Constraining the formation conditions of the ancient martian ALH 84001 carbonates

Thesis

CONSTRAINING THE FORMATION CONDITIONS OF THE ANCIENT MARTIAN ALH 84001 CARBONATES

Thesis submitted for the degree of

Doctor of Philosophy

by

Tim Tomkinson MSci

Department of Physical Sciences

THE OPEN UNIVERSITY

27th September 2012

DATE OF SUBMISSION : 10 SEPTEMBER 2012

DATE OF AWARD : 7 OCTOBER 2013

ABSTRACT

The martian meteorite ALH 84001 contains carbonates that provide information about the past aqueous conditions on Mars 3.9 Ga, and have been suggested to display signatures of martian organics. Determining the conditions under which the carbonates formed is crucial for addressing whether there was once life on Mars and the history of martian hydrosphere and atmosphere.

This study has combined new sample preparation techniques with fresh isotopic analyses of ALH 84001 carbonates and analogue materials, geochemical modelling and the testing of future equipment (WatSen) suitable for carbonate detection on Mars. The results from these investigations have provided quantitative constraints on the formation environment for the ALH 84001 carbonates and an instrument capable of detecting carbonates on Mars.

The microscale carbon and oxygen analyses of ALH 84001 carbonates provide the first combined transient study across the carbonates with $\delta^{13}C$ and $\delta^{18}O$ values correlated with chemical compositions. The $\delta^{13}C$ values range from -18.6‰ to +23.2‰ extending and lowering the previous ion microprobe $\delta^{13}C$ range found and suggests that reduced carbon is present in the carbonates. This component exists as either macromolecular carbon introduced through subsequent alteration, terrestrial contamination or martian organics. The $\delta^{18}O$ range -0.1‰ +27.1‰ is consistent with previous authors and displays a clear correlation with $\delta^{18}O$ enrichment with distance from the carbonates core to edge. An 18.6‰ range in $\delta^{18}O$ values was measured across analogue carbonates similar in size, shape and chemical variation which formed in a hydrothermal environment.

These sources of evidence combined with chemical and isotopic modelling are consistent with the ALH 84001 carbonates forming in a closed system with a single injection of a pH alkali (9.8), low temperature (<150°C) cooling Ca-, CO_2-rich hydrothermal fluid leaching the primary magmatic ALH 84001 composition. The 10 W/R ratios and timescales of formation (days to months) suggest that these carbonates were only subjected to a small transient quantity of water and for this reason are not favourable conditions for life.

ACKNOWLEDGEMENTS

I want to thank my supervisors, Professor Monica Grady, Dr Andrew Needham, Professor Ian Wright and Dr Axel Hagermann for their constant support and guidance throughout my thesis. I'm also incredibly grateful for the help from Dr Christelle Guillermier, Dr Ian Franchi and Dr Andrew Needham for help with training me and operating the NanoSIMS 50L for data used in Chapters 3 and 4. Furthermore, help by Dr Mabs Gilmour in training and collection of the 'true isotope' values on the gas bench in Chapter 3. Decent advice was also provided by Dr Jon Wade and Dr Henner Busemann in my first year which helped me plan my experimental campaign. Assistance and training on SEM and EPMA was provided and really appreciated by Dr Diane Turner and Dr Andy Tindle. Standard samples and analogue samples supplied for this thesis were kindly provided by Dr Mike Rumsey and Dr Andrew Steele, respectively. In addition, help preparing these samples for analyses was possible with the aid of Michelle Higgins and Kay Green.

For the financial support with which this thesis would not be possible I am indebted to the Science and Technology Facilities Council.

I am incredibly thankful for the support from my friends and work colleagues at the Open University.

Most importantly the love and support from my wife Rachel Tomkinson and parents David and Tora Tomkinson who have helped make this thesis an enjoyable experience.

PUBLICATION LIST

Some of the results from this thesis have been presented in conferences and a paper and are listed here along with the Chapters they refer.

Papers in Peer-reviewed Journals

Wolters S. D., Hagene J.K., Sund A.T., Bohman A., Guthery W., Sund B.T., Hagermann A., Tomkinson T., J. Romstedt., Morgan G.H., Grady M.M., 2013. WatSen: design and testing of a prototype mid-IR spectrometer and microscope package for Mars exploration. Experimental Astronomy (online) DOI 10.1007/s10686-012-9328-8. [Chapter 6].

Abstracts in international conference proceedings

Grady, M. M., M. M. Daswani, S. P. Schwenzer, T. Tomkinson, I. A. Franchi and I. P. Wright., 2012. Formation Environment of Noachian-Age Alteration Assemblages as Inferred from Secondary Minerals in ALH 84001. *Third Conference on Early Mars* 7086. [Chapter 2].

Tomkinson, T., C. Guillermier, A. W. Needham, I. A. Franchi, I. P. Wright, A. Hagermann and M. M. Grady., 2010. A Combined Carbon and Oxygen Isotopic Analysis of ALH 84001 Carbonates with NanoSIMS. *Meteoritical Society Abstracts* 5368. [Chapter 3].

Tomkinson, T., A. W. Needham, D. Johnson, C. Guillermier, I. A. Franchi and M. M. Grady., 2010. Determining the Carbon Isotopic Composition of ALH84001 rosettes with NanoSIMS. *Lunar and Planetary Science Conference Abstracts* 2717. [Chapter 3].

Tomkinson, T., S. D. Wolters, B. W. Guthery, B. Sund, A. T. Sund, A. F. Bohman, J. K. Hagene and M. M. Grady., 2010. Detection of Water and Magnesite with WatSen: The Next Generation of Instrumentation for Mars. *Lunar and Planetary Science Conference Abstracts* 2719. [Chapter 6].

Grady, M. M., T. Tomkinson, S. D Wolters, W.Guthery, A. F. Bohman and A. T. Sund., 2009. WATSEN — A Mid-IR Spectrometer, Humidity Sensor and Optical Microscope to Identify the Subsurface Water and Mineralogy of Mars. *The New Martian Chemistry Workshop* 8012. [Chapter 6].

Tomkinson, T., A. W. Needham, M. M. Grady, A. Hagermann and I. P. Wright., 2009. Understanding the Evolution of Martian Carbonates from a Combined Modelling and Synthesis Study. *The New Martian Chemistry Workshop* 8011. [Chapter 5].

Tomkinson, T., A. W. Needham, M. M. Grady, I. P. Wright, A. Hagermann, (2009). A Combined Synthesis and Modelling Approach to Investigate Formation of Carbonates on Mars. *Meteoritical Society Abstracts* 5333. [Chapter 5].

Tomkinson, T., S. D. Wolters, A. Hagermann, A. F. Bohman, A. T. Sund, J. K. Hagene, M. M. Grady., 2008. Insights into the Past Mineralogy & Fluvial Activity of Mars with WatSen. *Martian Phyllosilicates: Recorders of Aqueous Processes*. [Chapter 6].

Tomkinson, T., J. Wade, H. Busemann, I. A. Franchi, A. Hagermann, I. P. Wright, S. D. Wolters and M. M. Grady., 2008. Studying the Oxygen and Carbon Isotope Characteristics of Carbonate Analogues to ALH 84001. *Meteoritical Society Abstracts* 5286. [Chapter 4].

Tomkinson, T., S. D. Wolters , A. Hagermann, W. T. Fraser, A. F. Bohman, A. T. Sund, J. K. Hagene, M. M. Grady., 2008. WATSEN – A Minaturized Package to Detect Water on Mars. *Lunar and Planetary Science Conference Abstract* 2040. [Chapter 6].

Abstracts in UK conferences and workshops

Tomkinson, T., 2009. Using ALH 84001 Carbonates to Understand the Ancient Climate of Mars. *CEPSAR*, The Open University. [Chapters 1-7].

Tomkinson, T., H. Busemann, I. A. Franchi, I. P. Wright and M. M. Grady., 2008. Understanding Ancient Mars through Isotope Studies and Synthetic Formation of ALH 84001 Carbonate Rosettes. *UK Planetary Forum Early Career Meeting*, UCL, London. [Chapter 3].

Tomkinson, T., S. D. Wolters , M. M. Grady., 2008. WATSEN – An Instrument to gain Insights to the Subsurface of Early Mars. Network for Early Solar System Investigation (NESSI), RAS, London. [Chapter 6].

TABLE OF CONTENTS

List of Figures

CHAPTER 1

CHAPTER 2

CHAPTER 3

CHAPTER 4

CHAPTER 5

CHAPTER 6

CHAPTER 7

List of Tables

CHAPTER 1

CHAPTER 2

CHAPTER 3

CHAPTER 4

CHAPTER 5

CHAPTER 6

Chapter 1

1. CARBONATES FROM MARS

1.1 Introduction

Mars is a rocky planet, positioned fourth from the Sun in the Solar System and roughly half the size of Earth. Mars over the past six decades has been explored by numerous missions (flybys, orbiters, landers and rovers). Speculation over the presence of liquid water on Mars was rife until the first successful flyby of Mariner 4. While it was a disappointment not to find surface water deposits, the first pictures of the surface revealed valley networks as clear indication of past aqueous activity. Mars is now a dry planet but within the past decade there have been discoveries of water ice (Phoenix lander, 2008) and mineral phases associated with water (Spirit and Opportunity rovers, 2007; CRISM, 2009). These findings draw on numerous intriguing questions such as when and how did Mars lose its water? When did the climate change? And what was the past climate of Mars like?

1.1.1 Relevance

The research undertaken for this PhD seeks to infer environmental conditions on Mars through constraints imposed by the formation conditions of carbonates in the ancient martian meteorite ALH 84001. This subject is addressed through analyses of samples from the surface of Mars. Although no surface samples have been returned by missions to Mars, there are ~100 currently known meteorites (Meteoritical Bulletin Database) that have been ejected from Mars during impact and are available on Earth for study.

Martian meteorites provide insights into the lithosphere, atmosphere and hydrosphere of Mars and thus can help us to determine the environments in which they formed. Water is important in planetary-scale processes and has major implications for the evolution of a planet (including life) and its mineralogy. Primary igneous material is altered by water, forming secondary minerals. This occurs as the primary rocks are broken down through erosion by aqueous activity, wind and on Earth at least, by organisms. The rocks then dissolve in the surrounding waters only to reform as new minerals, such as anhydrite, gypsum and carbonates. Owing to the igneous origins of martian meteorites, formation of secondary alteration products on Mars is particularly intriguing since such components can cast light on their probable aqueous origins. Carbonates have been identified in some martian meteorites (Carr et al., 1985; Treiman, 1995; Jull et al., 1998; Bridges and Grady, 1999) and are an important part of martian meteorite studies. These minerals lead to potential insights into martian atmospheric and crustal interactions (Grady et al., 2007) and the possibility of associated organic molecules (Wright et al., 1989). It has been shown that under terrestrial conditions carbonates can be precipitated over a wide range of temperatures, affecting their final mineralogical and isotopic characteristics (Santos and Clayton., 1995; Socki et al., 2003; Niles et al., 2005; Sutter et al., 2007; Niles et al., 2010).

Production of carbonates on Earth is relatively well understood. This study aims to understand the production of carbonates in conditions found on ancient Mars, using the ALH 84001 meteorite as a case study. Allan Hills (ALH) 84 (1984 was the year of discovery) 001 (sample laboratory number) has the highest abundance of carbonates in any known martian meteorite (~1 vol. %; Romanek et al., 1994). There is also continuing debate regarding identification of possible biological signatures within the meteorite (McKay et al., 1996; Thomas-Keprta et al., 2010; Treiman and Essene, 2010). This Ph.D. thesis using a range of high precision instrumentation, newly established in house carbonate standards and unique

sample preparation techniques (Chapter 2) has characterised the fine-scale C and O isotope variations within secondary carbonate alteration in ALH 84001 (Chapter 3). A martian carbonate analogue from Svalbard, Norway, has also been studied to determine whether a hydrothermal environment can recreate the isotopic enrichments observed from the ALH 84001 carbonate investigation (Chapter 4). A variety of conditions are modelled to deduce the formation environment of carbonates on Mars (Chapter 5). Future surface exploration of Mars will be required to confirm the sites in which these carbonates formed. Hydrothermal settings are one of the main environments speculated in which these carbonates could have precipitated. In order to test this theory and with Mars' surface being covered in a layer of dust masking the geology it seems clear that an instrument capable of subsurface carbonate detection is required for future missions to Mars. Such an instrument exists and has been tested under martian conditions in this thesis. The detection limits of water and carbonate have also been assessed and its scientific merit will be discussed (Chapter 6). From this study it will be possible to infer the martian environmental conditions in which these ancient carbonates formed, and identify an instrument capable of sub-surface carbonate detection. These results will increase our current understanding and aid future *in situ* Mars investigations helping us to gain a more holistic knowledge of the red planet's evolution.

1.1.2 How we know the meteorites are from Mars

From the mid-1970s it was recognised that there was a group of igneous meteorites known as SNC, after their type specimens (Shergotty, Nakhla and Chassigny) with young crystallisation ages, suggesting an origin from a planetary body, rather than an asteroidal body. The Rb–Sr, Sm–Nd, Ar-Ar and Lu–Hf crystallisation ages suggest a formation ages of

~165-575 Ma, 1.3 Ga and 1.3 Ga for the S, N and C meteorites respectively (Nyquist et al., 2001, and references therein). These ages implied an origin from a body that was partially thermally active for as long as 4.4 Ga after the formation of the Solar System (4.57 Ga; Amelin et al., 2002). Smaller bodies such as asteroids would be unlikely to retain sufficient heat since the Solar System formed to produce the igneous meteorites. The candidates that remain are those with larger dimensions, i.e. Mercury, Venus, Earth's Moon, Earth and Mars; the probability of being removed from their surfaces by excavation following an impact is dependent on several parameters.

Taking these bodies in turn, the proximity of Mercury to the Sun means that the high escape velocity (67.7 kms^{-1}) required to overcome the Sun's gravitational pull is the dominating force, given that Mercury's planetary escape velocity is only 4.3 kms^{-1}. Venus has a higher planetary escape velocity (10.3 kms^{-1}) but the Sun has a lower gravitational pull on the planet (49.5 kms^{-1}). However, unlike Mercury, Venus has a dense atmosphere (~90 times that of Earth), a result of which is that aerodynamic stress would typically destroy an impactor before it reached the venusian surface. There is a finite chance that meteorites from Mercury and Venus have landed on Earth, and there are meteorites that lie on a separate oxygen isotope fractionation line from the SNC meteorites and which have been suggested as originating from Venus or Mercury but the evidence is not conclusive (Kuehner et al., 2006; 2007).

While impactors frequently bombard Earth and therefore it could be suggested that the SNC meteorites sample broken portions of the terrestrial surface, fusion crusts are observed on the outer portions of SNC meteorites proving re-entry into the Earths atmosphere from space. The SNC meteorites also fall on a distint line when plotting $^{18}O/^{16}O$ against $^{17}O/^{16}O$ which is clearly offset from all values acquired from terrestrial samples, therefore

these samples cannot originate from Earth. Returned Apollo samples and luna samples can be compared directly with the SNC meteorites. The lunar meteorites display obvious differences from the SNC meteorites. Two significant pieces of evidence that distinguish the lunar and SNC meteorites are their ages: (i) volcanism on the Moon ceased 1 Ga (Morota et al., 2011) and thus the moon is not a viable source for the shergottites, with the young ages of <575 Ma (Nyquist et al., 2001); (ii) the oxygen isotopic composition of lunar samples is practically indentical to that of Earth, and different from that of the SNC's, so they cannot come from the same parent body (Franchi et al., 1999). Hence on the basis of dynamic considerations, we are left with Mars as the most likely source of these meteorites.

Confirmation of a specific martian origin came from Elephant Moraine (EET) 79001, a meteorite found in Antarctica. The sample at the time of finding was unique in that it was the only meteorite to contain inclusions of black shattered glass throughout. This glass suggests shock melting as a result of an impact which probably initiated its journey to Earth. Trapped inside the glass is gas that has a composition (Bogard and Johnson, 1983) identical to atmospheric measurements from the Mars landers Viking 1 and 2 (Owen et al., 1977). This compositional match indicates that EET 79001 must be from Mars. In addition, the oxygen isotopic composition of EET 79001 lies on the same mass dependent fractionation line (Clayton and Mayeda 1983) as the oxygen isotopic composition of the other SNC meteorites. The inference is that these meteorites are related and, thus, martian (Clayton and Mayeda, 1996; Franchi et al., 1999; Spicuzza et al., 2007).

Deuterium and hydrogen isotopes have also been used to confirm the martian origin of the SNCs, although data are compromised by contamination of the samples by terrestrial water (Hallis et al., 2012). Deuterium isotopic composition can be diagnostic of martian

water signatures in the secondary minerals because preferential loss of atmospheric H to space through Jeans escape resulted in an enrichment of the D/H ratio (Owen et al., 1988). This has resulted in enriched δD within the martian alteration minerals (Watson et al., 1994; Leshin et al., 1996; Saxton et al., 2000; Boctor et al., 2003; Hallis et al., 2012; Usui et al., 2012) (Fig.1.1). Measurements on alteration minerals from Mars have been found to measure up to +1165‰ in phyllosilicate (Nakhla; Hallis et al., 2012) and +1196‰ in carbonate (ALH 84001; Greenwood et al., 2008) compared to the total δD terrestrial range of -400 to +50‰ (Hoefs, 2009).

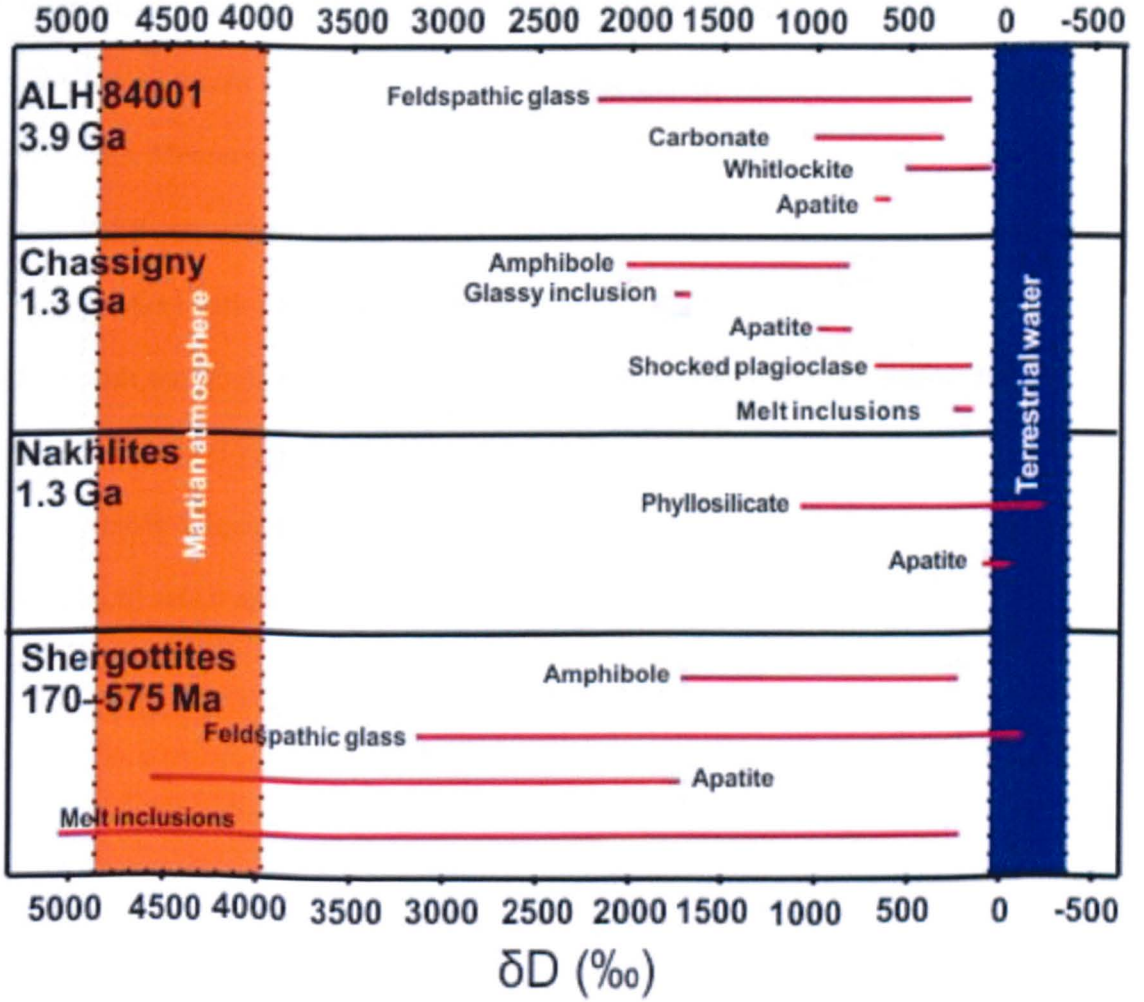

Figure 1.1 δD values from literature (Watson et., 1994; Leshin et al., 1996; Saxton et al., 2000; Boctor et al., 2003; Hallis et al., 2012; Usui et al., 2012) of martian meteorites.

Other sources of evidence include:

- Minerals found within the meteorites such as kaersutite, contain D/H ratios similar to the martian atmosphere (Watson et al., 1993).
- The basaltic shergottite meteorites and bounce rock (found on Mars by Opportunity rover, 2004) share very similar compositions (Zipfel et al., 2011).

Ironically, the young crystallisation ages of the Shergottites has been questioned. Pb-Pb isochrons of maskelynite and insoluble mineral fractions of shergottites suggest an older age of ~4 Ga (Bouvier et al., 2005). Since the general acceptance of a martian origin for the SNC meteorites, additional specimens have been recognised which extend the ranges of compositional variety and age. Material ejected from Mars' requires 5.0 km/s to overcome gravitational forces and 34.1 kms^{-1} to migrate out of the Solar System, however, unlike Venus and Mercury, inward migration is required to deliver martian samples to the Earth. ALH 84001, an orthpyroxenite is the oldest of the martian meteorites with a crystallisation age of 4.1 Ga (Lapen et al., 2010) and age of carbonates between 3.9 and 4.0 Ga (Borg et al., 1999) with the younger ages a result of resetting through aqueous interaction. The unusual breccia NWA 7034 has been dated with a crystallisation age of 2.1 Ga (Agree et al., 2013). NWA 7034's unique age and an order of magnitude more indigenous water (up to 6000 parts per million) sets it apart from other martian meteorites (Agree et al., 2013).

1.1.3 Why carbonates?

The motivation to search for carbonates on Mars is because these minerals are associated with water and carbon dioxide (Fig 1.2), both of which are believed to have existed in relative abundance on early Mars (Bridges et al., 2001, Bullock and Moore, 2007). Carbonates precipitate when carbon dioxide interacts with water forming carbonate anions (CO_3^{2-}) which bond with a range of cations such as calcium, iron and magnesium, typically present in the form of salts.

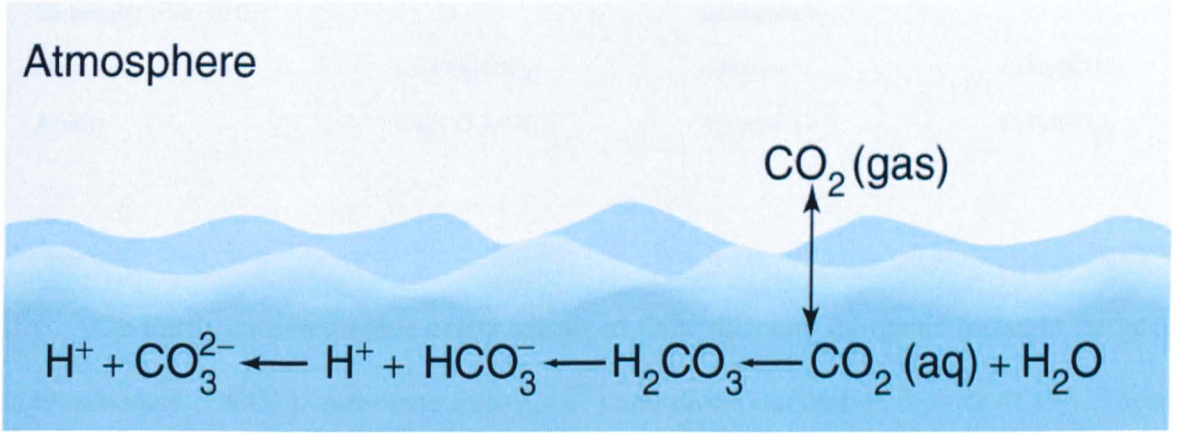

Figure 1.2 CO_2 dissolves in water to form carbonic acid which dissociates producing bicarbonate that again partly dissociates to form carbonates with a variety of cations. Collectively these reactants and products are known as Dissolved Inorganic Carbon (DIC – carbon dioxide (CO_2), carbonic acid (H_2CO_3), bicarbonate anions (HCO_3^-) and carbonate anions (CO_3^{2-}) (Table 1.1).

Table 1.1 Carbonates found on Earth. Note that, although calcite and aragonite are both $CaCO_3$, their different crystal structures lead to different physical and chemical properties affecting solubility.

Calcite group		**Aragonite group**	
(hexagonal)		(orthorhombic)	
Calcite	$CaCO_3$	Aragonite	$CaCO_3$
Magnesite	$MgCO_3$	Witherite	$BaCO_3$
Siderite	$FeCO_3$	Strontianite	$SrCO_3$
Rhodochrosite	$MnCO_3$	Cerussite	$PbCO_3$
Smithsonite	$ZnCO_3$		
(Monoclinic)		**Dolomite group**	
Carbonates with $(OH)^-$		(hexagonal)	
Malachite	$Cu_2CO_3(OH)_2$	Dolomite	$CaMg(CO_3)_2$
Azurite	$Cu_2(CO_3)_2(OH)_2$	Ankerite	$CaFe(CO_3)_2$

On Earth, carbon dioxide exists mainly in three different inorganic forms in the ocean: as bicarbonate (HCO_3^-), carbonate ions (CO_3^{2-}) and dissolved carbon dioxide (CO_2). There is also a fourth form, carbonic acid (H_2CO_3) but the concentration is so small (<0.3 %) compared to dissolved CO_2 it tends to be included in the CO_2 (aq) value.

$$[CO_2] = [CO_2(aq)] + [H_2CO_3] \qquad (1)$$

The stochiometric equilibrium constants mentioned above are dependent on temperature, salinity and pressure.

1.1.3 Stable isotope fractionation

In geochemistry, delta-(δ) values are used to express isotopic composition. For a compound A, whose isotopic composition is measured by mass spectrometry, its isotopic composition is derived as:

$$\delta_A = \left(\frac{R_A}{R_{st}} - 1\right) 10^3 (‰) \qquad (2)$$

Where R_A is the ratio of minor isotope to the major isotope (e.g. $^{13}C/^{12}C$ or $^{18}O/^{16}O$) and R_{st} is the same ratio in a standard (Hoefs, 2009). The values obtained are reported in parts per thousand (per mil, ‰). The international stable isotope standards normally used for carbon and oxygen isotopes are Peedee Belemnite (PDB) and Vienna Standard Mean Ocean Water (V-SMOW), respectively.

The enrichment of one isotope relative to another during a chemical or physical process is known as isotopic fractionation. This can either be dependent on the mass of the isotopes (mass-dependent fractionation) or not (mass-independent fractionation) depending on the specific process involved. Processes such as evaporation and condensation are mass dependent, and lead to changing vapour pressures of isotopic compounds and thereby lead to isotopic fractionations (Hoefs, 2009). In this scenario the lighter molecular species are preferentially enriched in the vapour phase yielding a more negative δ-value, with the extent of fractionation related to the temperature. This scenario can be explained as a Raleigh process (Fig. 1.3).

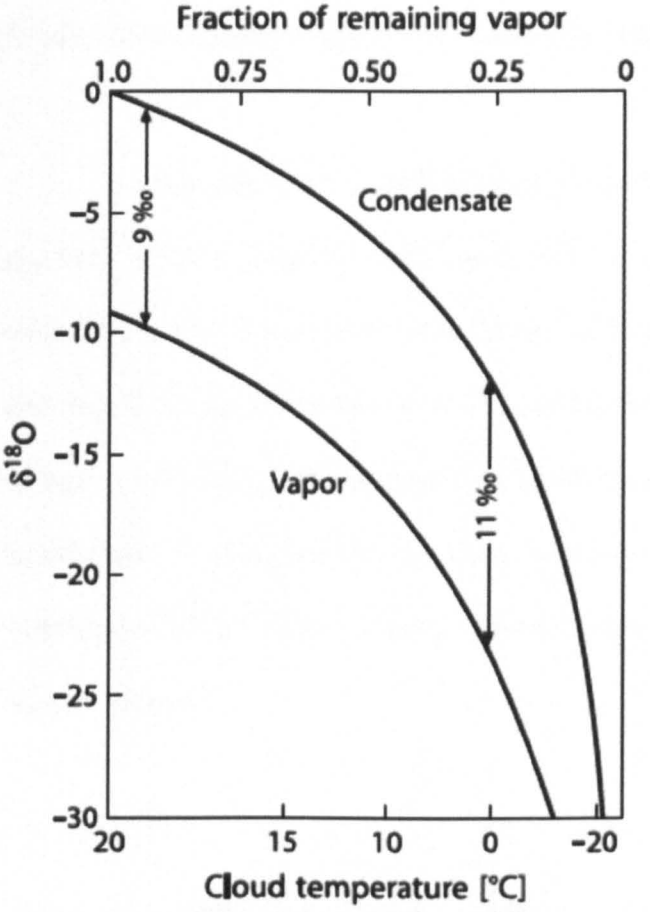

Figure 1.3 $\delta^{18}O$ for a cloud of vapour and condensate as a fraction of remaining vapour at a given temperature. The decrease in temperature is shown to increase the fractionation for this Rayleigh process (after Hoefs, 2009).

Equilibrium fractionation results in isotope redistribution of isotopes of an element among various species or compounds. So while the isotopic compositions of two or more compounds may not be identical, equilibrium between the ratios of the isotopes in each compound are constant for a given temperature. In equilibrium reactions, typically the heavier isotope accumulates in the compound with the higher oxidation state. In addition the denser the material involved is more likely to be enriched in the heavier isotope such as $\delta^{18}O$ values of $CO_2<HCO_3^-<CaCO_3$.

Kinetic fractionations are associated with unidirectional reactions, such as, biological reactions, diffusion and dissociation. These reactions are out of chemical and isotopic equilibrium and are dependent on the isotope mass ratios and their vibrational energies. Many

deviations from simple equilibrium processes are interpreted as different isotopic components having varied rates of reaction. The reaction products always show an enrichment in the lighter isotopes when measured across a unidirectional reaction.

In carbonates $\delta^{18}O$ and $\delta^{13}C$ can be used to infer the original isotope compositions of the fluid or CO_2 reservoir from which they formed. If precipitated in isotopic equilibrium with a fluid the $\delta^{18}O$ and $\delta^{13}C$ values in the carbonate depend on the temperature of formation and the dissolved carbon species (CO_2, H_2CO_3, HCO_3^-, and/or CO_3^{2-}) (Fig. 1.4). For example, isotope equilibrium exchange reactions for an inorganic system (atmospheric CO_2 – dissolved bicarbonate – solid carbonate) results in an enrichment of both ^{13}C (Fig. 1.4) and ^{18}O in carbonates. While kinetic isotope effects during photosynthesis concentrate ^{12}C into new organic material.

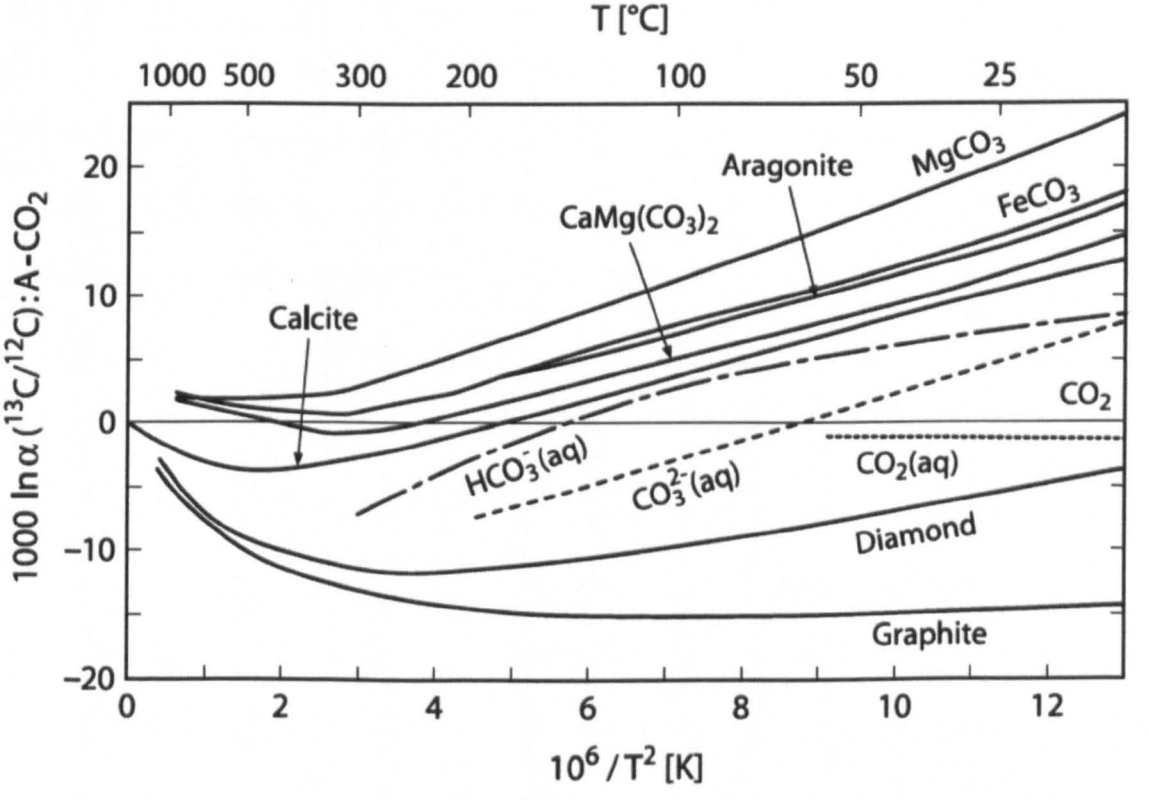

Figure 1.4 Carbon isotope fractionations of various materials and CO_2 (after Chacko et al. 2001).

In geochemistry there are two types of isotope system, open and closed. A chemically open system is where material is constantly removed or added and there is not necessarily isotopic equilibrium within the system. In this type of system the fractionation factor between materials remains constant.

In a closed system the isotopic difference between the material is controlled by the fractionation factor and the mass balance, isotopic equilibrium will always remain. Fractionation in an open system creates a much larger range in the reactants and products isotopic composition than in a closed system owing to the lack of back reactions in open systems.

1.2 Mars chronology

Previous studies referred to the history of Mars' surface as derived by Scott and Carr (1978) through crater counts. Data returned from an spectrometer known as Observatoire pour la Mineralogie, l'Eau, les Glaces et l'Activite (OMEGA) onboard Mars Express Orbiter (2003) led to a paper by Bibring et al. (2006) reclassifying the history of Mars in the context of mineralogy (Fig 1.5, discussed in detail, section 3.2).

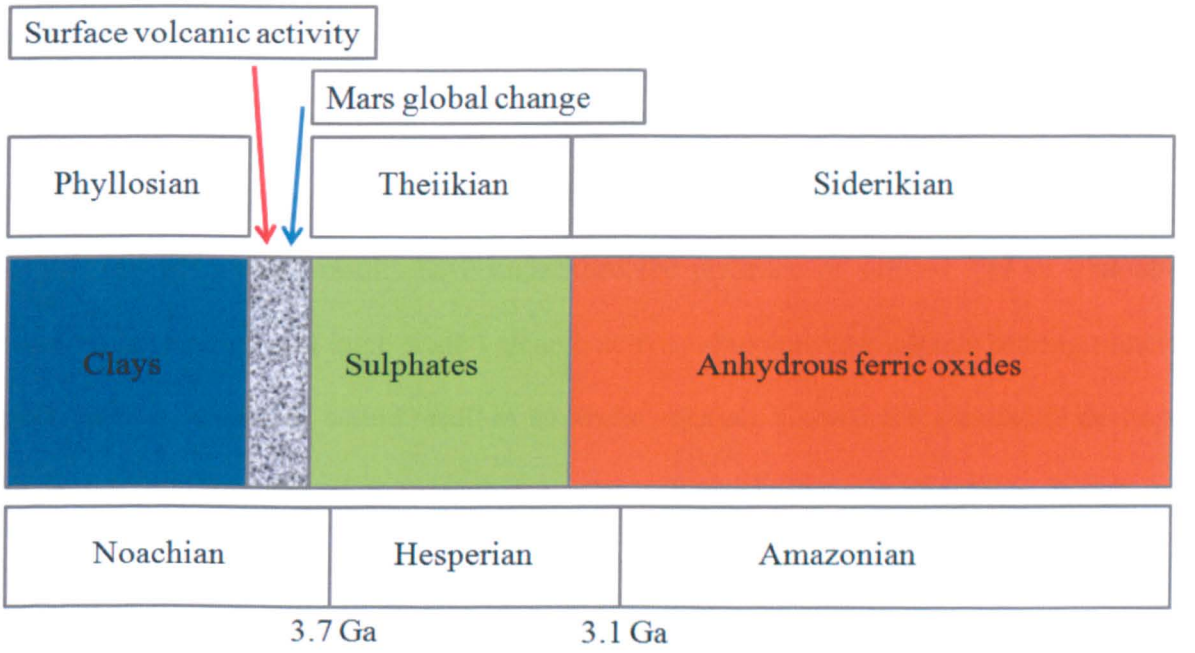

Figure 1.5 Displays the main mineralogies thought to have formed (blue, green and red) and the two derived chronologies (mineralogically based on top and based on crater count at the bottom) along with major events in the martian history. The figure is edited from Bibring et al. (2006) to include a timescale for the Noachian/Hesperian transition and the Hesperian/Amazonian (Hartmann and Neukum, 2001).

Three different alteration regimes have been defined from OMEGA results, namely 'Phyllosian', 'Theiikian' and 'Siderikian' characterised by clay minerals, sulphates and iron oxides respectively. These eras do not correspond directly with the crater count divisions

Noachian, Hesperian and Amazonian which were previously used to derive the chronology of the planet (Scott and Carr, 1978).

The eras suggested by Bibring et al. (2006) are characterised with surface alteration products and named after Greek words of the predominant minerals within each era. The first era, the 'Phyllosian' refers to a time of non-acidic aqueous alteration within the first ~0.6 Ga of the planet's formation.

The Phyllosian was followed by the 'Theiikian' era (sulphur), with the build-up of the Tharsis region caused by volatile outgassing from planet-wide volcanic activity also leading to climate change. In particular sulphur may have interacted with the atmospheric water vapour to produce acid rain resulting in acidic aqueous alteration.

The Mars rover results have underlined the presence of sulphur and its undoubted build up because of past large-scale volcanic activity. Sulphur and sulphur-bearing minerals are soluble in water and would result in an acidic solution. Carbonates are readily destroyed in acidic solutions and clay formation is also inhibited. Because the Mars Rovers and spectrometers CRISM and OMEGA have found sulphur in numerous regions of Mars, it might explain why carbonates are not detected on a planet-wide scale. Clays are mainly observed in the older terrain and OMEGA has detected sulphates on relatively younger plains. Clays and sulphates have yet to be detected in the same location.

During the late Noachian era (~3.7 Ga), vast amounts of volcanism associated with the Tharsis rise formation are believed to have occurred on Mars. A rise in SO_2 released into the martian atmosphere could be attributed to this volcanism. Through photochemical conversion of SO_2 to H_2SO_4 an acidic regime would have been introduced into the atmosphere and surface via precipitation and rainfall (Bullock and Moore, 2007).

$$CaCO_3\,(s) + H_2SO_4\,(aq) \rightleftharpoons CaSO_4\,(aq) + CO_2\,(g) + H_2O\,(l) \qquad (3)$$

This SO_2 enriched atmosphere could have inhibited the CO_2 precipitation of carbonates (equation 3) until the degassing of the planet slowed and sediments sequestered sufficient SO_2. Any remaining waters would become more alkaline allowing carbonate precipitation to form poorly consolidated patinas and fillings within rock fractures (Bullock and Moore, 2007). These carbonates would be vulnerable to weathering. This may have added to the atmospheric dust inventory as observed by the Thermal Emission Spectrometer (TES) onboard the Mars Global Surveyor (MGS; 1996: discussed in detail in section 1.5.1.1) and hence explain why large outcrops of carbonates are not observed on the present martian surface.

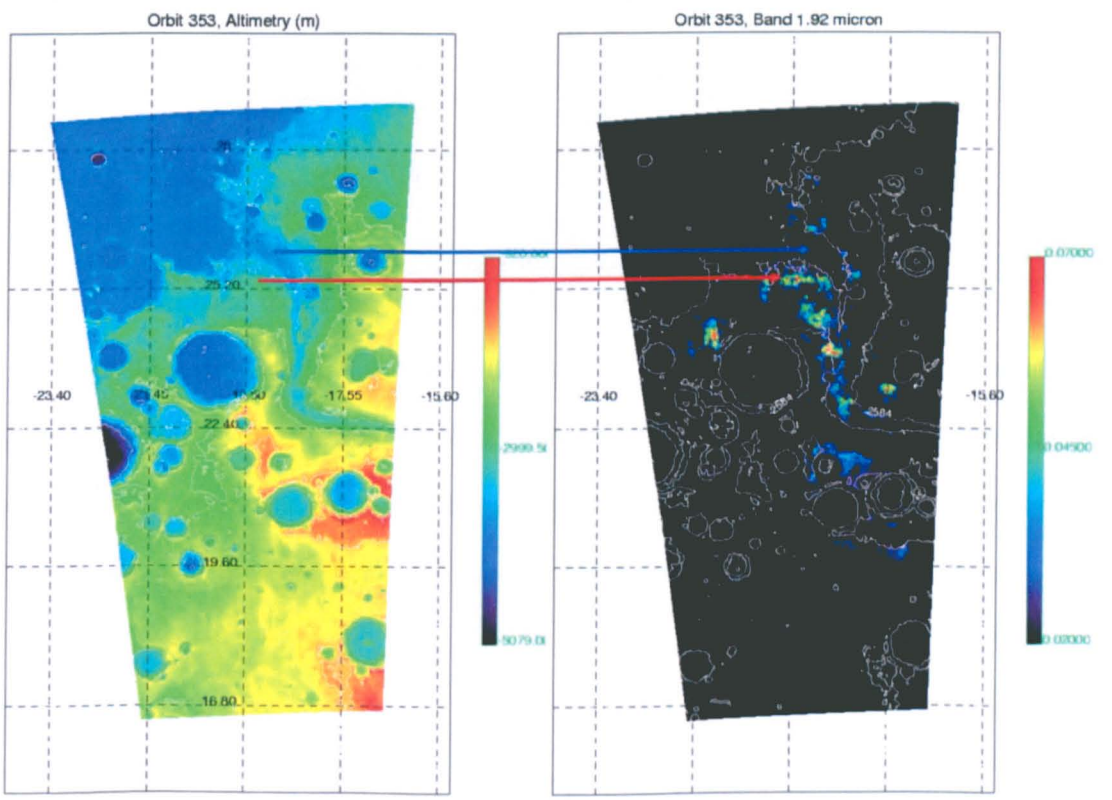

Figure 1.6 A view of the Marwth Vallis region of Mars, as seen by NASA Mars Global Surveyor's Mars Orbiter Laser Altimeter (MOLA) instrument. The OMEGA instrument on board ESA's Mars Express has mapped hydrated sites in this area, as shown in the right image (OMEGA data superimposed on the MOLA map). The hydrated minerals are not found in the channel (blue arrow), but in the eroded flanks and the cratered plateau (red arrow). This may be because dust has obscured horizontal surfaces but not vertical ones (Bibring et al., 2006).

As can be observed in Figure 1.6 hydrated minerals occur in localised areas. Four distinct assemblages have been detected on Mars: phyllosilicates, carbonates, sulphates and other hydrated minerals. The spectral resolution of OMEGA limits the ability to determine all the specific compositions of the hydrated sulphates, but two main identified forms are gypsum ($CaSO_4.2H_2O$) and kieserite ($MgSO_4.H_2O$) (Catling, 2007). The main locations of these hydrated sulphates are the dunes of Olympia Planitia (85°N 240°E; Langevin et al., 2005), the Northern polar cap (gypsum like compositions) and inside the Valles Marineris complex (10°S 73°5'W; Fig. 1.7).

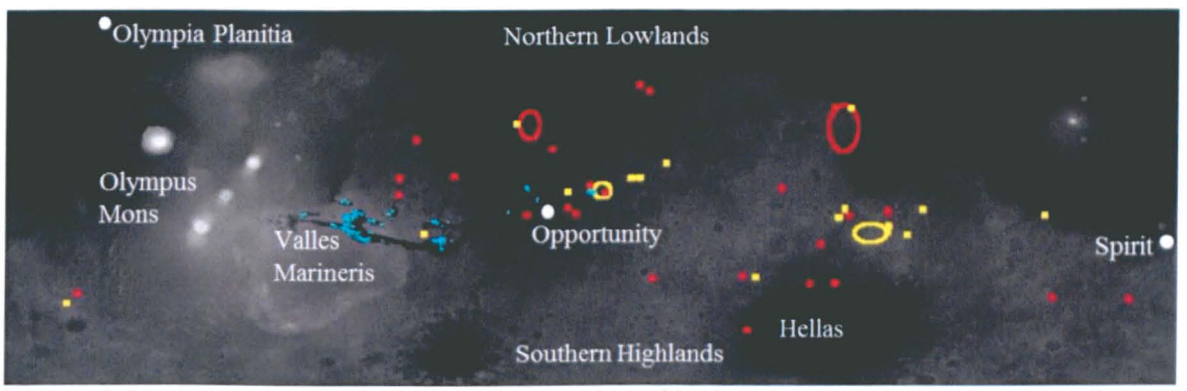

Figure 1.7 This image shows the global distribution of hydrated (water-rich) minerals as discovered by the OMEGA instrument on board Mars Express. The map is superimposed on an altitude reference map of Mars built with data from the Mars Orbiter Laser Altimeter (MOLA) instrument on board Mars Global Surveyor. The red marks indicate the presence of phyllosilicates, the blue ones indicate sulphates, and the yellow circles indicate other hydrated minerals (Bibring et al., 2006).

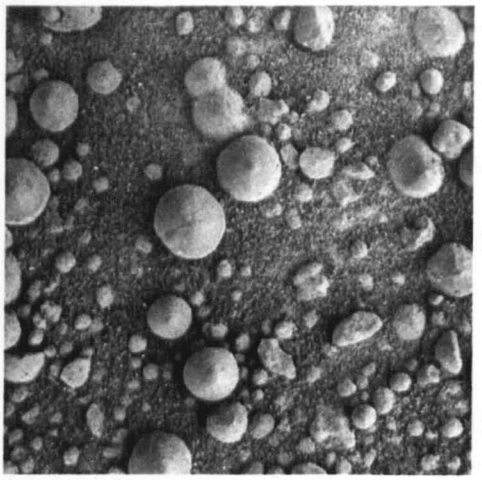

Figure 1.8 Hematite spherules imaged by Opportunity. Scale up to 5 mm in diameter .

In the Bibring et al. (2006) interpretation of Mars' chronology, the 'Siderikian' era is the final period where atmospheric aqueous-free alteration occurred, traced by ferric oxides that dominated the most recent history of Mars (~3.5 Ga to present). Following the acidic erosion of the ultramafic martian crust through sulphuric and carbonic acid weathering, the basalt could release Fe and Mg ions into any water present. The ferrous ions would then oxidize to ferric, Fe^{3+} ions (Fig. 1.8). This would make the water more acidic and when combined with sulphuric acid precipitate jarosite and Mg-sulphates. Such formations have been observed by MER "Opportunity" at Meridiani Planum (Fig. 1.6, 1.8). Dehydration of ferric sulphates could also produce the hematite spherules observed by Opportunity (Fig 1.7; Sefton-Nash and Catling, 2008).

1.3 The martian environment, past and present

The current atmosphere of Mars consists of 95% carbon dioxide, 3% nitrogen, 1.6% argon and traces of oxygen (0.13%) water (0.03%) and other traces of noble gases equating to a total of ~ 6.5 mbars.

The primordial climate of Mars has been of great interest since the Mariner 9 mission in the 1970s relayed images that were interpreted as fluvial channel systems (Schumm, 1974; Baker and Milton, 1974). The geomorphic evidence obtained since Mariner 9 has pointed towards a warmer, wetter era with a thicker atmosphere that created favourable conditions for the erosional features observed. Water derived valley networks extending up to thousands of kms across the martian surface are found concentrated in the southern highlands (Fig. 1.8). The majority of these networks are interpreted as Noachian in age (Fassett and Head, 2008). Martian outflow channels typically situated in the northern lowlands provide additional evidence that at least periodic liquid water existed. These channels are thought to have formed during the Hesperian by groundwater eruptions. Features such as alluvial fans (Fig. 1.9) are further indications of a past hydrological cycle on Mars (Moore and Howard, 2005). Mineral occurrences associated with these geomorphic features include layered phyllosilicate, sulphate and carbonate deposits (Ehlmann et al., 2011).

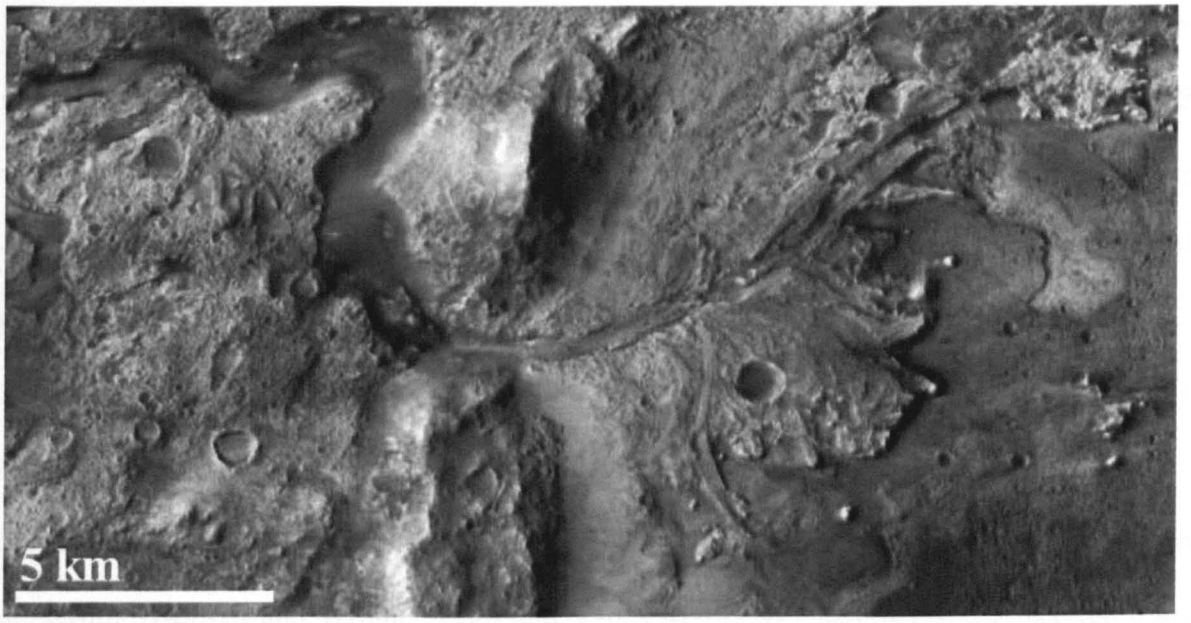

Figure 1.9 HiRISE image of valley leading into Jezero crater (Lat. 18.3°N Long: 77.5°E) with fan deposits known to contain phyllosilicates. Image from NASA website (CTX Image P02_001820_1984).

In the case of primordial Earth, water exposed to a rich CO_2 environment resulted in the precipitation of carbonates that produced sedimentary layers on the ocean floors. This same scenario may have been initially favourable on Mars during the Noachian (Phyllosian era). However, in order to achieve conditions favourable for carbonate precipitation from a fluvial environment an increase in temperature and pressure are required, enabling reservoirs of water to be stable on the martian surface. Currently, a 6.5 mbar atmospheric pressure exists on Mars but additional CO_2 reservoirs exist. CO_2 that is now locked as ice in the poles could have increased the atmospheric pressure by 40 mbars and another 40 mbars is thought to be sequestered in regolith (Fairén et al., 2004). Taking into account sputtering and impacts over the history of Mars, 95-99% of the CO_2 available in the Phyllosian atmosphere could have been removed. This implies possible CO_2 values of 800-4,000 mbars on a primordial Mars 4 Ga ago (Fairén et al., 2004).

An additional method for determining the primordial atmospheric conditions on Mars is to infer its relative CO_2 outgassing regime compared with those of Earth and Venus. If carbonates had not precipitated into Earth's early oceans the CO_2 partial pressure would be ~70 bar (Smith, 2000). Scaling this down using relative surface areas Mars' initial atmospheric pressure would be 51 bar.

Calculations on the quantity of sequestered CO_2 have been made referring to the 1 vol. % carbonate in ALH 84001 denoting a period before the end of the Noachian and within the new classified "Phyllosian" era. The current martian surface consists of 56% Noachian age terrain (Bridges and Wright, 2006) and Valles Marineris canyons displays layered units up to 7 km in depth. With the 1 vol. % carbonate value considered a potential 2,300 mbar pCO_2 could be sequestered within the martian crust. This calculation also accounts for a 95% loss to space through sputtering and impacts (Bridges and Wright, 2006).

The following text suggest methods of removal of this rich early CO_2 atmosphere -

Weathering - The rate and volume of the sequestering of CO_2 into carbonates is dependent on temperature and CO_2 partial pressure. The key issue is whether these factors can suppress CO_2 into the ground under realistic conditions on early Mars (Carr, 1999).

Sputtering - With the loss of Mars' magnetic field, the solar wind would have been effective in stripping the early atmosphere (Jakosky and Jones, 1997; Brain and Jakosky, 1998). While the exact date at which Mars' magnetic field ceased to effectively protect the atmosphere is not precisely known, it is thought to be before the end of the late heavy bombardment (LHB; 4.1-3.8 Ga; Cohen et al., 2000), as only ancient terrains retain magnetic anomalies (Carr, 1999).

Impact erosion – Is a process that will thin the early martian atmosphere through its removal by incident impactors (Melosh and Vickery, 1989). Early Mars had an active history

of impact bombardment which is recorded by the vast amount of visible impact sites over the martian surface

Carbonate recycling has been suggested for the retention of Mars' current CO_2 atmosphere (Carr, 1999). The process of volcanic burial (Pollack et al., 1987, Manning et al., 2006) and impacts (Carr, 1989) could replenish the diminished atmospheric CO_2. Volcanic burial of weathered rocks causes the buried layers to get progressively deeper with continuing volcanism. As the burial depth increases, so does the temperature and when temperatures are high enough CO_2 is released from the thermal decomposition of carbonates (Manning et al., 2006).

1.4 Water stability on Mars

The presence of water on Mars has been known to exist since the Mariner 9 spacecraft orbited the planet and observed river beds and canyons (Schumm, 1974; Baker and Milton, 1974). Furthermore, the occurrence of large volumes of subsurface water ice at depth was confirmed by Mars Express with its Mars Advanced Radar for Subsurface and Ionosphere Sounding (MARSIS) instrument (Plaut et al., 2007). Near surface deposits have also been observed by *in situ* studies by instruments onboard NASA's Phoenix lander that monitored subliming ice within the top few cm of the martian regolith (Smith et al., 2009; Rennó et al., 2009). Liquid water, however, has not been detected, even though there are abundant signs of its presence in Mars' history (Carr, 1995). The detection of water and whether it once existed on Mars is an intriguing topic as we commonly regard it as a key resource to support life. The discovery of water sources is also critical for the success of any future long term manned missions or colonisation of the planet.

Liquid water propagates the precipitation of carbonates from a CO_2 atmosphere until the triple point of water is reached at 6.11 mbars (Kahn, 1985) . This defines the lower limit for surface carbonate precipitation with water ice subliming at lower values omitting an intermediate liquid phase.

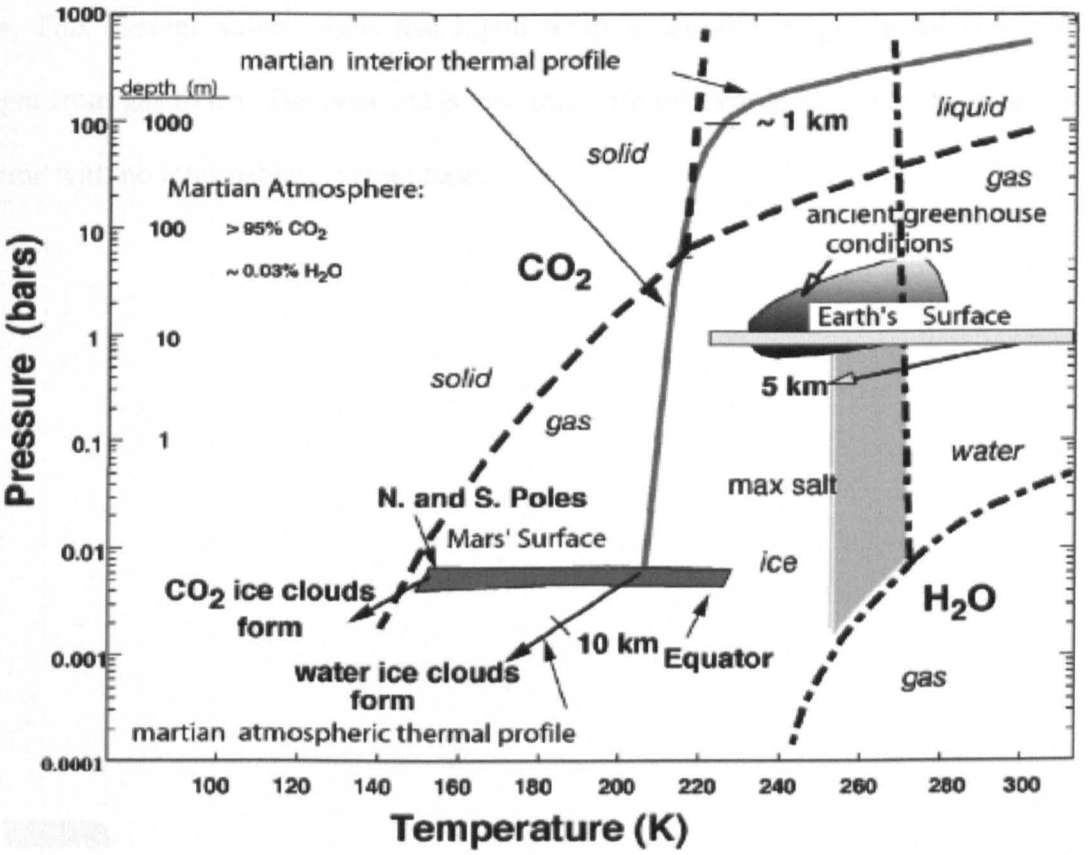

Figure 1.10 Pressure-temperature regimes of the martian atmosphere, surface, and regolith compared to phase relations of the pure H_2O (dash-dotted curves) and CO_2 (dashed curves) systems (Longhi, 2006).

It has been speculated that solid-solid and solid-gas reactions are not sufficient to precipitate carbonates at rates fast enough to produce significant deposits. The presence of water, even for short intermittent periods, is hence required to catalyse the reaction (Kahn, 1985). Currently liquid water is only stable where temperatures surpass 273 K and the partial pressure of water exceeds 6.1 mbar (Fig. 1.10). The water content of the martian atmosphere

was measured for a full Mars year by the Atmospheric Water Detector onboard the Viking orbiters. The results revealed that a total of 1 μm deep layer of water would precipitate on the CO_2 caps or 100 μm over the residual northern summer ice cap (Carr, 2006). The average partial pressure over the surface would be between $10^{-6} - 10^{-5}$ bars, this is 2-3 magnitudes lower than the minimum required partial pressure to sustain liquid water on the surface of Mars. This average value means that liquid water is unstable as precipitation would form straight from gas to ice. The opposite is also true with the heating of ice as it would instantly sublime with no intermediate water phase.

1.5 Carbonates on Mars

Spectral reflectance results have long been used to acquire information about the surface of Mars. The first studies utilized ground based telescopes (Sinton, 1959), with subsequent studies being conducted by ground-based (Pollack et al., 1990), space–based (Bell., 1997) and orbital instruments (Bibring et al., 2005; Poulet et al., 2005; Ehlmann et al., 2008). Some of the most important advances in martian studies have been aided by reflectance spectroscopy. These include the confirmation of martian meteorite findings with the identification of phyllosilicates, hydrated sulphates and carbonates (Gendrin et al., 2005; Langevin et al., 2005; Poulet et al., 2005; Ehlmann et al., 2008). However, the relatively limited detection of these aqueous alteration products on Mars has led to questions as to whether they are stable on the martian surface. Possibilities as to why they have not been detected in abundance are considered at the end of this section.

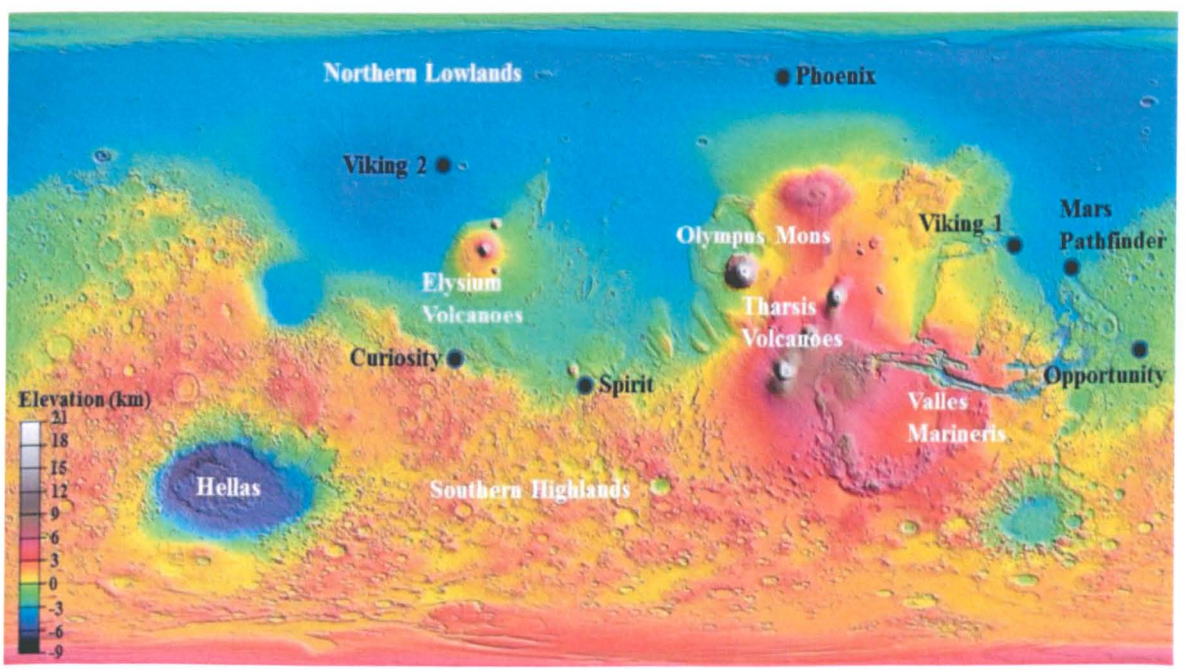

Figure 1.11 Global topographic map of Mars displaying locations of previous/current missions and landmarks on Mars.

1.5.1 Carbonate detection on Mars from space flight instrumentation

Over the past few decades, Mars has been investigated directly by means of numerous surface (Fig. 1.11) and orbital instruments. Despite various indications of 'presence of water' on the surface with the exception of Phoenix heating material to produce water droplets (Rennó et al., 2009) no direct detection of liquid water has been made. Indications of water's presence have been inferred through satellite images from orbit. These images show many features such as valleys and channels that indicate outflows of liquid at various times in Mars' history (Carr, 1995). The 1976 Viking missions sparked discussion that various salt forming materials such as carbonates (Gooding, 1978) and nitrates (Yung, 1989) should exist on the martian surface. The occurrence of these minerals on Earth is typically dependent on the presence of water. Surface measurements from Mössbauer spectrometers on the Spirit and Opportunity rovers have also indicated the presence of water with associated minerals e.g. hematite, jarosite (Morris et al., 2006) and recently carbonates (Morris et al., 2010).

Earth-based observations placed the upper limits of 1-3 vol. % for carbonates and 10-15 vol. % for sulphates and other hydrates present on the martian surface (Pollack et al., 1990).

The following section of instrumentation sent to Mars is organised according to the date of carbonate discovery.

1.5.1.1 Thermal Emission Spectrometer (TES) onboard the Mars Global Surveyor (MGS) (1996)

Initial results from TES placed the upper limits on carbonate concentration <10 wt. % to best fit the dust spectrum (Christensen et al., 1998). This upper limit has since been reduced, subsequent studies of martian dust observed by TES and compared with laboratory experiments displayed smaller concentrations (~2 – 5 wt. %) of carbonates (dominantly magnesite) with no obvious source and a planet wide distribution (Bandfield et al., 2003).

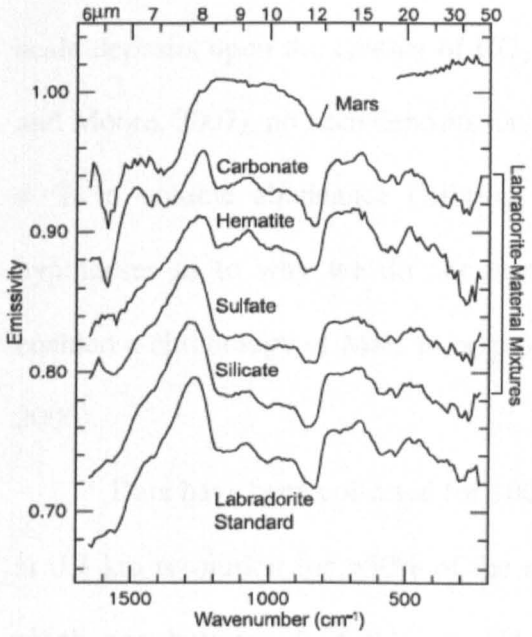

Figure 1.12 Various spectra of doped labradorite from Bandfield et al. (2003).

Work by Bandfield et al. (2003) showed how carbonate mixed with labradorite ($CaAl_2Si_2O_8$) was the best fit for reproducing the martian dust spectrum (Fig. 1.12). The observed emission peak at 1630 cm^{-1} can be accounted for by water but the high emissivities from 1350 to 1580 cm^{-1} cannot. Various carbonates such as calcite, dolomite, siderite and magnesite along with other non-carbonates including hematite, gypsum and silica glass were mixed with labradorite. The optimum spectral features were reproduced with ≥2 to 3 wt. % magnesite and grains 0 to 10 μm in diameter. The spectrum from Hebes Chasma has been used to estimate the upper limit abundances (5 wt. %).

1.5.1.2 Observatoire pour la Mineralogie, l'Eau, les Glaces et l'Activite (OMEGA) onboard Mars Express Orbiter (2003)

Despite the theoretical indication that carbonate minerals would have formed large-scale deposits upon the contact of CO_2 with liquid water (Kahn, 1985; Carr, 1999; Bullock and Moore, 2007), no such deposits have been observed within OMEGA's sensitivity limit of 4 % in volume abundance (Bibring et al., 2006). Results from OMEGA have led to hypotheses as to why we do not observe abundant quantities of carbonates. It has also enabled a chronology of Mars to be proposed based on mineralogy (Fig. 1.5) (Bibring et al., 2006).

Data have been collected for 100% of the surface at 1.5 to 5 km spatial resolution and at 0.3 km resolution for >50% of the surface (March, 2012). The spectrum range for each pixel was between 0.35-5.1 μm. The lack of observed carbonates could be because formations are smaller than OMEGA's spatial resolution (<300 m).

1.5.1.3 Compact Reconnaissance Imaging Spectrometer for Mars (CRISM) onboard Mars Reconnaissance Orbiter (2005)

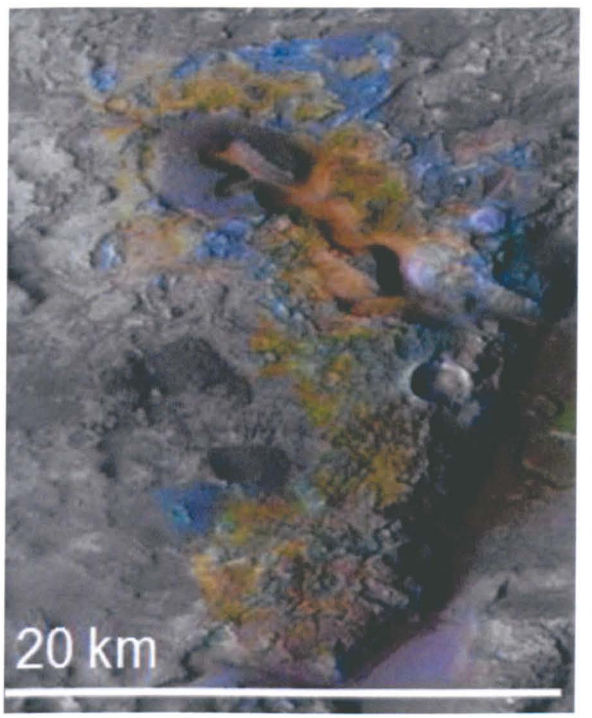

Figure 1.13 Displays carbonates associated with olivine (green), olivine-bearing rocks (yellow) and rocks bearing iron-magnesium smectite clay (blue). Image from NASA website.

CRISM is performing hyperspectral near-IR mapping with over 10 times higher spatial resolution than OMEGA (<300 m). It has the capability of targeting areas down to 15 metres per pixel in 554 colours of reflected sunlight. Coverage of the martian surface (March, 2012) at this spatial resolution is 3%, while 77% of the planet has been mapped at ~200 m per pixel. It is the planet's most detailed mineralogical study from orbit to date (2012). Carbonates in the form of magnesite + hydromagnesite have been discovered in the Nili Fossae region (Latitude 22°80' north of Mars' equator; Longitude: 76°8' east). The carbonates were associated with phyllosilicates and olivine bearing rock units that thought to have formed in the Noachian era (Fig. 1.13). The conditions in which they formed is still debated. Nevertheless, the evidence indicates a neutral to alkaline environment resulting from the alteration of olivine by surface interaction with water of hydrothermal fluids (Fig. 1.13) (Ehlmann et al., 2008).

1.5.1.4 Thermal and Evolved Gas Analyzer (TEGA) and Wet Chemistry Lab (WCL) onboard Phoenix lander (2008)

The WCL has been used to determine that the soil adjacent to Phoenix is alkaline with an average pH of 7.6±0.5 and to identify calcium carbonate. In addition, TEGA detected calcium carbonate and suggested there might be Mg and Fe carbonates present within the sample (CO_2 release between 400°C and 680°C). Despite these data the only clear endothermic transition was observed for $CaCO_3$ decomposition (725°C) (Boynton et al., 2009). A 3-5 wt. % of calcite was observed from the sample based on the results of WCL and TEGA. Measurements of the stable isotopes within the atmospheric CO_2 provided values of $\delta^{13}C_{VPDB}$ = 2.5±4.3 ‰ and $\delta^{18}O_{VSMOW}$ = 31.0±5.7 ‰ at the Phoenix landing site (Niles et al., 2010).

1.5.1.5 Mössbauer (MB), Mini-TES and the Alpha Particle X-Ray Spectrometer (APXS) onboard Spirit (2004)

An olivine-rich outcrop containing Mg-Fe-rich carbonate (16-34 wt. %) has been identified in the Columbia Hills of Gusev Crater (situated 15° degrees latitude south of Mars' equator at longitude 184°7' degrees west). The carbonates have molar quantities of $(Mg_{0.62}Fe_{0.25}Ca_{0.11}Mn_{0.02})CO_3$, assuming all the Mn and Ca is associated with the carbonates (Morris et al., 2010). The carbonates have formed in ultramafic rocks associated with Noachian alkaline-neutral volcanic activity (Morris et al., 2010). The associated volcanic activity suggests that these are hydrothermal deposits that have since been exposed through aeolian abrasion and chemical deposition from subsequent acidic volcanic fluids and vapours. The suggestions that these materials formed in the same era, with similar mineralogy to ALH

84001 further strengthens the case that ALH 84001 carbonates formed in a hydrothermal environment. In addition, the location of this carbonate outcrop is ~6300 km from those discovered by CRISM at Nili-Fossae (Lat. 22°80'N; Long. 76°8'E) suggesting that Mars may have had planet wide surface coverage carbonates in a warmer and wetter past climate.

1.5.2 What happened to all the carbonates?

Results from missions to Mars indicate the following reasons as to why carbonates are not as abundant on the current martian surface as might be expected on a planet with a history of surface water and a CO_2-rich atmosphere:

- Liquid water was not stable on the martian surface for prolonged periods of time, thus CO_2 from the primordial dense atmosphere had insufficient time to precipitate large quantities of carbonates.

- Carbonates may have been formed by impact or subsurface hydrothermal processes rather than by slow surface alteration within liquid water (Baker et al., 2000). This could explain the lack of surface deposits and why we observe carbonates within martian meteorites.

- Carbonates formed but then may have been removed by decomposition or acidic weathering.

- Mars never sustained a sufficiently rich CO_2 environment to accommodate carbonate precipitation. The only currently observed CO_2 reservoirs are within the atmosphere and a thin veneer of CO_2 ice over the southern pole.

- Theiikian volcanism initially favoured SO_2-rich conditions to precipitate Mg and Ca sulphates as opposed to carbonates (Chevrier et al., 2007; Bullock and Moore, 2007). The interaction of water with basaltic minerals could explain deposits of what was observed at Meridiani. Following the cessation of volcanic activity and thus a decrease in acidic gas production, more pH-neutral waters could have formed after the consolidation of sulphate layers. The remaining CO_2 atmosphere might then have been sequestered into small, poorly consolidated carbonate deposits. The current cold, low pressure martian conditions would cause water to freeze or sublime, leaving unconsolidated carbonates rather than aqueous layered sediments. Weathering could then have removed surface deposits into the atmosphere, reducing surface concentrations and increasing atmospheric traces.

1.5.3 Are carbonate formations possible in current martian conditions?

Thermodynamically, carbonates are stable on Mars in its current environment. This has been directly confirmed by instrumentation on the CRISM orbiter, Pheonix lander and Spirit rover (Ehlmann et al., 2008; Boynton et al., 2009; Morris et al., 2010). Owing to the alkaline nature of basalt a pH of 7.7 has been observed on the martian surface (Morris et al., 2010). The current martian conditions are not only stable for carbonates but favourable for

precipitation if the partial pressure of CO_2 interacted with a mixture of water, basalt and Mg. and Ca- rich salts.

It was suggested by Longhi (2006) that groundwater at the martian poles was saturated in CO_2 and therefore acidic, but results from Phoenix showed this not to be the case (Boynton et al., 2009). Regolith situated further from the ice mass of the poles could have come into contact with evaporating groundwater, causing dissolved ions to precipitate as salts and carbonates (Longhi, 2006). Over time, obliquity variations would alter the thermal balance at the poles. Low obliquity on Mars would cause a thinner atmosphere and poleward migration of the ice mass, and high obliquity a corresponding movement towards the equator. An extensive band of carbonates could thus have formed between latitudes at this boundary (Kieffer and Zent, 1992).

1.6 Martian meteorites

At the time of writing 100 separate meteorite samples are thought to have originated from Mars based on age, geochemistry and noble gas links with their parent body; see NASA's Mars Meteorite Compendium (Meyer, 2012) for reviews. Martian meteorites are classified into four groups on the basis of mineralogy: the single orthopyroxenite, ALH 84001; two chassignites (dunites); thirteen nakhlites (clinopyroxenites), and seventy-nine shergottites. This last group is divided into subgroups: basaltic, olivine-phyric, olivine-orthopyroxene-phyric and lherzolitic.

The martian meteorites comprise a range of igneous rocks hosting a variety of secondary minerals formed by aqueous processes. The secondary minerals are often observed within cracks in the olivine collectively described as "iddingsite" (Reid and Bunch, 1975; Ashworth and Hutchison, 1975). This term describes the secondary materials, typically containing a mix of smectite and illite clays, ferrihydrides and iron oxide. In addition to iddingsite secondary minerals such as salts are also found; precipitates include chlorides, sulphates and Ca-Mg-Fe-Mn carbonates with some zoned (both chemically and isotopically in ALH 84001) (Grady et al., 1988; Golden et al., 2001).

The following sections give a short overview of the martian meteorites including relevant carbonate information.

1.6.1 Shergottites (175 - 575 Ma)

The type specimen of the shergottites is Shergotty, which fell in Sherghati, India, in 1865. Since this discovery, samples have been collected from locations such as Antarctica and the Sahara desert resulting in the formation of the sub groups lherzolitic, basaltic (McSween and Treiman, 1998), olivine-orthopyroxene-phyric (Irving et al., 2004) and olivine-phyric shergottites (Goodrich, 2002).

On July 28th, 2011 a shergottite named Tissint was observed falling near Tata, Morocco. This sample is significant as most meteorites are obtained as finds, where their exposure to terrestrial contamination is unconstrained. This fall however, despite its rapid collection, is still observed to be contaminated by soil on the outer surface and tiny grains of carbonate in the interior of the sample (Aoudjehane et al., 2012.). While the carbonates in this study have been confirmed as martian in origin through petrographic relationships, a sample directly collected from Mars is required if any discoveries regarding martian organics are to be believed.

The presence of carbonate minerals in martian meteorites was first confirmed within the shergottite EETA 79001 by Carr et al., (1985). A subsequent study found that EETA 79001 displays calcite within druse cavities in the glassy region of the shergottite (Gooding et al., 1988).

1.6.2 Nakhlites (~1.3 Ga)

The first nakhlite was observed to fall at El-Nakhla, Alexandria, Egypt in 1911 and the most recent was found in the Saharan desert in 2009. There are currently thirteen known nakhlite samples.

Nakhlites are typically fine grained clinopyroxenites with green cumulate augite crystals, minor olivine content and small amounts of fine-grained mesostasis. This mesostasis can consist of maskelynite, oxides, sulphides, phosphate and pre-terrestrial weathering alteration products including carbonates and salts (Bridges and Grady., 1999; Treiman., 2005).

^{40}K-^{40}Ar and ^{40}Ar-^{39}Ar dating on seven of the known nakhlites indicate ages <1.3 Ga (Swindle et al., 2000 and 2004). Chronometric studies using ^{238}U-^{206}Pb, ^{147}Sm-^{143}Nd and ^{87}Rb-^{87}Sr isotopic ratios also provide near identical crystallisation ages (Shih et al., 1999; Misawa et al., 2005; Terada and Sano, 2004). As expected, the crystallisation age predates the 11 Ma martian ejection age that is calculated from cosmic ray exposure dating combined with terrestrial residence time (Eugster et al., 2002).

Nakhla is an olivine-bearing clinopyroxenite, probably formed within an basic-ultrabasic lava flow >100m thick or shallow intrusion by melt differentiation (Reid and Bunch., 1975; Bridges and Grady, 1999; Treiman., 2005; Bridges and Warren, 2006). Petrographic studies have shown carbonate, phyllosilicate and sulphate deposits along cracks, presumed to form during low-temperature, hydrous alteration (Treiman, 1993). Nakhla was an observed fall, part of it instantly collected and a second portion recovered two years later

(1913). The composition of the alteration minerals within Nakhla are similar to other nakhlites and are thus interpreted to result from weathering on Mars. This interpretation is supported by isotopic studies of the carbonates (Carr et al, 1985). Recent studies of the nahklites' by Mikouchi et al. (2006, 2012); Grady et al. (2007) and Changela and Bridges (2011) have all suggested a formation order based on petrography and mineralogy, $\delta^{13}C$ carbonate values and alteration materials, respectively. These models suggest how the nakhlites are linked within a single cumulate pile.

Trace amounts of Fe-Ca-Mn carbonate have been found within Lafayette (Vicenzi et al., 1997). Two carbonate settings were observed within a veinlet. The first was a distinct and continuous phase of carbonate with a composition range of $(Mg_{0-0.02}Fe_{0.27-0.67}Ca_{0.22-0.37}Mn_{0.04-0.35})CO_3$ (Bridges and Grady, 2000) and the second a mix with Fe-rich silicates (Vicenzi et al., 1997).

Governador Valaderes contains Fe-rich carbonate ($Mg_{0.09-0.29}Fe_{0.64-0.78}Ca_{0.04-0.11}Mn_{0.01-0.02}$) within fractures of olivine (Bridges and Grady, 2000).

NWA 998 contains calcite and ankeritic carbonate, both found along grain boundaries within cracks (Irving et al., 2002). The ankeritic carbonate is compositionally similar to that found in ALH 84001.

The nakhlites all appear to be weathered to varying extents. Changela and Bridges (2011) suggested a model that is consistent with a salt crystallisation sequence from which the secondary minerals are precipitants of impact generated hydrothermal heating. Some clay minerals within the nakhlites have been truncated by a fusion crust which acts as further evidence of a non-terrestrial origin (Gooding et al., 1991).

The remaining nine identified nakhlites all display alteration materials (typically clay, and Fe-oxides) but do not have any associated carbonates.

1.6.3 Chassignites (1.3 Ga)

The Chassigny meteorite was observed falling at Chassigny, Haute-Marne, France in 1815 and is the first of (currently, 2012) only two chassignites. The second was found in North-West Africa (August, 2000) and named NWA 2737 but also known as Diderot after the French encyclopaedist who was born just outside Chassigny. Common mineralogy linked the two samples and their oxygen isotopes confirmed a link to other martian meteorites (Beck et al., 2005). Chassignites are olivine cumulates (dunite) and their mineralogy implies a deeper origin than nakhlites. Aqueous alteration minerals are almost absent from Chassigny: Small quantities of calcite and Mg-rich carbonates have been observed in Chassigny, residing in veins within silicates. Whether this is because of terrestrial contamination still needs to be resolved (Wentworth and Gooding, 1994).

1.6.4 ALH 84001 (4.1 Ga)

ALH 84001 was originally classified as a diogenite (Score and MacPherson., 1985), but following its identification in 1994 as martian (Mittlefehldt, 1994), ALH 84001 was recognised as an important sample of the martian crust. In 1996, a paper by McKay et al. suggested evidence for life on Mars resided within the meteorite (Fig. 1.14). This paper subsequently made ALH 84001 one of the most studied rocks to date.

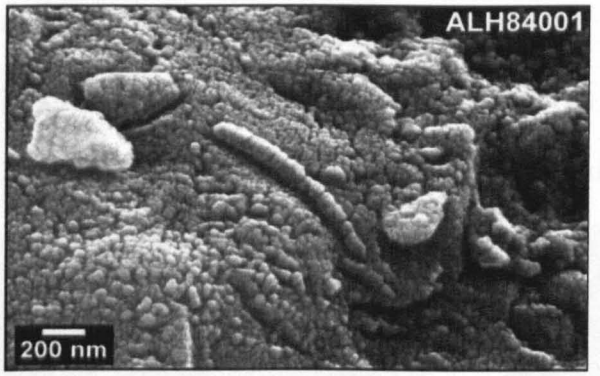

Figure 1.14 Martian meteorite ALH 84001 was reported as containing fossilized martian bacteria (McKay et al., 1996).

ALH 84001 is an orthopyroxenite, comprising ~ 97 vol. % Mg-rich orthopyroxene ($En_{69.4}Fs_{27.3}Wo_{3.3}$; Mittlefehldt, 1994). The general consensus is that ALH 84001 was formed in a slowly cooling magma chamber (Treiman, 1998; Corrigan and Harvey, 2004). Following crystallisation, multiple impacts gave ALH 84001 its highly fractured state (Treiman, 1995; 1998; Corrigan and Harvey, 2004). Treiman et al. (1998) inferred either four or five impact events to explain the deformation structures observed in ALH 84001. The impact-generated fracturing produced spaces in which secondary non-igneous alteration could occur through infiltration of fluid. The extensive fracturing is consistent with the ancient age of crystallisation, as the material was formed during the Solar System's LHB period (4.1-3.8 Ga; Cohen et al., 2000).

ALH 84001 contains ~1 vol. % carbonates (Romanek et al., 1994). These are heterogeneously distributed within the meteorite (Treiman, 1995). Half of the carbonates observed within ALH 84001 have been identified as circular shaped formations commonly

acquiring the name of "rosettes" (Fig. 1.15). The orange cores are Ca-Mg-Fe-rich ankerite and are typically surrounded by alternating layers of magnesite–siderite-magnesite (MSM). The siderite within the alternating layers is of particular interest to astrobiologists as it displays (single domain) magnetite that has been interpreted as biologically produced on Mars (McKay et al., 1996).

The origin of carbonates in ALH 84001 is still debated; potential formation hypotheses include evaporation (McSween and Harvey, 1998; Warren, 1998), high temperature reactions (Harvey and McSween, 1996), impact-induced melt (Scott et al., 1998) and low temperature precipitation (Golden et al., 2000). These theories all suggest different initial formation conditions and suggest both single and multi-stage events.

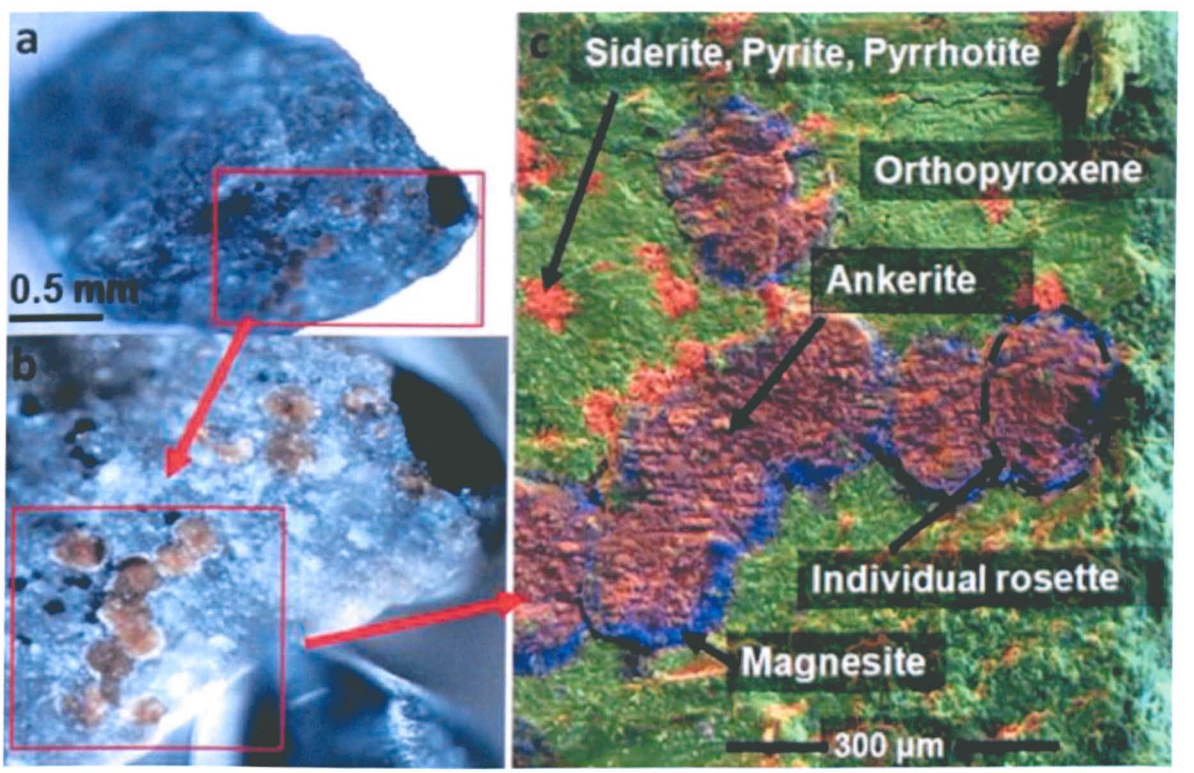

Figure 1.15 a-c Optical microscope and SEM images of the chip of ALH 84001 used for this thesis. The material rich in carbonates was broken from the larger piece of ALH 84001 (Fig. 1.15 a and b) and mounted without polishing, on an SEM stub for acquisition of the false coloured secondary electron image (Fig. 1.15 c). In Figure 1.15 a and b, the orange material is the ankerite carbonate, the

white rim surrounding the orange is magnesite. The small black areas are the siderite, pyrite and pyrrhotite. Figure 1.15 c is a false coloured secondary electron image of the unpolished surface with green (Si), red (Fe) and blue (Mg).

Variations in carbonate mineral chemistry, habit and texture suggest that ALH 84001 may contain several generations of carbonate (Treiman, 1998; Corrigan and Harvey, 2004). Complex carbonate regions in ALH 84001 include, as well as rosettes, planiform "slab" carbonates and "post-slab" magnesites with orthopyroxene, feldspathic and silica glass all in contact with each other (Fig. 1.16) (Corrigan and Harvey, 2004).

Corrigan and Harvey (2004) deduced that calcite-rich rosettes and slab carbonates were the first to form during a period of multiple impacts, followed by Magnesite-Siderite-Magnesite (MSM) layering. Post-slab magnesite is similar in major element composition but representative of a later carbonate generation which is associated with the silica glass deposition. After this final stage of carbonate formation, the feldspathic glass was introduced into the meteorite. In spite of this the carbonates show little or no alteration from thermal effects that must have occurred during the glass emplacement. The discontinuous interactions that must have occurred to produce the variety of carbonate formations would suggest an impact scenario. ALH 84001 with its 4.1 Ga (Lapen et al., 2010) history seems a likely candidate to have undergone remobilisation of fluids and fracturing resulting from impacts, explaining why a lack of silica enrichment is observed (Bridges et al., 2001). Thus ALH 84001 carbonates may not have required a long term martian hydrosphere to form as the liquid water may have been remobilised through multiple impacts.

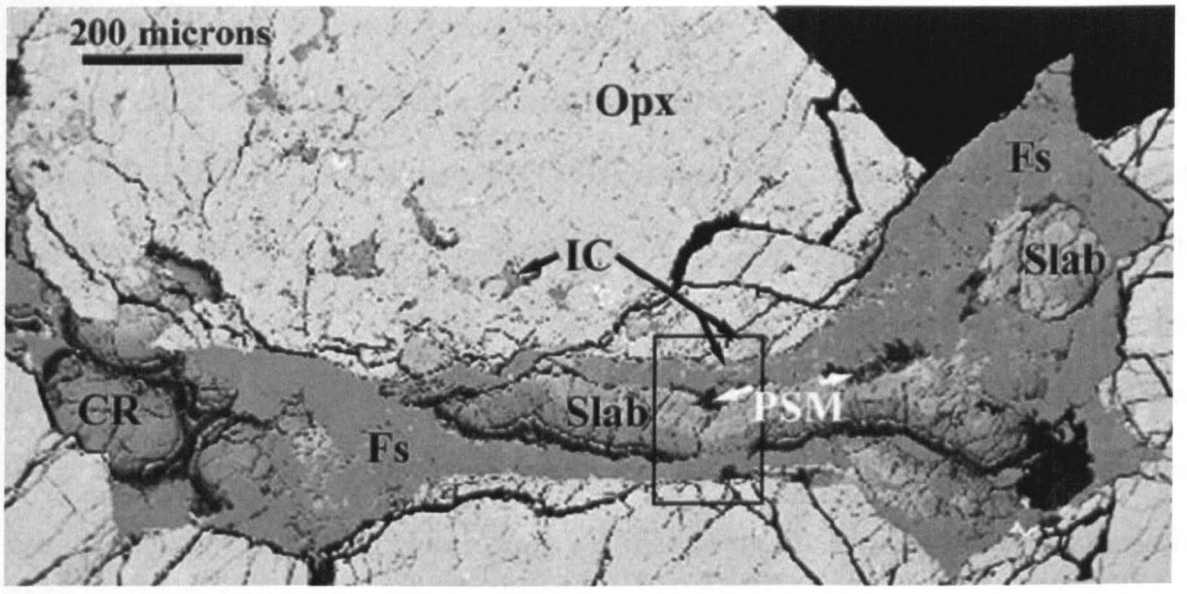

Figure 1.16 Backscatter electron image of ALH 84001 by Corrigan and Harvey (2004), displaying Slab carbonates, Post Slab Magnesites (PSM), Feldspar (Fs), Interstitial Carbonates (IC), Orthopyroxene (Opx) and Carbonate Rosettes (CR).

Golden et al. (2000, 2001) synthesised the mineral assemblage found in ALH 84001 (zoned Mg-Fe-Ca carbonates, Fe sulphide (pyrrhotite) and magnetite) from simple starting materials. The synthesis utilised low-temperature (25-150°C), hydrothermal processes and non-equilibrium conditions to produce carbonates using various Ca-Mg-Fe-S-CO_2-H_2O solutions. Subsequent brief heating of the reaction products at 470 °C was sufficient to form magnetite and pyrrhotite. Studies by Vecht and Ireland (2000) also produced carbonate structures similar to those observed in ALH 84001 at low temperature conditions. They suggested that the carbonates in ALH 84001 were initially vaterite ($CaCO_3$) formations as a precursor phase to calcite.

Measurements of carbon by ion microprobe on carbonates observed within ALH 84001 are ^{13}C-enriched (Niles et al., 2005) which has been taken to indicate interaction of

fluid with ^{13}C-enriched ancient martian atmospheric CO_2 (Romanek et al., 1994). This enriched early martian atmosphere is thought to derive from sputtering and hydrodynamic escape (Hunten et al., 1987; Wright et al., 1990, respectively). Analysis by the Phoenix lander has shown that Mars' current atmosphere is not ^{13}C-enriched (Niles et al., 2010). This depletion in the early ^{13}C has been accounted for through carbonate formation and mantle degassing, surpassing atmospheric loss. Results from the Curiosity rover, reported in March 2013, showed a completely different value for the isotopic composition of Mars' atmosphere, one that was enriched in ^{13}C (Jones et al., 2013). Additionally, oxygen isotopes suggest that ALH 84001 carbonates precipitated from a fluid within the martian crust (Romanek et al., 1994). These observations suggest carbonate formation through exchanges of the martian lithosphere and atmospheric CO_2.

The minimal silicate alteration and preservation of salts in ALH 84001 indicate relatively short timescales for exposure to fluids (Bridges et al., 2001). Experimental studies investigating the CO_2-H_2O interaction with basalt rocks have shown that carbonates can form at low temperatures over a period of a few days (Baker et al., 2000). Formation studies by Golden et al. (2000) looked at precipitation at 25 to 150°C with the solutions containing a mix of cations to reproduce the ALH 84001 rosette formation. The results showed how carbonate globules of similar magnitude and zoning could form at 150°C after 24 hrs, whereas after 96 hrs amorphous Fe-rich carbonates formed, followed by more Mg-rich carbonates.

The orthopyroxenite is characterised by a $^{176}Hf/^{177}Hf$-$^{176}Lu/^{176}Hf$ crystallisation age of 4.1 Ga (Lapen et al., 2010) with the formation of the carbonates thought to coincide with the outgassing of Ar from silicates (Nyquist et al., 2001). The age of the carbonates has not been so clearly defined. Initial dating with stepped heating and laser probe ^{39}Ar-^{40}Ar analyses by

Knott et al. (1995) reported an age of 3.6 Ga from a single carbonate/maskelynite grain. A subsequent $^{87}Sr/^{86}Sr$-$^{87}Rb/^{86}Sr$ analysis by Wadhwa and Lugmair (1996) inferred 1.39 ± 0.1 Ga age of formation from carbonate and maskelynite. Finally, $^{207}Pb/^{204}Pb$-$^{206}Pb/^{204}Pb$ dating of carbonate leachates by Borg et al. (1999) resulted in formation ages of 3.90 ± 0.04 and 4.04 ± 0.1 Ga respectively. The generally accepted consensus (Lapen et al., 2010; Niles et al., 2010) is that the carbonates $^{87}Sr/^{86}Sr$-$^{87}Rb/^{86}Sr$ age by Borg et al. (1999) is the most accurate to date with the carbonates post-dating their parent rock by 200 Ma.

The Cosmic-Ray Exposure (CRE) age of ALH 84001 has been determined by Eugster et al. (2002) from the radionuclide ^{81}Kr and stable Kr isotopes to be 15.4 ±5.0 Ma. Work by Nyquist et al. (2001) obtained a very similar CRE from stable noble gas compositions (14.7 ± 0.9 Ma). Jull et al. (1994) calculated a terrestrial age of 13 ka from ^{14}C. These studies that ALH 84001 was ejected from the martian surface less than ~16 Ma ago. It also suggests that prior to ejection, the secondary minerals were not remobilized or disturbed in the last ~3.9 Ga whilst on Mars.

1.7 Possible terrestrial formations

Each type of carbonate precipitates at a specific $\delta^{13}C$ and $\delta^{18}O$ range, which leads to the idea that the formation environment and mechanism in which they form is pertinent to their isotopic signature (Lacelle, 2007; Niles et al., 2010).

One of the characteristic marks of the ALH 84001 meteorite is the unique Mg-Fe-Ca carbonates within facture zones. The lack of associated salts, in particular sulphates, has led to problems when trying to explain their origin from brine evaporation (McSween and

Harvey, 1998). McSween and Harvey (1998) proposed that precipitation could occur in an alkali lake such as the outer edges of terrestrial lakes with zones of Mg enrichment without the presence of salts. The lake environment could be analogous to formerly flooded craters in the ancient highlands of Mars (McSween and Harvey, 1998).

Cryogenic formation of carbonates such as calcite form kinetically as a result of rapid CO_2 degassing during freezing of rich calcium bicarbonate fluids (Socki et al., 2003). The result is a depletion of ^{13}C in the remaining brine fluid and enrichment of ^{13}C within the precipitated calcite, linked to non-equilibrium reaction kinetics. Terrestrial conditions where this kind of formation is observed include Aufeis[1], caves and lake beds. Understanding these environments hence could be pertinent to potential formation conditions on present and even past Mars if a cold dry scenario is possible.

1.8 Outstanding questions

- What were the initial conditions under which carbonates observed within ALH 84001 formed? Were the rosettes produced at high or low temperatures?
- What was the composition of the starting solution that produced the carbonates? Could it have been sourced locally from surrounding material or was it injected from a separate location? Are the carbonates a single generation, or do they represent multiple generations of formation?

---

[1] Aufeis (icings) are layered ice sheets which form from successive ground water flows, typically observed in Arctic and subArctic conditions

- Where did these carbonates form? Was it on the martian surface such as a lake or ground frost, or subsurface in a hydrothermal system?
- What is the ideal instrument to detect these carbonates *in situ* on Mars?
- Are the magnetite formations found within the carbonates organic or inorganic? This question poses big implications for the formation of life on other planetary bodies and future landing sites for missions to Mars.

1.9 Purpose of this work

The work in the following chapters helps address some of the outstanding questions listed in the previous section through experimental and computational methods. The instrumentation and techniques that made these studies possible are described in Chapter 2. The first small-scale variability (~5 μm) of carbon and oxygen isotopes of ALH 84001 carbonate rosettes linked to their mineralogy is described in Chapter 3. This Chapter also includes the first matrix corrections for a comprehensive series of carbonates studied by NanoSIMS. A terrestrial analogue sample was also studied and oxygen isotope values measured to provide possible settings that may have been present on ancient Mars (Chapter 4). Chapter 5 gives the results of geochemical modelling combined with compositional and isotope data using Geochemist Workbench®. Finally, an investigation testing the next generation of detector was used to see whether current environments (specifically cold and dry) could be used to discover carbonate within basalt in the subsurface of Mars (Chapter 6).

Chapter 2

2. METHODS AND INSTRUMENATION

In order to determine the conditions under which carbonates in ALH 84001 were produced, the mineralogy and isotopic composition of components separated from the meteorite were analysed by Scanning Electron Microscope (SEM), Electron Microprobe (EMP) and ion microprobe (NanoSIMS). The experimental conditions under which these instruments were operated are described here; additional techniques (XRD, FTIR) were applied to specimens for specific purposes, and are described in the relevant chapters.

2.1 Sample preparation

Previous ion microprobe measurements of stable isotopes in ALH 84001 carbonates have endeavoured to produce flush, contamination free surfaces enabling acquisition of high precision reliable data sets. However, no previous ALH 84001 studies have obtained $\delta^{18}O$ and $\delta^{13}C$ measurements below 10x10 μm^2 (spot size) or prepared samples without impregnating and polishing with potential contaminants. These issues are significant as improved precision will help constrain existing formation models and producing contamination-free sample surfaces will ensure measurements from the ALH 84001

carbonates are reliable. To rectify this, NanoSIMS and Focussed Ion Beam (FIB) techniques were used to provide 5 μm measurements and flush ALH 84001 carbonate surfaces, respectively.

Of equal importance was the use of standards; since these are essential for Instrumental Mass Fractionation (IMF) corrections which need to be applied to NanoSIMS values to retrieve a true value for the stable isotope ratio within the ALH 84001 carbonates. The bulk elemental compositions of the carbonates within ALH 84001 are not simple end-members (calcite, dolomite, siderite and magnesite). Therefore, a large number of standards with varying Fe, Mg and Ca contents were required to deduce the IMF correction which needed to be applied to the NanoSIMS data. Previous studies have used corrections based on 9, or fewer, standards which typically involve end-member carbonates. In this thesis results from 14 carbonate standards are presented including samples used from previous investigations and newly classified standards (the latter chosen to aid IMF corrections for the intermediate composition carbonates found within ALH 84001).

While measurements from the standards were beneficial for IMF studies and corrections to data presented in Chapter 3 and 4, they also provided analytical challenges. Ideally when collecting measurements on any instrument the greatest chance of reproducibility occurs if all the samples are measured under the same analytical conditions. This is especially true for NanoSIMS measurements where even small lateral stage movements can have an effect on a measured value. As the most efficient way to conduct analyses it was therefore thought beneficial to have all the standards and samples within one holder. This is not a new concept and for instrumentation such as SEM and EMP, mineral standard blocks exist. For work in this thesis, it was deemed necessary to produce a holder which would allow samples to be placed in the machine at the same time as all of the standards. Additional requirements included mounting the samples in a material which would

not degas and ideally be conductive. These mounting materials needed to be placed within a conductive holder and provided a flush surface across all of the interchangeable samples. The relevance of the flush surface of the samples results from Kita et al. (2009), who showed 10-40 μm of sample relief would have a significant effect on the collected isotopic values (see section 2.4.6 for details).

2.1.1 Mounting medium

Mounting materials were first investigated where samples were mounted either by pressing them into indium, or by embedding them in korapox®. Indium is a soft metal into which samples can easily be pressed. The advantage of using indium is that it would not contaminate the sample with carbon and also act as a conductor therefore reducing issues with materials charging. Korapox® is a resin manufactured by Kömmerling (Germany). It is used for mounting samples for ion microprobe analysis because it bonds well, is low degassing, produces small gaps upon curing and leaves minimal induced relief when polished.

Terrestrial carbonate samples were used to test two mounting mediums prior to mounting the ALH 84001 carbonate rosettes. The terrestrial in-house standards (ankerite, calcite, dolomite, siderite and magnesite) were pressed into indium (heated to 60°C). This all sat in a 1 inch aluminium mount where the carbonate grains were then polished (Fig.2.1) as discussed in section 2.1.2. This initial setup was shown to have the following problems (Fig.2.1a):

- No interchanging of samples was possible once pressed into the indium within the aluminium mount.

- The indium smeared across the surface leaving pockets of contamination within vacancies and other carbonate lattice imperfections which proved difficult to remove with sonication.
- Indium has a soft and malleable texture and therefore would move in the mount when polished. This produced voids around the rim of the samples, increasing issues with charging and the possibility of samples falling out of the indium.
- Polishing pads were also easily contaminated (by indium sticking) and hard to clean, increasing chances of cross contamination.
- Samples would sometimes sink into the material as it was being polished making it hard to produce a uniform flat surface across all the samples.

From the above points it was clear that a new holder and resin was required to ensure future samples were provided the best opportunity of successful analysis, leading to the setup as shown in figure 2.1b.

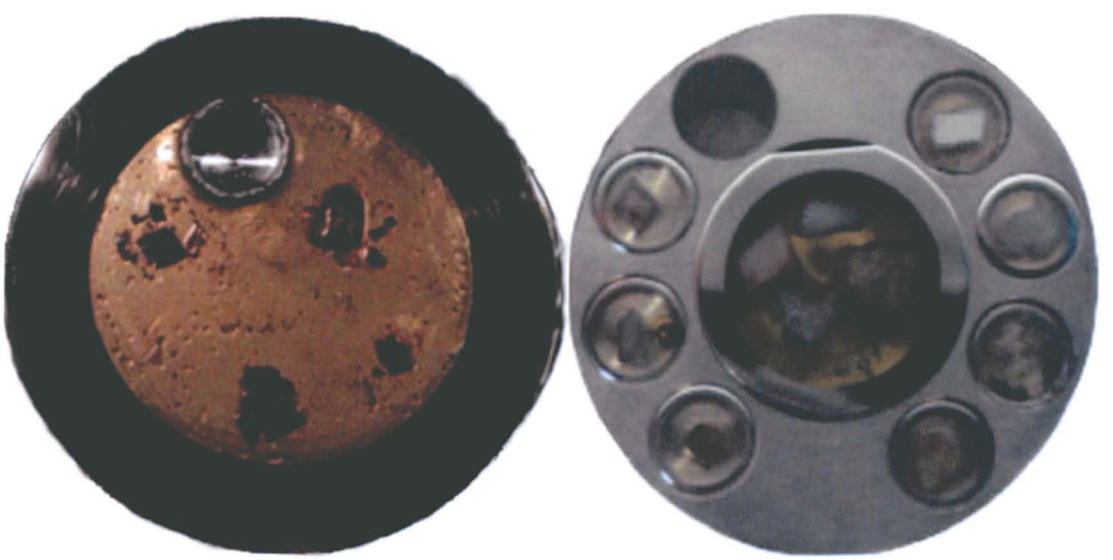

a **b**

Figure 2.1. Aluminium sample holders, 1 inch diameter. **Figure 2.1a** Gold-coated indium sample and resin imperfections are visible, voids can also be seen around some of the carbonate samples. The

hole in the indium (top of mount) was for placement of a 5 mm holder containing ALH 84001. **Figure 2.1b**, aluminium sample prior to coating. Samples embedded in resin can be polished more smoothly than samples pressed in indium. The holder was loaded with 12 carbonate samples.

2.1.2 Polishing

High precision analysis of samples by ion microprobe requires a sample surface that is as flat as possible so the specimens were polished. This was carried out in several stages, with increasingly finer grained polishing powders.

Stage 1: The samples were polished wet (18.2 Ω water[2]) and sequentially on magnetic 120, 220, 600 and 1200 grit diamond grinding discs[3] attached to an automatic polisher operating at ~300 rotations per minute (RPM). The polishing times varied between 5 to 15 minutes on each samples for all grits. Samples were therefore checked intermittently (~5 minutes) with a Nikon Eclipse LV100 microscope under reflected light (x50 mag) to see if the next grit could be applied. Samples were washed with 18.2 Ω water and isopropanol (IPA) between each polish to remove any grit and avoid compromising the next disc.

Stage 2: Once dried, the samples were polished by hand with 14 μm diamond paste on a TexMet® (Buehler) cloth. This was followed with 9, 6, 3, 1 and 0.5 μm diamond grit paste for ~5 minutes each. The microscope was used at each stage to check progress; time differed for various carbonate samples depending on their structure.

---

[2] 18.2 Ω water has been deionised.

[3] Grit sizes correspond to 125, 68, 25, 15 μm average grinding grain diameters respectively, as established by the FEPA (Federation of European Producers of Abrasives).

Stage 3: The samples were polished using aluminium oxide (~0.15 μm) for 30 seconds. After polishing the mounts were washed in a sonicator for 15 minutes each with 18.2 Ω water followed by IPA and dried in a vacuum oven (50°C).

2.1.3 Sample Coating

Following polishing the samples were imaged with the Nikon Eclipse LV100 under reflected light, prior to coating.

Samples were coated with gold for NanoSIMS experiments. For the gold coating a K575X Turbo Sputter Coater was used. A 40 A current was applied to the gold for 60 seconds with $1x10^{-1}$mbar of argon pressure resulting in 15 nm of coating. In subsequent EMP studies this gold coating was removed from the samples by either polishing or using the FIB (Chapter 3) and re-coated with 15 nm of carbon to ensure standard sample preparation procedure for calibrations was adhered to.

2.2 Scanning Electron Microscope (SEM)

The dual beam FEI Quanta 200 3D SEM was used to characterise the mineralogy and mineral chemistry of the samples, as well as to acquire images of the specimens. The SEM can be operated in one of several modes; owing to the requirements of each aspect of the research, different components of the SEM were utilised. Each sample was imaged using backscattered and secondary electrons with an accelerating voltage of 20 kV and a probe current of 0.6 nA. Results from the Oxford Instruments energy-dispersive X-ray (EDX) analyser were collected, reduced and stored by the INCA software program. The INCA

software was used for all the EDX elemental maps, false colour images and point analysis of samples. In 2010, the EDX lithium-drifted silicon detector (Si(Li)) was upgraded with an 80 mm^2 X-max Silicon Drift Detector (SDD) which reduced analysis times by an order of magnitude. The EDX maps and spot analyses as described in Chapter 4 were all collected with the new SSD. The SEM was run under high vacuum (10^{-7} mbar), with the samples gold-coated to reduce charging effects. Prior to analyses reference standards were measured using ZAF (Z: atomic number, A: X-ray absorption, F: secondary X-ray fluorescence) correction software (SEMQuant, Oxford Instruments).

2.3 Electron microprobe

A Cameca SX 100 electron microprobe with 5 separate wave dispersive X-ray (WDX) spectrometers characterized the carbonates used for matrix corrections. Smithsonian siderite, dolomite and calcite (Jarosewich and MacIntyre.,1983) were used to calibrate the instrument for Ca, Mg, Fe and Mn contents. Prior to analyses all samples were coated with 15 nm of carbon at the same time to ensure identical thickness. Spot sizes for standard quantification of carbonates were 15x15 μm^2 with analyses being conducted by taking 10 measurements diagonally across the surface of the sample. Analysis of the carbonate rosettes followed the NanoSIMS measurements with use of the FIB to remove the previous gold coating (Chapter 3) and smooth the surface before carbon coating and analysing the NanoSIMS pits (5x5 μm^2 measurements). An accelerating voltage of 20 kV and a probe current of 20 nA was used for all analyses.

2.4 NanoSIMS

Secondary ion mass spectrometry (SIMS) is a technique that links μm-scale isotopic analysis with high-resolution imaging. The resulting measurements provide valuable information about the elemental and isotopic compositions of small samples. The prime use of NanoSIMS in the field of cosmochemistry has been the study of presolar grains, aiding our understanding of the processes that occurred in the early Solar System (Messenger et al., 2003; Nittler., 2003, Davidson et al., 2009). There are many other applications of SIMS to specimen analysis, for example, looking at the isotopic composition of cells (Musat et al., 2008), proteins and nanoparticle interaction (Moreau et al., 2007), geological mineral sections (Sano et al., 2005) and trace element imaging for material research (Lozano-Perez et al., 2008).

2.4.1 Carbon and oxygen isotopes

Carbon and oxygen isotopes variations are normally measured as a ratio of their two most abundant isotopes. The way of denoting this is by using the delta notation (δ) and is the normalised difference between the sample and standard. In the case of $\delta^{18}O$ this can be displayed as:

$$\delta^{18}O = \left[\left(\frac{\frac{^{18}O}{^{16}O_{Sample}}}{\frac{^{18}O}{^{16}O_{Standard}}} \right) - 1 \right] \cdot 1000‰ \qquad (3)$$

and for $\delta^{13}C$:

$$\delta^{13}C = \left[\left(\frac{\frac{^{13}C}{^{12}C_{Sample}}}{\frac{^{13}C}{^{12}C_{Standard}}} \right) - 1 \right] \cdot 1000‰ \qquad (4)$$

2.4.2 NanoSIMS Operation

The NanoSIMS operates by focusing either a Cs^+ or O^- beam onto a sample which will then release secondary positive or negative ions (respectively). The secondary ions are then focussed through a second series of lenses and apertures for transmission into the mass spectrometer. Once within the mass spectrometer the secondary ions are separated according to their masses into seven detectors by magnetic and electric fields (Fig. 2.2).

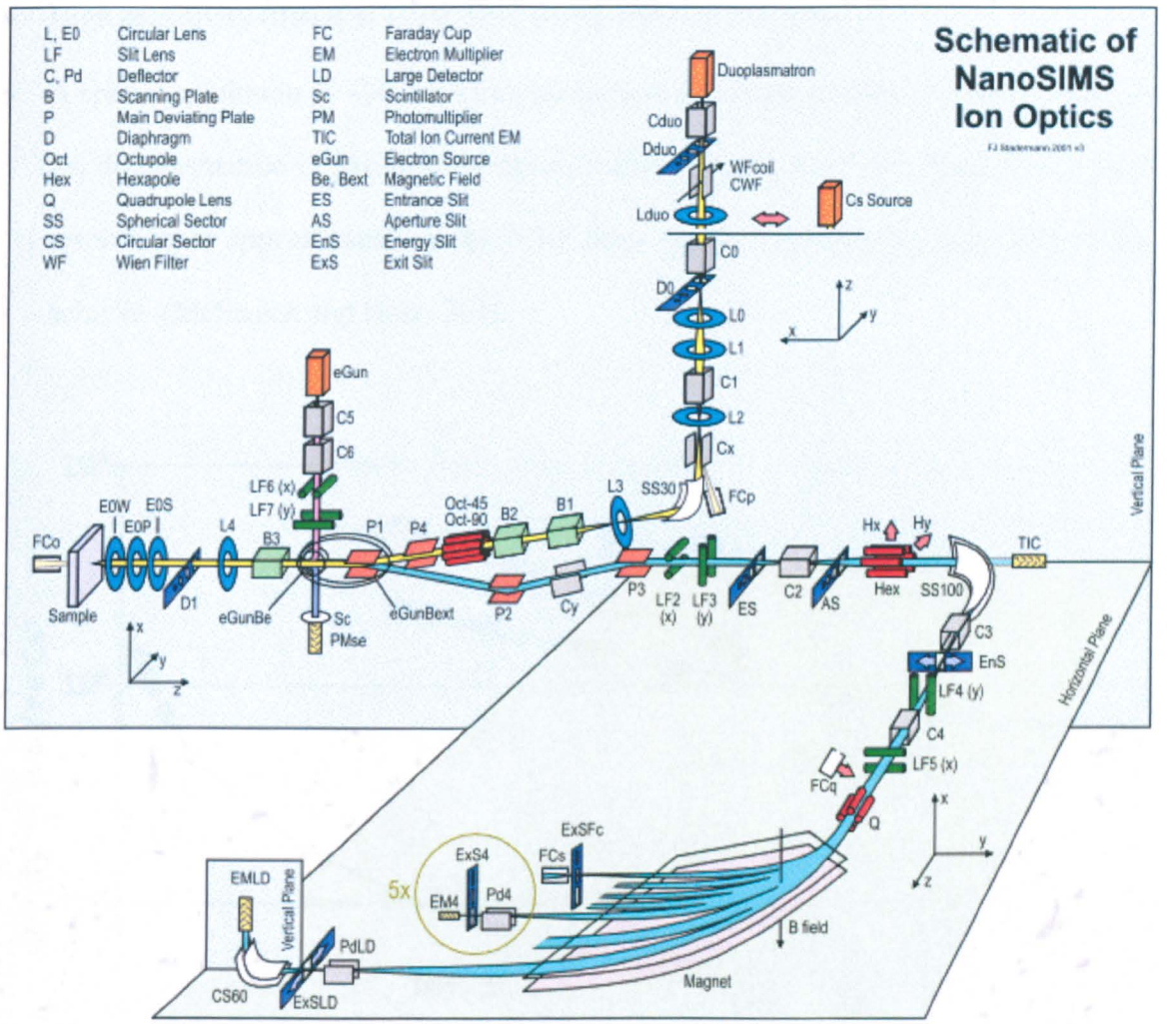

Figure 2.2 Schematic of NanoSIMS ion optics displaying all the slits and lens in the instrument. The yellow beam indicates the path of the oxygen ions and the blue beam represents the secondary ions. Figure from Stadermann et al., (1999).

The Cameca NanoSIMS 50L ion microprobe complements the conventional SIMS instruments (e.g. Cameca IMS-3f to IMS - 7f series) by combining –

- Higher resolution and mass resolving power (MRP; M/ΔM up to 9000 in this study; 7000 Fig 2.3).
- A multicollector which allows simultaneous collection of up to seven ion masses.

- High sensitivity (down to a few ppm during element imaging).
- A spatial resolution of ~30 nm when using the Cs^+ primary beam and 150 nm when using the duoplasmatron O^- primary ion beam. It also provides a depth resolution of 1 nm. This resolution is approximately a factor of three smaller than the Cameca IMS 1270 can achieve. (McSween and Huss, 2010).

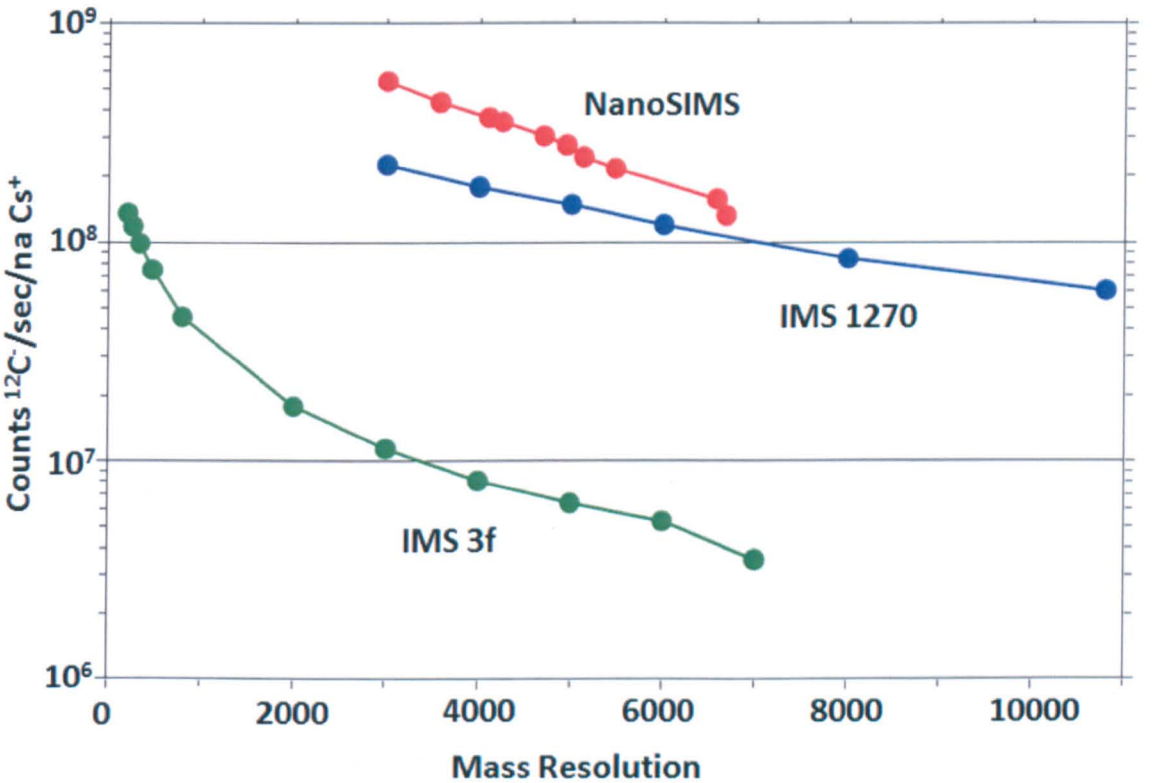

Figure 2.3 Comparison of results from three ion probes for secondary ion $^{12}C^-$ yields from presolar SiC grains at different mass resolutions. The NanoSIMS is roughly twice as efficient as the IMS 1270 and 40 times more efficient that the IMS 3f. Figure edited from Stadermann et al. (1999).

The key to the improved resolution and sensitivity is the design of the NanoSIMS optics (Fig. 2.4). The primary ion beam (Cs^+ or O^-) hits the sample at normal incidence rather than the oblique angle of the 3f ion probe family (Fig 2.4), so the primary beam implants more ions resulting in higher IMS ionization efficiency (improved transmission) and smaller shadowing effects. The secondary beam is co-axial with the primary beam. The NanoSIMS' immersion lens (part of the probe-forming and extraction optics) is set with a much smaller working distance than its predecessors (0.5 mm instead of 5 mm for the IMS-3f). This results in a shorter distance for the secondary ions to travel and thus their more rapid collection, thereby reducing the extent to which they will be dispersed.

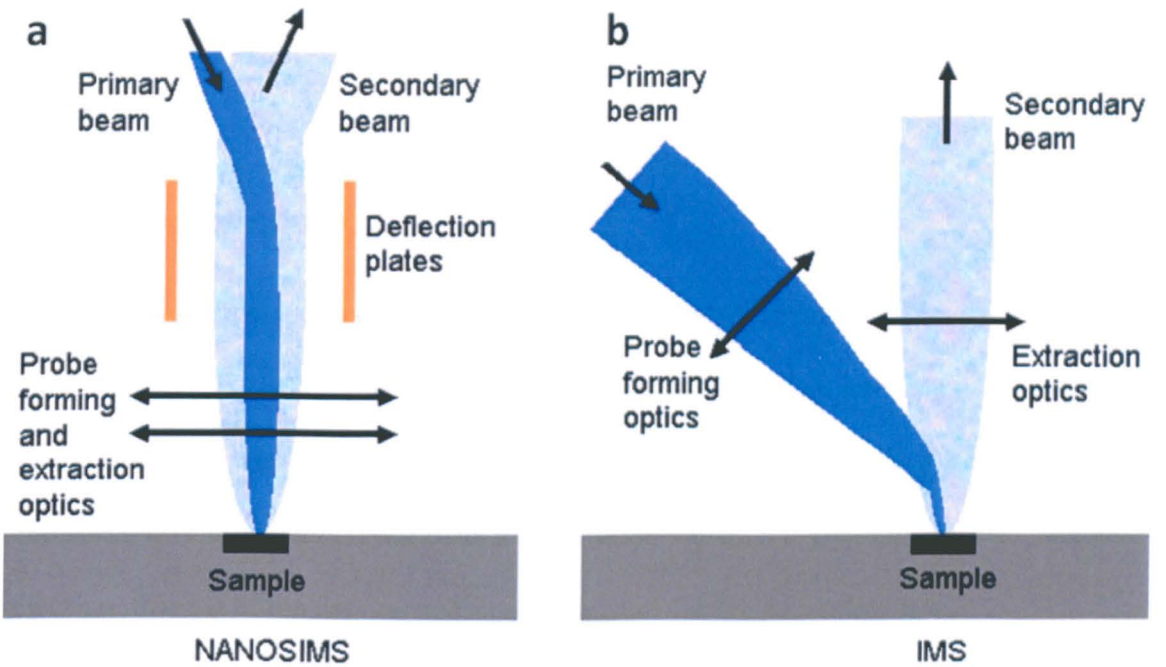

Figure 2.4 Diagrams showing how the beam sampling has been modified with the NanoSIMS (a) to produce superior analysis to previous IMS (b).

2.4.3 Sputtering and Ion Source

The work in this thesis uses Cs^+ ions as the primary ion beam. The Cs^+ ions are generated by a device that heats a caesium carbonate (Cs_2CO_3) pellet. The yield of secondary negatively charged ions depends on the concentration of caesium implanted into the top atomic layers of the sample (Slozdian et al., 1992). When sputtering on a fresh surface there is a period in which the yield varies before reaching an equilibrium state. Once achieved the removal rate of the implanted caesium ions equals the rate of arrival of the primary ions. Samples were pre-sputtered until counts of secondary ions plateaued or signs of contamination were removed ($^{28}Si^-$ monitoring), typical pre-sputter times of 2-3 minutes were recorded.

2.4.4 Detector setup

The instrument can detect up to seven masses simultaneously being equipped with three Faraday Cups (FC) and six Electron Multipliers (EM). Peak jumping is another analysis method available with the NanoSIMS or a combination of both may be employed. The NanoSIMS was used with fixed detector positions for this study. This was to increase the collection times, (i.e. ion counts) and hence statistics for the secondary ions.

Table 2.1 The two NanoSIMS trolley (EM, FC; Fig. 2.2) configurations used in this study for obtaining $\delta^{13}C$ and $\delta^{18}O$ values and performing Si, Mg, Ca and Fe checks.

FC	EM	EM	EM	EM	EM	EM
$^{16}O^-$	$^{17}O^-$	$^{18}O^-$	$^{28}Si^-$	$^{24}Mg^{16}O^-$	$^{40}Ca^{16}O^-$	$^{56}Fe^{16}O^-$
	$^{12}C^-$	$^{13}C^-$	$^{28}Si^-$	$^{24}Mg^{16}O^-$	$^{40}Ca^{16}O^-$	$^{56}Fe^{16}O^-$

$^{28}Si^-$ was observed to help determine the pre-sputter time and to ensure that, during analysis of ALH 84001, carbonate was being measured (i.e. the beam had not sputtered through the carbonate into underlying orthopyroxene). The $^{28}Si^-$ signal was also used to check that contamination was not present on the sample surface. $^{24}Mg^{16}O^-$, $^{40}Ca^{16}O^-$ and $^{56}Fe^{16}O^-$ were also monitored as checks to ensure any drift in acquiring isotope values was noted and that the carbonate mineralogy (i.e. relative proportions of Mg, Ca and Fe) in the single analysis remained constant. $^{17}O^-$ was recorded but at the time the analyses were made, the precision and MRP was not sufficient to draw conclusions from the $\delta^{17}O$ values.

The FC works by measuring the ion current hitting the metal cup, which is then converted into voltage by a high impedance amplifier (Fig. 2.5). This detector can measure a higher intensity of secondary ions produced by the ion beam than EM's, from ~$5x10^4$ upwards (Davidson et al., 2009). The FC was hence used to measure the $^{16}O^-$, the major stable isotope of oxygen, with a natural terrestrial abundance of 99.759% (Cook and Lauer, 1968).

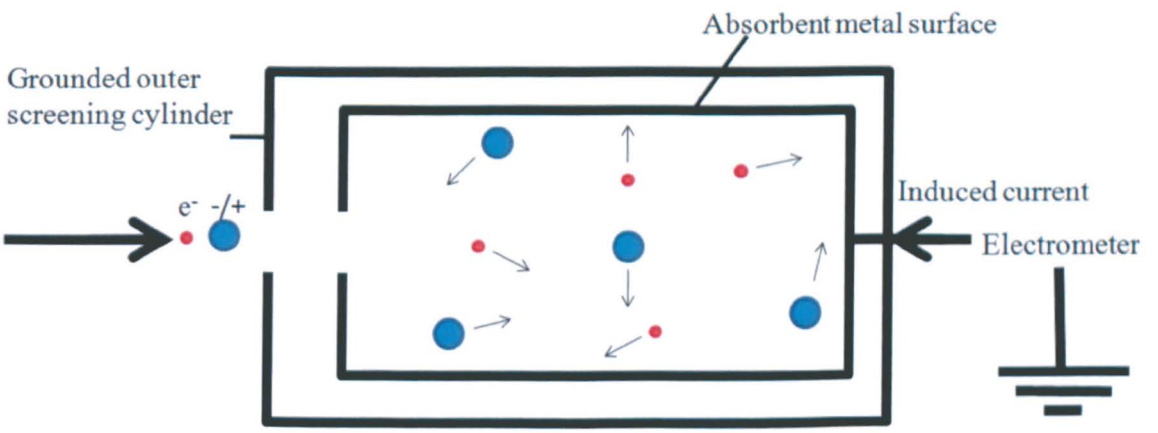

Figure 2.5 A faraday cup uses one dynode (absorbent metal surface) and therefore produces a single level of amplification. The faraday cup measures the electrical current as a charged particle beam (electron and ions) bombards the metal surfaces of the cup.

The EM uses a series of dynodes with potential differences across them to produce an accumulating quantity of electrons after each contact (Fig. 2.6). The resulting EM gain is of the range of 10^8. A preamplifier is used to convert the charge pulses into voltage pulses and amplifies them. The EM detectors were used for measurement of the $^{17}O^-$ and $^{18}O^-$ minor isotopes of oxygen, with terrestrial abundances of 0.037% and 0.204% respectively (Cook and Lauer, 1968).

Figure 2.6 An electron multiplier uses two series of dynodes, with an initial ion resulting in a subsequent shower of electrons. There is also an EM gain, the system is run under high vacuum (HV) with a preamplifier attached at the end for the charge pulses.

2.4.5 Sample charging

Charging problems can arise when insulating materials (e.g. carbonates, silicates) are sputtered with primary ions. The implanted charge can build up and cause the secondary ion beam to deflect to a point where it is no longer focused through the lenses into the mass

spectrometer, thus seriously reducing transmission efficiency. Carbonates were the main material studied within this research project. Carbonates are good insulators and are hence severely prone to charging (Fayek, 2009). A conductive layer of gold was added to the samples to help dissipate the implanted positive charge. To resolve this issue further, the NanoSIMS is equipped with an electron flood gun (Fig 2.2; eGun). An electron beam is deflected with magnets along the primary and secondary ion axis (Fig 2.2, C5, C6, LF6 (x) and LF7 (y)) and produces a cloud of low energy electrons (10-20 eV) just above the surface of the target. The cloud of electrons regulates the charge between the ion pulses and therefore reduces positive charging.

2.4.6 Mass interferences

When selecting specific ions, there are often other ions with similar masses (referred to as isobaric interferences), such that a single uniform peak within the atomic mass unit (a.m.u.) range is not always clearly identifiable (Fig. 2.7 a). Therefore, it is important when aligning the detectors to determine any isobaric interference so that only the species of interest were measured. The ability to separate between isobaric species is a function of the mass resolving power (MRP) of the instrument.

$$R = \frac{M}{\Delta M_{MRP}} = mass\ resolution \quad (1)$$

Where ΔM_{MRP} = mass resolving power and a larger resolution indicates a clearer separation of peaks.

$$MRP = \frac{M}{\Delta M} = mass\ resolving\ power \quad (2)$$

Where ΔM = resolution; defined as the minimum peak separation to define two ion species.

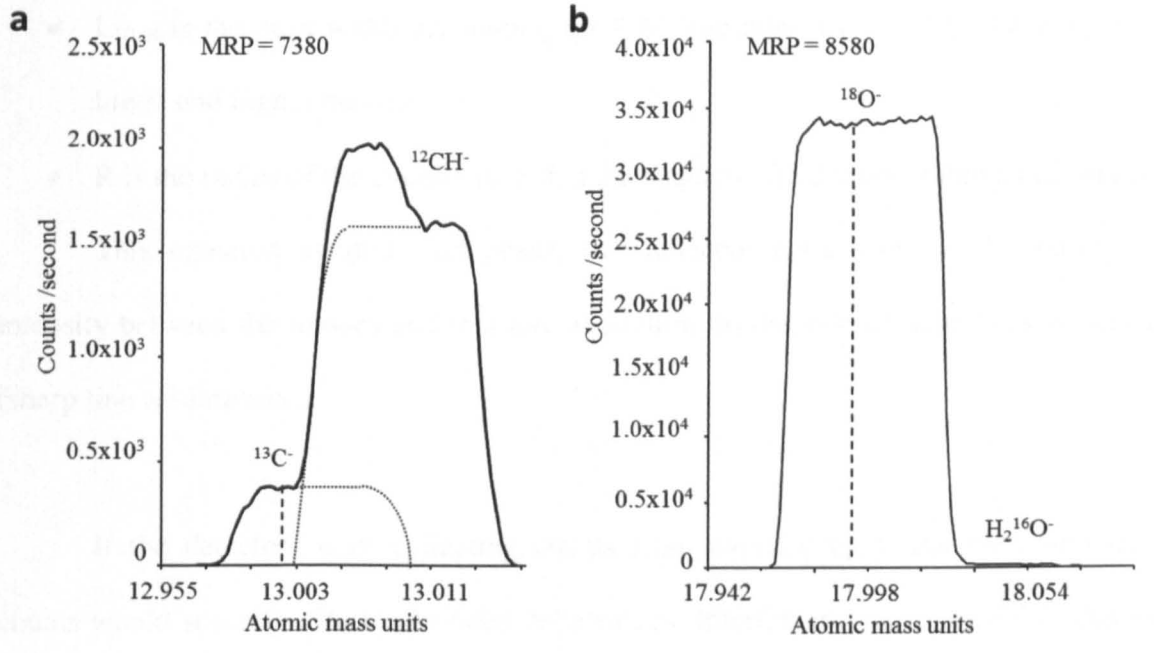

Figure 2.7 Scans of the mass spectra across the entrance slit of the detectors with MRP values corresponding to the mass selection line chosen for analysis (broken lines). These measurements were made using an ankerite carbonate sample with a 5x5 μm^2 ion beam spot size. In figure 2.7a, $^{13}C^-$ is resolved from $^{12}CH^-$. In fig 2.7b, $^{18}O^-$ is resolved from $H_2{}^{16}O^-$.

The NanoSIMS has a greatly improved MRP compared with other SIMS instruments, a property that is crucial to aid the identification of individual ion species. The MRP refers to the mass spectrometer's capability to separate ion beams with masses M and ΔM, which are given by the "Cameca definition" resolving power equation:

$$MRP_{Cam} = \frac{M}{\Delta M} = \frac{R}{4L_{10-90}} \qquad (3)$$

Where:

- M is atomic mass
- ΔM is the centre separation distance between two masses
- $L_{10\text{-}90}$ is the peak width accounting for 80% line intensity, i.e. 10% intensity at both lower and higher masses.
- R is the radius of the circular path that the magnetic field takes within a uniform field.

This equation assumes flat peaks, two adjacent masses of equal intensity, zero intensity between the masses and that any aberration on the side of their lines is neglected (sharp line assumptions).

If the detectors were collecting counts from overlapping peaks the combined ion counts would severely affect calculated delta values. Interferences encountered in this study were either resolvable or had a negligible contribution (Fig. 2.7). For example, when taking $^{13}C^-$ measurements the EM mass line was positioned on the left shoulder plateau (~13 a.m.u.) making it possible to differentiate between the $^{13}C^-$ and $^{13}CH^-$ isobaric interferences (Fig. 2.7a). The following equation gives the MRP value (2) required to clearly resolve the peak for $^{13}C^-$ (13.0035 a.m.u) from $^{13}CH^-$ (13.005 a.m.u):

$$MRP = \frac{13.0035}{(13.005 - 13.0035)} = 8869 \qquad (4)$$

The isotope species counts were monitored and re-centred over the peak for each analytical session to ensure that the collected ionic species did not change. Carbonates with the largest concentrations of ion species of interest (i.e. calcite for $^{40}Ca^{16}O^-$ tuning, magnesite

for $^{24}Mg^{16}O^-$ tuning etc.) were used to tune the instrument, typically reducing the quantity of interference peaks and decreasing tuning time.

2.4.6 Standard corrections

A full description of the specific correction factors applied to the NanoSIMS analyses of carbonates and the machine performance, is discussed in Chapter 3. This section gives a general outline of correction procedures. During NanoSIMS analysis, there are several stages with a high likelihood of instrumental mass fractionation (IMF) of the secondary ions. These include the ionization, extraction and sputtering stages, transmission and detection efficiencies. The first three of the stages mentioned produce IMFs which are mass-dependent but can also be artefacts of topography (Kita et al., 2009) and sample preparation. These were corrected using standards and by achieving submicron topography with sample preparation (section 3.3). Detection efficiencies can be affected by ageing of the electron multipliers, when production of secondary electrons starts to reduce. This can be compensated by checking the Pulse Height Distribution (PHD) of the detector and adjusting the voltage of the multiplier. The effects of transmission were controlled and kept constant for each analytical session.

The IMF was corrected in per mil (‰) using equation 5, where delta refers to either $\delta^{13}C$ or $\delta^{18}O$. The NanoSIMS standard measurements were normally spot values, though for imaging, an average value across the whole imaged area was taken. $Delta_{true}$ values were acquired by conventional analysis of splits of the carbonates, using acid dissolution and

measured with a Finnigan Advantage Mass Spectrometer. Additional details of the carbonate standards are given in Chapter 3.

$$IMF = \left[\frac{Delta_{Nanosims}}{Delta_{true}} - 1\right] \times 1000 \qquad (5)$$

The main issues in this study tended to arise from corrections for the "matrix effect", where the composition of the analysed material caused variation in the collected isotopic composition when compared to that of the true values. This was not a problem with the materials used for the standards but the carbonates of interest in ALH 84001 are complex solid solution phases that required a suite of similar carbonates that were isotopically and chemically homogenous. Such materials are hard to find in natural settings with the stability fields favouring end member carbonate formation (Fig. 2.8). It was on this basis that fourteen carbonates were sourced from mineralogies within the stability fields and were used to correlate the compositions required for correction of the IMF of ALH 84001 carbonate (see Chapter 3 for further discussion).

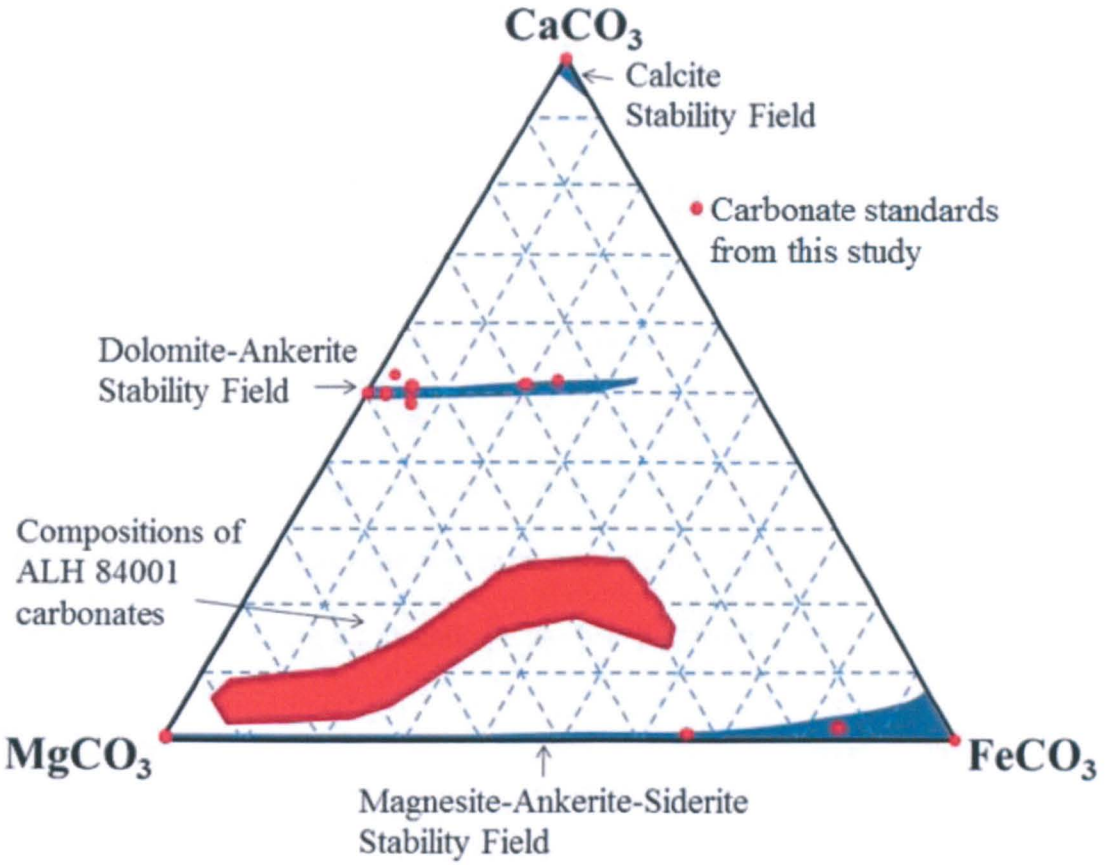

Figure 2.8 Ternary diagram of the solid solution stability phases for terrestrial Mg-Ca-Fe carbonates (blue) and the carbonate standards used in this study (red dots). The carbonates from ALH 84001 measured in this study (red region) fall between the Dol-Ank stability field and the Mag-Ank-Sid fields, suggesting that the carbonates are in disequilibrium. Diagram modified from Thomas-Keprta et al. (2009).

The long term reproducibility of the homogenous standards was recorded over a period of 6 months (Chapter 3). Standards were also monitored within each analytical session which varied between 6 and 56 hours. A common standard (typically siderite, $FeCO_3$) was used daily for each analytical session so that any changes in mass bias could be noted and adjusted for normalizing data. This ensured that all analytical sessions were comparable. No large isotopic variations (within the internal error of the standard) resulting from drift in the mass bias were observed in any analytical session.

2.4.7 Spot size of analysis

The target material for most of these studies is ALH 84001 carbonates (150 to 200 μm across). The micron-scale variations in the mineralogy and isotopes required the smallest spot size versus reproducibility to be determined. The most recent study of $\delta^{13}C$ in ALH 84001 was conducted by Niles et al. (2005). Errors (1σ) on standards range from ±1 to 4.1 ‰ based on two to fourteen analyses at each site and spot sizes ranging from 10x10 to 30x30 μm^2.

An "in house standard" ankerite sample obtained from the Natural History Museum, London was used to conduct the spot size study in this thesis. The 'true $\delta^{13}C$' value of the ankerite as measured using a conventional gas bench technique was -8.4 ‰ (Chapter 3.5).

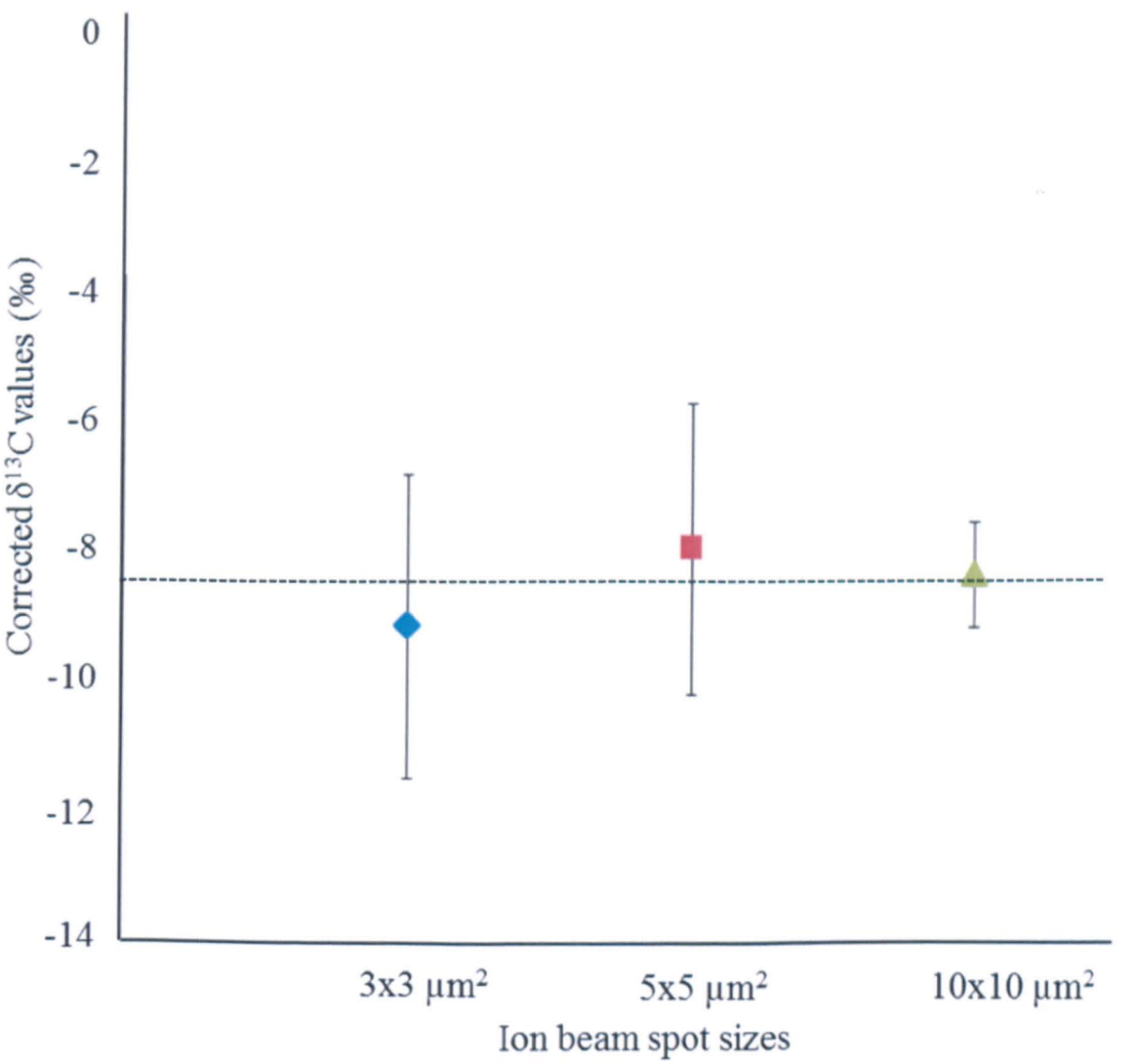

Figure 2.9 Results of ankerite analysis with varying spot sizes, size measurements were averaged over 5 analyses. Errors are reported to 1σ, corrected (equation 4) against '$\delta^{13}C$ true' value (-8.42‰; dotted line) obtained from measurements calibrated against NIST 19 international standard to V_{PDB} (Chapter 3.5).

The results of the analysis session showed no great difference in reproducibility errors between the 3x3 μm^2 (-9.2 ± 2.3 ‰) and the 5x5 μm^2 (-8.0 ± 2.3 ‰) micron spots, but a large improvement for 10x10 μm^2 (-8.4 ± 0.8 ‰). The 3x3 μm^2 spots required a deeper trench to be sputtered to reach the one per mil ^{13}C statistics. This was thought to be an issue, since formation of such relatively deep wells within the samples may potentially cause charging problems. The 5x5 μm^2 spot sizes were adopted for this study as they gave information on a scale not obtained from previous ALH 84001 carbonate studies whilst still producing data with a reasonable error.

Chapter 3

3. DETERMINING THE ISOTOPIC COMPOSITION OF ALH 84001 ROSETTES WITH NANOSIMS

3.1 Introduction

ALH 84001 is the oldest known martian meteorite we have on Earth (~4.1 Ga; Lapen et al, 2010) and the carbonates within ALH 84001 precipitated ~3.9 Ga (Borg et al, 1999). From the current martian meteorite collection, ALH 84001's carbonates are the most abundant (~1 vol. %) and the most varied in mineralogy; especially the carbonate "rosettes" that have an ankerite core leading to a layer of magnesite surrounded by small mixtures of pyrite siderite and magnetite (Fig. 3.1). The carbonates are widely believed to have formed in an ancient martian fluid. Through studies of the carbonates, information has been provided about their temperature, composition and pH (Romanek et al., 1994; Leshin et al., 1998; Niles et al., 2005). However, there is no single formation environment that has been recognised as the decisive path by which these carbonates formed. The age, abundance, isotope and mineralogy variations make the carbonates within ALH 84001 ideal candidates to provide insights into the primordial martian conditions in which they formed.

Many studies have previously tried to derive the formation conditions of these carbonates, with both high and low formation temperatures being proposed by authors. The range in temperatures from the literature vary from 5 to 700°C based on studies including micro-scale $\delta^{18}O$ and $\delta^{13}C$ isotopic variations, chemical analyses, petrographic relationships and laboratory synthesis. The speculated environments from these studies suggest scenarios such as thermal decomposition during an impact-induced event (Brearley, 1998; Corrigan and Harvey, 2004), evaporative deposits (McSween and Harvey., 1998; Warren, 1998), hydrothermal formations (Grady et al., 1994; Romanek et al., 1994), organic formation (McKay et al., 1996) and terrestrial contamination (Kopp and Humayun, 2003).

This study presents the first isotopic values for ALH 84001 using a 5 μm diameter spot to perform chain analysis across two rosettes with parallel $\delta^{18}O$ and $\delta^{13}C$ analysis. This reduced spot size doubles the number of analyses from the closest previous studies (10 μm, $\delta^{13}C$-Niles et al., 2005; $\delta^{18}O$-Holland et al., 2005) across a given area, allowing further correlations between mineralogy (also measured with 5 μm diameter spots in this study) and isotopic composition. A FIB was also used for the first time on a ALH 84001 sample, in preparation for ion probe analysis, to obtain a surface smooth at the micrometre scale. This method reduced potential contamination issues as epoxy resins and polish were not required for sample preparation. This study was the first undertaken on carbonates by the OU NanoSIMS, and so considerable effort was expended to determine the Instrumental Mass Fraction (IMF) corrections applied to the elemental data from a range of carbonate standards. In this chapter, results from analysis of carbonates in ALH 84001 are presented; they are discussed in terms of the corrections required to allow comparison with other studies. The implications of the data for interpretation of the environmental conditions pertaining on Mars during formation of the carbonates are contained in Chapter 7.

3.2 Petrographic context

The carbonates within ALH 84001 have been described in the literature as ellipsoids and slab carbonates. Slab carbonates are observed to conform to fractures and post slab magnesite and are thought to have formed as a late generation of carbonate (Corrigan and Harvey, 2004). However, most of the carbonate observed with ALH 84001 structures fall within the dimensions of ellipsoids varying between 10-300 μm along their major axis (Thomas-Keprta et al., 2009). The ALH 84001 carbonates studied in this sample were of a slight variation to previous elliptical shaped carbonates (rosettes) reported (Mittlefehldt, 1996; Treiman, 1998; Thomas-Keprta et al., 2009). Despite the appearance of zoned carbonate structures, their composition does not vary in mineralogy as commonly observed by other studies, which typically cited ankerite cores surrounded by an alternating layer of siderite-magnesite-siderite. Instead, these carbonates appear to have a core of ankerite (orange) followed by a rim of magnesite (white) (Fig. 3.1). Surrounding these carbonates are fine grained 10-50 μm spots of Fe sulphides commonly associated with observations of siderite and magnetite (black). The carbonates are also merged together, suggesting simultaneous nucleation and growth with no overlapping rims observed. The dominant surrounding material is orthopyroxene ($En_{70}W_{30}$), and a single large grain of chromite (Fig. 3.1).

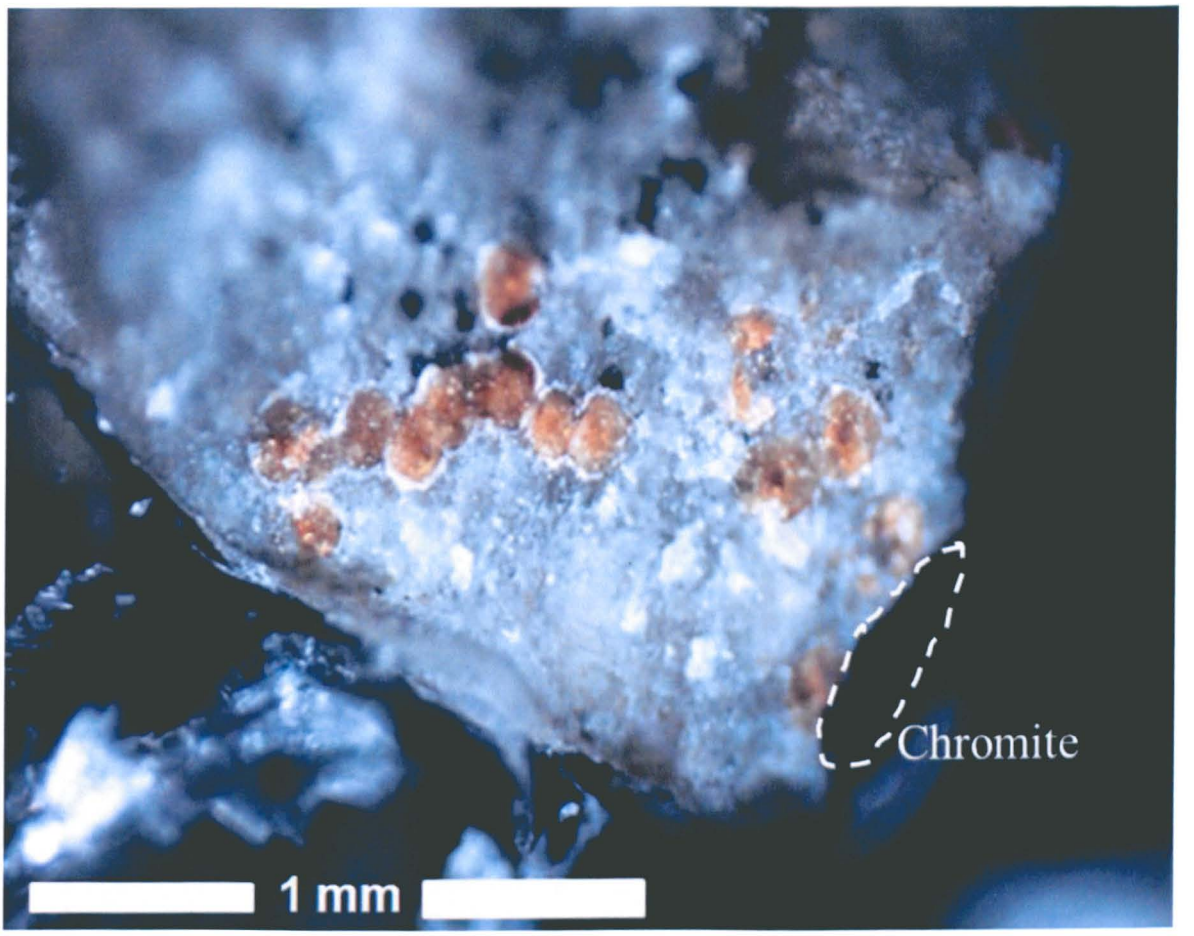

Figure 3.1 Optical binocular microscope image of rosettes within ALH 84001, split 126. The carbonates are elliptical formations that are observed as both associated groups and individually. The sizes of the rosettes in this study varied from 120-150 μm along the ellipsoids major axis. The white magnesite rims varied between 2-12 μm and the black Fe-rich material ~45 μm. The material to the bottom left of the image is the Körapox resin that did not contact the top surface. The dark patch to the bottom right of the carbonates is a chromite grain ~0.5 mm in diameter.

The rosettes when viewed with backscattered electrons (Fig. 3.2) have dark (magnesite) outer rings surrounding a lighter (ankerite) core. Both individual (complete circular ring) and combined rosettes can be observed with the only incomplete sample visible (top right). The surrounding regions of light material are enriched in Fe and S and from EDS point analysis indicate pyrite, siderite, magnetite and pyrrhotite.

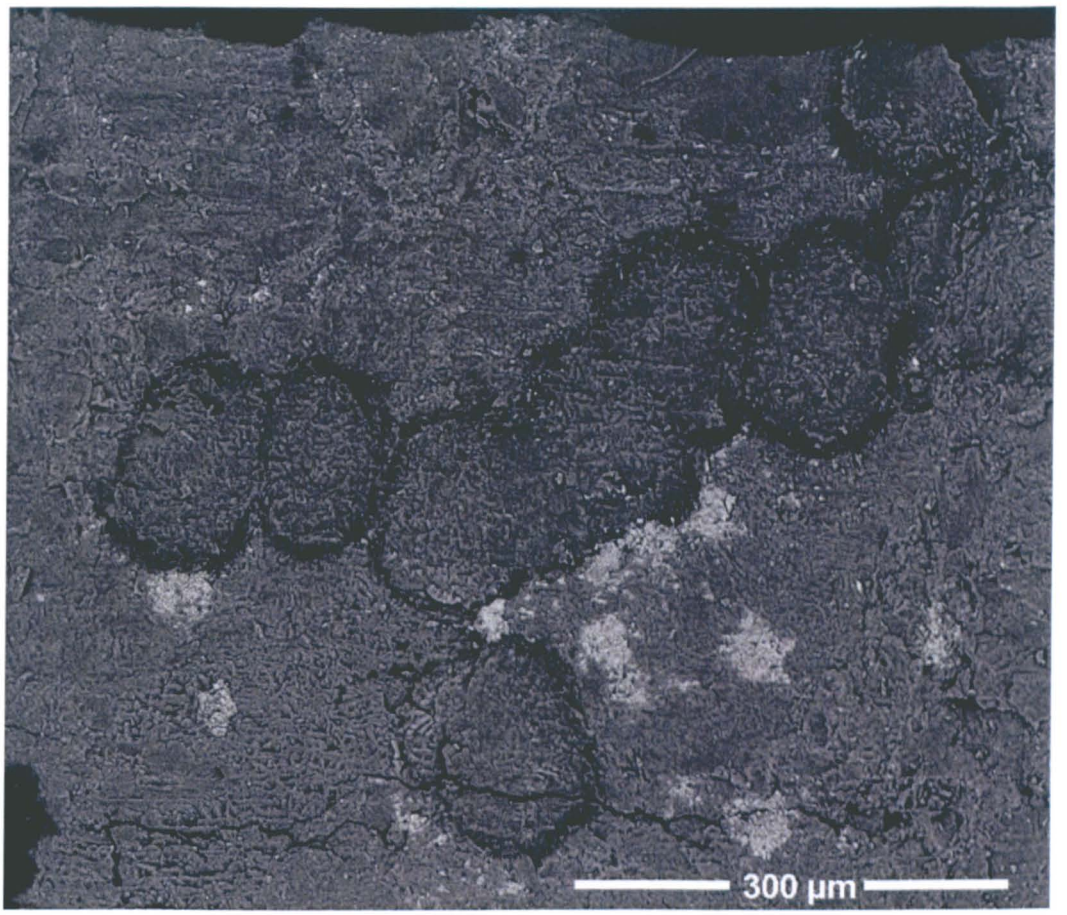

Figure 3.2 Backscatter electron image of multiple rosettes.

3.2.1 Rosette composition

Studies of the carbonate composition were conducted with a Nikon Eclipse LV100 reflected light microscope (Chapter 1.1.2), dual beam FEI Quanta 200 3D SEM (Fig. 3.3; see Chapter 2.3 for settings) and a Cameca SX 100 electron microprobe (Fig. 3.4; see Chapter 2.8 for settings).

The siderite, pyrite and pyrrhotite phase (Fig. 3.3) consists of a fine grain matrix of micron to sub-micron grains also associated with graphite and magnetite grains (Thomas-Keperta et al., 2009; Steele et al., 2012).

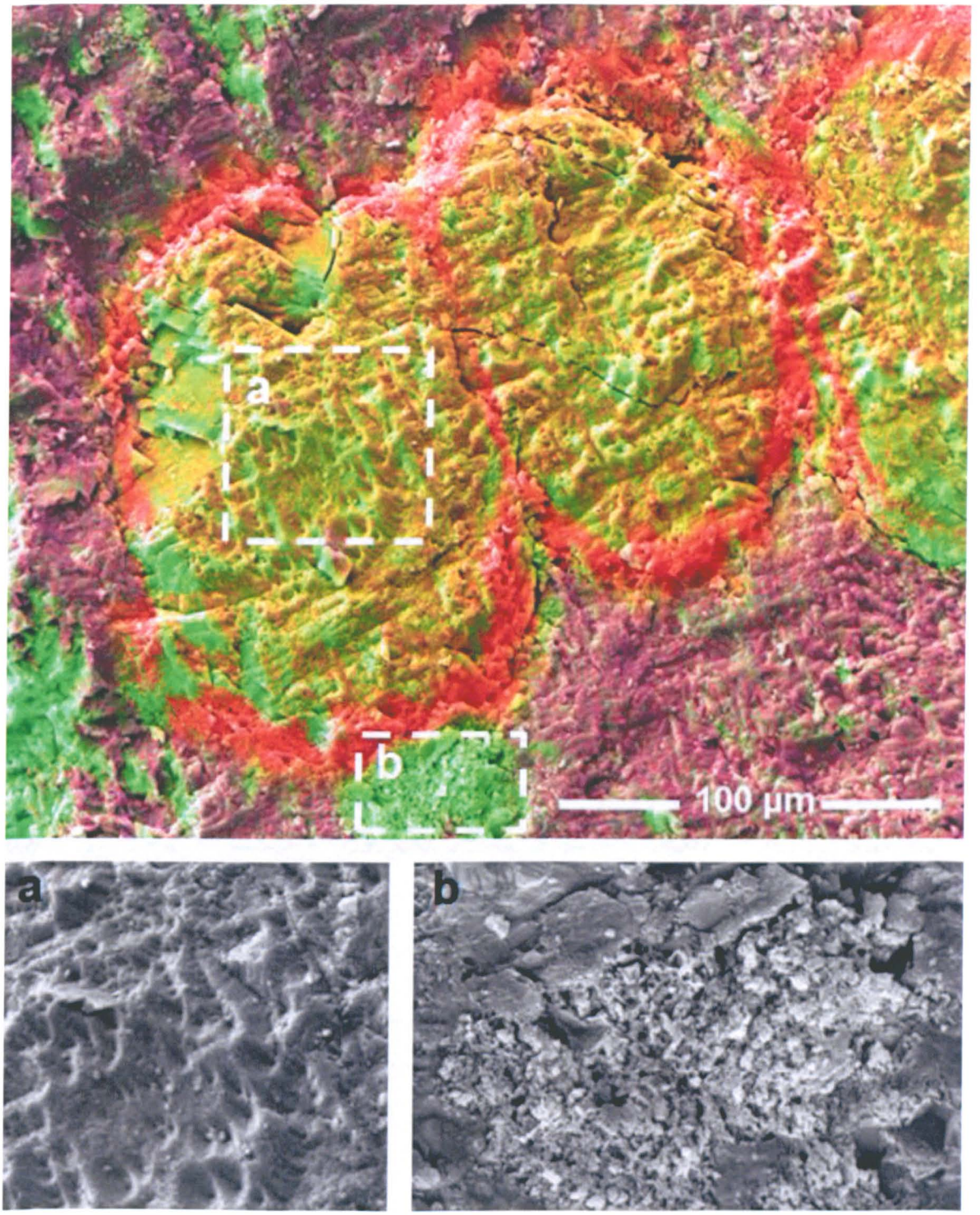

Figure 3.3 False coloured X-ray EDX map overlain on a SE image of two rosettes pre-FIB with Mg enrichments red, Fe – green and Si - blue. The dashed regions labelled (a) and (b) are shown at higher magnefication in the SE images below. Figure 3.3a an SE image of the pitted surface texture observed across magnesite and ankerite, identical to that noted by Thomas-Keperta et al. (2009). Figure 3.3b an

SE image of the fine grain patches of Fe-rich minerals such as pyrrhotite, pyrite, siderite and magnetite.

Evidence of mineral dissolution was observed on both fresh surfaces of carbonate and underlying orthopyroxene. The *'microdenticles'* in the orthopyroxene shown here (Fig. 3.4) and by Thomas-Keperta et al. (2009) show similarities to those found in terrestrially low-temperature aqueous alteration/weathered silicates such as pyroxene (Velbel 2007).

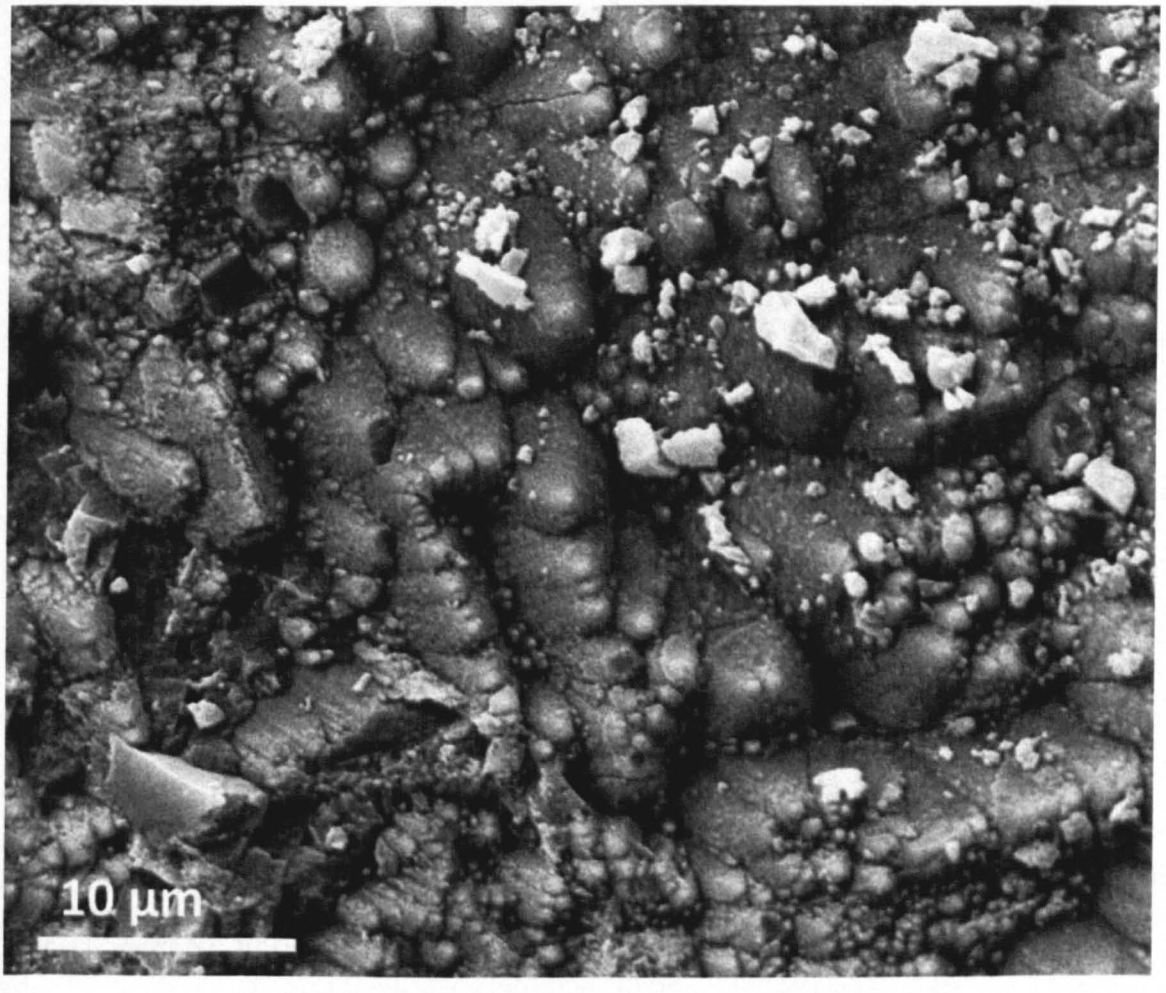

Figure 3.4 SEM image of micro-dentricular surface texture observed underneath the carbonate rossettes. Potential evidence of orthopyroxene dissolution as first noted in ALH 84001 by Thomas-Keperta et al. (2009).

The electron microprobe data (Fig. 3.5) represent molar abundances of $MgCO_3$, $CaCO_3$, $FeCO_3$ with a colour gradient for $MnCO_3$. The interior composition is the lower centre of the diagram representing the ankerite composition with the Mg-rich regions resulting from measurements of the magnesite rims.

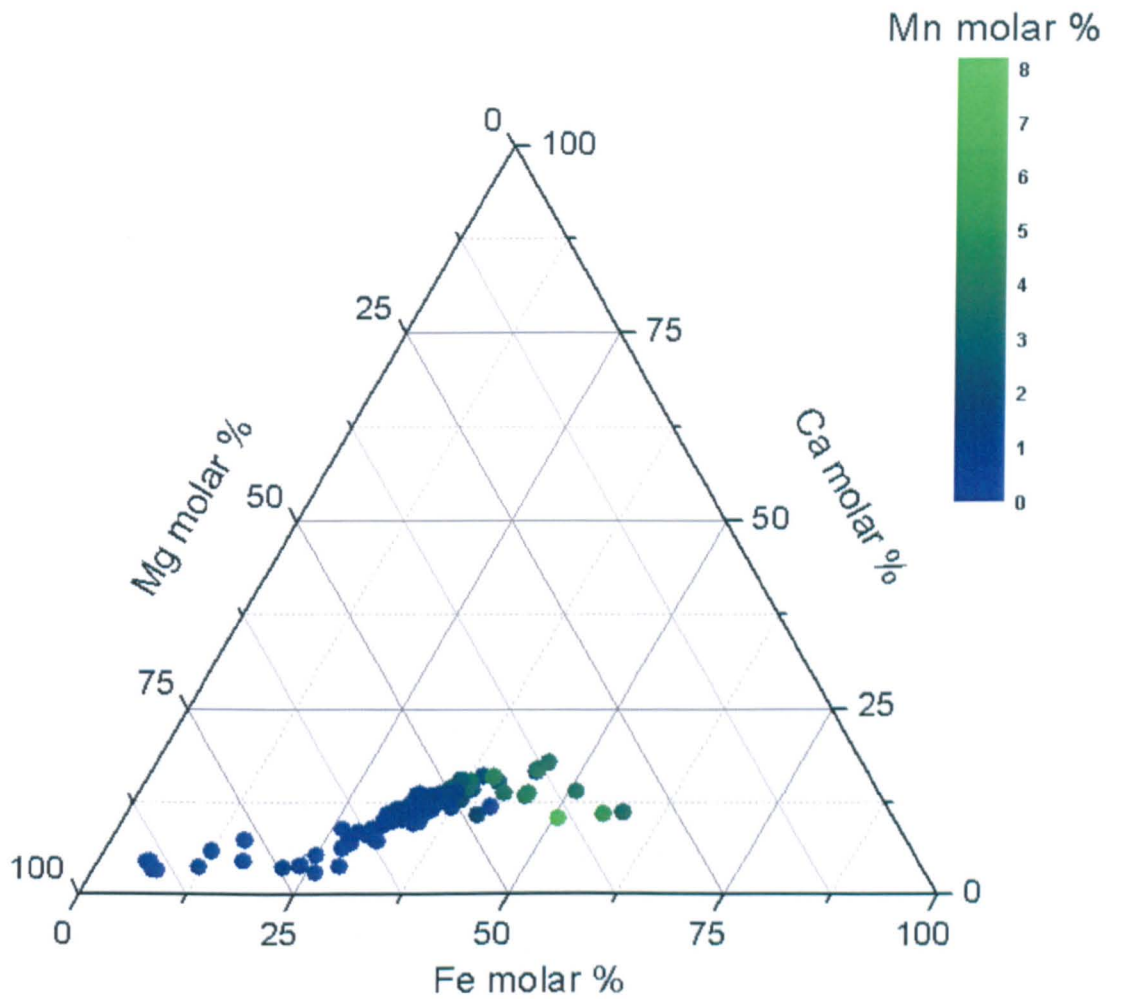

Figure 3.5 Ternary diagram of the major carbonate cations measured across two carbonate rosettes with a Cameca SX 100 electron microprobe (see Chapter 2.8).

3.3 Sample preparation

Measures were taken to reduce contamination by avoiding the use of resin, polishing materials and cleaning fluids. For this reason, thin sections were not used in this study.

Instead, a fresh ~5 mg grain from ALH 84001 split 126 was used. As the rosettes were heterogeneously distributed through the specimen, only a small surface of the overall split was found to be rich in carbonates. It was fractured into five pieces using applied pressure with a flat metal surface in a foil cup. The chip containing the largest quantity of rosettes (Fig. 3.1) was then partially inserted into Körapox resin with the rosette surface sitting proud (Fig. 3.6). The sample was then coated with 15 nm layer of gold using a K575X Turbo Sputter Coater. A further fracture was then required as it became clear that there was too much surface topography (>100 μm; Chapter 2.4.6; Kita et al., 2009) for NanoSIMS analysis. The scattered rosettes lying on a different plane to the clustered carbonates (Fig. 3.1) were removed and stored. A clean scalpel was used to make a 200 μm wide cut into the surface to separate the two planes (Fig. 3.6).

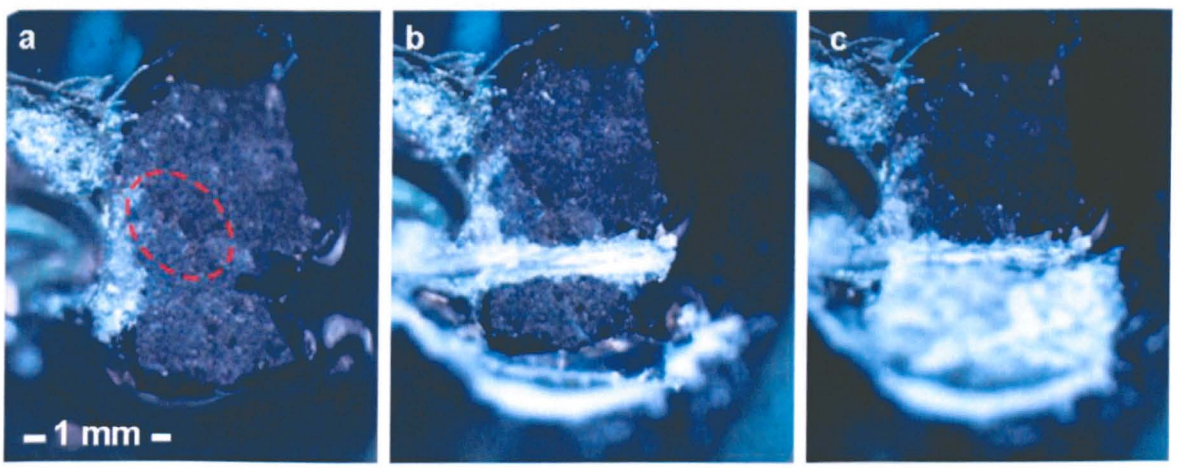

Figure 3.6 Reduction in topographic variability for NanoSIMS preparation, the scalpel cut was made just below nine carbonate rosettes (outlined with red dashes). Körapox resin (dark material) can be observed surrounding the top surface of the ALH 84001 split 126.

A FIB was used for the first time in martian isotopic studies to obtain a surface with <1 μm variation in topography for the NanoSIMS. This procedure was carried out using a FIB with a gallium source mounted at 52° to the tungsten filament scanning electron

microscope. The sample was mounted at a 50° axis that made it possible to FIB down the surface removing any topography (Fig. 3.7). The FIB was operated at 30 kV with a beam current of 1-5 nA. A trench approximately 50x2x100 μm^3 (x,y,z) was removed, leaving a smooth section through the middle of the rosette for NanoSIMS studies (Fig. 3.8).

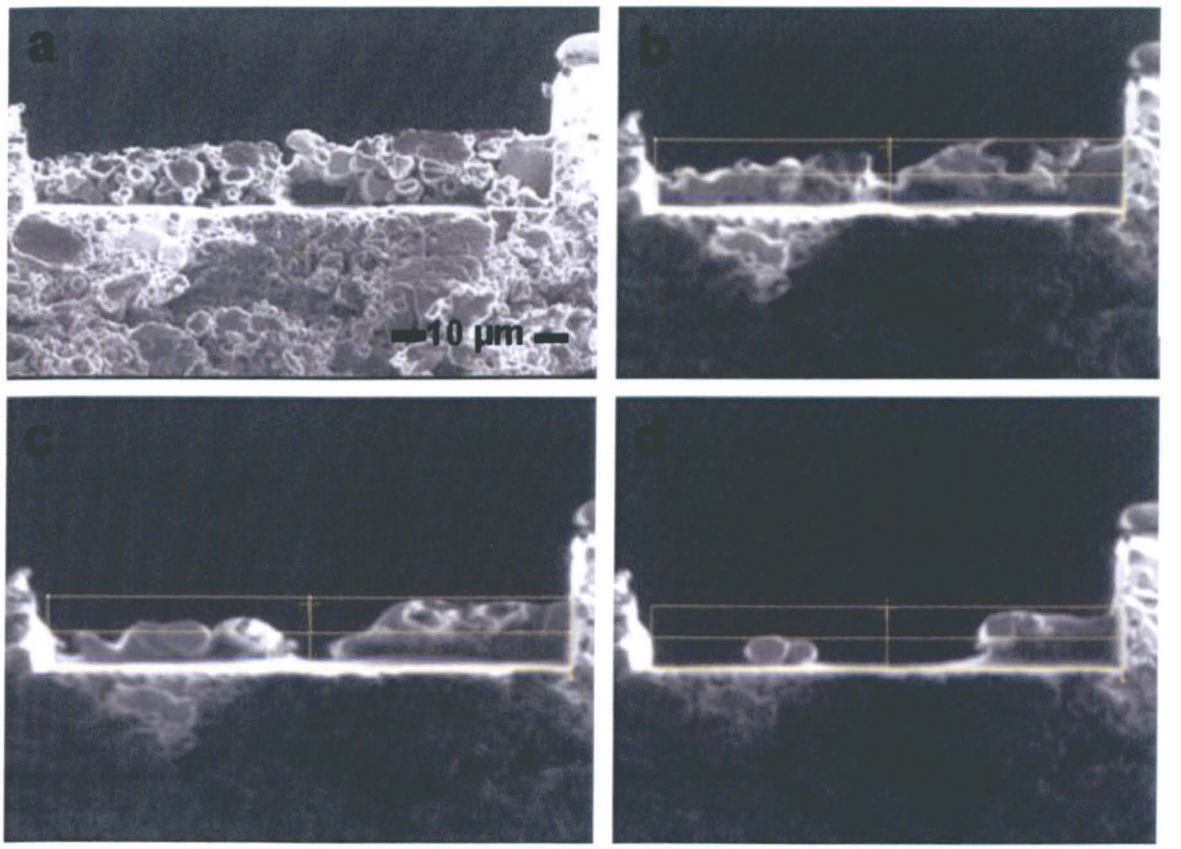

Figure 3.7 A side profile backscatter image of the Fe-sulphide and siderite material, Fig. 3.6a-d illustrating the removal of material across the top surface using a beam current for each step of 5 nA for 15 minutes at 30 kV.

An additional trench 30x4x100 μm^3 was formed at the top of the sample owing to the sample topography, this exposed a flat magnesite surface around the rim of the sample (Fig. 3.8a). Previous rosettes isotope studies have used epoxy and polish which are known to cause contamination affecting the isotopic values (Valley et al., 1997; Niles et al., 2005). In this study a FIB was used to achieve a flush surface (>1 µm) and avoid contamination.

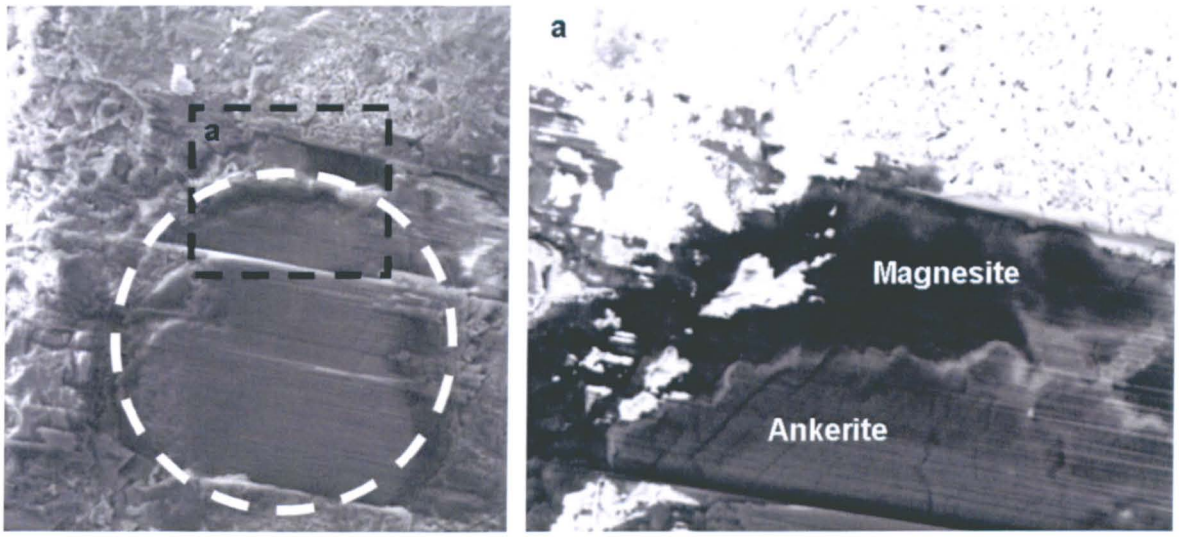

Figure 3.8 Backscatter image of a single rosette (white lines), the top surface smoothed with a FIB. 7a is a zoomed in image of area a ~80 μm across displaying clear boundary between the mineralogies and fractures suggestive of previous shock events.

3.4 NanoSIMS

3.4.1 Previous NanoSIMS work on carbonates

One previous example could be found in regard to high precision $\delta^{13}C$ carbonate studies with NanoSIMS. Guan et al. (2009) looked at carbonates within calcium-aluminium inclusions (CAIs) from the Murchison (CM) and Leoville (CV) carbonaceous chondrites. The carbonates viewed within Murchison were large 50x100 μm^2 calcite fragments and the well characterized Blue Angel altered hibonite inclusions containing 10-70 μm calcite grains. The Leoville calcite studied was in the form of narrow veins <10 μm. The NanoSIMS was a 50L ion microprobe, the beam size was 3x3 μm^2 with ~10 pA used to sputter the sample. $^{12}C^-$ and $^{13}C^-$ were detected simultaneously with EM's. Carbonate standards used to check matrix effects and IMF were calcite, dolomite, magnesite and siderite. Typical analytical errors were ~1-2‰ (1σ) for $\delta^{13}C$. IMF increased as a result of matrix effects across the carbonates by ~30‰ from calcite, dolomite, magnesite and siderite (Guan et al., 2009).

3.4.2 ALH 84001 carbonate $\delta^{13}C$ and $\delta^{18}O$ values from literature

There have been several investigations of the carbonate rosettes in ALH 84001 by ion microprobe (see Table 3.1). The studies all found a large range in isotopic compositions (~37‰ and ~34‰ variations in $\delta^{13}C$ and $\delta^{18}O$ respectively), indicating that a significant change in composition and/or fluid temperature must have occurred during formation. Studies of carbon and oxygen isotopes have been conducted on ALH 84001 carbonates using both bulk analysis and ion microprobes (Table 3.1). However, because of the small sizes of the rosettes (50-300 μm), few studies (Niles et al., 2005; Leshin et al., 1998; Saxton et al., 1998) have actually attempted to relate the mineralogical variations to isotopes. To rectify this, The Cameca NanoSIMS 50L has been used. This instrument combines submicron ion beam spot sizes with high sensitivity (see Chapter 2.2), making it an ideal analytical tool for studying isotope variations with alternating mineralogy.

Table 3.1 Summary of ALH 84001 carbonate isotope values from literature.

Summary of Isotopic Results from Carbonates in ALH 84001

Ion microprobe	**$\delta^{13}C$ (‰)**	**$\delta^{18}O$ (‰)**
Magnesite rims (overlapping)		
Valley *et al.* 1997		+20.6±1.3
Saxton *et al.* 1998		+22
Cores		
Valley *et al.* 1997	+36 to +55	+16.7±1.2 to +11.5±2.0
General structure		
Leshin et al. 1998		+5.4 to +25.3
Saxton *et al.* 1998		+7
Eiler *et al.* 2002		+1.7 to +26.9
Niles *et al.* 2005	+27 to +64	
Holland et al. 2005		-10 to + 24
Bulk (acid dissolution)		
Romanek *et al.* 1994	+39.5 to +40.2	+13.3 to +22.3
Jull *et al.* 1997	+32 to +40	+10 to +17
Farquhar *et al.*1998		+18.3±0.4
Bulk (stepped combustion)		
Grady *et al.* 1994	+40.1	
Wright et al. 1997	-61.8 to +4.2	
Jull *et al.* 1998	+32 to +40	

3.4.2.1 Carbon isotopes

The ion microprobe $\delta^{13}C$ measurements of carbonates in ALH 84001 vary from +27 to +64‰ (Valley et al., 1997; Niles et al., 2005). Studies using acid dissolution (Romanek et al., 1994; Jull et al., 1997) fall within this range, while stepped combustion of bulk material have lowered this range to -62‰ (Wright et al., 1997; Table 3.2). Two previous stepped combustion experiments fell within these values (Grady et al., 1994; Jull et al., 1995).

Table 3.2 Summary of ALH 84001 carbonate $\delta^{13}C$ values from literature. Values to left of dotted line have been associated with either terrestrial contamination or in some cases suggested as indigenous organics (see text below).

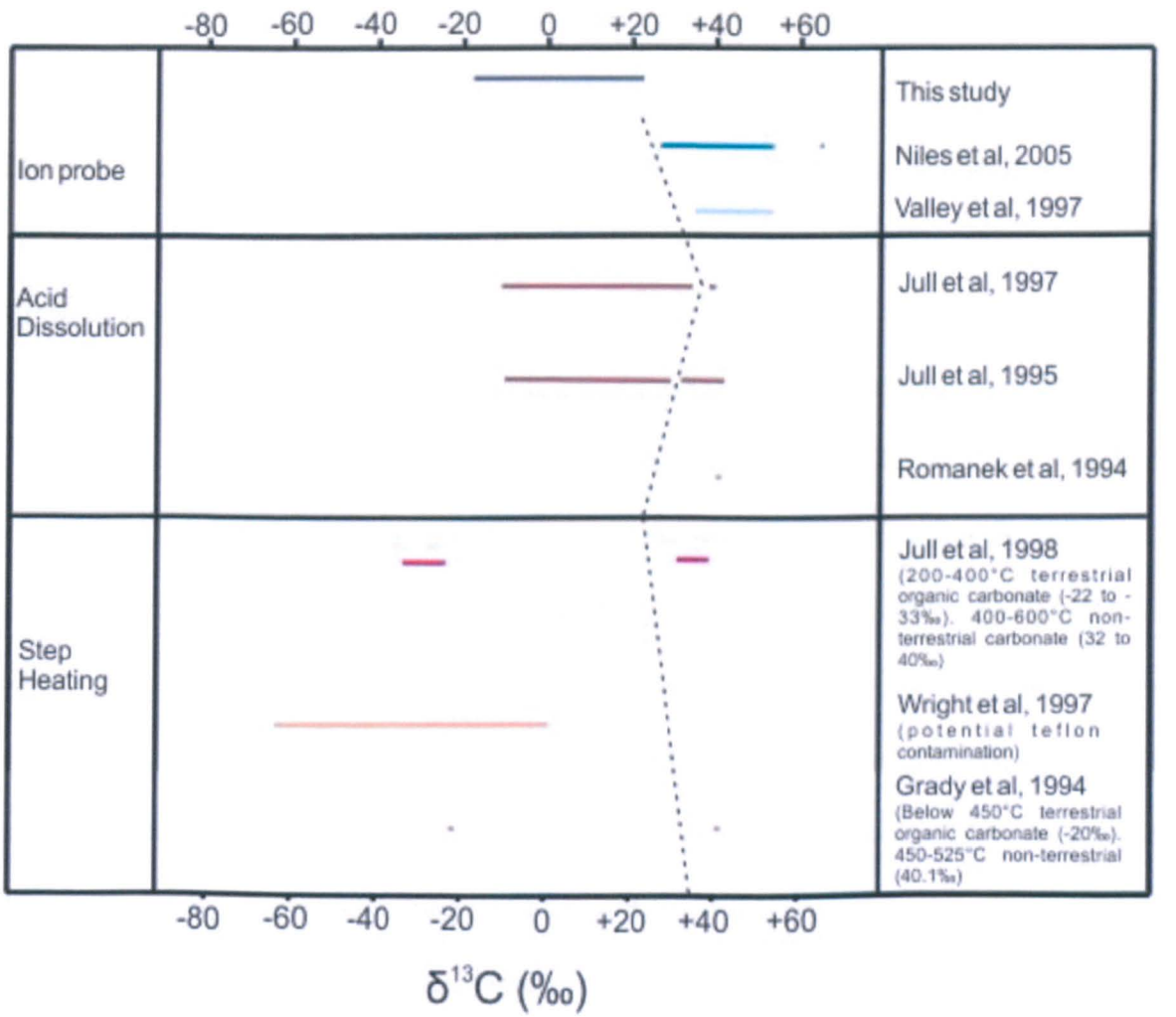

Grady et al. (1994) conducted the first $\delta^{13}C$ measurements on the ALH 84001 carbonates using stepped combustion on a whole rock sample. CO_2 released at temperatures <450°C had a $\delta^{13}C$ value of -21.5‰ and was surmised to correspond to terrestrial organic contamination. However, another $\delta^{13}C$ value of +40.1‰, recorded between 450-525°C was interpreted as the CO_2 released from the Fe, Mg-rich carbonate. Romanek et al. (1994) was one of only two authors (Niles et al., 2005) to link multiple isotopic and chemical compositions from $\delta^{13}C$ measurements of carbonate. The experiments were conducted using phosphoric acid on handpicked carbonate grains. A $\delta^{13}C$ value of +41.8‰ was obtained for the Mg-rich material which was calculated from the weighted means of CO_2 released between 4-24 hrs. The endmember isotopic composition was calculated assuming Ca, Fe-rich carbonates and first-order dissolution kinetics for the acid digestion process at +39.5‰. Both Grady et al. (1994) and Romanek et al. (1994) studies yielded similar values (~+40‰) using different methods. Furthermore, low $\delta^{13}C$ (-21.5‰) values were not obtained in the hand-picked carbonate samples suggesting organic contamination had limited coverage across the whole-rock samples.

Wright et al. (1997) significantly lowered the value range obtained from ALH 84001 $\delta^{13}C$ using a stepped heating experiment, obtaining values from +4.2 to -61.8‰ collected between 425-525°C. These unusually low values were obtained from 3 hand-picked carbonates that varied from orange to orange with speckled black. Issues of contamination from the Teflon container and/or a previous analysis on DuPont teflon foil were discussed and analysed reproducing similarly low $\delta^{13}C$ values (-47.4 to -58.5‰). However, it was also suggested that if these values are indigenous to the sample they could result from martian biological activity. Prior and subsequent experiments to this study have not found such low $\delta^{13}C$ values without scepticism of contamination.

Several papers published by Jull et al. (1995; 1997; 1998) have given a comprehensive overview for the sources of $\delta^{13}C$ and ^{14}C within the bulk ALH 84001 meteorite. In the first of these papers they confirm extraterrestrial enrichments of $\delta^{13}C$, they also observed carbonate that is terrestrial in origin existing within veins and cracks which was originally petrographically described by Mittlefehldt (1994). New measurements by Jull et al. (1997) extended this work and found similar results with short etch times corresponding to low $\delta^{13}C$ values and high ^{14}C (suggesting incorporation of terrestrial ^{14}C). These values took into account the inclusion of low levels of terrestrial ^{14}C providing a $\delta^{13}C$ range of +35.5 to +40.7‰.

It was also noted in the Jull et al. (1997) study that variations in terrestrial versus extraterrestrial components in different grain fractions are visible. The final paper by Jull et al. (1998) used stepped combustion using crushed and sieved bulk material. A large terrestrial component of ^{14}C (40-60%) and low values of $\delta^{13}C$ obtained -33 to -22‰ were released between 200 to 430°C (Jull et al., 1998). These are suggested to be derived from organic matter in agreement with Grady et al. (1994). Jull et al. (1998) measured a 32-40‰ $\delta^{13}C$ at higher temperatures (400-600°C) and a low terrestrial ^{14}C content. These $\delta^{13}C$ values agree with those observed by previous and subsequent authors (Grady et., 1994; Romanek et al., 1994; Valley et al., 1997 and Niles et al., 2005).

Jull et al. (1998) also verified Romanek et al. (1994) findings that there was heterogeneity in the carbonates' isotopic signature. A second combustion experiment on acid etched bulk ALH 84001 residue displayed low $\delta^{13}C$ values, -14.7 to -8.1‰, at temperatures associated with the release at 400-600°C of carbonate. While it is thought that this may represent an acid-insoluble carbonate phase or indigenous organics, it was favourably interpreted that these samples were similar to the Wright et al. (1997) suggestion of an organic terrestrial origin.

The variation in $\delta^{13}C$ requires a significant change in fluid composition and/or temperature during formation. However, because of the small size of the rosettes (50-300 μm), few studies have been able to relate micron-scale mineralogical variations with $\delta^{13}C$. Valley et al. (1997) took measurements of the orange-coloured, Fe-rich magnesites (called ankerite in this study) finding a core $\delta^{13}C$ value averaging near +46±8‰ (based on four measurements of +49, +36, +45, +55‰). The most recent $\delta^{13}C$ measurements of ALH 84001 (Niles et al., 2005) found enrichments of ~37‰ with increased magnesium content and order of crystallisation. The values obtained by Niles et al. (2005) revealed the first ion microprobe $\delta^{13}C$ values of the magnesite (+64‰) lay roughly ~20‰ higher than the next highest value of +41.8‰ found by Romanek et al. (1994). It must be noted that the magnesite typically forms as a small ~20 μm width layer around an ankerite core. The reduced $\delta^{13}C$ values could therefore be an average from a mixture of magnesite with ankerite in the hand-picked samples (Romanek et al., 1994; Wright et al. 1997), masking the true ^{13}C-enriched composition of Mg-rich carbonate.

3.4.2.2 Oxygen isotopes

The first measurements of $\delta^{18}O$ in ALH 84001 carbonates were conducted by Romanek et al. (1994) using acid dissolution (Table 3.3). They were the first to note a correlation between the ankerite and magnesite, similar to that observed in their carbon isotope data. They also noted a slight isotopic enrichment associated with Mg-content.

Table 3.3 Summary of ALH 84001 carbonate $\delta^{18}O$ values from literature.

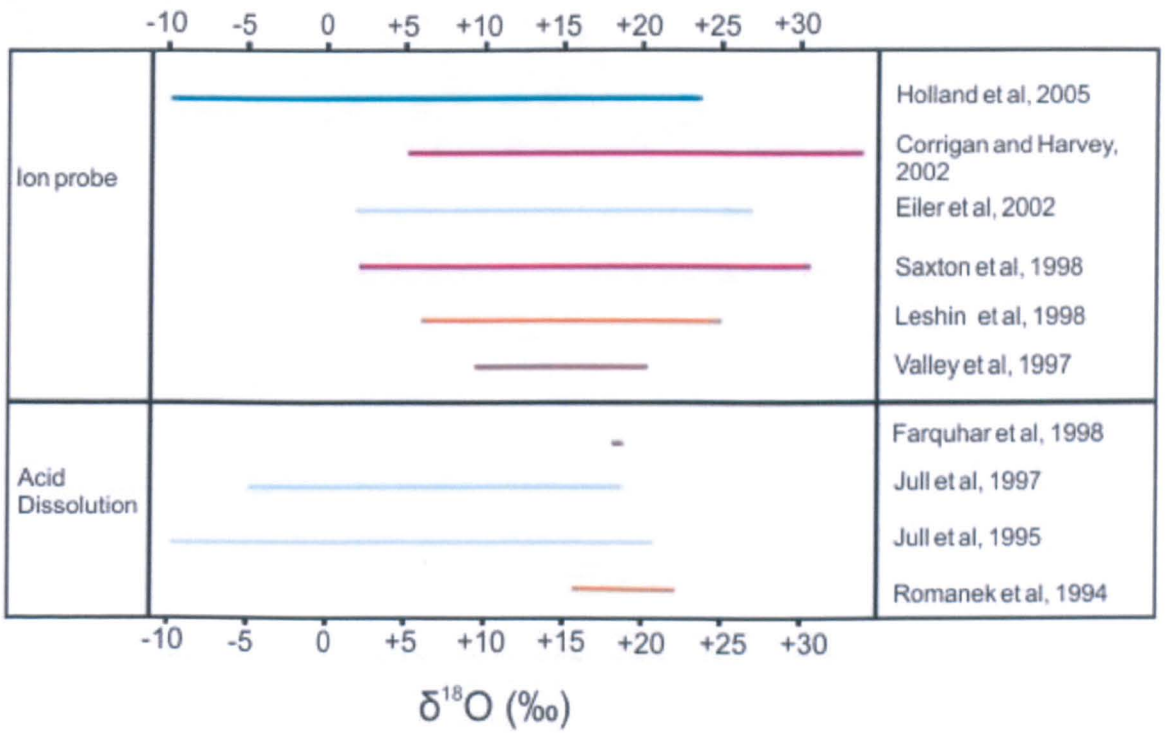

Studies by Leshin et al. (1998); Saxton et al. (1998) and Eiler et al. (2002) all found that the earliest forming carbonates were within the ankeritic carbonates (centre of rosette) with the lowest $\delta^{18}O$ values (~>+5.4‰). Meanwhile, the magnesite-rich material typically found on the outer rims of the rosettes was suggested to be the latest stage of growth with higher $\delta^{18}O$ values (~+25.3‰; Leshin et al., 1998). Furthermore, a direct link between the

Mg-content and $\delta^{18}O$ value was made by Leshin et al. (1998); Saxton et al. (1998); Eiler et al. (2002) and Holland et al. (2005) (Fig. 3.9).

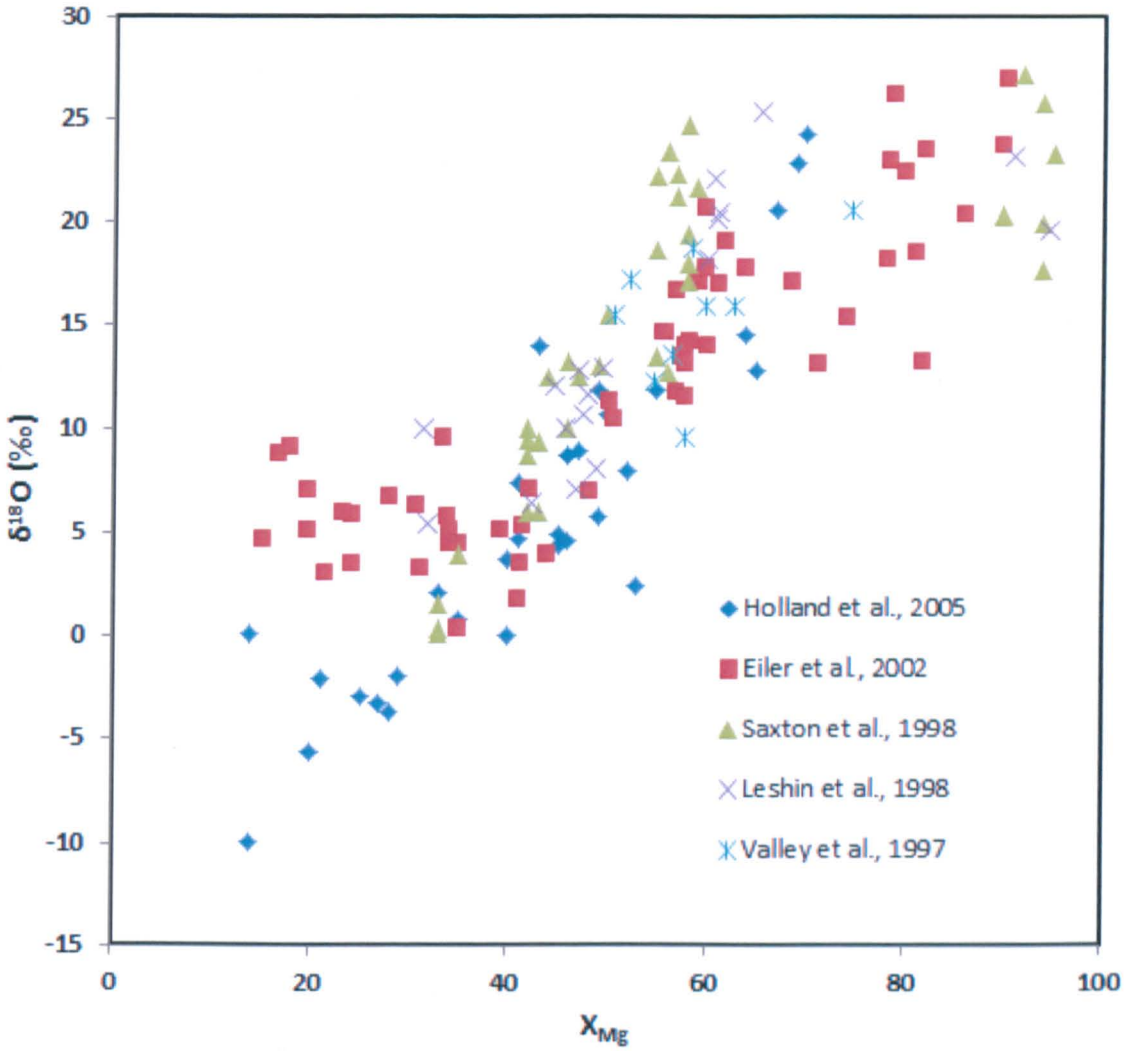

Figure 3.9 Data from previous ion microprobe studies on ALH 84001 carbonates where X_{Mg} represents Mg mole % found within the carbonate rosettes.

This correlation with Mg mole % (X_{Mg}) was not noted by Valley et al. (1997), their highest $\delta^{18}O$ value was associated with magnesite (+20.6‰; molar Mg content 74.7%; Fig. 3.8). However, values from the ankerite material varied between +9.5 to +18.7‰ and were not noted to correlate with molar Mg-contents (57.8% and 58.6% respectively). Even across the range of ankerite Mg-content (50.7% to 62.7%) little variation in $\delta^{18}O$ values were

observed; +15.5 to +15.9‰ respectively. However, as can be seen in Figure 3.9 these values fall within the range observed by other authors.

Corrigan and Harvey (2003) and Holland et al. (2005) examined Ca-rich carbonates which have been suggested to form under similar if not the same regime as the rosettes (Corrigan and Harvey. 2003) and found a larger $\delta^{18}O$ range. The isotopic compositions ranged from +4.2 to +34.7‰ (Corrigan and Harvey, 2003) and -10 to 0‰ (Holland et al., 2005) (Fig. 3.9). These studies were interesting, as they found a wider range of $\delta^{18}O$ values associated with different chemical composition. The study by Corrigan and Harvey (2003) discussed how these variations might imply that the fluid that formed the ALH 84001 carbonates was not present in large volumes (i.e. in an open system). Instead, it seemed possible that a closed system where individual pockets of different cation-enriched fluids could have produced the isotopic and chemical variations observed.

3.4.3 NanoSIMS Corrections

In order to determine accurately the isotopic composition of ALH 84001 with an ion microprobe, it is necessary to characterise the IMF of the instrument. This requires matching analyses of a sample with a standard of similar elemental composition. Unfortunately, with its unique and varying elemental composition, analysis of ALH 84001 harbours a challenge, as the ALH 84001 carbonate composition cannot be directly matched to terrestrial standards (see Chapter 2.5). The data from ALH 84001 were corrected using $\delta^{18}O$ and $\delta^{13}C$ values from

carbonate standards measured at the beginning and end of the analysis sessions with ankerite BM and siderite BM standards serving as checks.

3.4.3.1 IMF corrections for carbon isotopes

Valley et al. (1997) and Niles et al. (2005) used the same equation for isotope corrections.

$$\alpha_{SIMS} = \frac{\left({}^{13}C/{}^{12}C\right)_{SIMS}}{\left({}^{13}C/{}^{12}C\right)_{TRUE}} \quad (1)$$

Where α_{SIMS} is the instrument's correction factor, $({}^{13}C/{}^{12}C)_{SIMS}$ is the value taken by the ion probe and $({}^{13}C/{}^{12}C)_{TRUE}$ is the value from acid dissolution of material using a conventional gas bench system. A value of $\alpha_{SIMS}=1$ implies that there is no IMF.

Valley et al. (1997) found that the oxygen and carbon matrix correction varied non-linearly across the Ca-Mg junction but correlated well with the Fe molar % (X_{Fe} = Fe/(Fe+Mg+Ca+Mn) (for oxygen, $\alpha_{SIMS} = 0.968$ at $X_{Fe} = 100$ and $\alpha_{SIMS} = 0.927$ at $X_{Fe} = 0$ and for carbon $\alpha_{SIMS} = 0.956$ at $X_{Fe} = 100$ and $\alpha_{SIMS} = 0.932$ at $X_{Fe} = 0$; see Fig. 3.10). Niles et al. (2005) used the same IMF correction equation (α_{SIMS}) but applied the corrections according to X_{Mg} content. This inconsistency of correction method is also found within the literature for $\delta^{18}O$ values and is addressed in section 3.6.

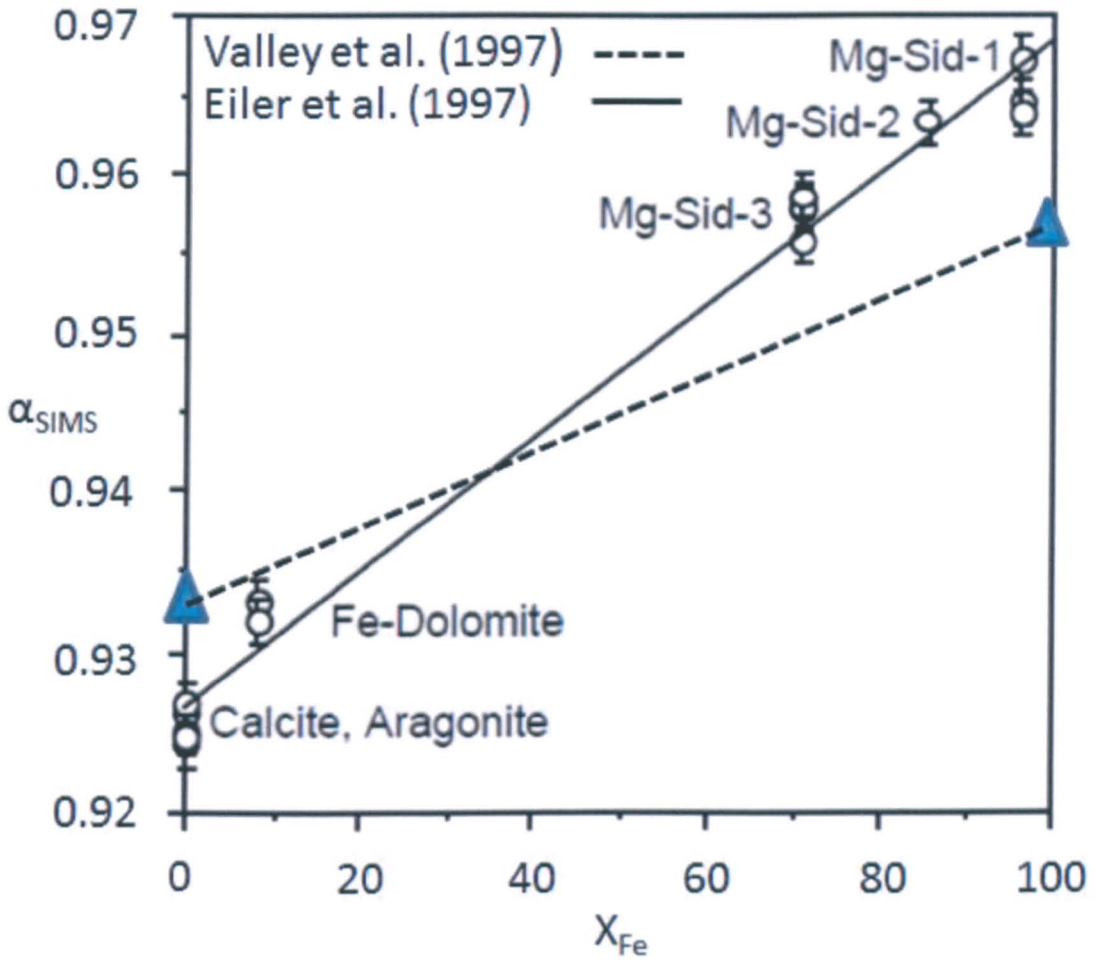

Figure 3.10 A demonstration of variations in IMF (α_{SIMS}) corrections based on standards plotted against X_{Fe} (Fe mole % in ALH 84001 rosettes), where values are obtained from Valley et al. (1997) (dotted line; based on two end-member values) and the remaining bold line and carbonate data values are from a linked study by Eiler et al. (1997).

The Valley et al. (1997) study found that during ion microprobe analysis, following initial steady count rates for carbon (within the first 1-4 μm sputtering depth) the counts increased and then dropped dramatically, indicating a decrease in $\delta^{13}C$ of ~50‰. Proposed hypotheses by Valley et al. (1997) as to why this occurred were either contamination or a change in mineralogy. The observed depth of these rosettes is only of the order of 10 μm (Thomas-Keprta et al., 2009) so it seems plausible that the second hypothesis, a change in

mineralogy, is more likely and that the rosette had been completely sputtered away by the ion beam.

3.4.3.2 IMF corrections for oxygen isotopes

The study by Leshin et al. (1998) found two different linear relationships in IMF with X_{Mg} for calcite-dolomite-magnesite and siderite-magnesite (Fig 3.11). They found no single correlation for all the materials, noting that there was no simple relationship between carbonate chemistry and IMF, even though the accuracy on the correction procedure for $\delta^{18}O$ ALH 84001 carbonates was better than 2‰. It was therefore suggested that small nonlinearities in the IMF should not affect the rosette measurements by more than ~2‰ (Leshin et al., 1998). In the following sections, results from my research demonstrate that this ~2‰ (Leshin et al., 1998) value is an underestimation (up to ~6‰) of the likely correction factor.

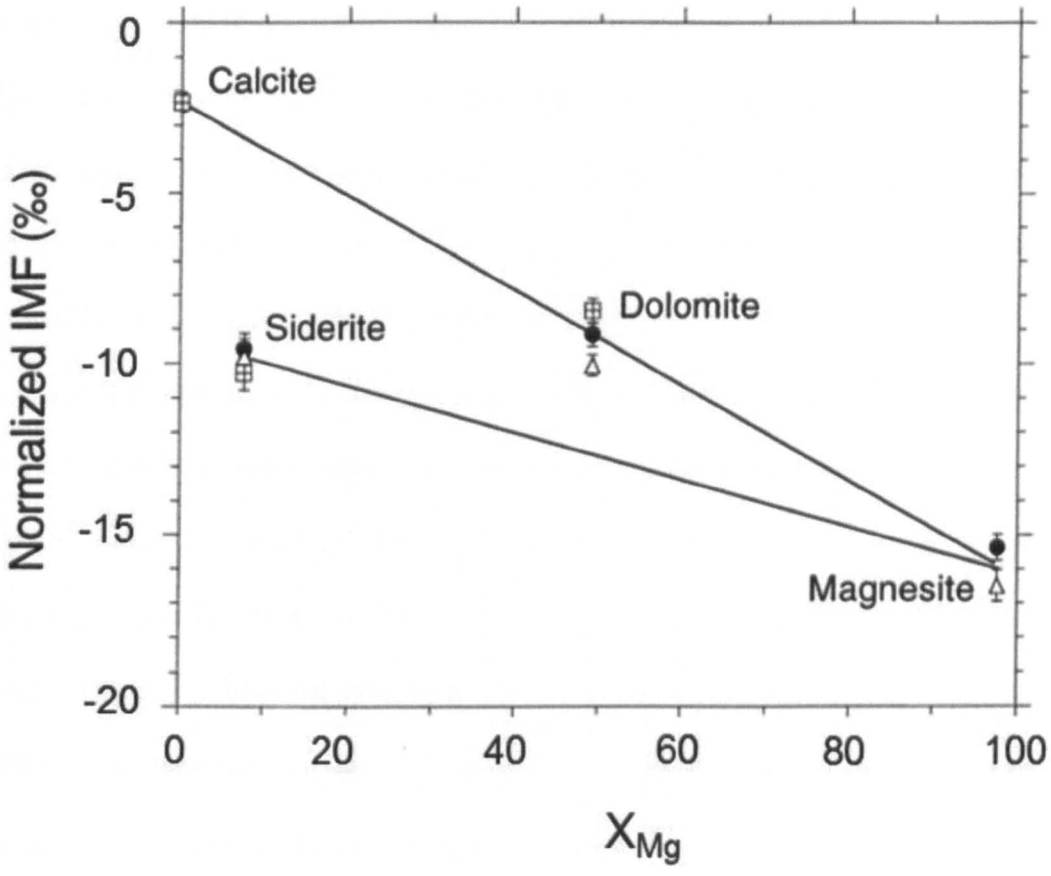

Figure 3.11 Plot from Leshin et al. (1998), where IMF values are normalized to calcite and each data point represents the weighted mean of ten measurements (with standard error). During the ALH 84001 data acquisition three standard analysis sessions were measured.

Saxton et al. (1998) applied a correction against the X_{Fe} content with $\alpha_{SIMS} = 0.956$ at X_{Fe}=100 and 0.932 at X_{Fe}=0 after finding a nonlinear relationship for IMF with Ca-Mg content in the Ca-Fe-Mg system. The large variations in correlation with compositional corrections led Saxton et al. (1998) to suggest that differences could be attributed to detection of different energy ions and/or charge neutralisation methods.

Riciputi and Greenwood (1998) conducted the most comprehensive study of carbonates to date in terms of sample quantity (20) and mineral variations (calcite, aragonite, siderite, rhodochrosite, witherite, strontianite, smithsonite, dolomite, magnesite and mid-

compositions). In their study they found that IMF for both oxygen and carbon was relatively well correlated with the X_{Fe+Mn} composition (Fig. 3.12) although some scatter existed but was typically related to Zn carbonate which is not relevant to analysis of ALH 84001; Zn carbonate was not included herein. A general correlation between a decrease in oxygen and carbon IMF and increasing atomic weight was discussed, but the trend was not constant and was mainly susceptible to Pb and Ba concentrations (again, carbonates of this composition were not examined in this study). The most revealing result related to the correlation of Mg, Ca, Fe and Mn carbonates to the X_{Fe+Mn} content and the oxygen and carbon IMF. This relationship was described as "not linear" and potentially open to significant errors, especially relating to Mg-enriched compositions. Riciputi and Greenwood (1998) also found positive correlations between α_{SIMS}, mean atomic weight, and the cps per nA of beam current. The α_{SIMS} correlation was shown to be similar to that observed in silicates.

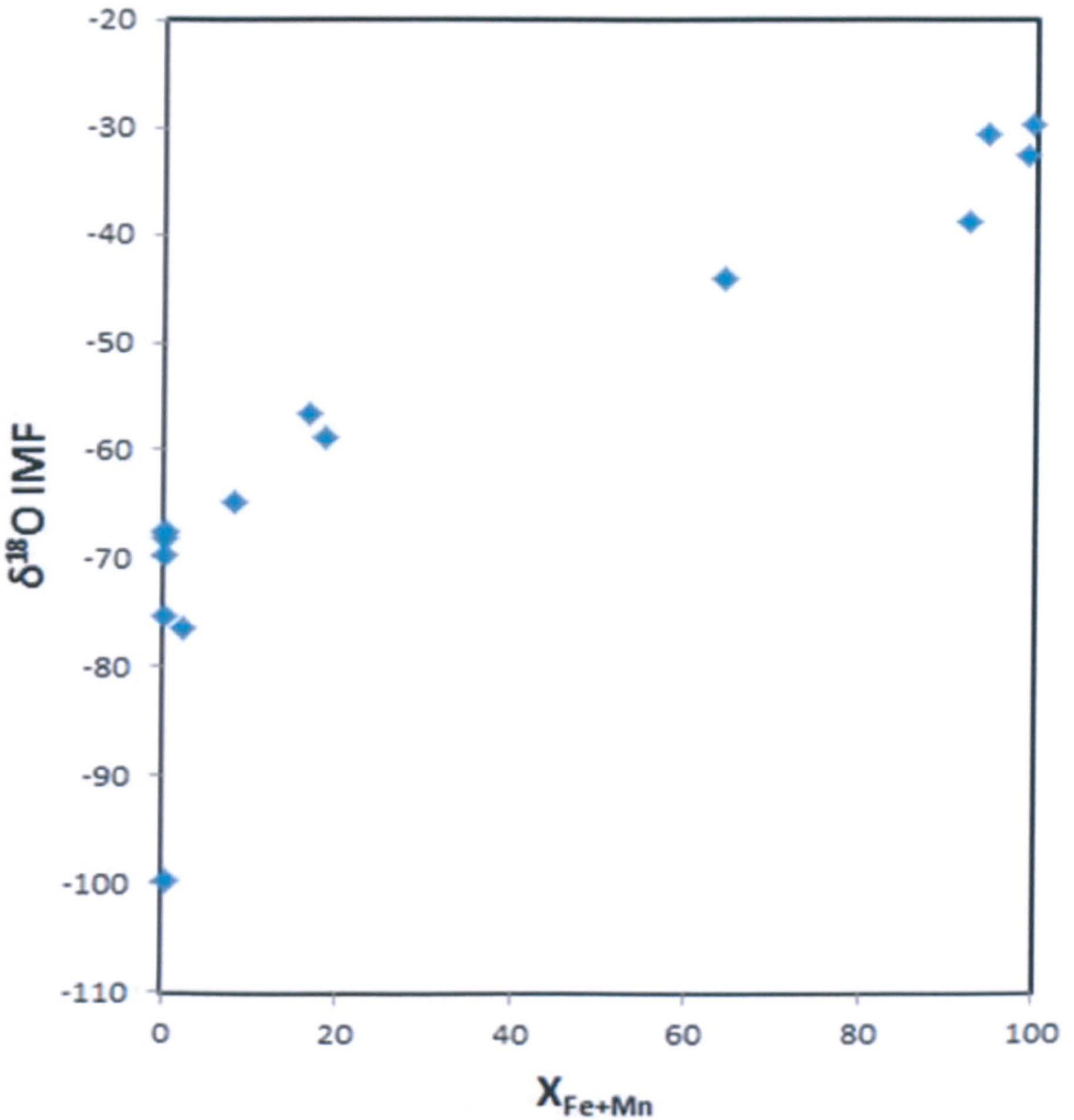

Figure 3.12 Data from Riciputi and Greenwood (1998) displaying $\delta^{18}O$ IMF corrections (‰) as a function of atomic proportion of X_{Fe+Mn} (mole %). Magnesite is the outlier from the dataset (bottom left).

Riciputi and Greenwood (1998) non-linear findings are in contrast to linear correlations interpreted from previous and subsequent literature relating to ALH 84001 (Table 3.4; Valley et al. 1997; Saxton et al. 1998; Eiler et al., 2002; Niles et al., 2005). These

results have interesting implications for corrections applied and the resulting effects on the reported $\delta^{18}O$ and $\delta^{13}C$ values for the ALH 84001 carbonates.

Table 3.4 Different IMF corrections observed by previous ion probe studies and number of Mg-Fe-Ca-Mn carbonate system standards.

Author	Correction	System	Correlation	No of standards
Valley et al. 1997	X_{Fe}	$\delta^{18}O$	Linear	9
Leshin et al. 1998	X_{Mg}	$\delta^{18}O$	Linear	4
Riciputi and Greenwood 1998	X_{Fe+Mn}	$\delta^{18}O$ and $\delta^{13}C$	Non linear	15
Saxton et al. 1998	X_{Ca}	$\delta^{18}O$	Linear	5
Eiler et al 2002	X_{Fe}	$\delta^{18}O$	Linear	9
Niles et al. 2005	X_{Mg}	$\delta^{13}C$	Linear	4
Holland et al. 2005	X_{Mg}	$\delta^{18}O$	Linear	5
This study	X_{Mg} and X_{Fe+Mn}	$\delta^{18}O$ and $\delta^{13}C$	Linear	14

3.5 Standards

3.5.1 Finnigan Advantage Mass Spectrometer (FAMS)

The true isotopic values for carbonate standards must be determined for NanoSIMS analyses. The values derived from the Finnigan Advantage Mass Spectrometer (FAMS) when combined with NanoSIMS analyses enable IMF corrections to be calculated for the standard carbonates. Therefore collecting these values from the FAMS is essential to determine the IMF corrections required to correct the isotopic values of the ALH 84001 carbonates. Fourteen standard carbonates samples were prepared using a hammer and pestle and mortar

to remove and grind three separate locations on each carbonate for analysis. Whole carbonate samples varied from 2x2x3 mm^3 to 5x4x3 cm^3 in size. In the case of the Smithsonian carbonates the samples were in grain form; typically three grains were used in each analysis. The FAMS was used to obtain values of $\delta^{13}C$ and $\delta^{18}O$ for the carbonate standards. These delta values were calibrated to a NIST 19 standard and a marble reference for V_{PDB} and V_{SMOW} values. Initial issues with the non-complete dissolution of siderite, dolomite and ankerite samples were resolved by moving samples to a heating block of 90°C (previously 70°C) for 6 hours before gas extraction. Any temperature fractionation factors were ignored as calcite samples values at both temperatures matched (within 0.1 ‰). Carbonate samples were run in triplicates in blocks of 40 samples and were interspaced with international standard NIST 19 and a marble internal house standard for calibration and corrections. A full list of standards used in this study can be found in Appendix A.

3.5.2 X-ray Diffraction (XRD)

XRD analyses were conducted to determine the purity/homogeneity of the carbonate standards. Analyses were performed at the Natural History Museum in London by Dr Kieran Howard. The X-Ray Diffractometer with an INEL curved position sensitive detector allowing x-rays to be collected across 120° of arc. Powdered carbonate samples (100 mg) were packed into a 1 mm deep circular aluminium well. These were then pressed and roughened with a spatula to produce randomness in the grain orientations (Howard et al., 2010).

The magnesite, siderite, calcite and dolomite samples all gave pure single phase results with only ankerite not showing a single phase. This is thought to be attributed to the ground sample being taken from a weathered surface.

3.6 Results

3.6.1 Standard compositions and true $\delta^{18}O$ and $\delta^{13}C$ values

The carbonate standards acquired for NanoSIMS corrections came from Edinburgh University (Edin) Scotland, UK, the Smithsonian Institution (SI), Washington, USA and the Natural History Museum (NHM), London. For all the standards, data were collected from Thermo-Finnigan DELTA Advantage mass spectrometer for $\delta^{13}C_{VPDB}$ and $\delta^{18}O_{SMOW}$ values (see section 3.5.1). Mineralogy analysis was conducted using XRD (NHM, UK; see section 3.5.2), EDX mapping (see section 2.2) and electron microprobe (see section 2.3).

Table 3.5 Standard composition, gas bench $\delta^{18}O$ and $\delta^{13}C$ values, associated errors (1σ) are ±0.6‰ and ±0.4‰ respectively. Compositions acquired via electron microprobe (see section 2.3). A full list of NanoSIMS values used for corrections can be found in Appendix B.

Mineral	Source	Sample No (name)	X_{Mg}	X_{Ca}	X_{Fe}	X_{Mn}	X_{Fe+Mn}	$\delta^{18}O$	$\delta^{13}C$
Magnesite	**NHM**	**BM**	98.9	1.1	0	0	0	23.4	-12.6
Dolomite	**SI**	**NMNH 10057**	49.7	50.2	0.1	0	0.2	12.9	-0.5
Dolomite	**NHM**	**BM**	49.2	50.6	0.1	0	0.2	25.1	2
Magnesite	**NHM**	**BM59199**	49.1	48.6	1.9	0.4	2.3	8.8	-5.3
Dolomite	**NHM**	**BM59191**	46.4	51.2	2.2	0.2	2.4	21.1	5.1
Dolomite	**NHM**	**BM1982**	46.3	47.3	6.1	0.2	6.3	20	0.1
Dolomite	**NHM**	**BM1917**	45.4	49.4	4.5	0.7	5.1	12.3	-3.7
Dolomite	**NHM**	**Dolomite Cornwall**	33.6	0.8	63.1	2.6	65.6	18.9	-11.9
Dolomite	**NHM**	**Ferroan Dolomite**	30.8	49.7	16.4	3.2	19.6	21.6	-0.7
Dolomite	**NHM**	**BM1990**	26.1	50.4	22.5	1	23.5	17	-10.1
Ankerite	**NHM**	**BM**	14.2	1.4	81	3.4	84.4	16.5	-8.4
Calcite	**Edin**	**LFC**	0.5	98.5	0.9	0.1	1	19	-1.7
Siderite	**SI**	**NMNH R2460**	0.4	0	95	4.5	99.5	8	-8
Siderite	**NHM**	**BM**	0.4	0	95.5	4.1	99.6	8	-7.9

Similar to studies by Niles et al. (2005) standards of rhodochrosite (pure $MnCO_3$) were not used owing to the low X_{Mn} observed in ALH 84001 (<8%) and the comparable effects of IMF correction to X_{Fe} similar to those observed for X_{Mn} (Riciputi and Greenwood 1998).

3.6.2 Oxygen IMF corrections

Resolving any potential correlations between the IMF corrections for the standards and their composition is essential in order to correct the ALH 84001 data. The carbonates studied here represent various chemical compositions and display a range of IMFs showing the difference between the measured $\delta^{18}O$ values from the NanoSIMS and the true gas bench measured $\delta^{18}O$ values (Table 3.6). These data are plotted against the molar % of Mg, Fe+Mn and Ca in the standards (Figs. 3.13-15). Each data point is the averaged value of five NanoSIMS measurements. The IMF errors (2σ) represent five analyses of each standard (the maximum observed error was 3.4‰).

Table 3.6 Carbonate IMF corrections for NanoSIMS 50L. Positive IMF values indicate ion probe measurements with greater $\delta^{18}O$ than the gas bench measured value. A full list of NanoSIMS values used for corrections can be found in Appendix B.

Mineral	Source	Sample No (name)	X_{Mg}	X_{Ca}	X_{Fe}	X_{Mn}	X_{Fe+Mn}	$\delta^{18}O$	Ave. δ_{IMF} Corr.	Stdev (1σ)
Magnesite	**NHM**	**BM**	98.9	1.1	0	0	0	23.4	-2.2	0.5
Dolomite	**SI**	**NMNH 10057**	49.7	50.2	0.1	0	0.2	12.9	6.5	0.9
Dolomite	**NHM**	**BM**	49.2	50.6	0.1	0	0.2	25.1	8.2	0.9
Magnesite	**NHM**	**BM59199**	49.1	48.6	1.9	0.4	2.3	8.8	11.9	0.6
Dolomite	**NHM**	**BM59191**	46.4	51.2	2.2	0.2	2.4	21.1	10	1.7
Dolomite	**NHM**	**BM1982**	46.3	47.3	6.1	0.2	6.3	20	12.6	1
Dolomite	**NHM**	**BM1917**	45.4	49.4	4.5	0.7	5.1	12.3	13.6	0.7
Dolomite	**NHM**	**Dolomite Cornwall**	33.6	0.8	63.1	2.6	65.6	18.9	3.8	0.8
Dolomite	**NHM**	**Ferroan Dolomite**	30.8	49.7	16.4	3.2	19.6	21.6	15.7	0.4
Dolomite	**NHM**	**BM1990**	26.1	50.4	22.5	1	23.5	17	18.9	1
Ankerite	**NHM**	**BM**	14.2	1.4	81	3.4	84.4	16.5	8.9	0.8
Calcite	**Edin**	**LFC**	0.5	98.5	0.9	0.1	1	19	15.9	0.6
Siderite	**SI**	**NMNH R2460**	0.4	0	95	4.5	99.5	8	9.2	0.8
Siderite	**NHM**	**BM**	0.4	0	95	4.1	99.6	8	13.3	0.9

Figure 3.13 shows a trend between 25-50 % X_{Mg} with only ankerite and dolomite cornwall falling off this trend. Pure magnesite has the lowest IMF correction as observed in previous studies (Riciputi and Greenwood 1998; Leshin et al., 1998; Saxton et al., 1998 and Eiler et al., 2002).

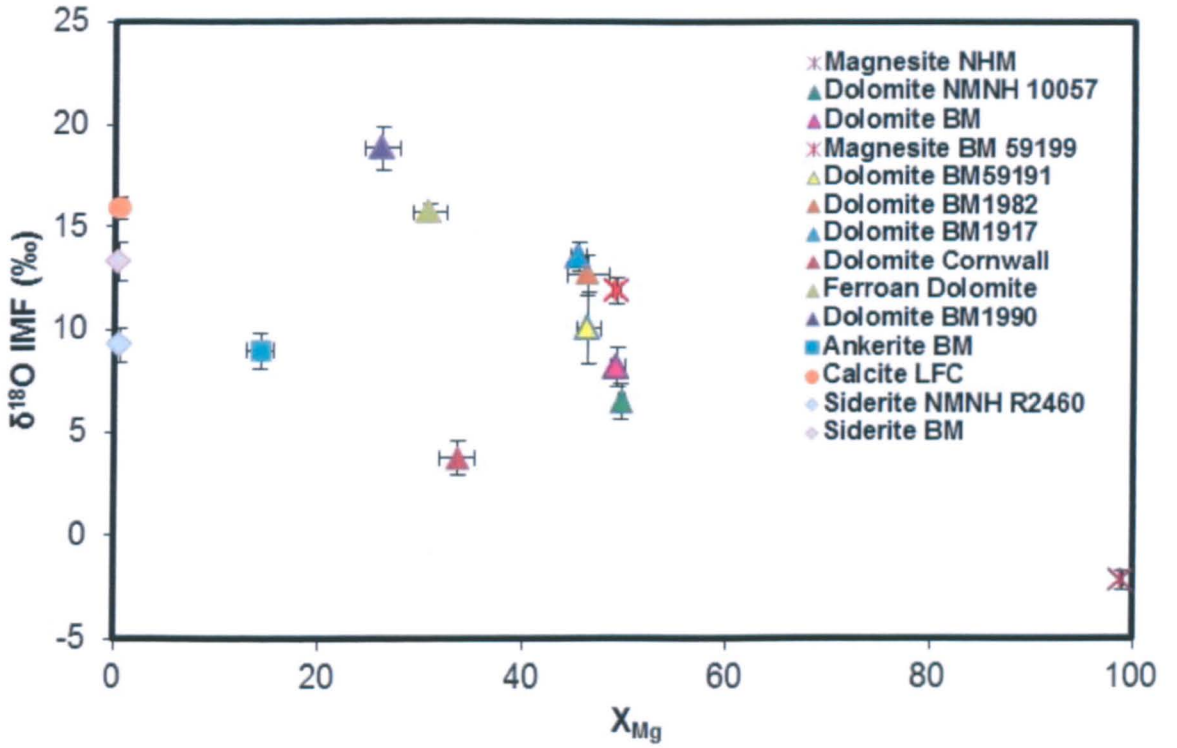

Figure 3.14 $\delta^{18}O$ Standard IMF corrections for X_{Mg}.

In Figure 3.14 there appears to be a large range in IMF corrections at each specific Ca content. This suggests that more than X_{Ca} content alone is responsible for the variation in the IMF correction.

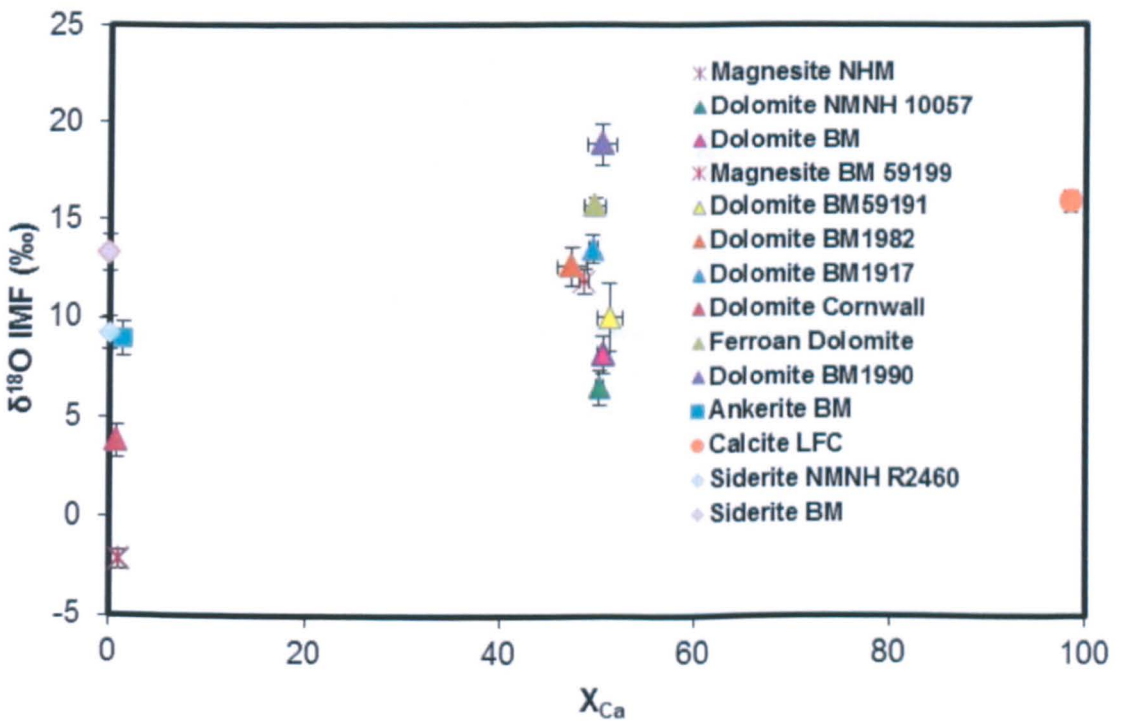

Figure 3.15 $\delta^{18}O$ standard IMF corrections for X_{Ca}.

There seems to be a distinct correlation between increasing Fe+Mn content and the highest IMF correction (Fig. 3.15). This relationship is not a linear relationship as can be observed within the first 24% X_{Fe+Mn} which displays an exponential trend as observed by Riciputi and Greenwood (1998). This exponential trend does not continue across the X_{Fe+Mn} content in a single curve as observed by Riciputi and Greenwood (1998) but appears to have an offset for the final 34% X_{Fe+Mn} with a more linear relationship observed between with IMF and X_{Fe+Mn} (Fig. 3.15). Unfortunately, we were unable to acquire a carbonate with X_{Fe+Mn} between 23.5 to 65.6%, so we do not know how the IMF would change across this X_{Fe+Mn} molar fraction.

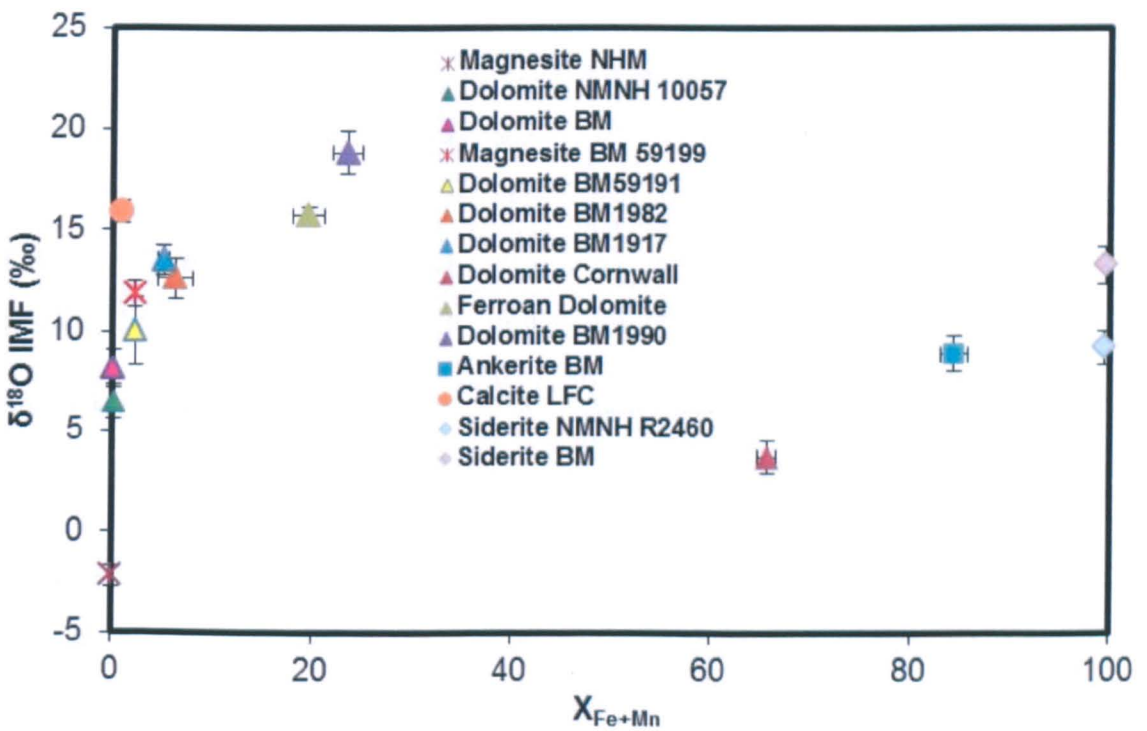

Figure 3.15 $\delta^{18}O$ standard IMF corrections for X_{Fe+Mn}.

3.6.3 Carbon IMF corrections

The $\delta^{13}C$ measurements appear to have less relationship with the mineralogical composition compared to the $\delta^{18}O$ values (Table 3.7).

Table 3.7 Carbonate IMF corrections for 50L NanoSIMS. Positive IMF values indicate ion probe measurements with greater $\delta^{13}C$ than the corrected gas bench measured value (Appendix A and B).

Mineral	Source	Sample No (name)	X_{Mg}	X_{Ca}	X_{Fe}	X_{Mn}	X_{Fe+Mn}	$\delta^{13}C$	Ave. $\delta_{IMF.}$ Corr.	Stdev (1σ)
Magnesite	**NHM**	**BM**	98.9	1.1	0	0	0	-12.6	-37.5	0.5
Dolomite	**SI**	**NMNH 10057**	49.7	50.2	0.1	0	0.2	-0.5	-35.6	1.1
Dolomite	**NHM**	**BM**	49.2	50.6	0.1	0	0.2	+2	-37.8	1.5
Dolomite	**NHM**	**BM59191**	46.4	51.2	2.2	0.2	2.4	+5.1	-33.8	1.7
Dolomite	**NHM**	**BM1982**	46.3	47.3	6.1	0.2	6.3	+0.1	-36.8	2.0
Dolomite	**NHM**	**BM1917**	45.4	49.4	4.5	0.7	5.1	-3.7	-36.3	0.9
Dolomite	**NHM**	**Dolomite Cornwall**	33.6	0.8	63.1	2.6	65.6	-11.9	-56.2	1.7
Dolomite	**NHM**	**Ferroan Dolomite**	30.8	49.7	16.4	3.2	19.6	-0.7	-37.6	0.9
Dolomite	**NHM**	**BM1990**	26.1	50.4	22.5	1	23.5	-10.1	-37.2	0.8
Ankerite	**NHM**	**BM**	14.2	1.4	81	3.4	84.4	-8.4	-55.8	0.7
Calcite	**Edin**	**LFC**	0.5	98.5	0.9	0.1	1	-1.7	-35.3	0.5
Siderite	**SI**	**NMNH R2460**	0.4	0	95	4.5	99.5	-8	-51.4	0.6
Siderite	**NHM**	**BM**	0.4	0	95.5	4.1	99.6	-7.9	-54.9	0.9

Figures 3.16-18 show two distinct patterns, the Fe+Mn-rich carbonates (siderite BM and NMHM 10057, ankerite BM and Cornwall dolomite BM) record the lowest IMF correction values (~55‰), with all the other carbonates measuring ~20‰ higher IMF values (-35‰).

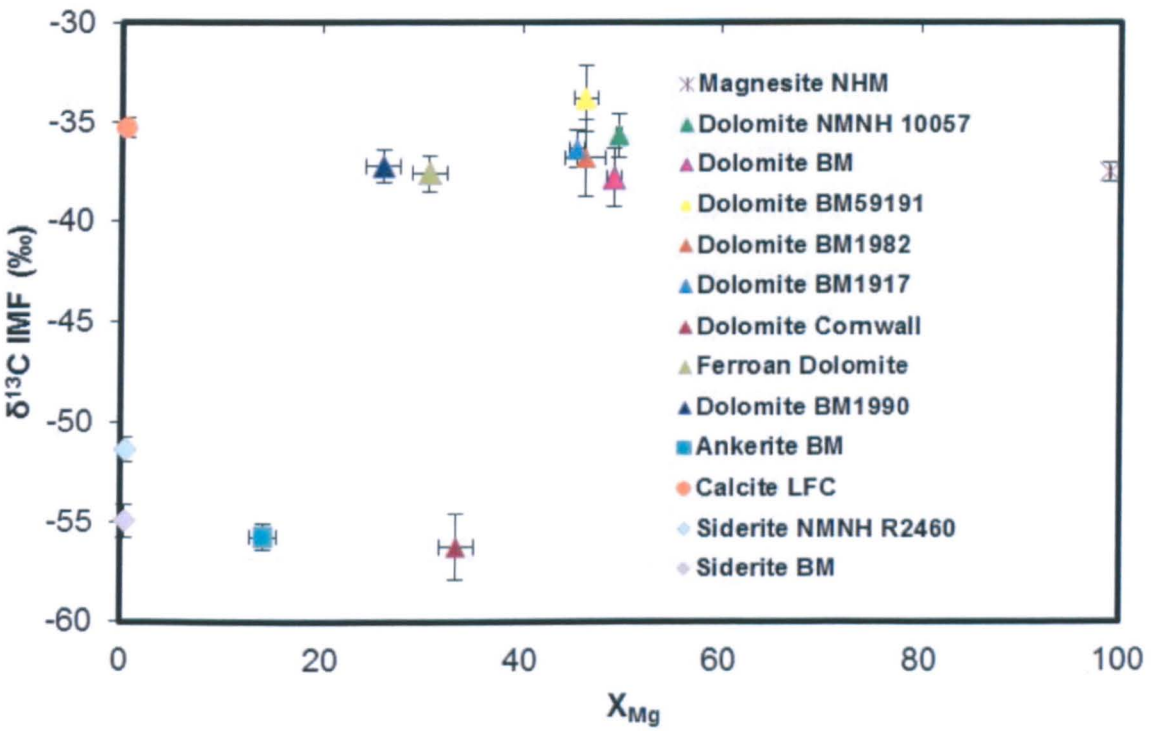

Figure 3.16 $\delta^{13}C$ standard IMF corrections for X_{Mg}.

The difference between the two lines of standards is ~20‰, this variation is lower than that observed by Guan et al., 2009 (~30‰), however, these differences may relate to the standards used or the setup of the NanoSIMS (e.g. 10 pA, Guan et al., 2009; 15 pA this study). Regardless, these variations in the IMFs from the standards emphasise the importance of applying the correct IMF correction.

With the exception of dolomite BM59191 (-33.8‰) and dolomite BM (-37.8‰) all of the X_{Fe+Mn} depleted carbonates plot within ~4‰ of each other (Fig.3.17). There is potentially

a trend in the data for X_{Fe+Mn} content (Fig. 3.17) and IMF but again, as for the oxygen plot, without data between X_{Fe+Mn} of 23.5 to 65.6% this cannot be confirmed.

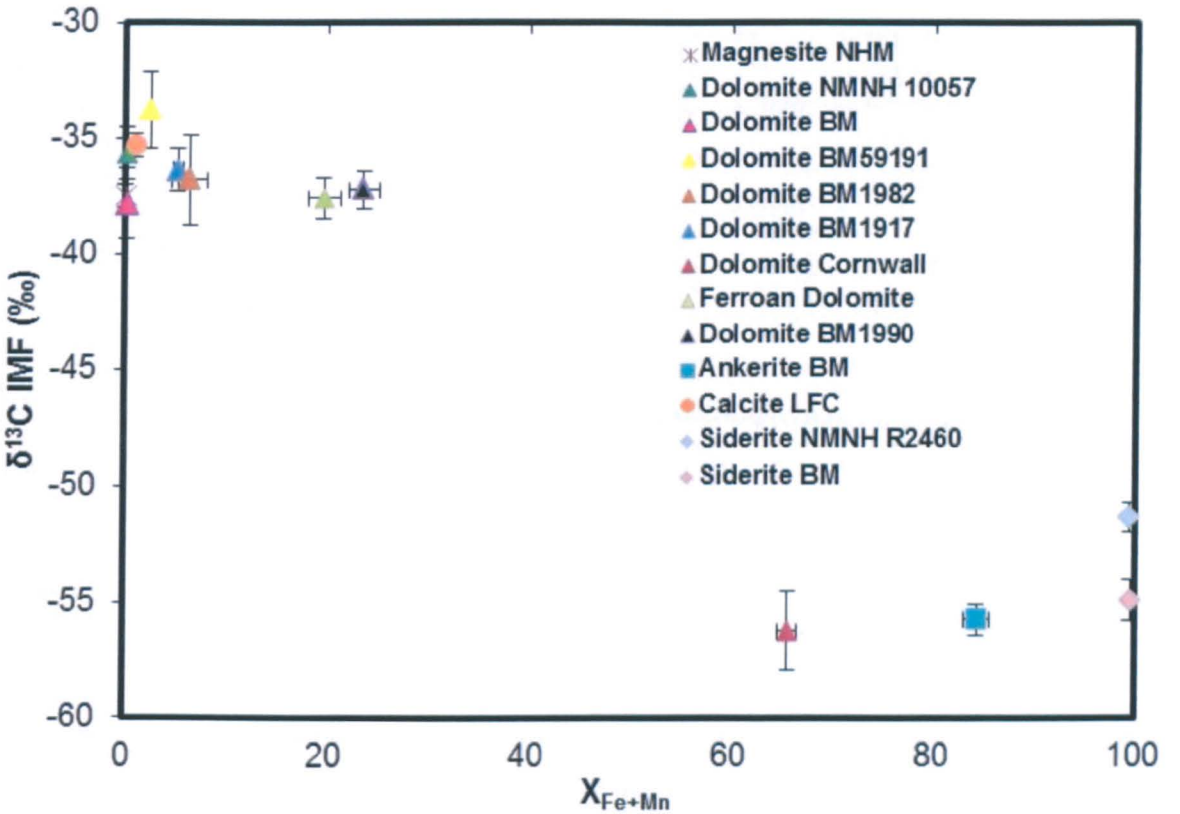

Figure 3.17 $\delta^{13}C$ standard IMF corrections for X_{Fe+Mn}.

Similarly to carbon IMF with X_{Mg} (Fig. 3.18) there appears to be no single correlation for X_{Ca} content (Fig. 3.18). There are potentially three lines of corrections with the Mg-Ca mixing line and either a straight Fe-Ca line or a non-linear line through the Fe-dolomite-Ca.

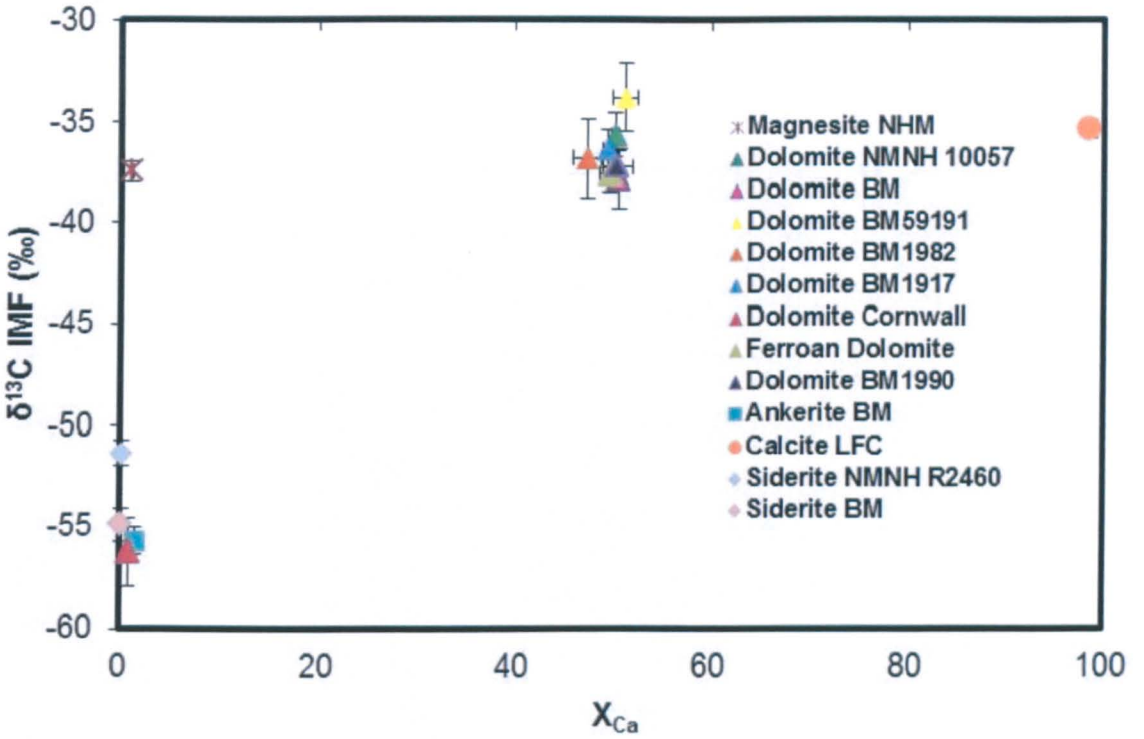

Figure 3.18 $\delta^{13}C$ standard IMF corrections for X_{Ca}

3.6.4 Sites of analysis

A key part of this study was the analyses of carbon and oxygen isotopic composition across two carbonate rosettes (Figs. 3.19-20).

Following NanoSIMS analyses the sites were analysed with the electron microprobe to determine each site's composition (see Chapter 2.3). The FIB was used to reduce the quantity of surface gold present around the analyses pits for recoating with carbon. Removing the gold with a FIB was an extra precaution as the electron microprobe beam spot size could focus in on each analysis pit (Fig. 3.21). In addition, the excitation volume of the electron beam meant that most of the analysed material existed beneath the top surface. Once the sample had been cleaned with the FIB it was recoated with a 15 nm layer of carbon. Freshly polished standards were coated at the same time to ensure equal coatings for electron

microprobe analyses. These measurements had to be completed after the sample had been analysed to avoid $\delta^{13}C$ contamination from the carbon coating.

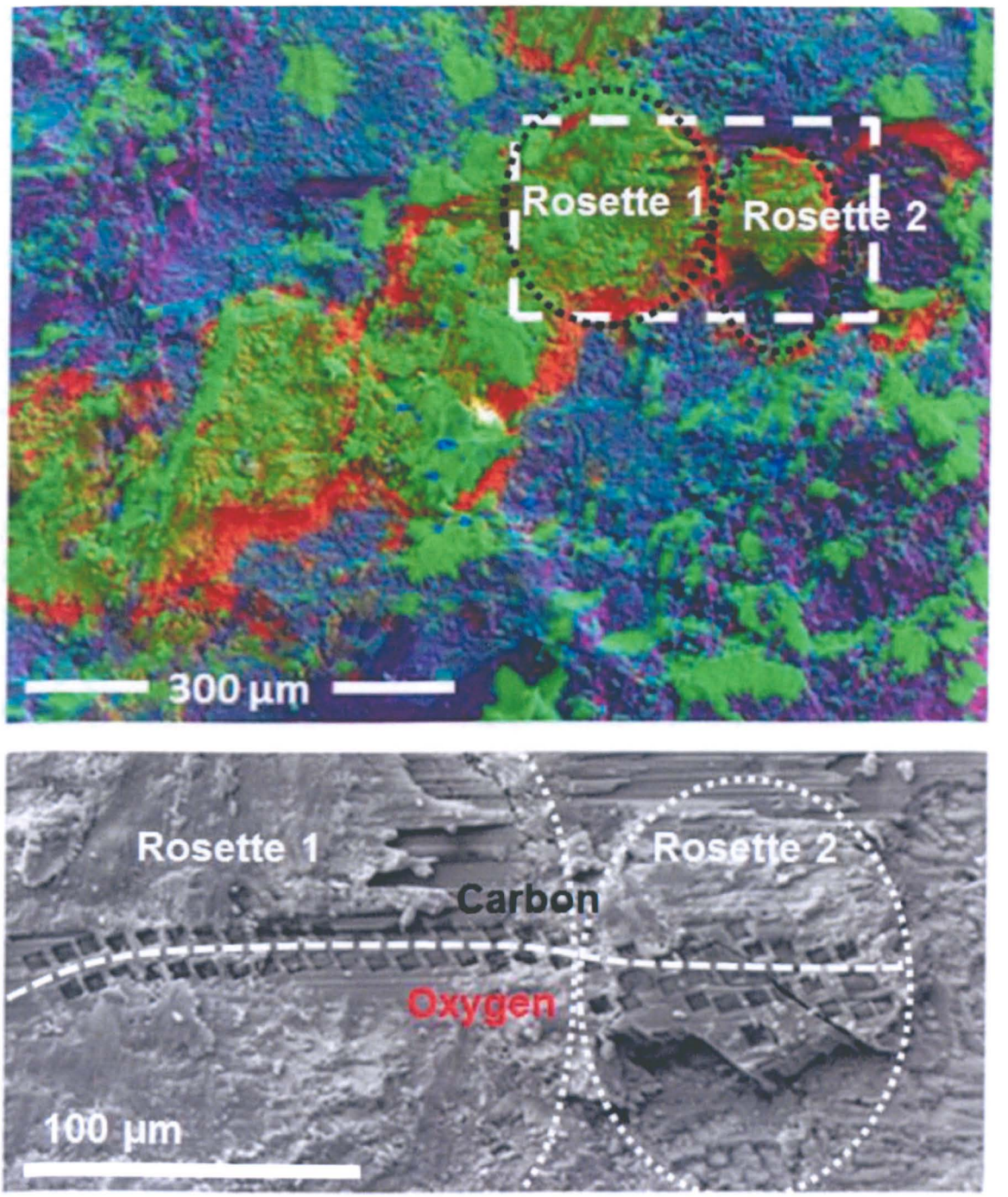

Figures 3.19-20 Rosette overview with false coloured image after FIB preparation (Mg enrichments are red, Fe – green and Si – blue). Figure 3.20 BSE image displaying points of 5x5 μm^2 NanoSIMS spot analysis with the dotted horizontal line representing border between the carbon and oxygen analyses.

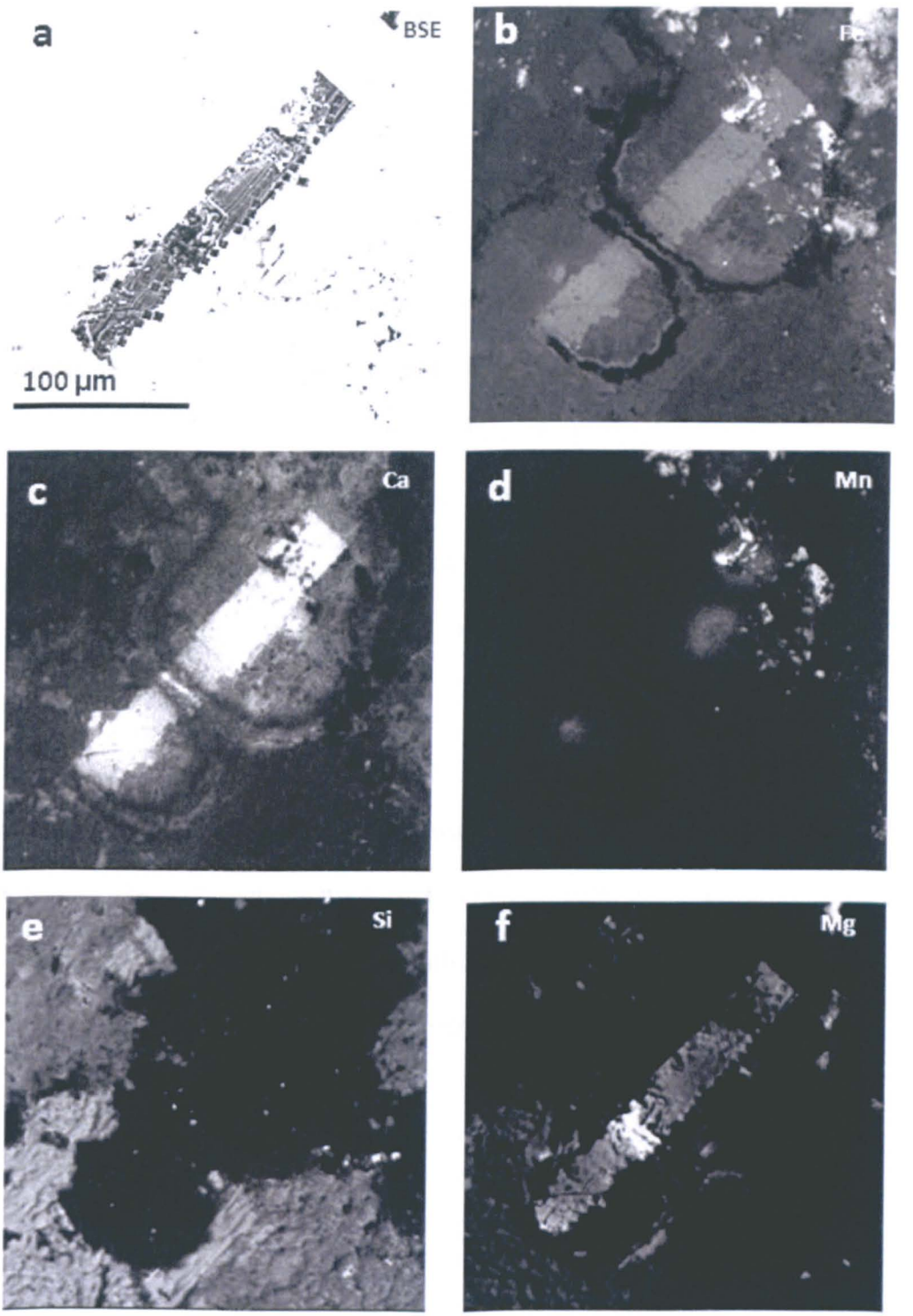

Figure 3.21 Backscatter image (BSE) and electron microprobe maps of Fe, Ca, Mn, Si and Mg element enrichments. The maps clearly show how the NanoSIMS analyses traverse across two ankerite cores and two rims of magnesite.

3.6.5 Oxygen results with corrections applied from Instrumental Mass Fractionations

In sections 3.6.2 and 3.6.3, data were plotted to show the range in isotopic composition of specific standards relative to their elemental composition. Knowing the composition of the carbonate in ALH 84001 (section 3.6.4), it is now possible to select the most appropriate suite of standards against which to correct the ALH 84001 data. All the possible candidate corrections are given in Appendix B, from there, two candidate trend lines were selected, based on X_{Mg} for $\delta^{18}O$ IMF corrections. These trends were 1) using data based on the same standards as Leshin et al., 1998 and 2) all carbonate data from this study which incorporate a larger suite of standards.

The same IMF correction procedure described by Leshin et al. (1998) and Valley et al. (1997) were applied for this section using only four of fourteen carbonate standards (Figs. 3.22-23). These corrections were used so that the isotope compositions of carbonates in ALH 84001 could be directly compared with results from other studies using the same carbonate compositions and applying similar corrections (Leshin et al., 1998; Saxton et al., 1998; Eiler et al., 2002 and Holland et al., 2005).

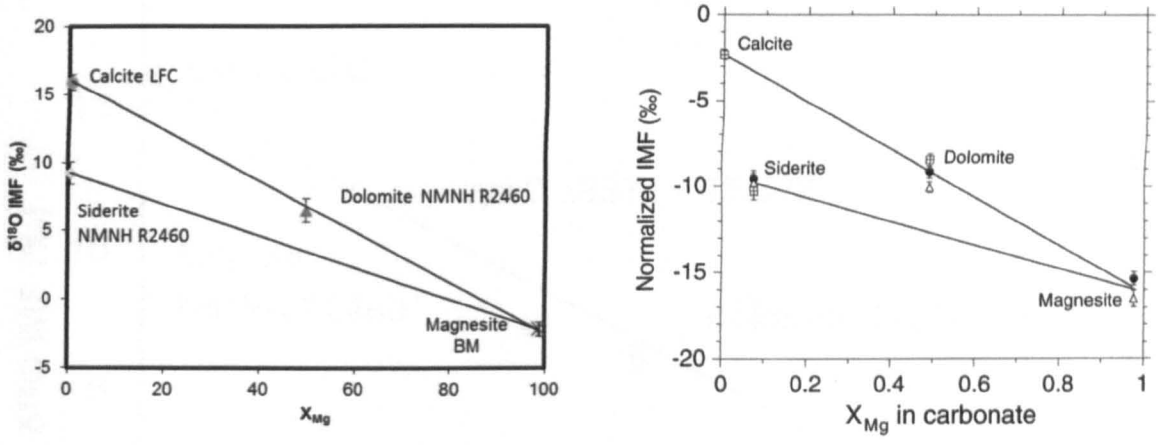

Figures 3.22-23 Relative compositions and IMF from this study (Fig. 3.22) are compared to Leshin et al. (1998) (Fig 3.23).

Two of the four standards (siderite NMNH R2460; dolomite NMNH 10057) used for this correction are the same standards as measured by Leshin et al. (1998). However, the siderite composition observed by Leshin et al. (1998) differs from this study's measured composition (0% X_{Mg} in siderite) and the initial study of the same material (Jarosewich and MacIntyre., 1983), suggesting either a heterogeneous siderite composition or a potential error in Leshin et al's. (1998) calculations. A correction along the calcite-dolomite-magnesite mixing line was applied to the carbonates measured in this Chapter (Figs. 3.24-5; Table 3.8)

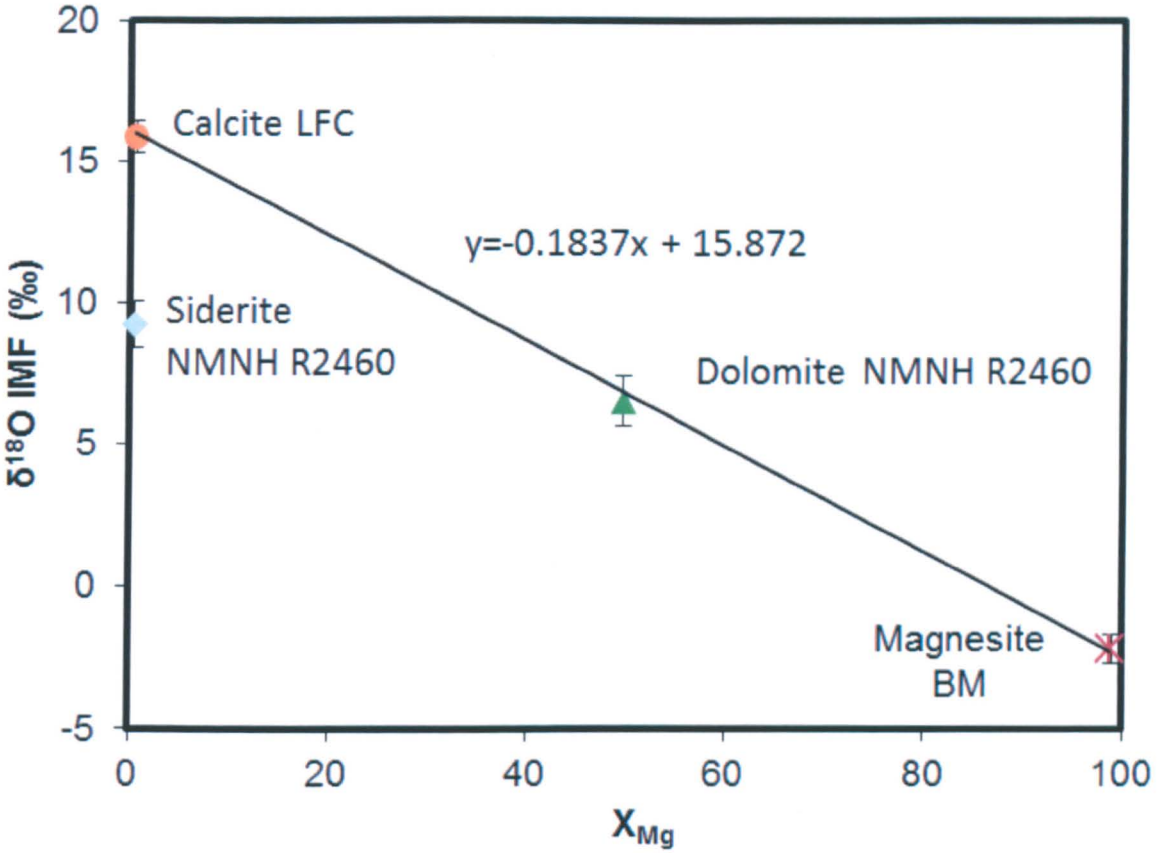

Figure 3.24 Applying IMF corrections to the data set using the calcite-dolomite-magnesite mixing trend as applied by Leshin et al. (1998).

Table 3.8 Compositions of rosettes when IMF corrections (Fig. 3.24) are applied. A maximum error of ±1.1‰ (1σ) was measured for $\delta^{18}O$.

Sample	X_{Mg}	X_{Ca}	X_{Fe}	X_{Mn}	X_{Fe+Mn}	$\delta^{18}O$	Error (1σ)
Rosette (1) 1	52.1	13.2	33.5	1.1	34.6	+13.9	0.4
Rosette (1) 2	47.1	14.2	36.5	2.2	38.6	+6.6	0.4
Rosette (1) 3	43.8	13.7	38.9	3.6	42.5	+1.1	0.7
Rosette (1) 4	36.5	17.9	42.2	3.4	45.6	+5.5	0.9
Rosette (1) 5	43.6	15.2	38.6	2.5	41.2	+6.7	0.9
Rosette (1) 6	49.0	13.9	35.4	1.8	37.1	+11.6	0.8
Rosette (1) 7	45.0	16.1	37.2	1.7	38.9	+5.5	1.1
Rosette (1) 8	48.3	14.8	33.6	3.4	36.9	-0.1	0.9
Rosette (1) 9	48.9	14.5	33.3	3.2	36.5	+3.2	0.6
Rosette (1) 10	48.4	14.2	33.9	3.4	37.3	+6.7	0.6
Rosette (1) 11	49.7	14.4	33.6	2.3	35.9	+9.2	0.6
Rosette (1) 12	57.5	11.4	30.3	0.8	31.1	+16.6	0.7
Rosette (1) 13	59.7	9.9	29.7	0.7	30.4	+15.1	0.7
Rosette (1) 14	81.7	5.8	11.9	0.5	12.5	+25.3	0.7
Rosette (1) 15	89.3	3.2	7.3	0.2	7.5	+27.1	0.7
Rosette (2) 16	72.5	3.9	23.4	0.3	23.7	+13.3	0.8
Rosette (2) 17	48.1	11.0	40.0	0.9	40.9	+8.9	0.9
Rosette (2) 18	58.7	10.9	29.6	0.7	30.3	+10.4	0.6
Rosette (2) 19	54.1	12.0	33.1	0.9	34.0	+0.3	0.7
Rosette (2) 20	51.9	12.5	34.6	1.0	35.6	+12.9	0.6
Rosette (2) 21	55.6	9.9	34.1	0.4	34.5	+15.2	0.6
Rosette (2) 22	65.4	7.0	27.3	0.3	27.6	+18.4	0.6
Rosette (2) 23	73.1	3.2	23.4	0.3	23.7	+23.3	0.6
Rosette (2) 24	72.5	3.8	23.4	0.3	23.7	+20.3	0.8

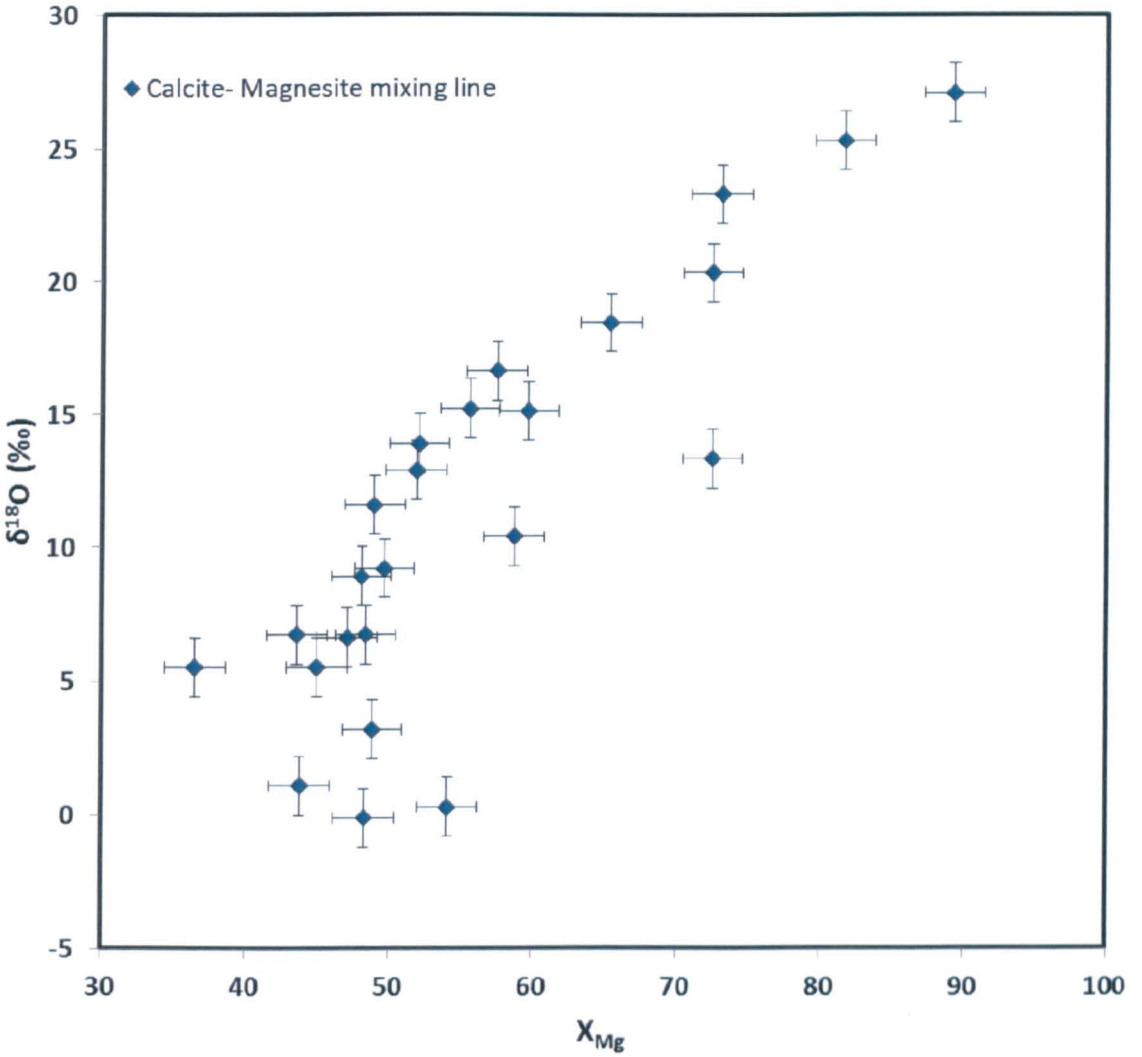

Figure 3.25 ALH 84001 $\delta^{18}O$ corrected values from this study showing trend against X_{Mg} as recognised by previous authors studies (Leshin et al., 1998; Saxton et al., 1998; Eiler et al., 2002 and Holland et al., 2005). Errors applied are max 1σ values from standards X_{Mg} (±2.1%) and $\delta^{18}O$ (±1.1‰).

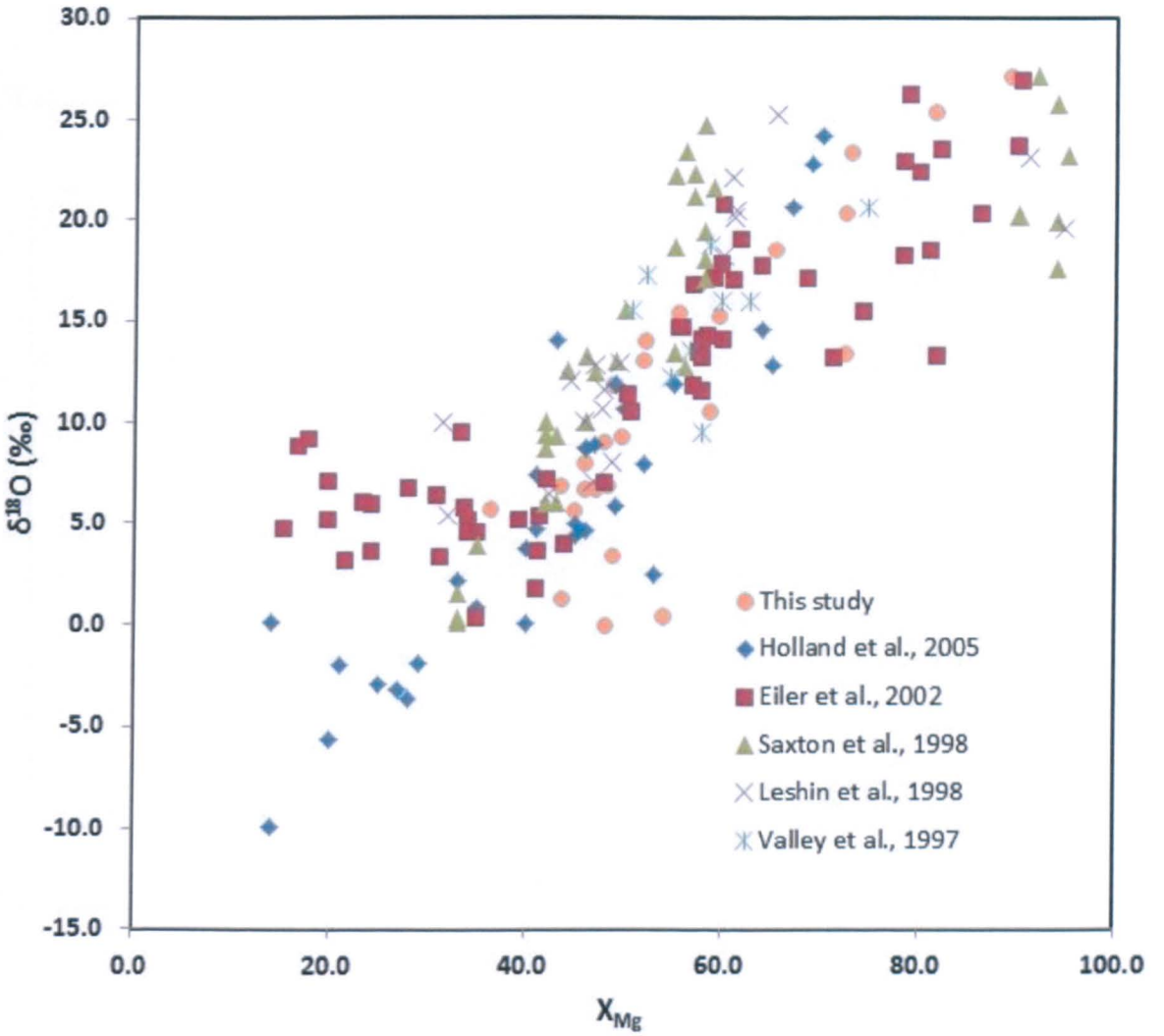

Figure 3.26 Values from this study and previous literature displaying the general trend of $\delta^{18}O$ with X_{Mg}.

Table 3.9 Values from this study plotted against previous authors.

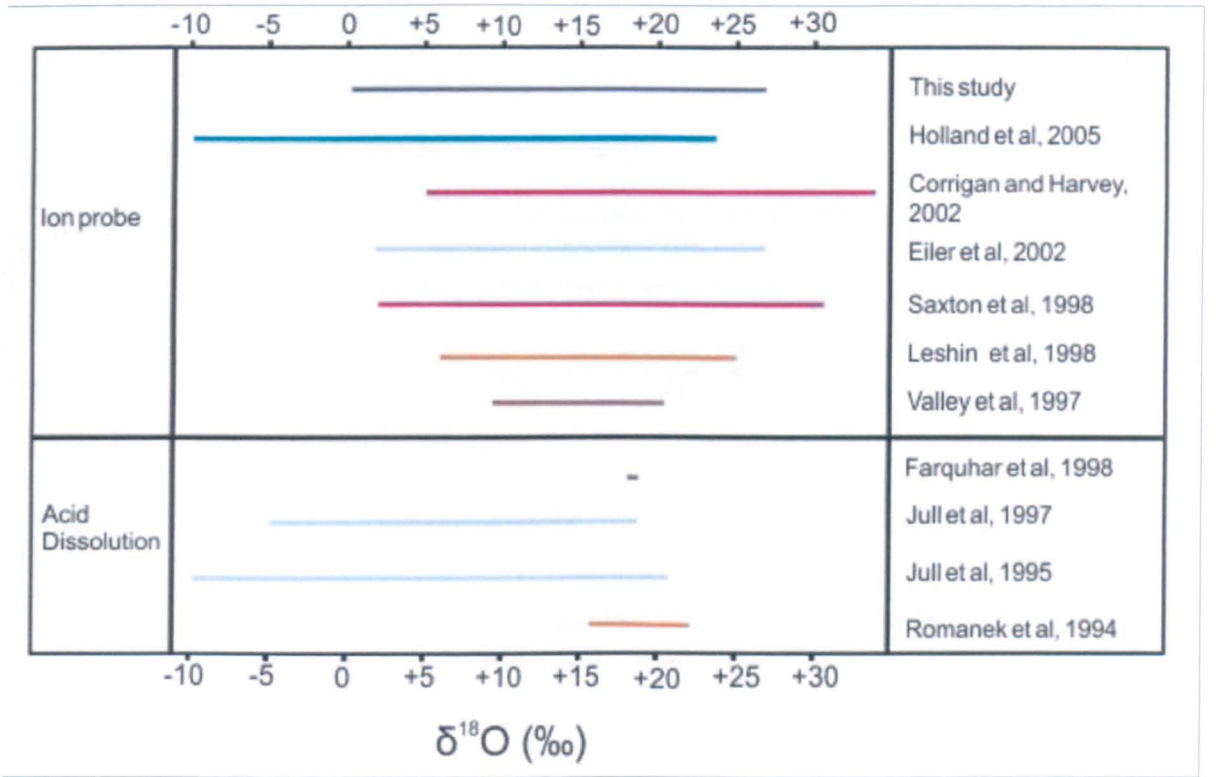

While most of the recorded values fall within observed trends, the higher $\delta^{18}O$ values correspond to a lower range of X_{Mg} compositions than previously observed and lack low $\delta^{18}O$ values with corresponding low X_{Mg} compositions. However, the IMF corrections used in all these studies potentially seriously underestimate the IMF corrections. An example of this can be observed when the data collected from twelve standards was compared to that collected by just four (Leshin et al., 1998). As can be observed from Figs. 3.22-23 when comparable standards are compared the resulting correction value looks like a similar linear correction. However, when the whole data set is added (further eight standards) it becomes clear that it not a simple linear correction (Fig. 3.27). An example of how the application of the IMF correction from the standards can result in a variation in the results can be observed if we apply a correction along the siderite-magnesite mixing line. (Fig. 3.28).

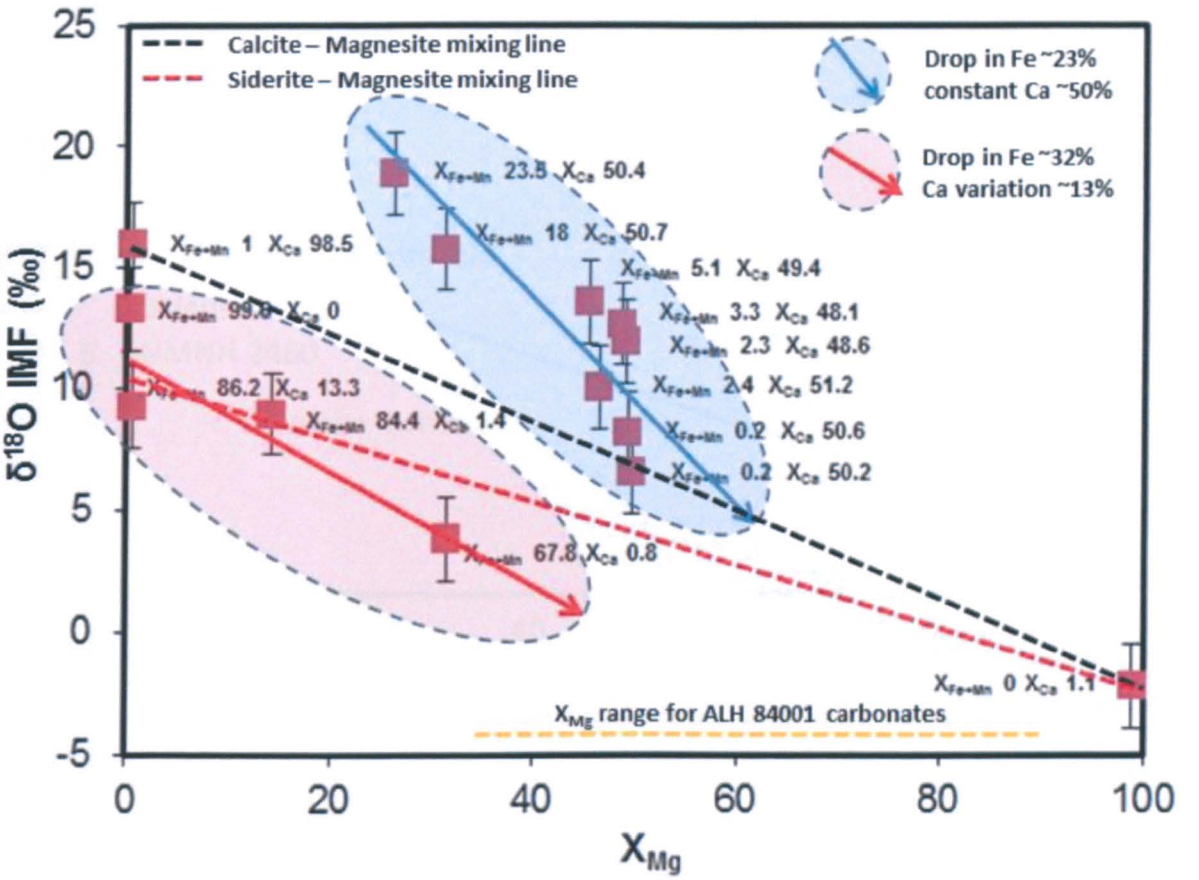

Figure 3.27 $\delta^{18}O$ IMF plotted against X_{Mg} highlighting trends in X_{Fe+Mn} and X_{Ca} two different mixing lines and the X_{Mg} range in ALH 84001 carbonates.

When considering that previous IMF corrections to the ALH 84001 carbonates have been applied according to dolomite and end member mixing lines (Fig. 3.27, red and black dotted lines) it can be observed that a large portion of the IMF standards with relevant compositions were not represented. A trend between the decreasing X_{Fe+Mn} component and a drop in IMF were clearly observed for the dolomites (Fig. 3.27, blue line). In addition a drop in X_{Fe+Mn} and X_{Ca} seemed to have a similar effect on the iron-rich dolomite cornwall, ankerite BM and siderites (Fig. 3.27, red line).

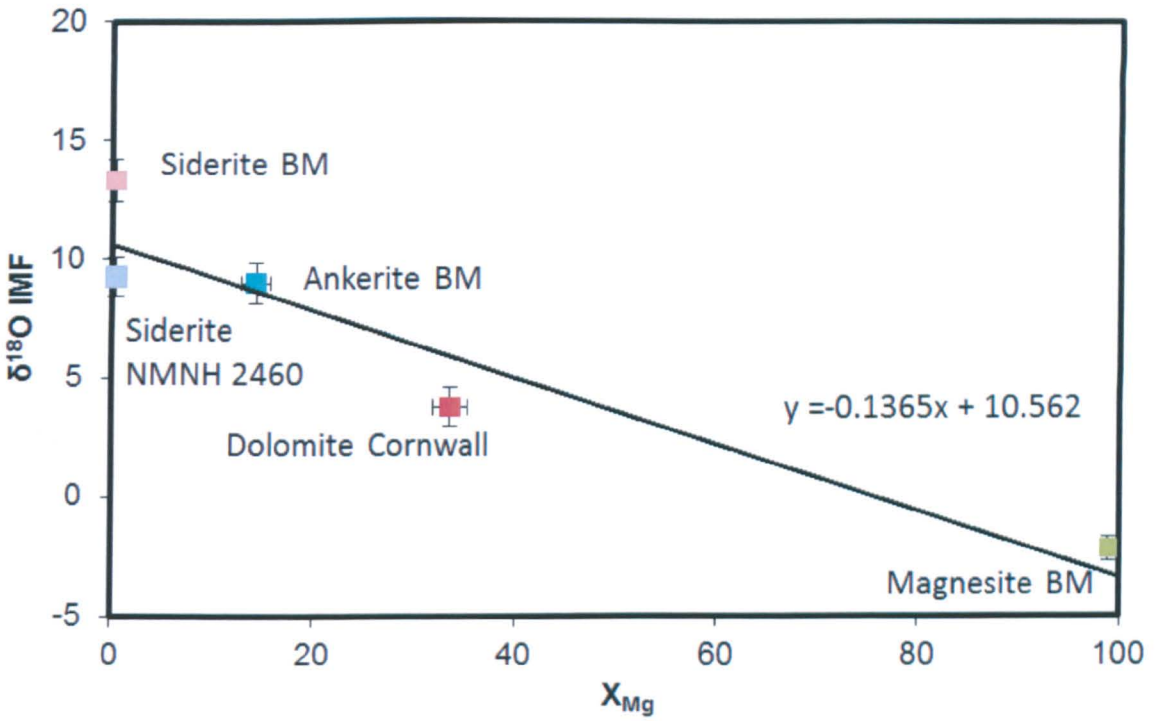

Figure 3.28 Plot displaying the siderite – magnesite mixing line and equation for line of best fit.

The variation on the IMF correction has a direct effect on the $\delta^{18}O$ values obtained for the rosette values (Fig. 3.29) with a difference of up to 6‰ (X_{Mg} 89.3%) when a correction along the siderite-magnesite mixing line is applied (Fig. 3.28). However, despite this difference there still appears to be a positive correlation between X_{Mg} and $\delta^{18}O$ which in turn suggests that the carbonates are getting continually greater $\delta^{18}O$ values with distance from the core of the rosettes.

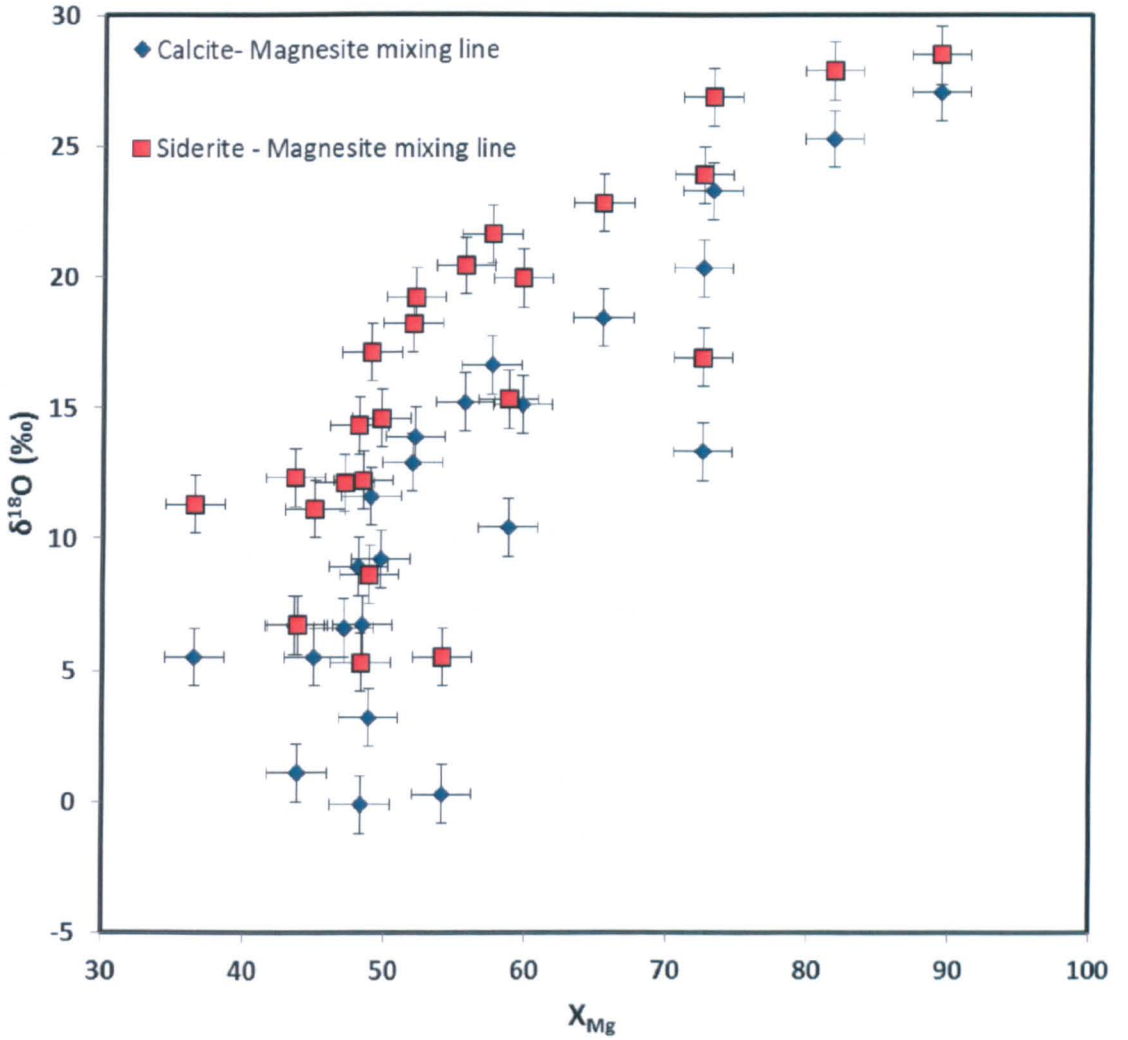

Figure 3.29 Values obtained for corrections based on different mixing line corrections (Fig. 3.25 and Fig. 3.28). Errors applied are max 1σ values from standards X_{Mg} (±2.1%) and max $\delta^{18}O$ (±1.1‰).

3.6.7 Carbon results with corrections applied from IMFs

Similarly to corrections applied to the oxygen isotopes sections 3.6.7 and 3.6.8 data were plotted to show the range in isotopic composition of specific standards relative to their elemental composition. Knowing the composition of the carbonate in ALH 84001 (section 3.6.4), it was possible to select the most appropriate suite of standards against which to correct the ALH 84001 data. All the possible candidate corrections are given in Appendix B,

from there the same method of IMF correction as that used by Valley et al. (1997) was applied to derive the equivalent $\delta^{13}C$ for this study (Fig. 3.30). Ion microprobe studies were also conducted by Niles et al. (2005) but no clear interpretation between composition and IMF correction could be deduced from the standards. In Figure 3.30 there appears to be only a poor correlation between composition (X_{Fe+Mn}) and $\delta^{13}C$ but in order to compare data from this study with published data, corrections according to Valley et al. (1997) were applied. Valley et al. (1997) observed a positive correlation of $\delta^{13}C$ with increase in X_{Fe+Mn}, while the data collected from this study demonstrates a negative correlation.

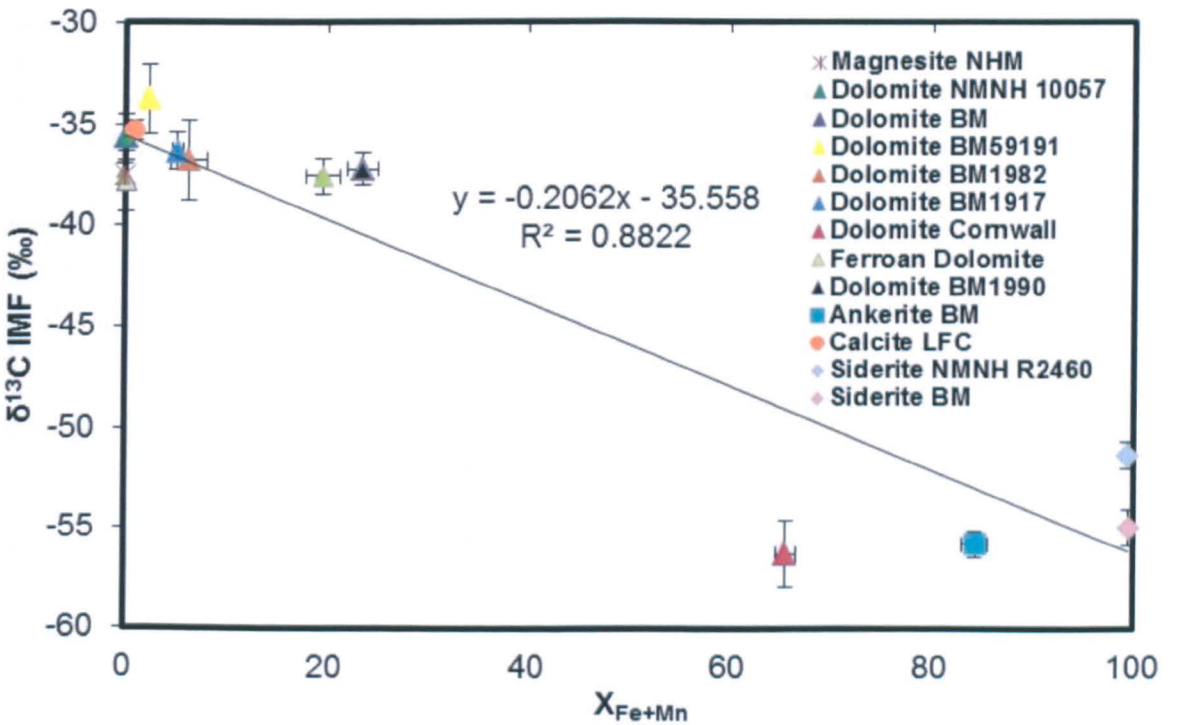

Figure 3.30 $\delta^{13}C$ values with change in X_{Fe+Mn} composition.

The total range in $\delta^{13}C$ values is large (41.8‰) in comparison to any previous ion probe measurements (Table 3.10-11). There is no overlap and no obvious correlation with magnesium content.

Table 3.10 $\delta^{13}C$ values of spot analysis across ALH 84001 rosettes. A maximum error of ±1.3‰ (1σ) was measured for $\delta^{13}C$.

Sample	X_{Mg}	X_{Ca}	X_{Fe}	X_{Mn}	X_{Fe+Mn}	$\delta^{13}C$	Error (1σ)
Rosette (1) 1	55.2	11.4	32.6	0.8	33.4	+16.1	1.0
Rosette (1) 2	51.8	12.5	34.7	1	35.7	+23.2	1.0
Rosette (1) 3	47.5	14.1	36.7	1.7	38.4	+16.5	1.0
Rosette (1) 4	49.6	13.6	34.4	2.4	36.8	-1.5	1.1
Rosette (1) 5	55.4	12.7	30.8	1	31.8	-13.5	0.9
Rosette (1) 6	56.5	11.6	31.1	0.8	31.9	+11.9	1.1
Rosette (1) 7	53.1	13.2	32.1	1.6	33.7	+5.7	0.9
Rosette (1) 8	37	17.1	42.7	3.2	45.9	+18	1.1
Rosette (1) 9	43.4	17.5	35.5	3.6	39	+15.6	1.2
Rosette (1) 10	30.3	19.4	46.4	3.8	50.3	+16.5	1.1
Rosette (1) 11	51	13.9	31.9	3.1	35.1	+19.8	1.0
Rosette (1) 12	49.7	13.8	34.6	1.9	36.5	+17.3	1.1
Rosette (1) 13	47.8	13.4	37.7	1.1	38.8	+15.3	1.1
Rosette (1) 14	62.7	7.4	29.6	0.3	29.9	+17.4	1.3
Rosette (1) 15	70.8	4.1	24.7	0.4	25.1	-18.6	0.8
Rosette (1) 16	74.4	7.4	17.5	0.7	18.3	-6.9	1.3
Rosette (2) 17	76	2.8	20.9	0.3	21.2	-6.9	1.1
Rosette (2) 18	62.2	8.6	29	0.3	29.3	-10.1	0.9
Rosette (2) 19	60.8	9.8	28.8	0.6	29.4	+6.8	1.0
Rosette (2) 20	61.9	9.6	27.9	0.6	28.6	+7.6	1.2
Rosette (2) 21	52.7	12	34.5	0.8	35.3	+19.5	1.0
Rosette (2) 22	50.6	13.4	35.2	0.8	36	+21.8	1.0
Rosette (2) 23	61.8	9.1	28.9	0.3	29.1	+21.8	1.0
Rosette (2) 24	43.5	8.4	47.7	0.4	48.1	+19.9	1.2

Most of the $\delta^{13}C$ data (~77%) plot between +23.2 to +5.7‰ with broadening range in $\delta^{13}C$ values with increasing Mg content (Table 3.8; Fig. 3.31) . The lowest values ($\delta^{13}C$ of -1.5 to -18.6‰) all occur at X_{Mg} contents above 50%, but there is no clear relationship between $\delta^{13}C$ and X_{Mg}. However, a potential $\delta^{13}C$ and X_{Fe+Mn} trend is apparent (Fig. 3.32) though this could be influenced by the chosen IMF correction (X_{Fe+Mn}). The low $\delta^{13}C$ values appear to be the result of an introduced reduced carbon component and are typically related to the outer portions of the rosettes (Mg-rich regions; Fig. 3.31). There have been

observations of graphite associated with the magnesite (Steele et al., 2012) other considered origins include organics and contamination which are discussed in Chapter 7.

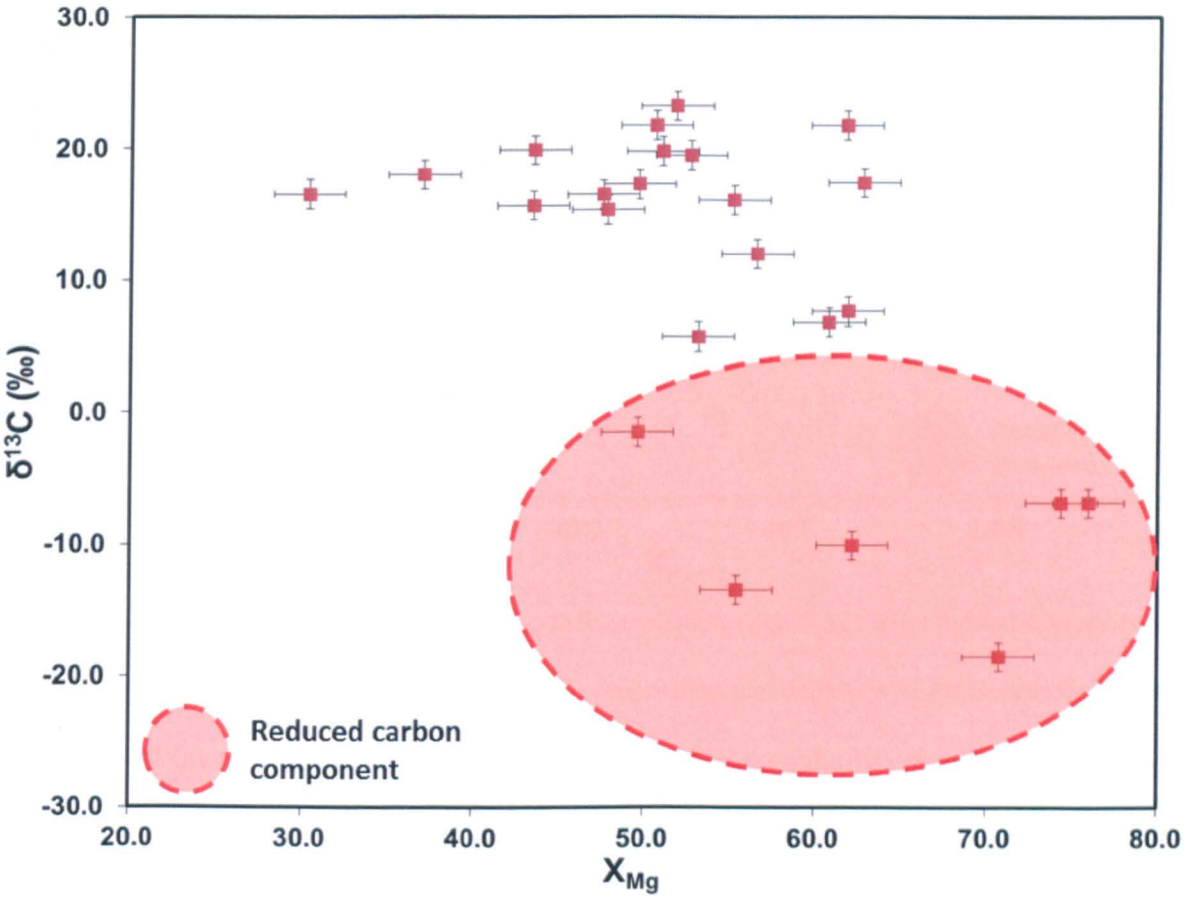

Figure 3.31 Values from applying X_{Fe+Mn} IMF correction (Fig. 3.30) and plotted against X_{Mg}.

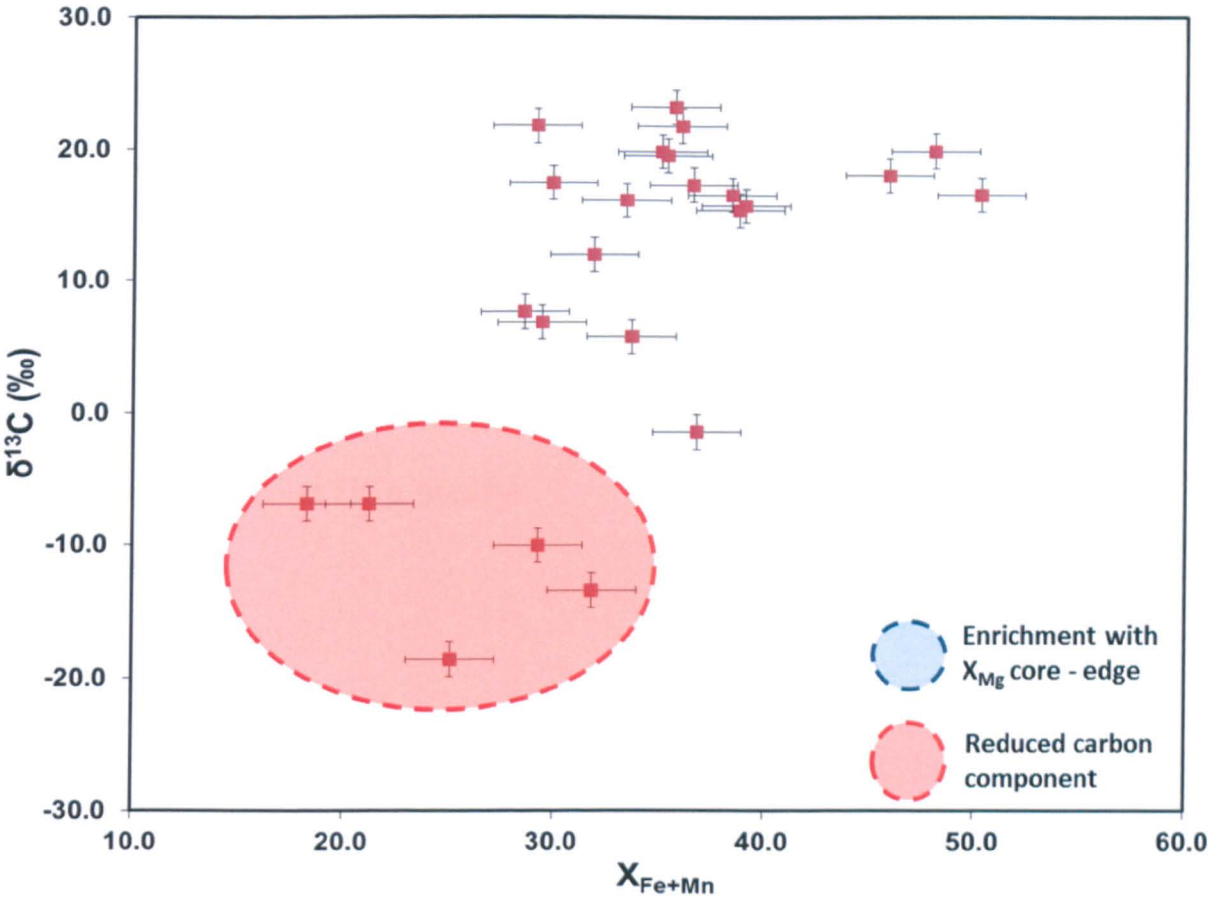

Figure 3.32 Values from applying X_{Fe+Mn} IMF correction (Fig. 3.32). Highlighted regions correspond to interpretation of a gradually enriched $\delta^{13}C$ composition and detection of a reduced component.

With the reduced carbon component portion potentially originating from a separate source there is a potential natural $\delta^{13}C$ enrichment of ~16‰ (+6.8 to +23.2‰). It is clear that the chemical composition of the carbonate is evolving as these rosettes are precipitating and therefore seems feasible that a CO_2 fractionation factor may be contributing to the variation in $\delta^{13}C$. Unfortunately, the magnitude of the fractionation is poorly constrained with the carbonates studied here, with the only theoretical upper limit for $\delta^{13}C$ fractionation factor of 4‰ at 25°C and decreasing for higher temperatures (Niles et al., 2005).

The isotope values collected from this study vary quite dramatically from those collected by Niles et al. (2005) (Fig. 3.33). However, the carbonate compositions studied in this Chapter vary from those measured by Niles et al. (2005). No observations of Fe-rich

carbonates were found to be associated with the carbonates in Niles et al., 2005 and they observed either homogenous magnesite or discontinuous to patchy carbonates rather than whole rosettes (this study) with Ca- and Fe-rich carbonate cores (described as ankerite in this study) to Mg-rich rims.

Figure 3.33 $\delta^{13}C$ values from corrections applied according to X_{Fe+Mn} content plotted against values obtained from Niles et al. (2005).

The range in $\delta^{13}C$ of 41.8‰ overlaps with all but one set of data from bulk analysis (Table 3.11; Romanek et al., 1994). However, while the data measured here agree with some of the bulk values, they do not correspond with any of the results from ion microprobe analyses (Valley et al., 1997; Niles et al., 2005; Table 3.11).

Table 3.11 Comparison of data with previous authors $\delta^{13}C$ measurements. Values to left of dotted line have been associated with either terrestrial contamination or in some cases suggested as indigenous organics.

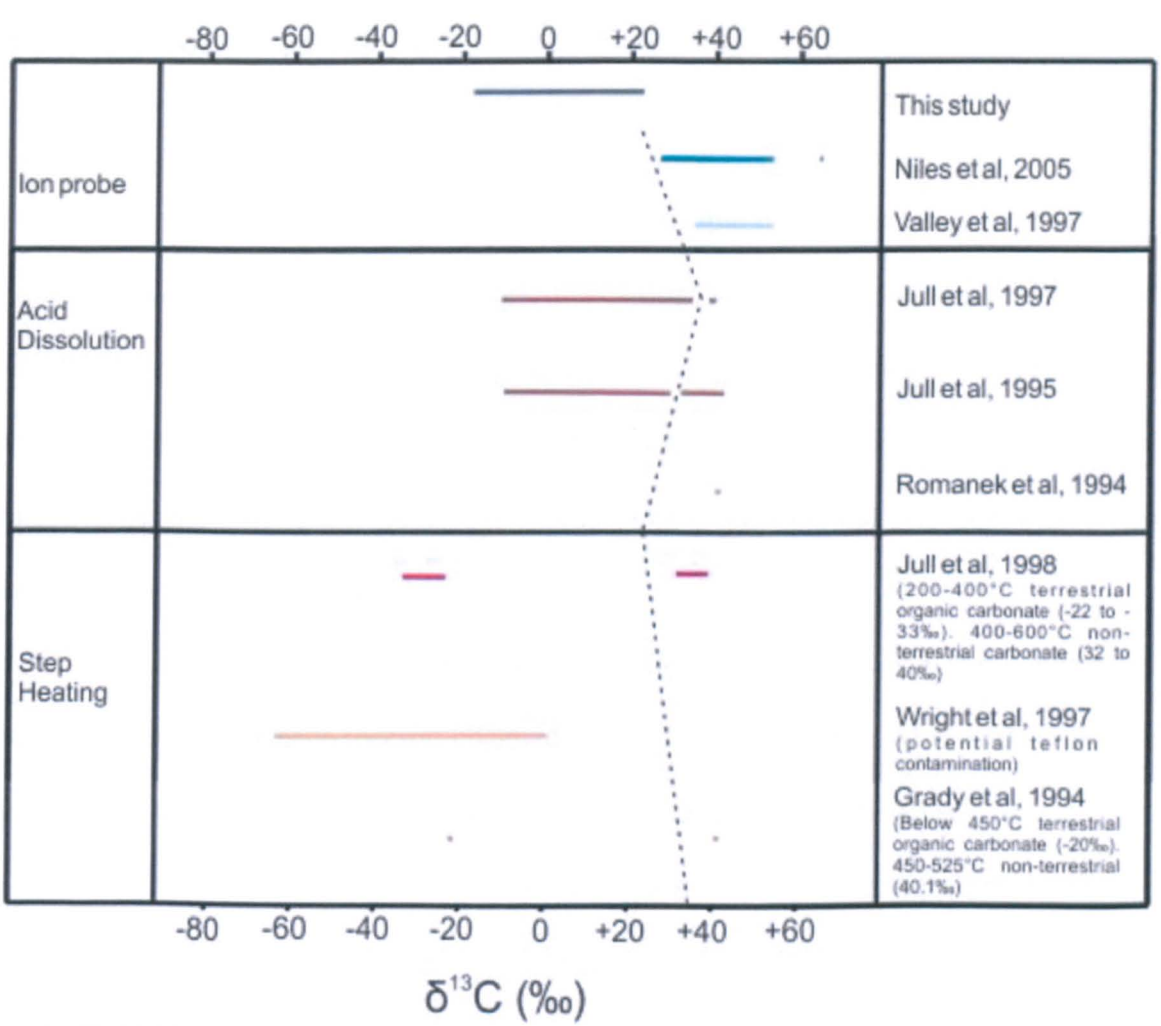

The data presented here are influenced by the presence of reduced carbon, the origin of these $\delta^{13}C$ values cannot be confirmed although the potential sources are discussed in Chapter 7. Despite this scatter in the data a potential positive correlation between X_{Mg} and

$\delta^{13}C$ also observed by Niles et al. (2005) (Fig. 3.33) might suggest that there is a progressive enrichment in $\delta^{13}C$ as the carbonate formation evolves. This in turn is supportive of a model with a progressive evaporating single fluid perhaps in a hydrothermal system.

3.7 Discussion

3.7.1 IMF corrections

This study shows that the $\delta^{18}O$ IMF is not a simple linear correction. A wider range of carbonates with various Ca-Fe-Mn-Mg compositions are required to resolve this issue in regards to precise corrections for measured data from unknown samples. However, the results presented here provide additional information about the relationship between carbonate composition and IMF and show that the transition elements Fe and Mn appear to influence the corrections differently from Mg and Ca.

The lack of a single clear trend for the $\delta^{18}O$ and $\delta^{13}C$ corrections suggests that materials sharing element-specific characteristics to those found in ALH 84001 carbonates are required to have confidence in martian carbonates ion microprobe data.

A $\delta^{18}O$ IMF variation of up to 18.6‰ for a single point measurement depending on which IMF correction was applied (see Appendix B (IV), Table 3.1, +12.1‰ compared to +30.7‰). The largest $\delta^{13}C$ IMF variation was 25.2‰ for a single point (see Appendix B (IV), Table 3.2, -10.4‰ compared to +15.8‰). These IMF variations obviously have large implications on the corrected values from this study and those reported from the literature.

Variations measured in this study only prove that the full range of $\delta^{18}O$ and $\delta^{13}C$ IMF have not been recorded, however, without measuring the large gap in the compositional record this issue cannot be resolved.

Eight studies (this study included) have used three different element molar contents to apply IMF corrections. Riciputi and Greenwood (1998) found a non-linear correlation with X_{Fe+Mn} (from fifteen carbonate samples), while six of the studies all found linear relationships for the IMF corrections (Table 3.4).

The IMF corrections applied to the ALH 84001 carbonates in this study use corrections methods suggested by previous authors (Valley et al., 1997; Leshin et al., 1998). However, the $\delta^{18}O$ dataset collected for this study use additional standards to Valley et al. (1997) and Leshin et al. (1998) and do not all fall on the linear trend inferred from dolomite and end-member carbonates. These additional standards with intermediate compositions show how essential it is to have a larger range of samples that better represent the compositions found within ALH 84001 carbonates. Half of the reported ion probe studies use fewer than five standards covering only end member compositions leaving intermediate compositions in which the ALH 84001 carbonates reside vacant (Fig. 3.34).

With the samples available it is beyond the scope of this PhD to determine the true source of these IMF differences. Reasons for these variations could depend on (1) the mass ratio of the isotopes; (2) the energy of the secondary ions; (3) the bond strength of the analysed ion and the matrix. This study (siderite BM and NHBM R2460) and research into the carbonates calcite and aragonite (both $CaCO_3$) have shown that materials with a similar chemical composition still provide variations in IMF (Rollion-Bard and Marin-Carbonne, 2011) suggesting even subtle variations in bond strength and crystal structure can affect the IMF.

The $\delta^{18}O$ values of dolomites with any Fe^{2+} component plot as outliers when a straight line is plotted through magnesite, calcite and dolomite (BM, LFC and NHBM 1990, respectively). This shows that the Ca-Mg mixing line may be a linear relationship (as suggested by Leshin et al., 1998) however, the incorporation of Fe^{2+} complicates the situation and hence using the Ca-Mg mixing line as a correction for ALH 84001 is compromised. This lack of understanding for the correct correction for the composition of ALH 84001 in the published literature (Leshin et al., 1998; Holland et al., 2005; Niles et al., 2005) is clearly displayed in Figure 3.34. Carbonate standards to date do not even overlap with any compositions other than the Mg-rich carbonates found within ALH 84001.

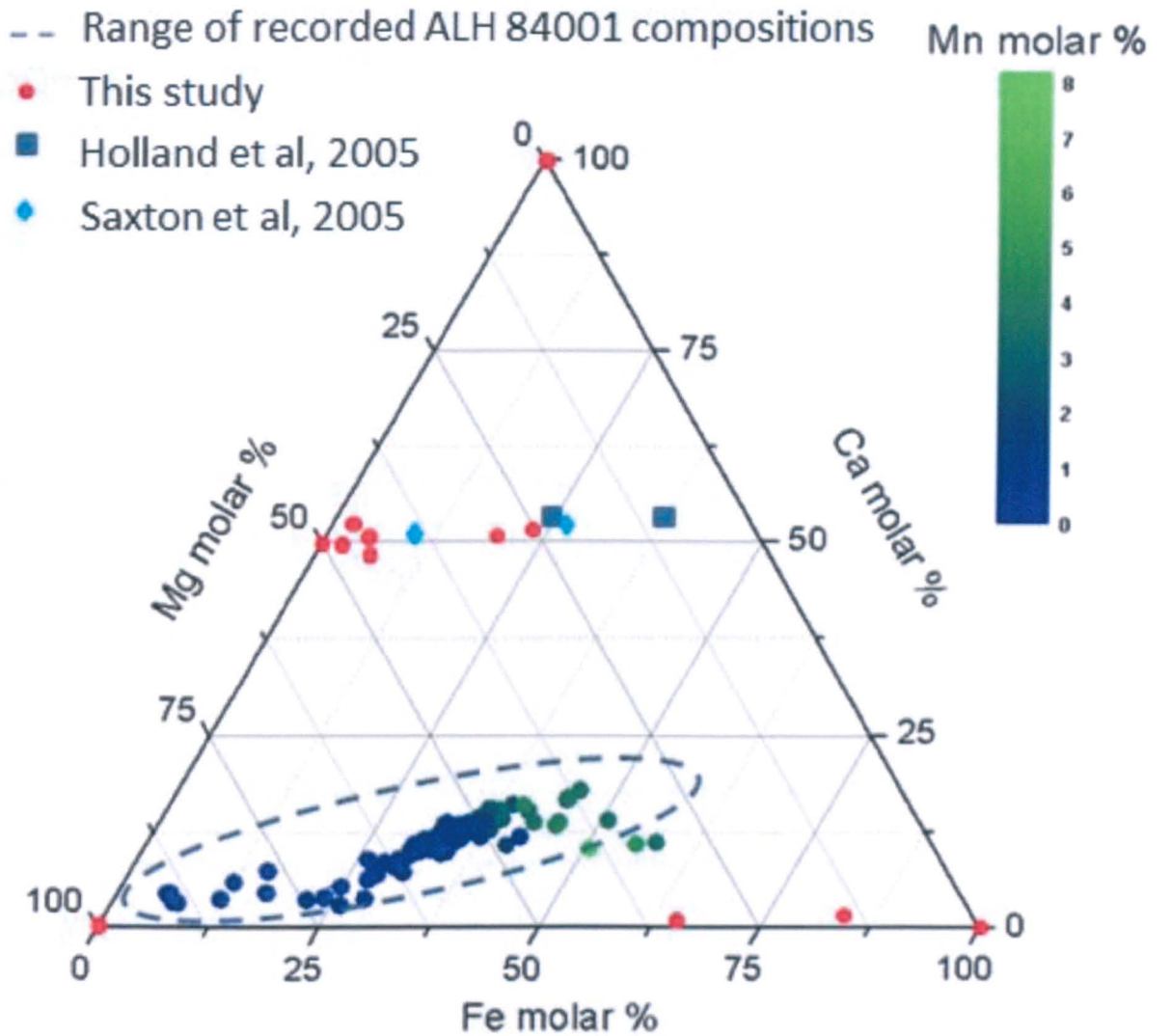

Figure 3.34 Ternary diagram of electron microprobe analyses of carbonate compositions found in standards and in ALH 84001 from this study and in the literature. Only values of intermediate-member carbonates from the SIMS literature have been included, as all previous studies have measured end-member compositions (siderite, dolomite, calcite and magnesite).

The large variations in IMF corrections for $\delta^{13}C$ values compared with those from $\delta^{18}O$ suggest that fractionation factors for carbon are greater than those for oxygen. This systematic difference implies that either one or all C-O, C-Ca, C-Fe, C-Mn and C-Mg bonds are strongly affected by the ion beam interaction and that there is preference for the lighter ^{12}C portion of the ions to be released upon excitation.

The significance of the uncorrected values in the literature has been discussed in this Chapter, however, $\delta^{18}O$ and $\delta^{13}C$ values are collected, published and not properly corrected from numerous SIMS studies. Issues found in this Chapter hence do not only have implications for Mars but any research field that investigates carbonates with SIMS such as studies of carbonates in chondrites, research in environmental studies such as stromatolites and other Mg-rich calcite corals and geothermometry relating to carbonates.

3.7.2 ALH 84001 carbonate values

The two parallel lines of analyses for $\delta^{18}O$ and $\delta^{13}C$ have rosette compositions that are relatively well matched aiding spatial isotopic interpretation. The $\delta^{18}O$ values measured in this study are in good agreement with those from previous authors (Leshin et al. 1998; Saxton et al. 1998 and Eiler et al. 2002). A trend between the X_{Mg} fraction and raised $\delta^{18}O$ values is clearly observed in addition to the first profile of a $\delta^{18}O$ increase from the core to edge of the rosettes (Fig. 3.35).

The $\delta^{13}C$ values display the opposite trend to $\delta^{18}O$ with the highest X_{Mg} fraction corresponding to low $\delta^{13}C$ values (Fig. 3.35). However, the relationship between X_{Mg} fraction and low $\delta^{13}C$ values does not apply to the first portion of the rosette 1 dataset with point 5 measuring -13.5‰. This region is suspect as the FIB has not produced a flush surface on this portion of the rosette which can cause IMFs (see Fig. 3.20), there is also a possibility that the NanoSIMS pre-sputter time was not sufficient and that top surface contamination may be affecting the $\delta^{13}C$ values (Fig. 3.21). This is normally detected by monitoring for high counts the $^{28}Si^-$ EM NanoSIMS. Values with high $^{28}Si^-$ counts or high Si wt. % (>0.5%) from electron microprobe measurements were discounted, i.e. values between points 4-5 for $\delta^{13}C$;

6-7 and 13-14 for $\delta^{18}O$ other non-reported values were used for tuning the NanoSIMS (Fig. 3.35).

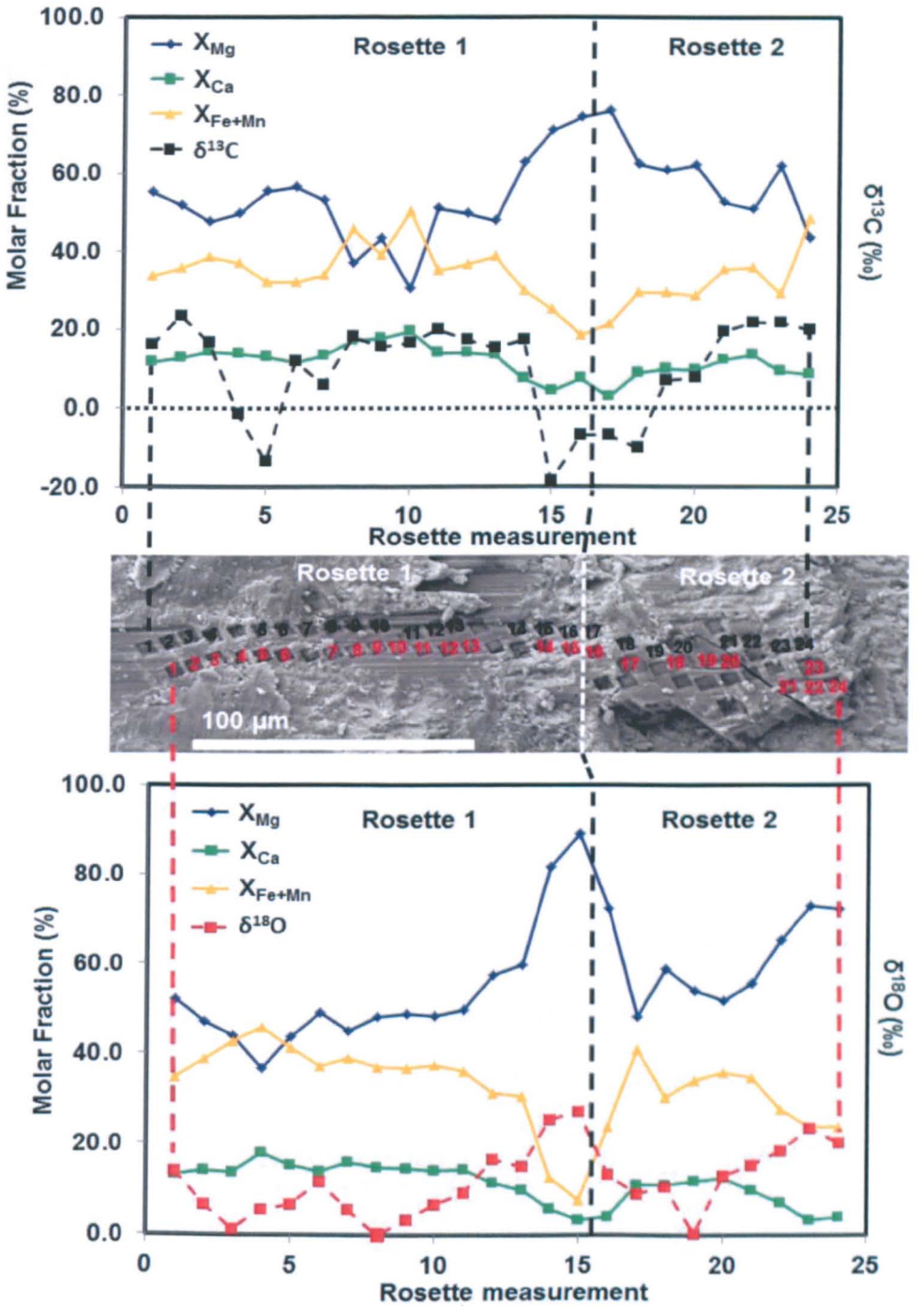

Figure 3.35 NanoSIMS and electron microprobe data plotted against analyses points displayed on BSE image of portions of two ALH 84001 rosettes.

Interpretations of the data for ALH 84001, in terms of implications for the environment in which the carbonates formed, is contained in Chapter 7.

3.7 Conclusions

- When $\delta^{18}O$ IMF corrections are applied with set of standards matching Leshin et al. (1998) a 27.2‰ variation (-0.1 to +27.1 ‰) is observed correlated with X_{Mg} enrichment (Fig. 3.35). These findings agree with previous microprobe studies suggesting the lowest $\delta^{18}O$ were the first to precipitate and the highest $\delta^{18}O$ values formed at the final stage of carbonate crystallisation (Figs. 3.26, 3.35).
- Additional standards show linear IMF corrections for $\delta^{18}O$ previously applied to ALH 84001 carbonates are not valid when carbonate standards with intermediate compositions are added to the IMF dataset.
- When different $\delta^{18}O$ IMF corrections to the siderite-magnesite mixing line are applied a variation of up to 18.6‰ is observed.
- A variation of 42‰ in $\delta^{13}C$ is observed with a potential inverse correlation with X_{Mg} but no other obvious correlations with composition, and no overlap observed between collected data and previous authors ion microprobe values.
- $\delta^{13}C$ values collected are lower than previous ion probe data but were consistent with measurements from bulk sample analyses.
- When different $\delta^{13}C$ IMF corrections are applied a variation of up to 25.2‰ is observed.

Chapter 4

4. MINERALOGY AND MICROSCALE CARBON AND OXYGEN ISOTOPE VARIABILITY IN ANALOGUE CARBONATES AND IMPLICATIONS FOR ALH 84001 CARBONATE FORMATION

4.1 Introduction

Studies of the martian surface have progressed leaps and bounds in recent times with orbital instruments and a handful of rovers and landers visiting Mars (Klingelhöfer et al., 2004; Bribing et al., 2005; Ehlmann et al., 2008; Boynton et al., 2009; Squyres et al., 2012). However, no mission has yet returned samples from our neighboring planet and meteorites therefore provide a unique insight into the martian crust. Typically they supply a few kgs of material to work with and no regional information as to their source, consequently interpreting the history of these materials can be challenging. However, finding sites on Earth which produce samples with the same petrographic makeup can provide an insight into the past conditions under which these materials formed on Mars. In this Chapter, I review potential terrestrial analogue collection sites and then describe in detail material returned from the Svalbard region of northern Norway.

4.2. ALH 84001 analogues

The bulk of ALH 84001 consists of the mineral orthopyroxene (97 vol. %; Mason et al., 1992) which is a common constituent of igneous and metamorphic rocks and which is found in locations across all the continents on Earth. It is also prevalent within extraterrestrial material, including meteorites (Mason, 1963) and material from the lunar highlands (Stöeffler et al., 1980). Unambiguous identification of orthopyroxene was first recorded on the martian surface by the Thermal Emission Spectrometer (TES) on board Mars Global Surveyor (MGS; Hamilton et al., 2003). While ALH 84001 is the only orthopyroxenite found within the current martian meteorites discovered on Earth, the NWA 998 nakhlite, Chassigny and at least six shergottites have all been noted to contain orthopyroxene.

Despite these well documented occurrences of the main constituent of ALH 84001, no other extraterrestrial samples have been found so far that display the unusual alteration: neither the heterogeneous composition nor the isotopic variations observed within the carbonates (~1 vol. %; Mittlefehldt, 1994; Treiman, 1995). There are also few places on Earth that have been found where a similar combination of igneous rock and heterogeneous carbonates exists. This may be because there is a lack of environments on Earth that mimic the conditions experienced on Mars that produced these carbonates. Although, another aspect may be that materials analagous to ALH 84001 are not examined to the same detail with instrumentation (i.e. ion probe instead of bulk analysis) and hence the isotopic and compositional variations within terrestrial carbonates are not detected or reported..

4.2.1 Warm and Arid environments

Analogue material for the carbonates observed with ALH 84001 has been collected from various sites around Earth. Carbonates that precipitate under conditions of very high water/rock ratios generally have approximately homogenous carbon and oxygen isotopic compositions. In contrast carbonates with heterogeneous isotopic variations are found to form in arid environments. An example of this environment is Sunset Crater, Arizona, USA where studies have found subariel caliches (calcite) forming on >3 Ma volcanic field basalts. These calcites, unfortunately, do not match the range of mineralogy observed within the ALH 84001 carbonates but do contain heterogeneous isotopic variations (Knauth et al., 2003; Volk et al., 2011). Both studies reported a kinetic effect as a consequence of evaporation with a combined $\delta^{13}C_{VPDB}$ range of +1.8 to +12.7‰, and $\delta^{18}O_{VSMOW}$ range of +21.5 to +32.0‰. These variations were observed over hundreds of microns, with the enrichments suggested to be a consequence of brief periods of precipitation, in parallel to CO_2 degassing and photosynthetic extraction from evaporating meteoric waters. The enrichments in $\delta^{13}C$ could be attributed to photosynthesis by organisms that selectively remove the lighter ^{12}C component as CO_2, leaving an enrichment in ^{13}C and thus higher $\delta^{13}C$. This aspect of the model leaves the $\delta^{18}O$ range unaffected but it is thought that enrichment in ^{18}O in the exterior was produced through evaporation of concentrated meteoric waters. Meanwhile, the interior of the sample retains evidence for the ambient temperatures of precipitation from the local meteoric waters, which yield $\delta^{18}O$ and $\delta^{13}C$ isotopic compositions that are characteristic of the isotopically-depleted fluids percolating through the soils. Despite the evaporated and potential biogenic scenarios explaining the isotope enrichments, the carbonates observed in ALH 84001 form large localized (~250 μm) isotope variations within the bulk of the sample.

Furthermore, the isotopic range in values observed in ALH 84001 is much wider and the range in carbonate compositions more diverse and not covariant.

4.2.2 Diagenesis

Variations in both $\delta^{18}O$ and $\delta^{13}C$ are also observed in carbonate concretions which form in diagenetic environments. An example of this is a study by Mozley and Burns (1993) who looked at marine diagenetic processes. They found that either interaction with meteoric water or temperature rises as a consequence of burial depth resulted in a variation of $\delta^{18}O$. As far as carbon isotopic variation is concerned, methanogenesis was suggested to explain the $\delta^{13}C$ enrichments, where microbes known as methanogens form methane and fractionate $\delta^{13}C$. The action of sulphate-reducing bacteria was another biological process suggested and known to produce $\delta^{13}C$ enrichments (Londry and Des Marais., 2003) in their study. However, the resulting carbonate concretions were observed to increase in $\delta^{13}C$ and decrease in $\delta^{18}O$, in contrast to the pattern in ALH 84001, where authors (Romanek et al., 1994; Valley et al., 1997; Niles et al., 2005) show progressive increases in $\delta^{18}O$ with distance from carbonate core values.

4.2.3 Cold arid conditions

Current environmental conditions on Mars cause liquid water to freeze rapidly and water ice to sublime on heating. It is not clear if at the time of carbonate formation in ALH 84001, some 3.9 Ga ago, whether conditions on Mars' surface were much warmer than current martian temperatures or if surface temperatures were similar conditions today, where only sparse quantities of water existed, which were likely to freeze and/or evaporate. Such cold arid conditions are present on Earth and carbonates produced in these environments exhibit covariant $\delta^{13}C_{(VPDB)}$ and $\delta^{18}O_{(VSMOW)}$ relationships.

An example of these cold conditions and the resulting isotopic enrichments observed with relation to ALH 84001 was conducted by Socki et al. (2009). The samples were collected from precambrian bedrock situated on Ellesmere Island (part of the Queen Elizabeth Islands in Northern Canada). The study focused on microscale variations in carbonate $\delta^{13}C_{(VPDB)}$ and $\delta^{18}O_{(VSMOW)}$ values from single crusts, in contrast to previous studies (Blake., 2005) which had looked at variations between multiple carbonate crusts with bulk analyses. Similar to the warm and arid environments (described in 4.2.1), enrichments in ^{13}C and ^{18}O are thought to result from CO_2 degassing and the action of photosynthetic organisms. However, unlike the warm environments (4.2.1), laboratory experiments demonstrated that a large isotopic fractionation effect occurs leading to enrichment in $\delta^{13}C$ in solution by ~20‰ during freezing (Clark and Lauriol., 1992; Socki et al., 2000). As the water is frozen out of solution, the concentration of the remaining solutes increases and isotopically light CO_2 is outgassed.

Four different Arctic carbonate crusts from Ellesmere Island were examined and all showed covariant isotopic trends (Socki et al., 2009). The sample's $\delta^{18}O$ were extracted for analysis on a gas bench using a micro-drill to remove swaths 200 x ~2000 μm along the growth planes (typically 5-6 swaths per sample). The sample's $\delta^{18}O$ values ranged from ~+15 to +20‰ and $\delta^{13}C$ from ~+0.6 to +14‰ with the largest individual sample enrichments of ~10‰ ($\delta^{13}C$) and 3.5‰ ($\delta^{18}O$). Isotopic composition corresponded to the spatial location of the samples, with the lowest $\delta^{13}C$ and $\delta^{18}O$ values found in samples in contact with the bedrock, and the highest values in the outer edge of the carbonate. These measurements are in agreement with the proposed hypothesis of formation (kinetic fractionation during precipitation) but deciphering the relative contributions to these enrichments is not possible. While cold and arid environmental conditions suggest another formation mechanism for the carbonation in ALH 84001, there are still problems within the mechanism, similar to the

problems observed with samples from the warm arid conditions. The size of the isotopic enrichment, the composition of the carbonate and the top surface crust formation are still not truly representative of the carbonates observed within ALH 84001.

4.2.4 Hydrothermal environments

Carbonates with varied chemical compositions and heterogeneous isotopic signatures have been found in freshwater spring environments. Studies have looked at variations within travertine systems exploring fractionation between isotopes formed within the carbonates and the waters from which they precipitated (Clark and Lauriol. 1992; Chafetz and Lawrence., 1994). However, in the case of Clark and Lauriol. (1992) the experimental and natural studied carbonates are not elementally complex ($CaCO_3$ and $BaCO_3$). They formed in water with high pH (>11.5), and display low isotopic values: -28‰ ($\delta^{13}C$) and -17‰ ($\delta^{18}O$).

Ihinger et al. (2002) studied a suite of rocks from over 40 dykes from the New England-Quebec igneous province. The samples (lamprophyres) were organized into different batches based on their water and CO_2 contents and some were found to contain significant concentrations of carbonates with major element compositions similar to those in ALH 84001. The lamprophyres that contained Ca-bearing magnesites and siderites similar to ALH 84001 carbonates had a high CO_2 and low water contents. These CO_2-rich samples were found in a specific dyke (Little Rattlesnake) in southern New Hampshire and were the focus of Ihinger et al. (2002) analogue carbonate study. The carbonates displayed a variation but not absolute values similar to that observed in ALH 84001 rosettes, with $\delta^{18}O$ values of +5 to +19‰ and $\delta^{13}C$ values from -1 to 7‰.

In addition to isotopic enrichment, the following similarities to ALH 84001 were found:

Size and shape

Major element composition

Association with magnetites and sulphides

Similar host rock (containing amorphous silica and forsteritic olivine).

4.2.5 Synthetic Samples

Further to terrestrial settings, laboratory experiments by Golden et al. (2000 and 2001) have successfully synthesized globules of carbonate compositionally similar to those found in ALH 84001 under low temperature (~150°C) conditions, however, no isotope data were collected.

4.3. Terrestrial Analogue from Svalbard

The Bockfjord Volcanic Complex on the Arctic islands of Svalbard is the only current terrestrial site where 'rosettes' directly comparable in composition to ALH 84001 have been found. The region consists of hot springs, volcanoes and permafrost, providing potential insights into the conditions from which these carbonates formed on Mars (Treiman et al., 2002). A joint venture between NASA, UK and Norwegian institutions have looked at the various research topics in Svalbard, including: formation and weathering of carbonate deposits, microbial activity, biological-geological interactions and biosensor technology testing (Steele et al., 2006). Results from NanoSIMS on the analogue carbonate isotope variations will directly contribute to research at this site and help determine if this site is truly indicative of conditions on ancient Mars. The sample (Figs. 4.1-4.2) has been provided by Dr

Andrew Steele, the current science leader for these expeditions, under NASA's "Astrobiology Science and Technology for Exploring Planets" programme.

Figure 4.1 Cross section of mantle lherzolite xenolith.

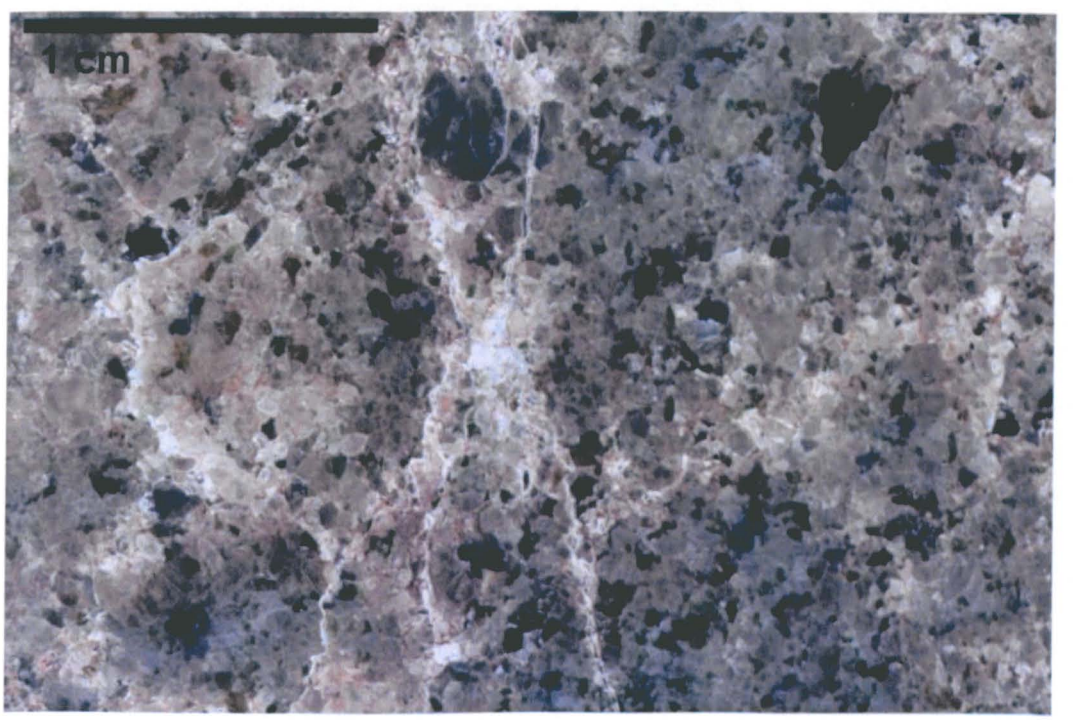

Figure 4.2 Close up of xenolith centred on veins of hydrothermal alteration (white).

4.4. Location and composition

The carbonates examined in this study are from the flanks of the Sverrefjell volcano, Quaternary basaltic volcanic province of northern Spitsbergen Island, Norway (Fig. 4.3). This location has provided numerous samples with carbonates of similar composition identified within ALH 84001 (Ionov 1998., Treiman et al., 2002). The xenoliths have been brought to the surface by alkaline magmas (Irving 1980) and present a great opportunity to study the circulation of fluid and associated variations in chemical and mineralogical compositions in the upper mantle.

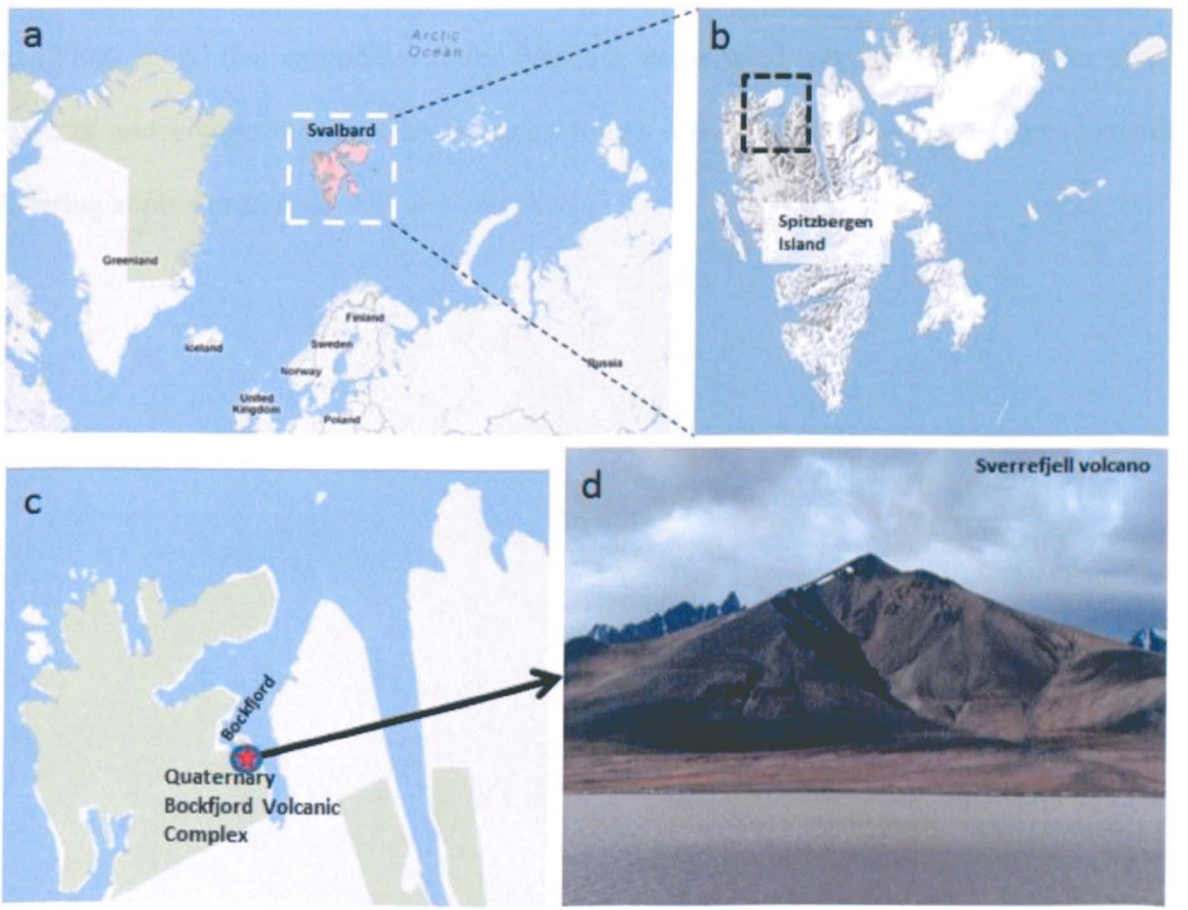

Figure 4.3 Location of the xenolith collected for this study. The sample was collected from the flanks of the Sverrefjell volcano.

The mantle xenolith used in this study was a spinel lherzolite. It consists of 47.5% olivine ($Fo_{91}Fa_9$), 41.2% clinoenstatite, 5.4%, Al-rich, Cr-augite, 2.4 % Cr-rich spinels or magnesiochromites with the approximate formula $Mg(Cr,Al,Fe)_2O_4$, 2.6% silica and 0.8% carbonate (Figs 4.4-5). However, pyroxenites and crustal xenoliths containing gneisses and granulites also exist within the location where this xenolith was collected (Treiman et al., 2002). A comprehensive study of the xenolith mineralogy of the Spitsbergen Quaternary volcanic province has been published by Grégoire et al. (2010). Previous studies have found that not all of the samples collected from Svalbard contain carbonate globules. The carbonates studied by Treiman et al. (2002) were found in locations similar to this study, within cracks and vesicles where dissolution has removed the olivines. However, Treiman et al. (2002) found that carbonates found within a single hand sample showed similar zoning patterns and compositions, while samples found within a metre of each other contained differing zoning orders.

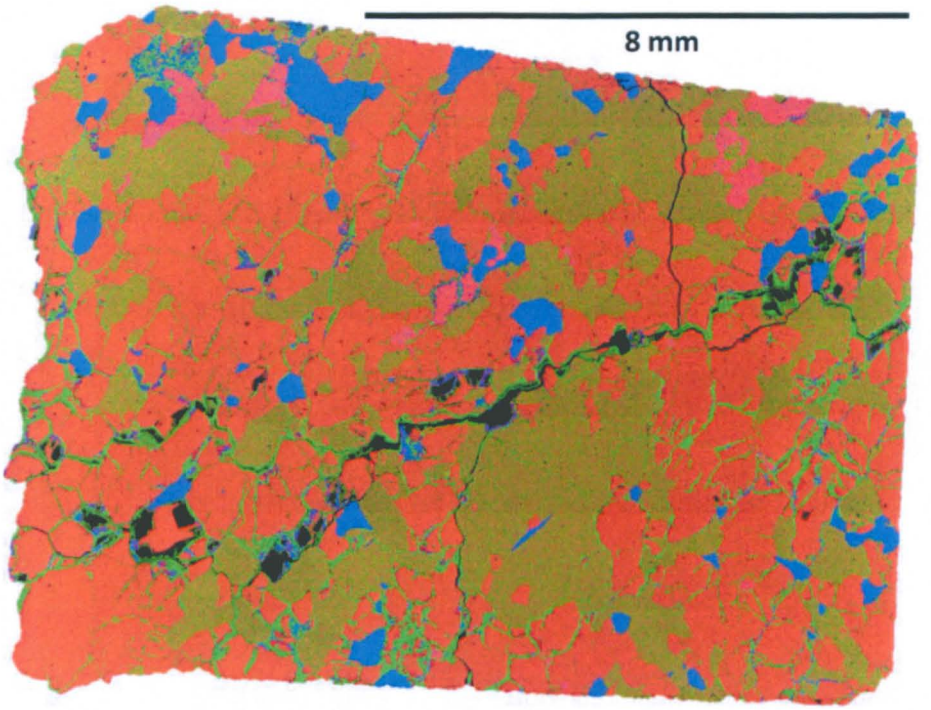

Figure 4.4 False coloured EDX image of lherzolite xenolith (ALH 84001 analogue) where Ca – blue, Si – green, Mg – red. The silica (bright green) can be observed lining some of the olivine (orange) and augite (blue) with some grains removed by the alteration.

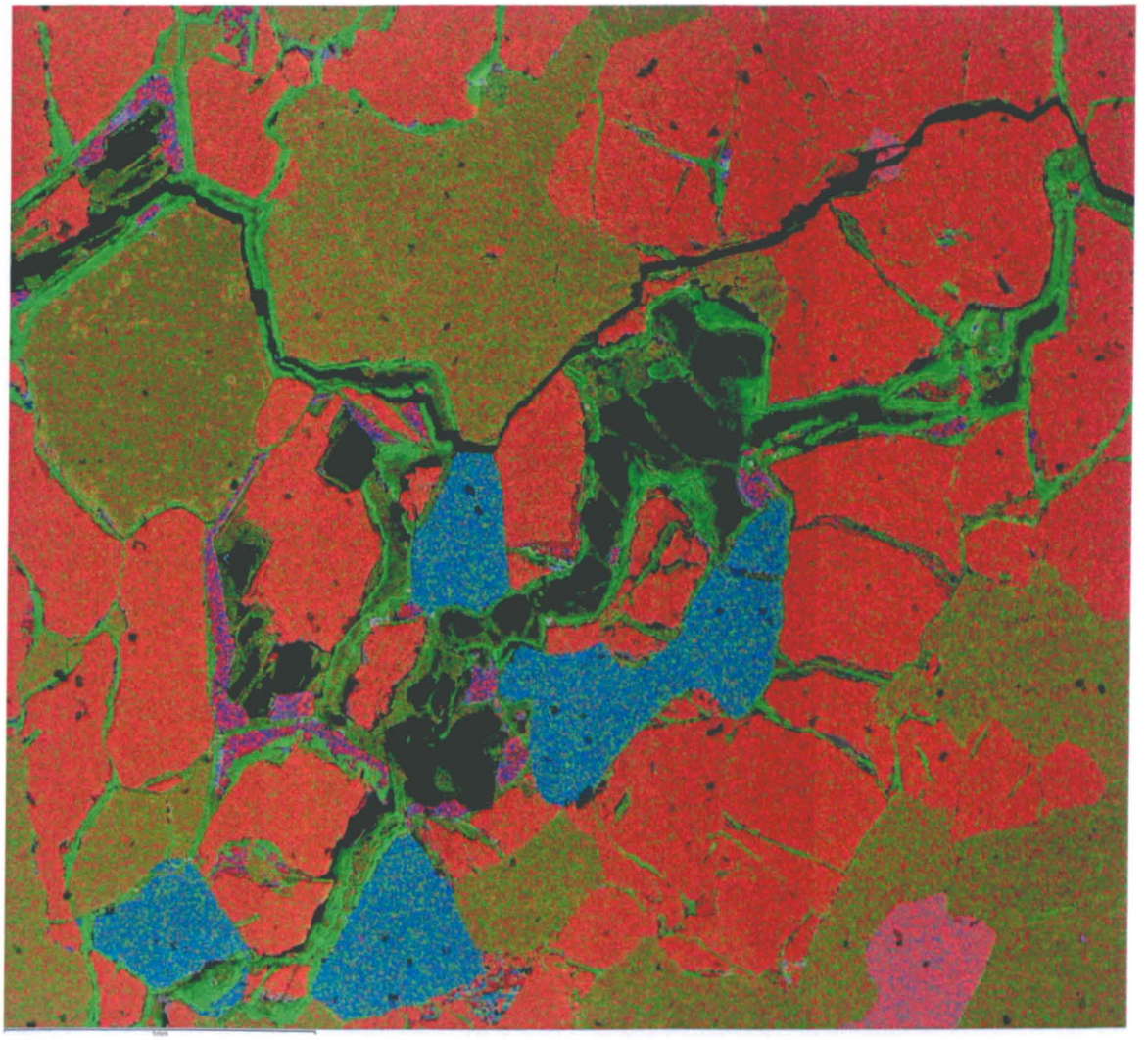

Figure 4.5 Grain boundaries are filled with silicate material (bright green). Layers of carbonate can be observed within the silica material (purple; Mg-rich carbonates - red).

The carbonate compositions appear to be influenced by the surrounding mineralogy with Ca enrichments found near augite crystals. They also appear to be associated with olivine and augite dissolution.

The types of carbonates found by Treiman et al. (2002) were variable in major element composition and were classified into two main compositional regions within the globule. There were the cores of either half ellipsoids or discs of ankerite, siderite, and

magnesite (ASM). The material typically surrounding these ASM carbonates are dolomite, magnesite, and/or calcite (DMC). The central ASM material varies concentrically in Fe/Mg/Ca ratios on a micron scale with rare grains of Fe-sulphide observed. Initial optical comparisons of ALH 84001 carbonates used in Chapter 3 (Fig. 4.6 a, c) and those found within the analogue sample (b, d) show a clear relation with sites of nucleation points of ankerite (orange) forming in a similar order to ALH 84001 carbonates. Figure 4.6 (d) displays the outer rim of magnesite-rich material with near identical scale of formation.

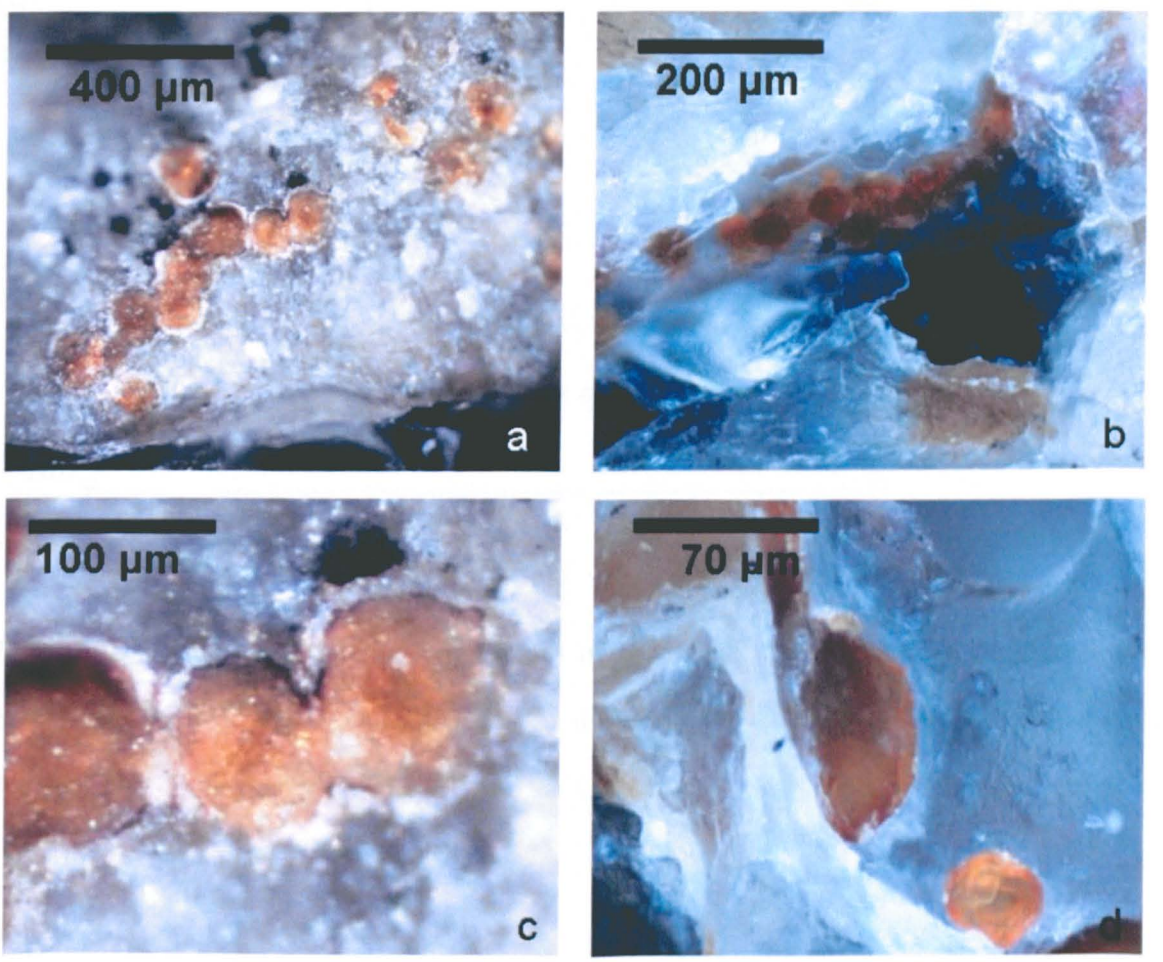

Figure 4.6 a-d Optical comparison of ALH 84001 carbonates from Chapter 3 (a, c) and the analogue carbonates (b, d).

All three of the carbonates in this study exhibit compositions similar to each other (Fig 4.6) and to those observed in ALH 84001 (Fig 4.7) values given in Table 4.1 in addition to $\delta^{18}O$.

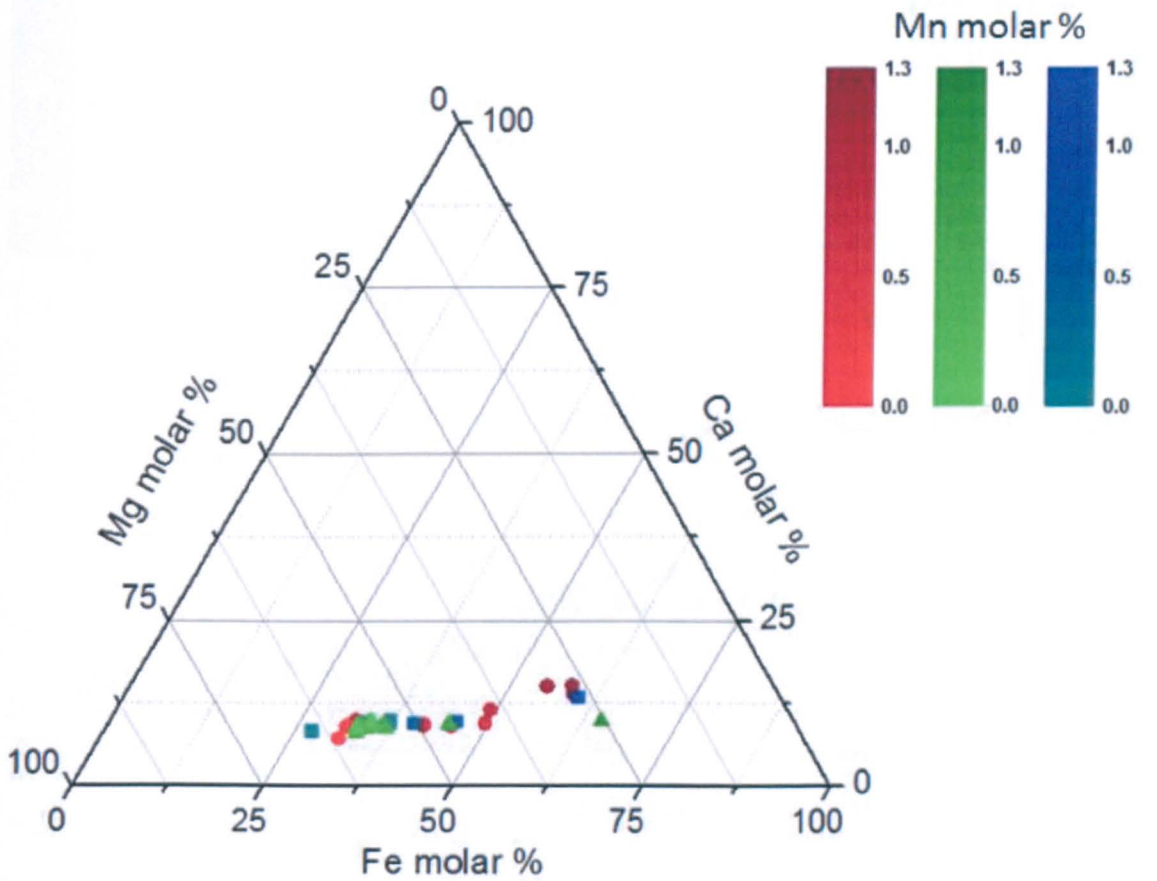

Figure 4.7 Ternary diagram for compositions of NanoSIMS analysis site for the three analogue carbonates. These data show molar abundances of $MgCO_3$, $CaCO_3$, and $FeCO_3$ with a colour gradient for $MnCO_3$. Colours refer to: red – Analogue Carbonate 1 (AC1); blue – Analogue Carbonate 2 (AC2); green-Analogue Carbonate 3 (AC3).

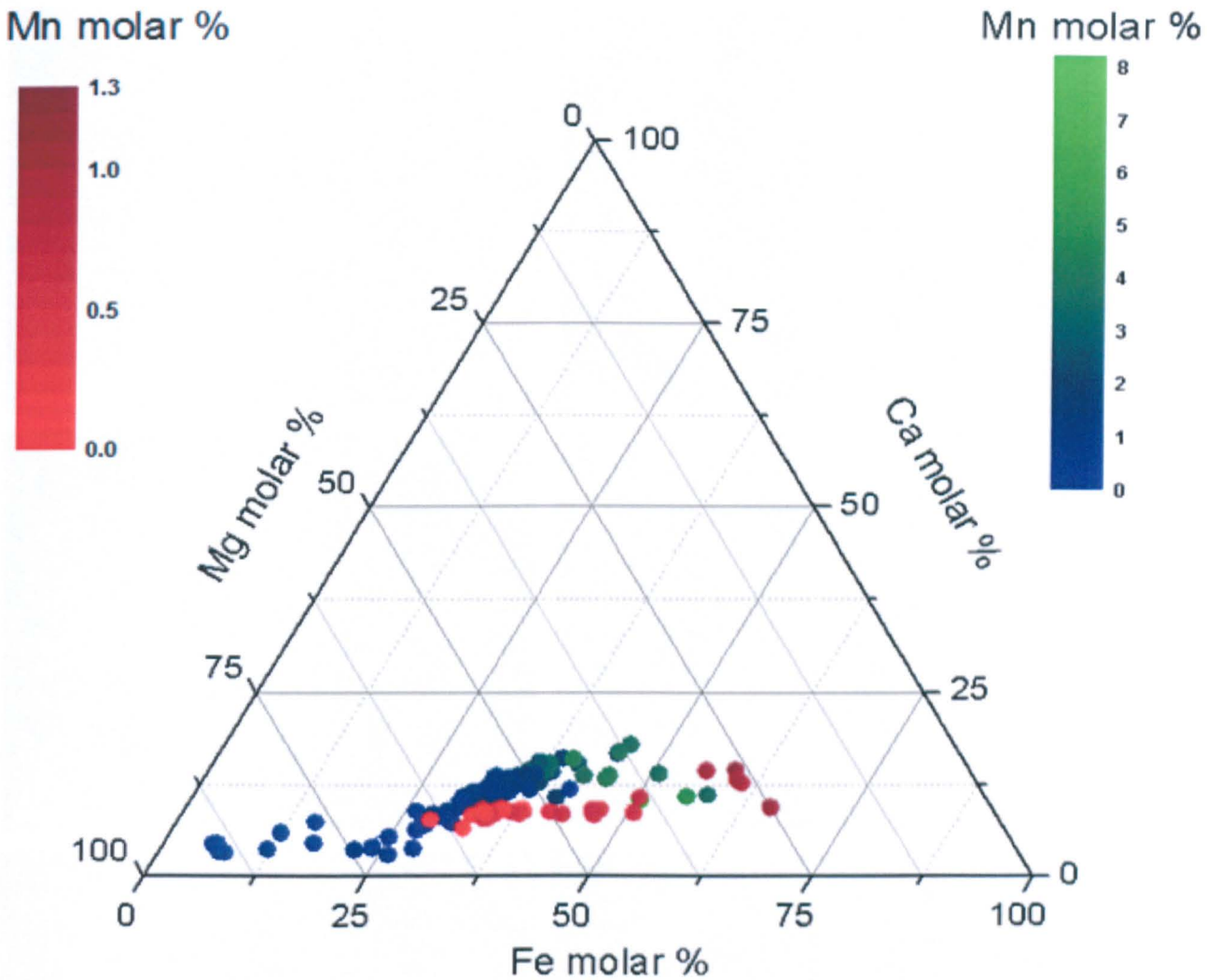

Figure 4.8 Ternary diagram comparing combined analogue compositions (EDX on SEM; red) with values from Chapter 3 ALH 84001 carbonate study (electron microprobe; blue-green; Fig. 3.5).

The diameters of the carbonates studied here range from 110 to 150 μm. Each candidate carbonate starts with an interior core of ankerite with a ~4-8 μm thick layer of magnesite followed by an 10-20 μm Fe-rich outer phase of carbonate (Figs. 4.9 a-f). The carbonates are themselves surrounded by magnesium-rich silicates. As studied in Chapter 3, the diameters of the carbonate structures were measured using NanoSIMS spot sizes of 5x5 μm^2.

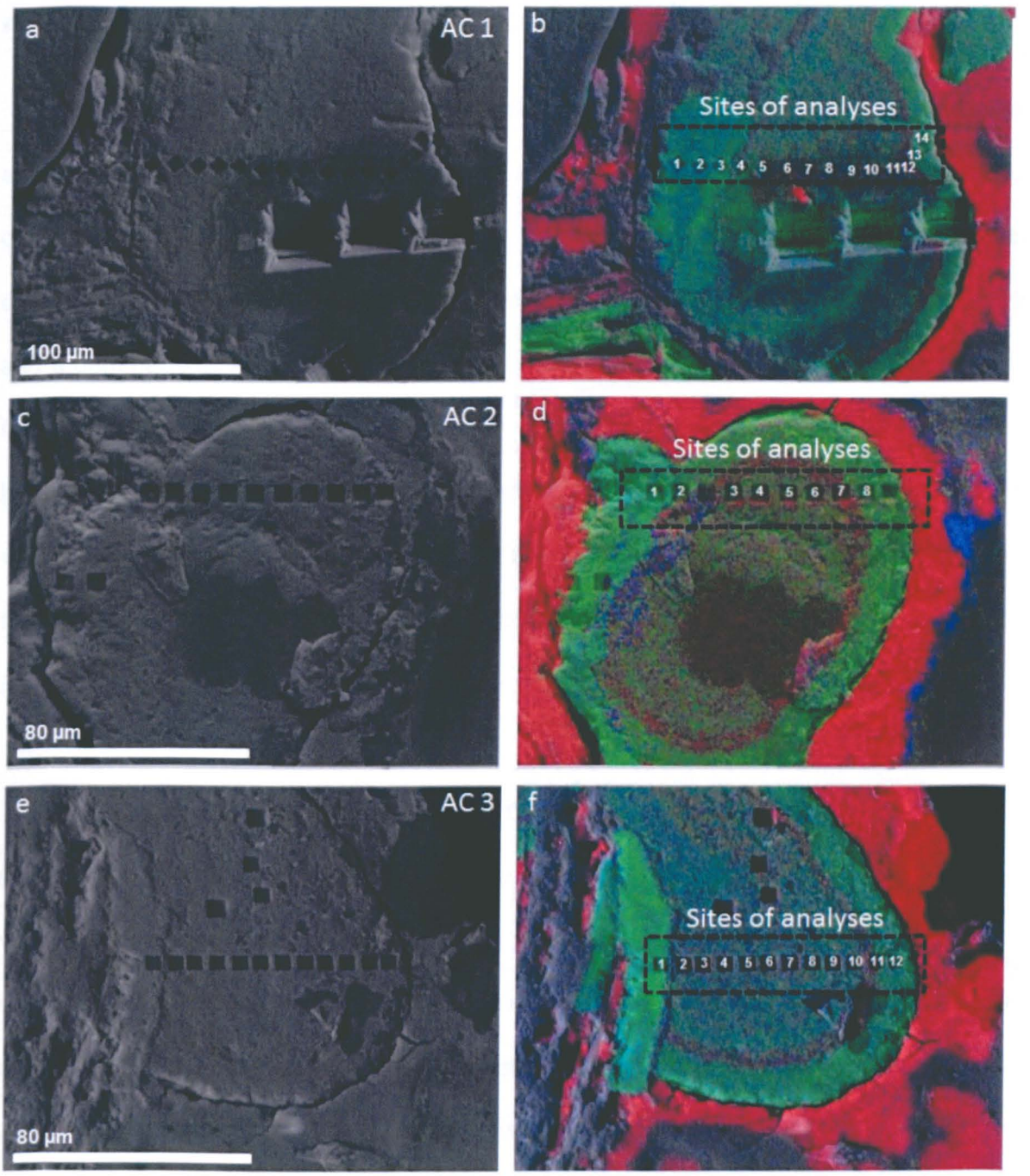

Figure 4.9 Secondary electron images of the three analogue carbonates (a,c,f) studied with NanoSIMS. Figures 4.9 b, d, f is a false coloured map of the carbonates where red (Mg); green (Fe) and blue (Ca). The numbers correspond to the NanoSIMS $\delta^{18}O$ analyses numbers.

4.5 Ion microprobe studies on ALH 84001 analogue

A single ion microprobe study has looked at the $\delta^{13}C$ and $\delta^{18}O$ within the Spitsbergen analogue carbonates with 25 μm diameter spots (Mojzsis et al., 1999). The Spitsbergen carbonates are known to have compositions similar to those of ALH 84001; however, the carbonate samples available for that study were a magnesian calcite referred to as SB43690 and a dolomite known as SX6. The authors concluded from the average isotopic values that the carbonates were not primary 'mantle' carbonate but were derived from CO_2–rich hydrothermal fluids which deposited carbonate of a crustal origin. While only small changes were observed in the magnesian calcite of $\delta\ ^{13}C_{PDB}$ <5‰ and $\delta^{18}O_{SMOW}$ <3‰ larger variations for the dolomite of $\delta^{13}C$ ~14‰ and $\delta^{18}O$ ~9‰ were measured (Mojzsis et al., 1999). The isotope range is smaller than those found in isotope studies of ALH 84001.

There were two important aspects of the Mojzsis et al. (1999) study that the work in this Chapter will build on. The first is the size of the analysis spots, as the isotopic variations were observed across such a small distance, using a 5 μm spot size compared to a 25 μm should allow us to understand the fine-scale variations. The second advance from the Mojzsis et al. (1999) study is that the major element compositional variations of the Spitsbergen specimens we studied were a better match to what we observe in ALH 84001.

4.6 Methods

The xenolith sample was sliced in half using a Buehler Lapro 24" slab saw lubricated with monopropylene glycol to avoid water absorption of the alteration. One half of the sample was then cut using a smaller manual feed saw to remove a specific region of interest (Fig. 4.1). After examining the interior of the sample it became clear that numerous hydrothermal veins existed within the xenolith. Two sections of alteration material were mounted using methods discussed in Chapter 2.1. The samples were imaged (BSE) with the SEM (Chapter 2). Chemical analyses and EDX maps were also acquired, using the same carbonate standards used in Chapter 3. Ion probe measurements were obtained with the NanoSIMS 50L using a 5x5 μm^2 analyses spots to perform chain analysis of ^{18}O and ^{16}O across the analogue 'rosettes'. Analyses were conducted with a primary beam of 15 pA and a mass resolving power >6000 (M/ΔM). NHM siderite was used to calibrate each NanoSIMS analysis session with previous IMF corrections made in Chapter 3.

4.7 Isotope results

The $\delta^{18}O$ values range of the carbonates from +11.3 to +29.9‰ relative to VSMOW. These data were corrected using NHM siderite measurements to calibrate to the IMFs (Fig. 4.10) calculated within Chapter 3.

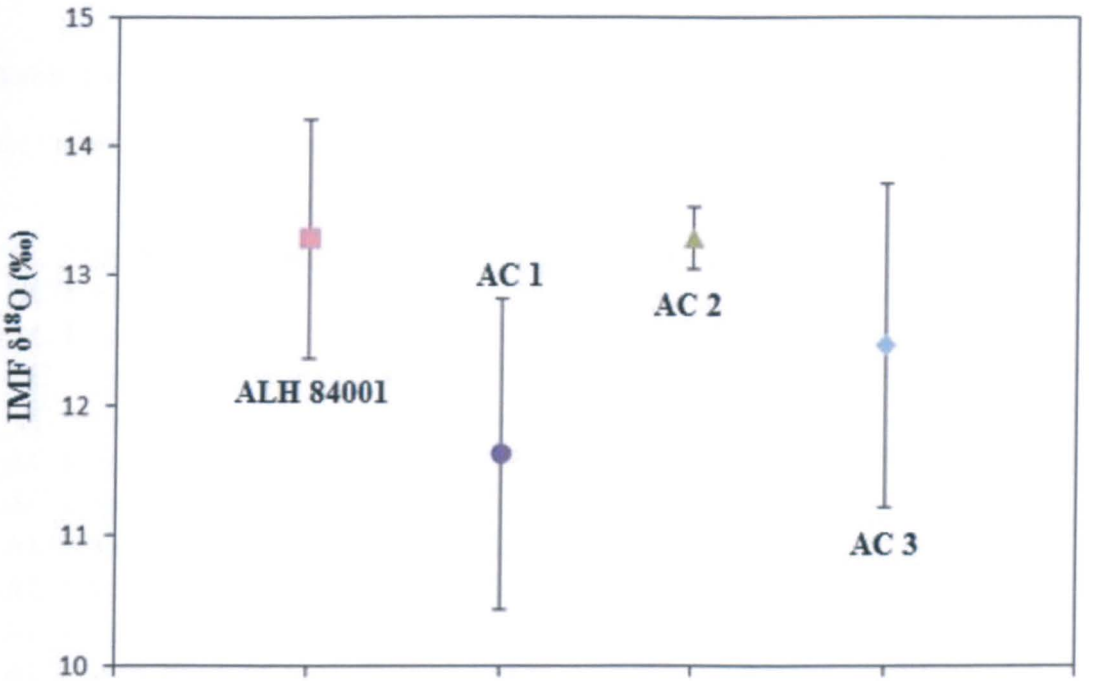

Figure 4.10 Plot of IMFs collected from siderite BM at time of standard correction and ALH 84001 carbonate analysis.

Carbonate compositions vary in X_{Mg} from 24.9 – 64.5% compared to 36.5-89.3% found in ALH 84001 carbonates (Table 3.5). The range in composition may be further enriched in X_{Mg} with only one spot sampling over the Mg-rich carbonate (X_{Mg} 64.5%; AC 2 spot 7; Fig. 4.9 d, Table 4.1) but owing to size of the Mg rich layers versus the EDX excitation volume (1 μm^3) portions of the surrounding carbonate are perhaps being sampled. Curiously AC 2 spot 7 also corresponds to the highest $\delta^{18}O$ value (Table 3.5). However, this may be linked to a slight bias in the IMF correction applied (according to X_{Mg}).

Table 4.1 Compositions of analogue carbonates when $\delta^{18}O$ IMF corrections (Fig. 3.24) are applied, the maximum recorded error is ±1.3‰ (1σ).

Sample	X_{Mg}	X_{Ca}	X_{Fe}	X_{Mn}	X_{Fe+Mn}	$\delta^{18}O$	Error (1σ)
AC 1, spot 1	26.4	14.8	57.6	1.3	58.9	+16.1	0.7
AC 1, spot 2	29.7	14.8	54.4	1.1	55.5	+24.2	0.3
AC 1, spot 3	26.8	13.6	58.5	1.1	59.5	+17.2	1.3
AC 1, spot 4	48.9	9.0	41.4	0.7	42.1	+17.1	0.3
AC 1, spot 5	39.0	11.3	49.0	0.8	49.7	+14.4	0.3
AC 1, spot 6	61.4	7.1	31.4	0.0	31.4	+17.6	0.3
AC 1, spot 7	57.6	9.7	32.1	0.5	32.6	+17.0	0.3
AC 1, spot 8	57.4	9.3	33.3	0.0	33.3	+22.0	0.3
AC 1, spot 9	57.5	8.6	33.4	0.5	34.0	+17.8	0.3
AC 1, spot 10	53.6	9.2	36.6	0.6	37.2	+17.5	1.1
AC 1, spot 11	56.9	9.3	33.3	0.5	33.8	+18.4	1.0
AC 1, spot 12	59.5	8.9	31.6	0.0	31.6	+20.8	1.0
AC 1, spot 13	45.4	9.0	45.0	0.6	45.6	+15.5	0.6
AC 1, spot 14	40.8	9.2	49.4	0.6	50.0	+13.0	0.8
AC 2, spot 1	26.6	13.2	59.2	1.0	60.2	+19.1	0.3
AC 2, spot 2	50.1	9.4	39.9	0.6	40.5	+20.9	0.3
AC 2, spot 3	56.2	9.5	33.7	0.6	34.3	+12.2	0.3
AC 2, spot 4	53.1	9.5	36.9	0.5	37.4	+26.7	0.3
AC 2, spot 5	56.5	9.4	34.1	0.0	34.1	+22.1	0.3
AC 2, spot 6	53.4	9.7	36.8	0.0	36.8	+27.7	0.8
AC 2, spot 7	64.5	8.3	27.2	0.0	27.2	+29.9	0.4
AC 2, spot 8	44.4	9.6	45.4	0.6	46.0	+18.8	0.3
AC 3, spot 1	45.2	9.6	44.6	0.6	45.2	+14.3	0.6
AC 3, spot 2	58.1	8.4	33.0	0.6	33.6	+22.0	0.7
AC 3, spot 3	53.8	9.1	36.6	0.5	37.1	+17.5	0.7
AC 3, spot 4	56.4	9.2	33.9	0.5	34.4	+13.7	0.6
AC 3, spot 5	54.4	9.3	35.8	0.5	36.3	+12.2	0.6
AC 3, spot 6	57.2	9.4	32.9	0.5	33.4	+17.5	0.6
AC 3, spot 7	57.1	9.2	33.2	0.5	33.7	+15.4	0.7
AC 3, spot 8	55.4	9.9	34.2	0.5	34.7	+16.8	0.6
AC 3, spot 9	55.7	9.7	34.7	0.0	34.7	+20.1	0.7
AC 3, spot 10	56.9	9.3	33.4	0.5	33.9	+13.1	0.6
AC 3, spot 11	57.9	9.3	32.8	0.0	32.8	+17.1	0.6
AC 3, spot 12	24.9	9.9	64.0	1.1	65.2	+11.3	0.7

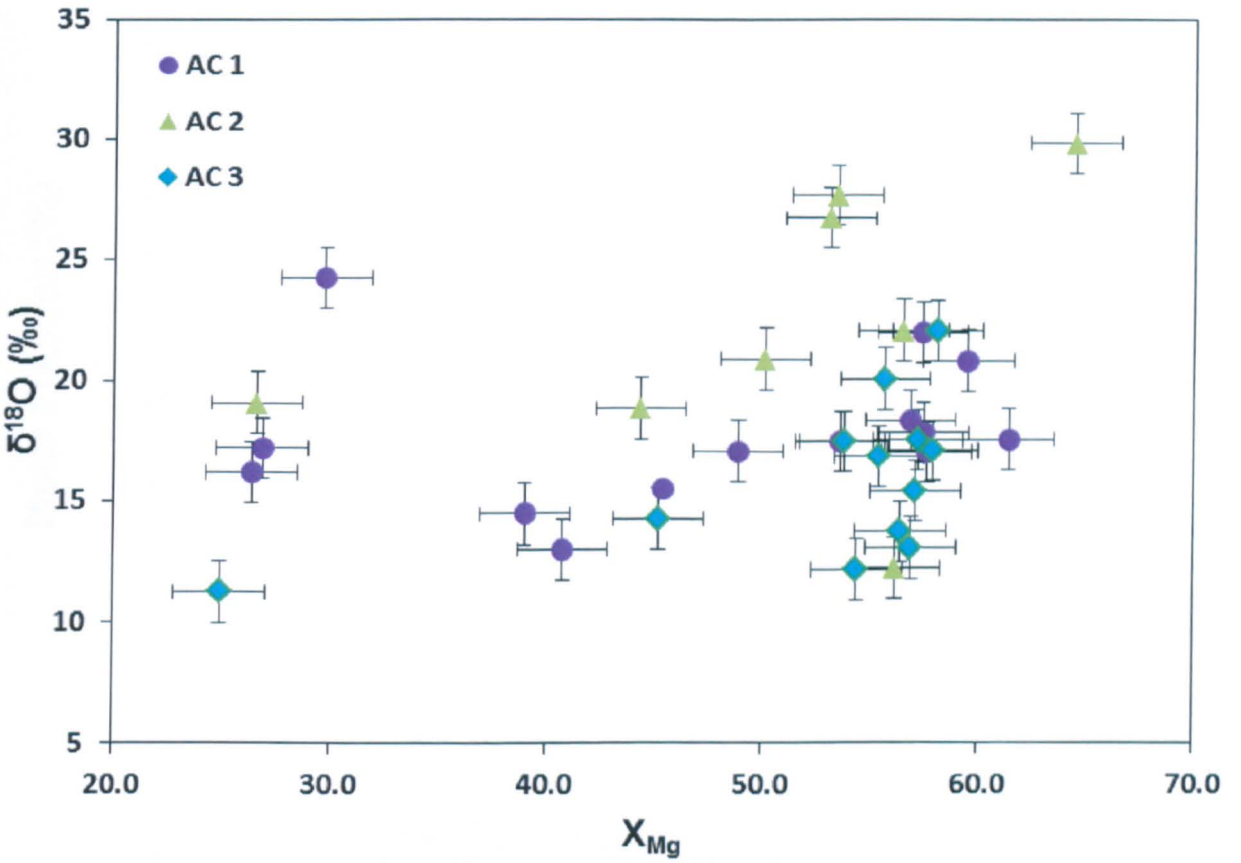

Figure 4.11 $\delta^{18}O$ values corrected according to the method described in Chapter 3.6.5.

The compositions of the individual carbonates show trends in X_{Fe+Mn} increasing in the outer layers with a drop in X_{Mg} (Figs. 4.12-4.14), X_{Ca} shows a slight enrichment with distance from the core in AC 1 and 2 (Figs. 4.12-13). The $\delta^{18}O$ values are variable but the greatest values were recorded on the outer portions of the carbonates (Figs. 4.12-13), while it was not consistent throughout the carbonates there was a general trend similar to the ALH 84001 carbonates. These observations were consistent with a gradually enriched $\delta^{18}O$ fluid precipitating the concentric carbonate layers. NanoSIMS spots (1-3) AC 1 sample the largest outer portion of Fe-rich carbonate found within the analogue samples (Fig. 4.9b, 4.12).

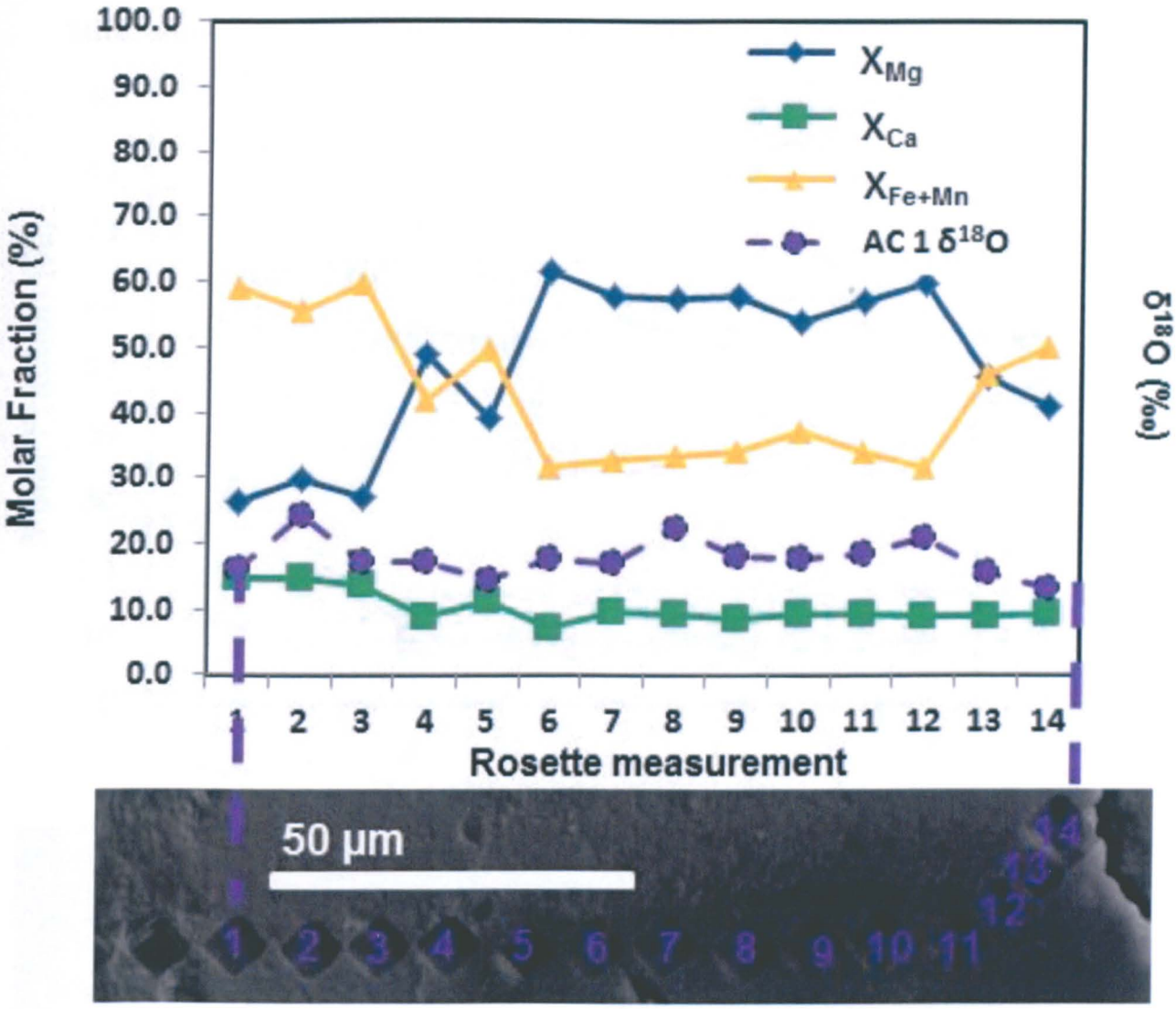

Figure 4.12 Molar fractions and $\delta^{18}O$ values for AC 1. Points left empty (far left) correspond to either instrument tuning points or analyses detected high Si content (Si > 1 wt. %).

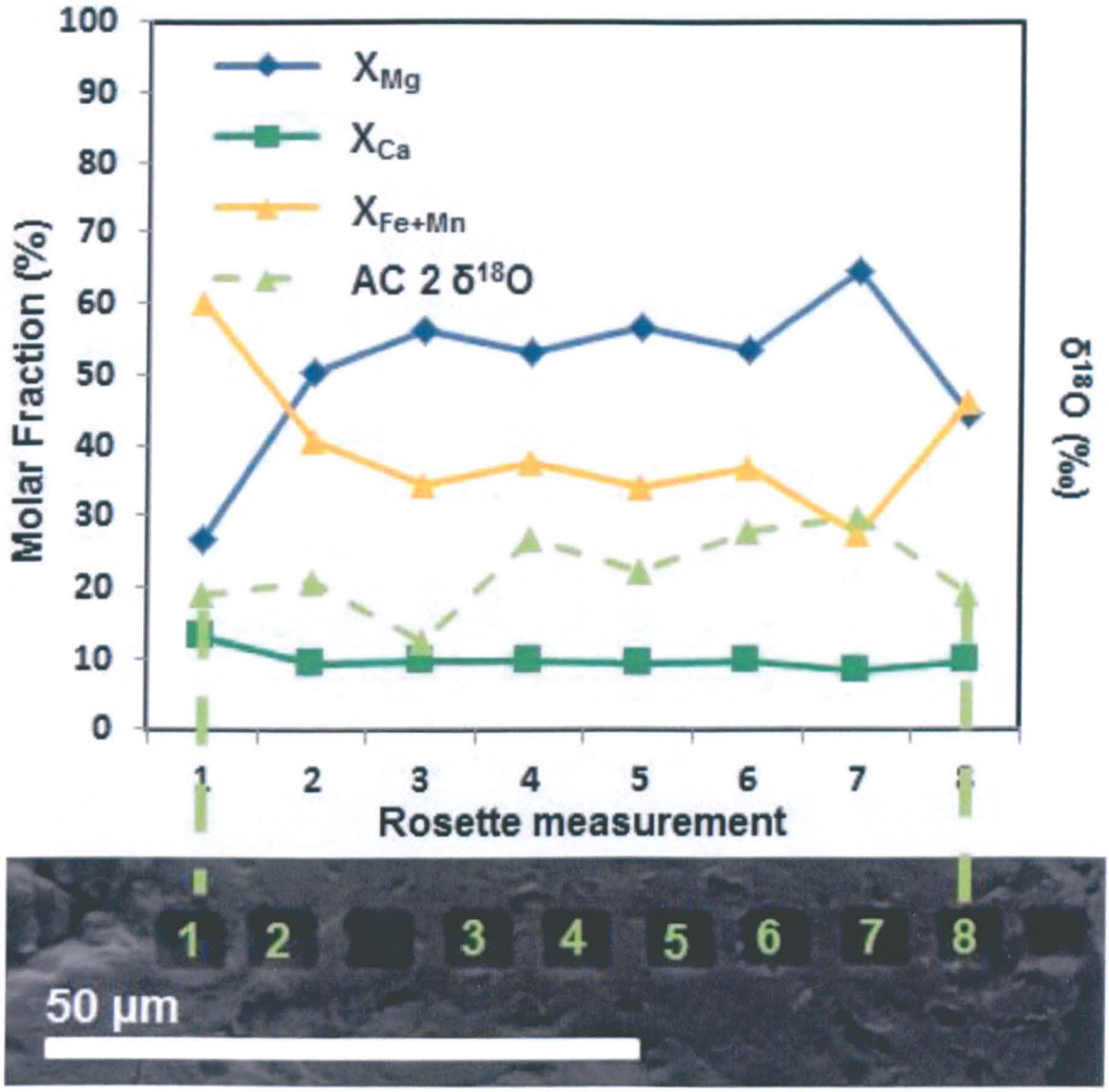

Figure 4.13 Molar fractions and $\delta^{18}O$ values for AC 2. Points left empty (between 2-3, after 8) correspond to either instrument tuning points or analyses detected high Si content (Si > 1 wt. %).

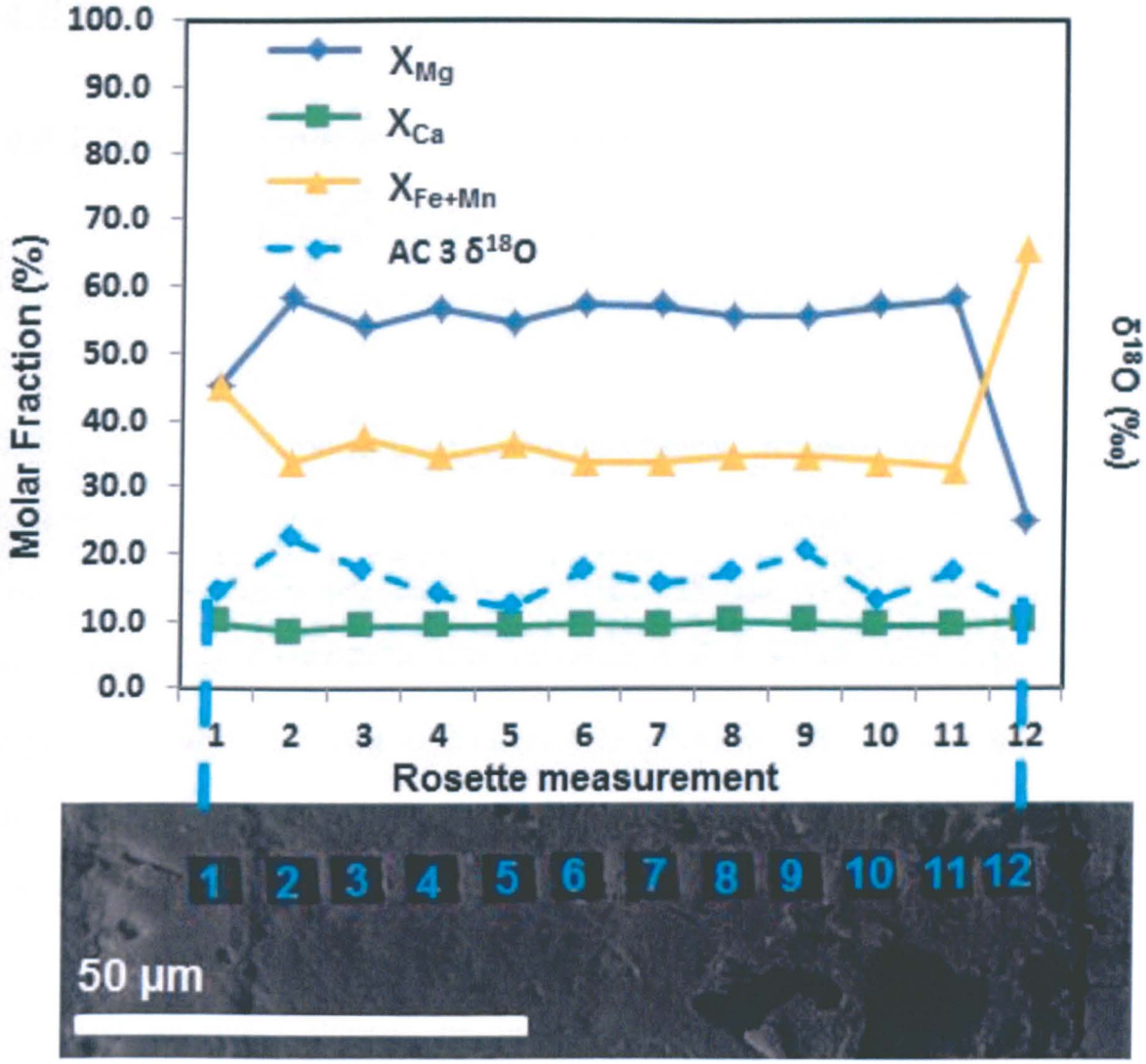

Figure 4.14 Molar fractions and $\delta^{18}O$ values for AC 3. Points left empty (Figs. 4.8 e, f) correspond to either instrument tuning points or analyses with high Si content (Si > 1 wt. %). $\delta^{18}O$ values corrected according to the method described in Chapter 3 (Section 3.6.5).

4.8 Discussion & Implications

4.8.1 Comparison with ALH 84001 carbonates

The carbonates found within this xenolith from Spitsbergen compare well with those in ALH 84001 in terms of size, shape, chemical compositions and zoning of structures (Figs. 3.3, 4.6, 4.8-9). The carbonates from both ALH 84001 and Spitsbergen range in size ~110-150 μm diameters, both sets of carbonates display ellipsoidal to disc shapes, are concentrically zoned in Mg and Fe-rich layers and occur as cementations filling interstitial spaces between grains. Strong zoning occurs in both carbonate structures over small scales ~5 μm and variations in $\delta^{18}O$ are also observed (Figs. 3.25, 4.12-4.14). While clear similarities apply between these carbonate structures there are of course differences, however, these can most likely be explained by variations in the hydrothermal systems and the more complex history of ALH 84001.

The variations in chemical composition between the Spitsbergen and ALH 84001 carbonates are minor. Although the carbonates within ALH 84001 have ankerite cores (similar to Spitsbergen carbonates), they go to a fine layer of Fe-rich carbonate before a ~10 μm layer of magnesite followed by an inconsistent outer region of Fe-rich carbonate (Fig. 3.3). The Spitsbergen carbonates vary from ankerite to a thin magnesite ~5 μm layer followed by a thicker ~ 20 μm outer rim of Fe-rich carbonate. Variations in X_{Ca} are also lower in the analogue carbonates (7.1 to 14.8%; Table 4.1) with high values associated with outer portions of the carbonates, but no obvious zoning. However, ALH 84001 carbonates vary in X_{Ca} from 3.2-17.9% with zoning observed from high core X_{Ca} values to low rim values (Fig. 4.15). The outer rims of the carbonates also differ, with an Fe-rich phase dominant in Spitsbergen compared to the Mg-rich carbonate found within ALH 84001.

Isotope analyses from the core show quite different starting $\delta^{18}O$ values for the analogue carbonates with all three carbonates initially decreasing in $\delta^{18}O$ as opposed to values from ALH 84001 which show a gradually increase from the core to edge. The $\delta^{18}O$ values then appear to gradually increase, similar to those within ALH 84001 until they reach the outer Fe-rich carbonate layer where a drop in $\delta^{18}O$ is observed.

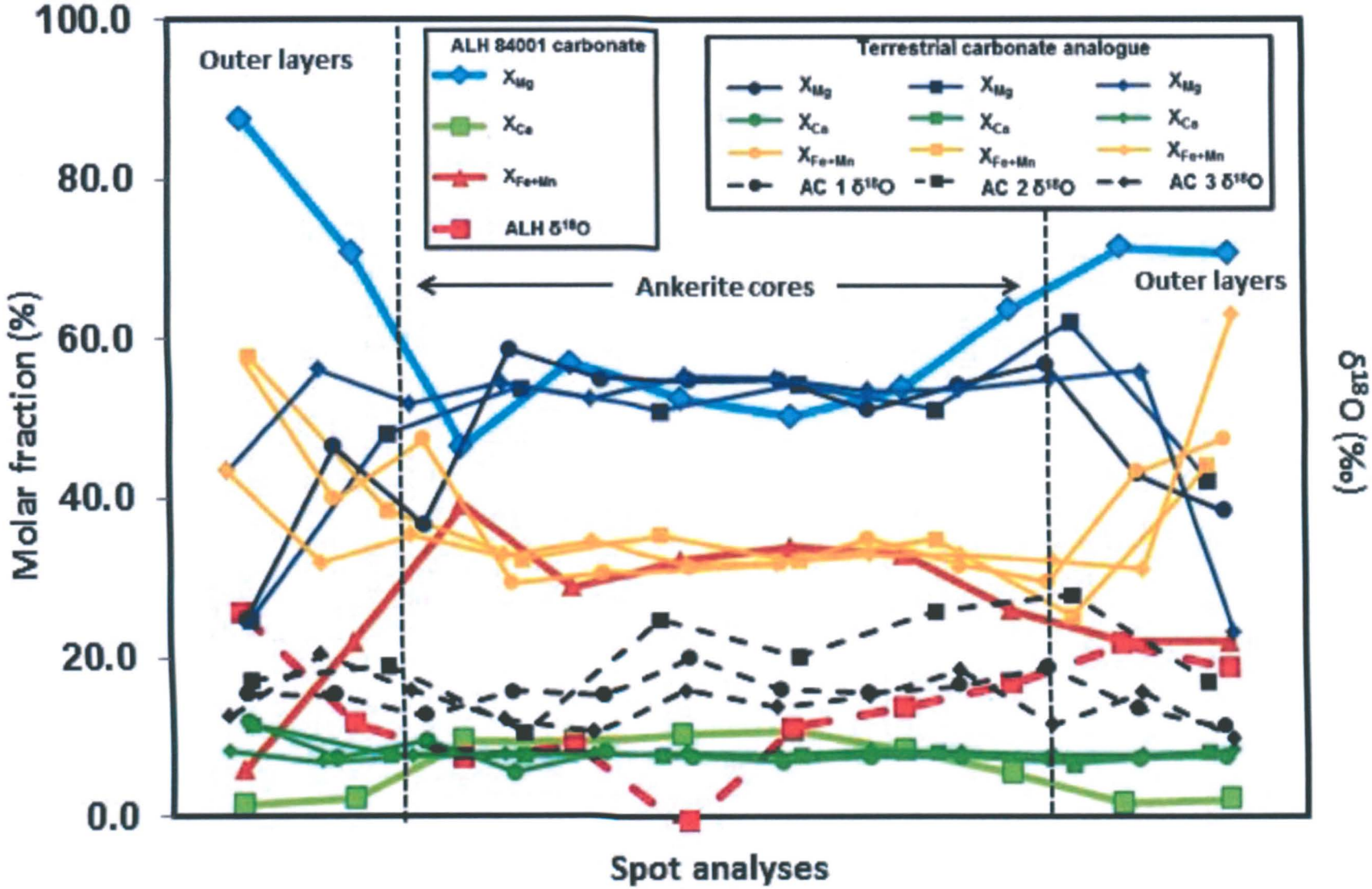
100.0
80.0
60.0
40.0
20.0
0.0
Molar fraction (%)
Outer layers
ALH 84001 carbonate
X_{Mg}
X_{Ca}
X_{Fe+Mn}
ALH $\delta^{18}O$
Terrestrial carbonate analogue
X_{Mg}
X_{Ca}
X_{Fe+Mn}
AC 1 $\delta^{18}O$
X_{Mg}
X_{Ca}
X_{Fe+Mn}
AC 2 $\delta^{18}O$
X_{Mg}
X_{Ca}
X_{Fe+Mn}
AC 3 $\delta^{18}O$
Ankerite cores
Outer layers
Spot analyses
$\delta^{18}O$ (‰)

Figure 4.15 Comparison of $\delta^{18}O$ values and molar fractions between ALH 84001 carbonates and Spitsbergen carbonates.

The major differences between the ALH 84001 and the analogue carbonates are the lack of silica in ALH 84001 but the inclusion of magnetite, pyrite and pyrrhotite. The origin of the magnetite in ALH 84001 could be the result of thermal decomposition, terrestrial contamination or organics. Experiments have shown that iron-rich carbonates have decomposed into fine grain iron oxides (De et al., 2001), this aspect of the origin of the magnetite are discussed in Chapter 7. The other main difference is the abundance of clays, while some silicates and clays have been cited in ALH 84001 their observations have been few and far between (Thomas-Keperta et al., 1997), meanwhile associated silicates are a common phase observed around the analogue carbonates (Figs. 4.4-5). The surrounding silicates phases appear to post-date the carbonate formations, similar to formations found in the some of the nakhlite martian meteorites. However, associated silicates in ALH 84001 are not found in this studies sample and are rarely cited, perhaps removed from the system. Meanwhile silica observed in the Spitsbergen sample remain within the pores and cracks closely associated with the carbonates (Fig. 4.5). There appears to be clear evidence of dissolution within the Spitsbergen samples and if this applies to ALH 84001 as suggested in Chapter 5, more silica should be observed. However, if the silica remained mobile in the precipitating fluids and were then cleared from the system, voids should at least remain. These voids could be accounted for by recorded subsequent shock events following carbonate deposition (Treiman et al., 2002; Corrigan and Harvey, 2002) crushing and closing any remaining open spaces or pores.

4.8.2 Implications for Mars

As noted by Treiman et al. (2002) caution has to be taken when extrapolating these alteration products as a regional formation. It is likely that similar to this analogue sample the formation of ALH 84001 carbonates are localized as a result of a small-scale hydrothermal system. The compositions studied for the analogue carbonates do not cover the full range measured in Chapter 3. The core compositions of the ALH 84001 carbonates are well represented in this Chapter while the outer rim is not as enriched in Mg. This difference in the carbonates is unfortunate but it potentially accounts for the difference in the $\delta^{18}O$. The analogue carbonates experienced an 18.6‰ (+11.3 to +29.9‰) enrichment compared with 27.2‰ (-0.1 to +27.1‰) from the carbonates within ALH 84001.

4.9 Conclusions

- Hydrothermal environments exist on Svalbard that can mimic the carbonate formations observed in ALH 84001.
- These carbonates appear to have formed in veins, cracks and voids produced by the dissolution of surrounding silicates.
- The variability of the compositions and order of formation over short relative distances suggest that the carbonates may only sample a small section of the local terrain and not represent wide scale alteration.
- The variation in $\delta^{18}O$ values (~20 ‰) suggest this mechanism of formation (hydrothermal) is a valid origin of the carbonate enrichments observed within ALH 84001.

- These conditions of formation are also plausible with the era in which they are thought to have formed on Mars (Phyllosian). At this time in Mars' past, liquid water is thought to have existed on the surface or subsurface and volcanic activity (hydrothermal) would have been widespread.

Chapter 5

5. Computational modelling of ALH 84001 carbonate formation

5.1 Introduction

The character of aqueous systems on Mars can provide us with important information regarding the history of water and the possibilities for environments once or currently favourable for the presence of martian life. Evidence of ancient aqueous systems have been preserved in carbonates found in the martian meteorite ALH 84001 whose crystallization age of 4.1 Ga indicates that it has experienced almost all of Mars' history. The 3.9 Ga age of the carbonates places their formation at a critical time on Mars that has been argued to have been `warm and wet' by previous studies (Bribing et al., 2005; Ehlmann et al., 2008). The carbonates in the ALH 84001 meteorite provide the best opportunity, among all of the martian meteorites, to understand the details of an ancient aqueous system on Mars. Their unique chemical, isotopic and mineralogical composition provides the opportunity to make conclusive statements about the geological conditions in which they formed including; formation temperature, chemistry of the fluids and isotopic reservoirs on early Mars.

Attempts have been made to model the carbonates conditions of formation in order to derive the environment in which they formed. Numerous investigations have been conducted

and suggest a range of formation scenarios such as evaporation, impact, biological and hydrothermal processes (e.g. Romanek et al., 1994; Scott et al., 1997; McKay et al., 1996; Leshin et al., 1998; McSween and Harvey, 1998; Niles et al., 2005; 2009; Berk et al., 2011) to account for the ALH 84001 carbonates. Obviously there are now more data sets available than previous models had and hence some of the models have been re-evaluated through time. However, there is no clear consensus on a single environmental setting and the range in $\delta^{18}O$ and $\delta^{13}C$ values from the carbonates has only increased providing a larger range of parameters for the models.

The work presented here aims to determine the temperature ranges, partial pressures, starting compositions, isotopic reservoirs and timescales required to reproduce the structures and isotopic values observed in ALH 84001 carbonates discussed within this thesis. The starting compositions used in this Chapter are those found within ALH 84001 consisting of orthropyroxene, maskelynite, chromite, pyrite, apatite and olivine (Mittlefehldt, 1994; Harvey and McSween, 1996). The new isotope data acquired for oxygen in Chapter 3 will be used to constrain further the formation conditions.

5.2 Low and high temperature models

Two main themes can be used to review the previous literature on formation conditions. Here the themes used are high (>200°C) and low (<200°C) temperature formation conditions.

5.2.1 Low temperature models

An initial formation temperature of ~100°C within a hydrothermal environment was suggested by Grady et al. (1994), based on measured $\delta^{13}C$ carbonate values resulting from the interaction of atmospheric CO_2 with the martian regolith. This proposed formation temperature was further reduced (cooling from 80-0°C) by Romanek et al. (1994) who measured both $\delta^{13}C$ and $\delta^{18}O$ values of the carbonates. However, it was the $\delta^{18}O_{SMOW}$ values (+13.3 to +22.3 ‰) which were used to model these temperatures in an open system with a constant H_2O/CO_2 ratio (0.58). The model derived this temperature decrease based on equilibrium fluid-mineral fractionation factors (similar to a model used by Clayton and Mayeda (1998) on carbonate in EETA 79001). Romanek et al. (1994) also suggested a closed system based on their $\delta^{18}O$ values. The system had varying H_2O/CO_2 ratios, steady temperatures and fluid constantly percolating through the rock, precipitating carbonates with smaller chemical variations.

Low temperature formation was also postulated by Treiman (1995) owing to the retention of zoning in the carbonates. Treiman (1995) argued that previous studies had demonstrated that high temperatures would effectively homogenize the carbonates within

unrealistically short timescales (days at 500°C and a ~month at 300°C; Rosenberg, 1963; 1967, respectively). Treiman (1995) also suggested from petrographic relationships that a single formation phase could account for the carbonates mineralogy instead of multiple alteration phases previously suggested by Mittlefehldt (1994). Subsequent $\delta^{18}O$ data collected by Leshin et al. (1998) and Eiler et al. (2002) suggested temperature drops from 125-0°C and 190-20°C respectively, explained the $\delta^{18}O$ variation.

Two new environments in which the carbonates precipitated were suggested by Niles et al. (2005). Both of these formation environments were inferred from acquired $\delta^{13}C$ values (+27 to +64‰) obtained with SIMS analyses. The first of the two models was an environment (such as a lake mixing with a spring) in which two isotopically distinct fluids could mix to produce the large variations in observed $\delta^{13}C$ values. Niles et al. (2005) described an analogue lake discovered in Turkey (Kazmierczak and Kempe, 2003) from which carbonates of similar size, shape, and chemical zoning were found. The second model describes an initially closed subsurface aqueous system where serpentinisation of the mafic rock increases the pH before being released as a high pH spring into a CO_2-rich atmosphere. Niles et al. (2005) suggested that this progression from a closed to an open system rapidly precipitated carbonate with varying isotopic and chemical compositions.

Niles et al. (2009) used equilibrium thermodynamic modelling to understand the zoning composition of the carbonates. They determined that starting fluid compositions with specific mole ratios of Mg/Ca (>~5.3) and Fe/Ca (>~1) would reproduce the zoning pattern observed in the ALH 84001 carbonates. The starting fluid was determined to form from subsurface aqueous alteration of an ALH 84001-type rock under low temperature (<100°C), pH 5-7 and an elevated CO_2 fugacity (0.1-1 bar). This fluid was then thought to precipitate carbonates following upwelling of the CO_2-rich fluid, where the CO_2 degassed and resulted in

increased pH. Berk et al. (2011) produced another thermodynamic model, however, they modelled a solid solution of carbonates assuming the isochemical equilibration of ALH 84001 minerals with pure water. CO_2 partial pressure reduction and low temperatures (10 – 0.0001 bar at 5°C or 60-0.0001 bar at 30°C) were suggested to form carbonates in the martian subsurface.

5.2.2 High temperature models

The first high temperature formation conditions (~700°C) were suggested by Mittlefehldt (1994). The temperature was derived from the magnesite-siderite molar compositions solvus limb of the Ca-Mg-Fe carbonate ternary diagram (Anovitz and Essene, 1987). Romanek et al., (1994) suggested a high temperature formation (>200°C) within a closed system. However, owing to changes in the cation composition of the carbonate an open instead of a closed system was deemed appropriate in which a low temperature (0-80°C) model was suggested. These temperatures were calculated from molar H_2O/CO_2 fluid ratios (Clayton and Mayeda., 1988; Wright et al., 1992). Wentworth and Gooding (1995) suggested a formation temperature below 300°C based on the well-developed carbonates and ZnS and Fe-sulphate accessories that they infer formed under reducing conditions.

A surge of papers suggesting formation of carbonate at high temperature (>200°C) conditions followed a paper in 1996 which claimed to observe remnants of past organics (McKay et al., 1996). These subsequent papers all directly contested the validity of McKay et al. (1996) findings with suggestions that organics would have not formed or been sustained under these high temperature conditions (Harvey and McSween, 1996; Gleason et al., 1997; Kring et al., 1998; Scott et al., 1997, 1998; Scott, 1999). A high temperature impact induced

origin was suggested by three studies (Harvey and McSween., 1996 and Scott et al., 1997; 1998). The three studies differ with CO_2-rich fluids being suggested to form the carbonates at rapidly cooling temperatures <300°C (Harvey and McSween., 1996) and an impact induced carbonate-rich melt forming the carbonates >500°C (Scott et al., 1997; 1998). Gleason et al. (1997) and Kring et al. (1998) both suggested that the carbonates formed from a hydrothermal event in which CO_2-rich fluids cooled from 300°C. Each case of carbonate formation was based on the replacement of maskelynite in a dissolution-precipitation reaction. The suggested timescale of formation was a few years based on dissolution rates of plagioclase at temperatures <300°C (Kring et al., 1998).

5.3 Composition of ALH 84001 and carbonates

The bulk composition of ALH 84001 used in this Chapter's model are based on ~95.6% orthopyroxene, 2% maskelynite, 1.9% chromite, 0.46% carbonate, 0.031% phosphate and 0.021% pyrite and traces of clinopyroxene (Dreibus et al. 1994; Mittlefehldt 1994; Treiman 1995) who combined thin section and inferred modal compositions from bulk dissolution values. However, traces of olivine (Harvey and McSween 1994), magnetite and silica (Thomas-Keprta et al. 1996) were subsequently discovered. Magnetite, silica and carbonate are assumed to be alteration phases are ignored in the model inputs. The primary phases are normalised (see Table 5.1). This process assumed equal amounts of the original bulk ALH 84001 composition dissolved into solution and precipitated the secondary phases. No modal values of olivine and augite could be found, so conservative values of 0.01 mol.% were used for both, having a minor effect on the model. Specific compositions of the phases are listed in the table along with any known isotopic compositions.

Table 5.1 Composition of assumed pre-altered minerals found in ALH 84001 and oxygen isotopic values. The oxygen isotopic values of orthopyroxene (Mittlefehldt, 1996[6]) are +4.6 ±1.2‰, olivine[1] +5.1±1.4‰ (2σ), (Shearer and Leshin, 1998[1]), maskelynite (Mittlefehldt, 1996[6]) +4.3 ± 0.26‰ (2σ) (3 spot average; Romanek et al., 1996[2]), chromite +2 ± 0.9‰ (2σ) (6 spot average, Eiler et al., 2002[3]), phosphate +3.4 ± 0.9‰ (2σ) (2 spot average, Greenwood et al., 2003[4]), pyrite and augite 4.6‰ (general value, Clayton.1993[5]).

			Composition	Isotopic values
		mol	Normalised (mol. %)	$\delta^{18}O$ (‰)
Orthopyroxene				4.6 ± 1.2[1]
$MgSiO_3$	Enstatite	66.6316		
$FeSiO_3$	Ferrosilite	26.211		
$CaSiO_3$	Wollastonite	3.16836		
$En_{69.4}Fs_{27.3}Wo_{3.3}$[6]			96.01	
Maskelynite				4.3 ± 0.13[2]
$NaAlSi_3O_8$	Albite	0.62467		
$NaAl_2Si_2O_8$	Anorthite	1.26943		
$KAlOSi_3O_8$	Orthoclase	0.11449		
$An_{31.1}Ab_{63.2}Or_{5.7}$[1]			2.01	
Chromite				2 ± 0.9[3]
$FeCr_2O_4$		1.54371		
$MgCr_2O_4$		0.36446		
$(Fe_{80.9}Mg_{19.1})Cr_2O_4$[3]			1.91	
Phosphate				
$Ca_5(PO_4)_3OH$	Hydroxyapatite	0.03	0.03	3.4 ± 0.9[4]
Pyrite				
FeS_2		0.02	0.02	4.6[5]
Olivine				5.1 ± 1.4[1]
Mg_2SiO_4	Forsterite	0.00653		
Fe_2SiO_4	Fayalite	0.00352		
$Fo_{65}Fa_{35}$[1]			0.01	
Augite				
$MgSiO_3$	Enstatite	0.00453		4.6[5]
$FeSiO_3$	Ferrosilite	0.00128		
$CaSiO_3$	Wollastonite	0.00424		
$En_{45.1}Fs_{12.7}Wo_{42.2}$[1]			0.01	

5.4 The model

The Geochemist WorkBench™ (GWB) program was used to model the Mg-Fe-Ca system within ALH 84001 carbonates (Fig. 5.1). The carbonate precipitation environment is constrained by modelling how changes in fluid composition, CO_2 fugacity, water/rock ratio (W/R) and temperature alter the chemistry of the final precipitation products. An initial inferred primary composition of ALH 84001 (Dreibus et al. 1994; Harvey and McSween 1994; Mittlefehldt 1994; Treiman 1995) is combined with a dilute NaCl brine solution. Cl^- and Na^+ were used to buffer the system and all ion species existing with ALH 84001 composition were added in very low (0.001) μmol concentrations. The output is a model of the evolution of the carbonate assemblage as equal mineral proportions of ALH 84001 are fed into the aqueous brine. Use of an initial brine solution is in agreement with theoretical predictions of martian groundwater (Clark and van Hart, 1981; Clifford, 1991). The model itself is closed and GWB only considers minerals of fixed compositions, therefore an assumed ideal behaviour of solid solutions is accepted with compositions of Ca-Mg-Fe carbonates based on mole % of calcite, dolomite, siderite and magnesite.

The model uses the Deybe-Hückel equation to provide stoichiometric calculations of the rate of alteration material precipitation in addition to cation and isotopic enrichment. The sequence of precipitation is well documented in numerous studies (e.g. Harvey and McSween, 1996; Corrigan and Harvey, 2002). In this Chapter the calcium-rich carbonates which are thought to have formed first were not addressed as these samples were not available for NanoSIMS analyses. Furthermore, the dispersed siderite phases surrounding the rosettes were also not modelled since owing to their friable nature no isotope values could be collected. Instead, this study concentrates on the main zoned phase of carbonate precipitation.

The thermodynamic script used for the modelling was from version 7 of GWB using thermo.com.v8.r6+.dat data set, which read data for 1768 aqueous species, 1122 minerals and 93 gases. This software provides simulations of chemical reactions giving outputs as stability diagrams, equilibrium states of fluids, models of reactive transport and traces reaction processes. "React" was the program used for tracing reaction paths for fluids, minerals and gases; this program was also used to predict the fractionation of the stable isotopes during the reaction. The results of the simulations were as x-y plots using GWB's Gtplot, the raw data exported as a spreadsheet for manipulation using Microsoft Excel.

The model follows a single step of formation representing an assumption that the initial fluid was evolving in composition as phases precipitated. The reasoning for this is to: (1) model accurately the reaction pathway observed from the microprobe analyses and mapping of the carbonate, which is not a single straight smooth varying composition from core to rim but rather a sharp transition from ankerite to a magnesite-rich carbonate. This transition has been smoothed in previous studies, owing to the large spot size of the analyses (i.e. Valley et al., 1997; Holland et al., 2005; Niles et al., 2005) and even in this study with a 5 μm diameter spot, there is still some overlap in composition; (2) for similar reasons regarding spot size we also see a relatively smooth transition in oxygen when IMF corrections similar to Leshin et al. (1998) are applied, however, no clear transition is observed with $\delta^{13}C$ (3) experiments by Golden et al. (2001) produced elemental compositions and single zoned structures with the use of multiple generations of fluid.

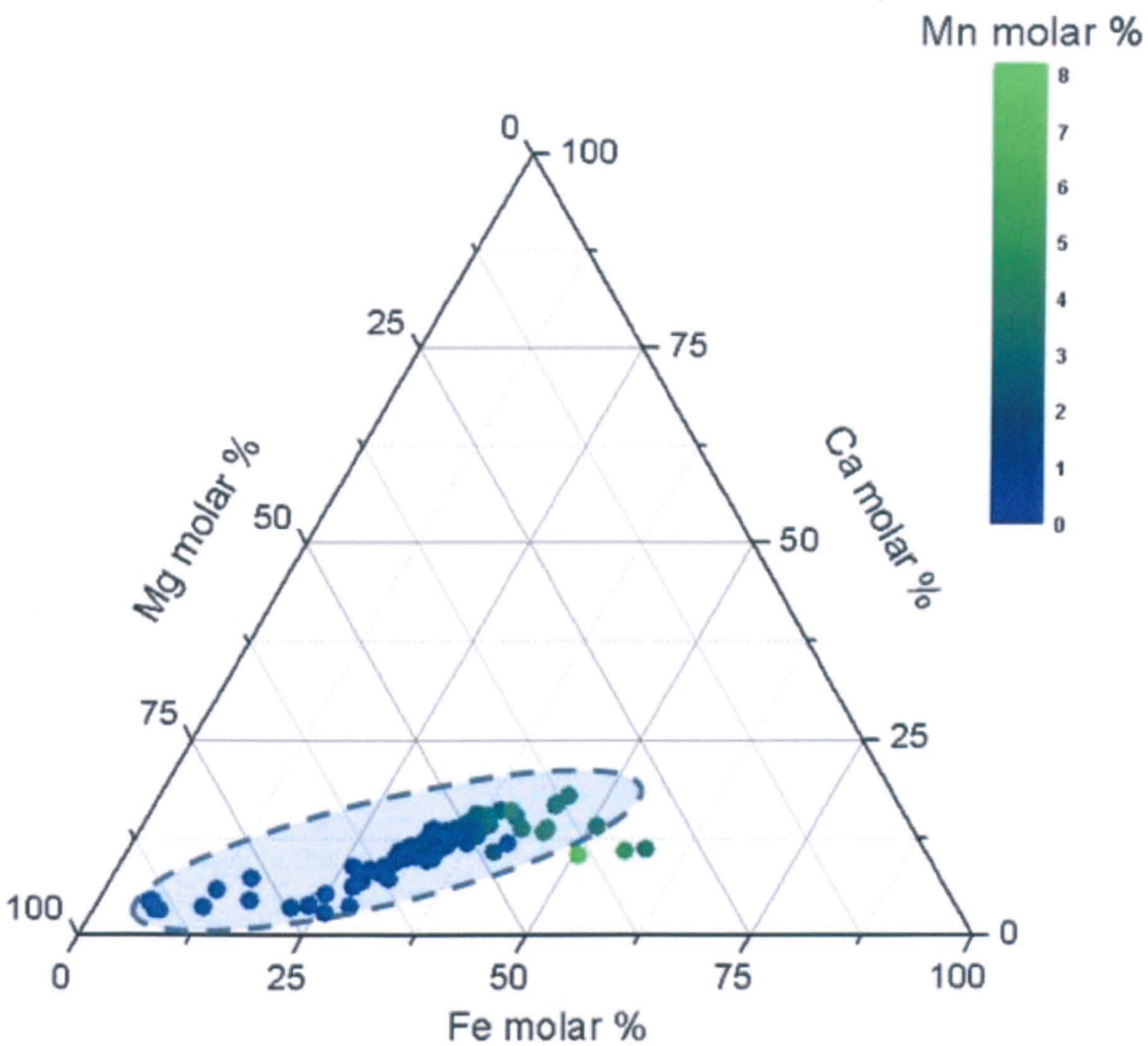

Figure 5.1 Path of ALH 84001 carbonate formation from data collected with the electron microprobe in Chapter 3, the Mg-rich carbonate (left corner) and the ankerite (centre).

Constraining the overall oxygen isotope system conditions proves difficult without knowledge of the isotopic composition of the water-bearing source and potential atmospheric component. The isotopic compositions of the carbonate (detailed in Chapter 3) and values from literature on ALH 84001 mineralogy were used as starting points to define a plausible initial isotopic composition of the brine fluid and CO_2 component.

5.5 Results

Modelling scenarios representing various system parameter changes were measured:

1) Looking at the variation of W/R ratios (5-1000)

2) Introduction of varying amounts of CO_2(g) into the system (0.1-2 mol)

3) Variations of temperature, including cooling, warming and constant temperature regimes (0-200°C; limits of GWB 0-300°C).

4) Addition of Ca^{2+} cations to the initial brine solution (0.3 mol to 0.001 μmol).

5) Isotope variations of $\delta^{18}O$ and $\delta^{13}C$ for the initial brine and CO_2 sources.

Assumptions:

1) Bulk compositional for ALH 84001 from literature is representative of the portion of sample analysed in this study.
2) Rates of dissolution are uniform for all minerals within ALH 84001.
3) Purely inorganic processes occurred in ALH 84001.
4) The system is closed.
5) Original rock is fractured sufficiently to derive a minimum W/R ratio 5 and a maximum of 1000.
6) An ideal behaviour of solid solutions assumed with Ca-Mg-Fe carbonates based on mole % of calcite, dolomite, siderite and magnesite.
7) A single evolving fluid interacted with the original ALH 84001 rock.
8) The accuracy and breadth of the thermodynamic dataset is representative of the minerals available on Mars.
9) Carbonates and phyllosilicates are not present at point of alteration.
10) All carbon contributions for $\delta^{13}C$ and carbonates are from CO_2(g).

5.5.1 Water to rock ratio effects on carbonate precipitation

A range of water/rock ratios were used to access this variable on the secondary minerals formed. The order of precipitation is displayed with arrows (Fig. 5.2 a, b), generally from a Ca-rich, to Mg-rich carbonate, however, at high (1000) and low (5) W/R ratios only calcite is observed.

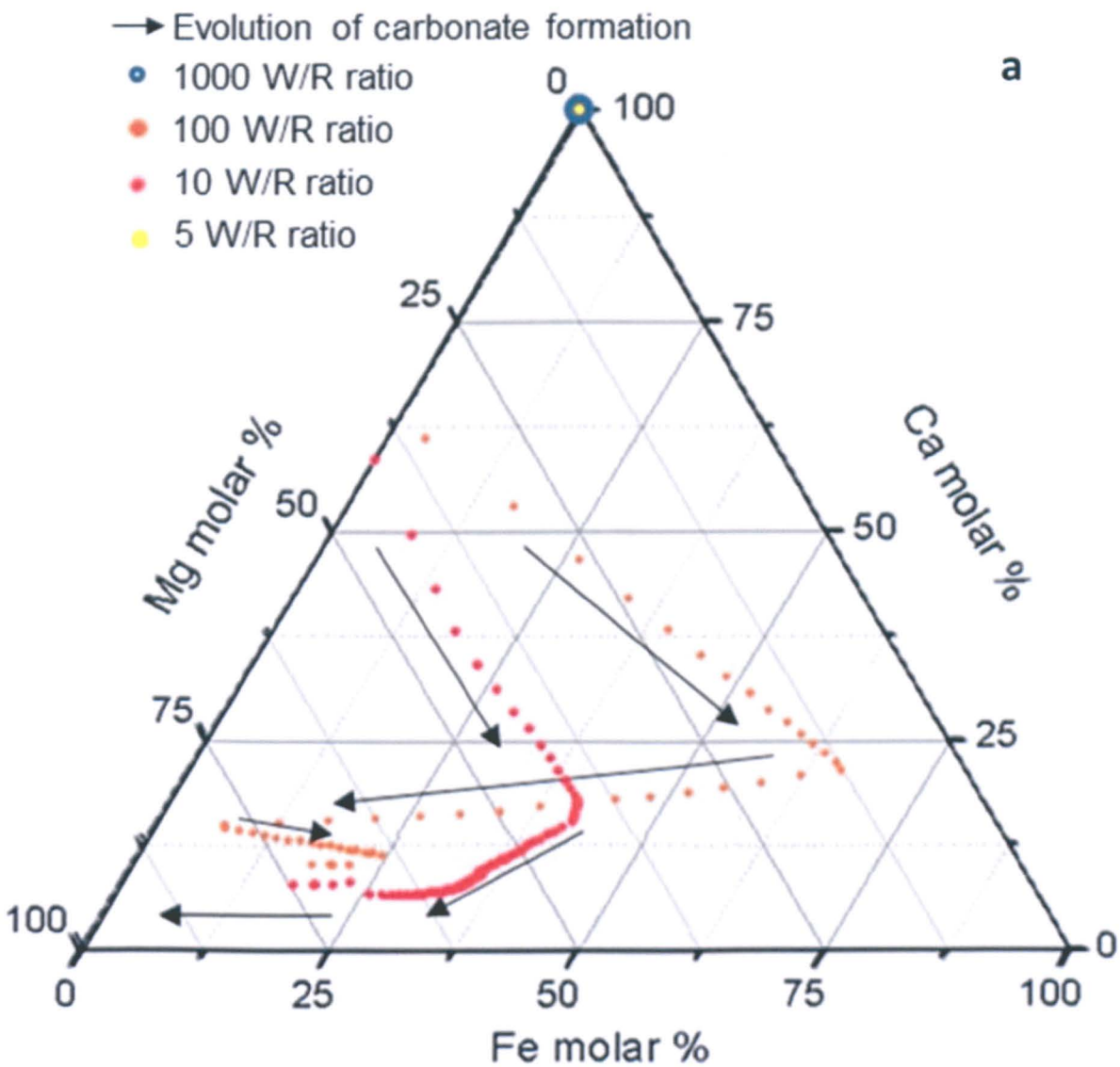

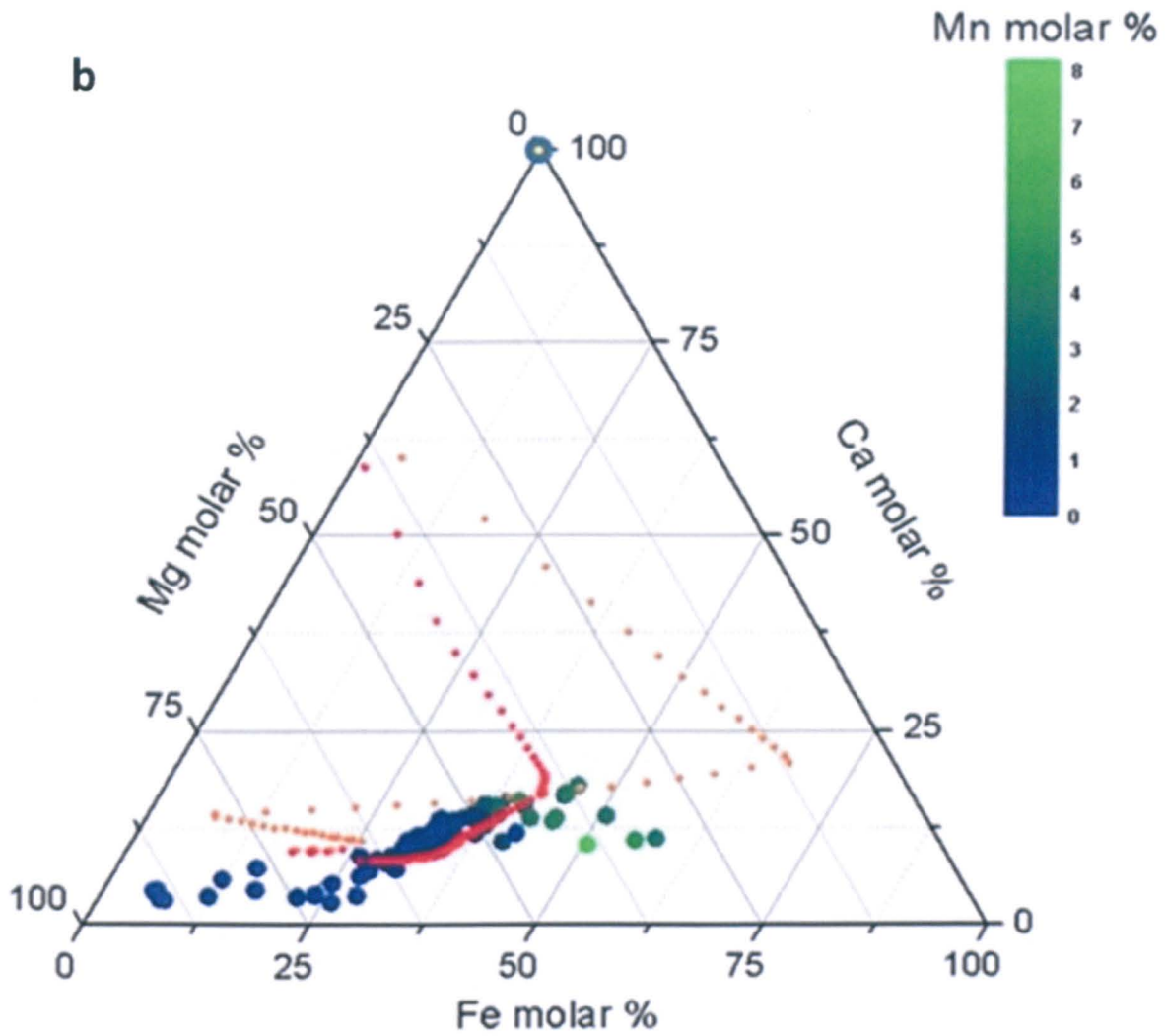

Figure 5.2 a, b Compositional variation modelled with GWB for various W/R ratios. Figure 5.2 b values from ALH 84001from this study are superimposed onto modelled values.

The minerals included are those that form in amounts <0.1 mole. The W/R 5 results in the instant precipitation of only calcite (Fig. 5.3a) in terms of carbonate with Mg and Fe cations precipitating as $MgCr_2O_4$ and pyrite. The W/R 10 precipitates all the carbonates required for the compositional match to those observed in ALH 84001, with siderite going back into solution in favour of $FeCr_2O_4$ precipitation and the enrichment of magnesite, as observed across the ALH 84001 rosettes (Fig. 5.3b). Similar to W/R 10 quartz is the most abundant mineral phase (which accounts for a large portion of the Si released from the ALH

84001 bulk composition). Magnesite, dolomite and calcite are all observed but siderite does not precipitate. For W/R (1000) ratios calcite does precipitate (>0.1 mole), however, the system is dominated by saponite-Na and magnetite, these both precipitate in relatively low abundances (Fig. 5.3d).

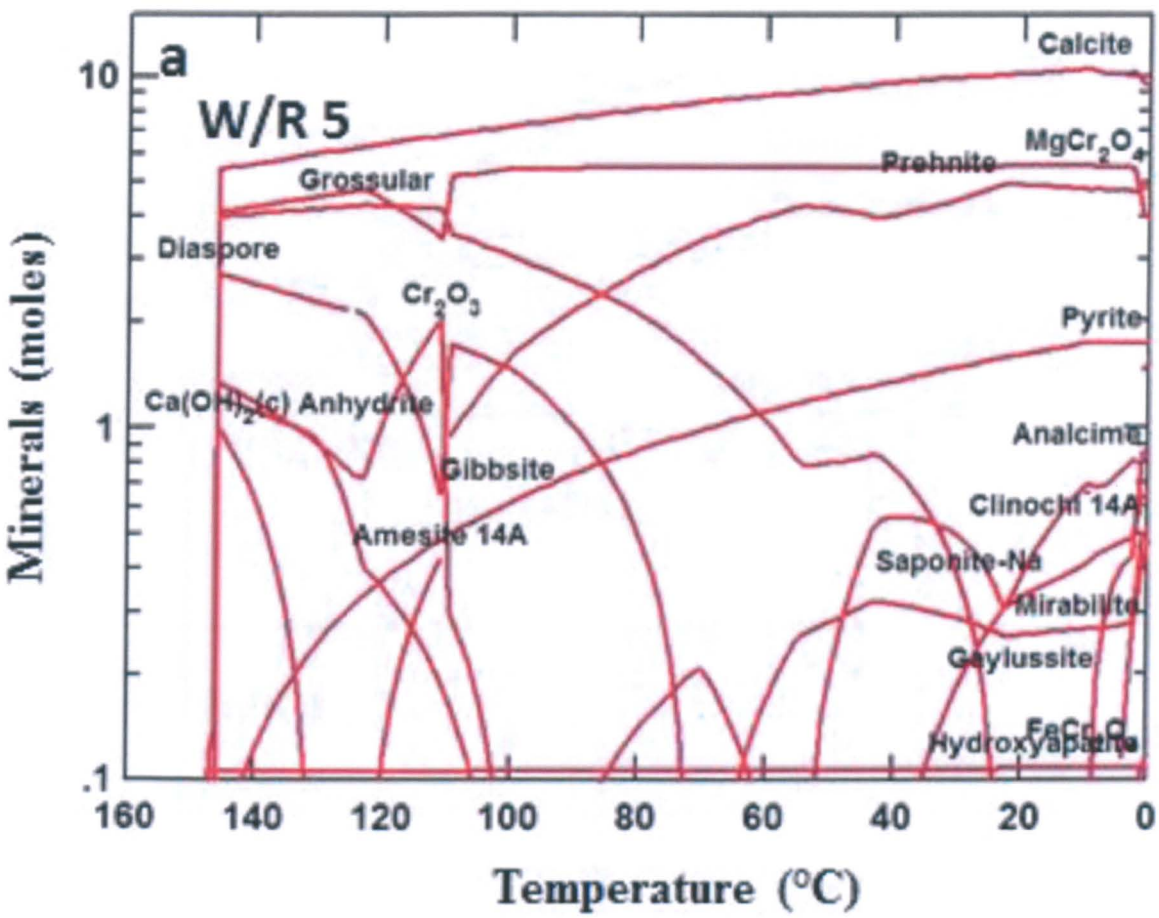

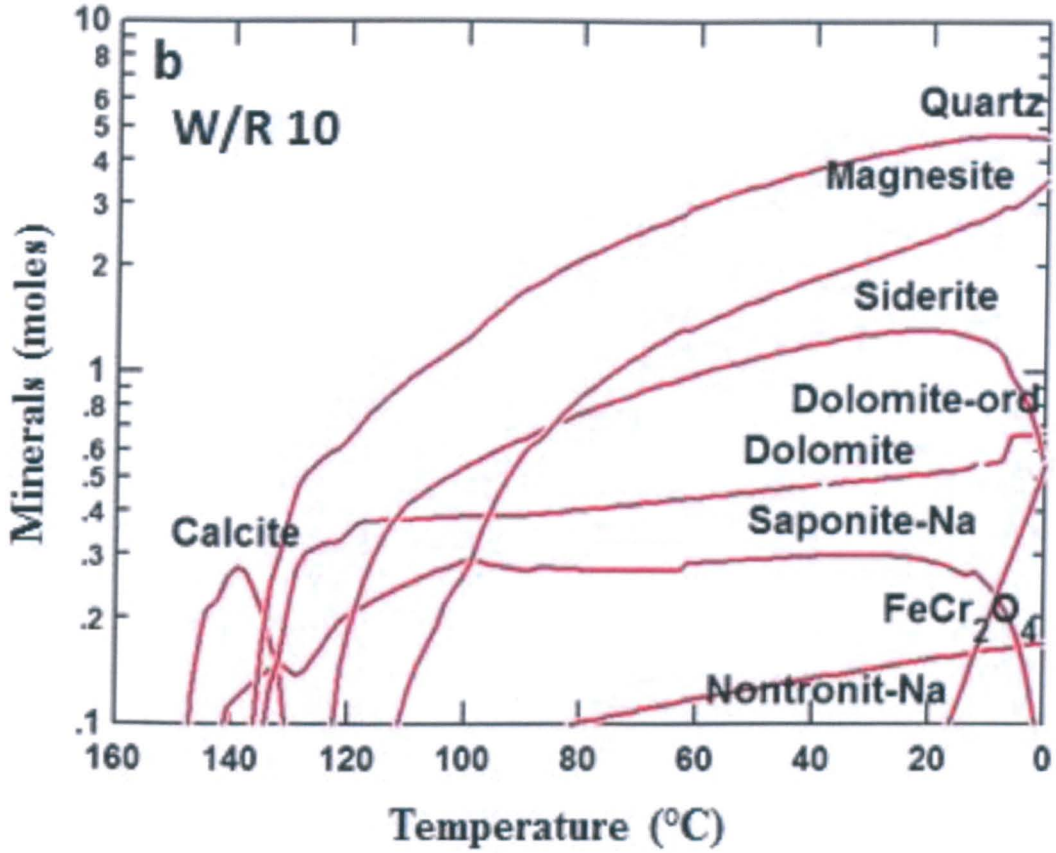
b
W/R 10
Quartz
Magnesite
Siderite
Dolomite-ord
Dolomite
Saponite-Na
Calcite
FeCr2O4
Nontronit-Na
Minerals (moles)
Temperature (°C)

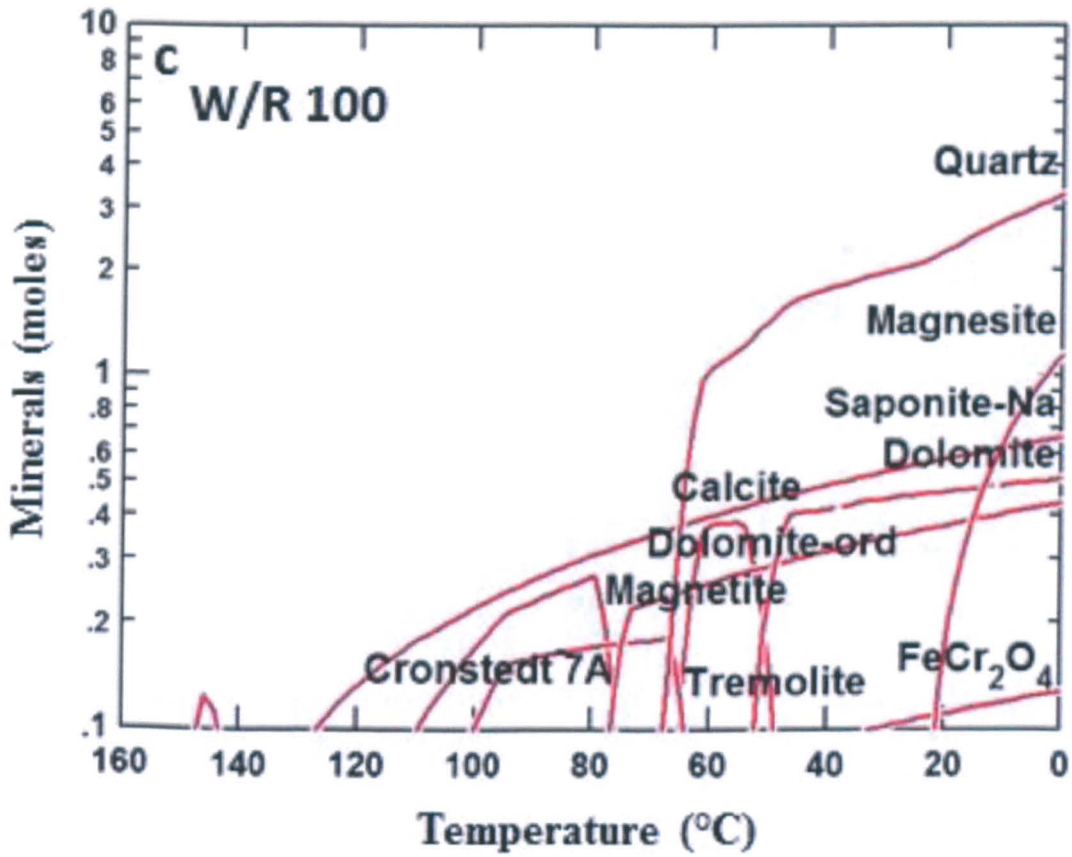
c
W/R 100
Quartz
Magnesite
Saponite-Na
Dolomite
Calcite
Dolomite-ord
Magnetite
Cronstedt 7A
Tremolite
FeCr2O4
Minerals (moles)
Temperature (°C)

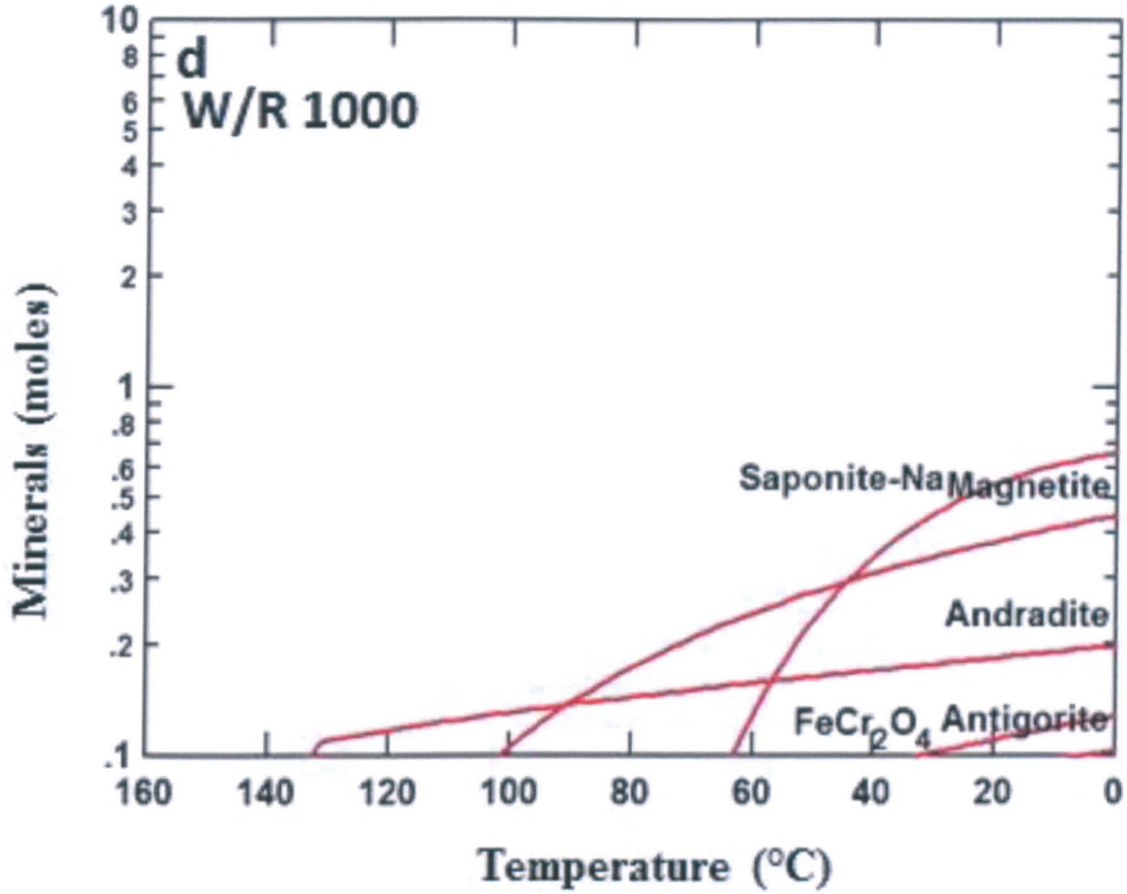

Figure 5.3 Composition (log scale of moles) of the phases that precipitate from a cooling fluid at a W/R of 5-1000 (a-d).

Minerals that precipitate below 0.1 mol are not displayed but a summary of the minerals are listed in Table 5.2. For all W/R ratios the precipitation of initial ALH 84001 $MgCr_2O_4$, calcite, antigorite, $FeCr_2O_4$, saponite-Na, hydroxyapatite, smectite phase is observed. However, W/R 10 were the only ratio in which the carbonates calcite, dolomite, magnesite, rhodochrosite and siderite are precipitated. Magnetite and pyrite were also precipitated at this W/R (10) and are commonly found to be associated with ALH 84001 carbonates.

Table 5.2 Minerals precipitated at various W/R ratios.

W/R 5	W/R 10	W/R 100	W/R 1000
$MgCr_2O_4$	$MgCr_2O_4$	$MgCr_2O_4$	$MgCr_2O_4$
Calcite	**Calcite**	**Calcite**	**Calcite**
Antigorite	Antigorite	Antigorite	Antigorite
$FeCr_2O_4$	$FeCr_2O_4$	$FeCr_2O_4$	$FeCr_2O_4$
Saponite-Na	Saponite-Na	Saponite-Na	Saponite-Na
Hydroxyapatite	Hydroxyapatite	Hydroxyapatite	Hydroxyapatite
Smectite	Smectite	Smectite	Smectite
Andradite	Andradite	Andradite	Andradite
Monticellite	Monticellite	Monticellite	
Brucite	Brucite	Brucite	
Diopside	Diopside	Diopside	
Pyrite	**Pyrite**	**Pyrite**	
Clinochlorine	Clinochlorine		
$Ca(OH)_2(C)$	$Ca(OH)_2(C)$		
Grossular	**Magnetite**	**Magnetite**	**Magnetite**
Anhydrite	Tremolite	Tremolite	
Cr_2O_3	Quartz	Quartz	
Diaspore	**Dolomite**	**Dolomite**	
Gibbsite	**Magnesite**	**Magnesite**	
Amesite	Tephroite	Cronstedt($Fe_4SiO_5(OH)_4$)	
Prehnite	**Rhodochrosite**		
Phlogopite	**Siderite**		
Analcime	Hematite		
Gaylussite	Nontronite-Na		
Mirabilite	Albite		
	Dawsonite		
	Vivianite		

An increasing W/R ratio can be observed to:

1) Generally precipitates fewer mineral phases (9; 1000 W/R instead of 26; 10 W/R).

2) A decreasing moles of carbonate precipitated at high W/R ratios (5 W/R, 10 moles; 1000 W/R; 0.01 moles).

3) Favourable precipitation of silicates rather than carbonates.

4) Magnetite precipitation is observed (Table 5.2).

5.5.2 Effects of CO_2

The incorporation of lower quantities of CO_2 generally appears to drive the carbonates to Fe-rich formations before changing to Mg-rich carbonates (Fig. 5.4 a, b). With the exception of 0.1 mol CO_2(g) higher values of CO_2 shift the compositions to Ca-rich carbonates (1.4 mol CO_2(g)). Exceptions to this is the inverse trend of the 2 mol CO_2(g) reaction where the carbonates form Mg-rich before Fe-rich carbonates.

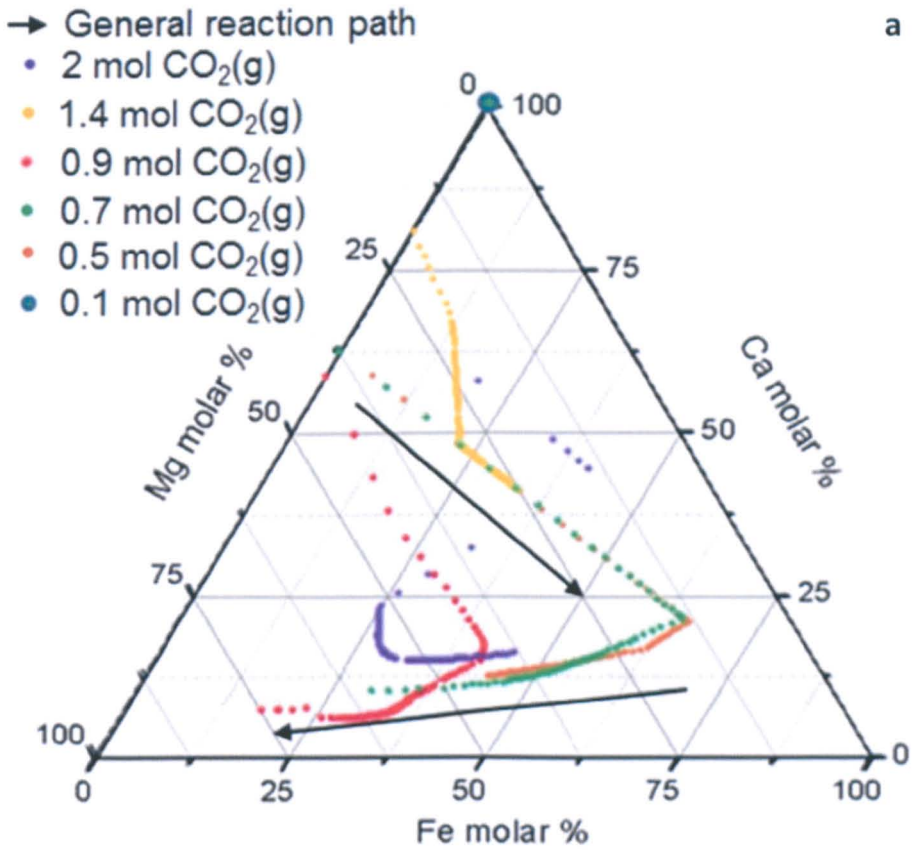

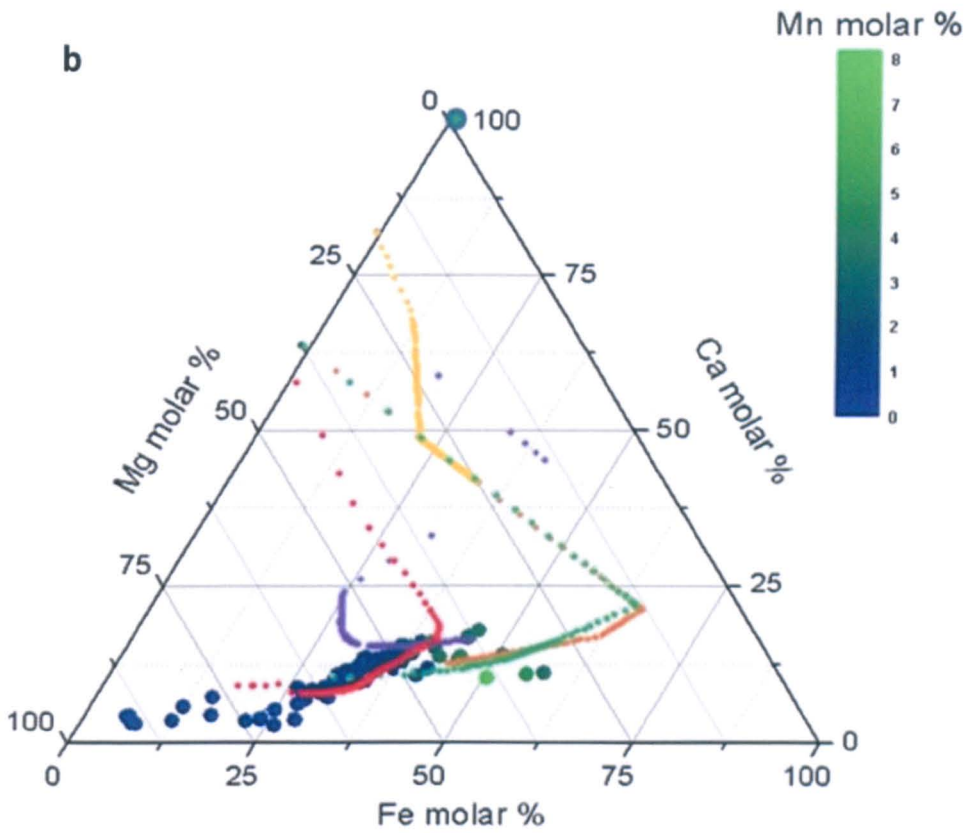

Figure 5.4 a, b Modelled CO_2 component effects on carbonate precipitation.

The carbonate formations that precipitate are the result of the CO_2 fugacity driving the pH and in the case of progression of the reaction Fe-rich to Mg-rich (Fig. 5.5 b, c, d; 0.5, 0.7 and 0.9 mol CO_2(g) carbonates, respectively) this forms when fugacity increases (drive towards lower pH, favourable for Fe-carbonates but then CO_2 drops off resulting in pH increase and Mg-rich carbonates). However, the 0.1 mol CO_2(g) component does not have sufficient CO_2 to increase the fugacity to the point at which any carbonates other than calcite formation occur (Fig. 5.5 a). In the case of higher CO_2 initial solutions (1.4 and 2 mol) there is enough CO_2 for the fugacity to increase constantly driving down the pH to such low values (~5.5 to 6) that there is a near constant Fe-enrichment with pH values not achieving the point where Mg-rich carbonate precipitation is favoured (Fig. 5.5 e, f).

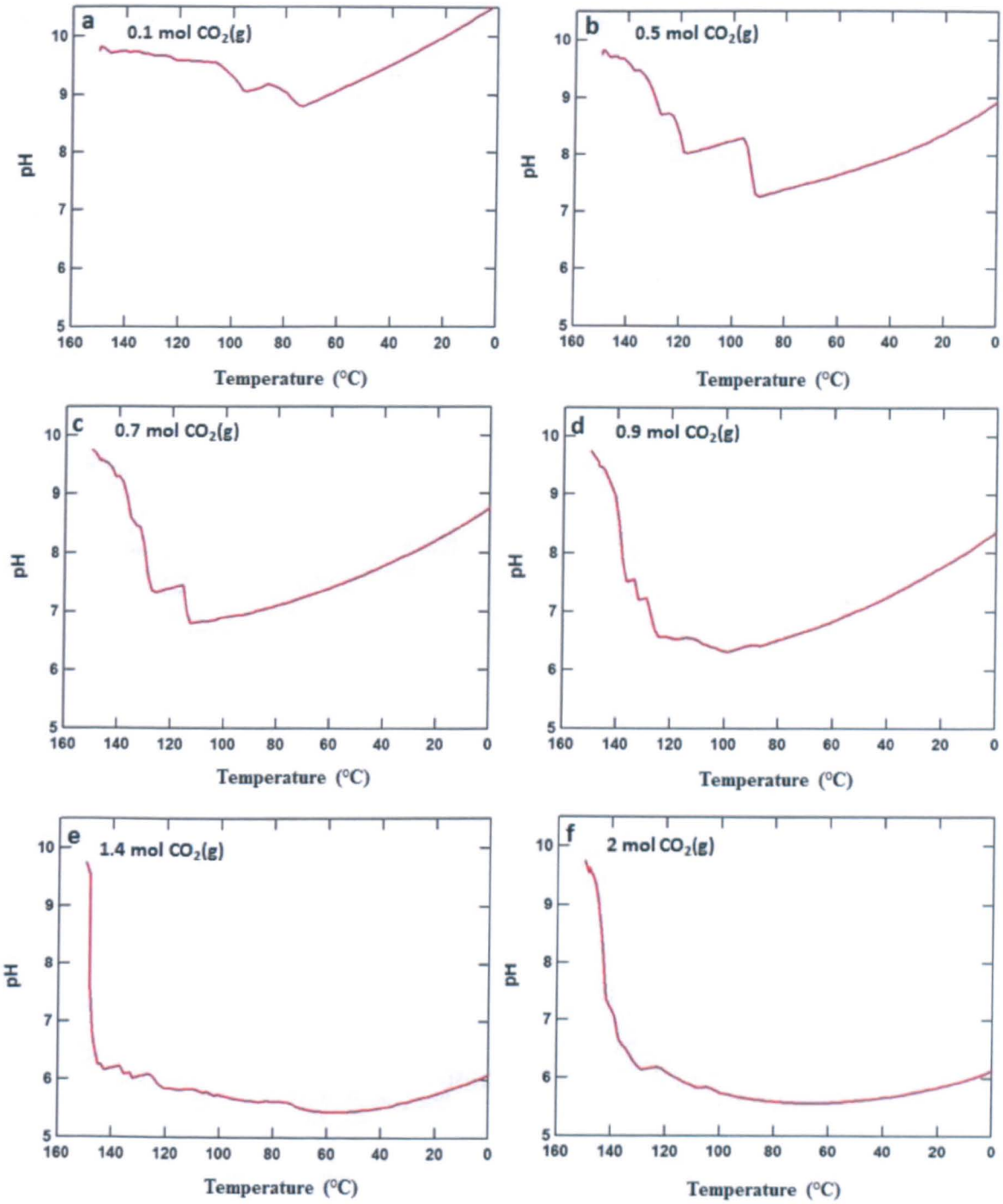

Figure 5.5 Modelled pH variation with temperature according to different CO_2 concentrations (mol).

5.5.3 Effects of various temperature regimes

Thus far, the temperatures of the modelled systems have been set to decrease with time in order to produce the observed isotopic enrichments. However, warming temperatures and isothermal temperature regimes have been considered with temperatures set at 25, 100, 150 and 200°C, to investigate their effects on the precipitated carbonates. These measurements were modelled at W/R ratio 10, starting pH 9.8 and a brine solution with 0.2 mol Ca^{2+} added to the system.

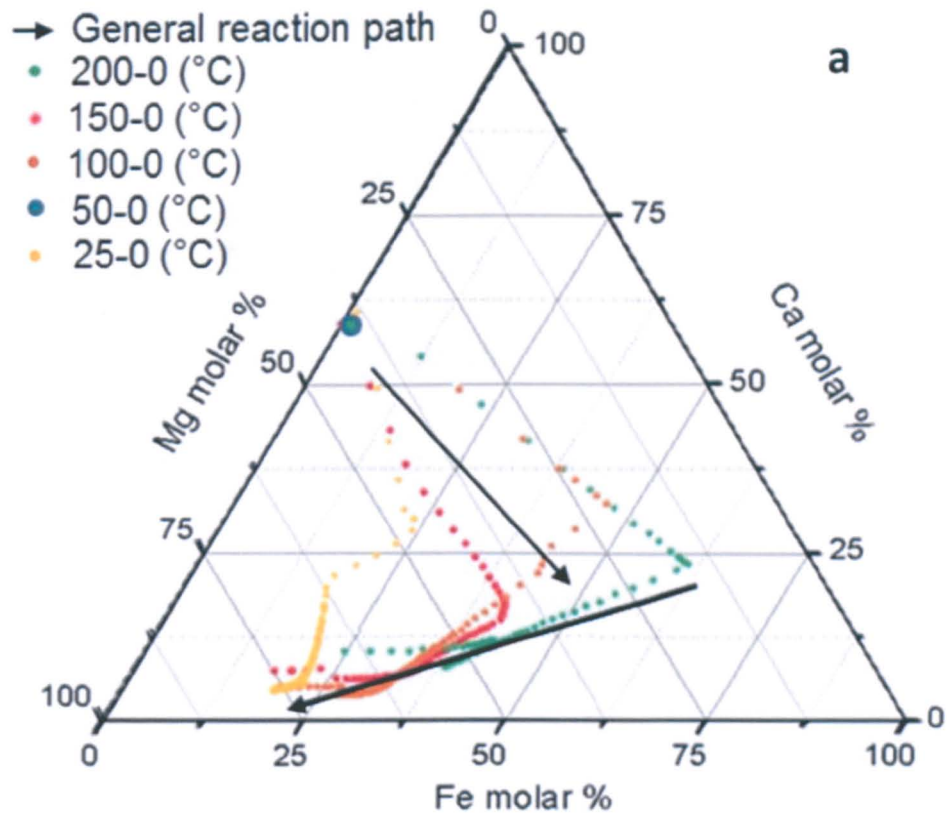

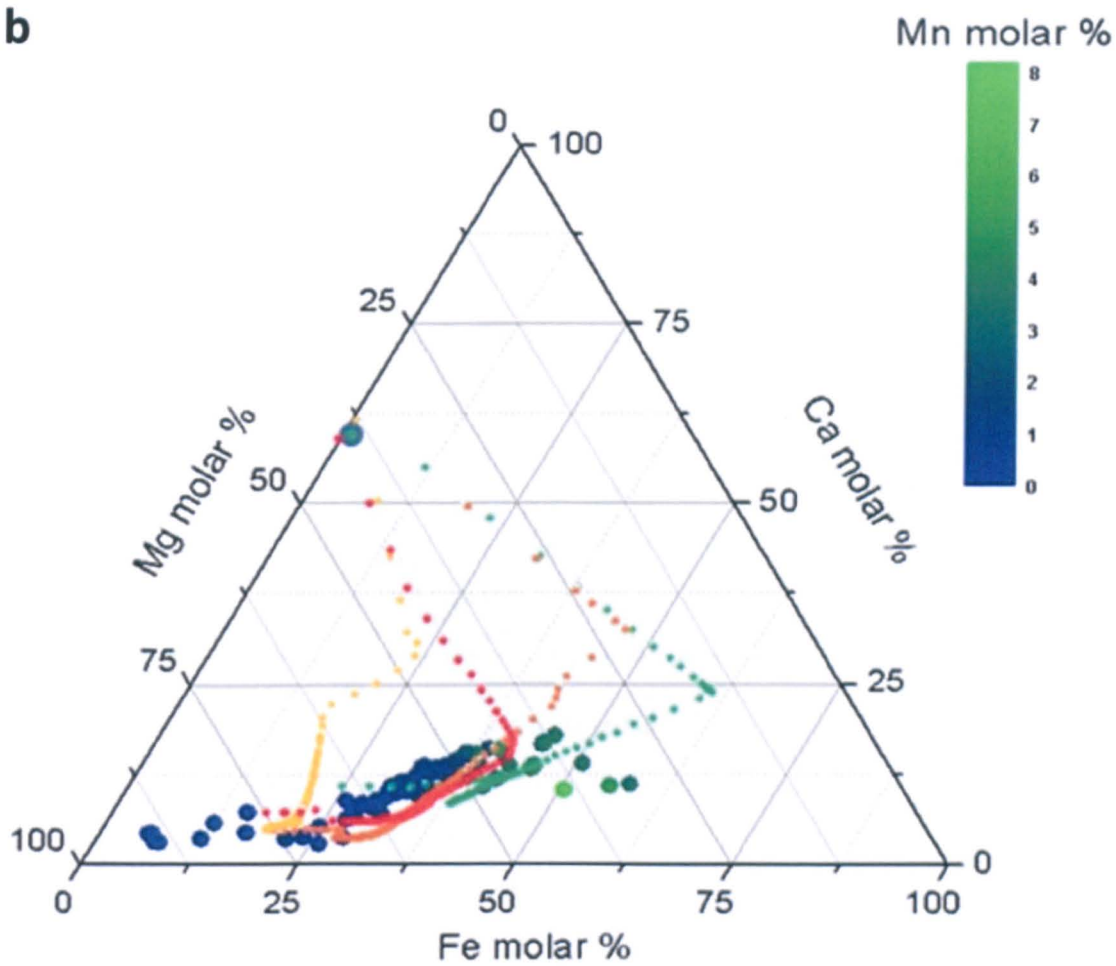

Figure 5.6 a, b Temperature variations on composition of carbonates (cooling scenarios).

The modelled zoning in a temperature decrease all typically followed a sequence where a cooling system favours Fe-rich carbonate before the Mg-rich carbonates. An optimum temperature of 150-0°C represents the closest formation of carbonates matching ALH 84001 while a temperature variation of 50°C either way precipitates carbonates with slightly elevated Fe-content (Fig. 5.6 a, b). When cooling from 50°C only dolomite forms while carbonates forming between 25-0°C are generally more Ca, Mg-rich.

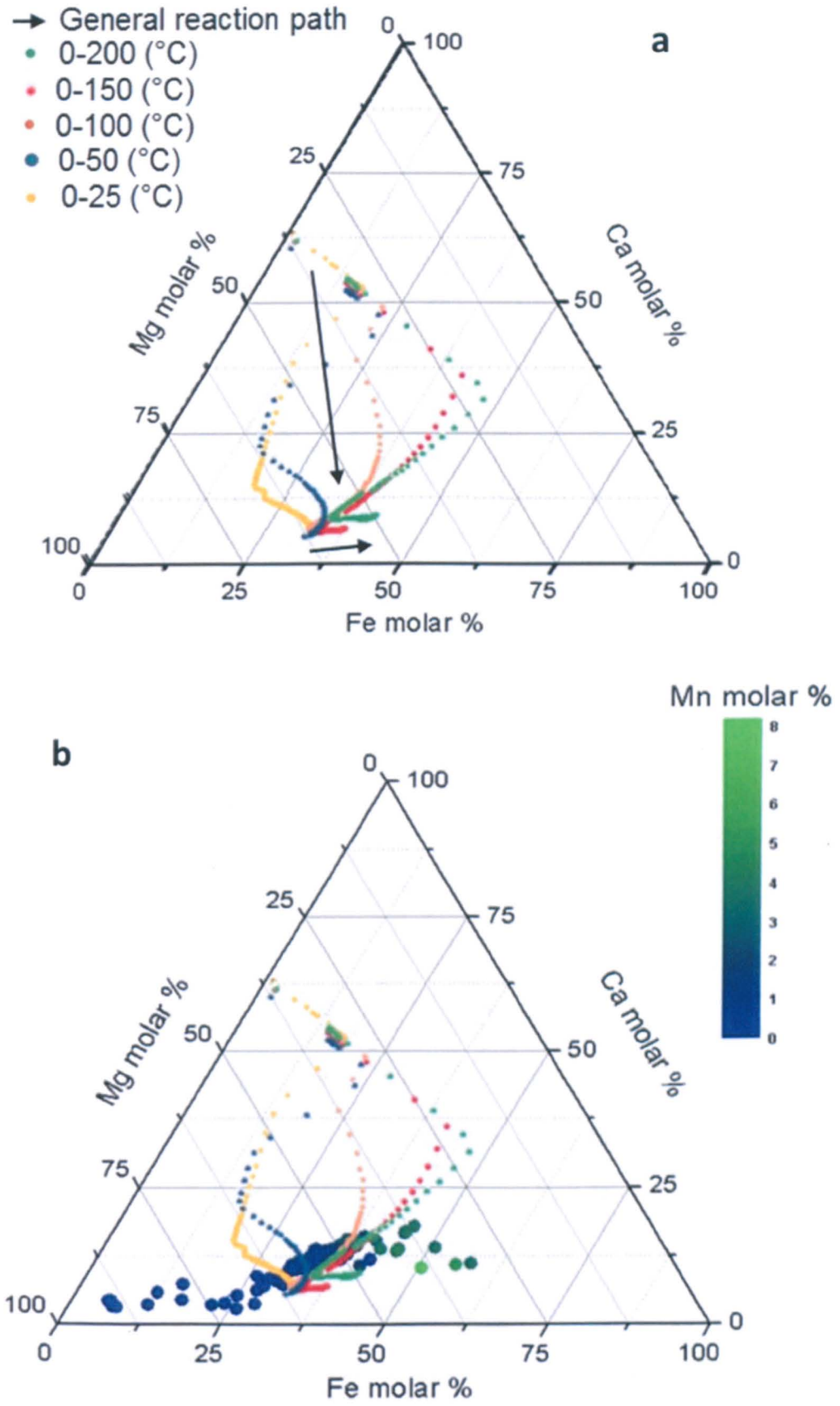

Figure 5.7a, b Temperature variations on composition of carbonates (heating scenarios).

The temperature increase still results in a Ca content decrease. The lower temperature ranges (50 and 25°C) result in an inverse reaction path to higher final temperatures (100, 150 and 200°C).

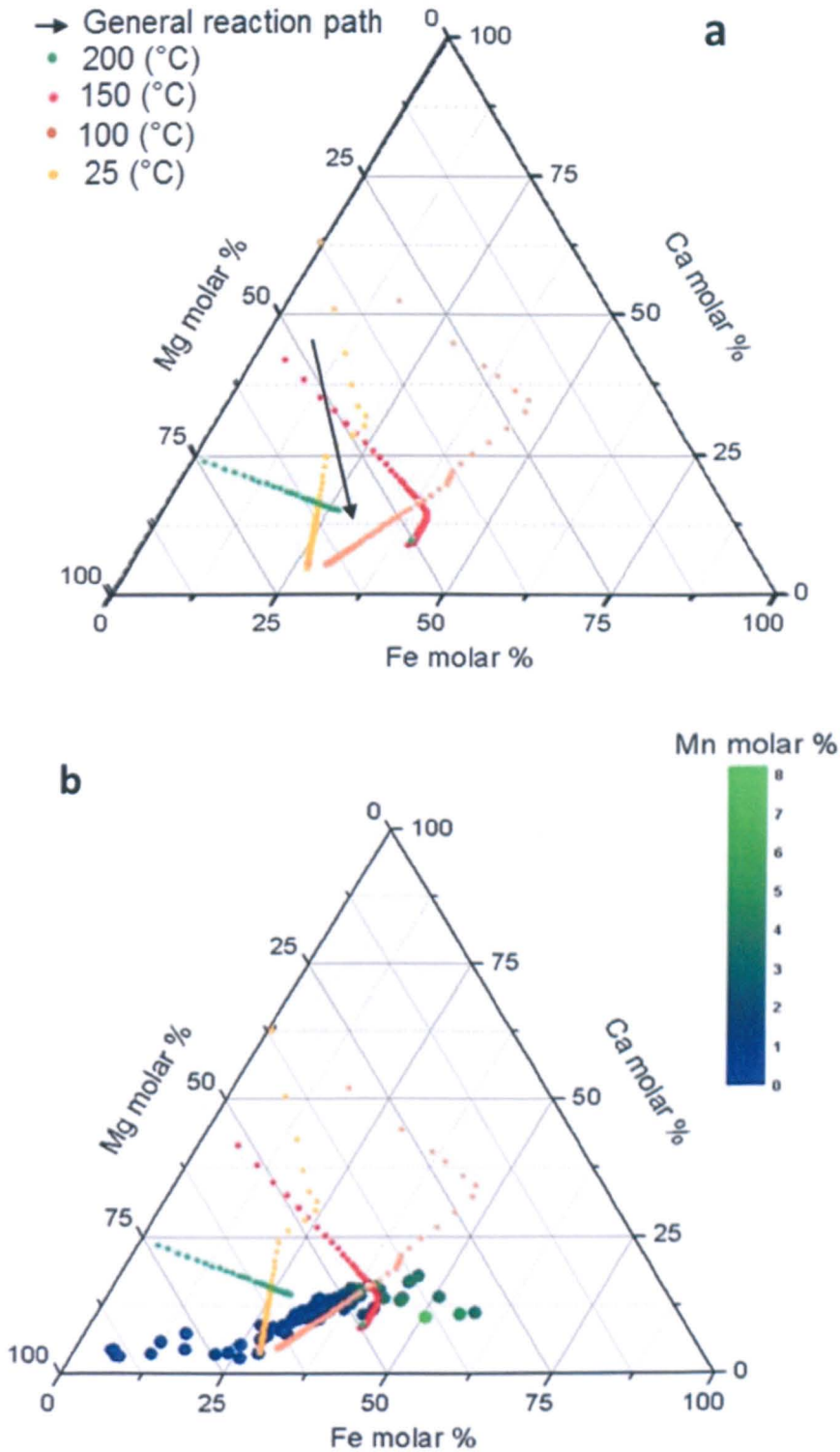

Figure 5.8 a, b Temperature variations on composition of carbonates (constant temperatures).

Constant values still result in carbonate evolution of precipitation from Ca-rich initial carbonates to more Mg, Fe-rich later formations. The carbonates which precipitated at 100°C are the closest representations of the true measured carbonate compositions.

5.5.4 Additional calcium

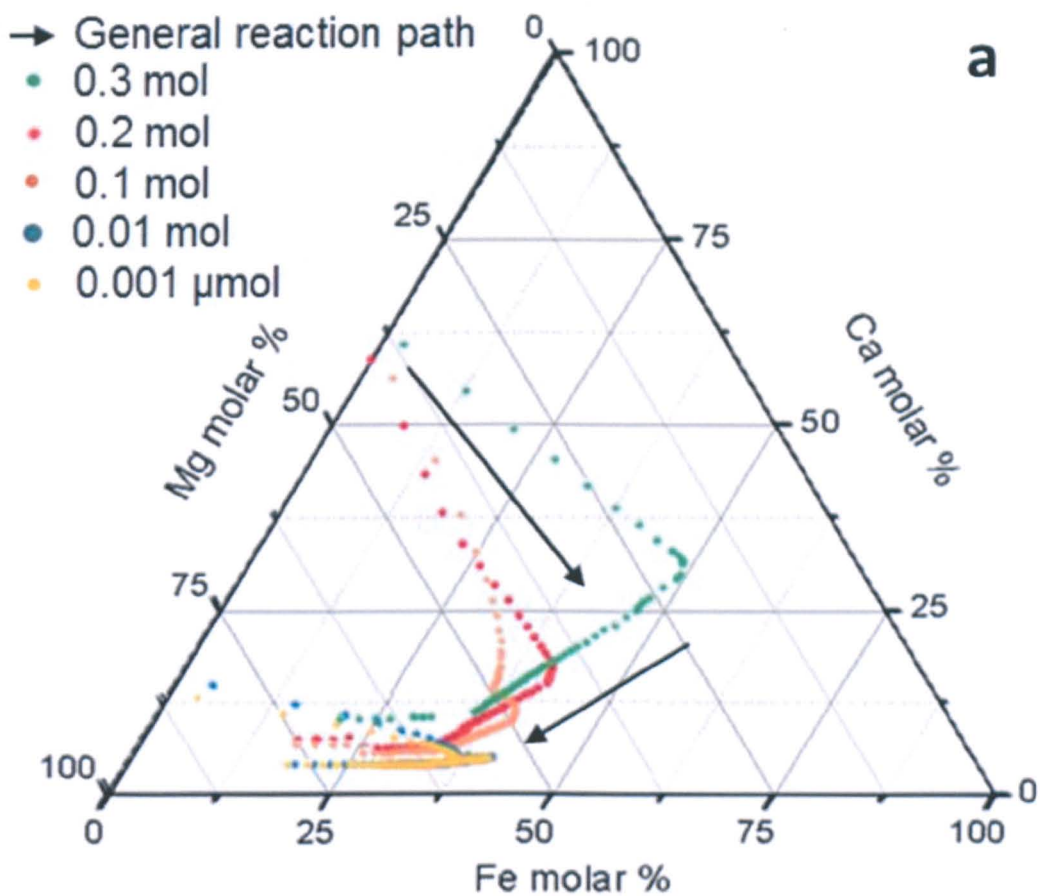

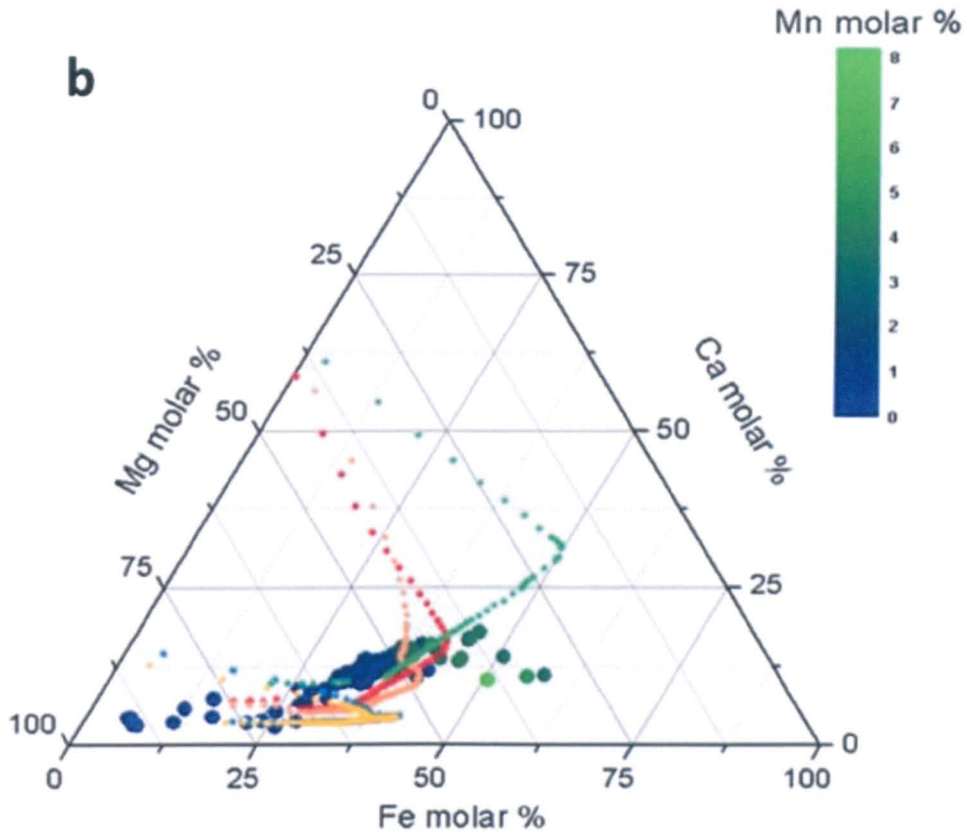

Figure 5.9 a, b Carbonate precipitation with the introduction of Ca^{2+} moles to initial brine solution.

A contribution of Ca^{2+} to the brine was required in addition to the bulk ALH 84001 sample to precipitate carbonates of a composition similar to the rosettes. The closest compositional match to ALH 84001 carbonates was produced with 0.2 mol of Ca^{2+}.

5.5.5 Isotopic values

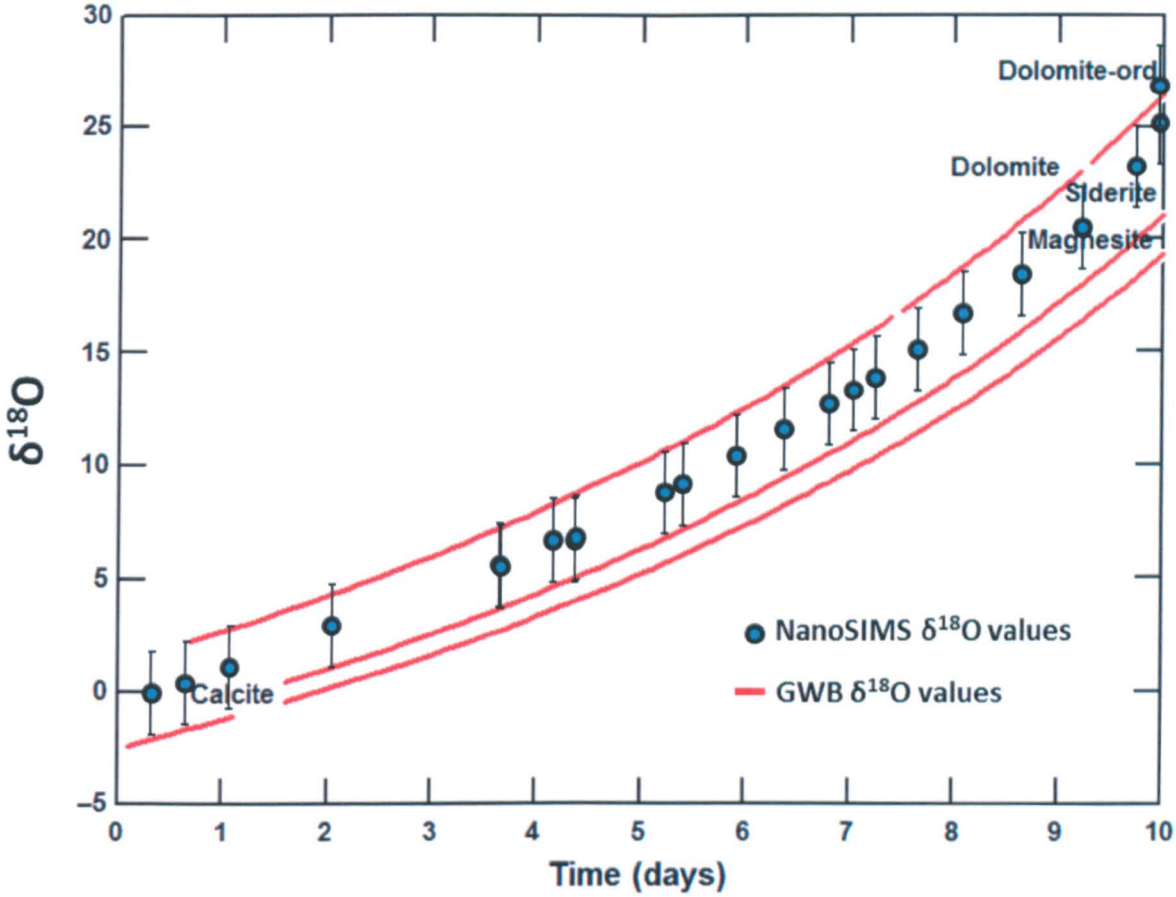

Figure 5.10 GWB $\delta^{18}O$ values for precipitated carbonates (red lines) over duration of formation at W/R ratio 10, pH 9.8 and decreasing temperature 150 to 0°C. Blue spots representing NanoSIMS data with ±2.2‰ error (2σ) plotted in increasing order to illustrate range in values.

The $\delta^{18}O$ values are seen here to be enriched with time, however, this $\delta^{18}O$ variation is really derived by the temperature change from 150 to 0°C (Fig. 5.10). These $\delta^{18}O$ values correspond to an initial brine solution (martian water reservoir) with a -15‰ $\delta^{18}O$, identical to that derived by Clayton and Mayeda (1988) for carbonates in martian meteorite EETA 79001. The NanoSIMS data range matches the GWB model with a comprehensive coverage of $\delta^{18}O$ values adding, demonstrating that a depleting ^{18}O fluid could result in an enriched ^{18}O carbonate. Owing to water being the dominant $\delta^{18}O$ phase in the formation of the

carbonates changing the CO_2 value has a negligible effect on the carbonates isotopic composition, therefore determining the original atmospheric $\delta^{18}O$ value is not possible in this model.

While the NanoSIMS data in chapter 3 displays a large variation in $\delta^{13}C$ the first portion of the data can be explained by either initial fluid or CO_2 reactants composition between 10-15‰ (Fig. 5.11).

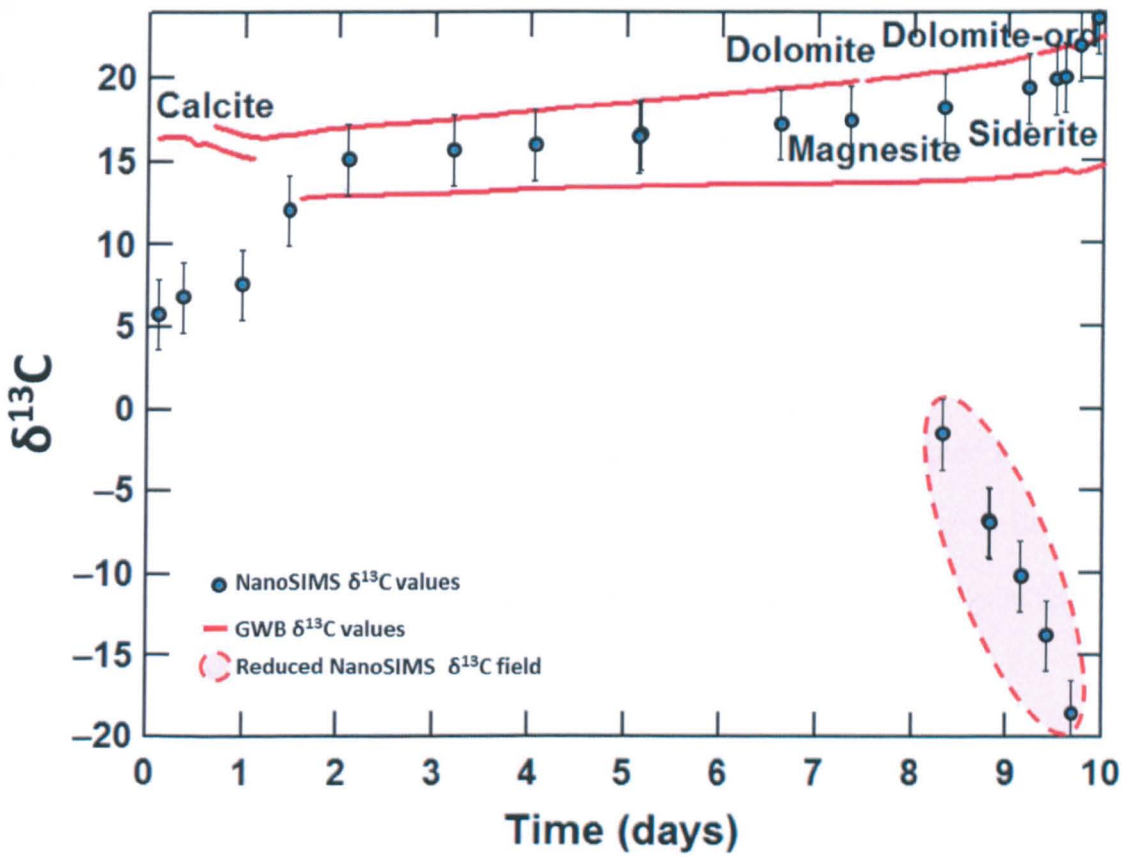

Figure 5.11 GWB $\delta^{13}C$ values for precipitated carbonates (red lines) over duration of formation at W/R ratio 10, pH 9.8 and decreasing temperature 150 to 0°C. Blue spots representing NanoSIMS data with ±2.6‰ error (2σ) plotted in increasing and descending order (reduced carbonate) to illustrate range in values.

Similarly to $\delta^{18}O$ the after an initial dip the $\delta^{13}C$ values are seen here to be enriched with time, however, the $\delta^{13}C$ variation is a much broader range suggesting different isotopic fractionation dependant on the carbonate composition. The final spread in $\delta^{13}C$ values (+14.5

to +22.5‰) corresponds with range of values from the first portion of the NanoSIMS data (+11.9 to +23.2‰). The low values recorded in the outer portions of the ALH 84001 carbonates cannot be modelled in this cooling system with values gradually increasing. It suggests that either a separate introduction of fluid or CO_2 composition with a lower $\delta^{13}C$ was introduced into the system or a subsequent heating event during carbonate precipitation. However, the steady precipitation of the increasing $\delta^{18}O$ values matching those obtained with the NanoSIMS from the same starting conditions suggests that something unique occurred to only the carbon component. These $\delta^{13}O$ values correspond to either an initial brine solution (martian water reservoir) with a +15‰ and CO_2 with +10‰ $\delta^{13}C$ or vice versa.

The reaction for oxygen and carbon appeared to favour Rayleigh fraction in a closed system equilibrium. The isotopic composition of the precipitated carbonates partitions ^{13}C and ^{18}O results relative to the fluid resulting in an enrichment of both $\delta^{13}C$ and $\delta^{18}O$. The low $\delta^{13}C$ values are offset from the fractionation trend and are perhaps related to the thermal decomposition of the magnesite or the incorporation of macromolecular carbon ((MMC) which has been observed within ALH 84001 with a -11‰ $\delta^{13}C$ value (Steele et al. 2012). The origins of the carbon are further discussed in Chapter 7.

5.6 Discussion

GWB modelling has produced carbonates with a similar composition to those identified with quantitative analyses in Chapter 3. The conditions placed on the model indicate; initially high CO_2 fugacities and low temperatures (<150°C) can reproduce the ALH 84001 carbonate 'rosette' formations over short timescales of hours/days (Niles et al., 2009; van Berk et al., 2011). The model varies from previous authors suggesting 1) a higher starting pH (9.8) in contrast to <7 pH (Niles et al., 2009; van Berk et al., 2011). In addition, 2) results show that a 0.2 mol Ca^{2+}-rich brine solution when mixed with bulk ALH 84001 compositions

can provide the source of Mg, Fe and Ca cations required to reproduce rosette carbonate formations. These findings are consistent with a high pH (10-12) and Ca-OH solutions formed through the hydrothermal serpentinisation of ultrabasic rocks in low-temperature conditions found on Earth (Bruni 2002). 3) SiO_2 and magnetite are also formed. 4) The water/rock ratios (10) required to form the carbonates in this study are far smaller than those observed by Niles et al. (2009; 100<W/R<10000) and van Berk et al. (2011; W/R=438).

5.7 Conclusion

The study has used the variable composition of the ALH 84001 carbonates to help define the condition in which they formed. This model has shown how the major component of the carbonates can form through the evolution of a single alteration phase in agreement with Niles et al. (2009). The water/rock mass ratios selected for the model varied from 5 to 100. In contrast to Niles et al. (2009) this study suggests that $<\sim10^2$ W/R ratio are likely with evidence of localised dissolution of the host rock observed in both ALH 84001 orthopyroxene and the analogue sample (Fig. 4.5). Values above 100 W/R are found in contrast to 1000

The conditions of formation provide an indication of the geological setting for the precipitation of Mg, Fe, Ca varying carbonate rosettes. The carbonates within ALH 84001 are 3.9 billion years old. The idea that these carbonates have not been substantially altered since the carbonate original formation event suggests a subsurface environment devoid of any long term water sources (hot spring, lake or ocean). While the model suggests no variation in the effects of formation timescale on the carbonates, Golden et al. (2001), have suggested days to weeks based on their experiments in which heterogeneous zoning was formed within the carbonates. A fracturing event induced by impact has been dated at 4 Ga (Ash et al. 1996). This event could have caused the initial conduit spaces for subsequent alteration.

Chapter 6

6. Carbonate and Water Detection with WATSEN

6.1 Introduction

A question commonly posed for Mars is "Were early environmental conditions warm and wet?" If the answer is positive, then conditions were therefore potentially favourable for life to arise, and also for carbonate precipitation to occur. Although there are many indicators that water was active on Mars' surface (Ehlmann et al., 2008) and water ice has been identified in the polar caps (Plaut et al., 2007; Smith et al., 2009), there has, as yet, been no direct detection of water (either liquid or frozen) within the regolith at more equatorial latitudes. To detect water directly, it is necessary to probe the martian regolith with a specific instrument. To this end, the Open University has been part of a consortium developing WatSen (Water Sensor). WatSen is a miniaturized instrument consisting of a combined Attenuated Total Reflectance (ATR) IR spectrometer and optical microscope. The consortium, of the OU, Norsk-Elektro Optikk and Navsys, was funded by ESA to produce a bread-board model of an instrument. The final description of the project was published as a technical note to ESA and has since been published (Wolters et al., 2013). My contribution to this project was to determine the detection limits for WatSen of hydromagnesite and water when mixed with basalt under current martian conditions, the result of this investigation is

presented here, following a brief explanation of why we tested the instrument using hydromagnesite, and a brief description of WatSen itself.

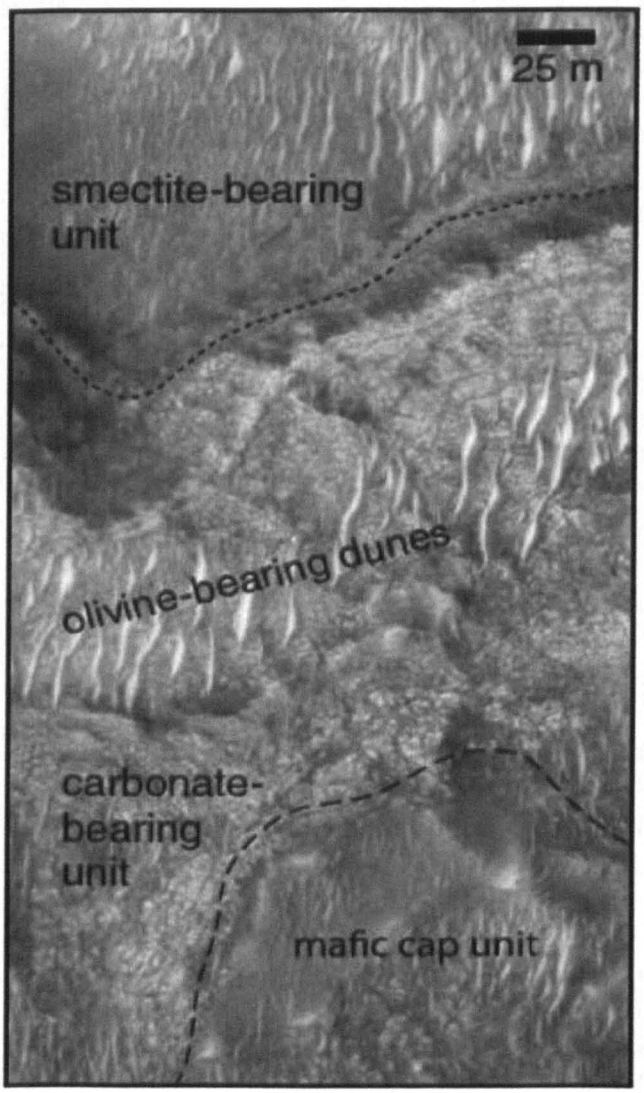

Figure 6.1 Image from CRISM, stratigraphic units found in Nili Fossae interpreted by Elhmann et al., 2008. Carbonate bearing phase consists of magnesite and hydromagnesite.

Hydromagnesite, $Mg_5(CO_3)4(OH)_2{\cdot}4(H_2O)$ is a hydrous Mg-bearing carbonate which incorporates water into its structure. Prior to its recent confirmation on Mars (Ehlmann et al., 2008) it was proposed as an explanation for some of the absorption bands in Mars spectra (Calvin et al., 1994; Bandfield et al., 2003). The region where this hydromagnesite outcrop was found is called Nili Fossae, and it covers an area <10 km^2. According to its cratering record, the terrain the outcrop resides in is Noachian, suggesting that this deposit formed on ancient Mars. Hydromagnesite forms at low-temperatures from Mg and CO_2-rich solutions (Hanchen et al., 2008; Konigsberger et al., 1999; Catling, 1999), and the phase has been identified as a weathering product on the exterior surfaces of Antarctic meteorites (Velbel et al., 1991). These conditions could still plausibly exist in the martian subsurface.

Mars is currently the main focus of extra-terrestrial planetary investigation in terms of the number of surface and orbital instruments deployed there. Several missions have scratched into the surface (most recently Phoenix), however, there have not been deeper measurements of the martian subsurface. Phoenix has discovered the surrounding soil to be comparable to soils found in Antarctica's Dry Valleys (Wentworth et al., 2005). The initial results show that the soil is alkaline (pH 8-9) and that water in the form of subliming ice has been involved in producing the soil. The presence of salts incorporating magnesium, sodium, chlorine and potassium further suggests the presence of water interacting with soil at some point in time. Since the current conditions at the martian surface are unfavourable for the presence of water, potential organic signatures (Gibson et al., 2007) and carbonates, it is necessary to look deeper into the subsurface.

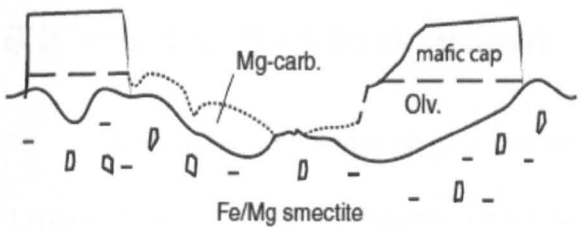

Figure 6.2 Schematic stratigraphy of mineralogical units within Nili Fossae region as interpreted by Elhmann et al., 2008. Only a small portion of carbonate layer being exposed under mafic cap unit.

Detection of vapour or liquid is dependent on whether atmospheric or subsurface pressure is higher than expected. A penetrating instrument could potentially reach below the zone of sublimation, depending on the porosity of the regolith (Grady, 2006). The zone of sublimation at different latitudes on Mars has yet to be determined accurately, although recent orbital data suggests H_2O ice is present in the upper metre with a concentration between 2-10% equatorially and above 55% in the northern latitudes (Mungas et al., 2007). It is likely that any sub-surface water discovered by a penetrating instrument will be in the form of H_2O ice. This may instantly sublime when the mole bores through or exposes the material to atmospheric pressures, as observed with the Phoenix lander. However, depending on the

porosity of the regolith and if the atmospheric or subsurface pressure is higher than anticipated, water may be sustained at depth or it may be detected as a brine.

6.2 The WatSen Instrument

WatSen is a combination of 3 instruments: a humidity sensor (not discussed further as it was not part of this thesis study), a microscope and an ATR detector. Numerous studies and current investigations of the martian surface are collecting data at visible and near infrared wavelengths. The WatSen ATR detector was originally designed to operate across the 5.5-11μm range for the following reasons: Sutter et al. (2007) examined Atacama Desert soils which have similar abundances of sulphate, phyllosilicates and carbonates to martian soils (Sutter et al., 2007). Their study showed that absorption features in the mid-infrared were the best indicators of carbonate (6.3-7.4 μm) with only very minor interferences from overlapping water and primary silicates in this region (Sutter et al., 2007). Water has a feature near 6 μm and silicates from 9 μm upwards (Roush et al., 1991).

WatSen is designed to be part of a suite of instruments on-board a mole on a planetary lander similar to that planned for the Heat Flow and Physical Properties Package (HP^3; Grott et al., 2009) developed for ESA's ExoMars mission. WatSen is 128 mm long with a circular cross-section 26 mm in diameter; and it weighs 180 g. This suite of sensors would be inserted into the martian regolith to make the first measurements of the non-oxidised subsurface. Depending on the length of the tether attached to the mole, WatSen could penetrate down to depths of 5 m potentially reaching past the zone of sublimation (Grady, 2006). At these depths and regolith porosities, liquid water may be sustained or detected in a brine solution,

as hinted by images from Phoenix (Rennó et al., 2009) and the compositions of the alteration within the nakhlite meteorites (Rao et al., 2006, Bridges and Grady, 2000).

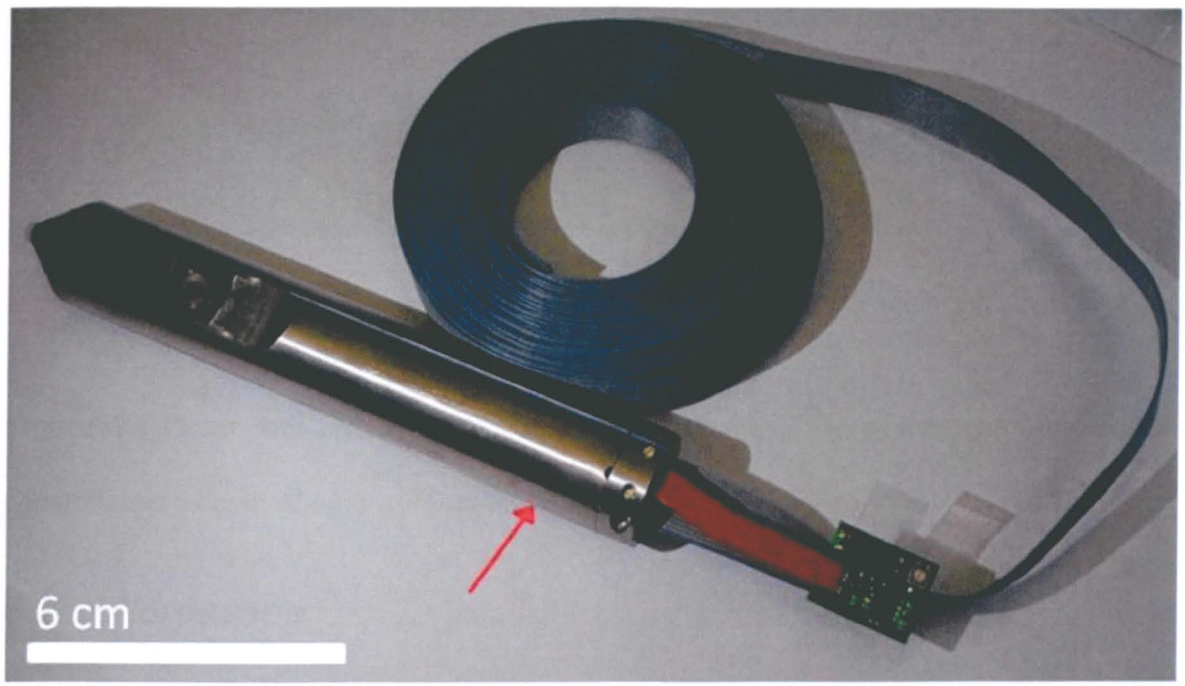

Figure 6.3 WatSen with grey flex cable attached. The electronics for the camera and the ATR spectrometer are encased in a titanium shell while the optical assembly is located behind the diamond window.

6.3.1 ATR spectrometer

The spectrometer detection covers the wavelength range 6.1 - 10.2 μm. This spread provides an ideal region to detect carbonates (6.3 - 7.4 μm) and water (6 - 7 μm). The ATR technique operates by introducing IR radiation into a diamond window where the beam is totally internally reflected with multiple "bounces" along the length of the window. The "bounces" form an evanescent or standing wave of radiation through the diamond. At each "bounce", the IR beam penetrates a finite (micron-scale) distance into any surrounding material, before being reflected to the detector. No sample preparation is required for the analysis, just a direct contact between the window and the specimen, so it is an ideal tool for

remote analysis. The instrument had a 0.015 $\Delta\lambda/\lambda$ resolution which is sufficient to resolve distinct spectral features. With a field of view of 14.5 x 8.5 mm^2 the microscope acted as an additional visual confirmation of the materials being detected and their grain sizes.

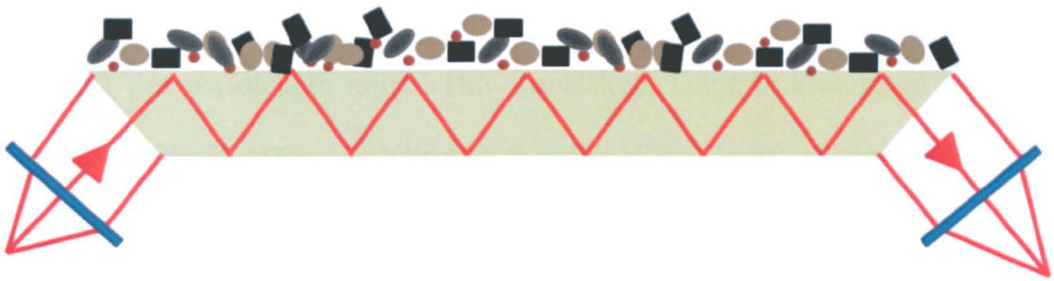

Figure 6.4 Beam path through lens and diamond window. The evanescent wave typically penetrates to a depth of ~1-3 μm into the samples surface.

6.3.2 Microscope

With a field of view of 14.5 x 8.5 mm the microscope acts as visual confirmation of the materials being detected and their grain sizes. The contact surface is illuminated by four Light Emitting Diodes (LED) positioned at each corner of the microscope lens barrel. Specific parameters are listed below.

Table 6.1 Parameters of WatSen microscope.

Parameter	**Centre**	**Edge**
Field of view, mm	-	14.5x8.5
Magnification	0.5x	0.33x
Spatial frequency (image) lp/mm	110	95
Spatial frequency (object) lp/mm	55	31
Resolution (object) (mm)	0.018	0.032
Contrast ,%	30	30
Pixel size on the object (μm)	7.2x7.2	approx. 11 x 11
Diagonal field of view	23 mm	
Field of view (Horizontal, Vertical) (approximate as FOV not rectangular because of distortion)	14.5 x 8.5 mm	

As can be observed in Table 6.1, performance changes quite significantly from the centre of the image to the edges, this change is a result of the barrel shape of the microscope.

Spectra from minerals characteristic of the surface of Mars and saturated with water were investigated using a Thermo Nicolet Nexus ATR Fourier Transform infrared spectrometer (FTIR), in order to construct a reference database (Fig. 6.5). The experiments showed that the soil components typical of Mars are uniquely identifiable within the chosen 6.1 - 10.2 μm wavelength range. This wavelength range is a trade-off between technical boundaries and scientific capability; H_2O absorption is stronger between 2 and 3 μm, but strong and distinct absorption peaks for minerals also occurs in the mid infrared spectrum (5 – 11 μm; Fig. 6.6). For example, carbonates, which have recently been identified by direct surface analysis, have features between 6.3 - 7.4 μm (Fig. 6.5). These characteristic spectra match the martian surface dust spectrum collected (TES, Mars Global Surveyor; Bandfield et al., 2003). Water IR spectral features are also displayed between 6 - 7 μm (6.2 μm; Fig. 6.6). Major features of anhydrous silicates occur at wavelengths greater than 9 μm (Fig. 6.5-6). Hydrated minerals such as clays display combined features of water and silicates (Montmorillonite, Fig. 6.5). WatSen's 0.015 $\Delta\lambda/\lambda$ resolution is sufficient to resolve distinct spectral features for water and minerals typical of Mars.

6.3.3 ATR FTIR

A commercial SpecArc Golden Gate™ attenuated total reflectance (ATR) accessory attached to a Thermo Nicolet Nexus Fourier Transform Infrared (FTIR) spectrometer was used to analyse powdered samples of hydromagnesite and basalt. The samples were analysed at room temperature (25°C) and atmospheric pressure. Spectra were obtained covering the wavelength range from 2.5 – 20 μm, this range adequately covered WatSen's 6.1 - 10.2 μm wavelength range.

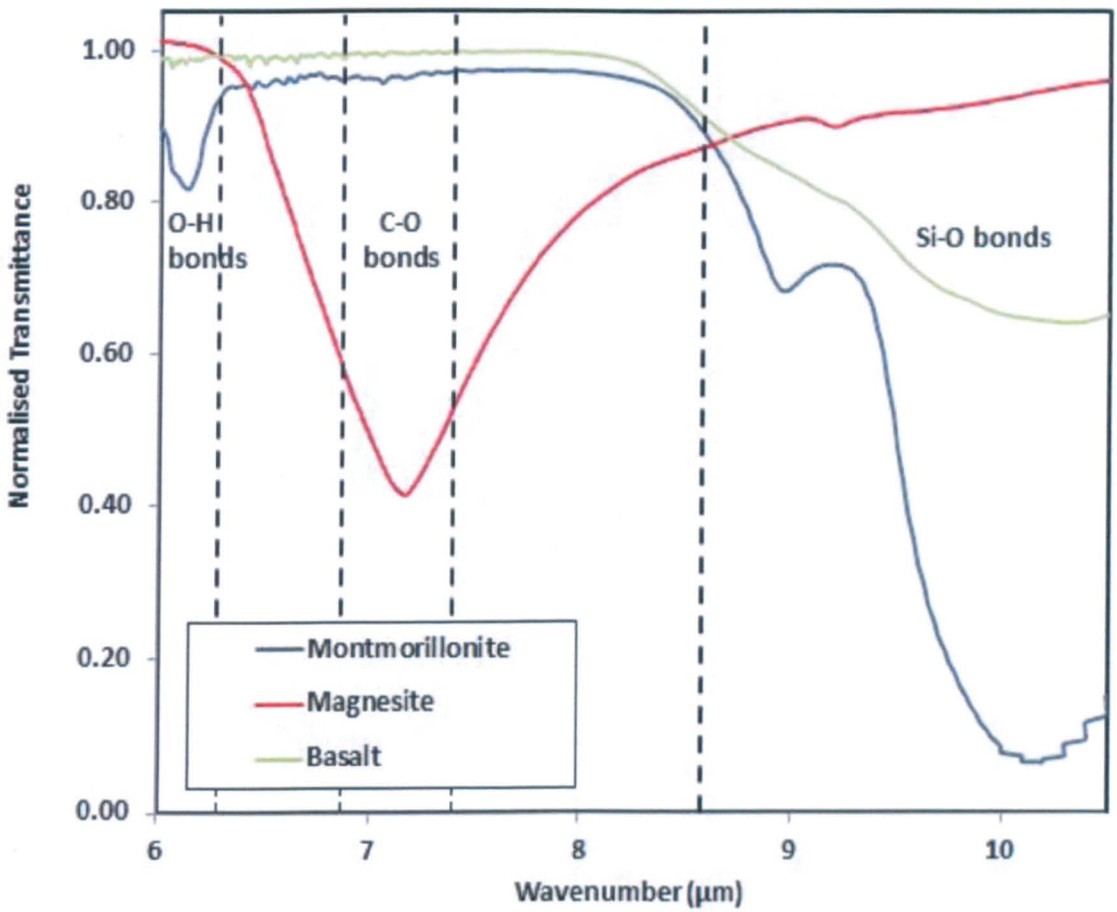

Figure 6.5 Spectra collected using a conventional ATR instrument for appropriate martian analogues. The spectra all displayed distinctive absorption features for carbonate (~7 μm), basalt (8.5-14 μm) and montmorillonite (~6 μm, 8.5-11 μm). Three spectra of montmorillonite which all overlapped were collected to demonstrate the reproducibility of ATR spectrometry.

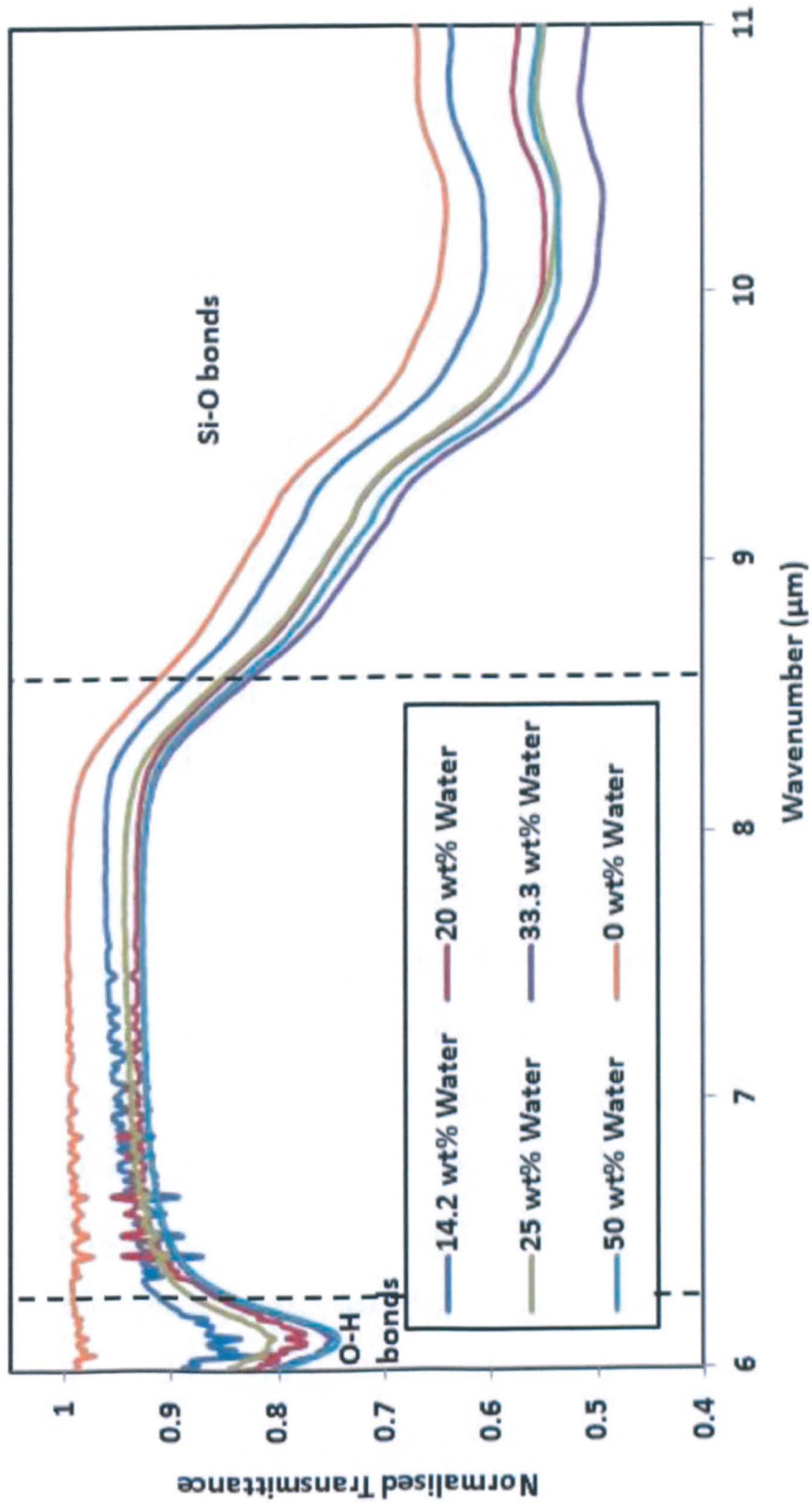

Figure 6.6 Water detection limits when mixed with basalt, measured on a commercial ATR instrument.

6.4 Method

6.4.1 The materials

Samples of basalt, hydromagnesite and water were employed to understand the limitations of WatSen in detecting water and carbonates within the martian subsurface. The basaltic sample was cut into 125 cm^3 pieces before being crushed in a hydraulic rock splitter. The basalt was crushed into small chips (> 2 mm) to simulate the grain sizes expected within the penetrated martian surface. The basalt was broken up using jaw crushers and sieved into requisite grain sizes (1-2 mm). The basalt was characterised with SEM for bulk composition. Pure hydromagnesite ($Mg_5(CO_3)4(OH)_2 \cdot 4(H_2O)$) was mixed with water and basalt in the final experimental runs (Figs. 6.7-9). The resulting range in grain sizes was further refined into sub mm using a sieve. The hydromagnesite arrived in the form of a compacted powder, these samples were broken up by hand (all sample preparation was conducted wearing dust masks within fume hoods). The hydromagnesite and basaltic material was dried over 24 hrs in an oven at 100°C. The material was then mixed together within a 3 litre round bottom flask. Initial tests of basalt to carbonate mix were conducted at room temperature and atmospheric pressure. Once rough wt. % detection limits were determined, a larger mix of material (~1 kg) was used to fill the assembly vessel containing WatSen.

A tether cable connecting WatSen to a laptop was fed though a slot in the vessels lid. Two thermistors were also placed within the vessel to monitor the general soil temperature and the soil temperature near the analysis diamond window. The lid was secured with four bolts to ensure soil remained in the vessel, the cable slot for the tether and thermistors allowed the vessel and chamber pressure to equilibrate and cool faster.

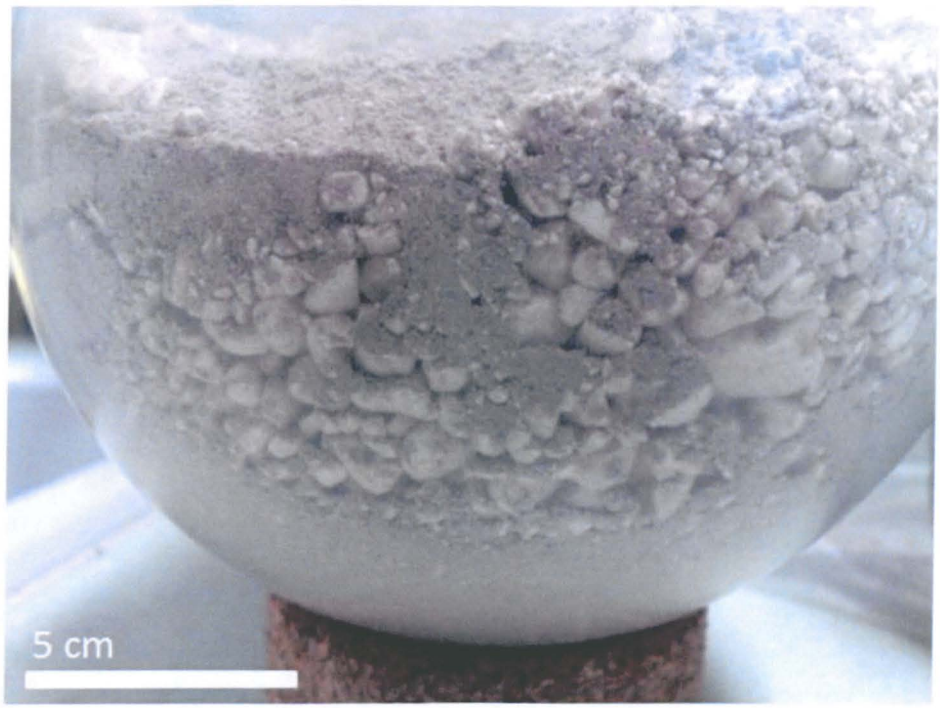

Figure 6.7 Initial mix of fine grained basalt (dark grey material) and light grey chunks of hydromagnesite.

Figure 6.8 Rotary evaporator used to break up coarse grains of hydromagnesite and then mixed with fine grained basalt and water.

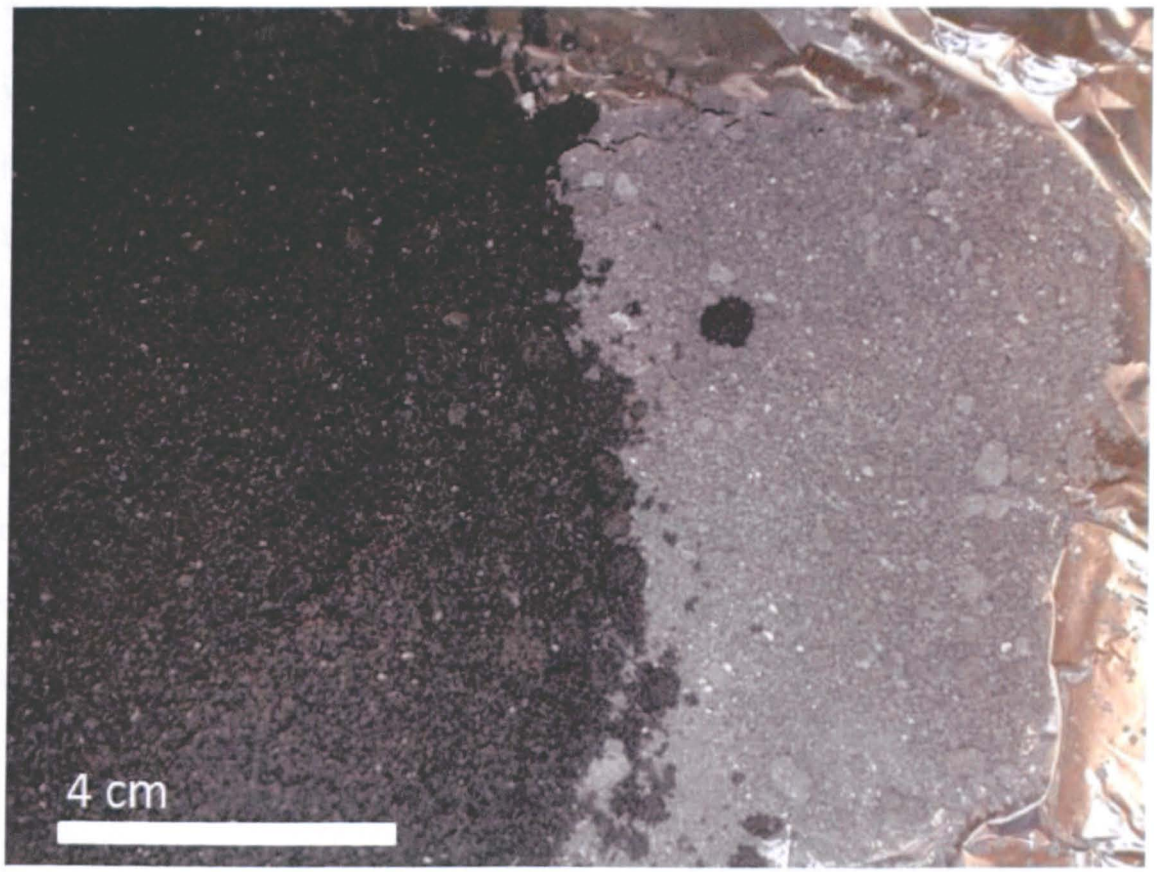

Figure 6.9 Results from using rotary evaporator on water saturated (left) and non-saturated (right) with 5 wt. % hydromagnesite and basalt mixtures. Fine grains of hydromagnesite are apparent (white specs), water saturated material tends to bunch together.

6.4.2 The martian environmental test chamber

Present-day martian surface conditions were simulated using one of the Open University's environmental chambers (Fig. 6.10). The chamber consisted of a stainless steel housing that could be sealed and evacuated, with several thermometers and a pressure gauge. The environmental test chamber for WatSen was connected to a turbo pump and equipped with thermistors, Euotherm temperature control and pressure detectors. The vessel that

WatSen sat within was placed on a cold plate. Liquid nitrogen from a Statebourne dewar tank was run through the system to achieve the desired temperature before testing. The base of the chamber was a liquid nitrogen cooled cold plate, upon which WatSen was placed within its martian analogue soil vessel. Thermometers were connected to a Pico datalogger, with the sensors attached 1. to the diamond window, 2. within the surrounding soil, 3. on the baseplate and 4. in the main chamber (Figs. 6.10-13). The temperature was fixed at -50(±2)°C and a pressure of 5.0±(0.6) mbars was maintained and monitored using a Eurotherm temperature controller. The pressure and temperature were decreased in steps from ambient terrestrial volumes to martian conditions to avoid additional atmospheric H_2O condensation within the soil vessel.

Figure 6.10 The martian simulation chamber with lid taken off, the interior of the chamber and the inside of the lid can be seen to be covered with foil for extra insulation.

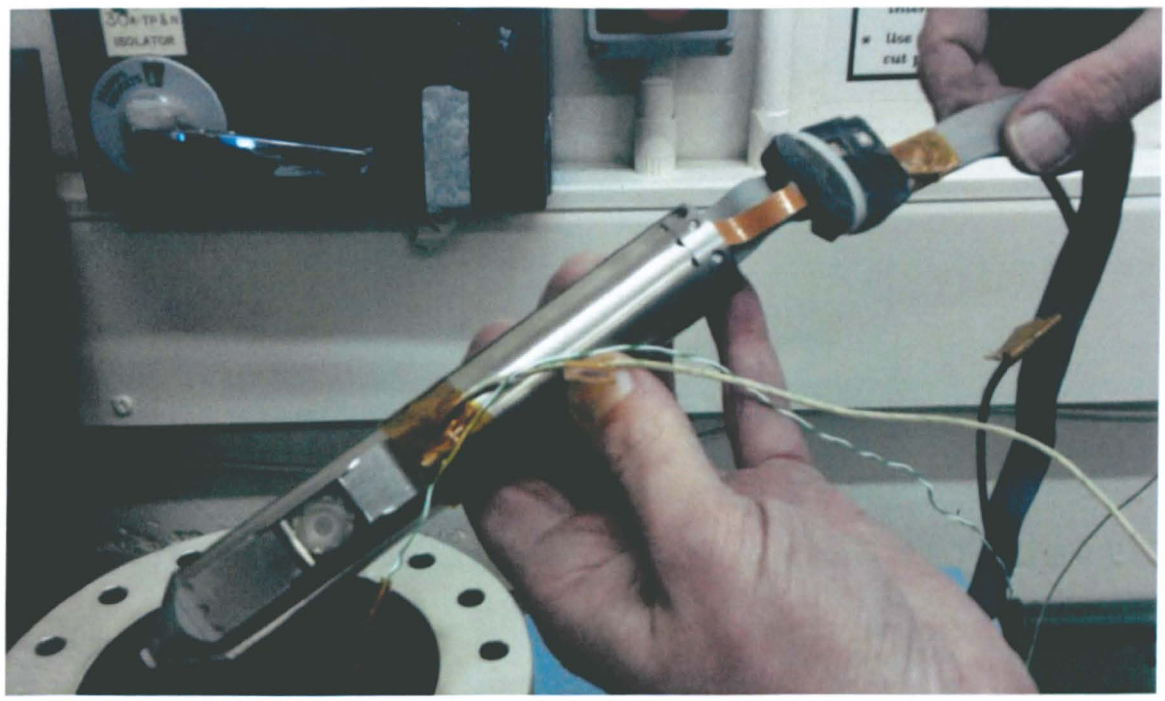

Figure 6.11 Watsen with thermistors attached to the side of the instrument and the second to sit in the soil just above the diamond window.

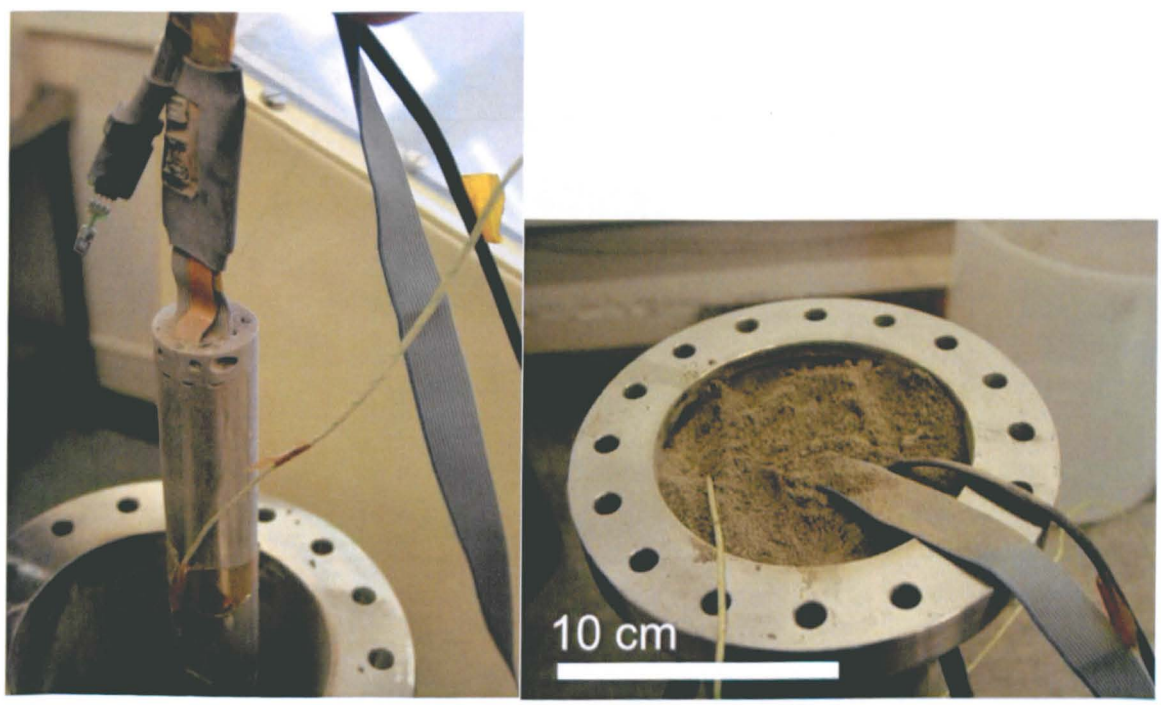

Figures 6.12-3 WatSen being lowered into the test vessel, then covered with 1 wt. % hydromagnesite and basalt mix.

6.5 Results

6.5.1 Basalt

The primary constituent of Mars's surface is basalt, hence it makes sense to try and detect hydromagnesite when it is mixed with a larger percentage of basalt. The terrestrial basalt, used for the experiment was characterised using a dual beam FEI Quanta 200 3D SEM (Chapter 2.2). The rock sample is medium-grained basalt, composed of low calcium pyroxene ($En_{62.7}Fs_{34.0}Wo_{3.3}$), high calcium pyroxene ($En_{37.4}Fs_{21.8}Wo_{40.8}$), plagioclase and olivine. The compositions of the pyroxene are shown to fall within the fields exhibited by martian meteorites (shaded areas; Fig 6.14).

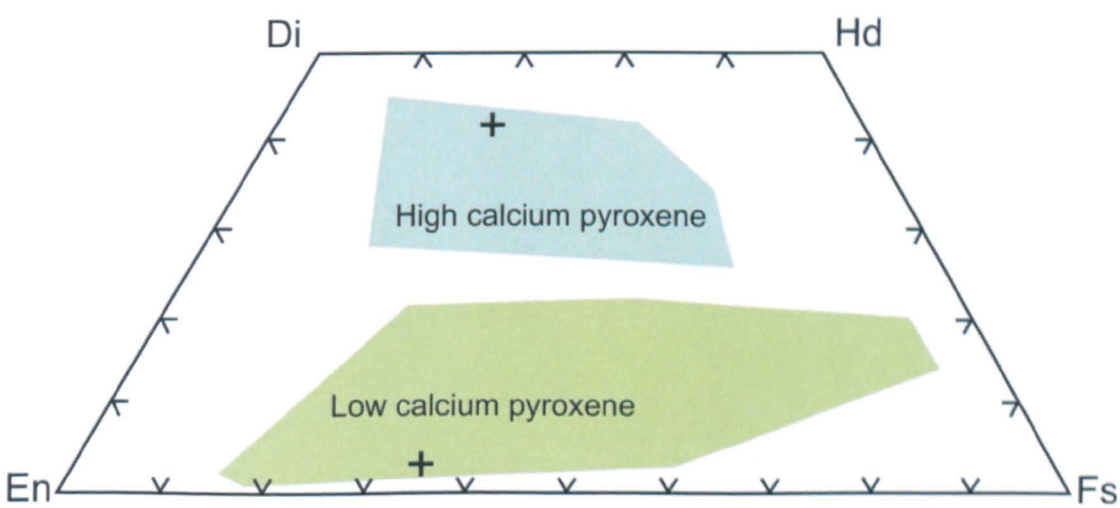

Figure 6.14 Pyroxene quadrilateral illustrating how the basalt composition provides a good representation of the compositions expected on Mars.

6.5.2 Detection limits of hydromagnesite

Initial experiments were performed at room temperature and atmospheric pressure in an open laboratory. Various wt. % of hydromagnesite were added to the fine-grained terrestrial basalt, to determine the detection limit for the carbonate before subjecting the sample to martian conditions (Fig. 6.15). The samples were mixed before being spread over the diamond window and pressed onto the surface with a spatula to simulate subsurface compaction and improve the sample to diamond window contact.

From the spectra the double peak (6.8 and 7.1μm) characteristic of hydromagnesite can be easily identified with 5 and 100 wt. % hydromagnesite, while 1 and 2 wt. % are not convincingly distinguished within spectrum. The basalt peak at 9.7 μm can be clearly observed (obviously no basalt spectrum detected in 100 wt. % hydromagnesite).

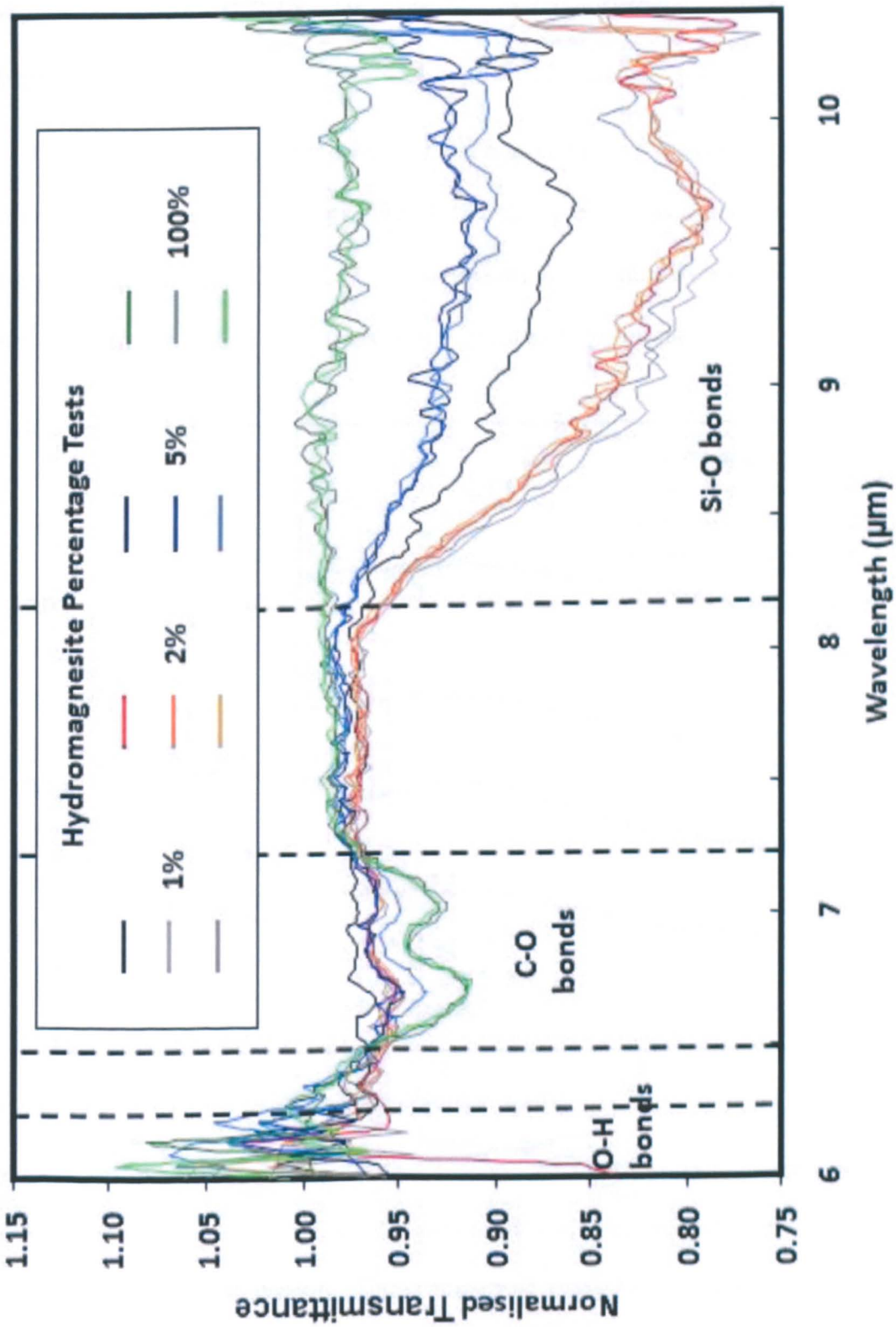

Figure 6.15 ATR spectra of hydromagnesite acquired at room temperature and pressure and normalised with master background spectrum. The spectra displayed distinctive absorption features for hydromagnesite (~6 µm, ~7 µm) and basalt (8.5-14 µm).

6.5.3 Detection limits of water with basalt and 5 wt. % hydromagnesite

The detection limit test for water content was conducted at room temperature within the environmental chamber (lid-off; Fig. 6.16). Samples of hydromagnesite + basalt + varying water content (5, 10, 15 wt. % and saturated) were coated over the diamond window and pressed to ensure a good contact and simulate subsurface compaction.

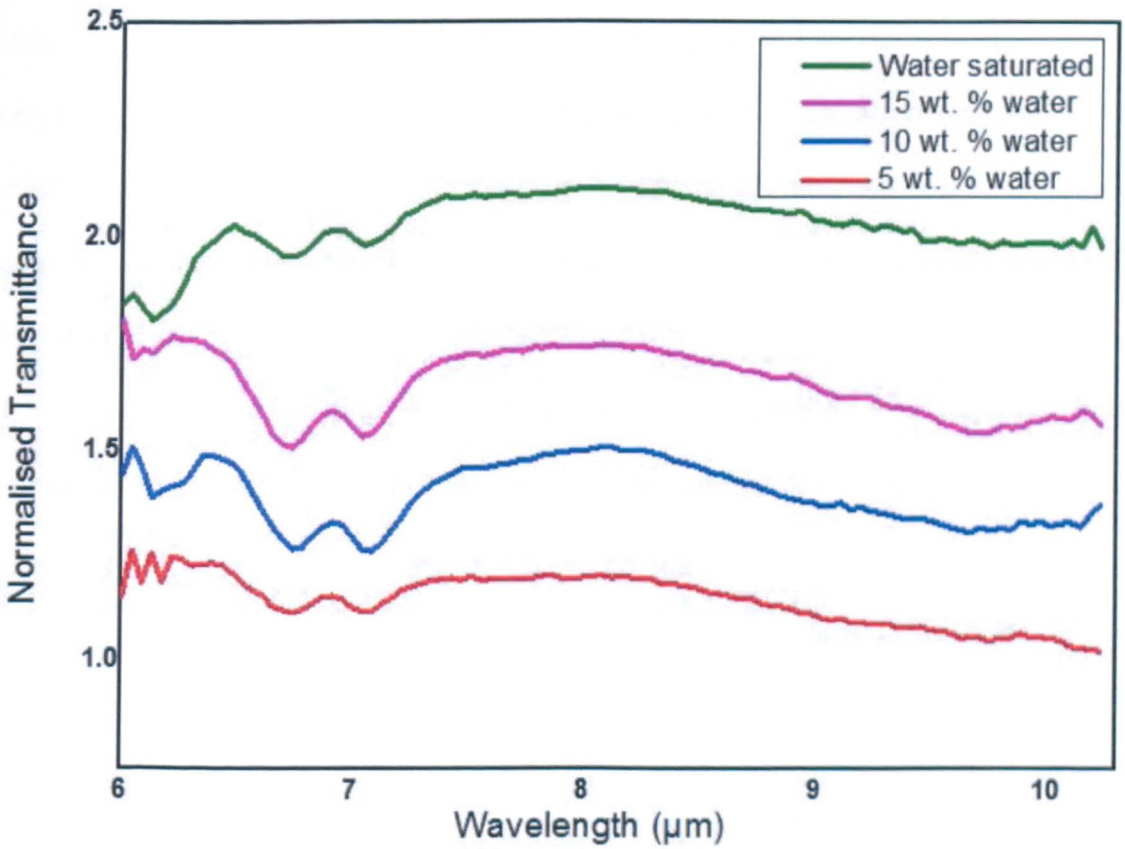

Figure 6.16 WatSen ATR spectra are offset for clarity, the spectra contain different water wt. % mixed with fine grain basalt and 5 wt. % hydromagnesite. Measurements were taken at room temperature and atmospheric pressure. The characteristic peaks for the hydromagnesite (6.8 and 7.1μm) are apparent in all the spectra, while the basalts are indistinguishable for all water contents.

6.5.4 Detection of basalt and 5 wt. % hydromagnesite under martian conditions

6.5.4.1 Test conditions

The cylindrical test vessel was filled with basalt mixed with 5 wt. % hydromagnesite before WatSen was slid into the compacted material (Fig. 6.12-13). This vessel was then sealed off before being screwed down onto the baseplate. Additional copper strapping was wrapped around the vessel and attached to the baseplate. Insulation foil was placed over the vessel to aid conduction and insulation (Fig. 6.10). The chamber was evacuated down to 5 mbar N_2 and then cooled to -50°C, on the baseplate which was chilled using liquid nitrogen (Fig. 6.18).

Spectra from the fine-grained basalt and hydromagnesite mix were acquired first without water so that any artefacts introduced by the addition of water could be monitored.

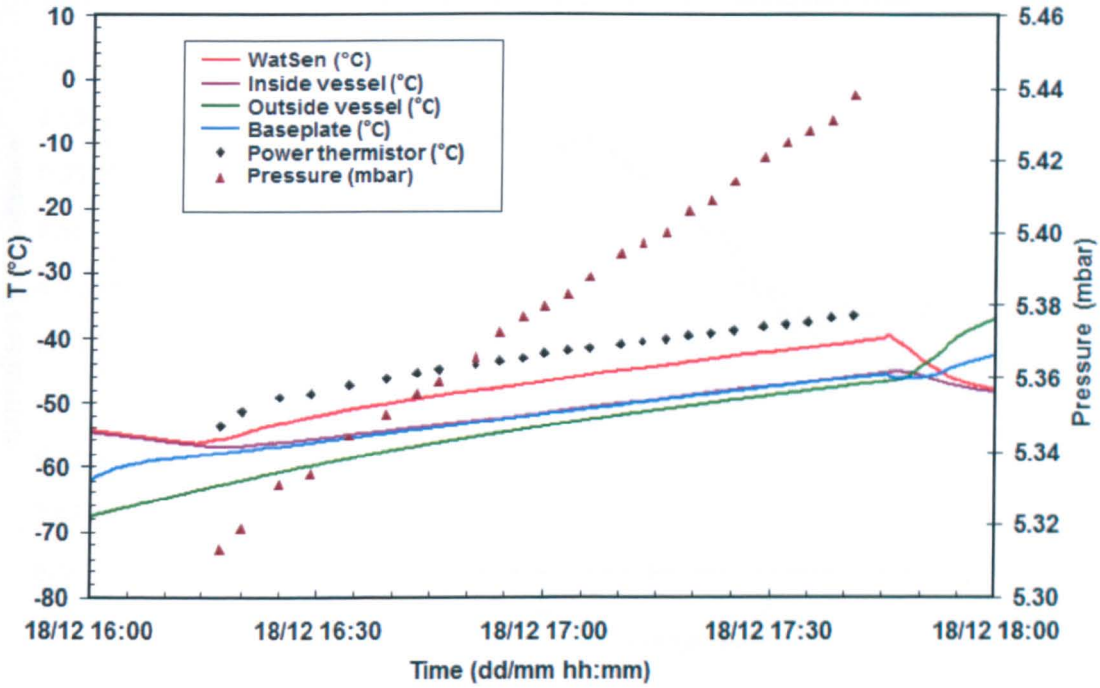

Figure 6.18 Experimental conditions while data was being collected with WatSen. Five thermistors were setup within the chamber, the WatSen sensor was placed on the instrument itself while the inside vessel thermistor was placed in the soil just above the diamond window.

It is possible to see that the desired conditions of ~-50°C and 5 mbar of pressure were obtained while the data were being collected (Fig. 6.18). The rise in temperature is a result of the instrument warming the surrounding soil upon activation, realistic to the scenario that would occur in the martian subsurface.

Twenty spectra from the sample and then against a ratio of the median background spectrum were taken under the low temperature and low atmospheric pressures (Fig. 6.19). The samples with 5 wt. % hyrdomagnesite and fine-grained basalt were easily identified from the spectrum and had good reproducibility.

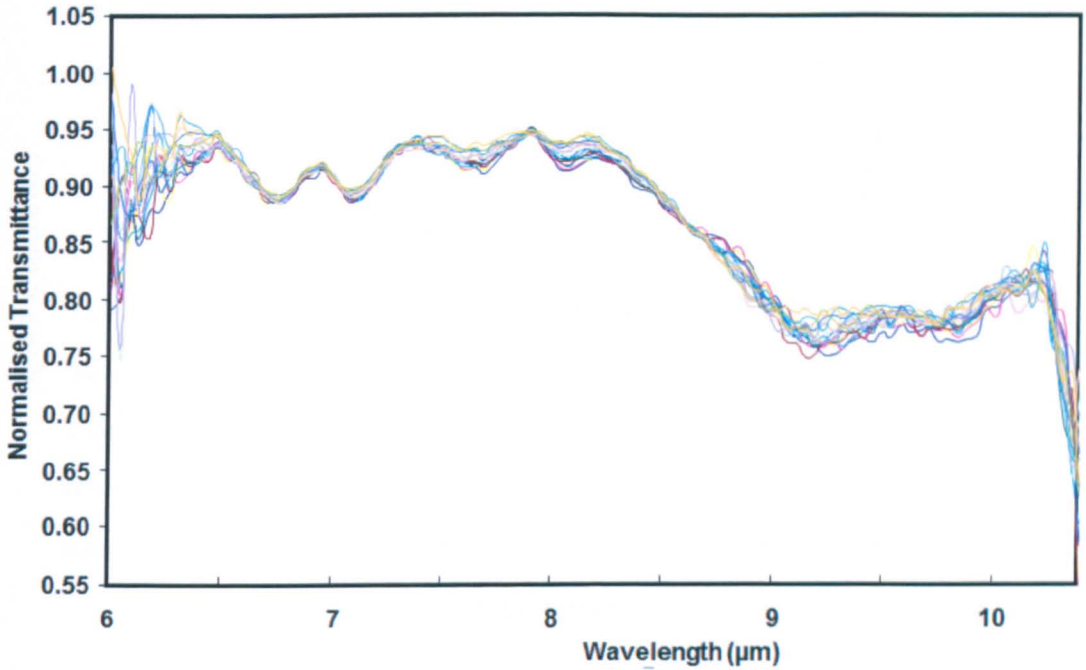

Figure 6.19 Combination of twenty spectra normalised with the master low temperature background spectrum.

The hydromagnesite and basalt absorption features did appear to shift under the change in conditions. There is an additional feature at 7.9 µm, which is not present in any of the room temperature magnesite and basalt measurements. While the backgrounds were measured in the same ambient conditions, the background spectrum did not take into account WatSen when surrounded by sample, and so the operational conditions (thermal variations) might be producing this feature. Furthermore, thermal changes can be clearly observed in the test period conditions (Fig. 6.18) however, the normalised master background file is an average and hence does not reflect each individual temperature variation.

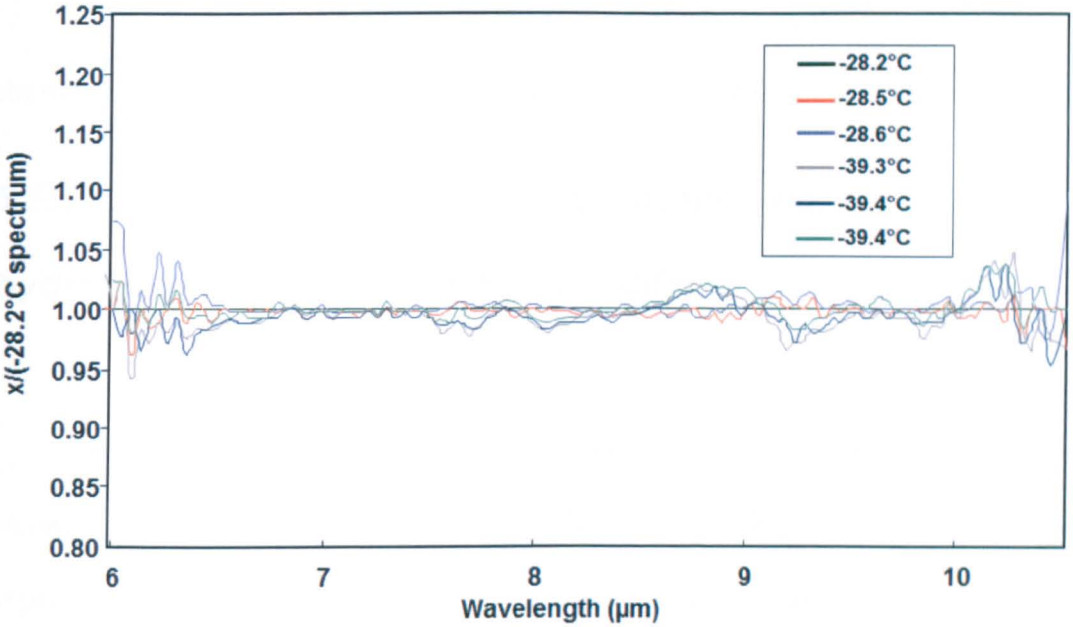

Figure 6.20 All background measured temperatures (-28.2 to -39.4°C) spectra are normalised against the -28.2°C spectrum. The pressure changes over this recording period were <1 mbar and are hence thought to have minimal effect on the spectra. The quoted temperatures were measured from within the vessel.

It is clear from the median of the temperatures that there is a variation in the collected backgrounds and future investigations/experiments would be required to further constrain background artefacts.

6.5.4.2 Potential issues

The seal around WatSen was thought to be gas-tight and has been baked and filled with dry nitrogen before assembly. However, the amount of water vapour contamination that might be finding its way into the instrument and interacting between the window and the IR sensor and source cannot be quantified.

Temperature is probably the main factor as thermal expansions have implications for changes in the refractive index, absorption losses and may affect optical coatings.

6.5.5 Detection of 20 wt. % water, basalt and 5 wt. % hydromagnesite under martian conditions

Following the initial detection limits of water with hydromagnesite a conservative quantity of 20 wt. % water content (basically saturating the sample) was used for the final experiment owing to concerns of water sublimation while cooling and venting the chamber (Fig. 6.21-22).

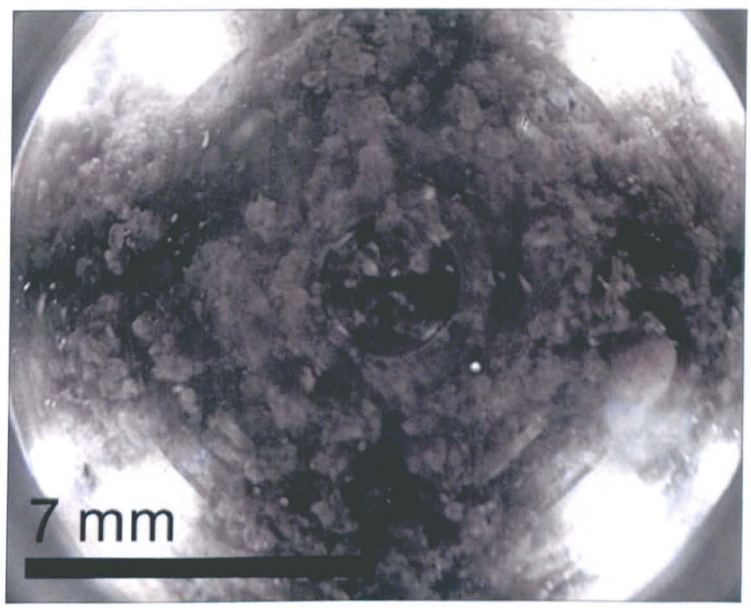

Figure 6.21 Sample at room temperature and atmospheric pressure. The material can be observed to clump into pockets of hydromagnesite and basalt mix bonded by water. Droplets of water can be observed forming on the left side of the window. A pre-test spectrum was taken showing a clear absorption features for water, hydromagnesite and basalt.

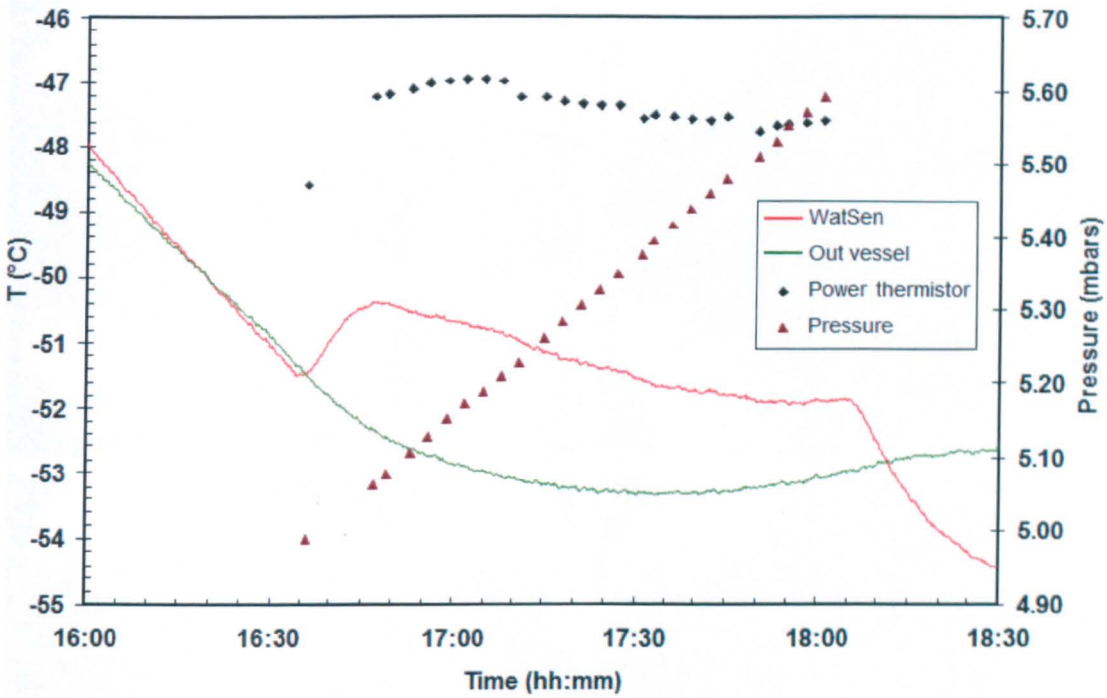

Figure 6.22 Conditions for final experimental investigations.

Only two of the four thermistors previously used were operational at the time of the experiment. However, they provided a good indication of the conditions within the chamber and of the analysed sample.

Images were taken over the space of an hour (16:48 to 15:48, Fig. 6.23). The water-ice can be clearly observed subliming (droplets shrinking; arrows) on the diamond window as the experiment progresses.

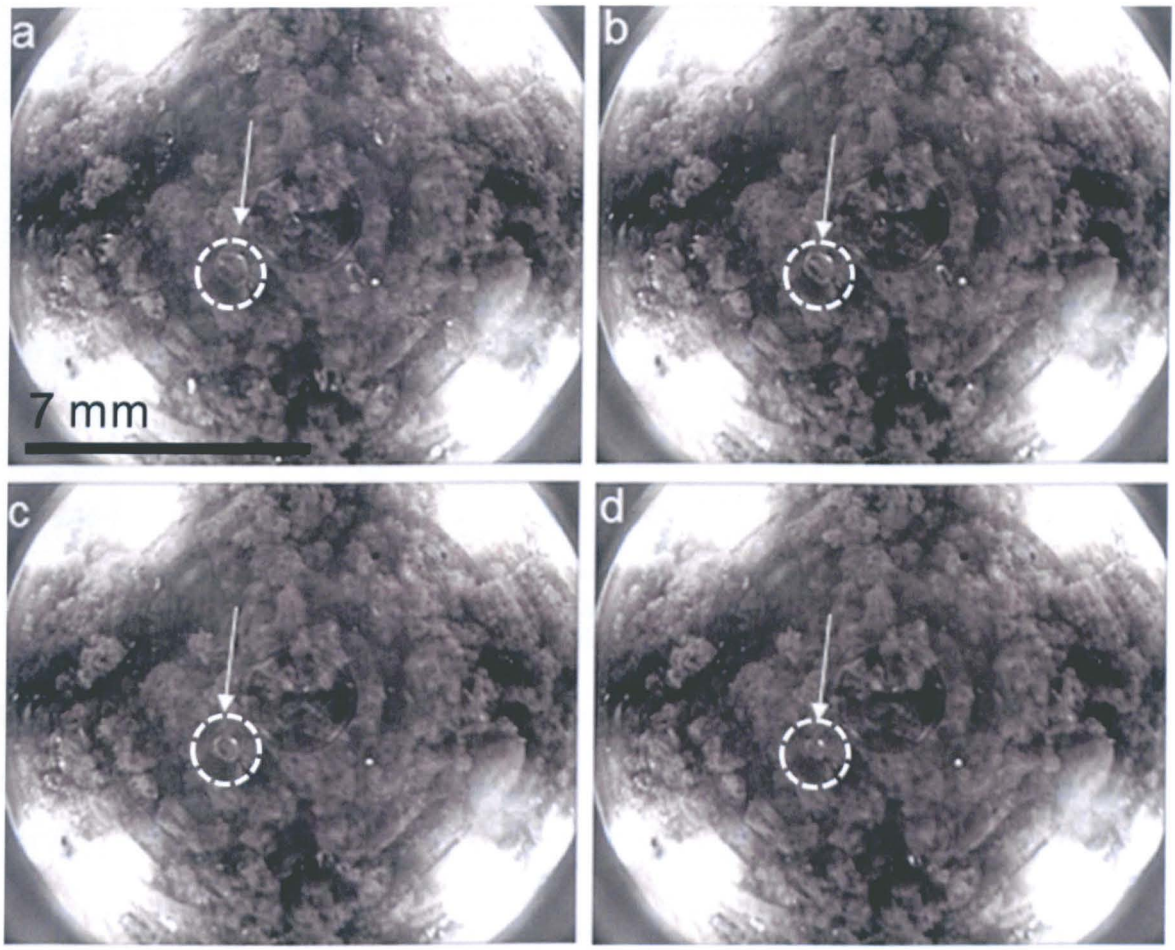

Figure 6.23 a-d Four corrected images of the sample between temperatures -50.47 to -51.77°C and pressures 5.062 to 5.478 mbar before each batch of spectrum recordings, with highlighted water sublimation spot (white arrow, dotted circle).

Despite the obvious presence of water ice on the microscope window (Fig. 6.23), the four batches (5 spectrum per batch) display noise in the water range of the spectrum and no obvious peak (6.24-25). Reasons to why the water absorption peak could not be observed include a downwards shift in the wavelength of the peak at low temperatures or/and loss and accumulation of water ice on non-sensitive sites on the diamond window.

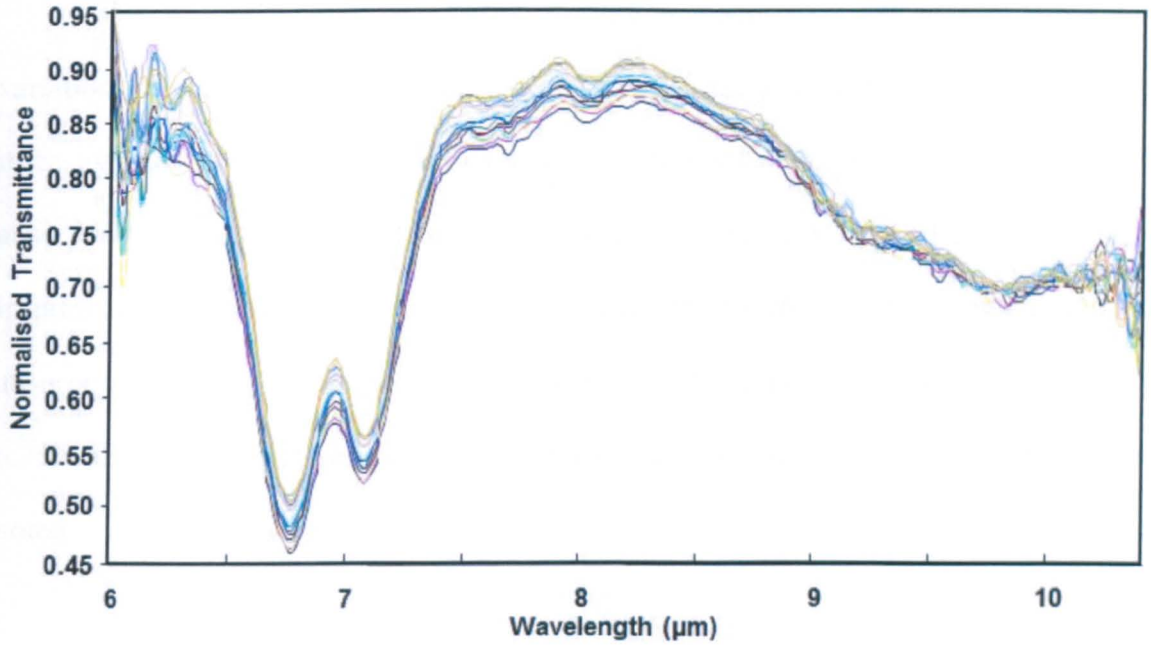

Figure 6.24 Twenty background normalised spectra collected under low temperature (~-50°C) and low pressure (5 mbar; N_2) conditions.

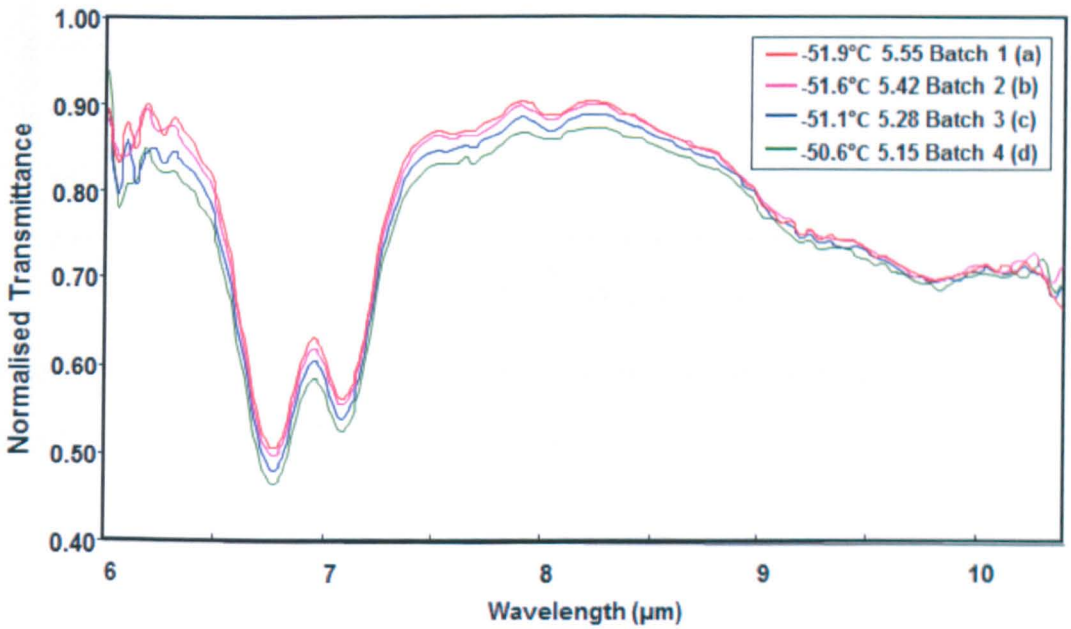

Figure 6.25 Average of five spectra for each of the four collected batches to improve signal-to-noise ratio.

The hydromagnesite and basalt absorption features do not exhibit large spectral variations under martian conditions. While no obvious peak shifts have occurred, small intensity variations were observed over the four batches of measurements (Fig. 6.25). The absorption features were seen to increase in intensity with a rise in temperature and decrease in pressure. Temperature variations seem to have affected the phase of water and hence its absorption feature shifting in down in wavelength. However, as can be observed in Figure 6.26 when the temperature is maintained and pressure is varied a clear change in intensity is noted.

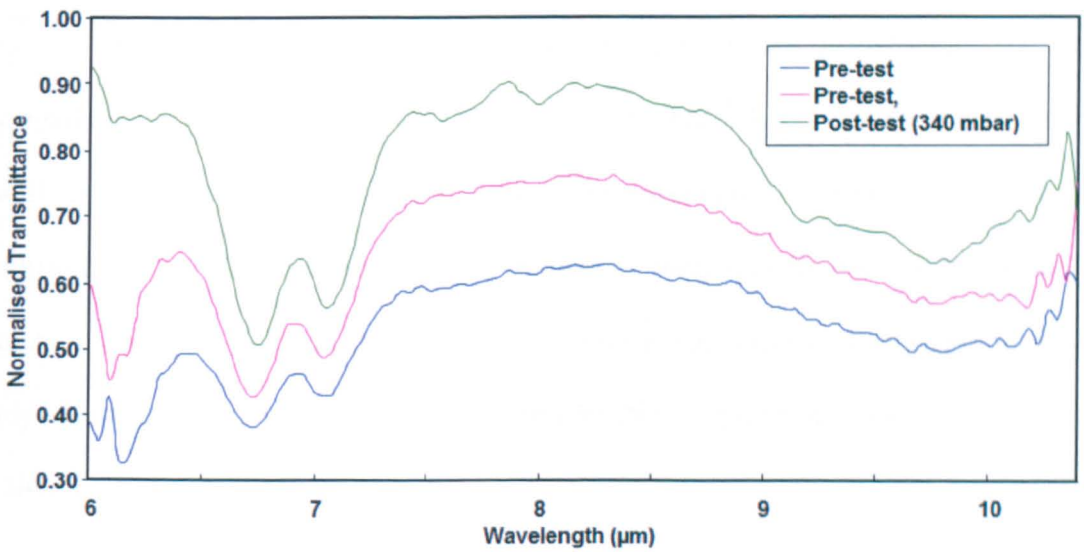

Figure 6.26 Three spectra acquired at room temperature and atmospheric pressure, apart from the post-test spectrum which was taken at 340 mbar.

The pre and post-test spectra all display absorption features for hydromagnesite and basalt, however, the post-test spectrum showed no sign of a water absorption feature below 6.4 μm.

6.6 Conclusion

WatSen has delivered on its specification of spectral identification and imaging of multiple mineral phases under martian conditions. Water and water-ice phases were clearly identifiable with imaging at room temperature and martian conditions. Spectral absorptions features were also detected at room temperature and 1 atm however, with a decrease in temperature the water-ice phase was no longer clearly identifiable and would have to be resolved before WatSen could be considered on the next mission to Mars.

The surface of Mars is constantly weathered by the planet-wide dust storms that spread and mix the loose surface soil components, but it is the layered subsoil material that will reveal Mars' history. In addition, the surface oxidizing solar radiation makes conditions inhospitable for life, however, beneath the surface there may exist briny solutions that would sustain organics. Rather than merely scratching the surface a penetrating mole would supersede its martian predecessors and with WatSen's instruments help characterize the past climate of Mars.

Chapter 7

7. Summary, Discussion and Further Work

7.1 Summary

This thesis set out to build on previous measurements of ALH 84001 using new methods of sample preparation and instrumentation (NanoSIMS) to derive the conditions in which the carbonates formed (GWB modelling) and to test whether WatSen was capable of detecting carbonates in the current martian subsurface.

A sample holder was developed and implemented to incorporate interchangeable carbonate standards and the unpolished ALH 84001 sample. The ALH 84001 sample was FIBed flush avoiding contamination issues experienced by previous SIMS analyses (Chapter 2). For the first time NanoSIMS was employed to measure $\delta^{18}O$ and $\delta^{13}C$ across ALH 84001 carbonate rosettes (Chapter 3) and $\delta^{18}O$ along an analogue carbonate (Chapter 4). NanoSIMS has allowed the smallest 5x5 μm spots of analysis to date to be recorded. In addition to carbonate standards used by previous authors new carbonate standards have been characterised and measured for IMF corrections. The $\delta^{18}O$ values corrected and applied to the ALH 84001 carbonates using the same IMF corrections and standards as previous authors (Leshin et al., 1998), result in the similar isotopic ranges 27.2‰ (-0.1 to 27.1‰; Chapter 3.7). The increased quantity and variety of measurements have shown that corrections from previous authors over simplify IMF corrections. This thesis has shown that an effect of 6‰ in $\delta^{18}O$ and potentially a difference in $\delta^{13}C$ of ~40‰ from previous ion microprobe studies. The ALH 84001 carbonate compositions and $\delta^{18}O$ values are of a comparable range to those

discovered in the analogue carbonates (Chapter 4), which are known to have formed in a hydrothermal processes on Earth (Treiman et al., 2002).

The formation of carbonates have been modelled the by applying the primary igneous modal mineralogy (Dreibus et al., 1994; Harvey and McSween 1994; Mittlefehldt 1994; Treiman 1995; Thomas-Keprta et al., 1996) and the $\delta^{18}O$ compositions (Romanek et al., 1996; Valley et al., 1997; Shearer and Leshin, 1998) within the literature. The addition of a dilute Ca^{2+}-rich brine solution and CO_2 formed carbonates with $\delta^{18}O$, $\delta^{13}C$ values and composition matching those found within ALH 84001 (Chapter 5). Following on from determining the formation conditions of ALH 84001 carbonates WatSen was proved capable of detecting carbonates and water within basalts (Chapter 6).

7.2 Discussion

The main aim of this project was to assess the conditions under which ALH 84001 formed; to this end the results have been conclusive of a hydrothermal formation. The additional observations/modelled parameters discovered from these findings therefore require a new model.

7.2.1 Implications for previous models

Findings from this study from analyses of elemental and isotopic composition and associated modelling of the formation fluids have implications for previous models.

7.2.1.1 High temperature models

The model in Chapter 5 has shown that in order to produce an enrichment in $\delta^{18}O$ a cooling system (>150°C) is required. The model suggests that a CO_2-rich fluid with an enrichment of Ca^{2+} dissolved the original mafic silicates through local dissolution (observed petrographically in Chapter 3). These results are in support of findings by Harvey and McSween (1996), who also suggest the dissolution of silicates prior to carbonate formation, however, there is a difference in formation temperatures (300°C). The high temperature models (Harvey and McSween 1996; Scott et al., 1997, 1998; Scott 1999) are not consistent with the composition of precipitated carbonates in this studies model, with a more sideritic composition found to precipitate at higher temperatures (Chapter 5; Fig. 5.6). Scott et al. (1997) also suggested a formation through carbonate melts which is inconsistent with the

chemical and $\delta^{18}O$ values found in this and previous studies (Romanek et al., 1994; Warren 1998).

Gleason et al. (1998) and Kring et al. (1998) suggested that the origins of the carbonate were from a high temperature (<300°C) dissolution-replacement or dissolution-precipitation of maskelynite, respectively. Treiman (1998) suggested the formation of the carbonates through the replacement of plagioclase glass which was then changed into maskelynite following high-temperature alteration. These hypotheses suggested a carbonic fluid was introduced into the system and Al, Si and Na were removed from the system. The dissolution-replacement of maskelynite or plagioclase as the sole reaction is not consistent with the carbonates association with orthopyroxene in this and previous studies (Treiman 1998; Scott 1999). While the model in Chapter 5 includes the dissolution of maskelynite, carbonate formation solely by replacement of plagioclase would not supply sufficient Fe, Mg, Ca cations. In addition, the multiple points of nucleation are not explained by this model or the intimate relationship to the orthopyroxene (mircodenticular structures) observed in this and previous studies (Thomas-Keprta et al., 2009). However, this study cannot rule out the low temperature formation of carbonates through replacement of other minerals such as plagioclase which were not present within the sample split 126 studied here.

7.2.1.2 Low temperature models

Findings from Chapter 3-5 show that a low temperature (<150°C) single fluid source can produce both the chemical and isotopic composition observed within the carbonates. Low temperature models consistent with the conditions discovered in this study include Romanek et al. (1994) who suggested a cooling system from 80-0°C derived from a model based on equilibrium fluid mineral fractionation factors. However, this model was based on $\delta^{18}O$

values with a range of +13.3 to +22.3‰. In order to obtain a greater chemical variety of carbonates and $\delta^{18}O$ range as discovered in chapter 3 a cooling system of 150-0°C is required, this is consistent with Clayton and Mayeda (1998) who observed similar carbonate $\delta^{18}O$ enrichments in EETA 79001. While the timescales in the model (Chapter 5) are dependent on the rate of release of cations into the fluid (rate of dissolution) high temperature models are shown to homogenize the carbonate under timescales of days to a month. While lower temperatures will further increase these timescales (rate of alteration/dissolution follows an Arrhenius trend) in order not to homogenise the carbonates timescales are likely to be less than a year, consistent with short term fluid-rock interaction in hydrothermal settings.

Warren (1998) suggested a Playa Lake or Sabkha Analog model in which a cataclysmic flood episode instead of a hydrothermal system formed the carbonates. A dolocrete analog model was also suggested where carbonates would form within ground waters that had become CO_3-rich. The argument for these environments related to the fluid-rock interaction timescales providing an enhanced level of alteration not compatible with observations in a hydrothermal setting. However, Warren (1998) study was prior to the detection of the analogue carbonates discovered in a hydrothermal setting (Trieman et al., 2002) studied in Chapter 4. The new data presented here clearly show how a hydrothermal system can provide chemical and isotopic compositions without replacing the whole sample.

Models by Niles et al. (2005) suggest a lake and a closed subsurface system both subsequently introducing a high pH spring. The model in Chapter 5 agrees with Niles et al. (2005) hydrothermal setting in which the pH is increased by the initial serpentinsation of the mafic rock to form the observed carbonates. The models vary in the pH levels and the concept of carbonates forming from a cooling system. Niles et al. (2005) argue that a cooling

system would progressively decrease the carbonates in solution resulting in the cessation of formation. This study differs from previous models by suggesting that dissolution and thereby the supply of cations is constantly being added to the fluid during cooling, therefore maintaining saturation of carbonates within the system. The system also needs to be cooling (150-0°C; Chapter 5) in order to produce the range in microscale $\delta^{18}O$ values across the carbonates, these finding are consistent with previous cooling hypotheses (Romanek et al., 1994; Saxton et al., 1998; Eiler et al., 2002a). In addition, if the low $\delta^{13}C$ values (-1.5 to -18.6‰) are presumed not to originate from hydrothermal activity, the $\delta^{13}C$ values (+5.7 to +23.2‰) are consistent with the $\delta^{13}C$ fractionation exhibiting a smaller range than $\delta^{18}O$ (Niles et al., 2005; Warren 1998).

7.2.2 New hydrothermal Model

The discussed models did not have the spatial resolution of $\delta^{18}O$ and $\delta^{13}C$ (Chapter 3) or the ability to model both the chemical and isotopic compositions determined in this study (Chapter 5). It is on this basis that a new comprehensive model of the ALH 84001 carbonate formation is proposed to constrain their martian environment in which they precipitated.

The rock surrounding ALH 84001 was originally fractured 4.0 Ga (Ash et al., 1996) soon after crystallising (4.1 Ga; Lapen et al., 2010). During the time between 4.1 Ga and 3.9 Ga (formation of the carbonates) the surface of Mars is cold, arid and icy. However, beneath the surface ground water exists in a warmer, wetter environment supported by geothermal heat (Ehlmann et al., 2011; Fig. 7.1a). Either a pulse of this geothermal heat or impacting caused the rapid rise of the underlying water table (brine) mixed with the CO_2-rich

atmosphere of Mars. The hot brine initiates serpentinisation of the surrounding impact induced permeable rocks which provide the high water/rock ratio (10), this reaction drives pH (9.8) up in the initial brine ($\delta^{18}O$ -15‰; $\delta^{13}C$ +10-15‰) and starts to precipitate carbonates (Fig. 7.1b). This reaction is common on Earth and does not require high temperatures (<150°C) to drive serpentinisation (Hofmann and Harris 2008). High pH spring environments interacting with CO_2 have been documented to produce carbonates with chemical (Clark et al., 1992; Treiman, 2002) and isotopic variations (Anders, 2006) consistent with observations from Chapter 3, 4 and modelled in Chapter 5. The carbonates crystallised from multiple point sources within the orthopyroxene followed by radial growth which has resulted in some of the carbonates overlapping (Fig 4.1). The carbonates nucleate on grain surfaces, actively dissolving orthopyroxene while precipitating, and thus forming the indented morphology observed in this study (Chapter 3; Fig. 3.3) and by Thomas-Keprta et al., 2009. Evidence of dissolution of the original orthopyroxene was found by examining the surface beneath the carbonates (Chapter 3; Fig. 3.4) which have also been identified in terrestrial studies to form by low temperature aqueous corrosion (Velbel 2007, 2011).

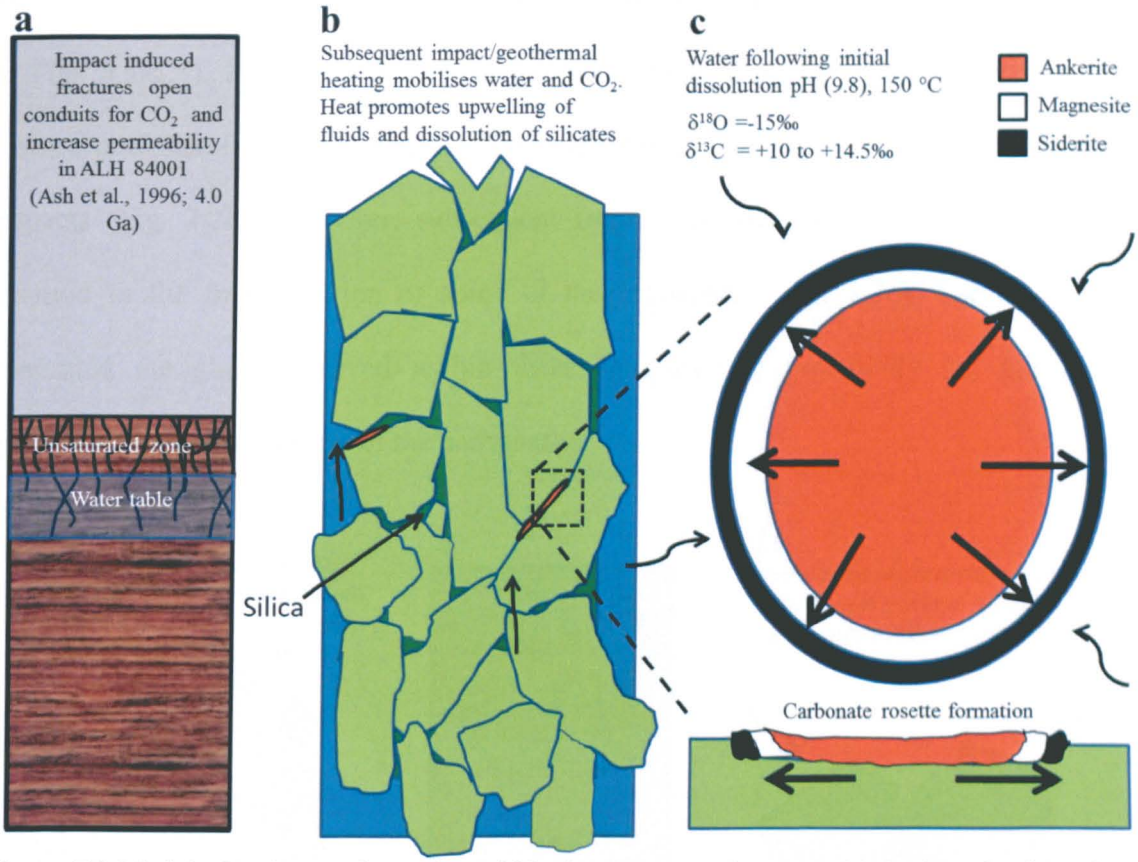

Figure 7.1 Model of carbonate formation within the upper martian crust (a) the introduction of water (b) and the starting conditions (c).

The carbonates formed from this single evolving fluid with the temperature (150°C) and pH drop resulting in a change of carbonate composition. This low temperature was consistent with the chemical diffusion rates required for these heterogeneous compositions (<200-400°C; Kent et al., 2001). The system was closed and localised resulting in an enrichment of $\delta^{18}O$ as the carbonates form.

The fluid-rock interaction timescale was short, probably less than a year by which point the carbonates had formed and the waters receded removing most of the unconsolidated phyllosilicates and quartz, but leaving the majority of the carbonates which were bound to the orthopyroxene surfaces (Fig. 7.2a). The receding silicate-rich waters left voids from the

initial dissolution. These voids can be observed in the ALH 84001 analogue sample (Chapter 4; Figs 4.4-4.5). Following this event the water table dropped further beneath the frozen surface and therefore did not remobilise and interact with ALH 84001 by any subsequent impacts (Fig. 7.2b). However, subsequent impacts of ALH 84001 closed the voids and resulted in the fragmentation of some of the carbonates (Fig. 7.2c). These impacts also generated the glass observed within these samples and potentially the magnetite and pyrhrrotite around the edges of the carbonates.

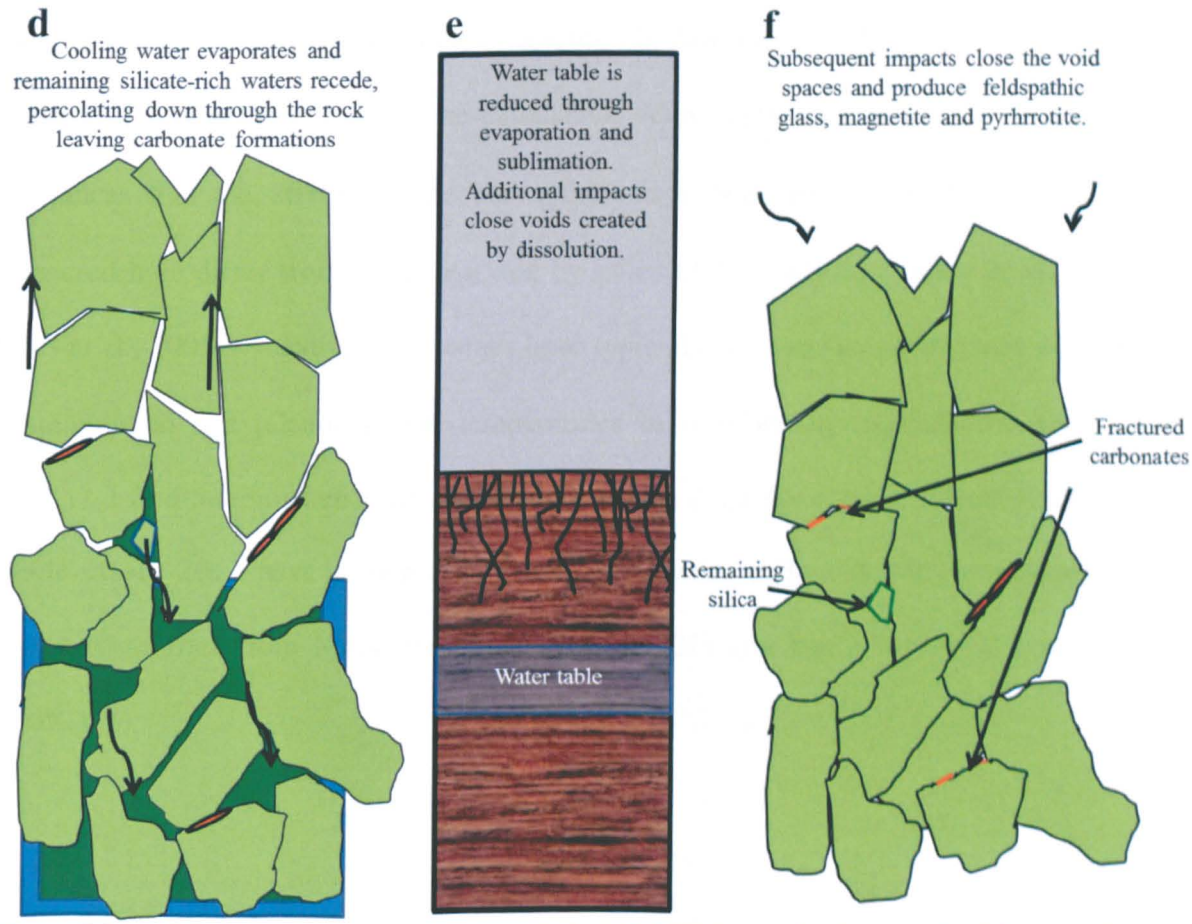

Figure 7.2 Model of retention of carbonates within ALH 84001(a), the closure of void spaces (b) and the fracturing of some carbonates (c).

7.2.3 Implications for interpreting $\delta^{18}O$ and $\delta^{13}C$ from martian carbonates

The work in Chapter 3 reveals the care which must be taken when inferring the true isotopic composition of the carbonates within ALH 84001 when measured by SIMS. To this end, it is essential to constrain these values before using them to deduce environmental conditions on Mars (e.g. Niles et al., 2010). Values from this thesis have shown how, when using the same standards as previous studies (Leshin, et al., 1997) and applying similar corrections, values for $\delta^{18}O$ can be calculated. With confidence in these $\delta^{18}O$ values and assurances that the effects of the NanoSIMS have been characterised, the $\delta^{13}C$ values measured here differ from those reported by other SIMS analyses (Valley et al., 1997 and Niles et al., 2005). Negative $\delta^{13}C$ values have typically been attributed to issues with organic contamination and release at low temperatures in step heating experiments (see Chapter 3.4.2.1). I find that no such conclusion can be drawn from my dataset. Recent findings from Steele et al., 2012 have shown that a macromolecular carbon (MMC) component exists within meteorites from Mars (including ALH 84001) and has a low $\delta^{13}C$ component (-11.0‰).

7.2.4 Implications for evolution of water $\delta^{18}O$ and atmospheric $\delta^{13}C$ from ALH 84001 carbonates

Niles et al., 2010 draws recent results from the atmospheric CO_2 measurements by the Phoenix lander and data from previous SIMS and acid dissolution experiments on martian meteorites (including ALH 84001) to infer an atmospheric-mantle CO_2 history of Mars (Fig. 7.3). As ALH 84001 is the only sample we have from the Noachian crust (chassignites and nakhlites sampling Mars some ~3 Ga later) determining the C and O found within its carbonates is key to understanding Mars' primordial $\delta^{13}C$ and $\delta^{18}O$ reservoirs.

While Niles et al. (2010) suggest they record a value from atmospheric CO_2, when $\delta^{13}C$ values from Niles et al. (2005) are combined with Holland et al. (2005) $\delta^{18}O$ measurements taken in Chapter 3 are more concurrent with a magmatic source with a sequentially introduced MMC component providing a more reduced initial $\delta^{13}C$ component than has been inferred by Niles et al. (2010). Recently values from the Sample Analysis at Mars (SAM) Suite Investigation in the Mars Science Laboratory (MSL) vary significantly from those measure in the Phoenix lander ($\delta^{13}C$ +45±4‰ and $\delta^{18}O$ +48±6‰ Webster et al. 2013; $\delta^{13}C$ -2.5±4.3‰ and $\delta^{18}O$ 31±5.7‰ Niles et al. 2010, respectively; Fig. 7.3).

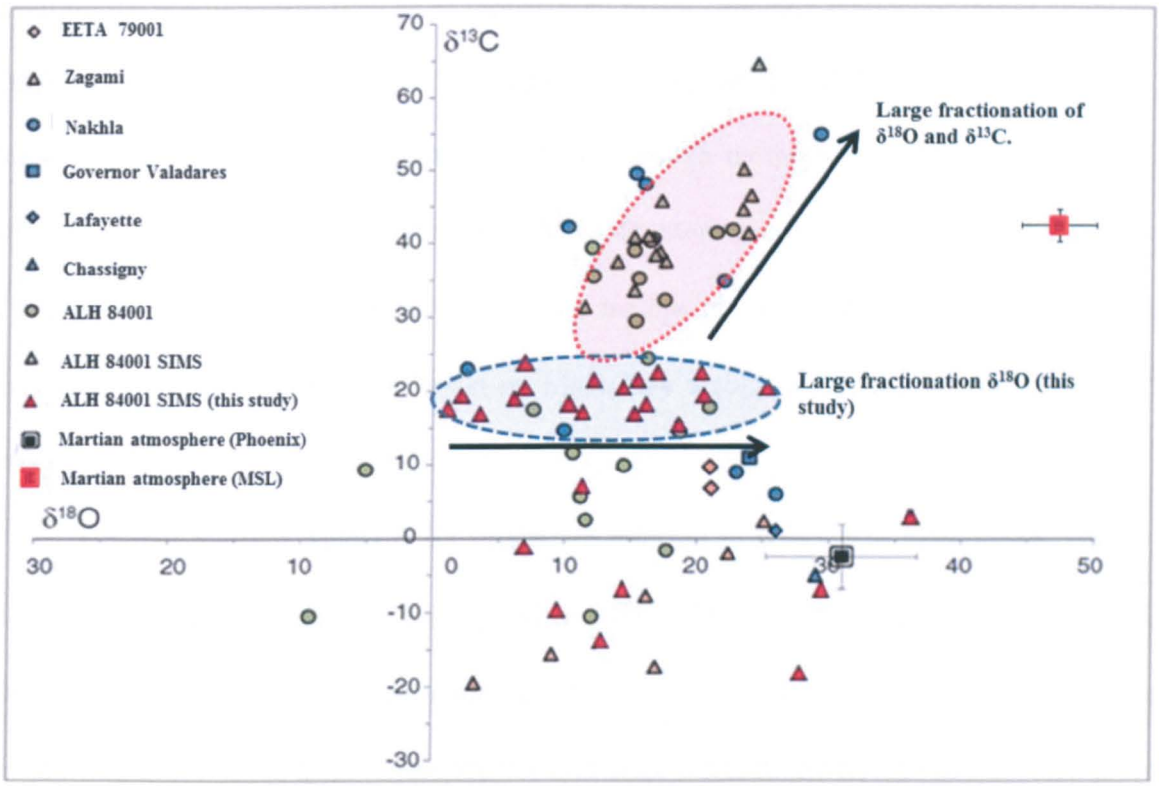

Figure 7.3 Measurements of $\delta^{13}C$ and $\delta^{18}O$ isotopes from martian meteorite carbonates. Values are derived from acid dissolution (Jull et al., 1995; 1997; 2000; Wright et al., 1988; 1992; Romanek et al., 1994; Clayton et al., 1988) apart from where noted as SIMS. The previous ALH 84001 SIMS analyses are based on values of $\delta^{13}C$ (Niles et al., 2005) coupled with measurements acquired on carbonates with similar Mg content for $\delta^{18}O$ (Holland et al., 2005) and Niles et al. 2010 inferred correlation (red dotted area). The $\delta^{13}C$ and $\delta^{18}O$ values from this study are coupled based on full compositional analyses. The atmosphere of Mars is believed to be +31.0±5.7‰ and –2.5±4.3‰ for $\delta^{18}O$ and $\delta^{13}C$ respectively from results collect from the Phoenix lander (black square; Niles et al., 2010). However, recent values from MSL record $\delta^{13}C$ +45±4‰ and $\delta^{18}O$ +48±6‰ from the martian atmosphere (Webster et al., 2013).

The values measured in this study record a $\delta^{13}C$ between 10-15‰ in the CO_2. Formation of carbonate readily removes ^{13}C from the atmosphere thereby decreasing $\delta^{13}C$ consistent with the Phoenix lander results, however, depending which measurement is most

accurate the martian crust may have sequestered major (Phoenix lander) or minor amounts of CO_2 (MSL results) in the form of carbonates. To explain the MSL data, scenarios such as degassing of a carbonate-rich primordial Mars through methods such as volcanic burial or impacts could explain the enrichment in $\delta^{13}C$. Sputtering could also favour an increase in $\delta^{13}C$ similar to δD (Fig. 1.1) where the lighter isotope is favourably removed. In addition, if biological processes ever existed/exist on Mars they would favour the incorporation of ^{12}C which would also increase the atmospheres $\delta^{13}C$ value.

Current martian waters $\delta^{18}O$ values are inferred to be ~-16‰ from measurement by the Phoenix lander which also correspond to EETA 79001 (-15‰) and this study (-15‰). This suggests that minimal fractionation of $\delta^{18}O$ in crustal waters has occurred over Mars' history and that limited high temperature water-rock interactions environments were present following the formation of ALH 84001 carbonates.

7.2.5 Implications for the past climate of Mars

There appears to be at least episodic evidence for lakes, valleys and channels on the surface of Mars (Schumm, 1974; Carr, 1995). However, greater cooling rates on Mars caused fracturing in the basaltic rocks which combined with impact induced fractures provided increased permeability and large subsurface deposits of liquid water. These large reservoirs of subsurface water could have been frozen by the point at which the ALH 84001 carbonates formed (3.9 Ga; Borg et al., 1999). The method by which this water was remobilised includes impact generated (in association with the late heavy impact bombardment) and geothermal heating. A geothermal and impact scenario fits ALH 84001 carbonate as the model shows how a closed system with a 10 W/R can reproduce the carbonates chemical and isotopically.

However, with no shock events recorded at the time of carbonate formation (3.9 Ga) a geothermal produced set of carbonates is favoured. In addition, Chapter 4 provides additional evidence of origin with analogue carbonates which are known to form from a geothermal rather than impact origin. This hydrothermal heating of subsurface water reservoirs on a large scale could explain observed ancient valley networks found on the southern terrain of Mars. Some of these valley networks are located close to impact sites or volcanic structures suggesting at least some of these sites are related to a hydrothermal origin similar to that which formed the ALH 84001 carbonates.

A similar process of a closed system subsurface clay mineral formation is also suggested to have occurred on ancient Mars (Ehlmann et al., 2011). Evidence for this subsurface formation environment exists from:

- Mineral formations of observed Fe, Mg-rich smectites and chlorite, forming under high pH conditions which would result from the dissolution of ultrabasic rock.
- Phases such as serpentine and illite/muscovite, which are known to form at high temperatures.
- The presence of the recently discovered clay mineral phases only being discovered in deep exposed crustal material.

The differences this thesis has discovered between the clay and carbonate formation environments on the ancient subsurface of Mars suggest an increase in W/R ratios and a decrease in CO_2 available will favour phyllosilicate precipitation over carbonates in a closed system. These results suggest that in locations with a greater potential of high W/R ratios such as ancient lake environments and heavily fracture crustal material, phyllosilicate formation would be favoured over carbonate precipitation.

7.2.6 Implications for life

Evidence presented from McKay et al. (1996) for life within the ALH 84001 carbonates is controversial with numerous authors contesting their findings (Harvey and McSween, 1996; Gleason et al., 1997; Kring et al., 1998; Scott et al., 1997, 1998; Scott 1999). Subsequent stepped heating measurements by Wright et al., 1997 provided the lowest recorded $\delta^{13}C$ values to date +4.2 to -61.8‰ (Fig. 7.4).

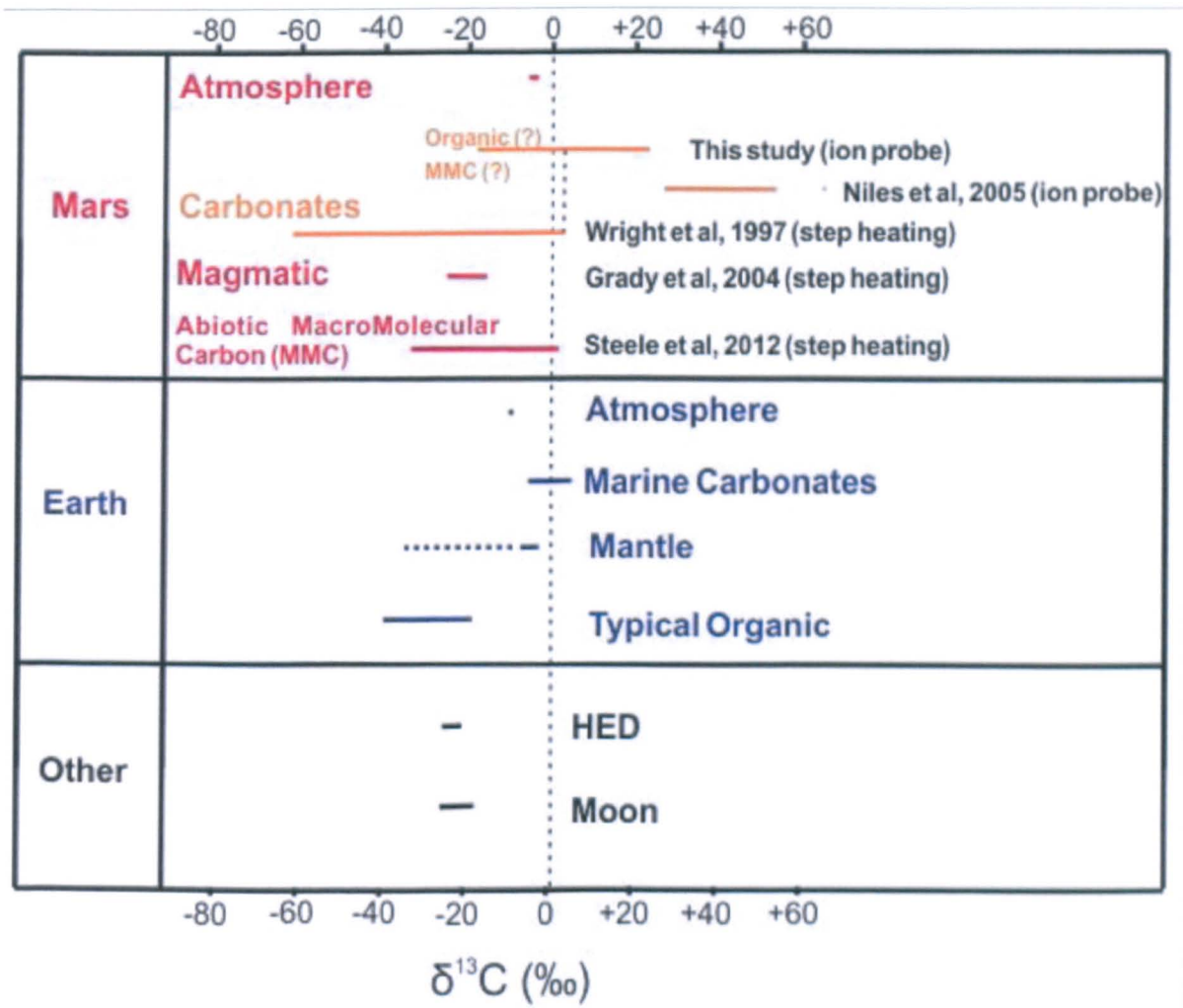

Figure 7.4 Summary of $\delta^{13}C$ values found the in Solar System and suggested origins.

Values measured from teflon foil (-58.7‰) used in the analysis of these samples were considered as contamination adding to a low $\delta^{13}C$ component. However, Wright et al. (1997) also noted a release of gas (i.e. 12.2% of the total carbon) at 200–300°C gave a $\delta^{13}C$ value of –37.7‰. Veins and grains of poorly crystalline graphite, magnetite and macromolecular carbon have been observed within ALH 84001 carbonates in intimate association with magnesite (Figs.7.5-6.Thomas-Keprta et al., 2009; Steele et al., 2007; 2012). This component corresponds to the outer portions of the carbonate rosettes and potentially the light carbon values measured in this study.

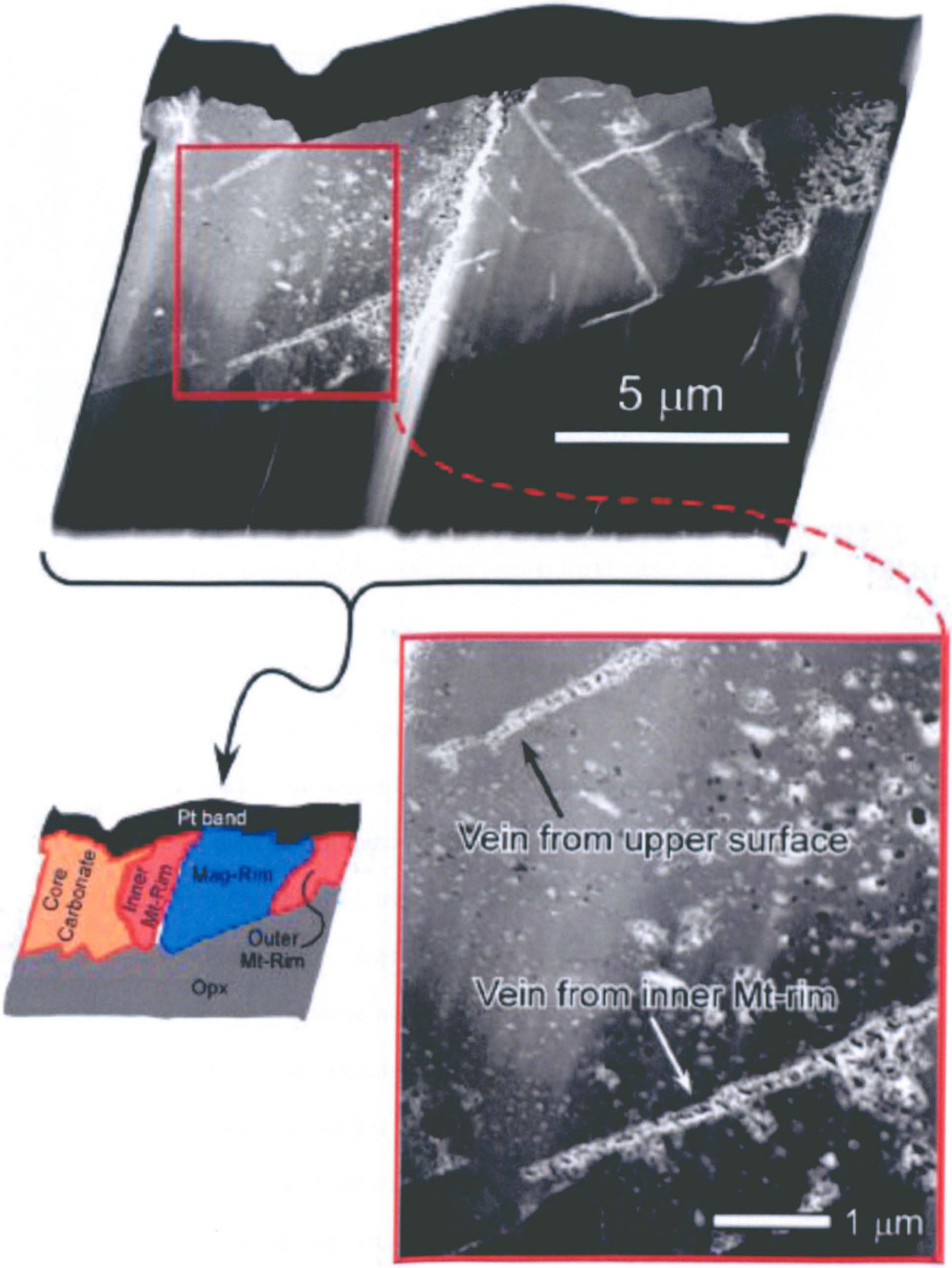

Figure 7.5 TEM image from Thomas-Keprta et al., 2009, displaying veins and grains of magnetite and recently identified graphite (Steele et al., 2012) cutting through the magnesite.

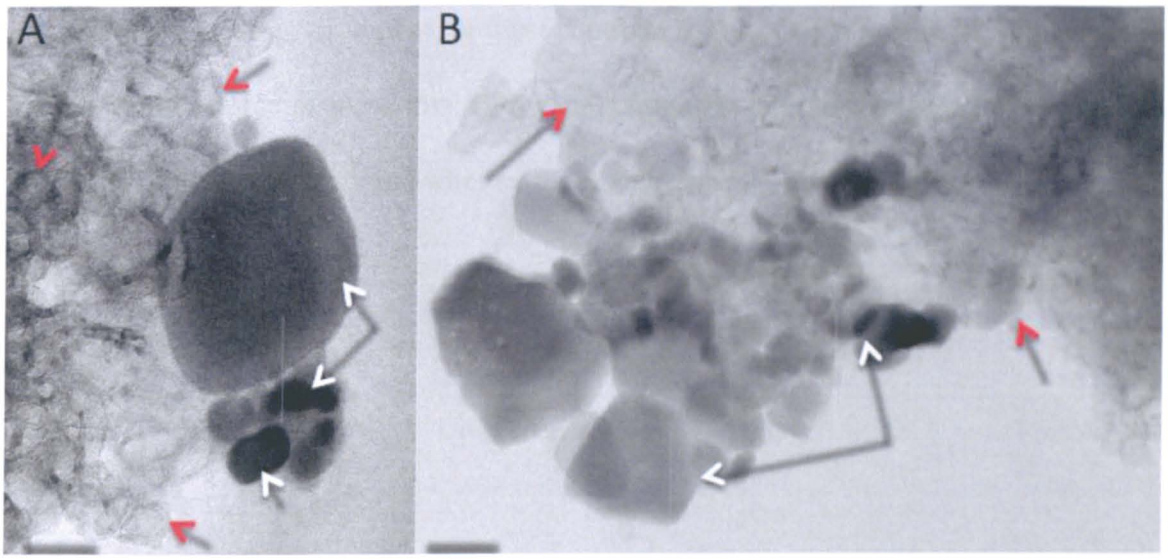

Figure 7.6 TEM image from Steele et al. (2012) of single-domain magnetite crystals (white arrows) associated with graphite spheres and filaments (red arrows) found within the outer portions of ALH 84001 carbonate globules.

The origins of this graphite can be explained by abiotic processes where (1) the graphite formed as part of the initial carbonate rosette and (2) forming from the thermal decomposition of the siderite-rich carbonate. The first mechanism of fluid-deposited graphite formation requires temperatures of at least 350°C (Luque et al., 1998, 2009; van Zuilen et al., 2003). The second mechanism requires temperatures over 600°C with the thermal decomposition of siderite producing magnetite + CO_2 + C (Treiman and Essene, 2010). A thermal heating event such as impact shock heating is thought to be consistent with the temperatures and pressures required to allow chemical equilibration on the micron-scale of the most iron-rich carbonates. While the incorporation of carbon in the form of graphite and macromolecular carbon by abiotic processes has been suggested, less clear is the mechanism by which the reduced carbon is incorporated. In addition to these arguments of an inorganic origin the carbonates themselves are believed to have formed through dissolution-

precipitation process from which the temperatures reduced to 0°C relatively rapid providing a less than hospitable environment for most common forms of organics. However, further work to deduce the source of these low $\delta^{13}C$ values found in the outer portions of the carbonates are required before determining whether these values have organic origins.

7.3 Suggested future work

7.3.1 Determining the isotopic composition of ALH 84001 rosettes with NanoSIMS (Chapter 3)

The collection of standards used for IMF corrections included fourteen carbonate standards. This quantity of carbonates should be extended to incorporate mid-ternary Ca, Fe, Mg carbonate compositions. In addition, carbonate with a large source region should be sampled as samples used in this study have been provided by ever depleting collections held at museums. While there are currently sufficient quantities obtained for this study to produce numerous standards, demands from external sources (Universities and commercial) of these standards would require larger deposits to be collected and re-characterised from their original sources. The inclusion of carbonates with large sources of material available will mean that large scale distances (m instead of cm) can be analysed and ensure samples are homogenous in both composition and stable isotopes. While the Smithsonian Institute provided microbeam standards with quantified compositions (Jarosewich and MacIntyre.1983), no isotope data were available when samples were requested despite numerous publications using these as standards. These samples had to be calibrated on a gas bench (Chapter 3.6.1), however, separate aliquots of calcite (USNM 136321) which has been used in previous studies of ALH 84001 carbonates (Leshin et al., 1998; Niles et al., 2005) produced values which varied by 4‰.

Synthesis of carbonate standards with the correct mineral composition is also a possibility. Precipitation of compositional and isotopically homogenous calcite has been achieved through the passing of carbon dioxide through water and a calcium oxide (Ghosh et al., 2006). The calcite grains produced were 40-50 μm and therefore would be suitable for

both gas bench and NanoSIMS analysis. With the addition of magnesium, iron and manganese to the calcium oxide it could be possible to produce carbonates with a composition similar to those found within the ALH 84001 carbonates.

Resolving the correct IMF corrections will aid determinations of the true isotopic composition of ALH 84001 carbonates and the sources and conditions on ancient Mars from which values derived. However, it will also have significant implications for other regions of science that use SIMS with carbonates such as environmental investigations, paleoclimatology and cosmochemistry.

7.3.2 Mineralogy and microscale carbon and oxygen isotope variability in analogue carbonates and implications for ALH 84001 carbonate formation (Chapter 4)

Carbon isotope data were not collected for the analogue carbonates because of the limited availability of NanoSIMS time for sample analyses. Oxygen data were collected relatively quickly (5 minutes per sample) however, carbon required a longer collection in order to achieve required resolution (30 minutes per analysis). Revisiting the analogue carbonate and measuring the $\delta^{13}C$ would prove beneficial for understanding the potential enrichments formed in a subsurface hydrothermal setting. In addition, while ALH 84001 is too precious to micromill (Charlier et al., 2006) a sample of the analogue carbonate could be directly analysed on the gas bench to ensure that the applied IMF corrections are accurate.

7.3.3 Computational modelling of ALH 84001 carbonate formation (Chapter 5)

To further these studies initial conditions and parameters determined by the model could be tested using other software packages. While geochemists workbench was specifically used for the application of both thermodynamic and isotopic simulations, other models which cannot simulate isotopic enrichments are capable of investigating subzero carbonate formations. Models such as CHILLER (Reed and Spycher. 2006) have been used to access the formation of alteration material within the martian nakhlites meteorites (Bridges and Schwenzer., 2012). In addition to testing the model parameters these initial values and composition of rock (ALH 84001) could be used to conduct laboratory experiments to attempt to physically reproduce these carbonates.

Experiments similar to this have already been conducted by Golden et al. (2001), however, conditions used in their formation scenario used ideal molar solutions. With the proposed model in Chapter 5, an orthopyroxenite with a similar composition to that found in ALH 84001 (potentially unaltered material from Chapter 4) could be used. This material could be fractured opening new fluid conduits and then reacted under an acidic regime with a brine solution containing an Ca^{2+} enrichment and premeasured dry CO_2 ice at high temperatures as suggested in Chapter 5 to mobilise candidate cations. Modelled conditions of cooling from 180 to 0°C with the introduction of CO_2 would then be applied. An initial brine solution could be added CP Grade Carbon dioxide 99.995% frozen and weighed as dried ice to ensure the correct ratio was added to the system. These initial components could then be place within Teflon vessels in a secured system such as a CEM Microwave Accelerated Reaction System (MARS 5). The chamber could fit 3 vessels simultaneously allowing

triplicates of each candidate solution to be run. MARS 5 is equipped with a RTP- 300 Plus fibre optical probe to measure the temperature (error ΔT = 2 K) and an ESP-1500 Plus pressure sensor both situated within a reaction vessel. Teflon should be used in favour of stainless steel owing to the leaching properties of the chloride solutions reacting with the inner walls of the reaction vessel.

These experiments would build on those made by Golden et al. (2001) as they would start with a candidate composition in whole rock form, provide sights for carbonate nucleation and attempt to also form similar relative isotope enrichments to that found in Chapter 3 and the GWB model ($\delta^{18}O$; 25‰).

7.3.4 Carbonate and Water Detection with WATSEN (Chapter 6)

An extension of the analyses conducted within this Chapter would include large samples collected from the analogue carbonate site in Svalbard which would provide a more direct comparison to ALH 84001. Alternatively while the low temperature and pressure cannot be conducted in the field (Svalbard) WatSen could be taken to this site as part of the AMASE team yearly outing.

The instrument was tested under low temperatures (-50°C), however, the temperature expected above the martian regolith at night is -80°C. By further reducing the temperature in the chamber (adding more insulation and setting up a constant supply of liquid nitrogen) the internal components and detection limits of WatSen could be tested.

An increase in the spectral range (currently 6.1-10.2 μm) would address the issues with the detection of water at low temperatures and provide additional absorption features for carbonates and phyllosilicates. This could be implemented by inserting two LVF filters side

by side, so that both spectral regions could be scanned. Such a task would require a new contract with Narsk-ElektroOptik and Navsys to refine the optical design and modify the software package. However, the resulting spectral range would provide WATSEN with the capabilities of scanning the same spectral range as the CRISM and OMEGA orbital spectrometers providing ground truth to their measurement and aiding interpretation of compositional mixtures with finescale imaging. The reflections from minerals illuminated by the LEDs can be reduced with post-processing, however, a control on the level of illumination would benefit imaging minerals with high reflectivity. An anti-reflection coating on the interior of the diamond window would also reduce reflections, but it is uncertain what effects this will have on the ATR spectrometer.

APPENDIX

Appendix A – Electron microprobe, SEM and the Finnigan Advantage Mass Spectrometer results

I. Carbonate standards

Table 1.1 Composition of carbonate standards measured on a Cameca SX 100 electron microprobe following $\delta^{13}C$ and $\delta^{18}O$ analyses. Data are reported as wt. % values.

Carbonate standards	Mg	Si	Ca	Mn	Fe	Au	O	Total
Siderite NMNH R2460	0.1	0	0	2.1	44.7	0.1	13.5	60.4
Siderite NMNH R2460	0.1	0	0	2.1	44.9	0	13.6	60.7
Siderite NMNH R2460	0.1	0	0	2.1	45	0	13.6	60.7
Siderite NMNH R2460	0.1	0	0	2.1	45	0	13.6	60.8
Dolomite NMNH 10057	13.3	0	22.2	0	0.1	0.1	17.6	53.3
Dolomite NMNH 10057	13.4	0	21.7	0	0.1	0.1	17.5	52.8
Dolomite NMNH 10057	13.3	0	22.5	0	0.1	0.1	17.8	53.7
Dolomite NMNH 10057	13.3	0	22.3	0	0.1	0	17.7	53.4
Dolomite NMNH 10057	13.4	0	22.2	0	0.1	0	17.7	53.3
Dolomite NHM 1917	12.1	0	21.8	0.4	2.8	0	17.6	54.7
Dolomite NHM 1917	12	0	21.2	0.4	2.6	0	17.2	53.4
Dolomite NHM 1917	11.6	0	21.5	0.3	2.5	0	17	52.9
Dolomite NHM 1917	11.7	0	21.5	0.4	3.1	0.1	17.3	54.1
Dolomite NHM 1917	12.1	0	21.2	0.4	2.4	0.2	17.2	53.4
Dolomite NHM 1917	11.7	0	21.4	0.5	3.1	0.1	17.3	54.1
Dolomite NHM 1917	11.8	0	21.1	0.5	2.9	0	17.2	53.5
Dolomite NHM 1917	12.3	0	21.2	0.3	2.2	0	17.3	53.3
Dolomite NHM 1917	11.8	0	21.1	0.4	2.8	0	17.1	53.3
Dolomite NHM 1917	11.8	0	21.4	0.3	2.4	0.1	17.1	53.2
Dolomite NHM 59191	12.7	0	22	0.2	1.3	0.1	17.6	53.8
Dolomite NHM 59191	11.9	0	23.3	0.1	1.2	0.1	17.5	54.1
Dolomite NHM 59191	12.6	0	22	0.1	1.3	0.1	17.5	53.7
Dolomite NHM 59191	12.6	0	21.8	0.1	1.3	0	17.5	53.4
Dolomite NHM 59191	12.3	0	22.1	0.2	1.4	0.1	17.4	53.4
Dolomite NHM 59191	11.9	0	22.2	0.1	1.3	0.1	17.2	52.9
Dolomite NHM 59191	12.4	0	21.5	0.1	1.4	0.1	17.2	52.8
Dolomite NHM 59191	11.8	0	22.9	0.1	1.3	0.1	17.3	53.6
Dolomite NHM 59191	12	0	22.2	0.1	1.4	0	17.2	52.8
Dolomite NHM 59191	11.9	0	22.8	0.1	1.2	0	17.4	53.4

Carbonate standards	Mg	Si	Ca	Mn	Fe	Au	O	Total
Dolomite Cornwall	8.1	0	0.4	1.2	34	0.1	15.6	59.4
Dolomite Cornwall	8.1	0	0.2	1.1	34.8	0.1	15.7	60
Dolomite Cornwall	7.9	0	0.2	1.4	34.2	0	15.5	59.2
Dolomite Cornwall	8.3	0	0.3	1.2	34.4	0	15.8	60.1
Dolomite Cornwall	2.6	0	0.3	3.5	40.3	0.2	14.4	61.4
Dolomite Cornwall	6.7	0	0.3	2.6	34.4	0	15.2	59.1
Dolomite Cornwall	8.1	0	0.4	1.3	34.5	0	15.8	60.1
Dolomite Cornwall	8.2	0	0.4	1.2	34.9	0	15.9	60.6
Dolomite Cornwall	8.1	0	0.4	1.2	34.2	0.1	15.6	59.6
Dolomite Cornwall	8.4	0	0.3	1.2	34.4	0	15.8	60.1
Ferroan Dolomite	7.6	0	21.7	1.9	7.8	0.2	16.5	55.7
Ferroan Dolomite	8.2	0	21.5	1.8	7.6	0	16.7	55.8
Ferroan Dolomite	7.7	0	21.3	1.7	8.5	0.1	16.5	55.9
Ferroan Dolomite	8	0	21.6	1.8	7.7	0.2	16.7	56
Ferroan Dolomite	7.3	0	21	2.1	9.8	0	16.6	56.7
Ferroan Dolomite	7.5	0	20.8	2.1	9.3	0.2	16.5	56.4
Ferroan Dolomite	8.3	0	20.6	2	8	0	16.6	55.6
Ferroan Dolomite	8.9	0	21.3	2	7.3	0.1	17	56.5
Ferroan Dolomite	7.4	0	20.6	2.4	9.2	0.1	16.5	56.2
Ferroan Dolomite	7.8	0	20.7	1.8	9.5	0	16.6	56.4
Dolomite NHM 1982	11.6	0	22	0.5	1.5	0	17	52.6
Dolomite NHM 1982	12.9	0	21.3	0.1	1.4	0.2	17.4	53.3
Dolomite NHM 1982	13.2	0	21.1	0.1	1.1	0	17.5	53
Dolomite NHM 1982	13.1	0	21	0.1	0.8	0.1	17.3	52.4
Dolomite NHM 1982	12.6	0	20.8	0.1	2.5	0	17.3	53.3
Dolomite NHM 1982	13.6	0	20.4	0	1.9	0.2	17.7	53.8
Dolomite NHM 1982	12.3	0	20.4	0.1	3.7	0.3	17.3	54.1
Dolomite NHM 1982	13.6	0	20.8	0	0.8	0	17.6	52.9
Dolomite NHM 1982	13	0	20.7	0	1.4	0	17.2	52.3
Dolomite NHM 1982	12.1	0	20.4	0.1	3.7	0.1	17.2	53.6
Ankerite NHM	2.9	0	0.5	1.8	41.2	0	14.5	60.9
Ankerite NHM	3.6	0	0.7	1.4	40.7	0.1	14.7	61.2
Ankerite NHM	3.5	0	0.6	1.4	40.8	0	14.6	60.9
Ankerite NHM	3.6	0	0.7	1.5	40.1	0	14.6	60.4
Ankerite NHM	3.1	0	0.6	1.7	41.3	0.1	14.6	61.4
Ankerite NHM	2.8	0	0.5	1.7	41.1	0	14.3	60.3
Ankerite NHM	3.2	0	0.5	1.6	41.3	0.1	14.7	61.4
Ankerite NHM	2.9	0	0.4	1.7	41.6	0.1	14.5	61.2
Ankerite NHM	2.8	0	0.3	2.3	40.9	0	14.3	60.6
Ankerite NHM	3	0	0.4	1.6	41	0	14.3	60.4
Dolomite NHM	13.1	0	22.1	0	0	0.2	17.5	53.1
Dolomite NHM	13.5	0	22.4	0	0	0.1	17.9	54
Dolomite NHM	13.4	0	22.5	0	0	0	17.8	53.8
Dolomite NHM	13.5	0	22.4	0	0	0	17.9	53.9
Dolomite NHM	13.3	0	22.2	0	0.1	0.1	17.7	53.5
Dolomite NHM	13	0	22.1	0	0	0.1	17.4	52.7
Dolomite NHM	12.7	0	22.5	0	0.3	0	17.4	52.8
Dolomite NHM	12.8	0	22.6	0	0.2	0.1	17.6	53.4
Dolomite NHM	13	0	22.5	0	0	0	17.6	53.1

Carbonate standards	Mg	Si	Ca	Mn	Fe	Au	O	Total
Dolomite NHM	13.6	0	22.2	0	0	0	17.8	53.7
Sidertie NHM	0.1	0	0	1.9	44.8	0	13.4	60.3
Sidertie NHM	0	0	0	2	45.6	0	13.7	61.3
Sidertie NHM	0.1	0	0	1.9	45.7	0	13.7	61.4
Sidertie NHM	0.1	0	0	1.9	44.5	0.2	13.4	60.1
Sidertie NHM	0.1	0	0	1.9	43.9	0	13.2	59.1
Sidertie NHM	0.1	0	0	1.9	44.5	0	13.4	59.8
Sidertie NHM	0.1	0	0	1.9	44.8	0	13.5	60.3
Sidertie NHM	0.1	0	0	1.8	45.1	0.1	13.5	60.7
Sidertie NHM	0.1	0	0	1.8	44.7	0.1	13.4	60.2
Sidertie NHM	0.1	0	0	1.8	44.8	0.1	13.4	60.3
Calcite LFC	0.1	0	38.4	0	0.5	0	15.6	54.7
Calcite LFC	0.1	0	38.3	0	0.6	0.1	15.6	54.7
Calcite LFC	0.1	0	39.3	0	0.4	0.1	15.9	55.9
Calcite LFC	0.1	0	39	0	0.3	0	15.7	55.1
Calcite LFC	0.1	0	38.4	0.1	0.5	0.1	15.6	54.7
Calcite LFC	0.1	0	38.4	0	0.6	0.3	15.6	55
Calcite LFC	0.1	0	39	0	0.5	0	15.8	55.5
Calcite LFC	0.1	0	38.8	0.1	0.5	0.1	15.7	55.3
Calcite LFC	0.1	0	38.5	0	0.6	0	15.6	54.9
Calcite LFC	0.1	0	38	0.1	0.6	0.1	15.5	54.4
Dolomite NHM 59199	12.8	0	21.1	0.2	1	0	17.2	52.4
Dolomite NHM 59199	13	0	21.2	0.3	1.1	0.1	17.4	53
Dolomite NHM 59199	13	0	20.6	0.3	1.1	0.1	17.2	52.4
Dolomite NHM 59199	13.1	0	20.9	0.3	1.2	0	17.4	52.8
Dolomite NHM 59199	13	0	20.8	0.3	1.1	0.2	17.3	52.7
Dolomite NHM 59199	12.9	0	21.1	0.3	1.2	0	17.3	52.8
Dolomite NHM 59199	12.7	0	21.1	0.2	1.1	0	17.1	52.3
Dolomite NHM 59199	12.9	0	21	0.2	1.1	0	17.2	52.4
Dolomite NHM 59199	12.5	0	20.8	0.3	1.2	0.1	17	51.7
Dolomite NHM 59199	12.5	0	20.6	0.3	1.1	0.2	16.8	51.4
Dolomite NHM 1990	7.4	0	20.6	0.4	11.5	0	16.6	56.6
Dolomite NHM 1990	7.2	0	20.9	0.4	11.4	0	16.5	56.5
Dolomite NHM 1990	6	0	20.5	0.5	13.4	0	16.2	56.6
Dolomite NHM 1990	6.2	0	20.4	0.6	13.4	0.1	16.3	56.9
Dolomite NHM 1990	6.4	0	20.3	0.6	13.3	0	16.3	57
Dolomite NHM 1990	6.2	0	21	0.6	13	0	16.4	57.1
Dolomite NHM 1990	6.2	0	20.5	0.6	13	0.1	16.1	56.4
Dolomite NHM 1990	6.5	0	20.3	0.5	12.7	0	16.2	56.2
Dolomite NHM 1990	6.4	0	20.7	0.6	12.9	0.1	16.3	57
Dolomite NHM 1990	6.1	0	20.4	0.6	13.5	0	16.2	56.7
Magnesite NHM	26.3	0	0.5	0	0	3.6	18	48.5
Magnesite NHM	28.2	0	0.5	0	0	1.6	19	49.2
Magnesite NHM	27.4	0	0.4	0	0	2.7	18.6	49.2
Magnesite NHM	26.8	0	0.5	0	0	3.7	18.3	49.2
Magnesite NHM	26.1	0	0.4	0	0	4.9	18	49.4
Magnesite NHM	27.1	0	0.5	0	0	3.3	18.4	49.3
Magnesite NHM	26.3	0	0.5	0	0	3.3	18	48.1
Magnesite NHM	27.8	0	0.5	0	0	2.2	18.8	49.5

Carbonate standards	Mg	Si	Ca	Mn	Fe	Au	O	Total
Magnesite NHM	26.6	0	0.5	0	0	4.3	18.3	49.7
Magnesite NHM	27.7	0	0.5	0	0	2.4	18.7	49.3
Dolomite NHM 1924	26.9	0	4.5	0	0.1	0.1	19.6	51.2
Dolomite NHM 1924	29.1	0	0.8	0	0.1	0.3	19.6	50
Dolomite NHM 1924	13.7	0	22.8	0	0.1	0	18.2	54.9
Dolomite NHM 1924	13.7	0	22.3	0	0	0.1	17.9	54.1
Dolomite NHM 1924	29.5	0	1.2	0	0.1	0	19.9	50.6
Dolomite NHM 1924	30	0	0.2	0	0.1	0	19.9	50.3
Dolomite NHM 1924	30.2	0	0.2	0	0.1	0.1	20	50.6
Dolomite NHM 1924	13.4	0	22.2	0	0	0.1	17.7	53.3
Dolomite NHM 1924	30.1	0	0.1	0	0.1	0.1	19.9	50.3
Dolomite NHM 1924	30	0	0.3	0	0.1	0	19.9	50.5
Magnesite NHM	29.1	0	0.5	0	0	0.1	19.4	49.1
Magnesite NHM	29.4	0	0.5	0	0	0.1	19.6	49.6
Magnesite NHM	29.4	0	0.4	0	0	0	19.5	49.4
Magnesite NHM	28.7	0	0.5	0	0	0	19.1	48.3
Magnesite NHM	27.9	0	0.5	0	0	0.5	18.7	47.7
Magnesite NHM	28.3	0	0.5	0	0	0	18.8	47.6
Magnesite NHM	28.6	0	0.4	0	0	0	19	48.1
Magnesite NHM	28.8	0	0.4	0	0	0	19.1	48.3
Magnesite NHM	29.5	0	0.5	0	0	0	19.7	49.8
Magnesite NHM	29.5	0	0.4	0	0	0.1	19.6	49.7
Magnesite BM 59199	12.5	0.0	20.9	0.3	1.2	0.0	17.0	52.0
Magnesite BM 59199	12.6	0.0	21.0	0.3	1.2	0.0	17.1	52.1
Magnesite BM 59199	12.6	0.0	21.4	0.3	1.1	0.1	17.3	52.8
Magnesite BM 59199	12.6	0.0	20.8	0.3	1.2	0.1	17.0	51.9
Magnesite BM 59199	12.5	0.0	20.7	0.2	1.2	0.3	17.0	51.9
Magnesite BM 59199	12.7	0.0	21.0	0.2	1.1	0.0	17.1	52.2
Magnesite BM 59199	12.6	0.0	20.8	0.3	1.3	0.0	17.0	52.0
Magnesite BM 59199	12.8	0.0	20.9	0.3	1.1	0.1	17.2	52.4
Magnesite BM 59199	12.6	0.0	20.9	0.3	1.2	0.1	17.1	52.2
Magnesite BM 59199	12.5	0.0	20.9	0.2	1.1	0.0	17.0	51.8

II. ALH 84001 carbonates

Table 1.2 Composition of ALH 84001 carbonates measured on a Cameca SX 100 electron microprobe following $\delta^{13}C$ analyses. Data are reported as wt. % oxide values.

ALH 84001 carbonates	SiO_2	Au_2O_3	MgO	CaO	MnO	FeO	Total
Rosette (1) 1	0.02	0.64	12.52	8.04	1.88	25.75	48.85
Rosette (1) 2	0.14	2.64	22.73	7.87	1.20	24.46	59.02
Rosette (1) 3	0.14	0.66	25.09	7.16	0.60	24.59	58.24
Rosette (1) 4	0.33	1.73	24.38	7.80	0.79	24.17	59.20
Rosette (1) 5	0.31	14.27	18.26	7.50	1.08	21.84	63.25
Rosette (1) 6	1.74	9.09	18.67	7.12	1.58	23.07	61.27
Rosette (1) 7	0.12	0.40	18.36	7.56	1.16	25.25	52.85
Rosette (1) 8	0.10	0.00	21.22	7.12	0.69	25.33	54.45
Rosette (1) 9	0.04	3.98	15.97	8.96	2.31	23.25	54.50
Rosette (1) 10	0.06	1.01	9.14	8.13	2.03	24.93	45.29
Rosette (1) 11	0.12	0.04	22.65	8.62	2.44	25.29	59.16
Rosette (1) 12	0.08	0.21	20.89	8.08	1.44	25.95	56.66
Rosette (1) 13	0.05	0.23	17.34	6.79	0.68	24.38	49.48
Rosette (1) 14	0.29	0.31	27.65	4.52	0.25	23.23	56.25
Rosette (1) 15	1.55	2.82	24.66	2.00	0.27	15.33	46.63
Rosette (1) 16	0.31	10.52	25.84	3.56	0.45	10.85	51.52
Rosette (2) 17	1.23	10.41	33.68	1.72	0.22	16.55	63.82
Rosette (2) 18	0.52	3.08	26.31	5.04	0.20	21.89	57.03
Rosette (2) 19	0.26	5.32	25.19	5.67	0.41	21.32	58.17
Rosette (2) 20	0.22	0.83	28.25	6.08	0.51	22.73	58.62
Rosette (2) 21	0.53	47.71	8.37	2.26	0.14	16.35	75.36
Rosette (2) 22	0.16	1.50	27.94	5.73	0.22	23.27	58.81
Rosette (2) 23	0.17	16.32	15.61	5.74	0.42	19.35	57.60
Rosette (2) 24	0.13	2.35	20.02	6.35	0.57	23.36	52.77

Table 1.3 Composition of ALH 84001 carbonates measured on a Cameca SX 100 electron microprobe following $\delta^{18}O$ analyses. Data are reported as wt. % oxide values.

ALH 84001 carbonates	SiO_2	Au_2O_3	MgO	CaO	MnO	FeO	Total
Rosette (1) 1	0.09	0.44	21.86	7.73	0.82	25.07	56.01
Rosette (1) 2	0.23	0.81	18.95	7.96	1.55	26.13	55.63
Rosette (1) 3	0.58	7.84	16.65	7.27	2.38	26.40	61.12
Rosette (1) 4	0.35	20.14	9.34	6.37	1.53	19.25	56.99
Rosette (1) 5	0.30	4.60	15.73	7.64	1.61	24.83	54.71
Rosette (1) 6	0.28	1.78	19.98	7.88	1.27	25.71	56.90
Rosette (1) 7	0.27	7.47	15.96	7.92	1.09	23.52	56.22
Rosette (1) 8	0.21	0.77	20.47	8.74	2.52	25.38	58.08
Rosette (1) 9	0.15	0.35	21.07	8.71	2.46	25.56	58.28
Rosette (1) 10	0.09	0.14	20.40	8.34	2.53	25.45	56.94
Rosette (1) 11	0.11	0.23	21.32	8.56	1.76	25.66	57.64
Rosette (1) 12	0.20	0.88	25.96	7.15	0.63	24.39	59.21
Rosette (1) 13	0.22	0.35	26.85	6.21	0.53	23.81	57.96
Rosette (1) 14	0.56	8.71	37.32	3.72	0.43	9.71	60.45
Rosette (1) 15	0.66	0.66	47.14	2.33	0.18	6.86	57.83
Rosette (2) 16	0.67	4.52	32.81	2.43	0.22	18.86	59.51
Rosette (2) 17	0.31	0.04	15.59	4.98	0.51	23.09	44.51
Rosette (2) 18	0.33	0.84	26.71	6.91	0.59	24.01	59.39
Rosette (2) 19	0.22	3.25	21.97	6.77	0.62	23.98	56.81
Rosette (2) 20	0.21	2.09	20.91	7.00	0.72	24.84	55.77
Rosette (2) 21	0.37	0.19	21.16	5.26	0.29	23.15	50.42
Rosette (2) 22	0.29	0.22	30.55	4.55	0.21	22.77	58.58
Rosette (2) 23	0.66	1.08	34.79	2.15	0.21	19.87	58.76
Rosette (2) 24	0.66	0.73	33.12	2.43	0.21	19.09	56.25

III. Analogue carbonates

Table 1.4 WDS compositions of analogue carbonates (AC) carbonates measured on a dual beam FEI Quanta 200 3D SEM following $\delta^{18}O$ analyses. Data are reported as wt. % normalised values.

Analogue carbonates	C	Mg	Si	Ca	Mn	Fe	Ni	Ga	O	Total
AC 1, spot 1	19.6	2.4	2.5	2.2	0.3	12.1			61.0	100
AC 1, spot 2	19.6	2.6	3.3	2.1	0.2	10.7			61.6	100
AC 1, spot 3	19.4	2.6	2.3	2.2	0.2	12.9			60.5	100
AC 1, spot 4	19.5	5.1	2.4	1.5	0.2	9.8			61.5	100
AC 1, spot 5	17.8	4.5	3.4	2.1	0.2	13.0			59.0	100
AC 1, spot 6	19.9	6.7	1.8	1.3		7.9	0.1		62.3	100
AC 1, spot 7	19.5	6.4	1.9	1.8	0.1	8.2	0.1	0.3	61.6	100
AC 1, spot 8	19.5	6.4	1.9	1.7		8.5	0.1	0.3	61.6	100
AC 1, spot 9	19.6	6.3	1.8	1.6	0.1	8.4	0.1	0.3	61.7	100
AC 1, spot 10	19.4	5.9	1.9	1.7	0.2	9.2	0.1	0.3	61.3	100
AC 1, spot 11	19.9	6.1	1.7	1.6	0.1	8.2		0.3	62.1	100
AC 1, spot 12	19.8	6.4	1.8	1.6		7.8	0.2	0.3	62.1	100
AC 1, spot 13	19.1	4.9	2.4	1.6	0.2	11.1	0.2		60.7	100
AC 1, spot 14	18.7	4.4	2.6	1.7	0.2	12.3	0.2		60.0	100
AC 2, spot 1	20.1	2.3	2.1	1.9	0.2	11.8			61.7	100
AC 2, spot 2	19.5	4.7	3.4	1.5	0.1	8.7	0.1		62.0	100
AC 2, spot 3	20.3	5.5	2.0	1.5	0.1	7.5	0.1		62.9	100
AC 2, spot 4	19.4	5.7	2.3	1.7	0.1	9.2	0.2		61.5	100
AC 2, spot 5	20.1	5.8	1.9	1.6		8.1	0.1		62.4	100
AC 2, spot 6	20.1	5.4	1.9	1.6		8.6	0.1		62.3	100
AC 2, spot 7	20.2	6.9	1.7	1.5		6.7	0.2		62.9	100
AC 2, spot 8	19.4	4.6	2.2	1.7	0.2	10.9	0.2		61.0	100
AC 3, spot 1	21.0	3.7	2.0	1.3	0.1	8.3	0.1		63.6	100
AC 3, spot 2	21.1	5.1	1.7	1.2	0.1	6.7	0.1		64.0	100
AC 3, spot 3	20.9	4.8	1.7	1.3	0.1	7.5	0.1		63.5	100
AC 3, spot 4	20.6	5.4	1.8	1.4	0.1	7.4	0.1		63.2	100
AC 3, spot 5	20.5	5.2	1.8	1.5	0.1	7.9	0.1		62.9	100
AC 3, spot 6	20.5	5.6	1.8	1.5	0.1	7.4	0.1		63.1	100
AC 3, spot 7	20.4	5.6	1.8	1.5	0.1	7.5	0.1		63.0	100
AC 3, spot 8	20.2	5.6	2.0	1.6	0.1	7.9			62.6	100
AC 3, spot 9	20.1	5.6	2.0	1.6		8.1			62.6	100
AC 3, spot 10	20.3	5.6	2.0	1.5	0.1	7.5	0.1		62.9	100
AC 3, spot 11	20.2	5.7	2.2	1.5		7.5			62.9	100
AC 3, spot 12	19.0	2.3	3.2	1.5	0.2	13.6			60.2	100

IV. Carbonate standards

Table 1.5 True isotopic values derived from the Finnigan Advantage Mass Spectrometer (FAMS).

Carbonate standards	δ13C vpdb	Error	δ18O vsmow	Error	δ18O vpdb	Error
Ankerite NHM	-8.39	0.06	16.63	0.12	-13.85	0.12
Ankerite NHM	-8.36	0.01	16.53	0.03	-13.95	0.03
Ankerite NHM	-8.42	0.02	16.58	0.04	-13.90	0.04
Ankerite NHM	-8.41	0.03	16.56	0.05	-13.92	0.05
Ankerite NHM	-8.52	0.03	16.35	0.03	-14.12	0.03
Calcite NHM	-12.01	0.03	15.41	0.03	-15.03	0.03
Calcite NHM	-12.07	0.02	15.43	0.04	-15.02	0.04
Calcite NHM	-12.07	0.04	15.57	0.03	-14.87	0.03
Calcite NHM	-12.11	0.02	15.44	0.04	-15.01	0.04
Calcite NHM	-12.03	0.06	15.45	0.05	-14.99	0.05
Dolomite NHM	1.97	0.04	25.12	0.04	-5.61	0.04
Dolomite NHM	2.01	0.02	25.13	0.08	-5.60	0.08
Dolomite NHM	2.10	0.02	25.32	0.02	-5.42	0.02
Dolomite NHM	2.05	0.03	25.34	0.05	-5.40	0.05
Dolomite NHM	2.08	0.11	25.08	0.11	-5.65	0.11
Dolomite NHM	1.70	0.06	24.58	0.05	-6.13	0.05
Magnesite NHM	-12.62	0.02	23.35	0.04	-7.33	0.04
Magnesite NHM	-12.68	0.04	23.46	0.07	-7.23	0.07
Magnesite NHM	-12.47	0.13	23.50	0.12	-7.18	0.12
Sidertie NHM	-7.92	0.02	7.81	0.06	-22.40	0.06
Sidertie NHM	-7.87	0.06	7.93	0.12	-22.29	0.12
Sidertie NHM	-7.88	0.03	8.04	0.03	-22.18	0.03
Sidertie NHM	-7.80	0.03	8.14	0.03	-22.08	0.03
Sidertie NHM	-7.72	0.11	8.23	0.12	-21.99	0.12
Sidertie NHM	-7.96	0.03	7.74	0.07	-22.47	0.07
Dolomite NHM 59191	5.17	0.07	21.18	0.07	-9.43	0.07
Dolomite NHM 59191	5.23	0.13	20.96	0.04	-9.64	0.04
Dolomite NHM 59191	4.97	0.08	21.01	0.05	-9.60	0.05
Dolomite NHM 1924	2.74	0.06	28.09	0.10	-2.73	0.10
Dolomite NHM 1924	2.75	0.04	28.60	0.28	-2.24	0.28
Dolomite NHM 1924	2.69	0.02	28.37	0.04	-2.47	0.04
Dolomite 1917	-3.51	0.04	12.19	0.02	-18.15	0.02
Dolomite 1917	-3.42	0.07	12.40	0.02	-17.95	0.02
Dolomite 1917	-3.95	0.01	12.38	0.05	-17.97	0.05
Dolomite 1917	-3.78	0.06	12.38	0.03	-17.97	0.03
Dolomite BM 1982	0.2	0.06	20.04	0.15	-10.54	0.15
Dolomite BM 1982	0.26	0.03	19.89	0.06	-10.69	0.06
Dolomite BM 1982	-0.12	0.02	20	0.08	-10.58	0.08
Magnesite BM59199	-5.4	0.04	8.67	0.11	-21.57	0.11
Magnesite BM59199	-5.37	0.04	8.55	0.1	-21.68	0.1
Magnesite BM59199	-5.22	0.07	9.25	0.23	-21	0.23
Dolomite NHM 1990	-10.42	0.04	16.84	0.06	-13.64	0.06
Dolomite NHM 1990	-10.68	0.02	17.9	0.07	-12.62	0.07
Dolomite NHM 1990	-9.04	3.86	16.29	5.73	-14.18	5.73

Ferroan Dolomite	-0.52	0.02	21.18	0.03	-9.43	0.03
Ferroan Dolomite	-0.82	0.07	21.91	0.11	-8.73	0.11
Dolomite Cornwall	-12.56	0.07	18.28	0.21	-12.25	0.21
Dolomite Cornwall	-11.57	0.01	19.18	0.07	-11.38	0.07
Dolomite Cornwall	-11.45	0.04	19.24	0.12	-11.32	0.12
Siderite NMNH R2460	-8.02	0.12	8.1	0.08	-22.13	0.08
Siderite NMNH R2460	-7.96	0.11	7.83	0.11	-22.38	0.11
Dolomite NMNH 10057	-0.51	0.029772	12.35541	0.090471	-18.00	0.090471

Appendix B – NanoSIMS data and IMF corrections

I. Carbonate standards

Table 2.1 $^{18}O^-$ and $^{16}O^-$ values of spot analyses (5x5 μm^2) across carbonate standards.

Carbonate standards	^{16}O Counts	^{16}O Rate	^{18}O Counts	^{18}O Rate	$^{18}O/^{16}O$ Ratio	$^{18}O/^{16}O$ Err Mean	$^{18}O/^{16}O$ Poisson
Siderite NHM	6.4E+09	3.1E+07	1.3E+07	6.4E+04	2.0E-03	2.7E-02	2.8E-02
Siderite NHM	6.6E+09	3.2E+07	1.4E+07	6.6E+04	2.1E-03	2.9E-02	2.7E-02
Siderite NHM	6.7E+09	3.3E+07	1.4E+07	6.8E+04	2.0E-03	2.5E-02	2.7E-02
Siderite NHM	6.6E+09	3.2E+07	1.4E+07	6.6E+04	2.0E-03	2.7E-02	2.7E-02
Siderite NHM	6.7E+09	3.2E+07	1.4E+07	6.7E+04	2.0E-03	2.9E-02	2.7E-02
Ankerite NHM	6.8E+09	3.3E+07	1.4E+07	6.8E+04	2.1E-03	2.8E-02	2.7E-02
Ankerite NHM	6.8E+09	3.3E+07	1.4E+07	6.8E+04	2.1E-03	2.7E-02	2.7E-02
Ankerite NHM	6.9E+09	3.3E+07	1.4E+07	6.9E+04	2.0E-03	2.5E-02	2.7E-02
Ankerite NHM	3.6E+09	1.8E+07	7.4E+06	3.6E+04	2.0E-03	4.4E-02	3.7E-02
Ankerite NHM	4.7E+09	2.3E+07	9.8E+06	4.8E+04	2.1E-03	3.5E-02	3.2E-02
Ankerite NHM	6.8E+09	3.3E+07	1.4E+07	6.8E+04	2.1E-03	2.8E-02	2.7E-02
Dolomite Cornwall	7.6E+09	3.7E+07	1.6E+07	7.6E+04	2.1E-03	2.7E-02	2.5E-02
Dolomite Cornwall	7.6E+09	3.7E+07	1.6E+07	7.6E+04	2.1E-03	2.7E-02	2.5E-02
Dolomite Cornwall	7.5E+09	3.7E+07	1.5E+07	7.6E+04	2.1E-03	2.8E-02	2.5E-02
Dolomite Cornwall	7.7E+09	3.8E+07	1.6E+07	7.7E+04	2.0E-03	2.6E-02	2.5E-02
Dolomite Cornwall	8.1E+09	4.0E+07	1.7E+07	8.1E+04	2.1E-03	2.5E-02	2.5E-02
Dolomite Cornwall	7.6E+09	3.7E+07	1.6E+07	7.6E+04	2.1E-03	2.5E-02	2.5E-02
Siderite NHM	3.3E+09	2.0E+07	6.8E+06	4.2E+04	2.1E-03	3.8E-02	3.8E-02
Siderite NHM	3.6E+09	2.2E+07	7.5E+06	4.6E+04	2.0E-03	3.6E-02	3.7E-02
Siderite NHM	4.1E+09	2.5E+07	8.4E+06	5.1E+04	2.0E-03	3.4E-02	3.5E-02
Siderite NHM	4.7E+09	2.8E+07	9.5E+06	5.8E+04	2.0E-03	3.2E-02	3.2E-02
Siderite NHM	4.6E+09	2.8E+07	9.5E+06	5.8E+04	2.0E-03	3.5E-02	3.2E-02
Siderite NMNH R2460	4.3E+09	2.6E+07	8.7E+06	5.3E+04	2.0E-03	3.2E-02	3.4E-02
Siderite NMNH R2460	4.3E+09	2.6E+07	8.8E+06	5.4E+04	2.0E-03	3.1E-02	3.4E-02
Siderite NMNH R2460	3.9E+09	2.4E+07	7.9E+06	4.8E+04	2.0E-03	3.7E-02	3.6E-02
Siderite NMNH R2460	4.0E+09	2.4E+07	8.1E+06	4.9E+04	2.0E-03	3.6E-02	3.5E-02
Siderite NMNH R2460	4.0E+09	2.4E+07	8.1E+06	4.9E+04	2.0E-03	3.6E-02	3.5E-02
Siderite NMNH R2460	5.0E+09	3.0E+07	9.9E+06	6.1E+04	2.0E-03	3.5E-02	3.2E-02
Siderite NMNH R2460	5.0E+09	3.1E+07	1.0E+07	6.2E+04	2.0E-03	3.2E-02	3.2E-02
Siderite NMNH R2460	5.1E+09	3.1E+07	1.0E+07	6.2E+04	2.0E-03	3.1E-02	3.1E-02
Siderite NMNH R2460	5.1E+09	3.1E+07	1.0E+07	6.3E+04	2.0E-03	3.2E-02	3.1E-02
Siderite NMNH R2460	5.0E+09	3.0E+07	1.0E+07	6.1E+04	2.0E-03	3.2E-02	3.2E-02
Calcite LFC	5.2E+09	1.7E+07	1.1E+07	3.5E+04	2.1E-03	2.9E-02	3.1E-02
Calcite LFC	5.2E+09	1.7E+07	1.1E+07	3.5E+04	2.1E-03	3.0E-02	3.1E-02
Calcite LFC	5.1E+09	1.7E+07	1.1E+07	3.4E+04	2.1E-03	3.2E-02	3.1E-02
Calcite LFC	4.9E+09	1.6E+07	1.0E+07	3.3E+04	2.1E-03	3.0E-02	3.2E-02

Carbonate standards	^{16}O Counts	^{16}O Rate	^{18}O Counts	^{18}O Rate	$^{18}O/^{16}O$ Ratio	$^{18}O/^{16}O$ Err Mean	$^{18}O/^{16}O$ Poisson
Calcite LFC	4.8E+09	1.6E+07	1.0E+07	3.3E+04	2.1E-03	3.0E-02	3.2E-02
Dolomite NHM	4.8E+09	1.5E+07	9.9E+06	3.2E+04	2.1E-03	3.3E-02	3.2E-02
Dolomite NHM	4.8E+09	1.6E+07	1.0E+07	3.3E+04	2.1E-03	3.1E-02	3.2E-02
Dolomite NHM	4.7E+09	1.5E+07	9.7E+06	3.2E+04	2.1E-03	3.3E-02	3.2E-02
Dolomite NHM	4.7E+09	1.5E+07	9.7E+06	3.2E+04	2.1E-03	3.1E-02	3.2E-02
Dolomite NHM	4.8E+09	1.6E+07	1.0E+07	3.3E+04	2.1E-03	3.1E-02	3.2E-02
Magnesite NHM	4.1E+09	1.3E+07	8.5E+06	2.8E+04	2.0E-03	3.6E-02	3.4E-02
Magnesite NHM	4.0E+09	1.3E+07	8.3E+06	2.7E+04	2.0E-03	3.7E-02	3.5E-02
Magnesite NHM	4.0E+09	1.3E+07	8.2E+06	2.7E+04	2.0E-03	3.5E-02	3.5E-02
Magnesite NHM	4.0E+09	1.3E+07	8.2E+06	2.7E+04	2.0E-03	3.4E-02	3.5E-02
Magnesite NHM	4.0E+09	1.3E+07	8.2E+06	2.7E+04	2.0E-03	3.3E-02	3.5E-02
Dolomite NMNH 10057	5.7E+09	1.8E+07	1.2E+07	3.8E+04	2.0E-03	3.0E-02	2.9E-02
Dolomite NMNH 10057	5.6E+09	1.8E+07	1.2E+07	3.8E+04	2.0E-03	3.1E-02	2.9E-02
Dolomite NMNH 10057	5.6E+09	1.8E+07	1.1E+07	3.7E+04	2.0E-03	3.1E-02	3.0E-02
Dolomite NMNH 10057	5.4E+09	1.8E+07	1.1E+07	3.6E+04	2.0E-03	3.2E-02	3.0E-02
Dolomite NMNH 10057	5.6E+09	1.8E+07	1.1E+07	3.7E+04	2.0E-03	3.0E-02	3.0E-02
Magnesite NHM 59199	4.4E+09	1.4E+07	9.0E+06	2.9E+04	2.1E-03	3.5E-02	3.3E-02
Magnesite NHM 59199	4.4E+09	1.4E+07	9.0E+06	2.9E+04	2.1E-03	3.5E-02	3.3E-02
Magnesite NHM 59199	4.3E+09	1.4E+07	8.8E+06	2.9E+04	2.1E-03	3.4E-02	3.4E-02
Magnesite NHM 59199	4.2E+09	1.4E+07	8.7E+06	2.8E+04	2.1E-03	3.1E-02	3.4E-02
Magnesite NHM 59199	4.2E+09	1.4E+07	8.5E+06	2.8E+04	2.1E-03	3.5E-02	3.4E-02
Dolomite NHM	4.9E+09	1.6E+07	1.0E+07	3.3E+04	2.1E-03	3.1E-02	3.2E-02
Dolomite NHM	5.3E+09	1.7E+07	1.1E+07	3.6E+04	2.1E-03	3.0E-02	3.0E-02
Dolomite NHM	5.3E+09	1.7E+07	1.1E+07	3.6E+04	2.1E-03	3.0E-02	3.0E-02
Dolomite NHM	5.3E+09	1.7E+07	1.1E+07	3.6E+04	2.1E-03	3.2E-02	3.0E-02
Dolomite NHM	5.2E+09	1.7E+07	1.1E+07	3.5E+04	2.1E-03	3.2E-02	3.1E-02
Magnesite NHM 59199	4.7E+09	1.5E+07	9.7E+06	3.2E+04	2.0E-03	3.3E-02	3.2E-02
Magnesite NHM 59199	4.8E+09	1.6E+07	9.9E+06	3.2E+04	2.0E-03	2.9E-02	3.2E-02
Magnesite NHM 59199	4.7E+09	1.5E+07	9.7E+06	3.1E+04	2.0E-03	3.2E-02	3.2E-02
Magnesite NHM 59199	4.7E+09	1.5E+07	9.7E+06	3.1E+04	2.0E-03	3.3E-02	3.2E-02
Magnesite NHM 59199	4.7E+09	1.5E+07	9.7E+06	3.2E+04	2.0E-03	3.4E-02	3.2E-02
Dolomite NHM 59191	5.7E+09	1.8E+07	1.2E+07	3.8E+04	2.1E-03	3.0E-02	2.9E-02
Dolomite NHM 59191	5.6E+09	1.8E+07	1.2E+07	3.8E+04	2.1E-03	3.0E-02	2.9E-02
Dolomite NHM 59191	5.6E+09	1.8E+07	1.2E+07	3.7E+04	2.1E-03	3.2E-02	3.0E-02
Dolomite NHM 59191	5.5E+09	1.8E+07	1.1E+07	3.7E+04	2.1E-03	2.9E-02	3.0E-02
Dolomite NHM 59191	5.2E+09	1.7E+07	1.1E+07	3.5E+04	2.1E-03	3.0E-02	3.1E-02
Dolomite NHM 1982	5.5E+09	1.8E+07	1.1E+07	3.7E+04	2.1E-03	2.8E-02	3.0E-02
Dolomite NHM 1982	5.5E+09	1.8E+07	1.1E+07	3.7E+04	2.1E-03	3.0E-02	3.0E-02
Dolomite NHM 1982	5.4E+09	1.8E+07	1.1E+07	3.6E+04	2.1E-03	3.1E-02	3.0E-02
Dolomite NHM 1982	5.5E+09	1.8E+07	1.1E+07	3.7E+04	2.1E-03	3.0E-02	3.0E-02
Dolomite NHM 1982	5.5E+09	1.8E+07	1.1E+07	3.7E+04	2.1E-03	3.0E-02	3.0E-02
Dolomite NHM 1990	4.4E+09	1.4E+07	9.2E+06	3.0E+04	2.1E-03	3.5E-02	3.3E-02
Dolomite NHM 1990	4.5E+09	1.5E+07	9.3E+06	3.0E+04	2.1E-03	3.3E-02	3.3E-02
Dolomite NHM 1990	4.3E+09	1.4E+07	9.0E+06	2.9E+04	2.1E-03	3.5E-02	3.3E-02

Carbonate standards	^{16}O Counts	^{16}O Rate	^{18}O Counts	^{18}O Rate	$^{18}O/^{16}O$ Ratio	$^{18}O/^{16}O$ Err Mean	$^{18}O/^{16}O$ Poisson
Dolomite NHM 1990	4.4E+09	1.4E+07	9.2E+06	3.0E+04	2.1E-03	3.3E-02	3.3E-02
Dolomite NHM 1990	4.4E+09	1.4E+07	9.1E+06	3.0E+04	2.1E-03	3.3E-02	3.3E-02
Ferroan Dolomite	5.7E+09	1.9E+07	1.2E+07	3.9E+04	2.1E-03	3.0E-02	2.9E-02
Ferroan Dolomite	5.8E+09	1.9E+07	1.2E+07	3.9E+04	2.1E-03	2.7E-02	2.9E-02
Ferroan Dolomite	5.8E+09	1.9E+07	1.2E+07	4.0E+04	2.1E-03	3.4E-02	2.9E-02
Ferroan Dolomite	5.8E+09	1.9E+07	1.2E+07	4.0E+04	2.1E-03	2.9E-02	2.9E-02
Ferroan Dolomite	5.7E+09	1.9E+07	1.2E+07	3.9E+04	2.1E-03	2.9E-02	2.9E-02
Dolomite 1917	5.6E+09	1.8E+07	1.1E+07	3.7E+04	2.1E-03	3.0E-02	3.0E-02
Dolomite 1917	5.4E+09	1.8E+07	1.1E+07	3.6E+04	2.1E-03	3.2E-02	3.0E-02
Dolomite 1917	5.4E+09	1.7E+07	1.1E+07	3.6E+04	2.1E-03	3.2E-02	3.0E-02
Dolomite 1917	5.3E+09	1.7E+07	1.1E+07	3.5E+04	2.1E-03	3.1E-02	3.0E-02
Dolomite 1917	5.2E+09	1.7E+07	1.1E+07	3.5E+04	2.1E-03	3.2E-02	3.0E-02
Sidertie NHM	1.7E+09	1.7E+07	3.5E+06	3.4E+04	2.0E-03	5.4E-02	5.4E-02
Sidertie NHM	1.7E+09	1.6E+07	3.4E+06	3.4E+04	2.0E-03	4.9E-02	5.4E-02
Sidertie NHM	1.7E+09	1.6E+07	3.4E+06	3.3E+04	2.0E-03	5.4E-02	5.4E-02
Sidertie NHM	1.7E+09	1.7E+07	3.5E+06	3.4E+04	2.0E-03	5.6E-02	5.4E-02
Sidertie NHM	1.7E+09	1.6E+07	3.4E+06	3.4E+04	2.0E-03	5.7E-02	5.4E-02
Sidertie NHM	1.6E+09	1.6E+07	3.3E+06	3.2E+04	2.0E-03	6.0E-02	5.5E-02
Ankerite NHM	1.8E+09	1.7E+07	3.7E+06	3.6E+04	2.1E-03	5.0E-02	5.2E-02
Ankerite NHM	1.8E+09	1.8E+07	3.7E+06	3.6E+04	2.1E-03	5.6E-02	5.2E-02
Ankerite NHM	1.8E+09	1.8E+07	3.7E+06	3.6E+04	2.1E-03	5.1E-02	5.2E-02
Ankerite NHM	1.8E+09	1.7E+07	3.7E+06	3.6E+04	2.1E-03	5.5E-02	5.2E-02
Ankerite NHM	1.8E+09	1.7E+07	3.6E+06	3.6E+04	2.1E-03	5.7E-02	5.2E-02
Dolomite Cornwall	1.6E+09	1.6E+07	3.3E+06	3.2E+04	2.1E-03	5.8E-02	5.5E-02
Dolomite Cornwall	1.5E+09	1.5E+07	3.1E+06	3.1E+04	2.0E-03	5.7E-02	5.7E-02
Dolomite Cornwall	1.5E+09	1.5E+07	3.1E+06	3.1E+04	2.0E-03	5.8E-02	5.7E-02
Dolomite Cornwall	1.6E+09	1.5E+07	3.2E+06	3.1E+04	2.1E-03	5.5E-02	5.6E-02
Dolomite Cornwall	1.6E+09	1.5E+07	3.2E+06	3.1E+04	2.1E-03	5.3E-02	5.6E-02
Magnesite NHM	6.7E+08	6.5E+06	1.4E+06	1.3E+04	2.1E-03	8.0E-02	8.5E-02
Magnesite NHM	6.7E+08	6.6E+06	1.4E+06	1.3E+04	2.0E-03	8.3E-02	8.5E-02
Magnesite NHM	6.6E+08	6.5E+06	1.4E+06	1.3E+04	2.1E-03	8.6E-02	8.6E-02
Magnesite NHM	6.6E+08	6.5E+06	1.4E+06	1.3E+04	2.0E-03	8.7E-02	8.6E-02
Magnesite NHM	6.8E+08	6.6E+06	1.4E+06	1.4E+04	2.1E-03	8.6E-02	8.5E-02

Table 2.2 $^{13}C^-$ and $^{12}C^-$ values of spot analyses (5x5 μm^2) across carbonate standards.

Carbonate standards	$^{12}C_{Counts}$	$^{12}C_{Rate}$	$^{13}C_{Counts}$	$^{13}C_{Rate}$	$^{13}C/^{12}C$ Ratio	$^{13}C/^{12}C$ Err Mean	$^{13}C/^{12}C$ Poisson
Dolomite Cornwall	1.6E+08	1.0E+05	1.6E+06	1.1E+03	1.0E-02	7.8E-02	7.9E-02
Dolomite Cornwall	1.6E+08	1.0E+05	1.7E+06	1.1E+03	1.0E-02	7.4E-02	7.8E-02
Dolomite Cornwall	1.6E+08	1.0E+05	1.7E+06	1.1E+03	1.0E-02	7.4E-02	7.8E-02
Dolomite Cornwall	1.6E+08	1.0E+05	1.7E+06	1.1E+03	1.0E-02	6.9E-02	7.8E-02
Dolomite Cornwall	1.5E+08	1.0E+05	1.6E+06	1.1E+03	1.0E-02	8.1E-02	7.9E-02
Edinburgh LFC	1.1E+08	8.2E+04	1.2E+06	8.9E+02	1.1E-02	8.6E-02	9.1E-02
Edinburgh LFC	1.1E+08	8.2E+04	1.2E+06	8.9E+02	1.1E-02	9.1E-02	9.1E-02
Edinburgh LFC	1.1E+08	8.3E+04	1.2E+06	8.9E+02	1.1E-02	9.6E-02	9.1E-02
Edinburgh LFC	1.1E+08	8.2E+04	1.2E+06	8.9E+02	1.1E-02	9.5E-02	9.1E-02
Edinburgh LFC	1.1E+08	8.2E+04	1.2E+06	8.9E+02	1.1E-02	9.0E-02	9.1E-02
Dolomite NHM	8.8E+07	5.8E+04	9.6E+05	6.2E+02	1.1E-02	1.1E-01	1.0E-01
Dolomite NHM	1.0E+08	6.6E+04	1.1E+06	7.2E+02	1.1E-02	9.4E-02	9.6E-02
Dolomite NHM	9.4E+07	6.1E+04	1.0E+06	6.7E+02	1.1E-02	9.7E-02	9.9E-02
Dolomite NHM	9.9E+07	6.5E+04	1.1E+06	7.0E+02	1.1E-02	9.0E-02	9.7E-02
Dolomite NHM	9.0E+07	5.9E+04	9.8E+05	6.4E+02	1.1E-02	9.9E-02	1.0E-01
Dolomite 1917	9.4E+07	6.1E+04	1.0E+06	6.6E+02	1.1E-02	9.3E-02	1.0E-01
Dolomite 1917	9.7E+07	6.3E+04	1.0E+06	6.8E+02	1.1E-02	1.0E-01	9.8E-02
Dolomite 1917	9.7E+07	6.3E+04	1.0E+06	6.8E+02	1.1E-02	1.0E-01	9.9E-02
Dolomite 1917	9.4E+07	6.1E+04	1.0E+06	6.6E+02	1.1E-02	9.7E-02	1.0E-01
Dolomite 1917	9.9E+07	6.5E+04	1.1E+06	6.9E+02	1.1E-02	9.9E-02	9.7E-02
Ferroan Dolomite	9.4E+07	6.1E+04	1.0E+06	6.6E+02	1.1E-02	1.1E-01	1.0E-01
Ferroan Dolomite	9.4E+07	6.1E+04	1.0E+06	6.6E+02	1.1E-02	1.1E-01	1.0E-01
Ferroan Dolomite	9.5E+07	6.2E+04	1.0E+06	6.7E+02	1.1E-02	9.2E-02	9.9E-02
Ferroan Dolomite	9.8E+07	6.4E+04	1.1E+06	6.9E+02	1.1E-02	9.6E-02	9.8E-02
Ferroan Dolomite	9.9E+07	6.4E+04	1.1E+06	6.9E+02	1.1E-02	1.0E-01	9.7E-02
Dolomite NHM 1982	8.1E+07	5.3E+04	8.8E+05	5.7E+02	1.1E-02	1.1E-01	1.1E-01
Dolomite NHM 1982	8.2E+07	5.3E+04	8.8E+05	5.7E+02	1.1E-02	1.0E-01	1.1E-01
Dolomite NHM 1982	8.4E+07	5.5E+04	9.1E+05	5.9E+02	1.1E-02	1.0E-01	1.1E-01
Dolomite NHM 1982	8.0E+07	5.2E+04	8.7E+05	5.6E+02	1.1E-02	1.1E-01	1.1E-01
Dolomite NHM 1982	8.4E+07	5.5E+04	9.1E+05	5.9E+02	1.1E-02	1.1E-01	1.1E-01
Siderite NHM	6.5E+07	4.2E+04	6.8E+05	4.4E+02	1.1E-02	1.3E-01	1.2E-01
Siderite NHM	6.6E+07	4.3E+04	6.9E+05	4.5E+02	1.1E-02	1.2E-01	1.2E-01
Siderite NHM	6.7E+07	4.4E+04	7.1E+05	4.6E+02	1.1E-02	1.2E-01	1.2E-01
Dolomite NHM 1924	6.2E+07	2.7E+04	6.9E+05	3.0E+02	1.1E-02	1.2E-01	1.2E-01
Dolomite NHM 1924	6.3E+07	2.7E+04	6.9E+05	3.0E+02	1.1E-02	1.2E-01	1.2E-01
Dolomite NHM 1924	5.0E+07	2.2E+04	5.5E+05	2.4E+02	1.1E-02	1.3E-01	1.4E-01
Dolomite NHM 1924	3.7E+07	1.6E+04	4.0E+05	1.8E+02	1.1E-02	1.6E-01	1.6E-01
Dolomite NHM 1924	3.6E+07	1.6E+04	4.0E+05	1.7E+02	1.1E-02	1.6E-01	1.6E-01
Magnesite NHM	2.0E+07	6.6E+03	2.2E+05	7.1E+01	1.1E-02	2.3E-01	2.1E-01
Magnesite NHM	2.9E+07	9.5E+03	3.1E+05	1.0E+02	1.1E-02	1.7E-01	1.8E-01
Magnesite NHM	2.3E+07	7.4E+03	2.5E+05	8.0E+01	1.1E-02	2.0E-01	2.0E-01
Magnesite NHM	2.1E+07	6.8E+03	2.2E+05	7.3E+01	1.1E-02	2.3E-01	2.1E-01
Magnesite NHM	2.2E+07	7.1E+03	2.3E+05	7.6E+01	1.1E-02	2.1E-01	2.1E-01
Magnesite NHM	2.0E+07	6.4E+03	2.1E+05	6.8E+01	1.1E-02	2.3E-01	2.2E-01
Magnesite NHM	1.6E+07	5.3E+03	1.7E+05	5.7E+01	1.1E-02	2.5E-01	2.4E-01
Magnesite NHM	1.6E+07	5.2E+03	1.7E+05	5.5E+01	1.1E-02	2.5E-01	2.4E-01
Carbonate standards	$^{12}C_{Counts}$	$^{12}C_{Rate}$	$^{13}C_{Counts}$	$^{13}C_{Rate}$	$^{13}C/^{12}C$	$^{13}C/^{12}C$	$^{13}C/^{12}C$

					Ratio	Err Mean	Poisson
Magnesite NHM	3.1E+07	1.0E+04	3.3E+05	1.1E+02	1.1E-02	1.8E-01	1.7E-01
Sidertie NHM	1.1E+05	6.5E+01	1.9E+09	1.2E+06	1.0E-02	1.3E-01	1.2E-01
Sidertie NHM	1.0E+05	6.2E+01	1.9E+09	1.2E+06	1.0E-02	1.3E-01	1.2E-01
Sidertie NHM	1.0E+05	6.1E+01	1.9E+09	1.2E+06	1.0E-02	1.3E-01	1.2E-01
Ankerite NHM	8.9E+07	5.8E+04	9.4E+05	6.1E+02	1.1E-02	1.0E-01	1.0E-01
Ankerite NHM	9.0E+07	5.8E+04	9.4E+05	6.1E+02	1.1E-02	1.1E-01	1.0E-01
Ankerite NHM	1.0E+08	6.6E+04	1.1E+06	6.9E+02	1.1E-02	1.0E-01	9.8E-02
Ankerite NHM	9.1E+07	5.9E+04	9.6E+05	6.2E+02	1.0E-02	1.0E-01	1.0E-01
Ankerite NHM	8.9E+07	5.8E+04	9.4E+05	6.1E+02	1.1E-02	1.0E-01	1.0E-01
Dolomite NHM 59191	1.0E+08	6.8E+04	1.1E+06	7.4E+02	1.1E-02	9.8E-02	9.4E-02
Dolomite NHM 59191	1.1E+08	7.0E+04	1.2E+06	7.6E+02	1.1E-02	9.2E-02	9.3E-02
Dolomite NHM 59191	1.1E+08	7.0E+04	1.2E+06	7.6E+02	1.1E-02	9.2E-02	9.3E-02
Dolomite NHM 59191	1.1E+08	6.9E+04	1.2E+06	7.5E+02	1.1E-02	9.2E-02	9.4E-02
Dolomite NHM 59191	9.6E+07	6.3E+04	1.0E+06	6.8E+02	1.1E-02	9.4E-02	9.8E-02
Dolomite NMNH 10057	7.5E+07	4.9E+04	8.1E+05	5.3E+02	1.1E-02	1.1E-01	1.1E-01
Dolomite NMNH 10057	7.5E+07	4.9E+04	8.1E+05	5.3E+02	1.1E-02	1.2E-01	1.1E-01
Dolomite NMNH 10057	7.4E+07	4.8E+04	8.0E+05	5.2E+02	1.1E-02	1.1E-01	1.1E-01
Dolomite NMNH 10057	7.2E+07	4.7E+04	7.8E+05	5.1E+02	1.1E-02	1.2E-01	1.1E-01
Dolomite NMNH 10057	7.3E+07	4.8E+04	7.9E+05	5.1E+02	1.1E-02	1.1E-01	1.1E-01
Siderite NMNH R2460	6.1E+07	4.0E+04	6.4E+05	4.2E+02	1.1E-02	1.2E-01	1.3E-01
Siderite NMNH R2460	6.2E+07	4.0E+04	6.5E+05	4.3E+02	1.1E-02	1.3E-01	1.2E-01
Siderite NMNH R2460	6.4E+07	4.1E+04	6.7E+05	4.4E+02	1.1E-02	1.2E-01	1.2E-01
Siderite NMNH R2460	6.4E+07	4.1E+04	6.7E+05	4.4E+02	1.1E-02	1.3E-01	1.2E-01
Siderite NMNH R2460	6.4E+07	4.2E+04	6.8E+05	4.4E+02	1.1E-02	1.2E-01	1.2E-01
Dolomite NHM 1990	2.9E+07	1.0E+04	3.1E+05	1.1E+02	1.1E-02	1.9E-01	1.8E-01
Dolomite NHM 1990	3.0E+07	1.1E+04	3.2E+05	1.1E+02	1.1E-02	1.9E-01	1.8E-01
Dolomite NHM 1990	2.9E+07	1.0E+04	3.2E+05	1.1E+02	1.1E-02	2.0E-01	1.8E-01
Dolomite NHM 1990	3.0E+07	1.0E+04	3.2E+05	1.1E+02	1.1E-02	1.9E-01	1.8E-01
Magnesite NHM	4.0E+07	7.1E+03	4.3E+05	7.6E+01	1.1E-02	1.5E-01	1.5E-01
Magnesite NHM	3.8E+07	6.8E+03	4.1E+05	7.2E+01	1.1E-02	1.6E-01	1.6E-01
Magnesite NHM	3.6E+07	6.4E+03	3.8E+05	6.8E+01	1.1E-02	1.6E-01	1.6E-01
Dolomite NHM 1924	7.6E+07	1.9E+04	8.3E+05	2.0E+02	1.1E-02	1.1E-01	1.1E-01
Dolomite NHM 1924	7.2E+07	1.8E+04	7.9E+05	1.9E+02	1.1E-02	1.2E-01	1.1E-01
Dolomite NHM 1924	7.0E+07	1.7E+04	7.6E+05	1.9E+02	1.1E-02	1.2E-01	1.2E-01
Dolomite NHM 1924	6.9E+07	1.7E+04	7.5E+05	1.8E+02	1.1E-02	1.2E-01	1.2E-01
Dolomite NHM 1924	6.7E+07	1.6E+04	7.3E+05	1.8E+02	1.1E-02	1.2E-01	1.2E-01

II. ALH 84001 carbonates

Table 2.3 $^{18}O^-$, $^{16}O^-$, $^{28}Si^-$, $^{24}Mg^{16}O^-$, $^{40}Ca^{16}O^-$, and $^{56}Fe^{16}O^-$ values of spot analyses (5x5 μm^2) across ALH 84001 carbonate rossettes. Owing to difficulties with the precision and insufficient MRP ^{17}O values are not reported as they would be misleading.

Rosette	^{16}O Counts	^{16}O Rate	^{18}O Counts	^{18}O Rate	$^{18}O/^{16}O$ Ratio	$^{18}O/^{16}O$ Err Mean	$^{18}O/^{16}O$ Poisson	^{24}Mg Counts	^{24}Mg Rate	^{40}Ca Counts	^{40}Ca Rate	^{56}Fe Counts	^{56}Fe Rate
1.1	3.6E+09	8.7E+06	7.3E+06	1.8E+04	2.0E-03	3.6E-02	3.7E-02	5.0E+07	1.2E+05	5.9E+06	1.4E+04	1.0E+08	2.5E+05
1.2	3.1E+09	7.6E+06	6.4E+06	1.6E+04	2.0E-03	4.1E-02	4.0E-02	3.9E+07	9.5E+04	4.4E+06	1.1E+04	8.4E+07	2.0E+05
1.3	1.3E+09	5.2E+06	2.6E+06	1.1E+04	2.0E-03	6.8E-02	6.2E-02	1.6E+07	6.6E+04	2.0E+06	8.0E+03	3.9E+07	1.6E+05
1.4	7.7E+08	3.1E+06	1.6E+06	6.3E+03	2.0E-03	8.8E-02	8.0E-02	9.2E+06	3.7E+04	1.2E+06	4.8E+03	1.9E+07	7.7E+04
1.5	8.7E+08	3.5E+06	1.8E+06	7.2E+03	2.0E-03	8.3E-02	7.5E-02	1.1E+07	4.3E+04	1.2E+06	4.7E+03	1.8E+07	7.4E+04
1.6	7.3E+08	3.0E+06	1.5E+06	6.1E+03	2.1E-03	8.2E-02	8.2E-02	8.7E+06	3.6E+04	9.5E+05	3.9E+03	1.5E+07	6.1E+04
1.7	4.1E+08	1.7E+06	8.4E+05	3.4E+03	2.1E-03	1.1E-01	1.1E-01	3.9E+06	1.6E+04	3.0E+05	1.2E+03	5.2E+06	2.1E+04
1.8	7.8E+08	3.2E+06	1.6E+06	6.5E+03	2.0E-03	8.5E-02	7.9E-02	9.2E+06	3.7E+04	1.1E+06	4.4E+03	1.5E+07	6.2E+04
1.9	1.2E+09	4.9E+06	2.5E+06	1.0E+04	2.0E-03	6.1E-02	6.4E-02	1.6E+07	6.6E+04	2.0E+06	8.1E+03	3.6E+07	1.5E+05
1.1	1.6E+09	4.9E+06	3.2E+06	9.8E+03	2.0E-03	2.9E+04	8.9E+01	1.1E+07	3.3E+04	2.6E+06	8.0E+03	4.5E+07	1.4E+05
1.11	1.4E+09	4.2E+06	2.8E+06	8.5E+03	2.0E-03	2.5E+04	7.6E+01	9.4E+06	2.9E+04	2.0E+06	6.2E+03	3.5E+07	1.1E+05
1.12	1.4E+09	4.2E+06	2.8E+06	8.5E+03	2.0E-03	2.3E+04	7.1E+01	9.4E+06	2.9E+04	2.1E+06	6.3E+03	3.4E+07	1.0E+05
1.13	9.5E+08	2.9E+06	2.0E+06	6.1E+03	2.1E-03	1.6E+04	5.0E+01	4.5E+06	1.4E+04	1.5E+06	4.6E+03	1.9E+07	5.9E+04
1.14	1.2E+09	3.8E+06	2.5E+06	7.7E+03	2.0E-03	2.0E+04	6.1E+01	6.9E+06	2.1E+04	1.8E+06	5.6E+03	2.8E+07	8.6E+04
1.15	1.2E+09	3.7E+06	2.5E+06	7.6E+03	2.0E-03	2.3E+04	6.9E+01	9.0E+06	2.7E+04	1.6E+06	4.9E+03	2.9E+07	8.9E+04
1.16	8.8E+08	2.7E+06	1.8E+06	5.5E+03	2.0E-03	1.8E+04	5.5E+01	5.9E+06	1.8E+04	1.3E+06	4.0E+03	2.0E+07	6.2E+04
2.1	7.7E+08	2.3E+06	1.6E+06	4.7E+03	2.0E-03	1.5E+04	4.4E+01	5.0E+06	1.5E+04	1.2E+06	3.7E+03	2.1E+07	6.4E+04
2.2	1.3E+09	4.0E+06	2.7E+06	8.1E+03	2.0E-03	2.3E+04	7.0E+01	8.0E+06	2.4E+04	2.2E+06	6.6E+03	3.4E+07	1.0E+05
2.3	1.2E+09	3.5E+06	2.4E+06	7.2E+03	2.0E-03	2.0E+04	6.2E+01	8.4E+06	2.6E+04	1.9E+06	5.8E+03	3.1E+07	9.4E+04
2.4	1.7E+09	5.2E+06	3.5E+06	1.1E+04	2.0E-03	3.1E+04	9.3E+01	1.5E+07	4.7E+04	2.9E+06	8.7E+03	5.3E+07	1.6E+05

Rosette	^{16}O Counts	^{16}O Rate	^{18}O Counts	^{18}O Rate	$^{18}O/^{16}O$ Ratio	$^{18}O/^{16}O$ Err Mean	$^{18}O/^{16}O$ Poisson	^{24}Mg Counts	^{24}Mg Rate	^{40}Ca Counts	^{40}Ca Rate	^{56}Fe Counts	^{56}Fe Rate
2.5	1.6E+09	4.9E+06	3.3E+06	1.0E+04	2.0E-03	2.8E+04	8.6E+01	1.6E+07	5.0E+04	3.0E+06	9.0E+03	4.8E+07	1.5E+05
2.6	1.6E+09	4.8E+06	3.2E+06	9.8E+03	2.0E-03	2.8E+04	8.6E+01	1.7E+07	5.3E+04	2.7E+06	8.3E+03	4.3E+07	1.3E+05
2.7	1.3E+09	4.0E+06	2.7E+06	8.1E+03	2.0E-03	2.3E+04	6.9E+01	1.4E+07	4.3E+04	2.3E+06	7.0E+03	3.1E+07	9.5E+04
2.8	7.8E+08	2.4E+06	1.6E+06	4.9E+03	2.1E-03	1.7E+04	5.0E+01	7.4E+06	2.3E+04	1.1E+06	3.3E+03	1.4E+07	4.2E+04
2.9	6.6E+08	2.0E+06	1.4E+06	4.1E+03	2.0E-03	1.4E+04	4.2E+01	6.4E+06	2.0E+04	8.8E+05	2.7E+03	1.2E+07	3.7E+04

Table 2.4 $^{13}C^-$, $^{12}C^-$, $^{28}Si^-$, $^{24}Mg^{16}O^-$, $^{40}Ca^{16}O^-$, and $^{56}Fe^{16}O^-$ values of spot analyses (5x5 μm^2) across ALH 84001 carbonate rossettes.

Rosette	$^{12}C_{Counts}$	$^{12}C_{Rate}$	$^{13}C_{Counts}$	$^{13}C_{Rate}$	$^{13}C/^{12}C$ Ratio	$^{13}C/^{12}C$ Err Mean	$^{13}C/^{12}C$ Poisson	^{28}Si Counts	$^{28}Si_{Rate}$	^{24}Mg Counts	$^{24}Mg_{Rate}$	^{40}Ca Counts	$^{40}Ca_{Rate}$	^{56}Fe Counts	$^{56}Fe_{Rate}$
1.1	1.0E+08	4.0E+04	1.1E+06	4.3E+02	1.1E-02	9.7E-02	9.5E-02	1.9E+07	7.5E+03	2.3E+08	8.9E+04	2.0E+07	7.9E+03	3.6E+08	1.4E+05
1.2	9.0E+07	3.5E+04	9.9E+05	3.9E+02	1.1E-02	9.9E-02	1.0E-01	8.2E+06	3.2E+03	2.3E+08	8.9E+04	2.3E+07	9.0E+03	4.0E+08	1.6E+05
1.3	1.1E+08	4.1E+04	1.2E+06	4.5E+02	1.1E-02	9.7E-02	9.4E-02	2.7E+07	1.1E+04	2.2E+08	8.5E+04	2.6E+07	1.0E+04	3.9E+08	1.5E+05
1.4	9.4E+07	3.7E+04	1.0E+06	3.9E+02	1.1E-02	1.0E-01	1.0E-01	8.7E+07	3.4E+04	1.3E+08	5.1E+04	1.5E+07	5.9E+03	2.6E+08	1.0E+05
1.5	1.4E+08	5.4E+04	1.5E+06	5.7E+02	1.1E-02	8.9E-02	8.3E-02	1.5E+08	5.8E+04	1.4E+08	5.4E+04	1.2E+07	4.8E+03	2.6E+08	1.0E+05
1.6	9.9E+07	3.9E+04	1.1E+06	4.2E+02	1.1E-02	1.1E-01	9.7E-02	3.3E+07	1.3E+04	1.9E+08	7.5E+04	1.9E+07	7.4E+03	3.5E+08	1.4E+05
1.7	1.4E+08	5.4E+04	1.5E+06	5.8E+02	1.1E-02	8.4E-02	8.2E-02	6.7E+07	2.6E+04	2.0E+08	7.9E+04	2.2E+07	8.7E+03	4.1E+08	1.6E+05
1.8	8.1E+07	3.2E+04	8.9E+05	3.5E+02	1.1E-02	1.0E-01	1.1E-01	1.3E+07	4.9E+03	1.6E+08	6.3E+04	2.2E+07	8.5E+03	3.5E+08	1.4E+05
1.9	7.4E+07	2.9E+04	8.0E+05	3.1E+02	1.1E-02	1.1E-01	1.1E-01	1.2E+07	4.5E+03	1.3E+08	5.2E+04	1.9E+07	7.6E+03	2.8E+08	1.1E+05
1.10	8.0E+07	3.1E+04	8.7E+05	3.4E+02	1.1E-02	1.1E-01	1.1E-01	6.8E+06	2.7E+03	1.6E+08	6.1E+04	2.2E+07	8.5E+03	3.0E+08	1.2E+05
1.11	9.7E+07	3.8E+04	1.1E+06	4.1E+02	1.1E-02	1.0E-01	9.8E-02	1.6E+07	6.3E+03	2.1E+08	8.2E+04	2.6E+07	1.0E+04	3.0E+08	1.2E+05
1.12	7.5E+07	2.9E+04	8.2E+05	3.2E+02	1.1E-02	1.1E-01	1.1E-01	1.8E+07	6.9E+03	1.6E+08	6.2E+04	1.7E+07	6.5E+03	1.5E+08	5.9E+04
1.13	8.2E+07	3.2E+04	8.9E+05	3.5E+02	1.1E-02	1.1E-01	1.1E-01	2.0E+07	7.7E+03	1.8E+08	6.9E+04	1.5E+07	5.9E+03	1.3E+08	5.2E+04
1.14	5.7E+07	2.6E+04	6.3E+05	2.9E+02	1.1E-02	1.3E-01	1.3E-01	9.7E+02	4.4E-01	2.2E+06	1.0E+03	5.3E+06	2.5E+03	2.3E+08	1.0E+05
1.15	1.8E+08	8.2E+04	1.9E+06	8.7E+02	1.1E-02	7.9E-02	7.3E-02	8.7E+03	4.0E+00	1.0E+07	4.7E+03	4.1E+06	1.9E+03	1.6E+08	7.5E+04
1.16	9.7E+07	4.5E+04	1.0E+06	4.8E+02	1.1E-02	1.3E-01	9.9E-02	3.5E+03	1.6E+00	3.4E+06	1.6E+03	3.1E+06	1.4E+03	9.5E+07	4.4E+04
2.1	1.1E+08	4.9E+04	1.1E+06	5.3E+02	1.1E-02	1.0E-01	9.4E-02	4.0E+03	1.8E+00	4.1E+06	1.9E+03	2.7E+06	1.2E+03	1.0E+08	4.8E+04

Rosette	$^{12}C_{Counts}$	$^{12}C_{Rate}$	$^{13}C_{Counts}$	$^{13}C_{Rate}$	$^{13}C/^{12}C$ Ratio	$^{13}C/^{12}C$ Err Mean	$^{13}C/^{12}C$ Poisson	^{28}Si Counts	$^{28}Si_{Rate}$	^{24}Mg Counts	$^{24}Mg_{Rate}$	^{40}Ca Counts	$^{40}Ca_{Rate}$	^{56}Fe Counts	$^{56}Fe_{Rate}$
2.2	1.4E+08	6.6E+04	1.5E+06	7.0E+02	1.1E-02	8.7E-02	8.2E-02	6.7E+03	3.1E+00	1.3E+07	5.9E+03	4.9E+06	2.3E+03	2.5E+08	1.2E+05
2.3	9.5E+07	4.4E+04	1.0E+06	4.7E+02	1.1E-02	1.0E-01	9.9E-02	2.4E+03	1.1E+00	6.6E+06	3.0E+03	6.5E+06	3.0E+03	3.3E+08	1.5E+05
2.4	7.0E+07	3.2E+04	7.6E+05	3.5E+02	1.1E-02	1.2E-01	1.2E-01	1.2E+03	5.6E-01	3.6E+06	1.7E+03	5.6E+06	2.6E+03	2.4E+08	1.1E+05
2.5	8.9E+07	4.1E+04	9.7E+05	4.5E+02	1.1E-02	9.9E-02	1.0E-01	3.2E+02	1.5E-01	1.7E+06	7.6E+02	1.0E+07	4.6E+03	4.1E+08	1.9E+05
2.6	9.0E+07	4.1E+04	9.9E+05	4.5E+02	1.1E-02	9.7E-02	1.0E-01	6.1E+02	2.8E-01	1.7E+06	7.7E+02	8.6E+06	4.0E+03	4.2E+08	1.9E+05
2.7	9.0E+07	4.1E+04	9.9E+05	4.5E+02	1.1E-02	9.6E-02	1.0E-01	6.7E+02	3.1E-01	2.0E+06	9.3E+02	8.6E+06	3.9E+03	4.4E+08	2.0E+05
2.8	7.8E+07	3.6E+04	8.6E+05	3.9E+02	1.1E-02	1.2E-01	1.1E-01	1.0E+03	4.8E-01	1.5E+06	6.8E+02	7.6E+06	3.5E+03	2.8E+08	1.3E+05

III. Analogue carbonates

Table 2.5 $^{18}O^-$ and $^{16}O^-$ values of spot analyses (5x5 μm^2) across analogue carbonates.

Analogue carbonates	^{16}O Counts	^{16}O Rate	^{18}O Counts	^{18}O Rate	$^{18}O/^{16}O$ Ratio	$^{18}O/^{16}O$ Err Mean	$^{18}O/^{16}O$ Poisson
AC 1, spot 1	7.8E+09	1.8E+07	1.6E+07	3.7E+04	2.1E-03	2.6E-02	2.5E-02
AC 1, spot 2	7.7E+09	1.8E+07	1.6E+07	3.6E+04	2.1E-03	2.6E-02	2.5E-02
AC 1, spot 3	7.6E+09	1.8E+07	1.6E+07	3.6E+04	2.1E-03	1.3E-01	2.5E-02
AC 1, spot 4	7.7E+09	1.8E+07	1.6E+07	3.6E+04	2.1E-03	2.6E-02	2.5E-02
AC 1, spot 5	7.7E+09	1.8E+07	1.6E+07	3.7E+04	2.1E-03	2.6E-02	2.5E-02
AC 1, spot 6	7.9E+09	1.8E+07	1.6E+07	3.7E+04	2.1E-03	2.6E-02	2.5E-02
AC 1, spot 7	6.5E+09	1.5E+07	1.3E+07	3.1E+04	2.1E-03	2.8E-02	2.7E-02
AC 1, spot 8	6.7E+09	1.5E+07	1.4E+07	3.2E+04	2.1E-03	2.8E-02	2.7E-02
AC 1, spot 9	6.7E+09	1.5E+07	1.4E+07	3.2E+04	2.1E-03	2.8E-02	2.7E-02
AC 1, spot 10	4.1E+08	9.4E+05	8.4E+05	1.9E+03	2.1E-03	1.1E-01	1.1E-01
AC 1, spot 11	6.5E+08	1.5E+06	1.3E+06	3.1E+03	2.1E-03	9.6E-02	8.6E-02
AC 1, spot 12	5.8E+08	1.3E+06	1.2E+06	2.7E+03	2.0E-03	1.0E-01	9.2E-02
AC 1, spot 13	1.4E+09	3.3E+06	2.9E+06	6.7E+03	2.1E-03	6.1E-02	5.9E-02
AC 1, spot 14	8.5E+08	2.0E+06	1.8E+06	4.1E+03	2.1E-03	7.9E-02	7.6E-02
AC 2, spot 1	5.7E+09	1.1E+07	1.2E+07	2.2E+04	2.1E-03	3.0E-02	2.9E-02
AC 2, spot 2	7.1E+09	1.3E+07	1.5E+07	2.7E+04	2.1E-03	2.8E-02	2.6E-02
AC 2, spot 3	7.3E+09	1.3E+07	1.5E+07	2.8E+04	2.1E-03	2.6E-02	2.6E-02
AC 2, spot 4	6.8E+09	1.2E+07	1.4E+07	2.6E+04	2.1E-03	2.8E-02	2.7E-02
AC 2, spot 5	6.4E+09	1.2E+07	1.3E+07	2.4E+04	2.0E-03	2.8E-02	2.8E-02
AC 2, spot 6	9.8E+08	1.8E+06	2.0E+06	3.8E+03	2.1E-03	8.1E-02	7.0E-02
AC 2, spot 7	4.5E+09	8.3E+06	9.2E+06	1.7E+04	2.1E-03	3.4E-02	3.3E-02
AC 2, spot 8	4.9E+09	9.0E+06	1.0E+07	1.9E+04	2.1E-03	3.2E-02	3.1E-02
AC 3, spot 1	1.4E+09	6.6E+06	2.9E+06	1.4E+04	2.0E-03	6.1E-02	5.9E-02
AC 3, spot 2	1.2E+09	5.4E+06	2.4E+06	1.1E+04	2.1E-03	6.7E-02	6.4E-02
AC 3, spot 3	1.3E+09	6.2E+06	2.8E+06	1.3E+04	2.0E-03	6.4E-02	6.0E-02
AC 3, spot 4	1.4E+09	6.3E+06	2.8E+06	1.3E+04	2.0E-03	6.1E-02	6.0E-02
AC 3, spot 5	1.4E+09	6.7E+06	3.0E+06	1.4E+04	2.0E-03	6.2E-02	5.8E-02
AC 3, spot 6	1.4E+09	6.4E+06	2.8E+06	1.3E+04	2.0E-03	5.8E-02	6.0E-02
AC 3, spot 7	1.3E+09	5.9E+06	2.6E+06	1.2E+04	2.1E-03	6.3E-02	6.2E-02
AC 3, spot 8	1.4E+09	6.4E+06	2.9E+06	1.3E+04	2.0E-03	6.2E-02	5.9E-02
AC 3, spot 9	1.4E+09	6.5E+06	2.9E+06	1.3E+04	2.1E-03	6.3E-02	5.9E-02
AC 3, spot 10	1.4E+09	6.5E+06	2.9E+06	1.3E+04	2.0E-03	6.2E-02	5.9E-02
AC 3, spot 11	1.4E+09	6.5E+06	2.9E+06	1.3E+04	2.0E-03	5.8E-02	5.9E-02
AC 3, spot 12	1.2E+09	5.5E+06	2.4E+06	1.1E+04	2.1E-03	6.7E-02	6.4E-02

IV. Additional IMF corrections

Various compotisional correlations are assessed for both $\delta^{18}O$ and $\delta^{13}C$ to appreciate the composition of the standards against those in ALH 84001 (Fig. 3.1) and to choose the most suitable IMF correction.

Oxygen IMF corrections

Figure 3.1 illustrates the various compositions of standards measured in this study and those found in ALH 84001. In addition, mixing lines and the region of dolomites are marked on the ternary diagram to clarify the relevance ALH 84001 compositions to the carbonate standards.

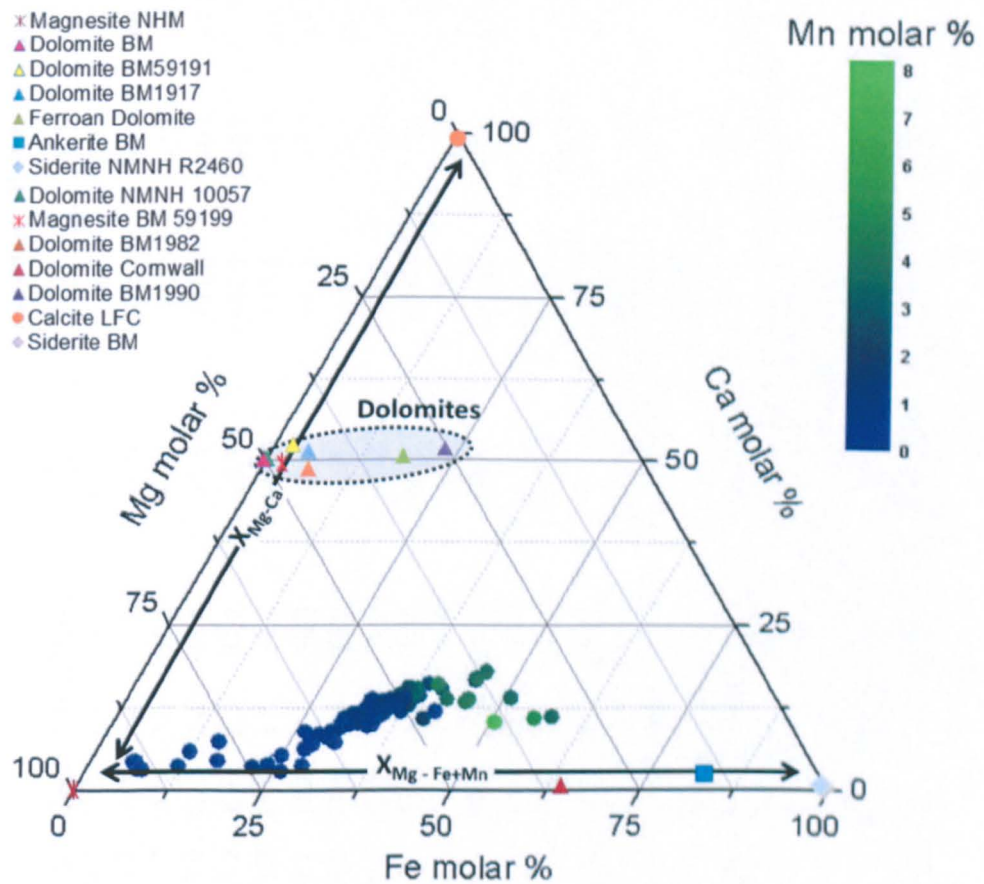

Figure 3.1 Summary of carbonate standards and ALH 84001 carbonate rosettes Mg-Fe-Ca compositions measured in this study.

Table 3.1 Composition and corrected $\delta^{18}O$ values of ALH 84001 carbonate rosettes according to various IMF corrections.

						This study (line)	Line	Line	Line	Exponential	Exponential	Polynomial
						X_{Mg}-X_{Ca}	X_{Fe+Mn}-X_{Mg}	Dolomites	X_{Fe+Mn}	X_{Mg}-X_{Ca}	All	X_{Mg}-X_{Ca}
Sample	X_{Mg}	X_{Ca}	X_{Fe}	X_{Mn}	X_{Fe+Mn}	$\delta^{18}O$	$\delta^{18}O$	$\delta^{18}O$	$\delta^{18}O$	$\delta^{18}O$	$\delta^{18}O$	$\delta^{18}O$
Rosette (1) 1	52.1	13.2	33.5	1.1	34.6	+13.9	+19.2	+11.5	+12.5	+6.3	+9.7	+13.3
Rosette (1) 2	47.1	14.2	36.5	2.2	38.6	+6.6	+12.1	+3.2	+6.1	-0.2	+3.2	+4.2
Rosette (1) 3	43.8	13.7	38.9	3.6	42.5	+1.1	+6.7	-2.8	+1.4	-5	-1.6	-2.3
Rosette (1) 4	36.5	17.9	42.2	3.4	45.6	+5.5	+11.3	+0.1	+7.2	+0.6	+4.1	+0.2
Rosette (1) 5	43.6	15.2	38.6	2.5	41.2	+6.7	+12.3	+2.7	+7	+0.6	+4	+3.2
Rosette (1) 6	49	13.9	35.4	1.8	37.1	+11.6	+17.1	+8.7	+10.9	+4.6	+8	+9.9
Rosette (1) 7	45	16.1	37.2	1.7	38.9	+5.5	+11.1	+1.7	+5.5	-0.9	+2.6	+2.4
Rosette (1) 8	48.3	14.8	33.6	3.4	36.9	-0.1	+5.3	-3.2	-0.7	-7	-3.6	-2.1
Rosette (1) 9	48.9	14.5	33.3	3.2	36.5	+3.2	+8.6	+0.3	+2.5	-3.8	-0.4	+1.5
Rosette (1) 10	48.4	14.2	33.9	3.4	37.3	+6.7	+12.2	+3.6	+6	-0.2	+3.2	+4.8
Rosette (1) 11	49.7	14.4	33.6	2.3	35.9	+9.2	+14.6	+6.3	+8.2	+2	+5.4	+7.7
Rosette (1) 12	57.5	11.4	30.3	0.8	31.1	+16.6	+21.6	+15.3	+14.2	+8.1	+11.4	+18.1
Rosette (1) 13	59.7	9.9	29.7	0.7	30.4	+15.1	+19.9	+14.2	+12.2	+6.2	+9.5	+17.4
Rosette (1) 14	81.7	5.8	11.9	0.5	12.5	+25.3	+27.9	+28.9	+18	+13.2	+16	+35.3
Rosette (1) 15	89.3	3.2	7.3	0.2	7.5	+27.1	+28.5	+32.3	+18.2	+14	+16.5	+38.6
Rosette (2) 16	72.5	3.9	23.4	0.3	23.7	+13.3	+16.9	+15	+8	+2.3	+5.5	+20.4
Rosette (2) 17	48.1	11	40	0.9	40.9	+8.9	+14.3	+5.7	+8.3	+1.9	+5.3	+6.9
Rosette (2) 18	58.7	10.9	29.6	0.7	30.3	+10.4	+15.3	+9.3	+7.7	+1.7	+5	+12.3
Rosette (2) 19	54.1	12	33.1	0.9	34	+0.3	+5.5	-1.6	-1.4	-7.5	-4.2	+0.5
Rosette (2) 20	51.9	12.5	34.6	1	35.6	+12.9	+18.2	+10.5	+11.6	+5.3	+8.7	+12.2
Rosette (2) 21	55.6	9.9	34.1	0.4	34.5	+15.2	+20.4	+13.6	+13.2	+7	+10.4	+16
Rosette (2) 22	65.4	7	27.3	0.3	27.6	+18.4	+22.8	+18.7	+14.5	+8.6	+11.8	+23
Rosette (2) 23	73.1	3.2	23.4	0.3	23.7	+23.3	+26.9	+25.1	+17.8	+12.1	+15.3	+30.7
Rosette (2) 24	72.5	3.8	23.4	0.3	23.7	+20.3	+23.9	+22	+15	+9.3	+12.4	+27.5

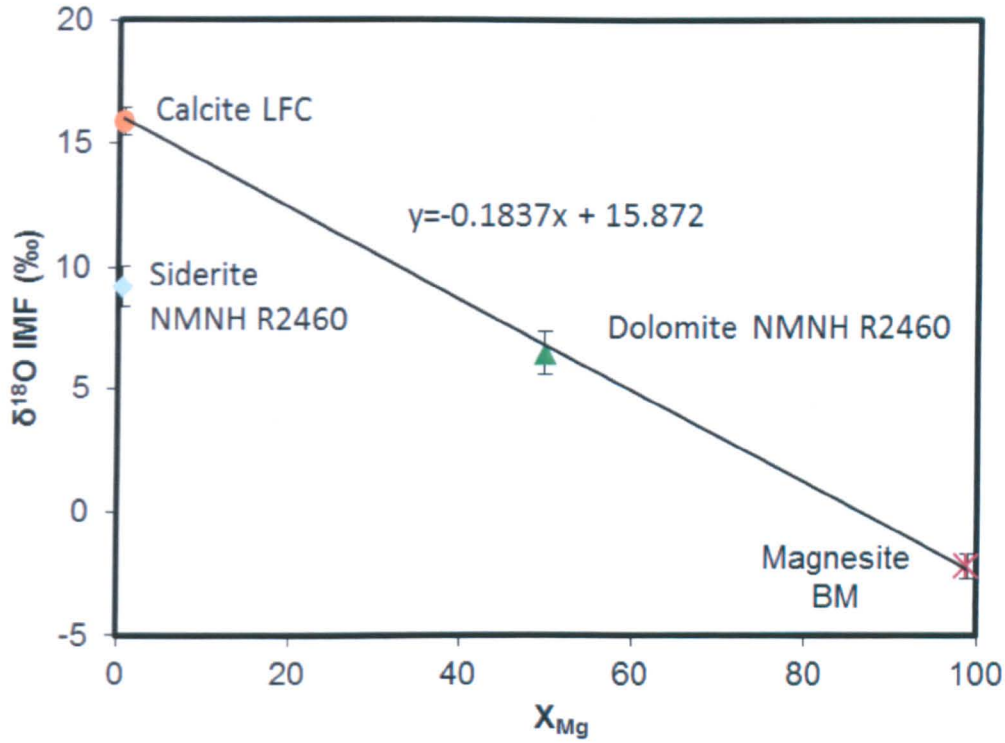

Figure 3.2 Applying IMF corrections to the data set using the calcite-dolomite-magnesite mixing line as applied by Leshin et al. (1998).

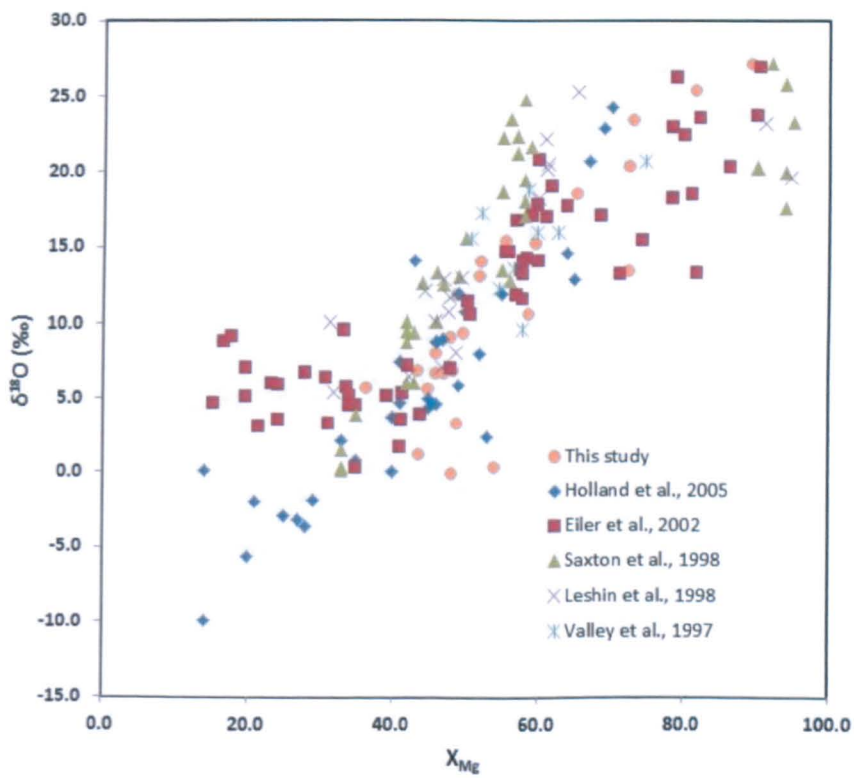

Figure 3.3 Values from this study and previous literature displaying the general trend of $\delta^{18}O$ with X_{Mg} when applying the calcite-dolomite-magnesite mixing line (Fig. 3.2).

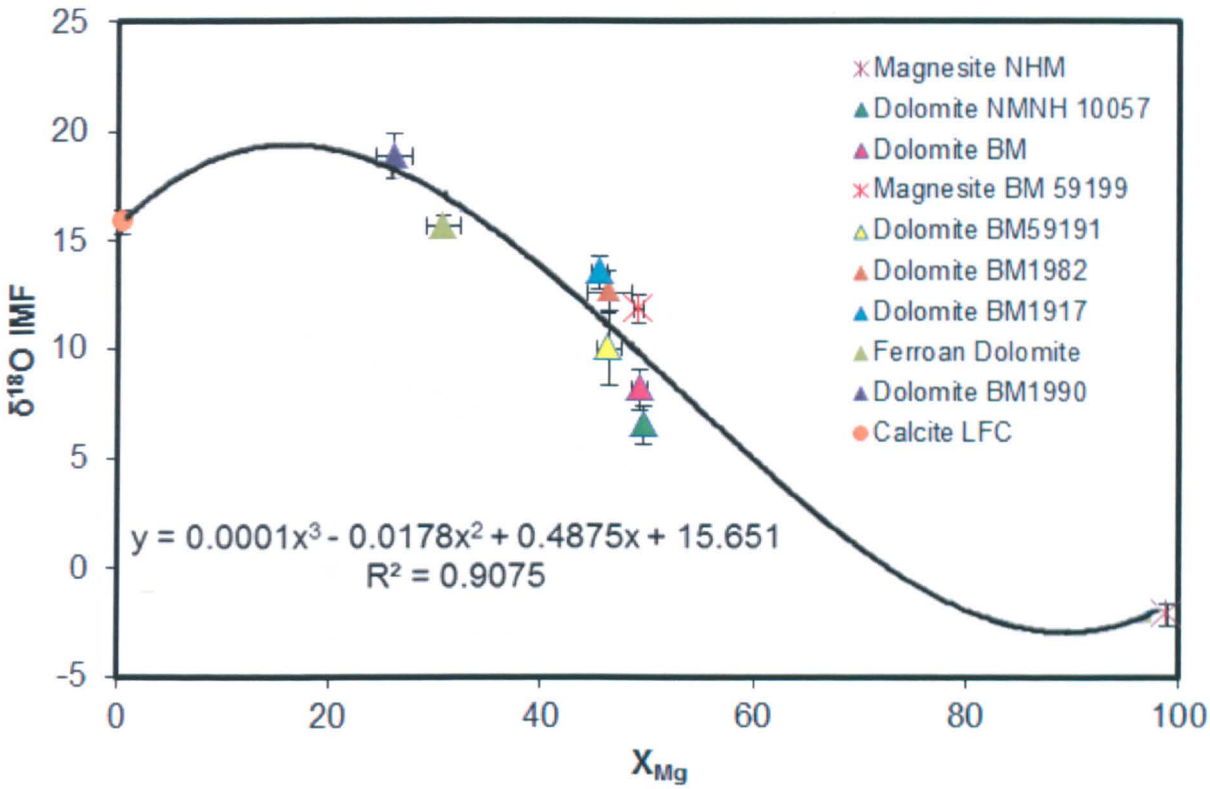

Figure 3.4 Polynomial fit for $X_{Mg\text{-}Ca}$-rich carbonate standards.

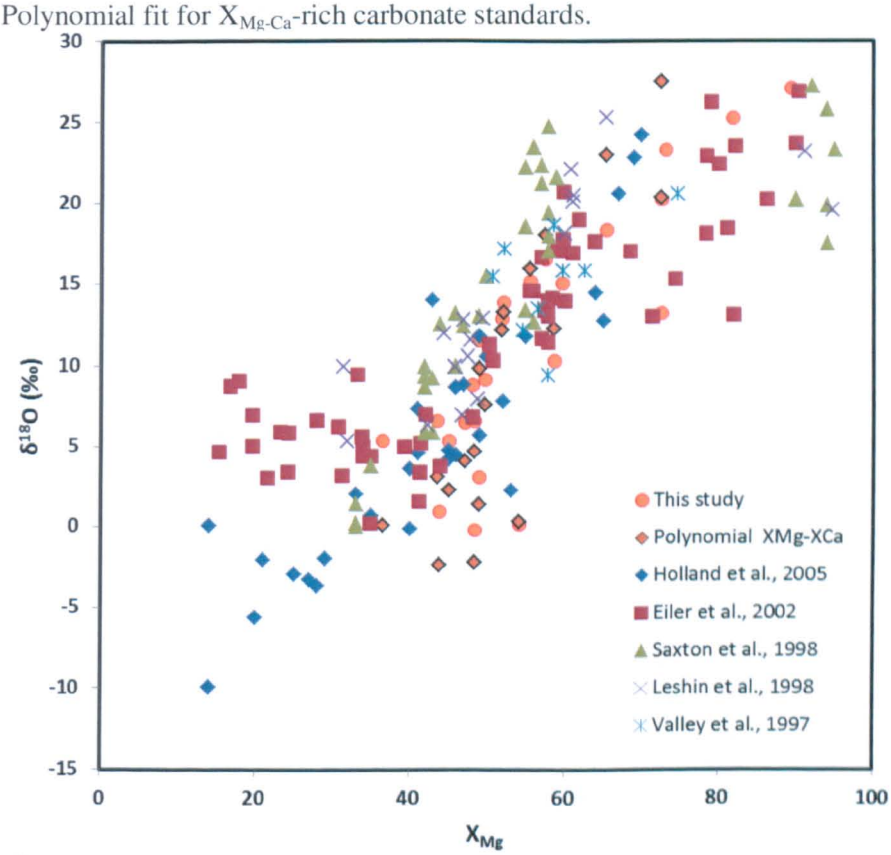

Figure 3.5 $\delta^{18}O$ values against Mg content (X_{Mg}) from that used in this study, previous literature and when applying a polynomial IMF correction using $X_{Mg\text{-}Ca}$-rich standards (Fig. 3.4).

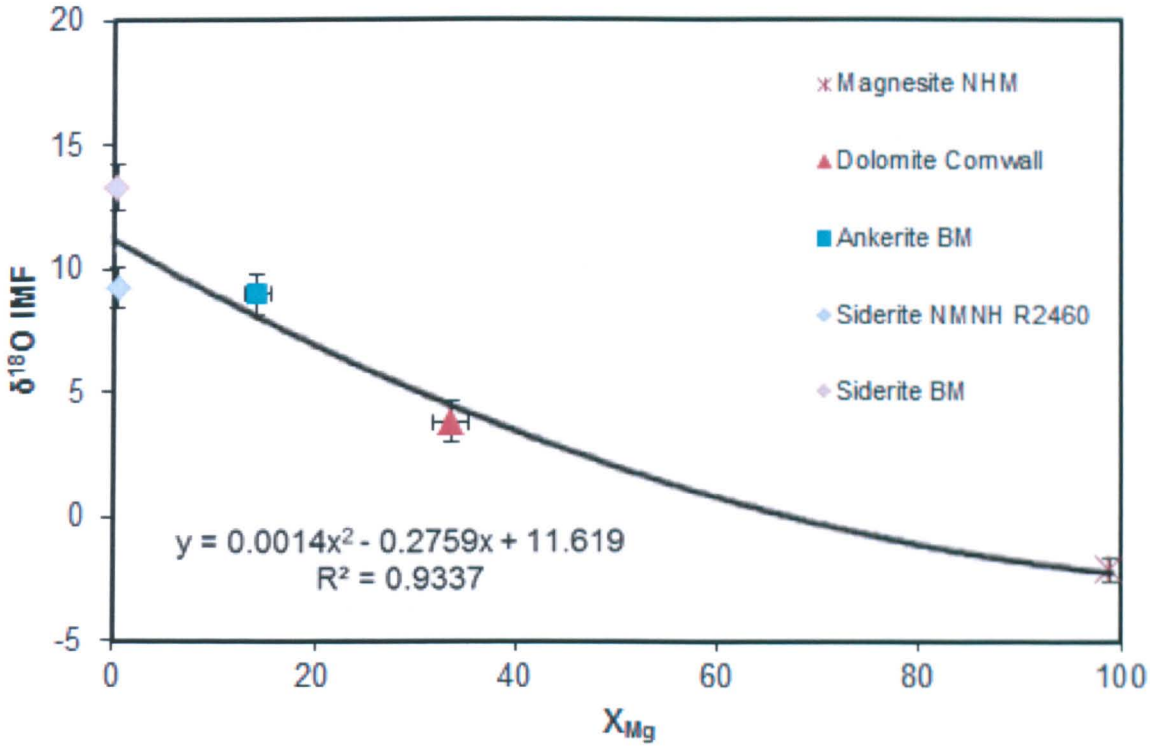

Figure 3.6 Exponential fit for magnesite-siderite mixing line according to their Mg content (X_{Mg}).

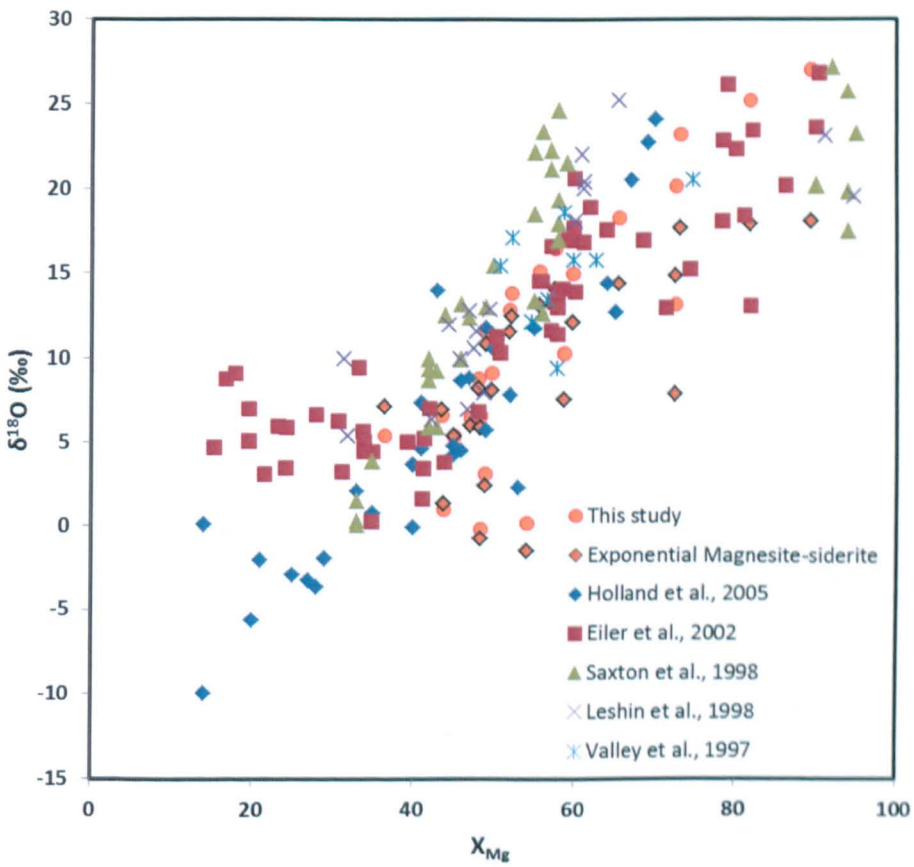

Figure 3.7 $\delta^{18}O$ values against Mg content (X_{Mg}) from that used in this study, previous literature and when applying a exponential IMF correction using magnesite-siderite mixing line (Fig. 3.6).

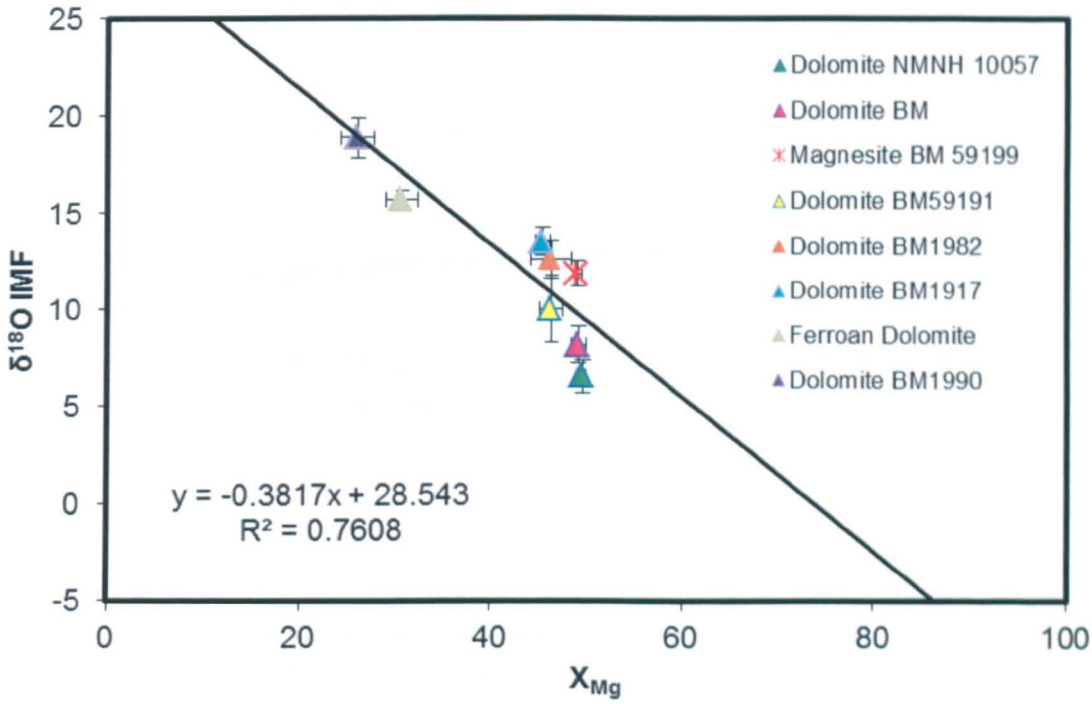

Figure 3.8 Linear fit for dolomite standards according to their Mg content (X_{Mg}).

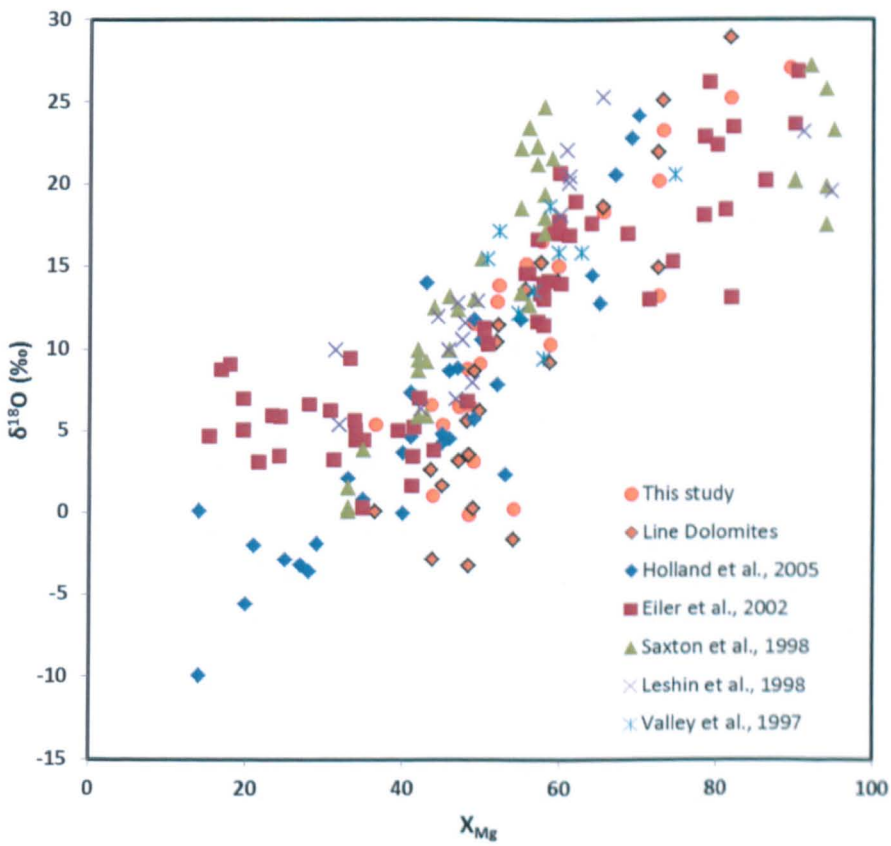

Figure 3.9 $\delta^{18}O$ values against Mg content (X_{Mg}) from that used in this study, previous literature and when applying a linear IMF correction using dolomite standards (Fig. 3.8).

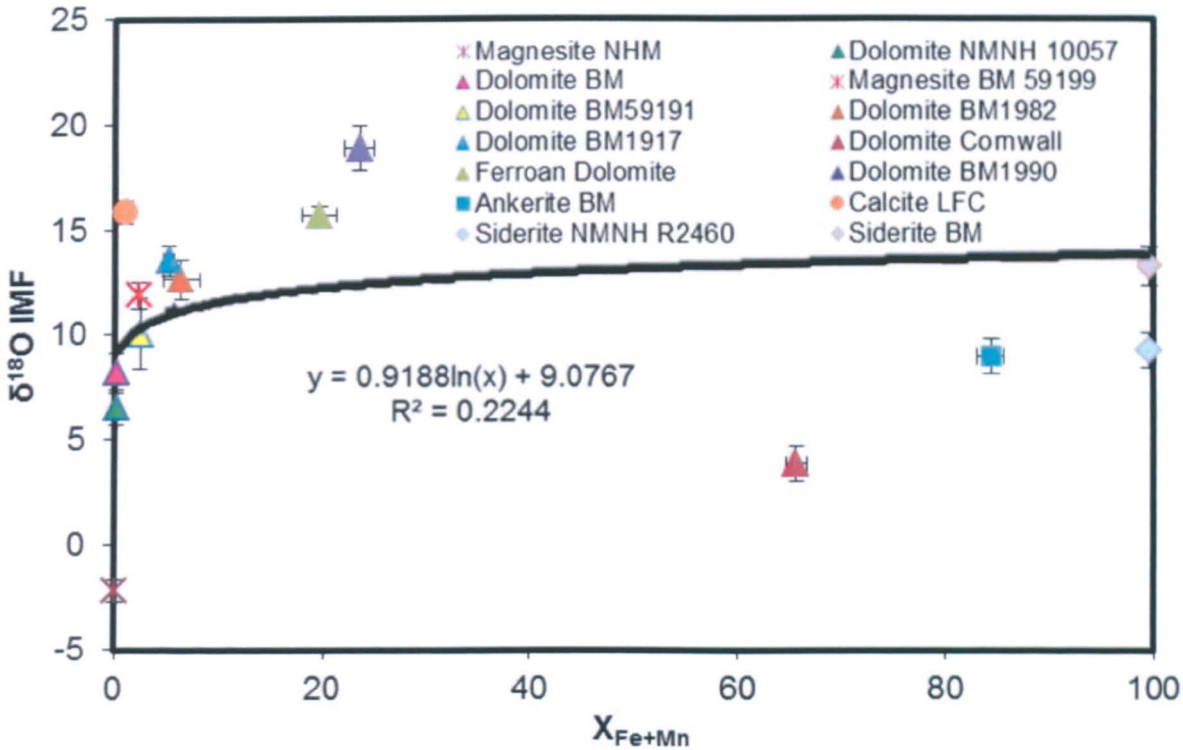

Figure 3.10 Exponential fit for all standards according to their Fe+Mn content (X_{Fe+Mn}).

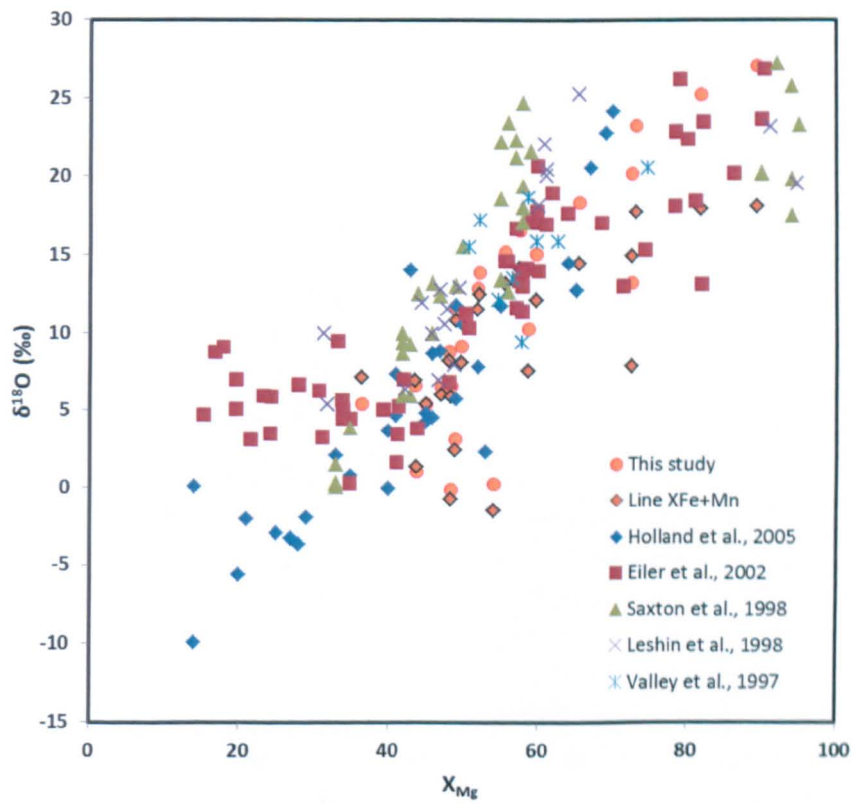

Figure 3.11 $\delta^{18}O$ values against magnesium content (X_{Mg}) from that used in this study, previous literature and when applying a exponential IMF correction using all standards (Fig. 3.10).

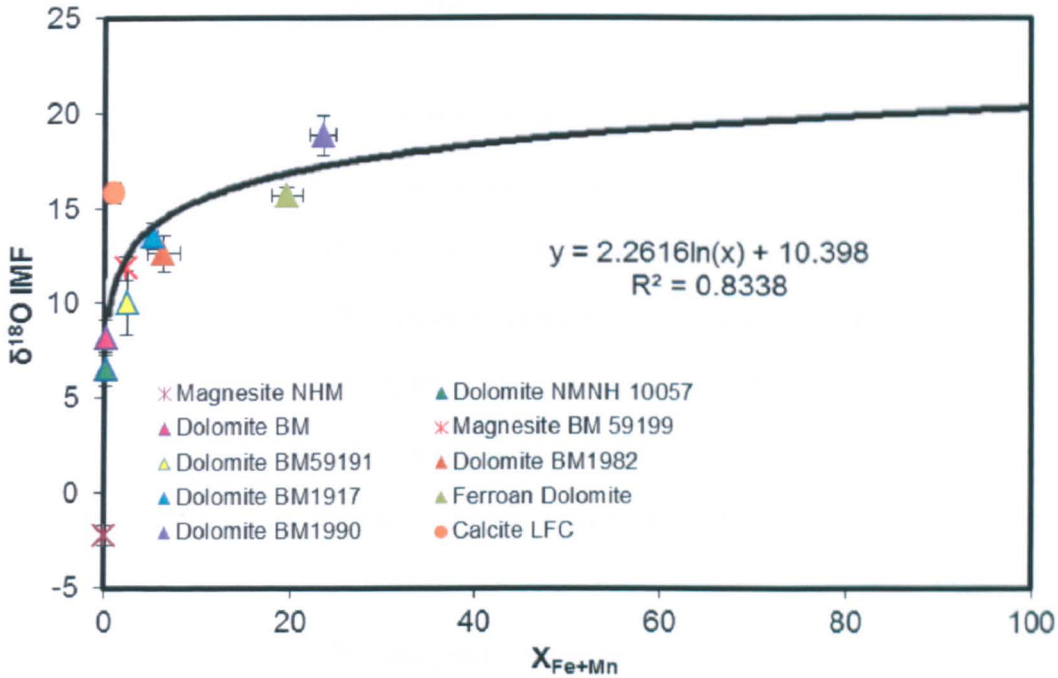

Figure 3.12 Exponential fit for $X_{Mg\text{-}Ca}$-rich carbonate standards according to their Fe+Mn content (X_{Fe+Mn}).

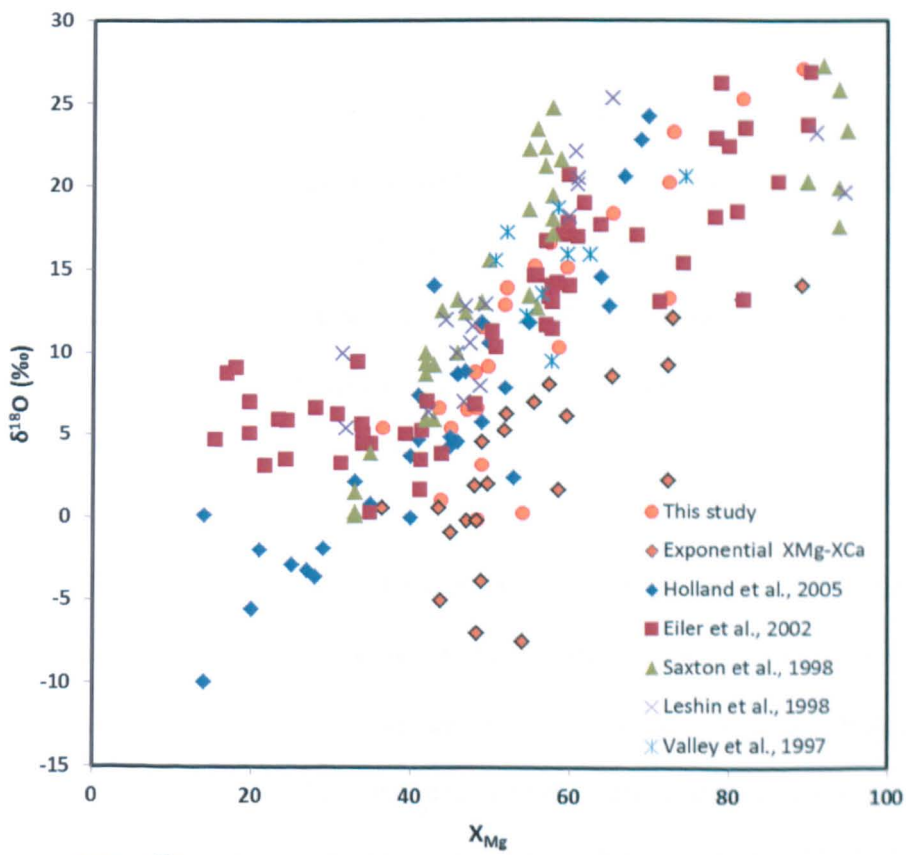

Figure 3.13 $\delta^{18}O$ values against magnesium content (X_{Mg}) from that used in this study, previous literature and when applying an exponential IMF correction using $X_{Mg\text{-}Ca}$-rich standards (Fig. 3.12).

Choice of $\delta^{18}O$ IMF correction

When the carbonates are separated into two components (siderite-magnesite mixing line and $X_{Mg\text{-}Ca}$ rich) there were good IMF correlations when applying a polynomial trend to $X_{Mg\text{-}Ca}$ rich carbonates (Figs. 3.4 and 3.5; R^2=0.9075) and a exponential trend to siderite-magnesite mixing line (Figs 3.6 and 3.7; R^2=0.9337). A poor IMF correlation exists for the all the carbonate data when an exponential trend is applied (Figs 3.8 and 3.9; R^2=0.2244). A reasonable IMF correlation exists for the dolomites as shown in Figures 3.8 and 3.9, in addition a correlation between an increase in X_{Mg} and a decrease in X_{Fe+Mn} is also noted in Chapter 3 (Fig. 3.27; reproduced here Fig. 3.12). There was a good IMF correlation of $X_{Mg\text{-}Ca}$-rich carbonates when applying a exponential trend (Figs 3.12 and 3.13; R^2=0.8338), however, the $\delta^{18}O$ values did not compare well with previous studies. In summary all the IMF corrections apart from the $X_{Mg\text{-}Ca}$-rich carbonates exponential trend (Figs. 3.10 and 3.11; typically lower $\delta^{18}O$ values) provided a good correlation with the existing $\delta^{18}O$ values from literature.

The calcite-dolomite-magnesite mixing lines does form a central line from which all the carbonates measured in this study are spread around (Fig. 3.14). The standards used for this mxining line directly correspond to those measured by Leshin et al. (1998) and the line appears to provide the most general incorporation of all the carboantes. Therefore the calcite-dolomite-magnesite IMF correction was applied rather than a smaller spread of carbonate standards unrepresentative of the range of carbonates found in ALH 84001 (Fig. 3.1 and 3.14).

The ALH 84001 carbonates $\delta^{18}O$ values were shown to vary by up to 18.6‰ for a single point measurement depending on the which IMF correction was applied (Table 3.1; Rosette (2) 23; exponential X_{Mg}-X_{Ca} (+12.1‰) compared to polynomial X_{Mg}-X_{Ca}(+30.7‰)). This variation obviously has large implications for the compositions of the starting waters in which these carbonates formed and therefore the evolution of water $\delta^{18}O$ on Mars (Chapter 7.2.6). The ideal correction will only be

resolved with the addition of carbonate standards that are representative of the ALH 84001 carbonate composition, until then the best infered IMF corrections will be used (Figs. 3.2 and 3.3).

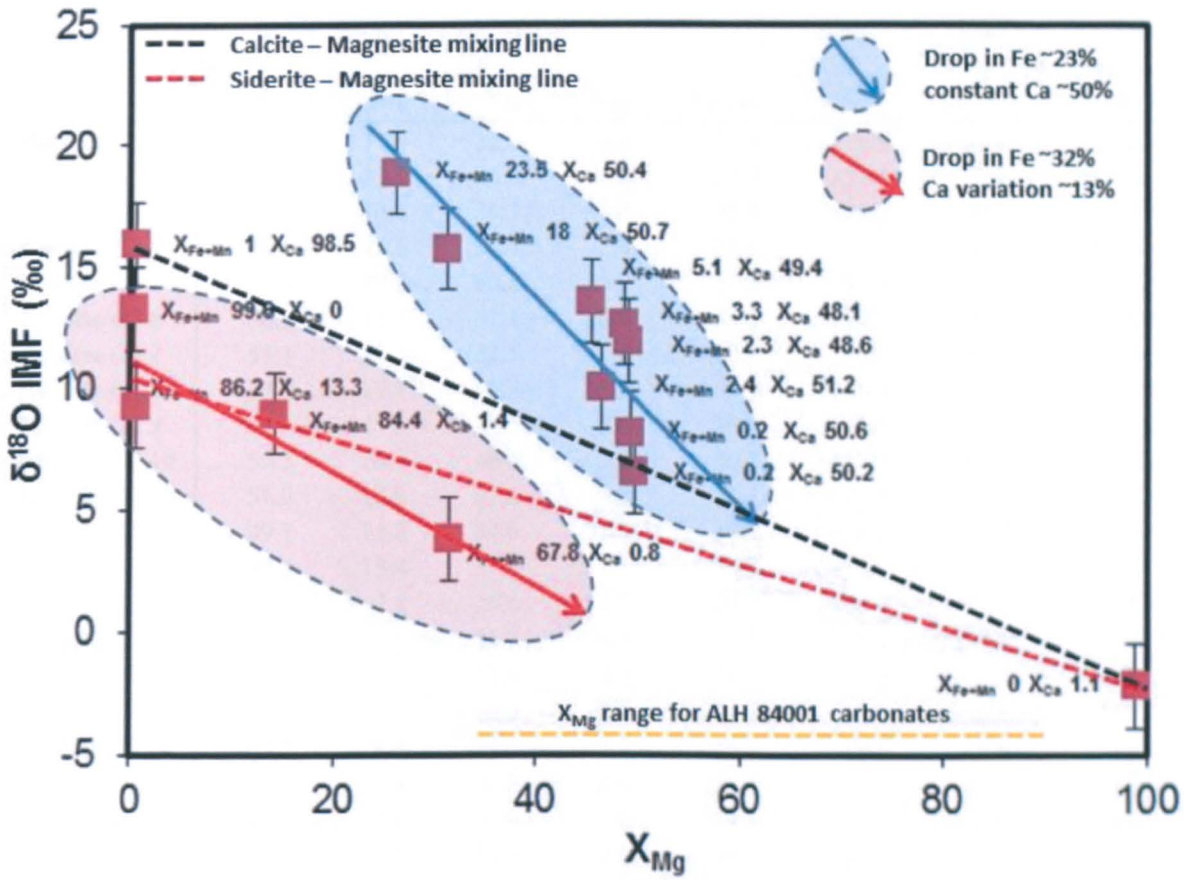

Figure 3.14 $\delta^{18}O$ IMF plotted against X_{Mg} highlighting trends in X_{Fe+Mn} and X_{Ca} two different mixing lines and the X_{Mg} range in ALH 84001 carbonates.

Carbon isotope IMF corrections

Table 3.2 Compositions and corrected $\delta^{13}C$ values of ALH 84001 carbonate rosettes according to various IMF corrections.

Sample	X_{Mg}	X_{Ca}	X_{Fe}	X_{Mn}	X_{Fe+Mn}	Line All $\delta^{13}C$	Line X_{Fe+Mn}-rich $\delta^{13}C$	Line X_{Mg-Ca}-rich $\delta^{13}C$
Rosette (1) 1	55.2	11.4	32.6	0.8	33.4	+16.8	10.6	34.4
Rosette (1) 2	51.8	12.5	34.7	1.0	35.7	+24.3	17.5	41.1
Rosette (1) 3	47.5	14.1	36.7	1.7	38.4	+17.2	9.9	32.9
Rosette (1) 4	49.6	13.6	34.4	2.4	36.8	-1.6	-8.4	14.4
Rosette (1) 5	55.4	12.7	30.8	1.0	31.8	-14.1	-19.7	3.3
Rosette (1) 6	56.5	11.6	31.1	0.8	31.9	+12.4	6.7	30.4
Rosette (1) 7	53.1	13.2	32.1	1.6	33.7	+6.0	-0.2	23.1
Rosette (1) 8	37.0	17.1	42.7	3.2	45.9	+18.9	9.7	31.8
Rosette (1) 9	43.4	17.5	35.5	3.6	39.0	+16.3	+8.8	+31.4
Rosette (1) 10	30.3	19.4	46.4	3.8	50.3	+17.3	+7.1	+28.5
Rosette (1) 11	51.0	13.9	31.9	3.1	35.1	+20.7	+14.1	+37.5
Rosette (1) 12	49.7	13.8	34.6	1.9	36.5	+18.0	+11.1	+34.4
Rosette (1) 13	47.8	13.4	37.7	1.1	38.8	+16.0	+8.6	+31.6
Rosette (1) 14	62.7	7.4	29.6	0.3	29.9	+18.2	+12.9	+37.4
Rosette (1) 15	70.8	4.1	24.7	0.4	25.1	-19.4	-23.4	+0.9
Rosette (1) 16	74.4	7.4	17.5	0.7	18.3	-7.2	-9.7	+15.3
Rosette (2) 17	76.0	2.8	20.9	0.3	21.2	-7.2	-10.4	+14.8
Rosette (2) 18	62.2	8.6	29.0	0.3	29.3	-10.5	-15.6	+8.2
Rosette (2) 19	60.8	9.8	28.8	0.6	29.4	+7.1	+1.9	+26.0
Rosette (2) 20	61.9	9.6	27.9	0.6	28.6	+7.9	+2.9	+27.1
Rosette (2) 21	52.7	12.0	34.5	0.8	35.3	+20.4	+13.7	+37.3
Rosette (2) 22	50.6	13.4	35.2	0.8	36.0	+22.8	+15.9	+39.4
Rosette (2) 23	61.8	9.1	28.9	0.3	29.1	+22.7	+17.6	+42.1
Rosette (2) 24	43.5	8.4	47.7	0.4	48.1	+20.8	+11.3	+34.0

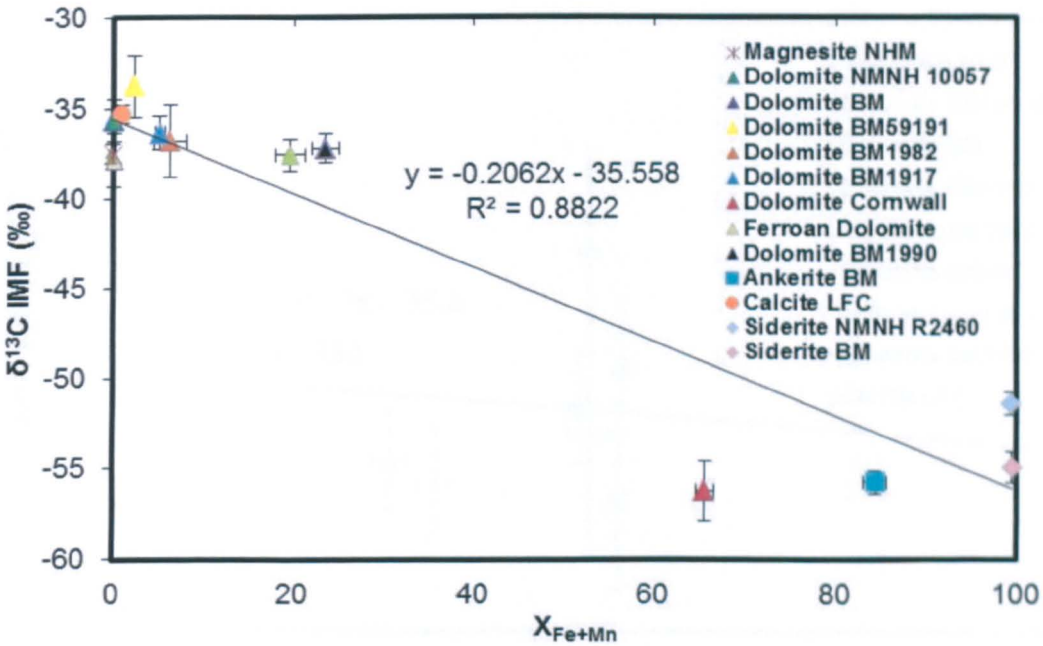

Figure 3.15 Linear fit for all carbonate standards according to their Fe+Mn content (X_{Fe+Mn}).

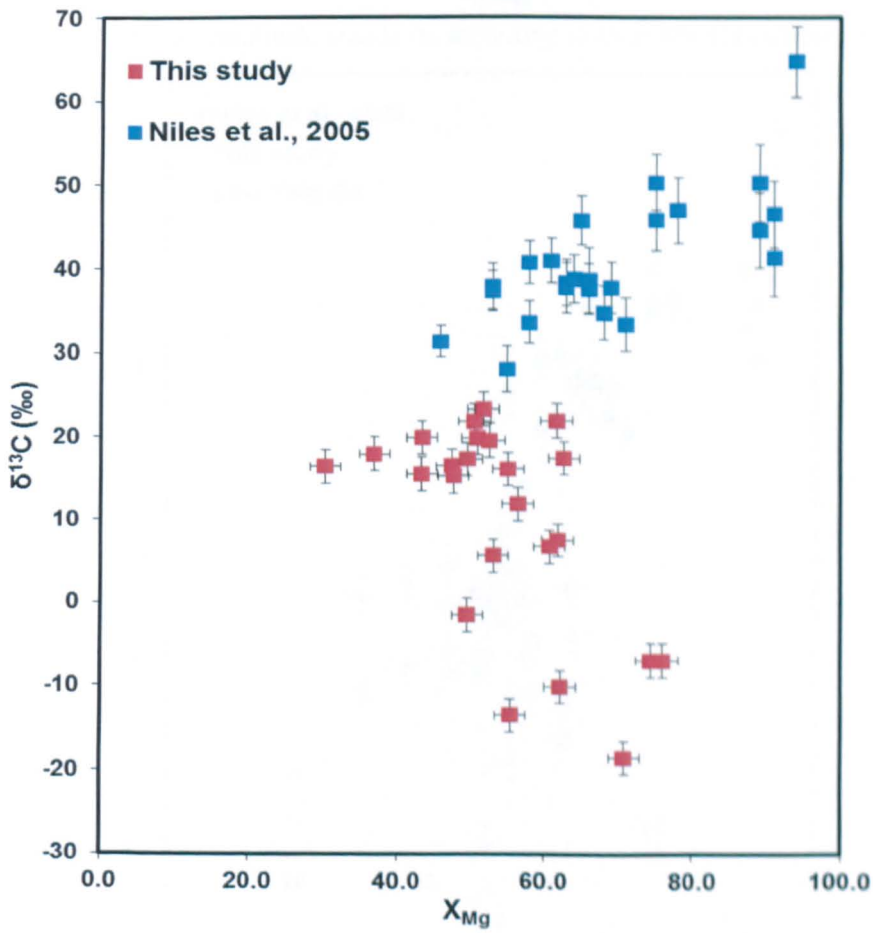

Figure 3.16 Values from this study and previous literature displaying the general trend of $\delta^{13}C$ with Mg content (X_{Mg}).

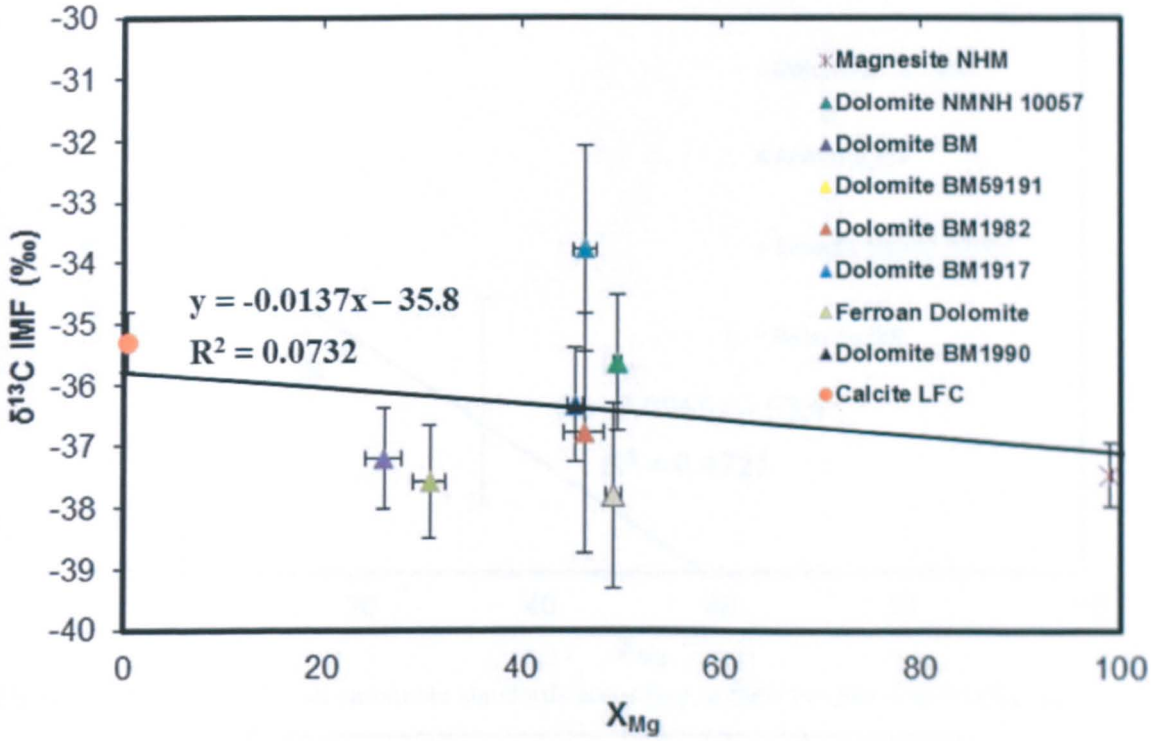

Figure 3.17 Linear fit for all carbonate standards according to their Mg-Ca content ($X_{Mg\text{-}Ca}$).

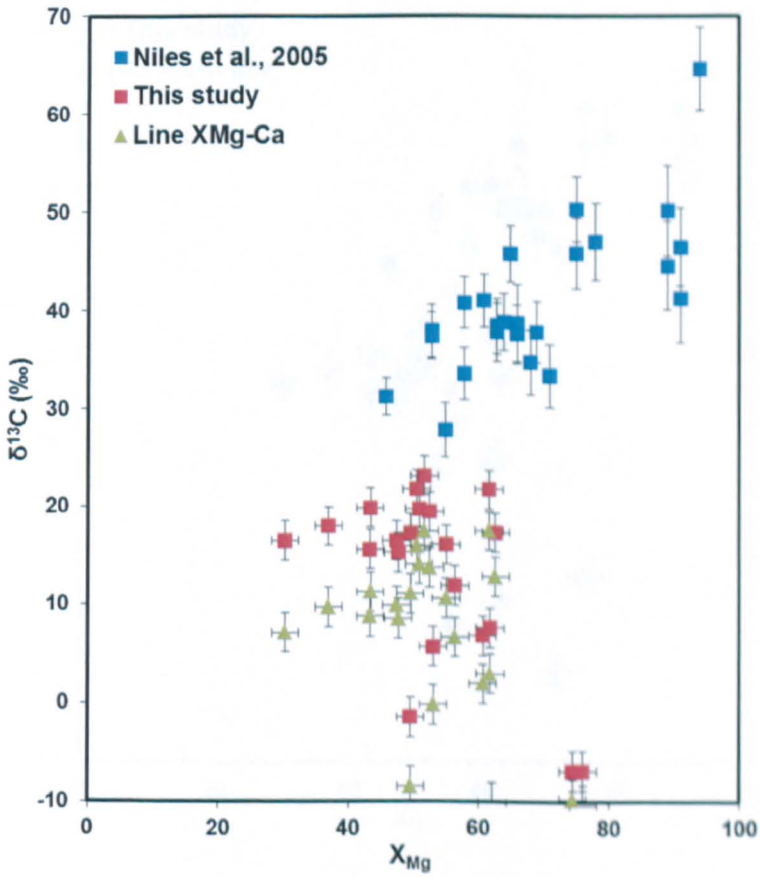

Figure 3.18 $\delta^{13}C$ values against magnesium content (X_{Mg}) from that used in this study, previous literature and when applying a linear IMF correction using $X_{Mg\text{-}Ca}$-rich standards (Fig. 3.17).

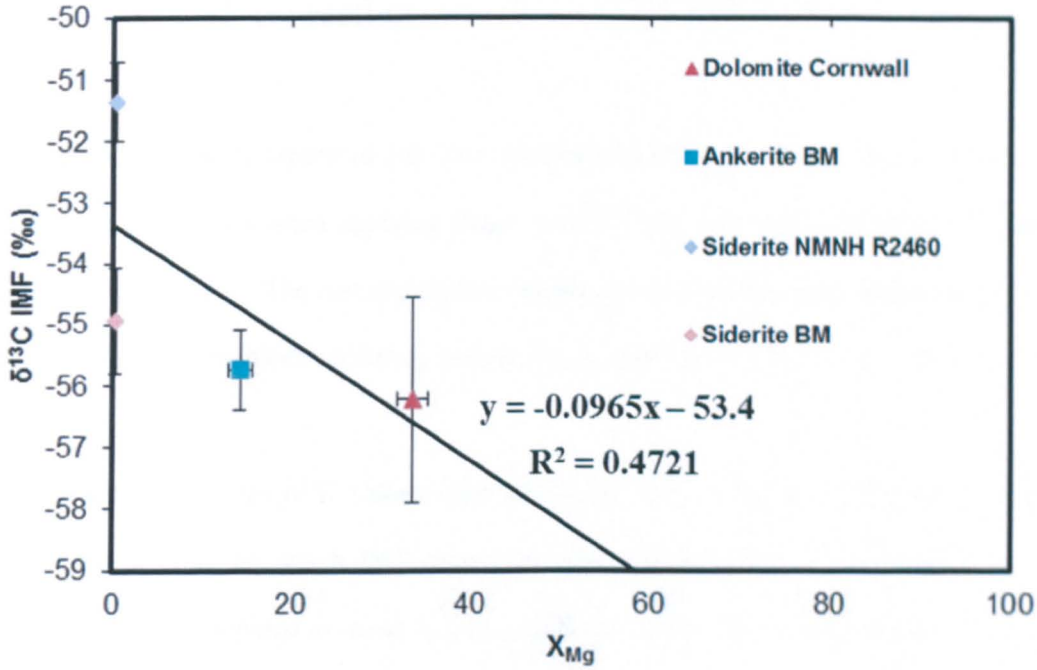

Figure 3.19 Linear fit for all carbonate standards according to their Fe+Mn content (X_{Fe+Mn}).

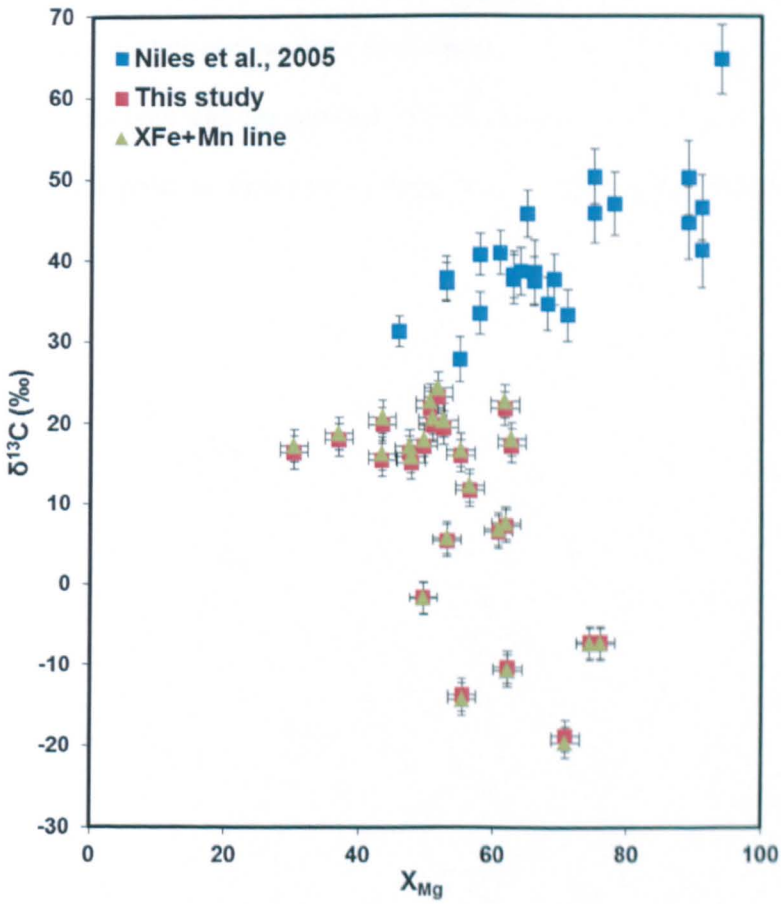

Figure 3.20 $\delta^{13}C$ values against magnesium content (X_{Mg}) from that used in this study, previous literature and when applying a linear IMF correction using X_{Fe+Mn}-rich standards (Fig. 3.19).

Choice of $\delta^{13}C$ IMF correction

When the carbonates were separated into two components ($X_{Mg\text{-}Ca}$-rich and X_{Fe+Mn}-rich) poor IMF correlations were observed when applying linear trends (Figs. 3.17 and 3.18; R^2=0.0732 and Figs. 3.19 and 3.20; R^2=0.4721). The best correlation was the one used in this study when applying a linear trend against all of the standards according to their X_{Fe+Mn}-content (Fig. 3.15 and 3.16; R^2=0.8822).

The ALH 84001 carbonates $\delta^{13}C$ values were shown to vary by up to 25.2‰ for a single point measurement depending on which IMF correction was applied (Table 3.2, Rosette (2) 17; linear X_{Fe+Mn}-rich (-10.4‰) compared to linear X_{Mg}-X_{Ca}–rich (+15.8‰)). This variation obviously has large implications for the isotopic compositions of the atmospheric CO_2 from which these carbonates formed and therefore the evolution of water $\delta^{13}C$ on Mars (Chapter 7.2.6). Simliarly to $\delta^{18}O$ an ideal correction will only be resolved with the addition of carbonate standards that are representative of the ALH 84001 carbonate composition, until then the best infered trends will be used (Figs. 3.2 and 3.3).

Appendix C – Geochemist work bench results

The first (0, 1 and 2) and final (105, 109 and 112) steps are included in the appendix, however the additional 96 steps are available on disc or can be requested through direct correspondence.

Step # 0 Xi = 0.0000
Time = 0 secs (0 days)

Temperature = 150.0 °C Pressure = 4.665 bars
pH = 9.800 log fO_2 = -17.604
Eh = 0.0246 volts pe = 0.2931
Ionic strength = 2.507557
Activity of water = 0.918307
Solvent mass = 15.000000 kg
Solution mass = 17.582200 kg
Solution density = 1.006 g/cm^3
Chlorinity = 2.918506 molal
Dissolved solids = 146864 mg/kg sol'n
Rock mass = 0.000000 kg
Carbonate alkalinity= 0.00 mg/kg as $CaCO_3$

Reactants	moles remaining	moles reacted	grams reacted	cm^3 reacted
Albite	0.04181	0	0	0
Anorthite	0.08502	0	0	0
CO_2(g)	6.03	0	0	0
Enstatite	4.462	0	0	0
Fayalite	0.000268	0	0	0
$FeCr_2O_4$	0.1035	0	0	0
Ferrosilite	1.755	0	0	0
Forsterite	0.000469	0	0	0
H_2O	0	0	0	0
Hydroxyapatite	0.00201	0	0	0
$MgCr_2O_4$	0.02439	0	0	0
Pyrite	0.00134	0	0	0
Sanidine high	0.007638	0	0	0
Wollastonite	0.2124	0	0	0

No minerals in system.

Aqueous species	molality	mg/kg sol'n	act. coef.	log act.
Na^+	2.484	4.87E+04	0.6003	0.1735
Cl^-	2.476	7.49E+04	0.5103	0.1016
NaCl	0.4369	2.18E+04	1	-0.3596
OH^-	0.0262	380.1	0.5577	-1.8353
NaOH	0.01266	432	1	-1.8975
$CaCl^+$	0.005461	351.9	0.6003	-2.4844
Ca^{++}	0.005235	179	0.1296	-3.1685
$CaOH^+$	0.002638	128.5	0.6003	-2.8004

(only species > 1e-8 molal listed)

Mineral saturation states

	log Q/K		log Q/K
Portlandite	0.2282s/sat	Halite	-1.1698
Ca(OH)2(c)	0.2282s/sat	Ferrite-Ca	-1.2961
Hydroxyapatite	-0.5604	Goethite	-2.271
Bixbyite	-0.7087	Pyrolusite	-2.5444
Hausmannite	-0.8322		

(only minerals with log Q/K > -3 listed)

Gases	fugacity	log fug.
Steam	4.142	0.617
$CO_2(g)$	1.07E-12	-11.971
$O_2(g)$	2.49E-18	-17.604
$H_2(g)$	8.13E-19	-18.09
$CH_4(g)$	4.49E-75	-74.348
$H_2S(g)$	1.33E-75	-74.877
$S_2(g)$	6.63E-129	-128.178

	Original basis Total moles mg/kg	In fluid moles mg/kg	Sorbed moles L/kg
Al^{+++}	1.00E-09	1.00E-09	1.53E-06
Ca^{++}	0.2	0.2	456
Cl^{-}	43.8	43.8	8.83E+04
Cr^{+++}	1.00E-09	1.00E-09	2.96E-06
Fe^{++}	1.00E-09	1.00E-09	3.18E-06
H^{+}	-0.622	-0.622	-35.7
H_2O	833	833	8.54E+05
HCO_3^{-}	1.00E-09	1.00E-09	3.47E-06
HPO_4^{--}	1.00E-09	1.00E-09	5.46E-06
K^{+}	1.00E-09	1.00E-09	2.22E-06
Mg^{++}	1.00E-09	1.00E-09	1.38E-06
Mn^{++}	1.00E-09	1.00E-09	3.12E-06
Na^{+}	44	44	5.75E+04
$O_2(aq)$	1.00E-09	1.00E-09	1.82E-06
SO_4^{--}	1.00E-09	1.00E-09	5.46E-06
$SiO_2(aq)$	1.00E-09	1.00E-09	3.42E-06

Elemental composition	Total moles	In fluid moles mg/kg	Sorbed moles mg/kg
Aluminum	1.00E-09	1.00E-09	1.54E-06
Calcium	0.2	0.2	455.9
Carbon	1.00E-09	1.00E-09	6.83E-07
Chlorine	43.78	43.78	8.83E+04
Chromium	1.00E-09	1.00E-09	2.96E-06
Hydrogen	1666	1666	9.55E+04
Iron	1.00E-09	1.00E-09	3.18E-06
Magnesium	1.00E-09	1.00E-09	1.38E-06
Manganese	1.00E-09	1.00E-09	3.13E-06
Oxygen	833.3	833.3	7.58E+05
Phosphorus	1.00E-09	1.00E-09	1.76E-06
Potassium	1.00E-09	1.00E-09	2.22E-06
Silicon	1.00E-09	1.00E-09	1.60E-06
Sodium	44	44	5.75E+04
Sulfur	1.00E-09	1.00E-09	1.82E-06

Step # 0 Xi = 0.0000
Time = 0 secs (0 days)

Temperature = 150.0°C Pressure = 4.665 bars
pH = 9.737 log fO_2 = -17.444
Eh = 0.0333 volts pe = 0.3965
Ionic strength = 2.503787
Activity of water = 0.918277
Solvent mass = 15.000000 kg
Solution mass = 17.578805 kg
Solution density = 1.006 g/cm^3
Chlorinity = 2.918506 molal
Dissolved solids = 146700 mg/kg sol'n
Rock mass = 0.003395 kg
Carbonate alkalinity= 0.00 mg/kg as $CaCO_3$

Reactants	moles remaining	moles reacted	grams reacted	cm^3 reacted
Albite	0.04181	0	0	0
Anorthite	0.08502	0	0	0
CO_2(g)	6.03	0	0	
Enstatite	4.462	0	0	0
Fayalite	0.000268	0	0	0
$FeCr_2O_4$	0.1035	0	0	0
Ferrosilite	1.755	0	0	0
Forsterite	0.000469	0	0	0
H_2O	0	0	0	
Hydroxyapatite	0.00201	0	0	0
$MgCr_2O_4$	0.02439	0	0	0
Pyrite	0.00134	0	0	0
Sanidine high	0.007638	0	0	0
Wollastonite	0.2124	0	0	0

Minerals in system	moles	log moles	grams	volume (cm^3)
$Ca(OH)_2$(c)	0.04582	-1.339	3.395	1.515
(total)		3.395	1.515	

Aqueous species	molality	mg/kg sol'n	act. coef.	log act.
Na^+	2.485	4.88E+04	0.6001	0.1736
Cl^-	2.477	7.49E+04	0.5103	0.1017
NaCl	0.4372	2.18E+04	1	-0.3593
OH^-	0.02264	328.5	0.5576	-1.8988
NaOH	0.01094	373.5	1	-1.9609

Aqueous species	molarity	mg/kg sol'n	act. coef.	log act.
$CaCl^+$	0.004327	278.9	0.6001	-2.5856
Ca^{++}	0.004146	141.8	0.1296	-3.2698
$CaOH^+$	0.001805	87.94	0.6001	-2.9652

(only species > 1e-8 molal listed)

Mineral saturation states

	log Q/K		log Q/K
$Ca(OH)_2(c)$	0.0000 sat	Hydroxyapatite	-1.3211
Portlandite	0.0000 sat	Ferrite-Ca	-1.519
Bixbyite	-0.7625	Goethite	-2.2683
Hausmannite	-0.9528	Pyrolusite	-2.5314
Halite	-1.1695		

(only minerals with log Q/K > -3 listed)

Gases	fugacity	log fug.
Steam	4.141	0.617
$CO_2(g)$	1.50E-12	-11.825
$O_2(g)$	3.60E-18	-17.444
$H_2(g)$	6.77E-19	-18.169
$CH_4(g)$	3.02E-75	-74.521
$H_2S(g)$	8.56E-76	-75.067
$S_2(g)$	3.987E-129	-128.399

Original basis	In fluid total moles mg/kg	Sorbed moles mg/kg	Kd moles L/kg
Al^{+++}	1.00E-09	1.00E-09	1.53E-06
Ca^{++}	0.2	0.154	352
Cl^-	43.8	43.8	8.83E+04
Cr^{+++}	1.00E-09	1.00E-09	2.96E-06
Fe^{++}	1.00E-09	1.00E-09	3.18E-06
H^+	-0.622	-0.531	-30.4
H_2O	833	833	8.54E+05
HCO_3^-	1.00E-09	1.00E-09	3.47E-06
HPO_4^{--}	1.00E-09	1.00E-09	5.46E-06
K^+	1.00E-09	1.00E-09	2.22E-06
Mg^{++}	1.00E-09	1.00E-09	1.38E-06
Mn^{++}	1.00E-09	1.00E-09	3.13E-06
Na^+	44	44	5.75E+04
$O_2(aq)$	1.00E-09	1.00E-09	1.82E-06
SO_4^{--}	1.00E-09	1.00E-09	5.46E-06
$SiO_2(aq)$	1.00E-09	1.00E-09	3.42E-06

Elemental composition		In fluid	Sorbed
	total moles	moles	moles
		mg/kg	mg/kg
Aluminum	1.00E-09	1.00E-09	1.54E-06
Calcium	0.2	0.1542	351.5
Carbon	1.00E-09	1.00E-09	6.83E-07
Chlorine	43.78	43.78	8.83E+04
Chromium	1.00E-09	1.00E-09	2.96E-06
Hydrogen	1666	1666	9.55E+04
Iron	1.00E-09	1.00E-09	3.18E-06
Magnesium	1.00E-09	1.00E-09	1.38E-06
Manganese	1.00E-09	1.00E-09	3.13E-06
Oxygen	833.3	833.2	7.58E+05
Phosphorus	1.00E-09	1.00E-09	1.76E-06
Potassium	1.00E-09	1.00E-09	2.22E-06
Silicon	1.00E-09	1.00E-09	1.60E-06
Sodium	44	44	5.75E+04
Sulfur	1.00E-09	1.00E-09	1.82E-06

Step # 1 Xi = 0.0100
Time = 3.15576e+012 secs (3.6525e+007 days)

Temperature = 148.5°C Pressure = 4.481 bars
pH = 9.612 log fO_2 = -51.973
Eh = -0.6742 volts pe = -8.0589
Ionic strength = 2.502355
Activity of water = 0.918031
Solvent mass = 15.001981 kg
Solution mass = 17.575332 kg
Solution density = 1.007 g/cm^3
Chlorinity = 2.918121 molal
Dissolved solids = 146418 mg/kg sol'n
Rock mass = 0.017223 kg
Carbonate alkalinity= 9.47 mg/kg as $CaCO_3$

Reactants	moles remaining	moles reacted	grams reacted	cm^3 reacted
Albite	0.04139	0.000418	0.1096	0.04191
Anorthite	0.08417	0.00085	0.2365	0.08569
CO_2(g)	5.97	0.0603	2.654	
Enstatite	4.418	0.04462	4.48	1.396
Fayalite	0.000265	2.68E-06	0.000546	0.000124
$FeCr_2O_4$	0.1025	0.001035	0.2317	0.04556
Ferrosilite	1.738	0.01755	2.316	0.6618
Forsterite	0.000464	4.69E-06	0.00066	0.000205
H_2O	0	. 0	0	
Hydroxyapatite	0.00199	2.01E-05	0.0101	0.003208
$MgCr_2O_4$	0.02414	0.000244	0.0469	0.01062
Pyrite	0.001327	1.34E-05	0.001608	0.000321
Sanidine high	0.007562	7.64E-05	0.02126	0.008325
Wollastonite	0.2103	0.002124	0.2467	0.08481

Minerals in system	moles	log moles	grams	volume (cm^3)
Andradite	0.009304	-2.031	4.728	1.225
Brucite	0.004058	-2.392	0.2367	0.09996
Calcite	0.05811	-1.236	5.816	2.146
Hydroxyapatite	2.01E-05	-4.697	0.01009	0.003207
$MgCr_2O_4$	0.001279	-2.893	0.246	0.05571
Monticellite	0.03953	-1.403	6.186	2.035
(total)			17.22	5.565

Aqueous species	molality	mg/kg sol'n	act. coef.	log act.
Na^+	2.493	4.89E+04	0.6019	0.1762
Cl^-	2.484	7.52E+04	0.5121	0.1045
NaCl	0.4322	2.16E+04	1	-0.3643
OH^-	0.01637	237.6	0.5595	-2.0383
NaOH	0.007979	272.4	1	-2.0981
$CaCl^+$	0.002287	147.5	0.6019	-2.8611
Ca^{++}	0.002195	75.09	0.1307	-3.5423
$CaOH^+$	0.000677	33	0.6019	-3.3898
$Al(OH)_4^-$	0.000146	11.86	0.6019	-4.0552
$CH_4(aq)$	0.000141	1.936	1.5419	-3.6615
$H_2(aq)$	5.37E-05	0.09239	1.5419	-4.082
K^+	4.79E-06	0.1597	0.5121	-5.6107
NaH_3SiO_4	2.42E-06	0.2441	1	-5.616
CO_3^{--}	1.77E-06	0.09074	0.0755	-6.8738
HCO_3^-	1.64E-06	0.0854	0.6401	-5.979
HS^-	1.39E-06	0.03929	0.5595	-6.1086
$CaCO_3$	8.01E-07	0.06847	1	-6.0961
S^{--}	3.93E-07	0.01076	0.0931	-7.4363
$H_3SiO_4^-$	3.62E-07	0.02936	0.6019	-6.6621
KCl	3.05E-07	0.01943	1	-6.5152
$NaHCO_3$	2.52E-07	0.01806	1	-6.5988
$MgOH^+$	1.71E-07	0.006023	0.6019	-6.988
$H_2SiO_4^{--}$	1.52E-07	0.01219	0.059	-8.0476
$SiO_2(aq)$	5.31E-08	0.002722	1.5419	-7.0871
$NaCO_3^-$	3.17E-08	0.002244	0.6019	-7.7197
Mg^{++}	2.89E-08	0.0006	0.2091	-8.2184
$MgCl^+$	2.85E-08	0.001455	0.6019	-7.7651
$CaHCO_3^+$	2.45E-08	0.002113	0.6874	-7.7738
$Al(OH)_3$	1.47E-08	0.000978	1	-7.8332

(only species > 1e-8 molal listed)

Mineral saturation states

	log Q/K		log Q/K
Brucite	0.0000 sat	Ferrite-Ca	-1.425
Andradite	0.0000 sat	Gibbsite	-1.4619
$MgCr_2O_4$	0.0000 sat	Monohydrocalcite	-1.7105
Monticellite	0.0000 sat	Boehmite	-1.7271
Calcite	0.0000 sat	Ca_2SiO_4(gamma)	-1.879
Hydroxyapatite	0.0000 sat	Akermanite	-1.9043
$FeCr_2O_4$	-0.0703	Goethite	-1.9295
Aragonite	-0.1614	Cr_2O_3	-2.0848
Clinochl-14A	-0.4803	Merwinite	-2.2282
$Ca(OH)_2(c)$	-0.5735	Ca_2SiO_4^7/6H_2O	-2.2562

	log Q/K		log Q/K
Portlandite	-0.5735	Smectite-Reykjan	-2.2883
FeO(c)	-0.6726	Magnetite	-2.3419
Grossular	-0.6749	Hematite	-2.4165
Wollastonite	-0.8839	$Fe(OH)_2$(ppd)	-2.4939
Amesite-14A	-0.9889	Forsterite	-2.5588
Pseudowollastoni	-1.0746	Wustite	-2.6615
Diopside	-1.1262	Larnite	-2.7954
Halite	-1.1693	Nepheline	-2.8135
Diaspore	-1.3315	Hercynite	-2.9739
Chrysotile	-1.409		

(only minerals with log Q/K > -3 listed)

Gases	fugacity	log fug.
Steam	3.982	0.6
CH_4(g)	0.1741	-0.759
H_2(g)	0.09366	-1.028
CO_2(g)	1.83E-07	-6.737
H_2S(g)	3.18E-09	-8.498
S_2(g)	1.90E-30	-29.722
O_2(g)	1.07E-52	-51.973

Original basis	In fluid Total moles mg/kg	Sorbed moles mg/kg	moles L/kg
Al^{+++}	0.00219	0.00219	3.37
Ca^{++}	0.203	0.0774	177
Cl^-	43.8	43.8	8.83E+04
Cr^{+++}	0.00256	6.24E-15	1.85E-11
Fe^{++}	0.0186	1.07E-08	3.41E-05
H^+	-0.71	-0.382	-21.9
H_2O	833	833	8.54E+05
HCO_3^-	0.0603	0.00219	7.6
HPO_4^{--}	6.03E-05	1.13E-08	6.15E-05
K^+	7.64E-05	7.64E-05	0.17
Mg^{++}	0.0449	3.42E-06	0.00474
Mn^{++}	1.00E-09	1.00E-09	3.13E-06
Na^+	44	44	5.76E+04
O_2(aq)	-4.69E-05	-0.0047	-8.56
$SO4^{--}$	2.68E-05	2.68E-05	0.146
SiO_2(aq)	0.0675	4.48E-05	0.153

Elemental composition	total moles	In fluid moles mg/kg	Sorbed moles mg/kg
Aluminum	0.002195	0.002195	3.37
Calcium	0.2031	0.07742	176.5
Carbon	0.0603	0.002189	1.496
Chlorine	43.78	43.78	8.83E+04
Chromium	0.002558	6.25E-15	1.85E-11
Hydrogen	1666	1666	9.55E+04
Iron	0.01861	1.07E-08	3.41E-05
Magnesium	0.04488	3.42E-06	0.004736
Manganese	1.00E-09	1.00E-09	3.13E-06
Oxygen	833.6	833.1	7.58E+05
Phosphorus	6.03E-05	1.13E-08	1.99E-05
Potassium	7.64E-05	7.64E-05	0.1699
Silicon	0.06749	4.48E-05	0.07162
Sodium	44	44	5.76E+04
Sulfur	2.68E-05	2.68E-05	0.04889

Step # 2 Xi = 0.0200
Time = 6.31152e+012 secs (7.305e+007 days)

Temperature = 147.0 C Pressure = 4.304 bars
pH = 9.481 log fO_2 = -51.919
Eh = -0.6554 volts pe = -7.8623
Ionic strength = 2.502557
Activity of water = 0.917787
Solvent mass = 15.002155 kg
Solution mass = 17.571248 kg
Solution density = 1.008 g/cm^3
Chlorinity = 2.918087 molal
Dissolved solids = 146210 mg/kg sol'n
Rock mass = 0.031661 kg
Carbonate alkalinity= 19.64 mg/kg as $CaCO_3$

Reactants	moles remaining	moles reacted	grams reacted	cm^3 reacted
Albite	0.04097	0.000836	0.2193	0.08383
Anorthite	0.08332	0.0017	0.4731	0.1714
CO_2(g)	5.909	0.1206	5.308	
Enstatite	4.373	0.08924	8.959	2.791
Fayalite	0.000263	5.36E-06	0.001092	0.000249
$FeCr_2O_4$	0.1014	0.00207	0.4634	0.09111
Ferrosilite	1.72	0.03511	4.632	1.324
Forsterite	0.00046	9.38E-06	0.00132	0.000411
H_2O	0	0	0	
Hydroxyapatite	0.00197	4.02E-05	0.02019	0.006416
$MgCr_2O_4$	0.0239	0.000488	0.09379	0.02125
Pyrite	0.001313	2.68E-05	0.003215	0.000642
Sanidine high	0.007485	0.000153	0.04252	0.01665
Wollastonite	0.2081	0.004248	0.4934	0.1696

Minerals in system	moles	log moles	grams	volume (cm^3)
Andradite	0.01861	-1.73	9.456	2.451
Antigorite	0.002645	-2.578	5.998	4.626
Calcite	0.1158	-0.936	11.59	4.278
Clinochl-14A	0.001964	-2.707	1.092	0.4068
Diopside	0.0139	-1.857	3.009	0.9184
Hydroxyapatite	4.02E-05	-4.396	0.02017	0.006409
$MgCr_2O_4$	0.002558	-2.592	0.4919	0.1114
(total)		31.66	12.80	

Aqueous species	molality	mg/kg sol'n	act. coef.	log act.
Na^+	2.5	4.91E+04	0.6037	0.1788
Cl^-	2.49	7.54E+04	0.514	0.1072
NaCl	0.4272	2.13E+04	1	-0.3693
OH^-	0.01166	169.2	0.5613	-2.1843
NaOH	0.005731	195.7	1	-2.2418
$CaCl^+$	0.000627	40.42	0.6037	-3.4221
Ca^{++}	0.000602	20.6	0.1318	-4.1005
$CH_4(aq)$	0.0003	4.112	1.5416	-3.3346
$CaOH^+$	0.00013	6.319	0.6037	-4.1064
$H_2(aq)$	3.77E-05	0.06491	1.5416	-4.2355
$Al(OH)_4^-$	3.08E-05	2.494	0.6037	-4.7314
NaH_3SiO_4	2.81E-05	2.829	1	-4.5519
K^+	9.57E-06	0.3196	0.514	-5.308
HCO_3^-	8.32E-06	0.4335	0.6419	-5.2724
CO_3^{--}	6.75E-06	0.346	0.0763	-6.288
$H_3SiO_4^-$	4.11E-06	0.3337	0.6037	-5.6053
HS^-	2.99E-06	0.08442	0.5613	-5.7751
$NaHCO_3$	1.33E-06	0.09511	1	-5.8775
$H_2SiO_4^{--}$	1.23E-06	0.09853	0.0597	-7.1353
$CaCO_3$	8.23E-07	0.07033	1	-6.0846
$SiO_2(aq)$	8.18E-07	0.04196	1.5416	-5.8994
KCl	6.09E-07	0.03878	1	-6.2152
S^{--}	5.80E-07	0.01586	0.094	-7.2637
$NaCO_3^-$	1.28E-07	0.009092	0.6037	-7.1109
$MgOH^+$	9.21E-08	0.00325	0.6037	-7.2547
$CaHCO_3^+$	3.40E-08	0.002931	0.6892	-7.6307
Mg^{++}	2.25E-08	0.000467	0.2105	-8.3241
$MgCl^+$	2.19E-08	0.00112	0.6037	-7.8779
$CO_2(aq)$	1.01E-08	0.00038	1	-7.995

(only species > 1e-8 molal listed)

Mineral saturation states

	log Q/K		log Q/K
Antigorite	0.0000 sat	Cr_2O_3	-1.6746
Calcite	0.0000 sat	Monohydrocalcite	-1.6996
$MgCr_2O_4$	0.0000 sat	Diaspore	-1.8737
Hydroxyapatite	0.0000 sat	Saponite-Na	-1.9692
Diopside	0.0000 sat	Gibbsite	-1.9956
Clinochl-14A	0.0000 sat	Forsterite	-2.1951
Andradite	0.0000 sat	Enstatite	-2.2605
Monticellite	-0.0846	Boehmite	-2.2732

	log Q/K		log Q/K
Aragonite	-0.1613	Saponite-Ca	-2.2778
Chrysotile	-0.2289	Nepheline	-2.3062
$FeCr_2O_4$	-0.2308	Amesite-14A	-2.3911
Brucite	-0.4118	Ca_2SiO_4(gamma)	-2.4265
Wollastonite	-0.5513	Goethite	-2.4385
Smectite-Reykjan	-0.5798	Phlogopite	-2.5231
Pseudowollastoni	-0.7438	Clinochl-7A	-2.7372
Grossular	-0.7484	Prehnite	-2.7705
Halite	-1.1691	Ca_2SiO_4^7/6H_2O	-2.7945
FeO(c)	-1.2545	Saponite-Mg	-2.8111
$Ca(OH)_2$(c)	-1.4454	Dolomite-ord	-2.8382
Portlandite	-1.4454	Dolomite	-2.8396
Akermanite	-1.6631	Merwinite	-2.8657

(only minerals with log Q/K > -3 listed)

Gases	fugacity	log fug.
Steam	3.827	0.583
CO_2(g)	0.3727	-0.429
O_2(g)	0.06621	-1.179
H_2(g)	1.22E-06	-5.913
CH_4(g)	1.02E-08	-7.991
H_2S(g)	2.61E-29	-28.583
S_2(g)	1.20E-52	-51.919

Original basis	In fluid Total moles mg/kg	Sorbed moles mg/kg	moles L/kg
Al^{+++}	0.00439	0.000461	0.708
Ca^{++}	0.206	0.0204	46.5
Cl^-	43.8	43.8	8.83E+04
Cr^{+++}	0.00512	7.93E-15	2.35E-11
Fe^{++}	0.0372	2.96E-09	9.41E-06
H^+	-0.797	-0.261	-15
H_2O	833	833	8.54E+05
HCO_3^-	0.121	0.00476	16.5
HPO_4^{--}	0.000121	1.40E-07	0.000767
K^+	0.000153	0.000153	0.34
Mg^{++}	0.0898	2.05E-06	0.00284
Mn^{++}	1.00E-09	1.00E-09	3.13E-06
Na^+	44	44	5.76E+04
O_2(aq)	-9.38E-05	-0.0094	-17.1
SO_4^{--}	5.36E-05	5.36E-05	0.293
SiO_2(aq)	0.135	0.000513	1.76

Elemental composition	total moles	In fluid moles mg/kg	Sorbed moles mg/kg
Aluminum	0.00439	0.000461	0.7084
Calcium	0.2061	0.02039	46.52
Carbon	0.1206	0.004765	3.257
Chlorine	43.78	43.78	8.83E+04
Chromium	0.005116	7.93E-15	2.35E-11
Hydrogen	1666	1666	9.56E+04
Iron	0.03722	2.96E-09	9.41E-06
Magnesium	0.08975	2.05E-06	0.002835
Manganese	1.00E-09	1.00E-09	3.13E-06
Oxygen	833.9	833	7.59E+05
Phosphorus	0.000121	1.40E-07	0.000248
Potassium	0.000153	0.000153	0.3399
Silicon	0.135	0.000513	0.8204
Sodium	44	44	5.76E+04
Sulfur	5.36E-05	5.36E-05	0.0978

Step # 102 Xi = 0.9000
Time = 2.84018e+014 secs (3.28725e+009 days)

Temperature = 15.0°C Pressure = 1.013 bars
pH = 7.860 log fO2 = -75.711
Eh = -0.2991 volts pe = -5.2309
Ionic strength = 2.863162
Activity of water = 0.904083
Solvent mass = 14.993677 kg
Solution mass = 17.578140 kg
Solution density = 1.093 g/cm^3
Chlorinity = 2.919737 molal
Dissolved solids = 147027 mg/kg sol'n
Rock mass = 0.946857 kg
Carbonate alkalinity= 995.80 mg/kg as $CaCO_3$

Reactants	moles remaining	moles reacted	grams reacted	cm^3 reacted
Albite	0.004181	0.03763	9.867	3.772
Anorthite	0.008502	0.07652	21.29	7.713
CO_2(g)	0.603	5.427	238.8	
Enstatite	0.4462	4.016	403.2	125.6
Fayalite	2.68E-05	0.000241	0.04915	0.01119
$FeCr_2O_4$	0.01035	0.09316	20.85	4.1
Ferrosilite	0.1755	1.58	208.4	59.56
Forsterite	4.69E-05	0.000422	0.05939	0.01848
H_2O	0	0	0	
Hydroxyapatite	0.000201	0.001809	0.9087	0.2887
$MgCr_2O_4$	0.002439	0.02195	4.221	0.9561
Pyrite	0.000134	0.001206	0.1447	0.02887
Sanidine high	0.000764	0.006874	1.913	0.7493
Wollastonite	0.02124	0.1912	22.2	7.633

Minerals in system	moles	log moles	grams	volume (cm^3)
Dawsonite	0.0824	-1.084	11.86	4.886
Dolomite	0.5253	-0.28	96.88	33.81
$FeCr_2O_4$	0.1151	-0.939	25.77	5.066
Hydroxyapatite	0.02004	-1.698	10.07	3.198
Magnesite	2.549	0.406	214.9	71.41
Nontronit-Na	0.08332	-1.079	35.43	14.16
Pyrite	0.001206	-2.919	0.1447	0.02887
Quartz	4.793	0.681	288	108.7
Saponite-Na	0.2656	-0.576	102.7	36.31
Siderite	1.391	0.143	161.2	39.83
(total)			946.9	317.4

Aqueous species	molality	mg/kg sol'n	act. coef.	log act.
Cl-	2.85	8.62E+04	0.589	0.2249
Na+	2.842	5.57E+04	0.6682	0.2785
NaCl	0.0639	3185	1	-1.1945
NaHCO3	0.01488	1066	1	-1.8275
HCO3-	0.006788	353.3	0.7011	-2.3225
MgCl+	0.006064	309.1	0.6682	-2.3924
Mg++	0.005017	104	0.2912	-2.8353
CH4(aq)	0.001389	19.01	1.9167	-2.5747
K+	0.000449	14.96	0.589	-3.5781
NaHPO4-	0.000212	21.48	0.6682	-3.8494
CO2(aq)	0.000199	7.451	1	-3.7023
NaCO3-	0.000146	10.37	0.6682	-4.0095
MgHCO3+	0.000103	7.485	0.6682	-4.1629
CO3--	9.48E-05	4.853	0.1312	-4.9052
HPO4--	7.77E-05	6.362	0.1082	-5.0751
CaCl+	6.60E-05	4.251	0.6682	-4.3557
SiO2(aq)	3.37E-05	1.725	1.9167	-4.1904
Ca++	2.09E-05	0.7151	0.2015	-5.3752
Fe++	1.33E-05	0.6343	0.2015	-5.5713
MgCO3	1.21E-05	0.8678	1	-4.9184
NaH3SiO4	1.19E-05	1.199	1	-4.9245
FeCl+	1.06E-05	0.8246	0.6682	-5.1503
KCl	9.87E-06	0.6279	1	-5.0055
MgHPO4	8.52E-06	0.874	1	-5.0696
FeCl2	6.27E-06	0.6783	1	-5.2025
H2PO4-	3.02E-06	0.2494	0.6682	-5.6959
MgPO4-	1.27E-06	0.1294	0.6682	-6.0707
H3SiO4-	6.45E-07	0.05234	0.6682	-6.3654
FeHCO3+	4.93E-07	0.04911	0.6682	-6.4826
OH-	4.71E-07	0.006838	0.6311	-6.5265
CaHCO3+	4.16E-07	0.03585	0.7413	-6.5112
NaOH	3.54E-07	0.01208	1	-6.4511
FeCO3	3.03E-07	0.02995	1	-6.5185
MgH2PO4+	1.22E-07	0.01258	0.6682	-7.0901
MgOH+	9.15E-08	0.003223	0.6682	-7.2138
FeHPO4	7.56E-08	0.009787	1	-7.1216
CaCO3	7.42E-08	0.00633	1	-7.1299
PO4---	4.53E-08	0.00367	0.0052	-9.6269
CH3COO-	4.24E-08	0.002136	0.7011	-7.5268
KHPO4-	2.62E-08	0.00302	0.6682	-7.7566
FePO4-	1.96E-08	0.002524	0.6682	-7.8823
CaHPO4	1.68E-08	0.001948	1	-7.7751
H+	1.56E-08	1.34E-05	0.8847	-7.8598

(only species > 1e-8 molal listed)

Mineral saturation states

	log Q/K		log Q/K
		Maximum	
Quartz	0.0000 sat	Microcli	-1.3664
Dolomite	0.0000 sat	K-feldspar	-1.3679
Pyrite	0.0000 sat	Amrph^silica	-1.3693
FeCr2O4	0.0000 sat	Gibbsite	-1.4504
Hydroxyapatite	0.0000 sat	Dolomite-dis	-1.6196
Saponite-Na	0.0000 sat	Saponite-H	-1.6571
Dawsonite	0.0000 sat	Calcite	-1.6918
Siderite	0.0000 sat	Hematite	-1.7175
Magnesite	0.0000 sat	Greenalite	-1.7566
Nontronit-Na	0.0000 sat	Mordenite-Na	-1.8222
Dolomite-ord	-0.0000 sat	FeO(c)	-1.8261
Smectite-Reykjan	-0.0519	Aragonite	-1.8578
Tridymite	-0.1754	Ferrosilite	-1.8627
Chalcedony	-0.2807	Graphite	-1.9842
Vivianite	-0.4205	Mordenite-K	-1.9888
Saponite-Mg	-0.5393	Pyrrhotite	-2.0691
Nontronit-Mg	-0.5405	Albite high	-2.0826
Cristobalite	-0.5738	Cr2O3	-2.1541
Albite low	-0.6964	Annite	-2.1818
Albite	-0.6964	Troilite	-2.2433
Talc	-0.8014	Diaspore	-2.2877
Nontronit-K	-0.9083	Jadeite	-2.3192
Saponite-K	-0.9117	Magnetite	-2.3921
Analcime	-0.9284	Kaolinite	-2.4375
Phengite	-0.9587	Smectite-low-Fe-	-2.5394
Saponite-Ca	-0.9587	Cronstedt-7A	-2.5835
Nontronit-Ca	-0.9588	Sanidine high	-2.6337
Minnesotaite	-1.0563	Monohydrocalcite	-2.7099
Halite	-1.0597	Phlogopite	-2.7846
Whitlockite	-1.1297	Muscovite	-2.8211
Goethite	-1.3435	Chrysotile	-2.8559

(only minerals with log Q/K > -3 listed)

Gases	fugacity	log fug.
Steam	1.506	0.178
$CO_2(g)$	0.01513	-1.82
$O_2(g)$	0.00418	-2.379
$H_2(g)$	3.19E-06	-5.496
$CH_4(g)$	7.53E-09	-8.123
$H_2S(g)$	1.26E-32	-31.899
$S_2(g)$	1.94E-76	-75.711

Original basis	In fluid Total moles mg/kg	Sorbed moles mg/kg	moles L/kg
Al^{+++}	0.198	9.37E-08	0.000144
Ca^{++}	0.627	0.00131	2.99
Cl^{-}	43.8	43.8	8.83E+04
Cr^{+++}	0.23	8.28E-15	2.45E-11
Fe^{++}	1.67	0.000466	1.48
H^{+}	-8.6	0.0198	1.14
H_2O	834	832	8.53E+05
HCO_3^{-}	5.43	0.354	1.23E+03
HPO_4^{--}	0.0646	0.00454	24.8
K^{+}	0.00687	0.00687	15.3
Mg^{++}	4.04	0.168	232
Mn^{++}	1.00E-09	1.00E-09	3.13E-06
Na^{+}	44	43.8	5.73E+04
$O_2(aq)$	-0.00422	-0.0417	-75.8
SO_4^{--}	0.00241	1.53E-07	0.000834
$SiO_2(aq)$	6.07	0.000693	2.37

Elemental composition	total moles	In fluid moles mg/kg	Sorbed moles mg/kg
Aluminum	0.1975	9.37E-08	0.000144
Calcium	0.6268	0.001311	2.988
Carbon	5.427	0.354	241.9
Chlorine	43.78	43.78	8.83E+04
Chromium	0.2302	8.30E-15	2.45E-11
Hydrogen	1666	1665	9.55E+04
Iron	1.675	0.000466	1.481
Magnesium	4.039	0.168	232.3
Manganese	1.00E-09	1.00E-09	3.13E-06
Oxygen	863.2	833.3	7.59E+05
Phosphorus	0.06465	0.004536	7.993
Potassium	0.006874	0.006874	15.29
Silicon	6.074	0.000693	1.107
Sodium	43.99	43.8	5.73E+04
Sulfur	0.002412	1.53E-07	0.000279

Step # 105 Xi = 0.9300
Time = 2.93486e+014 secs (3.39683e+009 days)

Temperature = 10.5°C Pressure = 1.013 bars
pH = 7.994 log fO_2 = -77.157
Eh = -0.3024 volts pe = -5.3724
Ionic strength = 2.870942
Activity of water = 0.903809
Solvent mass = 14.992757 kg
Solution mass = 17.578182 kg
Solution density = 1.096 g/cm^3
Chlorinity = 2.919916 molal
Dissolved solids = 147081 mg/kg sol'n
Rock mass = 0.977879 kg
Carbonate alkalinity= 1067.04 mg/kg as $CaCO_3$

Reactants	moles remaining	moles reacted	grams reacted	cm^3 reacted
Albite	0.002927	0.03888	10.2	3.898
Anorthite	0.005952	0.07907	22	7.97
CO_2(g)	0.4221	5.608	246.8	
Enstatite	0.3124	4.15	416.6	129.8
Fayalite	1.88E-05	0.000249	0.05079	0.01156
$FeCr_2O_4$	0.007246	0.09627	21.55	4.237
Ferrosilite	0.1229	1.633	215.4	61.55
Forsterite	3.28E-05	0.000436	0.06137	0.0191
H_2O	0	0	0	
Hydroxyapatite	0.000141	0.001869	0.939	0.2983
$MgCr_2O_4$	0.001707	0.02268	4.361	0.988
Pyrite	9.38E-05	0.001246	0.1495	0.02983
Sanidine high	0.000535	0.007103	1.977	0.7743
Wollastonite	0.01487	0.1975	22.94	7.887

Minerals in system	moles	log moles	grams	volume (cm^3)
Dawsonite	0.08097	-1.092	11.66	4.802
Dolomite-ord	0.535	-0.272	98.65	34.42
FeCr2O4	0.1189	-0.925	26.63	5.235
Hydroxyapatite	0.01998	-1.699	10.04	3.189
Magnesite	2.73	0.436	230.2	76.48
Nontronit-Na	0.1294	-0.888	55.04	22
Pyrite	0.001246	-2.904	0.1495	0.02983
Quartz	4.906	0.691	294.8	111.3
Saponite-Na	0.2438	-0.613	94.22	33.32
Siderite	1.351	0.131	156.5	38.68
(total)			977.9	329.5

Aqueous species	molality	mg/kg sol'n	act. coef.	log act.
Cl^-	2.857	8.64E+04	0.5795	0.219
Na^+	2.849	5.59E+04	0.657	0.2723
NaCl	0.05593	2788	1	-1.2523
$NaHCO_3$	0.01562	1119	1	-1.8062
HCO_3^-	0.006721	349.8	0.6893	-2.3342
$MgCl^+$	0.006607	336.8	0.657	-2.3624
Mg^{++}	0.005089	105.5	0.2873	-2.8351
$CH_4(aq)$	0.002158	29.53	1.9447	-2.3771
K^+	0.000465	15.49	0.5795	-3.57
$NaHPO_4^-$	0.000214	21.75	0.657	-3.8513
$NaCO_3^-$	0.000196	13.87	0.657	-3.8903
$CO_2(aq)$	0.000152	5.699	1	-3.8187
CO_3^{--}	0.000115	5.873	0.1298	-4.8269
$MgHCO_3^+$	0.000101	7.313	0.657	-4.1803
HPO_4^{--}	9.67E-05	7.913	0.1072	-4.9846
$CaCl^+$	6.03E-05	3.885	0.657	-4.402
$SiO_2(aq)$	2.71E-05	1.39	1.9447	-4.2777
Ca^{++}	1.73E-05	0.5921	0.1991	-5.4624
$MgCO_3$	1.30E-05	0.9336	1	-4.8866
Fe^{++}	1.24E-05	0.5899	0.1991	-5.6081
NaH_3SiO_4	1.13E-05	1.143	1	-4.9453
$MgHPO_4$	9.80E-06	1.005	1	-5.0089
KCl	9.25E-06	0.5883	1	-5.0337
$FeCl^+$	8.05E-06	0.6268	0.657	-5.2767
$FeCl_2$	4.64E-06	0.5021	1	-5.3331
$H_2PO_4^-$	2.90E-06	0.2398	0.657	-5.7201
$MgPO_4^-$	1.78E-06	0.1806	0.657	-5.9331
$H_3SiO_4^-$	6.29E-07	0.05099	0.657	-6.3841
$FeHCO_3^+$	5.08E-07	0.05062	0.657	-6.4767
OH^-	4.44E-07	0.006445	0.6207	-6.5594
$FeCO_3$	4.41E-07	0.0436	1	-6.3553
$CaHCO_3^+$	3.33E-07	0.02875	0.7287	-6.6145
NaOH	3.21E-07	0.01094	1	-6.4939
$MgH_2PO_4^+$	1.09E-07	0.01127	0.657	-7.1453
$MgOH^+$	8.22E-08	0.002897	0.657	-7.2674
$FeHPO_4$	7.93E-08	0.01027	1	-7.1007
PO_4^{---}	6.82E-08	0.005526	0.0052	-9.4483
$CaCO_3$	6.82E-08	0.00582	1	-7.1664
CH_3COO^-	6.48E-08	0.003261	0.6893	-7.3504
$KHPO_4^-$	2.93E-08	0.003375	0.657	-7.7156
$FePO_4^-$	2.49E-08	0.003197	0.657	-7.787
$CaHPO_4$	1.58E-08	0.001833	1	-7.8014
H^+	1.17E-08	1.00E-05	0.869	-7.9941

(only species > 1e-8 molal listed)

Mineral saturation states

	log Q/K		log Q/K
Magnesite	0.0000 sat	K-feldspar	-1.3365
Saponite-Na	0.0000 sat	Goethite	-1.3635
Nontronit-Na	0.0000 sat	Amrph^silica	-1.4082
Dawsonite	0.0000 sat	Gibbsite	-1.5048
Pyrite	0.0000 sat	Dolomite-dis	-1.6546
Hydroxyapatite	0.0000 sat	Saponite-H	-1.6966
FeCr2O4	0.0000 sat	Calcite	-1.7211
Dolomite-ord	0.0000 sat	Greenalite	-1.7219
Siderite	0.0000 sat	Hematite	-1.7712
Quartz	0.0000 sat	FeO(c)	-1.8614
Dolomite	0	Aragonite	-1.8877
Smectite-Reykjan	-0.11	Ferrosilite	-1.8891
Tridymite	-0.1799	Mordenite-Na	-1.8906
Vivianite	-0.2247	Graphite	-1.9245
Chalcedony	-0.2851	Mordenite-K	-1.9704
Saponite-Mg	-0.5638	Pyrrhotite	-2.098
Nontronit-Mg	-0.5655	Annite	-2.1269
Cristobalite	-0.5844	Cr2O3	-2.1771
Albite low	-0.7594	Albite high	-2.1772
Albite	-0.7595	Troilite	-2.2641
Talc	-0.8027	Jadeite	-2.3813
Nontronit-K	-0.8872	Diaspore	-2.3834
Saponite-K	-0.8924	Magnetite	-2.4615
Phengite	-0.9016	Kaolinite	-2.5796
Saponite-Ca	-0.9892	Cronstedt-7A	-2.5961
Nontronit-Ca	-0.9893	Smectite-low-Fe-	-2.6222
Analcime	-0.9941	Sanidine high	-2.6335
Minnesotaite	-1.0367	Monohydrocalcite	-2.7327
Halite	-1.0559	Phlogopite	-2.7713
Whitlockite	-1.1557	Chrysotile	-2.8684
Maximum Microcli	-1.3345	Muscovite	-2.9343

(only minerals with log Q/K > -3 listed)

Gases	fugacity	log fug.
Steam	2.233	0.349
$CO_2(g)$	0.01129	-1.947
$O_2(g)$	0.002824	-2.549
$H_2(g)$	2.56E-06	-5.591
$CH_4(g)$	4.53E-09	-8.344
$H_2S(g)$	2.34E-33	-32.631
$S_2(g)$	6.97E-78	-77.157

Original basis	Total moles mg/kg	In fluid moles mg/kg	Sorbed moles L/kg
Al^{+++}	0.204	5.49E-08	8.43E-05
Ca^{++}	0.636	0.00117	2.67
Cl^{-}	43.8	43.8	8.83E+04
Cr^{+++}	0.238	6.76E-15	2.00E-11
Fe^{++}	1.73	0.000392	1.25
H^{+}	-8.87	0.0296	1.7
H_2O	835	832	8.53E+05
HCO_3^{-}	5.61	0.376	1.31E+03
HPO_4^{--}	0.0648	0.00488	26.7
K^{+}	0.0071	0.0071	15.8
Mg^{++}	4.17	0.177	245
Mn^{++}	1.00E-09	1.00E-09	3.13E-06
Na^{+}	44	43.8	5.73E+04
$O_2(aq)$	-0.00436	-0.0647	-118
SO_4^{--}	0.00249	1.22E-07	0.000667
$SiO_2(aq)$	6.28	0.000586	2

Elemental composition	total moles	In fluid moles mg/kg	Sorbed moles mg/kg
Aluminum	0.2041	5.49E-08	8.43E-05
Calcium	0.6361	0.00117	2.668
Carbon	5.608	0.376	256.9
Chlorine	43.78	43.78	8.83E+04
Chromium	0.2379	6.79E-15	2.01E-11
Hydrogen	1666	1665	9.55E+04
Iron	1.731	0.000392	1.245
Magnesium	4.173	0.1772	245.1
Manganese	1.00E-09	1.00E-09	3.13E-06
Oxygen	864.2	833.3	7.58E+05
Phosphorus	0.06483	0.004885	8.607
Potassium	0.007103	0.007103	15.8
Silicon	6.277	0.000586	0.9367
Sodium	44	43.79	5.73E+04
Sulfur	0.002492	1.22E-07	0.000223

Step # 109 Xi = 0.9700
Time = 3.06109e+014 secs (3.54293e+009 days)

Temperature = 4.5°C Pressure = 1.013 bars
pH = 8.182 log fO_2 = -79.150
Eh = -0.3068 volts pe = -5.5700
Ionic strength = 2.881297
Activity of water = 0.903455
Solvent mass = 14.986719 kg
Solution mass = 17.573713 kg
Solution density = 1.100 g/cm^3
Chlorinity = 2.921092 molal
Dissolved solids = 147208 mg/kg sol'n
Rock mass = 1.023768 kg
Carbonate alkalinity= 1201.29 mg/kg as $CaCO_3$

Reactants	moles remaining	moles reacted	grams reacted	cm^3 reacted
Albite	0.001254	0.04055	10.63	4.066
Anorthite	0.002551	0.08247	22.94	8.312
CO_2(g)	0.1809	5.849	257.4	
Enstatite	0.1339	4.328	434.5	135.4
Fayalite	8.04E-06	0.00026	0.05297	0.01206
$FeCr_2O_4$	0.003105	0.1004	22.48	4.419
Ferrosilite	0.05266	1.703	224.6	64.19
Forsterite	1.41E-05	0.000455	0.06401	0.01992
H_2O	0	0	0	
Hydroxyapatite	6.03E-05	0.00195	0.9794	0.3112
$MgCr_2O_4$	0.0007316	0.02366	4.549	1.03
Pyrite	4.02E-05	0.0013	0.1559	0.03112
Sanidine high	0.0002291	0.007409	2.062	0.8076
Wollastonite	0.006372	0.206	23.93	8.226

Minerals in system	moles	log moles	grams	volume (cm^3)
Dawsonite	0.07217	-1.142	10.39	4.28
Dolomite-ord	0.6474	-0.189	119.4	41.65
$FeCr_2O_4$	0.1241	-0.906	27.77	5.46
Magnesite	2.95	0.47	248.8	82.66
Nontronit-Na	0.2382	-0.623	101.3	40.49
Pyrite	0.0013	-2.886	0.1559	0.03112
Quartz	4.981	0.697	299.3	113
Saponite-Na	0.1883	-0.725	72.77	25.74
Siderite	1.113	0.047	129	31.87
Vivianite	0.02989	-1.524	14.99	5.596
(total)			1024	350.8

Aqueous species	molality	mg/kg sol'n	act. coef.	log act.
Cl^-	2.867	8.67E+04	0.5644	0.2091
Na^+	2.858	5.60E+04	0.6396	0.262
NaCl	0.04622	2304	1	-1.3352
$NaHCO_3$	0.01665	1193	1	-1.7787
$MgCl^+$	0.007423	378.3	0.6396	-2.3235
HCO_3^-	0.006653	346.2	0.6709	-2.3503
Mg^{++}	0.005149	106.7	0.2806	-2.8403
CH_4(aq)	0.003973	54.35	1.9857	-2.103
K^+	0.000486	16.2	0.5644	-3.5618
$NaCO_3^-$	0.000289	20.47	0.6396	-3.7329
$NaHPO_4^-$	0.000211	21.42	0.6396	-3.8696
CO_3^{--}	0.000149	7.641	0.1272	-4.7214
HPO_4^{--}	0.000125	10.22	0.1051	-4.8819
CO_2(aq)	0.000105	3.954	1	-3.9774
$MgHCO_3^+$	9.70E-05	7.06	0.6396	-4.2072
$CaCl^+$	5.31E-05	3.42	0.6396	-4.469
SiO_2(aq)	2.00E-05	1.027	1.9857	-4.4002
$MgCO_3$	1.39E-05	0.9995	1	-4.857
Ca^{++}	1.33E-05	0.4528	0.1947	-5.5884
$MgHPO_4$	1.12E-05	1.15	1	-4.9504
Fe^{++}	1.11E-05	0.5295	0.1947	-5.6645
NaH_3SiO_4	1.05E-05	1.058	1	-4.9785
KCl	8.37E-06	0.5321	1	-5.0773
$FeCl^+$	5.49E-06	0.4272	0.6396	-5.4548
$FeCl_2$	3.02E-06	0.326	1	-5.5206
$H_2PO_4^-$	2.63E-06	0.2176	0.6396	-5.774
$MgPO_4^-$	2.62E-06	0.2662	0.6396	-5.7763
$FeCO_3$	7.28E-07	0.07189	1	-6.1381
$H_3SiO_4^-$	6.07E-07	0.04922	0.6396	-6.411
$FeHCO_3^+$	5.28E-07	0.05264	0.6396	-6.4713
OH^-	4.10E-07	0.005947	0.6044	-6.6058
NaOH	2.77E-07	0.009436	1	-6.5581
$CaHCO_3^+$	2.47E-07	0.0213	0.709	-6.7566
CH_3COO^-	1.16E-07	0.005838	0.6709	-7.1091
PO_4^{---}	1.15E-07	0.009286	0.0052	-9.2258
$MgH_2PO_4^+$	8.87E-08	0.009179	0.6396	-7.246
$FeHPO_4$	8.01E-08	0.01037	1	-7.0963
$MgOH^+$	7.09E-08	0.002499	0.6396	-7.3433
$CaCO_3$	6.01E-08	0.005126	1	-7.2214
$KHPO_4^-$	3.31E-08	0.003808	0.6396	-7.6748
$FePO_4^-$	3.22E-08	0.004138	0.6396	-7.6866
$CaHPO_4$	1.38E-08	0.001596	1	-7.8615

(only species > 1e-8 molal listed)

Mineral saturation states

	log Q/K		log Q/K
Nontronit-Na	0.0000 sat	K-feldspar	-1.2896
Dolomite-ord	0.0000 sat	Goethite	-1.3922
$FeCr_2O_4$	0.0000 sat	Amrph^silica	-1.463
Quartz	0.0000 sat	Gibbsite	-1.5765
Magnesite	0.0000 sat	Greenalite	-1.676
Vivianite	0.0000 sat	Dolomite-dis	-1.7029
Dawsonite	0.0000 sat	Saponite-H	-1.7517
Pyrite	0.0000 sat	Calcite	-1.7614
Siderite	0.0000 sat	Graphite	-1.841
Saponite-Na	0.0000 sat	Hematite	-1.8462
Dolomite	-0.0001	FeO(c)	-1.9103
Hydroxyapatite	-0.0646	Ferrosilite	-1.9258
Tridymite	-0.1862	Aragonite	-1.929
Smectite-Reykjan	-0.1865	Mordenite-K	-1.9413
Chalcedony	-0.2912	Mordenite-Na	-1.9784
Saponite-Mg	-0.5978	Annite	-2.0487
Cristobalite	-0.5991	Pyrrhotite	-2.1377
Nontronit-Mg	-0.6002	Cr_2O_3	-2.208
Talc	-0.806	Troilite	-2.2929
Phengite	-0.8209	Albite high	-2.3029
Albite	-0.8417	Jadeite	-2.4622
Albite low	-0.8417	Diaspore	-2.511
Nontronit-K	-0.8572	Magnetite	-2.5583
Saponite-K	-0.866	Cronstedt-7A	-2.6158
Minnesotaite	-1.0109	Sanidine high	-2.6294
Saponite-Ca	-1.0315	Smectite-low-Fe-	-2.7318
Nontronit-Ca	-1.0315	Phlogopite	-2.7506
Halite	-1.0514	Monohydrocalcite	-2.7671
Analcime	-1.0805	Kaolinite	-2.768
Whitlockite	-1.2338	Chrysotile	-2.8879
Maximum Microcli	-1.2867		

(only minerals with log Q/K > -3 listed)

Gases	fugacity	log fug.
$CH_4(g)$	3.843	0.585
Steam	0.007523	-2.124
$CO_2(g)$	0.001645	-2.784
$H_2(g)$	1.89E-06	-5.724
$H_2S(g)$	2.28E-09	-8.643
$S_2(g)$	2.29E-34	-33.641

$O_2(g)$	7.08E-80	-79.15

Original basis	Total moles mg/kg	In fluid moles mg/kg	Sorbed moles L/kg
Al^{+++}	0.213	2.47E-08	3.79E-05
Ca^{++}	0.648	0.000999	2.28
Cl^{-}	43.8	43.8	8.83E+04
Cr^{+++}	0.248	5.12E-15	1.52E-11
Fe^{++}	1.8	0.000315	1
H^{+}	-9.22	0.0542	3.11
H_2O	835	832	8.53E+05
HCO_3^{-}	5.85	0.419	1.45E+03
HPO_4^{--}	0.0651	0.00529	28.9
K^{+}	0.00741	0.00741	16.5
Mg^{++}	4.35	0.19	263
Mn^{++}	1.00E-09	1.00E-09	3.13E-06
Na^{+}	44	43.8	5.73E+04
$O_2(aq)$	-0.00455	-0.119	-217
SO_4^{--}	0.0026	9.00E-08	0.000492
$SiO_2(aq)$	6.55	0.000467	1.6

Elemental composition	total moles	moles mg/kg	In fluid moles mg/kg	Sorbed
Aluminum	0.2129	2.47E-08	3.79E-05	
Calcium	0.6484	0.000999	2.279	
Carbon	5.849	0.4186	286.1	
Chlorine	43.78	43.78	8.83E+04	
Chromium	0.2481	5.18E-15	1.53E-11	
Hydrogen	1666	1664	9.55E+04	
Iron	1.805	0.000315	1	
Magnesium	4.353	0.1903	263.2	
Manganese	1.00E-09	1.00E-09	3.13E-06	
Oxygen	865.5	833	7.58E+05	
Phosphorus	0.06507	0.005287	9.319	
Potassium	0.007409	0.007409	16.48	
Silicon	6.547	0.000467	0.7461	
Sodium	44	43.78	5.73E+04	
Sulfur	0.0026	9.00E-08	0.000164	

Step # 112 Xi = 1.0000
Time = 3.15576e+014 secs (3.6525e+009 days)

Temperature = 0.0°C Pressure = 1.013 bars
pH = 8.330 log fO_2 = -80.697
Eh = -0.3103 volts pe = -5.7255
Ionic strength = 2.887854
Activity of water = 0.903238
Solvent mass = 14.984396 kg
Solution mass = 17.572844 kg
Solution density = 1.103 g/cm^3
Chlorinity = 2.921545 molal
Dissolved solids = 147298 mg/kg sol'n
Rock mass = 1.055702 kg
Carbonate alkalinity= 1354.58 mg/kg as $CaCO_3$

Reactants	moles remaining	moles reacted	grams reacted	cm3 reacted
Albite	-5.43E-17	0.04181	10.96	4.191
Anorthite	2.31E-17	0.08502	23.65	8.569
CO_2(g)	3.18E-15	6.03	265.4	
Enstatite	2.57E-15	4.462	448	139.6
Fayalite	1.83E-19	0.000268	0.05461	0.01243
$FeCr_2O_4$	1.23E-16	0.1035	23.17	4.556
Ferrosilite	-2.72E-15	1.755	231.6	66.18
Forsterite	-3.96E-19	0.000469	0.06599	0.02054
H_2O	0	0	0	
Hydroxyapatite	-2.29E-18	0.00201	1.01	0.3208
$MgCr_2O_4$	-1.25E-17	0.02439	4.69	1.062
Pyrite	6.95E-19	0.00134	0.1608	0.03208
Sanidine high	2.11E-18	0.007638	2.126	0.8325
Wollastonite	-3.03E-16	0.2124	24.67	8.481

Minerals in system	moles	log moles	grams	volume (cm^3)
Dawsonite	0.05842	-1.233	8.412	3.464
Dolomite-ord	0.6567	-0.183	121.1	42.25
FeCr2O4	0.1279	-0.893	28.63	5.629
Magnesite	3.316	0.521	279.6	92.92
Nontronit-Na	0.3833	-0.416	163	65.17
Pyrite	0.00134	-2.873	0.1608	0.03208
Quartz	4.957	0.695	297.9	112.5
Saponite-Na	0.1048	-0.98	40.49	14.32
Siderite	0.8738	-0.059	101.2	25.02
Vivianite	0.03027	-1.519	15.18	5.666
(total)		1056.	366.9	

Aqueous species	molality	mg/kg sol'n	act. coef.	log act.
Cl^-	2.874	8.69E+04	0.5513	0.1998
Na^+	2.864	5.62E+04	0.6246	0.2526
NaCl	0.0396	1973	1	-1.4023
$NaHCO_3$	0.01745	1250	1	-1.7582
$MgCl^+$	0.00809	412.2	0.6246	-2.2965
HCO_3^-	0.006628	344.9	0.655	-2.3624
CH_4(aq)	0.006395	87.48	2.0191	-1.889
Mg^{++}	0.005151	106.8	0.2744	-2.8496
K^+	0.000502	16.74	0.5513	-3.5579
$NaCO_3^-$	0.000388	27.48	0.6246	-3.6153
CO3--	0.000184	9.398	0.1247	-4.6402
$NaHPO_4^-$	0.000174	17.62	0.6246	-3.9646
HPO_4^{--}	0.000126	10.28	0.1031	-4.888
$MgHCO_3^+$	9.41E-05	6.846	0.6246	-4.2309
CO_2(aq)	7.96E-05	2.987	1	-4.0991
$CaCl^+$	4.78E-05	3.081	0.6246	-4.5247
SiO_2(aq)	1.58E-05	0.808	2.0191	-4.497
$MgCO_3$	1.43E-05	1.026	1	-4.8454
Ca^{++}	1.07E-05	0.3646	0.1907	-5.6916
Fe^{++}	1.01E-05	0.4828	0.1907	-5.7138
$MgHPO_4$	1.01E-05	1.039	1	-4.9942
NaH_3SiO_4	9.83E-06	0.9899	1	-5.0074
KCl	7.67E-06	0.4877	1	-5.1151
$FeCl^+$	4.05E-06	0.3151	0.6246	-5.5972
$MgPO_4^-$	2.85E-06	0.2901	0.6246	-5.7493
$FeCl_2$	2.12E-06	0.2293	1	-5.6733
$H_2PO_4^-$	2.01E-06	0.1665	0.6246	-5.9006
$FeCO_3$	1.06E-06	0.1045	1	-5.9754
$H_3SiO_4^-$	5.92E-07	0.04801	0.6246	-6.4321
$FeHCO_3^+$	5.43E-07	0.05408	0.6246	-6.4699
OH^-	3.86E-07	0.0056	0.5902	-6.6422
NaOH	2.45E-07	0.008341	1	-6.6116
$CaHCO_3^+$	1.96E-07	0.01693	0.6922	-6.8667
CH_3COO^-	1.82E-07	0.009182	0.655	-6.9228
PO_4^{---}	1.42E-07	0.01147	0.0051	-9.1398
$FeHPO_4$	6.59E-08	0.008527	1	-7.1814
$MgOH^+$	6.31E-08	0.002223	0.6246	-7.4044
$MgH_2PO_4^+$	6.19E-08	0.006398	0.6246	-7.413
$CaCO_3$	5.40E-08	0.004607	1	-7.2678
$FePO_4^-$	3.18E-08	0.004092	0.6246	-7.7018
$KHPO_4^-$	3.02E-08	0.00348	0.6246	-7.7242
$CaHPO_4$	1.01E-08	0.001171	1	-7.996

(only species > 1e-8 molal listed)

Mineral saturation states

	log Q/K		log Q/K
Quartz	0.0000 sat	Goethite	-1.4152
Pyrite	0.0000 sat	Whitlockite	-1.4661
$FeCr_2O_4$	0.0000 sat	Amrph^silica	-1.5064
Siderite	0.0000 sat	Gibbsite	-1.6298
Dolomite-ord	0.0000 sat	Greenalite	-1.6419
Dawsonite	0.0000 sat	Dolomite-dis	-1.7404
Vivianite	0.0000 sat	Graphite	-1.7753
Magnesite	0.0000 sat	Calcite	-1.7927
Saponite-Na	0.0000 sat	Saponite-H	-1.7948
Nontronit-Na	0.0000 sat	Hematite	-1.9051
Dolomite	-0.0001	Mordenite-K	-1.9158
Tridymite	-0.1911	FeO(c)	-1.9483
Smectite-Reykjan	-0.2433	Ferrosilite	-1.9544
Chalcedony	-0.2959	Aragonite	-1.961
Hydroxyapatite	-0.3733	Annite	-1.986
Cristobalite	-0.6104	Mordenite-Na	-2.0414
Saponite-Mg	-0.6243	Pyrrhotite	-2.1684
Nontronit-Mg	-0.6273	Cr_2O_3	-2.2313
Phengite	-0.7566	Troilite	-2.3152
Talc	-0.8097	Albite high	-2.3968
Nontronit-K	-0.8333	Jadeite	-2.5214
Saponite-K	-0.8457	Diaspore	-2.6071
Albite	-0.902	Sanidine high	-2.6233
Albite low	-0.902	Cronstedt-7A	-2.6327
Minnesotaite	-0.9918	Magnetite	-2.6344
Halite	-1.0489	Phlogopite	-2.7329
Saponite-Ca	-1.0644	Monohydrocalcite	-2.7959
Nontronit-Ca	-1.0644	Smectite-low-Fe-	-2.8136
Analcime	-1.1442	Gaylussite	-2.8818
Maximum Microcli	-1.2467	Chrysotile	-2.9048
K-feldspar	-1.2506	Kaolinite	-2.9089

(only minerals with log Q/K > -3 listed)

Gases	fugacity	log fug.
$CH_4(g)$	5.86	0.768
Steam	0.005485	-2.261
$CO_2(g)$	0.001082	-2.966
$H_2(g)$	1.49E-06	-5.826
$H_2S(g)$	1.35E-09	-8.871
$S_2(g)$	3.77E-35	-34.423
$O_2(g)$	2.01E-81	-80.697

Original basis	Total moles mg/kg	In fluid moles mg/kg	Sorbed moles L/kg
Al^{+++}	0.219	1.27E-08	1.94E-05
Ca^{++}	0.658	0.000881	2.01
Cl^{-}	43.8	43.8	8.83E+04
Cr^{+++}	0.256	4.11E-15	1.22E-11
Fe^{++}	1.86	0.00027	0.858
H^{+}	-9.48	0.088	5.05
H_2O	835	832	8.53E+05
HCO_3^{-}	6.03	0.468	1.63E+03
HPO_4^{--}	0.0653	0.00471	25.7
K^{+}	0.00764	0.00764	17
Mg^{++}	4.49	0.2	277
Mn^{++}	1.00E-09	1.00E-09	3.13E-06
Na^{+}	44	43.8	5.73E+04
$O_2(aq)$	-0.00469	-0.192	-349
SO_4^{--}	0.00268	7.14E-08	0.00039
$SiO_2(aq)$	6.75	0.000392	1.34

Elemental composition	total moles	moles mg/kg	In fluid moles mg/kg	Sorbed
Aluminum	0.2195	1.27E-08	1.94E-05	
Calcium	0.6576	0.000881	2.008	
Carbon	6.03	0.4681	319.9	
Chlorine	43.78	43.78	8.83E+04	
Chromium	0.2558	4.20E-15	1.24E-11	
Hydrogen	1666	1664	9.55E+04	
Iron	1.861	0.00027	0.858	
Magnesium	4.488	0.2002	276.9	
Manganese	1.00E-09	1.00E-09	3.13E-06	
Oxygen	866.5	832.9	7.58E+05	
Phosphorus	0.06525	0.004714	8.309	
Potassium	0.007638	0.007638	16.99	
Silicon	6.749	0.000393	0.6273	
Sodium	44	43.78	5.73E+04	
Sulfur	0.00268	7.14E-08	0.00013	

REFERENCES

Agee, C. B., Wilson, N. V., McCubbin, F. M., Ziegler, K., Polyak, V. J., Sharp, Z. D., Asmerom, Y., Nunn, M. H., Shaheen, R., Thiemens, M. H., Steele, A., Fogel, M. L., Bowden, R., Glamoclija, M., Zhang, Z., Elardo S. M., 2013. Unique Meteorite from Early Amazonian Mars: Water-Rich Basaltic Breccia Northwest Africa 7034. *Science* **339**, 780-785.

Aoudjehane, H. C., Avice, G., Barrat, J.-A., Boudouma, O., Chen, G., Duke, M. J. M., Franchi, I. A., Gattacceca, J., Grady, M. M., Greenwood, R. C., Herd, C. D. K., Hewins, R., Jambon, A., Marty, B., Rochette, P., Smith, C. L., Sautter, V., Verchovsky, A., Weber, P., and Zanda, B., 2012. Tissint martian meteorite: a fresh look at the interior, surface, and atmosphere of mars. *Science* **338**, 785–788.

Amelin Y, Krot A. N., Hutcheon I. D., and Ulyanov A. A. 2002. Lead isotopc ages of chondrules and calcium-aluminum-rich inclusions. *Science* **297**, 1678-1683.

Anovitz L. M. and Essene E. J., 1987. Phase-equilibria in the system $CaCO_3$-$MgCO_3$-$FeCO_3$. *Journal of Petrology* **28**, 389-414.

Ash R. D., Kontt S. F., and Turner G., 1996. A 4-Gyr shock age for a Martian meteorite and implications for the cratering history of Mars. *Nature* **380**, 57–59.

Ashworth, J. R., and Hutchison, R., 1975. Water in non-carbonaceous stony meteorites. *Nature* **256**, 714–715.

Baker, V. R. and Milton, D. J., 1974. Erosion by catastrophic floods on Mars and Earth. *Icarus* **23**, 27-41.

Baker, L. L., Agenbroad, D. J., and Wood, S. A., 2000. Experimental hydrothermal alteration of a Martian analog basalt: Implications for Martian meteorites. *Meteoritics and Planetary Science* **35**, 31-38.

Bandfield, J. L., Glotch, T. D., and Christensen, P. R., 2003. Spectroscopic Identification of Carbonate Minerals in the Martian Dust. *Science* **301**, 1084-1087.

Barber, D., and Scott, E. R. D., 2003. Transmission electron microscopy of minerals in the Martian meteorite, Allan Hills 84001. *Meteoritics and Planetary Science* **38**, 831-848.

Beck, P., Barrat, J-A., Gillet, Ph., Franchi, I. A., Greenwood, R. C., Van de Moortele, B., Reynard, B., Bohn, M., and Cotten, J., 2005. The Diderot meteorite: The second chassignite. *Lunar and Planetary Institute Conference Abstracts*, 1326.

Bell III, J. F., Wolff, M. J., James, P. B., Clancy, R. T., Lee, S. W., and Martin, L. J., 1997. Mars surface mineralogy from Hubble Space Telescope imaging during 1994-1995:

Observations, calibration, and initial results. ***Journal of Geophysical Research*** 102, 9109-9123.

Bibring, J.-P., Langevin, Y., Gendrin, A., Gondet, B., Poulet, F., Berthe, M., Soufflot, A., Arvidson, R., Mangold, N., Mustard, J., Drossart, P., and the OMEGA team, 2005. Mars Surface Diversity as Revealed by the OMEGA/Mars Express Observations. *Science* **307**, 1576-1581.

Bibring, J.-P., Langevin, Y., Mustard, J. F., Poulet, F. O., Arvidson, R., Gendrin, A., Gondet, B., Mangold, N., Pinet, P., and Forget, F., 2006. Global Mineralogical and Aqueous Mars History Derived from OMEGA/Mars Express Data. *Science* **312**, 400-404.

Blaney, D. L., and McCord, T.B., 1989. An observational search for carbonates on Mars. *Journal of Geophysical Research* **94**, 159-10.

Blake, W. Jr., 2005. Holocene carbonate precipitates on Precambrian bedrock in the High Arctic: age and potential for paleoclimatic information. *Geografiska Annaler* **87**, 175–192.

Boctor, N. Z., Alexander, C. M. O'D., Wang, J. and Hauri, E., 2003. The sources of water in martian meteorites: Clues from hydrogen isotopes. *Geochimica et Cosmochimica. Acta* **67**, 3971-3989.

Bogard, D. D., and Johnson, P., 1983. Martian gases in an Antarctic meteorite? *Science* **221**, 651-654.

Borg, L. E., Connelly, J. N., Nyquist, L. E., Shih, C. Y., Wiesmann, H., and Reese, Y., 1999. The age of the carbonates in martian meteorite ALH84001. *Science* **286**, 90-94.

Bouvier, A., Blichert-Toft J., Vervoort, J. D., and Albarède, F., 2005. The age of the SNC meteorites and the antiquity of the Martian surface. *Earth and Planetary Science Letters* **240**, 221-233.

Boynton, W.V., Ming, D. W., Kounaves, S. P., Young, S. M. M., Arvidson, R. E., Hecht, M. H., Hoffman, J., Niles, P. B., Hamara, D. K., Quinn, R. C., Smith, P. H., Sutter, B., Catling, D. C., and Morris, R. V., 2009. Evidence for Calcium Carbonate at the Mars Phoenix Landing Site. *Science* **325**, 61-64.

Bradley J.P., McSween H.Y. Jr. and Harvey R.P., 1998. Epitaxial growth of nanophase magnetite in Martian meteorite ALH84001: Implications for biogenic mineralization. *Meteoritics and Planetary Science* **33**, 765-774.

Brearley A. J., 1998. Magnetite in ALH84001: Product of the decomposition of ferroan carbonate. *Lunar and Planetary Institute Conference Abstracts*, 1451.

Brain, D. A. and Jakosky, B. M., 1998. Atmospheric loss since the onset of the Martian geologic record: Combined role of impact erosion and sputtering. *Journal of Geophysical Research* **103**, 22689-22694.

Bridges, J. C., Catling, D. C., Saxton, J. M., Swindle, T. D., Lyon, I. C., and Grady, M. M., 2001. Alteration Assemblages in Martian Meteorites: Implications for Near-Surface Processes. *Space Science Reviews* **96**, 365-392.

Bridges, J. C. and Grady, M. M., 1999. A halite-siderite-anhydrite-chlorapatite assemblage in Nakhla: mineralogical evidence for evaporites on Mars. *Meteoritics and Planetary Science* **34**, 407-415.

Bridges, J. C. and Grady, M. M., 2000. Evaporite mineral assemblages in the nakhlite (martian) meteorites. *Earth and Planetary Science Letters* **176**, 267-279.

Bridges, J. C., Catling, D. C., Saxton, J. M., Swindle, T. D., Lyon, I. C., Grady, M. M., 2001. Alteration assemblages in martian meteorites: Implications for near-surface processes. *Space Science Reviews* **96**, 365-392.

Bridges, J. C., and Wright, I. P., 2006. Atmospheric Thickness on Ancient Mars: Constraints from SNC Meteorites. *Lunar and Planetary Institute Conference Abstracts*, 1990.

Bridges, J. C., and Warren, P. H., 2006. The SNC meteorites: basaltic igneous processes on Mars. *Journal of the Geological Society* **163**, 229–251.

Bruni, J., Canepa, M., Chiodini, G., Cioni, R., Cipolli, F., Longinelli, A., Marini, L., Ottonello, G., Zuccolini, M. V., 2002. Irreversible water–rock mass transfer accompanying the generation of the neutral, Mg-HCO_3 and high-pH, Ca-OH spring waters of the Genova province, Italy. *Applied Geochemistry* **17**, 455–474.

Bullock, M. A., and Moore, J. M., 2007. Atmospheric conditions on early Mars and the missing layered carbonates. *Geophysical Research Letters* **34**, L19201, doi:10.1029/2007GL030688.

Calvin, W. M., King, T. V. V., Clark, R. N., 1994. Hydrous carbonates on Mars?: Evidence from Mariner 6/7 infrared spectrometer and ground-based telescopic spectra. *Journal of Geophysical Research* **99**, 659-675.

Carr R. H., Grady M. M., Wright I. P., and Pillinger C. T., 1985. Martian atmospheric carbon-dioxide and weathering products in SNC meteorites. *Nature* **314**, 248-250.

Carr, M.H., 1989. Recharge of the early atmosphere of Mars by impact-induced release of CO_2. *Icarus* **79**, 311-327.

Carr, M. H., 1995. The Martain drainage system and the origin of valley networks and fretted channels. *Journal of Geophysical Research* **100**, 7479-7507.

Carr, M. H., 1999. Retention of an atmosphere on early Mars. *Journal of Geophysical Research* **104**, 21897-21910.

Carr, M. H., 2006. *The Surface of Mars*. Cambridge Planetary Science Series, Cambridge University Press.

Catling, D. C., 1999. A chemical model for evaporites on early Mars: Possible sedimentary tracers of the early climate and implications for exploration, *Journal of Geophysical Research*, **104** 453-470.

Catling, D. C., 2007. Mars: Ancient fingerprints in the clay. *Nature* **448**, 31-32.

Chacko. T,, Cole D. R., and Horita J., 2001. Equilibrium oxygen, hydrogen and carbon fractionation factors applicable to geologic systems. *Reviews in Mineralogy and Geochemistry* **43**, 1–81.

Chafetz, H. S., and Lawrence, J. R., 1994. Stable isotopic variability within modern travertines. *Geographie Physique et Quaternaire* **48**, 257-273.

Changela, H .G., and Bridges, J. C., 2011. Alteration assemblages in the nakhlites: Variation with depth on Mars. *Meteoritics and Planetary Science* **45**, 1847-1867.

Chevrier, V., Poulet, F., and Bibring, J.-P., 2007. Early geochemical environment of Mars as determined from thermodynamics of phyllosilicates. *Nature* **448**, 60-63.

Christensen, P. R., Anderson, D. L., Chase, S. C., Clancy, R. T., Clark, R. N., Conrath, B. J., Kieffer, H. H., Kuzmin, R. O., Malin, M. C., Pearl, J. C., Roush, T. L., and Smith, M. D., 1998. Results from the Mars Global Surveyor Thermal Emission Spectrometer. *Science* **279**, 1692-1698.

Clark B. C., and Van Hart D. C., 1981. The salts of Mars. *Icarus* **45**, 370–378.

Clark I. D., and Lauriol B., 1992. Kinetic enrichment of stable isotopes in cryogenic calcites. *Chemical Geology* **102**, 217-228.

Clayton, R.N., Onuma, N., Ikeda, Y., Mayeda, T.K., Hutcheon, I. D., Olsen, E. J., and Molini-Velsko, C., 1983. Oxygen isotopic compositions of chondrules in Allende and ordinary chondrites, in Chondrules and Their Origins, edited by King, E. A., pp 37-43, Lunar and Planetary Institute, Houston.

Clayton R. N. and Mayeda T. K., 1988. Isotopic composition of carbonate in EETA-79001 and its relation to parent body volatiles. *Geochimica et Cosmochimica Acta* **52**, 925-927.

Clayton R. N. 1993. Oxygen isotope analysis of ALH84001. In *Antarctic Meteorite Newsletter* **16**, 4.

Clayton R. N. and Mayeda T. K., 1996. Oxygen isotope studies of achondrites. *Geochimica et Cosmochimica. Acta* **60**, 1999-2017.

Clifford, S. M. 1991. The role of thermal vapor diffusion in the subsurface hydrologic evolution of Mars. *Geophysical Research Letters* **18**, 2055–2058.

Cohen, B. A., Swindle, T. D., and Kring, D. A., 2000. Support for the Lunar Cataclysm 570 Hypothesis from Lunar Meteorite Impact Melt Ages. *Science* **290**, 1754-1755.

Cook, G. A., Lauer, C. M., 1968. Oxygen. In: Clifford, A.Hampel (Ed.), The Encyclopedia of the Chemical Elements. Reinhold Book Corporation, New York, pp. 499–512. LCCN 68-29938.

Corrigan C. M. and Harvey R. P., 2002. Unique carbonates in martian meteorite Allan Hills 84001. *Lunar and Planetary Institute Conference Abstracts*, 1051.

Corrigan C. M. and Harvey R. P., 2003. Evidence for a second generation of magnesite in martian meteorite Allan Hills 84001. *Lunar and Planetary Institute Conference Abstracts,* 1255.

Corrigan, C. M. and Harvey, R. P., 2004. Multi-generational carbonate assemblages in martian meteorite Allan Hills 84001: Implications for nucleation, growth, and alteration. *Meteoritics and Planetary Science* **39**, 17-30.

Davidson, J., Busemann, H., Alexander, C. M. O'D., Nittler, L. R., Schrader, D. L., Orthous-Daunay, F. R., Quirico, E., Franchi, I. A., and Grady, M. M. 2009. Presolar SiC abundances in primitive meteorites by NanoSIMS raster ion imaging of insoluble organic matter. *Lunar and Planetary Institute Conference Abstracts,* 1853.

De, S., Bunch, T., Treiman, A.H., Amundsen, H.E.F., Blake, D.F., Carbonate globules from Spitsbergen, Norway: terrestrial analogs of the carbonates in martian meteorite ALH84001? 2001. *Geological Society of America.* Abstract. **33**. A311.

Dreibus, G., Burghele A., Jochum K.P., Spettel B., Wlotzka F. and Wänke H. 1994. Chemical and mineral composition of ALH84001: A Martian orthopyroxenite. *Meteoritics* **29**, 461.

Ehlmann, B.L., Mustard, J.F., Murchie, S.L., Poulet, F., Bishop, J.L., Brown, A.J., Calvin, W.M., Clark, R.N., Des Marais, D.J., Milliken, R.E., Roach, L.H., Roush, T.L., Swayze, G.A., Wray, J.J., 2008. Orbital identification of carbonate-bearing rocks on Mars. *Science* **322**, 1828–1832.

Ehlmann, B. L., Mustard, J. F., Swayze, G. A., Clark, R. N., Bishop, J. L., Poulet, F., Marais, D. J. D., Roach, L. H., Milliken, R. E., Wray, J. J., Barnouin-Jha, O. and Murchie, S. L., 2009. Identification of hydrated silicate minerals on Mars using MRO-CRISM: geologic context near Nili Fossae and implications for aqueous alteration. *Journal of Geophysical Research* **114**.

Ehlmann, B. L., Mustard, J. F., Murchie, S. L., Bibring J. P., Meunier, A., Fraeman, A A, and Langevin, Y. 2011. Subsurface water and clay mineral formation during the early history of Mars. *Nature* **479**, 53–60.

Eiler, J. M., Graham, C. M., and Valley, J. W., 1997. SIMS Analysis of Oxygen Isotopes: Matrix Effects in Complex Minerals and Glasses. *Chemical Geology* **138**, 221-244

Eiler, J. M., Valley J. W., Graham C. M., and Fournelle J., 2002. Two populations of carbonate in ALH84001: Geochemical evidence for discrimination and genesis. *Geochimica et Cosmochimica. Acta* **66**, 1285-1303.

Eugster, O., 1994. Orthopyroxene ALH 84001: Ejection from Mars (?) 15 Ma. *Meteoritics* **29**, 464.

Eugster, O., Busemann, H., Lorenzetti, S., and Terribilini, D., 2002. Ejection ages from krypton-81-krypton-83 dating and pre-atmospheric sizes of martian meteorites. *Meteoritics and Planetary Science* **37**, 1345-1360.

Fairén, A. G., Fernández-Remolar, D., Dohm, J. M., Baker, V. R., and Amils, R., 2004. Inhibition of carbonate synthesis in acidic oceans on early Mars. *Nature* **431**, 423-426.

Farquhar, J., Thiemens, M. H., and Jackson, T. 1998. Atmosphere-surface interactions on Mars: Delta O-17 measurements of carbonate from ALH 84001. *Science* **280** 1580-1582.

Fassett, C. I., and Head, J. W., 2008. The timing of Martian valley network activity: constraints from buffered crater counting. *Icarus* **195**, 61–89.

Fayek, M., 2009. Hydrogen, carbon, nitrogen and sulfur isotope microanalysis by Secondary Ion Mass Spectrometry. In: Fayek, M. (Ed.), *MAC Short Course: Secondary Ion Mass Spectrometry in the Earth Sciences* 65–83.

Formisano, V., Atreya, S., Encrenaz, T., Ignatiev, N., and Giuranna, M., 2004. Detection of Methane in the Atmosphere of Mars. *Science* **306**, 1758-1761.

Franchi I. A., Wright I. P., Sexton A. S., and Grady M. M., 1999. The oxygen isotopic composition of the Earth and Mars. *Meteoritics & Planetary Science* **34**, 657-661.

Gendrin, A. N., Mangold, N., Bibring, J.-P., Langevin, Y., Gondet, B., Poulet, F., Bonello, G. Quantin, C., Mustard, J. Arvidson, R., LeMoue'lic, S., 2005. Sulfates in Martian layered terrains: The OMEGA/Mars Express view. *Science* **307**, 1587–1591.

Ghosh, P., Adkins, J., Affek, H., Balta, B., Guo, W., Schauble, E. A., Schrag, D., Eiler J. M., 2006. ^{13}C-^{18}O bonds in carbonate minerals: A new kind of paleothermometer. *Geochimica et Cosmochimica Acta* **70**, 1439-1456.

Gibson, E. K., McKay, D. S., Thomas-Keprta, K. L., Clemett, S. J., Wentworth, S. J., 2007. Conditions on Early Mars Might Have Fostered Rapid and Early Development of Life. . *Seventh International Conference on Mars*, **1353.**

Gleason J. D., Kring D. A., Hill D. H., and Boynton W. V., 1997. Petrography and bulk chemistry of Martian orthopyroxenite ALH84001: Implications for the origin of secondary carbonates. *Geochimica et Cosmochimica Acta* **61**, 3503-3512.

Golden, D. C., Ming, D. W., Schwandt, C. S., Morris, R. V., Yang, S. V., and Lofgren, G. E., 2000. An experimental study on kinetically-driven precipitation of calcium-magnesium-iron carbonates from solution: Implications for the low-temperature

formation of carbonates in martian meteorite Allan Hills 84001. *Meteoritics and Planetary Science* **35**, 457-466.

Golden, D. C., Ming, D. W., Schwandt, C. S., Lauer, H. V., Socki, R. A., Morris, R. V., Lofgren, G. E., and McKay, G. A., 2001. A simple inorganic process for formation of carbonates, magnetite and sulfides in Martian meteorite ALH84001. *American Mineralogist* **86**, 2370–375.

Gooding, J. L., 1978. Chemical weathering on Mars - Thermodynamic stabilities of primary minerals /and their alteration products/ from mafic igneous rocks. *Icarus* **33**, 483-513.

Gooding, J. L., Wentworth, S. J., and Zolensky, M. E., 1988. Calcium carbonate and sulfate of possible extraterrestrial origin in the EETA 79001 meteorite. *Geochimica et Cosmochimica Acta* **52**, 909-915.

Gooding J.L., Wentworth S.J., and Zolensky M.E., 1991. Aqueous alteration of the Nakhla meteorite. *Meteoritics* **26**, 135-143.

Goodrich, C. A., 2002. Olivine-phyric martian basalts: A new type of shergottite. *Meteoritics and Planetary Science.* **37**, B31-B34.

Goreva, J. S., Guan, Y., and Leshin, L. A., 2002. Isotopic Composition of Carbon in Martian Magmatic Minerals: Insights into Martian Carbon Reservoirs. *Lunar and Planetary Institute Conference Abstracts*, 2014.

Goreva, J. S., Leshin, L. A., and Guan, Y., 2003. Ion Microprobe Measurements of Carbon Isotopes in Martian Phosphates: Insights into the Martian Mantle. *Lunar and Planetary Institute Conference Abstracts*, 1987.

Grady, M. M., Wright, I. P., Swart, P. K., and Pillinger, C. T., 1988. The carbon and oxygen isotopic composition of meteoritic carbonates. *Geochimica et Cosmochimica Acta* **52**, 2855-2866.

Grady, M. M., Wright, I. P., Douglas, C., and Pillinger, C. T., 1994. Carbon and nitrogen in ALH84001. *Meteoritics* **29**, 469-469.

Grady, M. M., Verchovsky, A. B., Wright, I. P., 2004. Magmatic carbon in martian meteorites: Attempts to constrain the carbon cycle on Mars. *International Journal of Astrobiology* **3**, 117-124.

Grady, M. M., 2006. WatSen: searching for clues for water (and life) on Mars. *International Journal of Astrobiology*, **5**, 211–219.

Grady, M. M., Anand, M., Gilmour, M. A., Watson, J. S., and Wright, I. P., 2007. Alteration of the Nakhlite Lava Pile: Was Water on the Surface, Seeping Down, or at Depth, Percolating Up? Evidence (Such as It Is) from Carbonates. *Lunar and Planetary Institute Conference Abstracts*, 1826.

Greenwood, J. P., Blake, R. E. and Coath, C. D., 2003. Ion microprobe measurements of

18O/16O ratios of phosphate minerals in the Martian meteorites ALH84001 and Los Angeles, *Geochimica Cosmochimica Acta,* **67**, 2289– 2298.

Grégoire, M., Chevet. J., and Maaloe, S., Composite xenoliths from Spitsbergen: evidence of the circulation of MORB-related melts within the upper mantle. *Geological Society, London, Special Publications*, **337**, 71-86.

Grott, M., Spohn, T., Banerdt, W. B., Smreker, S. E., Hudson, T. L., Zoest, T. V., Korgl, G., Morgan, P., and Wieczorck, M. A., 2011. Measuring Heat Flow on Mars: The Heat Flow and Physical Properties Package on GEMS. *EPSC Abstracts* **6**, EPSC-DPS2011.

Guan, Y., Paque, J. M., Burnett, D.S., and Eiler, J. M., 2009. Preliminary NanoSIMS Analysis of Carbon Isotope of Carbonates in Calcium-Aluminum-rich Inclusions. *Meteoritics and Planetary Science Supplement*, 5364.

Hallis, L. J., Taylor, G. J., Nagashima, K., Huss G. R., Needham, A. W., Grady, M. M., and Franchi, I. A., 2012. Hydrogen isotope analyses of alteration phases in the nakhlite martian meteorites. *Geochimica et Cosmochimica Acta* **97**, 105–119.

Hamilton, V. E., Christensen, P. R., McSween, H. Y., Bandfield, J. L., 2003. Searching for the source regions of Martian meteorites using MGS TES; integrating Martian meteorites into the global distribution of igneous materials on Mars, *Meteoritics and Planetary Science*, **38**, 871-885.

Hamilton, V. E., and P. R. Christensen 2005. Evidence for extensive, olivine-rich bedrock on Mars. *Geology* **33**, 433– 436.

Hartmann, W. K. and Neukum, G., 2001. Cratering Chronology and the Evolution of Mars. *Space Science Reviews* **96**, 165-194.

Hanchen, M., Prigiobbe, V., Baciocchi, R., Mazzotti, M., 2008. Precipitation in the Mg-carbonate system—effects of temperature and CO_2 pressure. *Chemical Engineering Science* **63**, 1012–1028.

Harvey R. P., and McSween H. Y. Jr., 1994. Ancestor's Bones and Palimpsests: Olivine in ALH84001 and orthopyroxene in Chassigny. *Meteoritics* **29**, 472.

Harvey R. P., and McSween H. Y., 1996. A possible high-temperature origin for the carbonates in the Martian meteorite ALH84001. *Nature* **382**, 49-51.

Hofmann, A., and Harris, C., 2008. Silica alteration zones in the Barberton greenstone belt: A window into subseafloor processes 3.5–3.3 Ga ago. *Chemical Geology* **257**, 221-239.

Holland, T. J. B., and Powell, R., 1998. An internally-consistent thermodynamic dataset for phases of petrological interest. *Journal of Metamorphic Geology* **16**, 309-344.

Holland, G., Saxton, J. M., Lyon, I. C., Turner, G., 2005. Negative $\delta^{18}O$ values in Allan Hills 84001 carbonate: Possible evidence for water precipitation on Mars. *Geochimica et*

Cosmochimica Acta **69**, 1359-1370.

Howard K. T., Benedix G. K., Bland P. A., Cressey, G., 2010. Modal mineralogy of CV3 chondrites by X-ray diffraction (PSD-XRD) *Geochimica et Cosmochimica Acta*, **74**, 5084-5097.

Hunten, D. M., Pepin, R. O., and Walker J. C. G., 1987. Mass fractionation in hydrodynamic escape. *Icarus* **69**, 532–549.

Ihinger, P. D., Chamberlin, S., and Smith, S. C., 2002. Inorganic Terrestrial analog for Carbonate-Magnetite-Pyrite Assemblage in ALH-84001, *Lunar and Planetary Institute Conference Abstracts*, 2057.

Ionov, D., 1998. Trace Element Composition of Mantle-derived Carbonates and Coexisting Phasesin Peridotite Xenoliths from Alkali Basalts. *Journal of Petrology* **39**, 1931-1941.

Irving, A. J., 1980. Petrology and Geochemistry of Composite Ultramafic Xenoliths in Alkalic Basalts and Implications for Magmatic Processes within the Mantle. *American Journal of Science* **280**, *389-426.*

Irving A. J., Kuehner S. M., Rumble D. III, Carlson R. W., Hupé A. C. and Hupé G. M. 2002. Petrology and isotopic composition of orthopyroxene-bearing Nakhlite NWA 998. *Meteoritics and Planetary Science*. A70.

Irving, A. J., Bunch, T. E., Kuehner, S. M., and Wittke, J. H., 2004, Petrology of Primitive Olivine-Orthopyroxene-Phyric Shergottites NWA 2046 and NWA 1195: Analogies with Terrestrial Boninites and Implications for Partial Melting of Hydrous Martian Mantle. *Lunar and Planetary Institute Conference Abstracts*, 1444.

Jakosky, B. and Jones, J. 1997. The history of Martian volatiles. *Reviews of Geophysics* **35**, 8755-1209.

Jarosewich, E, and MacIntyre, I. G. 1983. Carbonate reference samples for electron microprobe and scanning electron microscope analyses. *Journal of Sedimentary Research* **53**, 677-678.

Jones, J. H., Niles, P.B., Webster, C. R., Mahaffy, P. R., Flesch, G. J., Christensen, L. E., Leshin, L.A., Franz, H., Wong, M., Atreya, S. K., Conrad, P. G., Manning, H., Navarro-Gonzalez, R., Owen, T., Pepin, B., Stern, J. C., Trainer, M., and Schwenzer, S. P., 2013. Preliminary Interpretations of Atmospheric Stable Isotopes and Argon from Mars Science Laboratory (SAM). *Lunar and Planetary Institute Conference Abstracts*, 2781.

Jull, A. J. T., Donahue, D. J., Eastoe, C. J., Swindle, T. D., Burkland, M. K., and Herzog, G. F., 1994. Isotopic evidence for extraterrestrial carbonates in the SNC meteorites Allan Hills 84001 and Nakhla. *Meteoritics* **29**, 479.

Jull, A. J. T., Eastoe, C. J., Xue, S., and Herzog, G. F., 1995. Isotopic composition of carbonates in the SNC meteorites Allan Hills 84001 and Nakhla. *Meteoritics* **30**, 311.

Jull, A. J. T., Eastoe, C. J., and Cloudt, S., 1997. Isotopic composition of carbonates in the SNC meteorites, Allan Hills 84001 and Zagami. *Journal of Geophysical Research* **102**, 1663-1670.

Jull, A. J. T., Courtney, C., Jeffrey, D. A., and Beck, J. W., 1998. Isotopic Evidence for a Terrestrial Source of Organic Compounds Found in Martian Meteorites Allan Hills 84001 and Elephant Moraine 79001. *Science* **279**, 366-369.

Kahn, R., 1985. The evolution of CO_2 on Mars. *Icarus* **62**, 175-190.

Karner, J., Papike, J. J., and Shearer, C. K., 2006. Comparative planetary mineralogy: Pyroxene major- and minor- element chemistry and partitioning of vanadium between pyroxene and melt in planetary basalts. *American Mineralogist* **91**, 1574-1582.

Kazmierczak, J., and Kempe, S., 2003. Modern terrestrial analogues for the carbonate globules in Martian meteorite ALH84001. *Naturwissenschaften* **90**, 167-172.

Kent, A. J. R., Hutcheon, I. D., Ryerson, F. J., and Phinney, D. L., 2001 The temperature of formation of carbonate in Martian meteorite ALH84001: Constraints from cation diffusion. *Geochimica et Cosmochimica Acta*, **65**, 311–321.

Kieffer, H. H., and Zent. A. P., 1992. Quasi-periodic climate change on Mars. In Mars. Kieffer, H. H., Jakosky, B. M., Snyder, C. W., and Matthews, M. S., Eds., 1180–1218. Univ. of Arizona Press, Tucson.

Kita, N. T., Ushikubo, T., Fu, B., Valley, J. W., 2009. High precision SIMS oxygen isotope analysis and the effect of sample topography. *Chemical Geology* **264**, 43–57.

Klingelhöfer, G., Morris, R.V., Bernhardt, B., Schröder, C., Rodionov, D.S., de Souza, P.A., Yen, A., Gellert, R., Evlanov, E.N., Zubkov, B., Foh, J., Bonnes, U., Kankeleit, E., Gütlich, P., Ming, D.W., Renz, F., Wdowiak, T., Squyres, S.W., and Arvidson, R.E., 2004. Jarosite and hematite at Meridiani Planum from Opportunity's Mössbauer spectrometer. *Science* **306**, 1740-1745.

Knauth L. P., Brilli M., and Klonowski S., 2003. Isotope geochemistry of caliche developed on basalt. *Geochimica et Cosmochimica Acta* **67**, 185-195.

Konigsberger, E., Konigsberger L.-C., and Gamsjager, H., 1999. Low-temperature thermodynamic model for the system Na_2CO_3–$MgCO_3$–$CaCO_3$–H_2O. *Geochimica et Cosmochimica Acta* **63**, 3105–3119.

Kopp, R.E. III and Humayun, M., 2003. Kinetic model of carbonate dissolution in Martian meteorite ALH84001, *Geochimica et Cosmochimica Acta*, **67**, 3247-3256

Kring D. A., Swindle T. D., Gleason J. D., and Grier J. A., 1998. Formation and relative ages of maskelynite and carbonate in ALH84001. *Geochimica et Cosmochimica Acta* **62**,

2155–2166.

Knott, S. F., Ash, R. D., and Turner, G., 1995. 40Ar-39Ar Dating of ALH 84001: Evidence for the Early Bombardment of Mars. *Lunar and Planetary Institute Conference Abstracts*, 765-766.

Kuehner S. M., Irving A. J., Bunch T. E., Wittke J. H., Hupé G. M., and Hupé A. C., 2006. Coronas and symplectites in plutonic angrite NWA 2999 and implications for Mercury as the angrite parent body. *Lunar and Planetary Institute Conference Abstracts*, 1344.

Kuehner S. M., and Irving, A. J., 2007. Grain boundary glasses in the plutonic angrite NWA 4590: Evidence for rapid decompressive partial melting and cooling on Mercury? *Lunar and Planetary Institute Conference Abstracts*, 1522.

Lacelle, D., 2007. Environmental setting, (micro) morphologies and stable C O isotope composition of cold climate carbonate precipitates---a review and evaluation of their potential as paleoclimatic proxies. *Quaternary Science Reviews* **26**, 1670-1689.

Langevin, Y., Poulet, F., Bibring, J.-P., and Gondet, B., 2005. Sulfates in the north polar region of Mars detected by OMEGA/Mars Express. *Science* **307**, 1584-1586.

Lapen, T. J., Righter, M., Brandon, A. D., Debaille, V., Beard, B. L., Shafer, J. T., and Peslier, A. H., 2010. A younger age for ALH84001 and its geochemical link to shergottite sources in Mars. *Science* **328**, 347-351.

Lellouch, E., Encrenaz, T., Graauw, T., Erard, S., Morris, P., Crovisier, J., Feuchtgruber, H., Girard, T., and Burgdorf, M., 2000. The 2.4–45μm spectrum of Mars observed with the infrared space observatory. *Planetary and Space Science* **48**, 1393-1405.

Leshin L. A., Epstein S., and Stolper E. M., 1996. Hydrogen isotope geochemistry of SNC meteorites. *Geochimica et Cosmochimica Acta* **60**, 2635-2650.

Leshin L. A., McKeegan K, Carpenter P, Harvey R. P., 1998. Oxygen isotopic constraints on the genesis of carbonates from Martian meteorite ALH84001. *Geochimica et Cosmochimica Acta.* **62**, 3–13.

Londry, K. L. and Des Marais, D. J., 2003. Stable carbon isotopic fractionation by sulfate-reducing bacteria. *Applied and Environmental Microbiology* **69**, 2942-2949.

Longhi, J., 2006. Phase equilibrium in the system CO_2-H_2O: Application to Mars. *Journal of Geophysical Research (Planets)* **111**, 06011.

Lozano-Perez S., Schröder M., Yamada T., Terachi, T., English, C. A., and Grovenor, C. R. M., 2008. Using NanoSIMS to map trace elements in stainless steels from nuclear reactors. *Applied Surface Science* **255**, 1541–1543.

Luque, F. J., Pasteris, J. D., Wopenka, B., Rodas, M., and Barrenechea, J. F., 1998. Natural fluid deposited graphite: Mineralogical characteristics and mechanisms of formation.

American Journal of Science **298**, 471–498.

Luque, F. J., Ortega, L., Barrenechea, J. F., Millward, D., Beyssac, O., and Huizenga, J.-M., 2009. Deposition of highly crystalline graphite from moderate-temperature fluids. *Geology* **37**, 275–278.

Manning, C. V., McKay, C. P., and Zahnle, K. J., 2006. Thick and thin models of the evolution of carbon dioxide on Mars. *Icarus* **180**, 38-59.

Mason, B., 1963. The Hypersthene Achondrites. *American Museum Novitates* **2155**, 13.

Mason, B., MacPherson, G. J., Score, R., Martinez, R., Satterwhite, C., Schwarz, C., and Gooding, J. L., 1992. Descriptions of stony meteorites; *In* U.B. Marvin and G.J. MacPherson, eds., Field and Laboratory Investigations of Antarctic Meteorites Collected by United States Expeditions, 1985-1987. *Smithsonian Contributions to the Earth Sciences* **30**, 17-35. Smithsonian Institution Press.

McKay, D. S., Gibson, E. K., Thomas-Keprta, K. L., Vali, H., Romanek, C. S., Clemett, S. J., Chiller, X. D. F., Maechling, C. R., and Zare, R. N., 1996. Search for past life on Mars: Possible relic biogenic activity in martian meteorite ALH84001. *Science* **273**, 924-930.

McSween, H. Y. and Harvey, R. P.,1998. Brine Evaporation: an Alternative Model for the Formation of Carbonates in Allan Hills 84001. *Meteoritics & Planetary Science,* **33**, A103.

McSween, H. Y., and Treiman, A. H., 1998. Martian Meteorites in *Planetary Materials* edited by Papike, J. J., Washington D. C. Minerological Society of America.

McSween, H. Y. and Huss, G. R., 2010. Cosmochemistry: probing the origin and chemical evolution of the solar system. Cambridge University Press. ISBN 978-0-521-87862-3.

Melosh, H. J., and Vickery A. M., 1989. Impact erosion of the primordial atmosphere of Mars. *Nature* **338**, 487–489.

Messenger, S., Stadermann, F. J., Floss, C., Nittler, L. R., and Mukhopadhyay. S., 2003. Isotopic signatures of presolar materials in interplanetary dust, *Space Science Review* **106**, 155-172.

Meyer, C., 2012. Mars Meteorite Compendium, NASA JSC.

Mikouchi, T., Miyamoto, M., Koizumi, E., Makishima, J., and McKay, G., 2006. Relative burial depths of nakhlites: An update. *Lunar and Planetary Institute Conference Abstracts*, 1865.

Mikouchi T., Makishima J., Kurihara T., Hoffmann V. H., and Miyamoto M. 2012. Relative burial depth of nakhlites revisited. *Lunar and Planetary Institute Conference Abstracts*, 2363.

Misawa K., Shih C.-Y., Wiesmann H, Garrison D. H., Nyquist L. E. and Bogard D. D. 2005. *Antarctic Meteorite Research (NIPR)* **18**, 133-151.

Mittlefehldt D. W., 1994. ALH84001, a cumulate orthopyroxenite member of the SNC meteorite group. *Meteoritics* **29**, 214-221.

Mittlefehldt, D. W., 1996. ALH 84001, A Cumulate Orthopyroxenite Member of the Martian Meteorite. *Meteoritics*, **29**, 214-221.

Mojzsis S. J., Coath C. D., Bunch T. E., Blake D., Treiman A. H., and Amundsen H. E. F., 1999 Carbonate "rosettes" in xenoliths from Spitzbergen; SIMS analysis of O and C isotope ratios in a potential terrestrial analogue to Martian meteorite ALH84001. *Lunar and Planetary Institute Conference Abstracts,* 2032.

Moore, J. M., and Howard, A. D., 2005, Large alluvial fans on Mars. *Journal of Geophysical Research,* **110**, E04005.

Moreau, J. W., Weber, P. K., Martin, M. C., Gilbert, B., Hutcheon, I. D., Banfield, J. F., 2007. Extracellular proteins limit the dispersal of biogenic nanoparticles. *Science* **316**, 1600-1603.

Morota, T., Haruyama, J., Ohtake, M., Matsunaga, T., Honda, C., Yokota, Y., Kimura, J., Ogawa, Y., Hirata, N., Demura, H., Iwasaki, A., Sugihara, T., Saiki, K., Nakamura, R., Kobayashi, S., Ishihara, Y., Takeda, H., and Hiesinger, H. 2011. Timing and characteristics of the latest mare eruption on the Moon. *Earth and Planetary Science Letters* **302**, 255–266.

Moroz, V. I., Huntress, W. T., Shevalev, I. L. 2002, Planetary Missions of the 20th Century* *Cosmic Research* **40**, 419–445.

Morris, R. V., Klingelhöfer, G., Schröder, C., Rodionov, D. S., Yen, A., Ming, D. W., de Souza, P. A., Wdowiak, T., Fleischer, I., Gellert, R., Bernhardt, B., Bonnes, U., Cohen, B. A., Evlanov, E. N., Foh, J., Gütlich, P., Kankeleit, E., McCoy, T., Mittlefehldt, D. W., Renz, F., Schmidt, M. E., Zubkov, B., Squyres, S. W., and Arvidson, R. E., 2006. Mössbauer mineralogy of rock, soil, and dust at Meridiani Planum, Mars: Opportunity's journey across sulfate-rich outcrop, basaltic sand and dust, and hematite lag deposits. *Journal of Geophysical Research (Planets)* **111**, E12S15.

Morris, R. V., Ruff, S. W., Gellert, R., Ming, D. W., Arvidson, R. E., and Clark, B. C., 2010. Identification of carbonate-rich outcrops on Mars by the Spirit rover. *Science* **329**, 421-424.

Mozley P. S., and Burns S. J., 1993. Oxygen and carbon isotopic composition of marine carbonate concretions - an overview. *Journal of Sedimentary Petrology* **63**, 73-83.

Mukhin, L. M., Koscheevi, A. P., Dikov, Y. P., Huth, J., and Wänke, H., 1996. Experimental simulations of the photodecomposition of carbonates and sulphates on Mars. *Nature* **379**, 141-143.

Mungas, G. S., Peters, G. H., Smith, J. A., Bearman, G. H., Beegle, L. W., Struthers, C., and Glucoft, J., 2007. H_2O Sublimation Alteration of Icy Martian Samples Due to Mechanical Work, Heat and Mass Transport. *Lunar and Planetary Institute Conference Abstracts*, 1338.

Musat, N., Halm H., Winterholler, B., Hoppe, P., Peduzzi, S., Hillion, F., Horreard, F., Amann, R., Jørgensen, B. B., and Kuypers, M. M. M., 2008 A single-cell view on the ecophysiology of anaerobic phototrophic bacteria. *Proceedings of the National Academy of Sciences of the United States of America* **105**, 17861-17866.

Mumma, M. J., Villanueva, G. L., Novak, R. E., Hewagama, T., Bonev, B. P., DiSanti, M. A., Mandell, A. M., Smith, M. D., 2004. Detection of Methane in the Atmosphere of Mars. *Science* **306**, 1758-1761.

Nadeau, S. L., Epstein, S., and Stolper, E., 1999. Hydrogen and carbon abundances and isotopic ratios in apatite from alkaline intrusive complexes, with a focus on carbonatites. *Geochimica et Cosmochimica Acta* **63**, 1837-1851.

Neumann, G. A., Mazarico, E. M., 2009. Planetary Science Seeing the Missing Half. *Science* **323**, 885-887.

Niles, P. B., Leshin, L. A., and Guan, Y., 2005. Microscale carbon isotope variability in ALH84001 carbonates and a discussion of possible formation environments. *Geochimica et Cosmochimica Acta* **69**, 2931-2944.

Niles, P. B., Zolotov, M. Y., Leshin, L. A., 2009. Insights into the formation of Fe- and Mg-rich aqueous solutions on early Mars provided by the ALH 84001 carbonates. *Earth and Planetary Science Letters* **286**, 122-130.

Niles, P. B., Boynton, W. V., Hoffman, J. H., Ming, D. W., Hamara, D., 2010. Stable Isotope Measurements of Martian Atmospheric CO_2 at the Phoenix Landing Site. *Science* **329**, 1334-1337.

Nittler, L. R. 2003. Presolar stardust in meteorites: recent advances and scientific frontiers, *Earth and Planetary Science Letters* **209**, 259-273.

Nyquist, L. E., Bogard, D. D., Shih, C. Y., Greshake, A., Stöeffler, D., and Eugster, O., 2001. Ages and Geologic Histories of Martian Meteorites. *Space Science Reviews* **96**, 105-164.

Owen, T., Biemann, K., Rushneck, D. R., Biller, J. E., Howarth, D. W., and LaFleur, A.L., 1977. The composition of the atmosphere at the surface of Mars. *Journal of Geophysical Research* **82**, 4635-4639.

Parnell, J., Boyce, A. J., Blamey, N. J. F., 2010. Follow the methane: the search for a deep biosphere, and the case for sampling serpentinites, on Mars. *International Journal of Astrobiology* **9**, 193-200.

Plaut, J. J., Picardi, G., Safaeinili, A., Ivanov, A. B., Milkovich, S. M., Cicchetti, A., Kofman, W., Mouginot, J., Farrell, W. M., Phillips, R. J., Clifford, S. M., Frigen, A., Orosei, R., Federico, C., Williams, I. P., Gurnett, D. A., Nielson, E., Hagfors, T., Heggy, E., Stofan, E. R., Plettemeier, D., Watters, T. R., Leuschen, C. J., and Edenhofer, P., 2007. Subsurface Radar Sounding of the South Polar Layered Deposits of Mars. *Science* **316**, 92-95.

Pollack, J. B., Kasting, J. F., Richardson, S. M., and Poliakoff, K., 1987. The case for a wet, warm climate on early Mars. *Icarus* **71**, 203-224.

Pollack, J. B., Roush, T., Witteborn, F., Bregman, J., Wooden, D., Stoker, C., and Toon, O. B., 1990. Thermal emission spectra of Mars (5.4-10.5 microns) - Evidence for sulfates, carbonates, and hydrates. *Journal of Geophysical Research* **95**, 14595-14627.

Poulet, F., Bibring, J.-P., Mustard, J. F., Gendrin, A., Mangold, N., Langevin, Y., Arvidson, R. E., Gondet, B., and Gomez C. 2005. Phyllosilicates on Mars and implications for early Martian climate. *Nature* **438**, 623–628.

Rao, M. N., McKay, D. S., Wentworth, S. J., Garrison, D. H. 2006. Martian Brines: Clues from Sulfur and Chlorine in Salts from Some Martian Meteorites and MER Samples Lunar and Planetary Institute Conference Abstracts, 1969.

Reid, A.M., Bunch, T.E., 1975. The nakhlites—II: where, when, and how. *Meteoritics* **10**, 317–324.

Rennó, N. O., Bos, B. J., Catling, D., Clark, B. C., Drube, L., Fisher, D., Goetz, W., Hviid, S. F., Keller, H. U., Kok, J. F., Kounaves, S. P., Leer, K., Lemmon, M., Madsen, M. B., Markiewicz, W. J., Marshall, J., McKay, C., Mehta, M., Smith, M., Zorzano, M. P., Smith, P.H., Stoker, C., Young, S.M.M. 2009. Possible physical and thermodynamical evidence for liquid water at the Phoenix landing site. *Journal of Geophysical Research* **114**, 1-11.

Riciputi L.R. and Greenwood J.P., 1998. Analysis of sulfur and carbon isotope ratios in mixed matrices by secondary ion mass spectrometry: Implications for mass bias corrections. *International Journal of Mass Spectrometry* **178**, 65-71.

Rollion-Bard, C. and Marin-Carbonne, J., 2011. Determination of SIMS matrix effects on oxygen isotopic compositions in carbonates. *Journal of Analytical Atomic Spectrometry* **26**, 1285-1289.

Romanek, C. S., Grady, M. M., Wright, I. P., Mittlefehldt, D. W., Socki, R. A., Pillinger, C. T., and Gibson, E. K., Jr., 1994. Record of Fluid / Rock Interactions on Mars from the Meteorite ALH:84001. *Nature* **372**, 655.

Romanek, C. S., Perry, E. C., Gibson, E. K. Jr., and Socki, R. A. 1996. Stable isotope analysis of diatomic oxygen from SNC meteorites. *Lunar and Planetary Institute Conference Abstracts,* 1097-1098.

Rosenberg, P.E., 1963. Subsolidus relations in the system $CaCO_3$-$FeCO_3$. *American Journal*

of Science. **261**, 683-689.

Rosenberg, P.E., 1967. Subsolidus relations in the system $CaCO_3$-$MgCO_3$-$FeCO_3$. *The American Mineralogist*. **52**, 787-796.

Roush. T., Pollack. J., and Orenberg, J., 1991. Derivation of Midinfrared (5-25 μm) Optical Constants of Some Silicates and Palagonite. *Icarus* **94**, 191-208.

Sano, Y., Shirai, K., Takahata, N., Hirata, T., Sturchio N.C., 2005. Nano-SIMS analysis of Mg, Sr, Ba and U in natural calcium carbonate. *Analytical sciences: the international journal of the Japan Society for Analytical Chemistry* **21**, 1091-1097.

Santos, R. V. and Clayton, R. N., 1995. Variations of oxygen and carbon isotopes in carbonatites: A study of Brazilian alkaline complexes. *Geochimica et Cosmochimica Acta*. **59**, 1339-1352.

Saxton J.M., Lyon I.C., and Turner G., 1998. Correlated chemical and isotopic zoning in carbonates in the martian meteorite ALH84001. *Earth and Planetary Science Letters* **160**, 811-822.

Saxton J. M., Lyon I. C., and Turner G., 2000. Ion probe studies of deuterium/hydrogen in the nakhlite meteorites. *Meteoritics & Planetary Science*, A142-A143.

Schumm, S. A., 1974. Structural origin of large Martian channels. *Icarus* **22**, 371-384.

Score R., and MacPherson G., 1985. Macroscopic and thin section description of ALH84001. In *Antarctic Meteorite Newsletter* **8**, 5.

Scott, D. H. and Carr, M. H. 1978. Geologic map of Mars. United States Geological Survey Miscellaneous Investigation Series Map 1-1083. 1:25000000 scale.

Scott E. R. D., Yamaguchi A., and Krot A. N., 1997. Petrological evidence for shock melting of carbonates in the Martian meteorite ALH84001. *Nature* **387**, 377-379.

Scott E. R. D., Krot A. N., and Yamaguchi A., 1998. Carbonates in fractures of Martian meteorite Allan Hills 84001: Petrologic evidence for impact origin. *Meteoritics & Planetary Science* **33**, 709-719.

Scott E. R. D., 1999. Origin of carbonate-magnetite-sulfide assemblages in Martian meteorite ALH84001. Journal of Geophysical Research **104**, 3803–3813.

Sefton-Nash, E. and Catling, D. C., 2008. Hematitic concretions at Meridiani Planum, Mars: Their growth timescale and possible relationship with iron sulfates. *Earth and Planetary Science Letters* **269**, 366-376.

Shearer C. K., and Papike J. J., 1996. Evaluating the evidence for past life on Mars. *Science* **274**, 2119-2125.

Shearer C. K., and Leshin L. A., 1998. The origin of olivine in Martian Meteorite ALH84001.

The oxygen isotopic systematics of the olivine. *Lunar and Planetary Institute Conference Abstracts,* 1268.

Shih C.-Y., Nyquist L.E. and Wisemann H. 1999. Samarium-neodymium and rubidium-strontium systematics of the nakhlite Governador Valadares. *Meteoritics & Planetary Science* **34**, 647-656.

Sinton, W. M., 1959. Further Evidence of Vegetation on Mars. *Science* **130,** 1234-1237.

Slodzian, G., Daigne, B., Girard, F., Boust, F.,and Hillion, F., 1992. Scanning secondary ion analytical microscopy with parallel detection. *Biology of the Cell* **74**, 43-50.

Smith R. (ed.) 2000. Encyclopedia of the Solar System, Fitzroy Dearborn, 785.

Smith, P. H., Tamppari, L. K., Arvidson, R. E., Bass, D., Blaney, D., Boynton, W. V., Carswell, A., Catling, D. C., Clark, B. C., Duck, T., DeJong, E., Fisher, D., Goetz, W., Gunnlaugsson, H. P., Hecht, M. H., Hipkin, V., Hoffman, J., Hviid, S. F., Keller, H. U., Kounaves, S. P., Lange, C. F., Lemmon, M. T., Madsen, M. B., Markiewicz, W. J., Marshall, J., McKay, C. P., Mellon, M. T., Ming, D. W., Morris, R. V., Pike, W. T., Renno, N., Staufer, U., Stoker, C., Taylor, P., Whiteway, J. A., Zent, A. P. 2009. H_2O at the Phoenix landing site. *Science* **325**, 58–61.

Socki R. A., Romanek C. S., and Gibson E. K. Jr., 2000. Formation of C-13 Enriched Carbonates on the Planet Mars: Clues from Laboratory-produced Cryogenic Calcite. *Lunar and Planetary Institute Conference Abstracts,* 1885.

Socki, R. A., Gibson, E. K., Jr., Golden, D. C., Ming, D. W., and McKay, G. A., 2003. Kinetic Fractionation of Stable Isotopes in Carbonates on Mars: Terrestrial Analogs. *Lunar and Planetary Institute Conference Abstracts*, 1983.

Socki, R. A., Niles, P. B., Blake, W., Leveille, R., 2009. Covariant C and O Isotope Trends in Arctic Carbonate Crusts and ALH84001: Potential Biomarker or Indicator of Cryogenic Formation Environment? *Lunar and Planetary Institute Conference Abstracts,* 2218.

Spicuzza, M. J., Day, J. M. D., Taylor, L.A., Valley, J.W., 2007. Oxygen isotope constraints on the origin and differentiation of the Moon. *Earth and Planetary Science Letters* **253**, 254-265.

Squyres, S. W., Arvidson, R. E., Bell, J. F., Calef, F., Clark, B. C., Cohen, B. A., Crumpler, L. A., De Souza, P. A., Farrand, W. H., Gellert, R., Grant, J., Herkenhoff, K. E., Hurowitz, J. A., Johnson, J. R., Jolliff, B. L., Knoll, A. H., Li, R., McLennan, S. M., Ming, D. W., Mittlefehldt, D. W., Parker, T. J., Paulsen, G., Rice, M. S., Ruff, S. W., Schroder, C., Yen, A. S., Zacny, K., Ancient Impact and Aqueous Processes at Endeavour Crater, Mars. *Science* **336**, 570-576.

Stadermann, F., Walker, R., Zinner, E., 1999. Sub-micron isotopic measurements with the CAMECA NanoSIMS. *Lunar and Planetary Institute Conference Abstracts,* 1407.

Starke, V, DS Mckay, SJ Wentworth, and KL. 2002. Carbonate Globules in Columbia River Basalt-The Search for Life in Terrestrial Subsurface Environments as Possible Martian Analogs. *Lunar and Planetary Institute Conference Abstracts,* 1475.

Steele, A., Fries, M., Amundsen, H.E.F., Mysen, B., Fogel, M., Schweizer, M., Boctor, N., 2006. A comprehensive imaging and Raman spectroscopy study of ALH84001 and a terrestrial analogue from Svalbard. *Lunar and Planetary Institute Conference Abstracts*, 2096.

Steele, A., McCubbin, F. M., Fries, M., Kater, L., Boctor, N. Z., Fogel, M. L., Conrad, P. G., Glamoclija, M., Spencer, M., Morrow, A. L., Hammond, M. R., Zare, R. N., Vicenzi, E. P., Siljeström, S., Bowden, R., Herd, C. D. K., Mysen, B. O., Shirey, S. B., Amundsen, H. E. F., Treiman, A. H., Bullock, E. S., Jull, A. J. T., 2012. A Reduced Organic Carbon Component in Martian Basalts. *Science* **337**, 212-215.

Stöeffler, D., Knoell, H. D., Marvin, U. B., Simonds, C. H., and Warren, P. H., 1980. Recommended classification and nomenclature of lunar highland rocks- A committee report. *Conference of Lunar Highlands Crust* (eds Papike, J. J. and Merrill, R. B.) 51–70.

Sutter, B., Dalton, J. B., Ewing, S. A., Amundson, R., and McKay, C. P., 2007. Terrestrial analogs for interpretation of infrared spectra from the Martian surface and subsurface: Sulfate, nitrate, carbonate, and phyllosilicate-bearing Atacama Desert soils. *Journal of Geophysical Research,* **112**.

Swindle T.D., Treiman A.H., Lindstrom D.J., Burkland M.K., Cohen B.A., Grier J.A., Li B., and Olson E.K. 2000. Noble gases in iddingsite from the Lafayette meteorite: Evidence for liquid water on Mars in the last few hundred million years. *Meteoritics & Planetary Science* **35**, 107-116.

Swindle T.D., and Olson E.K. 2004. ^{40}Ar-^{39}Ar studies of whole rock nakhlites: Evidence for the timing of formation and aqueous alteration on Mars. *Meteoritics & Planetary Science* **39**, 755-766.

Terada K., and Sano Y. (2004) Ion microprobe U-Th-Pb dating and REE analyses of phosphates in the nakhlites Lafayette and Yamato-000593/000749. *Meteoritics & Planetary Science* **39**, 2033-2041.

Thomas-Keprta K. L., Romanek C. S., Wentworth S. J., McKay D. S., Fisler D., Golden D. C., and Gibson E. K. 1997. TEM analysis of fine-grained minerals in the carbonate globules of martian meteorite ALH 84001. *Lunar and Planetary Institute Conference Abstracts*, 1433-1434.

Thomas-Keprta K.L., Clemett S.J., McKay D.S., Gibson E.K., Wentworth S.J. 2009. Origins of magnetite crystals in Martian meteorite ALH84001. *Geochimica et Cosmochimica Acta*, **73**, 6631-6677.

Treiman, A. H., 1993. The parent magma of the Nakhla (SNC) meteorite: Reconciliation of composition estimates from magmatic inclusions and element partitioning. *Lunar and*

Planetary Institute Conference Abstracts, 1441-1442.

Treiman, A. H., 1995. A petrographic history of martian meteorite ALH84001: Two shocks and an ancient age. *Meteoritics* **30**, 294.

Treiman, A. H., 1998. The history of ALH 84001 revised: Multiple shock events. *Meteoritics and Planetary Science* **33**, 753-764.

Treiman A.H., Amundsen. H.E.F., Blake D.F., and Bunch T., 2002. Hydrothermal origin for carbonate globules in Martian meteorite ALH84001: A terrestrial analogue from Spitsbergen (Norway). *Earth and Planetary Science Letters* **204**, 323-332.

Treiman A.H., 2005. The nakhlite (Martian) meteorites: Augite-rich igneous rocks from Mars. *Chemie der Erde* **65**, 203-270.

Treiman A.H., and Essene E.J. 2010 Metamorphic origin of sub-micron magnetite crystals in ALH 84001: Re-evaluation of equilibria, compositions, and experiments. *Astrobiology Science Conference Abstract,* 1159.

Thomas-Keprta K. L., Romanek C. S., Wentworth S. J., McKay D. S., Fisler D., Golden D. C., and Gibson E. K. 1997. TEM analysis of fine-grained minerals in the carbonate globules of martian meteorite ALH 84001. *Lunar and Planetary Institute Conference Abstracts,* 1433-1434.

Thomas-Keprta, K.L., S.J. Clemett, D.S. McKay, E.K. Gibson, and S.J. Wentworth. 2009. Origins of magnetite nanocrystals in Martian meteorite ALH84001. *Geochimica et Cosmochimica Acta* **73**, 21.

Thomas-Keprta K.L., Clemett S.J., Wentworth S.J., McKay D.S., and Gibson E.K.Jr. 2010. New insights into the origin of magnetite crystals in ALH 84001 carbonate disks. *Lunar and Planetary Institute Conference Abstracts,* 1064.

Tobias, O., Biemann, K., Rushneck, D. R., and Biller, J. E., 1977. The composition of the atmosphere at the surface of Mars. *Journal of Geophysical* **82**, 4635-4639.

Usui, T., Alexander, C. M. O'D.; Wang, J., Simon, J. I., and Jones, J. H., 2012. Origin of water and mantle–crust interactions on Mars inferred from hydrogen isotopes and volatile element abundances of olivine-hosted melt inclusions of primitive Shergottites. *Earth and Planetary Science Letters* **357**, 119-129.

Valley, J. W., Eiler, J. M., Graham, C. M., Gibson, E. K., Jr., and Romanek, C. S., 1997. Ion microprobe analysis of oxygen and carbon isotope ratios in the ALH84001 meteorite. *Lunar and Planetary Institute Conference Abstracts*, 1445.

Valley J. W., Eiler J. M., Graham C. M., Gibson E. K., Romanek C. S., and Stolper E. M., 1997. Low-temperature carbonate concretions in the Martian meteorite ALH84001: Evidence from stable isotopes and mineralogy. *Science* **275**, 1633-1638.

Van Berk, W., Ilger, J.-M., Fu, Y., and Hansen, C., 2011. Decreasing CO_2 partial pressure triggered Mg–Fe–Ca carbonate formation in ancient Martian crust preserved in the ALH84001 Meteorite. *Geofluids* **11**, 6–17.

Van Zuilen, M.A., Lepland, A., Teranes, J., Finarelli, J., Wahlen, M., and Arrhenius, G., 2003. Graphite and carbonates in the 3.8 Ga old Isua Supracrustal Belt, southern West Greenland. *Precambrian Research* **126**, 331–348.

Vecht, A. and Ireland, T. G., 2000. The role of vaterite and aragonite in the formation of pseudo-biogenic carbonate structures: implications for Martian exobiology. *Geochimica et Cosmochimica Acta* **64**, 2719-2725.

Velbel, M. A., Long, D. T., and Gooding, J. L., 1991. Terrestrial weathering of Antarctic stone meteorites: Formation of Mg-carbonates on ordinary chondrites. *Geochimica et Cosmochimica Acta*, **55**, 67-76.

Velbel M. A., 2007. Surface textures and dissolution processes of heavy minerals in the sedimentary cycle: examples from pyroxenes and amphiboles. *In Heavy Minerals in Use* (eds. M. A. Mange and D. T. Wright). Elsevier, Doorwerth, The Netherlands, 113–150.

Velbel, M. A., 2011. Microdenticles on naturally weathered hornblende. *Applied Geochemistry* **26**, 1594–1596.

Vicenzi, E. P., Tobin, K., Heaney, P. J., Onstott, T. C., and Chun, J., 1997. Carbonate in Lafayette Meteorite: A Detailed Microanalytical Study. *Meteoritics & Planetary Science* **32**, A132.

Volk, K. E., Niles, P. B., and Socki, R. A., 2011. Covariant C and O Isotope Trends in some Terrestrial Carbonates and ALH 84001: Possible Linkage through Similar Formation Processes. *Lunar and Planetary Institute Conference Abstracts*, 1975.

Wadhwa, M. and Lugmair, G. W., 1996. The Formation Age of Carbonates in ALH84001. *Meteoritics & Planetary Science* **31**, 145.

Warren, P. H. 1998. Petrologic evidence for low-temperature, possibly flood evaporitic origin of carbonates in the ALH84001 meteorite. *Journal of Geophysical Research-Planets* **103**, 16759-16773.

Watson, L. L., Hutcheon, I. D., Epstein, S., and Stolper, E. M., 1993. High D/H ratios of water in magmatic amphiboles in Chassigny: Possible constraints on the isotopic composition of magmatic water on Mars. *Lunar and Planetary Science Conference*. 1493-1494.

Watson L. L., Hutcheon I. D., Epstein S., and Stolper E. M., 1994. Water on Mars: Clues from D/H and water contents of hydrous phases in SNC meteorites. *Science* **265**, 85-90.

Webster, C. R., Mahaffy, P. R., Leshin, L. A., Atreya, S. K., Flesch, G. J., Stern, J., Christensen, L. E., Vasavada, A. R., Owen, T., Niles, P. B., Jones, J. H., and Franz, H., 2013. Mars Atmospheric Escape Recorded by H, C and O Isotope Ratios in Carbon Dioxide and Water Measured by the Sam Tunable Laser Spectrometer on the Curiosity Rover. *Lunar and Planetary Science Conference.* 1365.

Wentworth, S. J. and Gooding, J. L., 1994. Carbonates and sulfates in the Chassigny meteorite: Further evidence for aqueous chemistry on the SNC parent planet. *Meteoritics* **29**, 860-863.

Wentworth S. J. and Gooding J. L., 1995. Carbonates in the Martian Meteorite, ALH 84001: Water-borne But Not Like the SNCs. *Lunar and Planetary Institute Conference Abstracts,* 1489.

Wentworth, S. J., Gibson, E.K., Velbel, M. A., and McKay, D. S., 2005. Antarctic Dry Valleys and indigenous weathering in Mars meteorites: implications for water and life on Mars. *Icarus* **174**, 382-395.

Wolters S. D., Hagene J.K., Sund A.T., Bohman A., Guthery W., Sund B.T., Hagermann A., Tomkinson T., J. Romstedt., Morgan G.H., Grady M.M., 2013. WatSen: design and testing of a prototype mid-IR spectrometer and microscope package for Mars exploration. Experimental Astronomy (online) DOI 10.1007/s10686-012-9328-8.

Wright, I. P., Grady, M. M., and Pillinger, C. T., 1989. Organic Materials in a Martian Meteorite. *Nature* **340**, 220-222.

Wright, I. P., Grady, M. M., and Pillinger, C. T., 1990. The Evolution of Atmospheric CO_2 on Mars: The Perspective From Carbon Isotope Measurements. *Journal of Geophysical Research* **95**, 14,789–14,794.

Wright I.P., Grady M.M., and Pillinger, C.T., 1992. Chassigny and the nakhlites: Carbon-bearing components and their relationship to martian environmental conditions. *Geochimica et Cosmochimica Acta* **56**, 817–826.

Wright, I.P., Grady, M.M., and Pillinger, C.T., 1997. Isotopically light carbon in ALH 84001: Martian metabolism or Teflon contamination? *Lunar and Planetary Institute Conference Abstracts, 1414.*

Yung, Y. L., 1989. Is the Martian Atmosphere Denitrified by Ice Clouds? *Bulletin of the American Astronomical Society.*

Zipfel, J., Schröder, C., Jolliff, B.L., Gellert, R., Rieder, R., Anderson, R., Bell III, J.F., Brückner, J., Crisp, J.A., Christensen, P.R., Clark, B.C., Souza Jr. P.A., Dreibus, G., d'Uston, C., Economou, T., Gorevan, S.P., Hahn, B.C., Herkenhoff, K.E., Klingelhöfer, G., McCoy, T.J., McSween Jr. H.Y., Ming, D.W., Morris, R.V., Rodionov, D.S., Squyres, S.W., Wänke, H., Wright, S.P., Wyatt, M.B., and Yen, A.S., 2011. Bounce Rock: A Shergottite-Like Basalt Encountered at Meridiani Planum, Mars. *Meteoritics and Planetary Science*, **46**, 1-20.